Nanoscale Calibration Standards and Methods

Edited by
G. Wilkening, L. Koenders

Nanoscale Calibration Standards and Methods: Dimensional and Related Measurements in the Micro- and Nanometer Range.
Edited by Gunter Wilkening, Ludger Koenders
ISBN: 3-527-40502-X

Nanoscale Calibration Standards and Methods

Dimensional and Related Measurements in the Micro- and Nanometer Range

Edited by
Günter Wilkening, Ludger Koenders

WILEY-VCH Verlag GmbH & Co. KGaA

Editors

Prof. Dr. Günter Wilkening
National Metrology Institute (PTB),
Nano- und Micrometrology Department
Guenter.Wilkening@ptb.de

Dr. Ludger Koenders
National Metrology Institute (PTB),
Nano- und Micrometrology Department
Ludger.Koenders@ptb.de

Cover Picture
Illustration: Hans-Ulrich Danzebrink

Library of Congress Card No.: Applied for
British Library Cataloguing-in-Publication Data:
A catalogue record for this book is available from the British Library.

Bibliographic information published by Die Deutsche Bibliothek
Die Deutsche Bibliothek lists this publication in the Deutsche Nationalbibliografie; detailed bibliographic data is available in the Internet at <http://dnb.ddb.de>.

Composition hagedorn kommunikation, Viernheim
Printing Strauss GmbH, Mörlenbach
Bookbinding J. Schäffer GmbHiG, Grünstadt

Printed in the Federal Republic of Germany.
Printed on acid-free paper.

ISBN-13: 978-3-527-40502-2
ISBN-10: 3-527-40502-X

Contents

List of Contributors

Chapter 1
H.-U. Danzebrink, F. Pohlenz, G. Dai, and C. Dal Savio
National Metrology Institute (PTB), Braunschweig, Germany
Hans-Ulrich.Danzebrink@ptb.de

Chapter 2
M. Bisi, E. Massa, A. Pasquini, G. B. Picotto, and M. Pisani
CNR – Institute of Metrology "G. Colonnetti", Torino, Italy
g.picotto@imgc.cnr.it

Chapter 3
A. Yacoot
National Physical Laboratory, Teddington, Middlesex, UK
Andrew.Yacoot@npl.co.uk

Chapter 4
E. Manske, R. Mastylo, T. Hausotte, N. Hofmann, and G. Jäger
Technical University Ilmenau, Institute of Process- and Sensor Engineering, Ilmenau, Germany
eberhard.manske@tu-ilmenau.de

Chapter 5
D. Hüser, R. Petersen, and H. Rothe
Measurement and Information Technology, University of the Federal Armed Forces, Hamburg, Germany
doro@unibw-hamburg.de

Chapter 6
G. Dai, F. Pohlenz, H.-U. Danzebrink, M. Xu, K. Hasche, and G. Wilkening
Physikalisch-Technische Bundesanstalt (PTB), Braunschweig, Germany
gaoliang.dai@ptb.de

Chapter 7
K. Dirscherl[1] and K. R. Koops[2]
[1] National Metrology Institute (PTB), Braunschweig, Germany
[2]Nederlands Meetinstituut, Van Swinden Laboratorium (NMi-VSL), Delft, The Netherlands
kai.dirscherl@ptb.de

Chapter 8
A. Sikora, D. V. Sokolov, and H. U. Danzebrink
National Metrology Institute (PTB), Braunschweig, Germany
Hans-ulrich.danzebrink@ptb.de

Chapter 9
G. Dai, F. Pohlenz, H.-U. Danzebrink, K. Hasche, and G. Wilkening
National Metrology Institute (PTB), Braunschweig, Germany
gaoliang.dai@ptb.de

Chapter 10
D. V. Sokolov, D. V. Kazantsev, J. W.G. Tyrrell, T. Hasek, and H.-U. Danzebrink
National Metrology Institute (PTB), Braunschweig, Germany
hans-ulrich.danzebrink@ptb.de

Chapter 11
A. Sikora, T. Gotszalk, and R. Szeloch
Faculty of Microsystems Electronics and Photonics, Wroclaw University of Technology, Poland
andrzej.sikora@pwr.wroc.pl

Chapter 12
L. Doering[1], E. Peiner[2], V. Nesterov[1], and U. Brand[1]
[1]National Metrology Institute (PTB), Braunschweig, Germany;
[2]Institute for Semiconductor Technology, Technical University of Braunschweig, Germany
Lutz.Doering@ptb.de

Chapter 13
T. Dziomba, L. Koenders, and G. Wilkening
National Metrology Institute (PTB), Braunschweig/Berlin, Germany
Thorsten.Dziomba@ptb.de,

Chapter 14
J. Garnaes, A. Kühle, L. Nielsen, and F. Borsetto
Danish Institute of Fundamental Metrology, Lyngby, Denmark
jg@dfm.dtu.dk

Chapter 15
L. Koenders[1] and F. Meli[2]
[1] National Metrology Institute (PTB), Braunschweig und Berlin, Germany
[2] Swiss Federal Office of Metrology and Accreditation (METAS), Bern, Switzerland
Thorsten.Dziomba@ptb.de

Chapter 16
A. Grant, L. McDonnell, and E. M. Gil Romero
Centre for Surface & Interface Analysis, Department of Applied Physics & Instrumentation, Cork Institute of Technology, Ireland
lmcdonnell@cit.ie

Chapter 17
J. Schöbel and E. Westkämper
Institute of Industrial Manufacturing and Management, University of Stuttgart, Germany
ins@ipa.fraunhofer.de

Chapter 18
L. Koenders, T. Dziomba, P. Thomsen-Schmidt, and G. Wilkening
National Metrology Institute (PTB), Berlin/Braunschweig, Germany
Ludger.koenders@ptb.de

Chapter 19
S. Gröger and M. Dietzsch
Institute of Production Measuring Technology and Quality Assurance, Chemnitz, Germany
sophie.groeger@mb.tu-chemnitz.de

Chapter 20
R. Krüger-Sehm, T. Dziomba, and G. Dai
National Metrology Institute (PTB), Braunschweig, Germany
Rolf.Krueger-Sehm@ptb.de

Chapter 21
M. Senoner[1], Th. Wirth[1], W. Unger[1], W. Österle[1], I. Kaiander[2], R. L. Sellin[2], and D. Bimberg[2]
[1]Federal Institute for Materials Research and Testing (BAM), Berlin, Germany
[2] Institut für Festkörperphysik, Technische Universität Berlin, Germany
mathias.senoner@bam.de

Chapter 22
T. Machleidt, R. Kästner, and K.-H. Franke
Computer Graphics Program, Technical University of Ilmenau, Germany
Torsten.machleidt@tu-ilmenau.de

Chapter 23
S. Czerkas, T. Dziomba, and H. Bosse
National Metrology Institute (PTB), Braunschweig, Germany
slawomir.czerkas@ptb.de

Chapter 24
Y.-L. Chen, C.-J. Chen, and G.-S. Peng
Center for Measurement Standards/ ITRI, Taiwan, Republic of China
Gwo-sheng.peng@cms.tw

Chapter 25
V. Nascov
National Institute for Laser, Plasma and Radiation Physics,
Bukarest, Romania
nv@ifin.nipne.ro

Chapter 26
G. Sparrer and A. Abou-Zeid
National Metrology Institute (PTB), Braunschweig, Germany
gerald.sparrer@ptb.de

Chapter 27
F. Meli
Swiss Federal Office of Metrology and Accreditation (METAS),
Bern, Switzerland
Felix.meli@metas.Admin.ch

Chapter 28
C. G. Frase*, S. Czerkas, H. Bosse
Physikalisch-Technische Bundesanstalt (PTB), Braunschweig, Germany.
Carl. g.frase@ptb.de

Chapter 29
C. G. Frase, W. Häßler-Grohne, E. Buhr, K. Hahm, and H. Bosse
National Metrology Institute (PTB), Braunschweig, Germany
Carl. G.Frase@ptb.de

Chapter 30
J. Flügge
National Metrology Institute (PTB), Braunschweig, Germany
Jens.Fluegge@ptb.de

Chapter 31
P. Bariani, G. Bissacco, H. N. Hansen, and L. De Chiffre
Department of Manufacturing, Engineering and Management, Technical University, Lyngby, Denmark
pbl@ipl.dtu.dk

Chapter 32
C. Zerrouki[1], L.R Pendrill[2]
J. M. Bennett[3], Y. Haidar[4], F. de Fornel[4], and P. Pinot[1]
[1]BNM-INM/Cnam, 292, Paris, France
[2]Swedish National Testing and Research Institute, Boras, Sweden
[3]Naval Air Warfare Center, China Lake, USA
[4]Equipe Optique de Champ Proche LPUB, Dijon, France
Zerrouki@cnam.fr

Chapter 33
U. Jacobsson[1] and P. Sjövall[2]
[1]Measurement Technology,
[2]Chemistry and Materials Technology, SP Swedish National Testing and Research Institute, Boras, Sweden
ulf.jacobsson@sp.se

Chapter 34
Št. Lányi
Slovak Academy of Science, Institute of Physics, Bratislava, Slovakia
lanyi@savba.sk

Chapter 35
P. Klapetek[1], I. Ohlídal[2] and J. Bílek[1,2]
[1]Czech Metrology Institute, Brno, Czech Republic
[2]Department of Physical Electronics, Faculty of Science, Masaryk University, Brno, Czech Republic
pklapetek@cmi.cz

Chapter 36
D. Shuman
NanoMc Company, New York, USA
david.shuman@nanomc.com

Chapter 37
J. Keller, D. Vogel, and B. Michel
Fraunhofer Institute for Reliability and Microintegration (IZM), Dept. Mechanical Reliability and Micro Materials, Berlin, Germany
Michel@izm.fhg.de

Chapter 38
R. Schödel and A. Abou-Zeid
National Metrology Institute (PTB), Braunschweig, Germany
rene.schoedel@ptb.de

Part I
Instrumentation – Overview

Nanoscale Calibration Standards and Methods: Dimensional and Related Measurements in the Micro- and Nanometer Range.
Edited by Gunter Wilkening, Ludger Koenders
ISBN: 3-527-40502-X

1
Metrological Scanning Probe Microscopes – Instruments for Dimensional Nanometrology

Hans-Ulrich Danzebrink, Frank Pohlenz, Gaoliang Dai, and Claudio Dal Savio

Abstract

An overview of PTB's activities in the field of dimensional nanometrology using scanning probe microscopes (SPMs) is presented. The chapter is divided into two parts: the development of (1) high-resolution probing systems and (2) complete SPM metrology systems. The subject of SPM-probing system design comprises, among other things, the concept of the "sensor objective" to combine conventional microscopy with scanning probe techniques. In the field of complete metrological SPM systems, the measuring properties of one of the existing SPM metrology systems have been significantly improved by including laser interferometers directly into the position control loop and by a clear reduction of the nonlinearity of the interference signals. In addition, the application spectrum of metrological SPM has been considerably extended by the establishment of an SPM system with a measuring volume of 25 mm $\times$ 25 mm $\times$ 5 mm.

1.1
Introduction

In many fields of material sciences, biology, and medicine, conventional scanning probe microscopes (SPMs) serve to visualize small structures with dimensions down to atoms and molecules as well as to characterize object-specific properties (magnetism, friction, thermal conductivity, and the like). For a large part of the investigations, the image information obtained with the SPM is completely sufficient for the qualitative investigation of the sample. Because of their high spatial resolution, use of these microscopes is also of great interest for metrological applications. This is why the PTB has begun using SPMs in dimensional metrology as one of the first national metrology institutes [1, 2].

A fundamental requirement for precise length measurements is, however, the addition of a length measuring system to the microscope scanning system. For this purpose, the piezo actuators that serve for positioning and scanning of sam-

Nanoscale Calibration Standards and Methods: Dimensional and Related Measurements in the Micro- and Nanometer Range.
Edited by Gunter Wilkening, Ludger Koenders
ISBN: 3-527-40502-X

ple or measuring head, are in many cases position-controlled via additional sensors (strain gauges, capacitive or inductive sensors) by which disadvantages of piezo elements, such as hysteresis or creeping, are compensated [3–10]. The use of these additional sensor systems does not release the user from performing regular calibrations. In the majority of cases, the SPM is calibrated with the aid of special standards with microstructures of defined geometry. Detailed information on such calibration standards can be found in another article of this edition [11]. The disadvantage of discrete calibration via standards is, however, that linearization of the positioning measuring systems is based on a few reference points only which are given by the material measure. This leads to higher calibration effort when objects of different height or structure periods are to be measured.

This is why users with high demands on the uncertainty of SPM measurements have in the past few years proceeded to equip the individual axes of the positioning system with laser interferometers. This allows the positioning values to be continuously traced back to the wavelength of the laser light and thus to the SI unit "meter". The fundamental idea is to treat the SPM like a miniaturized three-coordinate measuring machine and to correct its metrological properties with the device's control software.

As in the case of coordinate measuring machines, the SPM measuring systems can be divided into probing system and positioning unit. The structure of the present chapter reflects this aspect. The first part describes the PTB activities in the development of high-resolution probing systems based on scanning probe microscope techniques. The second part deals with precise positioning units and with the complete SPM measuring and calibration devices that are available at PTB.

1.2 High-Resolution Probing Systems

PTB's development of probing systems based on SPMs is aimed at constructing and optimizing these measuring heads for use in dimensional nanometrology. Needless to say that the sensor systems described cannot only be used for metrological applications, but are of general interest for scanning probe microscopy and coordinate measuring techniques.

The scanning force microscopes (SFMs) are those of the family of SPMs that are of special importance for dimensional metrology. This is mainly due to the fact that their use is not limited to conductive surfaces as it is, for example, the case for scanning tunnel microscopes. The design principle of an SFM is shown in Figure 1.1. In this case, the deflection detection system of the cantilever moving relative to the surface is based on an optical beam deflection principle, thus keeping the cantilever with the integrated measuring tip in a constant distance to the surface. The sample is then investigated line by line, and the profiles are subsequently composed in a computer to form an image.

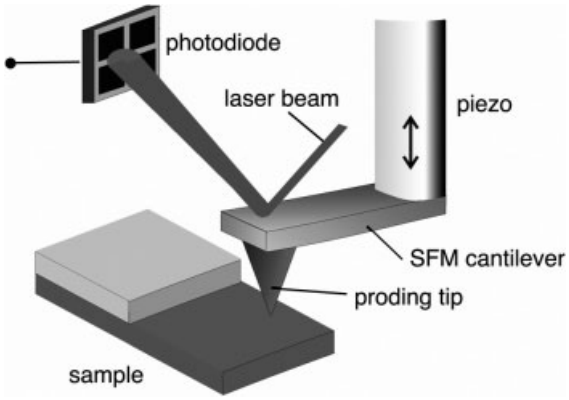

Fig. 1.1 Sketch of a scanning force microscope (SFM) with cantilever probe and beam deflection detection.

In addition to the properties important from the viewpoint of metrology such as stability, sensitivity, and noise behavior, different other aspects have been incorporated into PTB's device development:

- Combination of the SPM measuring heads with optical microscopes: here, the optical function extends from visualization to quantitative dimensional or analytical methods.
- The use of different detection principles: the movement and position of the measuring tip is measured by an external optical procedure or via an intrinsic electrical measuring principle.
- The use of different measuring tip materials: in recent developments, special diamond tips are used in addition to silicon and silicon nitride tips.

1.2.1 Sensor Objective with Beam Deflection Detection

As the name already suggests, the concept of the so-called sensor objective directly takes up the combination of microscope objective and sensor, the sensor in this case working as a scanning probe microscope. The special feature of this sensor head development is that existing optical standard microscopes are used as a basis: because of the compact geometry and the special design, the sensor objective (composed of SPM module and imaging optics) can be directly screwed into the turret of an optical microscope [12]. This allows two microscopy worlds to be ideally combined.

In measuring operation, the advantages of the combined system become obvious. Firstly, the well-proven conventional light microscopy is used for fast and extensive surface investigation. The spectrum of tasks extends from the orientation on the measurement object to quantitative optical measurements (see Section 1.2.4). Then local measurement is performed with the slower serial scanning probe procedure in the measurement area defined for calibration or, generally, at those points of the sample which require a high resolution.

Figure 1.2 shows a version of the sensor objective screwed into a standard microscope. During measurement the sample is scanned with a piezo scanning stage whose position is controlled with capacitive sensors. In this objective design, the optical part of the measuring head consists of a combination of mirror optics. These allow the cantilever with the integrated measuring tip to be viewed simultaneously with the sample surface. This clearly improves user-friendliness as far as the adjustment and the selection of the measurement area are concerned. When optionally operated as optical near-field microscope, the same optics can be used for coupling and/or for collecting optical radiation into or from the near-field probe [12]. This allows very local optical investigations and spectroscopic surface characterizations to be performed even on submicroscopic structures [13].

In topography mode (SFM mode), even single atomic terraces of a GaAs substrate wafer (step height: approx. 0.28 nm) have been resolved with this measuring setup despite the relatively large measuring circle (sample, microscope body, granite stand, positioning stages – cf. Figure 1.2) [13]. These measurements were performed in a dynamic SFM mode using conventional silicon cantilever probes. Traditional beam deflection technique was applied to detect the bending of the cantilever. All optoelectronic elements of the beam deflection system have been arranged outside the measuring head, since a spatial integration was not intended when this version of the measuring head was constructed. This arrangement can be optimized, in particular, with respect to its mechanical stability. The further objective of the PTB development went, however, beyond the integration of the beam deflection system into the measuring head. This is why measuring heads based on probes with monolithically integrated deflection detection have been developed (see Sections 1.2.2 and 1.2.3).

Fig. 1.2 Conventional standard microscope with screwed-in sensor objective – the version shown here allows the device to be operated as optical near-field microscope in addition to scanning force and optical microscopy. The enlarged image section in addition shows a diagrammatic representation of the beam path inside the objective.

1.2.2
Sensor Objective with Piezolever Module

One possibility of integrating the deflection detection system into the sensor probe (i. e., as near as possible to the measuring tip) consists in utilizing the piezoresistive effect of the cantilever material (here silicon) [14]. Comparable to the strain gauge principle, the movement of the cantilever can thus be directly converted into a measurable electrical signal. This means that an adjustment of a light beam on the cantilever is not necessary. This improves user-friendliness of the system and avoids possible errors as a result of inexact adjustment. Step-height measurements have, for example, shown that scattered light or reflections from the surface can lead to disturbing interference patterns or that the roughness of the rear side of the cantilever affects the measurement when optical methods are used for deflection detection. These error sources are avoided by monolithically integrated deflection sensors.

For realization of the piezoresistive cantilevers (briefly referred to as "piezolevers"), the piezoresistive elements were arranged in the form of a complete Wheatstone bridge and incorporated into the silicon cantilevers by ion implantation. This work was performed in cooperation with NanoWorld Services GmbH, Forschungszentrum Jülich and Surface Imaging Systems (SIS) GmbH [15]. As a special option, one of the Wheatstone resistors is realized as an electrically controllable resistor that allows the measuring bridge to be nulled.

During the design of our very compact SFM measuring head, which is based on these piezolevers, special attention was directed toward the requirement for detachable contacts of the cantilever chips [16]. In the piezolever SFMs so far realized, the cantilever chips were glued on small ceramic boards and the contacts were bonded. To avoid these complex additional process steps, the cantilever chips should be directly clamped and, at the same time, electrically contacted. To achieve this spring contacts were used that are made of gold-plated platinum beryllium (see Figure 1.3(b)). These "fingers" are arranged on a steel spring that is pressed-on or flapped-back with the aid of a very small cam to allow the probes to be exchanged. The complete holder must be exactly preadjusted and work free from mechanical play in order to contact the electrodes on the rear side of the chip reproducibly with the fingers, to exert enough force on the chip and to achieve good contacting. As can be seen in Figure 1.3(b), the contacts are only 50 μm apart from each other. The latter emphasizes the desired mechanical precision of the contacting mechanism.

The dimensions of the whole SFM module that comprises both a piezo element for the dynamic excitation of the cantilever and the electrical connections for the sensor signals were reduced to 4 mm × 3.5 mm × 35 mm only (see Figure 1.3(c)). This compact design allows the combination with different measuring heads and measuring microscope objectives. Topographic measurement results obtained with this piezolever module are described and shown in Section 1.2.4 (Figure 1.6) together with interference-optical measurements.

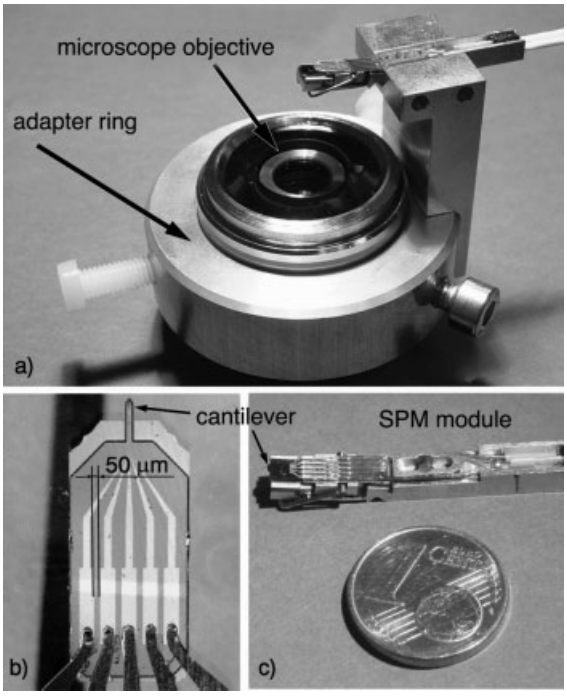

Fig. 1.3 Piezolever module combined with a standard microscope objective. Part (b) shows the finger contacts for fastening and electrical contacting.

A great advantage of the mirror optics used in the sensor objective version described above (Section 1.2.1) was the fact that the dimensions and the optical parameters could be calculated by optical computational programs and manufactured with diamond turning machines. This finally allowed the whole sensor objective to be designed and constructed at our own options and the space required for the SFM module and the positioning mechanics to be taken into account. As described, the compact piezolever module does not require so much space. This is why these aspects are no longer important and the combination with a commercial microscope objective as shown in Figure 1.3(a) furnishes a solution that is more universal. This combination – microscope objective and SPM module – has been realized for all measuring head versions so far developed (cf. also Figure 1.4(a)).

1.2.3
Sensor Objective with Tuning Fork Module

Another possibility of integrating the deflection detection system into the measuring probe consists in using a cantilever arm made of quartz [17]. In operation, this quartz is – just like the tuning fork in a quartz clock – excited to swing after an electrical voltage has been applied. The measurement of the distance between the probe and the surface and thus imaging the surface is performed by recording the

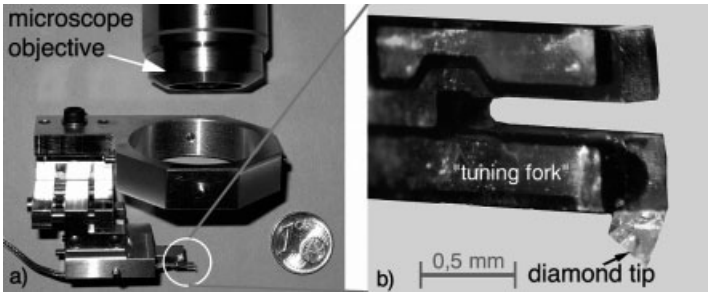

Fig. 1.4 "Tuning fork" module with positioning mechanics and adapter ring for the microscope objective as well as a micrograph of the tuning fork lever arm with the diamond tip (b).

current flowing through the quartz. This signal is proportional to the lever arm vibration and reacts very sensitive to changes of the damping when the distance between the tip and the surface varies.

Diamond tips designed at PTB are fastened on these tuning forks to allow high lateral resolution of the measurement (tip radii $<$ 100 nm) [18]. Figure 1.4(b) shows a quartz probe with tip. The selection of diamond as tip material is based on both the mechanical properties (stability and resistance to abrasion) and the optical properties that are important for the future use of the probes in optical near-field microscopy.

To test the efficiency of the tuning fork measuring head, topographic measurements were performed on structures with dimensions in the nanometer range. The samples used here are made of self-organized InAs quantum dots on a GaAs substrate. These quantum dots have pyramidal geometries (width approx. 20–30 nm, height approx. 4–6 nm). The mechanical stability of the whole microscope is sufficiently high to image such nanostructures. Investigations of the noise resulted in values of less than 0.6 nm (root mean square value) on a profile 2 μm in length.

Because of their extremely slim construction and their adjustment-free deflection detection, the tuning fork sensors can be tilted relative to the surface without any problem. This also allows measurements to be performed on object areas difficult to access such as structure edges or inclined areas. These properties allow these as well as the piezolever sensors to be used as sensitive probes in a coordinate measuring machine. Relevant developments have already been initiated at PTB.

1.2.4
Sensor Head for Combined Scanning Probe and Interference Microscopy

Up to now, imaging optics in SFMs only served as visualization tools to determine the area of interest for the measurement and to aid during probe alignment. In the sensor head realization described in this chapter, the functionality has been

considerably progressed. The combination of SFM and interference microscope allows an optical measuring technique to be integrated into the measuring head that can be traced back to the SI unit "meter" [19, 20].

This measuring system is based on the developments of the compact SFM measuring heads so far described and has been conceived so that it can be operated in different interference microscopes. For the PTB measuring setup, a commercial interference microscope (MicroMap, Nikon) was selected as the basic instrument. Because of the identical mechanical connecting plate, the newly developed sensor only replaces the exchangeable interference objective (see Figure 1.5). The basic instrument makes use of both the evaluation software and the displacement mechanics for phase-shifting interferometry or white light interferometry.

For the realization of the sensor head, two possibilities came into consideration: (1) modification of a commercial interference objective by adding an SFM module with the aid of an adapter (cf. Sections 1.2.2 and 1.2.3) or (2) new internal development of the whole interferential sensor head with additional SFM module. A solution according to (1) can directly be achieved by adapting the adapter ring mentioned in Section 1.2.2 and shown in Figure 1.3(a). In view of the planned improvement of the optical properties of the objective, which will be explained

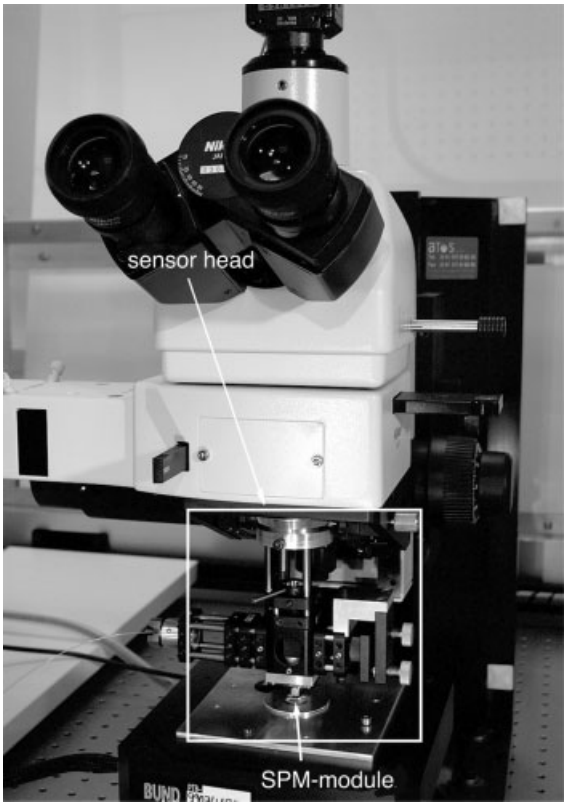

Fig. 1.5 View of the combined SFM and interference microscope composed of sensor head and commercial basic instrument.

in the following, preference has, however, been given to the internal development of the measuring head.

Core piece of the newly developed sensor head is a Michelson interferometer in which the illumination is not performed via the internal, filtered microscope white light lamp, but via external laser sources coupled to optical fibers. This way, an essential heat source is removed from the measuring setup and the mechanical stability is improved. Even more important is the fact that due to the small illumination aperture of the optical fiber aperture correction becomes negligible in the interference-microscopic evaluation. This clearly reduces the measurement uncertainty.

At present, a HeNe laser ($\lambda = 632.80$ nm) or a frequency-doubled Nd-YAG laser ($\lambda = 532.26$ nm) can optionally be used as external laser sources in the measuring setup. If desired, this allows operation in the multiwavelength interferometry mode by which, compared to operation with only one wavelength, the range of unambiguous measurements of the interference microscope is extended.

For combination with a scanning probe microscope, the compact SFM module with piezolevers already described in Section 1.2.2 was mounted on the sensor head below the beam splitting cube. The cantilever can be seen in the image section of the optical microscope (both in the "live image" and in the interference-microscopic image; see Figure 1.6: on the left above) so that measurement area selection is very user-friendly. The interference-optical measurement (e. g., in phase-shifting mode) is performed simultaneously over the whole image section; in the current configuration, the optical measuring range amounts to approx. 900 μm × 900 μm. It can, however, also be varied by using different optical systems. In the case of a higher optical magnification it has, however, to be taken into account that the depth of focus is reduced and the advantage of an optical survey image is no longer valid. In a second step, the object area to be investigated with a high lateral resolution is moved below the SFM measuring tip with the aid

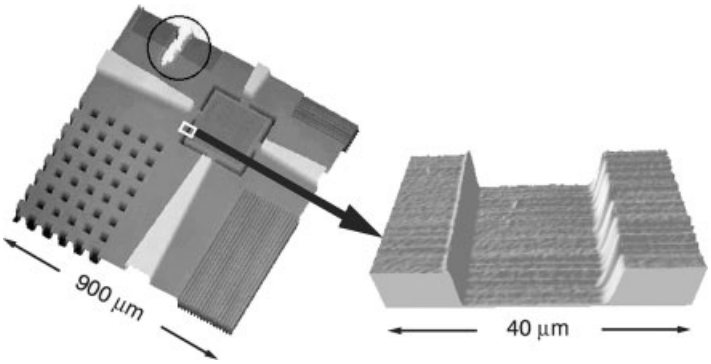

Fig. 1.6 Topography image of an 80-nm step-height standard (H80) (a) image recorded in the interference-optical mode (range 900 μm × 900 μm) – the SFM cantilever can be seen in the circle marked at the upper-left corner; (b) Section measured with the integrated SFM module (range 40 μm × 20 μm).

of a manually operated linear *x*, *y*-stage. After the surface has been successfully approached to the tip, the measurement object is moved line by line with a position-controlled piezo scanning stage (maximum operating range: approx. 100 μm × 100 μm).

The extraordinary advantage of this combined measuring system consists in the possibility of a direct *z*-calibration of the SFM. As soon as SFM and interference microscope are measuring at the same place of the sample, the interference-optical result can be used as calibration value for the SFM. Special step-height standards are suited to be used as precise standards for heights from a few nanometers up to some micrometers [11].

Comparison measurements performed at PTB with the newly established measuring system and the reference interference-optical microscope showed for step-height measurements on 80 nm and 260 nm calibration standard deviations of less than 1 nm [20]. Figure 1.6 shows a comparison of the results of measurements performed on an 80 nm standard in the interference-microscope mode and in the SFM mode.

Another advantage of this combined device becomes obvious in the case of heterogeneous objects. As soon as the optical constants of substrate and measurement structure differ, the optical wave in the interference microscope experiences different phase jumps on reflection. This leads to a measurement error as long as the relevant optical constants are not taken into account in the interference-microscopic evaluation. Determination of these constants for thin layers in the nanometer range is, however, quite time-consuming and often imprecise, so this correction is only conditionally possible. This is different in the case of the device on hand: Here, the measured value of the interference microscope is corrected by the SFM module that had been calibrated before. It is worthwhile pointing out that the SFM calibration was, as already described, performed with the same interference microscope, although on a sample with homogeneous surface. This example shows the complementary properties of the two independent measuring principles combined in one measuring instrument [20].

1.3 Metrology Systems Based on Scanning Probe Microscopes

In addition to other development activities in the field of SPM metrology, two commercial SFMs have been extended by miniaturized homodyne laser interferometers and their data acquisition system has been improved in the past 2 years. The positioning system of a third device developed into a large range SFM at PTB has already been equipped with laser interferometers by the manufacturer. These laser interferometers were developed in cooperation with the Technical University IImenau and SIOS Messtechnik GmbH. In the case of all devices, special attention was already paid during the construction of the interferometer extension and the instrument design to the fact that principles as minimization of Abbe errors and tilting were complied with. At PTB, the SFMs

described serve for the calibration of standards and the general characterization of microstructures. In the following, the SFMs equipped with laser interferometers will be referred to as metrological SFMs.

1.3.1 Scanning Force Microscopes of Type Veritekt

Since 1995, two metrological SFMs with integrated laser interferometers have been constructed on the basis of the commercial SFM Veritekt-3 of Carl Zeiss, Jena. These devices allow measurement objects to be characterized in "contact" SFM mode with a measuring range of $70 \times 15 \times 15\ \mu m^3$ (x, y, z). Compared to other instruments, the advantage of these SFMs is that a precise flexure hinge stage is used as the basis for the positioning system and that position-controlled piezo actuators (with integrated capacitive sensors) are used for each axis of motion. A skilful geometry of the flexure hinges allows factors such as cross-talk of the axes and nonorthogonality of the directions of motion to be minimized.

The operating principle of the integrated laser interferometers and the procedure of how they are used to calibrate the capacitive sensors in the piezo actuators is described in detail in [21, 22]. Figure 1.7 shows the diagrammatic sketch of the two Veritekt SFMs. Veritekt B that has been completed in 1996 and optimized in the following years with respect to a minimization of the Abbe error, is used for calibrations at PTB. The results of international and internal comparisons [23, 24] have confirmed suitability of this SFM for calibration tasks.

On the basis of the experience gained with Veritekt B, another metrological SFM, Veritekt C (see Figure 1.8), has been developed in the years until 2002. Essential subassemblies of the commercial basic instrument were adopted and supplemented by modern measuring and evaluation electronics. The arrange-

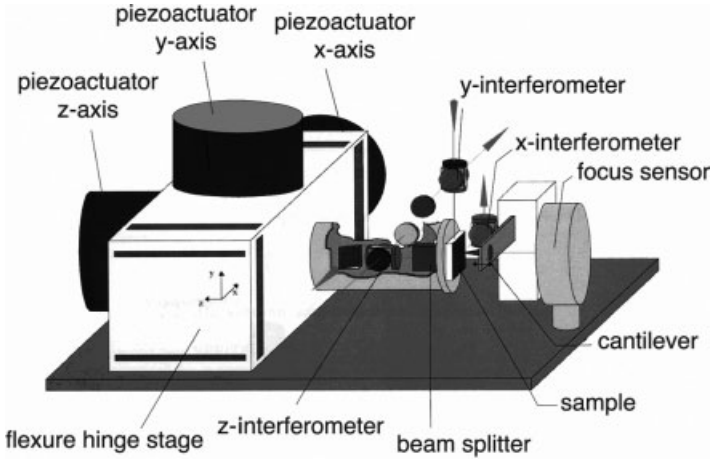

Fig. 1.7 Sketch of the metrological scanning force microscope Veritekt with integrated laser interferometers (source: TK Ilmenau).

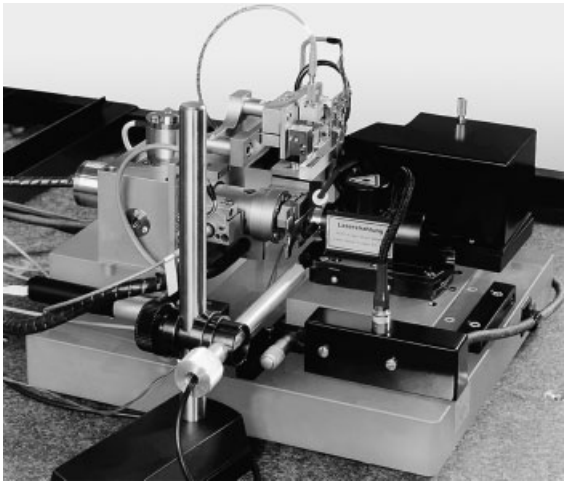

Fig. 1.8 View of the SFM Veritekt C.

ment of the laser interferometers was revised in such a way that it is now also possible to adapt measuring heads working in different SFM modes.

Contrary to the measuring strategy used for Veritekt B, in which the laser interferometers are used for calibration of the capacitive sensors at discrete measurement points ($\lambda/2$ zero points of the interferometer signals) and calculation of correction values, Veritekt C directly includes the interferometer values in the SFM's control loop. To allow the interferometers to be used as measuring and control systems, the data acquisition electronics were completely changed and signal processing realized on the basis of a fast signal processor [5]. Integration of these data acquisition electronics into Veritekt C allows the resolution of the interferometer values to be increased to 0.04 nm and the interferometers to be operated at a data rate of 20 kHz.

As nonlinearity of the interferometer signals (which amounts to approx. 3 nm in the uncorrected form) is a limiting factor when measurement uncertainties in the range of a few nanometers are concerned, diverse correction procedures for the nonlinearity were investigated when the measuring electronics was modified. Finally, a procedure that follows the principle developed by Heydemann [25] was embedded into the control loop of the interferometers. This procedure corrects the deviations of the interferometers' electrical signals u_1^d and u_2^d in amplitude, offset, and phase by an ellipse fitting method:

$$u_1^d = u_1 + p \qquad u_2^d = \frac{1}{r}(u_2 \cos\alpha - u_1 \sin\alpha) + q.$$

In view of the calculation effort involved, this algorithm is usually not implemented as online method. The investigations performed on Veritekt C have, however, shown that the ellipse parameters p, q, r, and α can be assumed to be constant over a sufficiently long period of time and need not, therefore, be permanently determined during correction. This allows the procedure to be integrated into

the interferometer's measuring circle without restriction of the data rate. The correction described allowed remaining nonlinearities of the interferometer signals to be reduced to 0.3 nm.

After the interferometer data rate had been successfully increased, the measuring principle of the SFM was revised to accelerate data acquisition of all signals. On this basis, a new measuring mode was developed for scanning of the sample. Central triggering of all measuring and control elements installed in the SFM then allows the measurement object to be scanned with constant velocity and to simultaneously determine the measurement data of both the positioning system and the SFM sensor acting as null indicator. This makes deceleration of the movement during acquisition of the measurement point data unnecessary; this "scan-on-the-fly" measuring principle allows the measurement velocity in the *x*-direction (fast scan axis) to be increased to up to 25 μm/s as a function of the topography to be investigated. Because of the fast data acquisition, the influence of thermal drift and other environmental factors can be reduced.

Modernization of the data acquisition software, an automated sample positioning system, and the efforts taken to realize automatic measuring processes (batch processes) have further improved the handling of the device. Because of the use of laser interferometers as displacement measuring sensors, calibration of the measuring system so far required can be dispensed. This leads to a reduction of the whole measuring time.

1.3.2
Metrological Large Range Scanning Force Microscope

For an increasing number of practical applications of scanning probe microscopy – also in the field of SPM metrology – the measuring range of piezo scanning stages (x, $y < 100$–200 μm) is too small. These applications comprise, for example, the determination of roughness in accordance with written standards and investigations on lateral standards whose evaluation requires measurements in the millimeter range. For the reasons mentioned, different concepts have been developed to extend the measuring range of SFMs with the aim of increasing the displacement range of piezo actuators [26] or using alternative positioning systems [27].

The PTB decided to develop and manufacture a positioning system on the basis of the so-called nano measuring machine [27] that meets the specific metrological requirements of industrial metrology. This device was combined with a measuring head based on a focus sensor known from the Veritekt SFM. A measuring instrument is thus available that combines a positioning range of $25 \times 25 \times 5\ \text{mm}^3$ with the detection principles of scanning force microscopy – the so-called metrological large range scanning force microscope (LR-SFM). Its operating principle is shown in Figure 1.9.

The object stage is moved via three linear driving systems that are position controlled by laser interferometers. Two angle-measuring systems have been included in the control unit to correct for guidance errors of the motion stage.

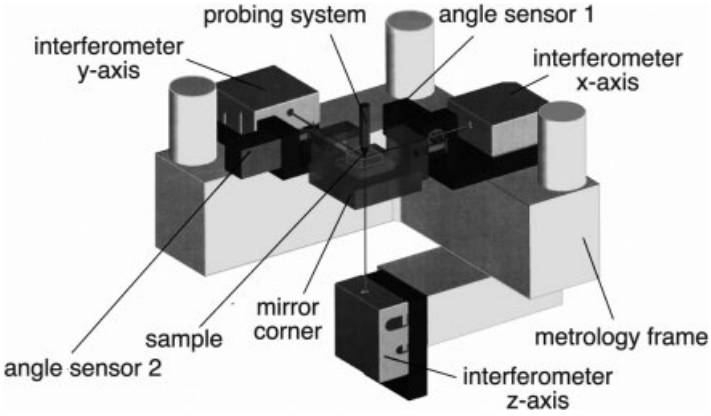

Fig. 1.9 Diagrammatic sketch of the metrological large range SFM (LR-SFM) (components such as drives and rails are not shown for reasons of clarity), (source: TK Ilmenau).

Similar to the Veritekt SFMs, the reference system is formed by plane mirrors; in the case of the LR-SFM, the mirrors have been combined to form a cube corner. The resolution of the measuring system amounts to 0.08 nm or 0.001, respectively. The construction of the device is aimed at achieving coincidence of measuring and reference plane to minimize Abbe errors.

To increase the dynamics of the positioning system, a compact vertically moving piezo stage was arranged on the sample stage of the NMM. This one allows fast scanning with a range of up to 2 μm. Its compact and stiff design results in a high mechanical resonance frequency f_r of 20 kHz. The movement of this stage is measured and its position controlled via a capacitive sensor arranged in the middle of three symmetrically arranged piezo actuators. During scanning of the sample, the lateral movement is performed exclusively with the NMM, whereas the height adjustment results from a combined movement of the vertically adjustable z piezo stage and the NMM. The whole device is controlled via two signal processor systems. One is responsible for the NMM, the other realizes height adjustment and data acquisition. More detailed information about the measuring techniques used and the control systems implemented can be found in [28, 29]. The photo in Figure 1.10 shows the metrological LR-SFM.

After finishing the design of the measuring software for the complete device, extensive investigations into the metrological properties of the LR-SFM were carried out. As an example, the first results of measurements performed on a flatness standard and on a sinusoidal lattice standard are shown.

The topographic image of the flatness standard (Figure 1.11) can be used to estimate the quality of the motion (influenced by the guidance mechanism) and to evaluate the instrument's noise behavior. The image shows that the structure measured is very flat and that artifacts as they may, for example, be caused by the ball bearings, are not detectable. The residual instrument noise (3 nm p-v)

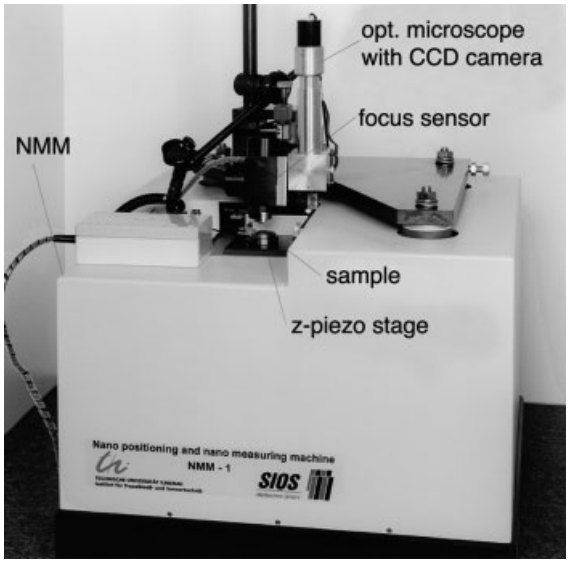

Fig. 1.10 View of the metrological large range SFM (LR-SFM).

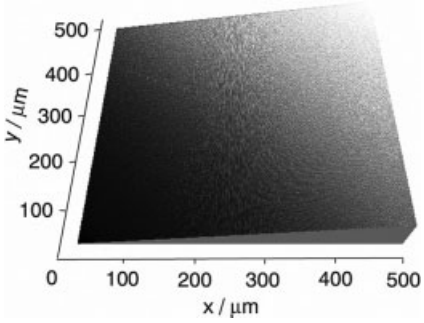

Fig. 1.11 Investigations into the guiding properties and noise behavior of the LR-SFM Topography image of a flatness standard.

is mainly due to external influences such as building vibrations and acoustic excitations, and it should be reduced by optimizing the environmental conditions.

Suitability of the LR-SFM for measurements on lateral standards and determination of the structure period is illustrated by the example of a sinusoidal lattice. Figure 1.12 shows the scan image of a one-dimensional lattice that has been scanned in the *x*-direction with a measuring range of 1.35 mm (this corresponds to 20 times the scanning range of the Veritekt SFMs!). As calculation of the structure period is based on a statistical procedure, a larger number of structures allows us to improve the measurement uncertainty of the measuring procedure, provided the sample structure is homogeneous. Repeated measurements on this sinusoidal lattice showed an identical periodic value of 416.67 nm. This result agrees with the reference value from diffractrometric optical measurements within two decimal places.

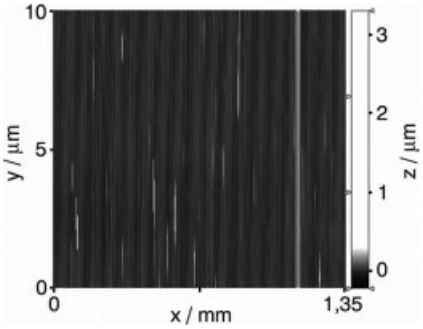

Fig. 1.12 Determination of the lattice constant on a sinusoidal lattice with approx. 3000 periods (measuring range in the *x*-direction 1.35 mm).

Further measurements on nanostructures and step heights have confirmed the high spatial resolution of the measuring instrument and agreement of the measured values with reference values from international comparisons.

The investigations initiated to optimize the LR-SFM and extend it by alternative detection principles are permanently continued and are to demonstrate that the measuring system is also suitable for the measurement of structures with a topography up to the millimeter range. Measurement tasks such as calibration of tip geometries on indenters for hardness measurement, investigation of structures on photo masks from semiconductor industry, determination of dimensional parameters on parts in the field of microsystem technology and the like are already demanded by industry and represent potential fields of application for the metrological LR-SFM.

1.4 Summary

Special emphasis in the field of dimensional nanometrology at PTB is placed on the development and optimization of measuring instruments for SPM metrology. The development of sensor heads comprises, among other things, the concept of the "sensor objective" to combine conventional microscopy with scanning probe techniques. It is characterized by its extraordinary versatility that is due to the use of different measuring heads and detection principles. In the field of complete metrological SFM systems, the measuring properties of one of the existing Veritekt systems have been significantly improved by including laser interferometers directly into the position control loop and by a clear reduction of the nonlinearity of the interference signals. In addition, the application spectrum of metrological scanning probe microscopy has been considerably extended by the establishment of an SFM system with a measuring volume of 25 mm × 25 mm × 5 mm.

The experience gained in the past few years has shown that it is precisely the performance of development work in the field of SPM instrumentation at PTB that is of decisive importance for the quality and understanding required for subsequent use of these devices and their calibration. No study of operating instruc-

tions or training courses can replace the know-how gained in this work. Many development projects have produced innovative solutions to reply to metrological questions. In accordance with our philosophy, these activities are carried out almost exclusively together with partners from industry and are, if possible, based on commercially available components. Several examples of successful technology transfer (among others Physik Instrumente (PI) GmbH, SIOS Messtechnik GmbH, Surface Imaging Systems (SIS) GmbH) can be shown; they have been implemented in many industrial products in the whole world.

Because of the continuing miniaturization in many high-technology fields and the increasing number of metrological applications of SPMs, scanning probe microscopy will be of outstanding importance for the future work in the field of dimensional nanometrology at PTB.

Acknowledgments

We wish to thank all colleagues of the "Micro- and Nanometrology" Department and the Working Group "Quantitative Scanning Probe Microscopy" for the good cooperation. Especially Dr. L. Koenders, Dr. R. Krüger-Sehm, Dr. J. W.G. Tyrrell, Dipl.-Phys. Th. Dziomba, H. Wolff, M. Kempe, Dr. M. Xu, Dr. D. V. Sokolov, Dr. D. V. Kazantsev and Dipl.-Ing.(FH) D. Schulz have contributed to the work being a success. Furthermore, we thank Professor Dr. K. Hasche and Dr. G. Wilkening for their support. Thanks are also due to our partners from industry: Surface Imaging Systems (SIS) GmbH (among others Dr. H.-A. Fuß), NanoWorld Services GmbH/Nanosensors GmbH (among others Dipl.-Phys. Th. Sulzbach), Ilmenau Technical University and SIOS Messtechnik GmbH (among others Prof. G. Jäger and Dr. T. Hausotte) and Physik Instrumente (PI) GmbH (among others Dr. H. Marth und K. Pollak).

References

1 O. Jusko, X. Zhao, H. Wolff, and G. Wilkening, Design and three dimensional calibration of a measuring scanning tunneling microscope for metrological applications, Rev. Sci. Instrum. **65**, 2514ff (1994).

2 H. Geuther, K.-P. Schröder, H.-U. Danzebrink, and W. Mirandé, Rastermikroskopie im Nah- und Fernfeld an Strukturen im Submikrometerbereich, tm-Technisches Messen **61**, 390–400 (1994).

3 S. Gonda, T. Doi, T. Kurosawa, et al., Real-time, interferometrically measuring atomic force microscope for direct calibration of standards, Rev. Sci. Instrum. **70**(8), 3362ff (1999).

4 J. Haycocks and K. Jackson, in *Proc. of the 2nd Euspen Conference, Torino, Italy, May 27th–31st* (2001) 392ff.

5 G. Dai, F. Pohlenz, H.-U. Danzebrink, K. Hasche, and G. Wilkening, Improving the performance of interferometers in metrological scanning probe microscopes, Meas. Sci. Technol. **15**, 444–450 (2004).

6 G. B. Picotto and M. Pisani, Ultramicroscopy **86**, 247ff (2001).

7 M. Bienias, S. Gao, K. Hasche, R. Seemann, and K. Thiele, A metrological scanning force microscope used for coating thickness and other topographical measurements, Appl. Phys. A **66**, 837ff (1998).

8 R. Dixson, R. Köning, J. Fu, and T. Vorburger, Accurate dimensional metrology with atomic force microscopy, *SPIE Metrology, Inspection, and Process Control for Microlithography XIV, February 28 – March 2, 2000, Santa Clara, Ca,* Vol. 3998.

9 G. Garnaes, N. Kofod, A. Kühle, and C. Nielsen, Calibration of step heights and roughness measurements with atomic force microscopes, Prec. Eng. **27**, 91ff (2003).

10 F. Meli, and R. Thalmann, Long-range AFM profiler used for accurate pitch measurements, Meas. Sci. Technol. **9**, 1087–1092 (1998).

11 L. Koenders, T. Dziomba, P. Thomsen-Schmidt, and M. Senoner, Normale für die dimensionelle und analytische Nanometrologie, PTB-Mitteilungen **114**, 16–24 (2004).

12 C. Dal Savio, H. Wolff, T. Dziomba, H.-A. Fuß, and H.-U. Danzebrink, A compact sensor-head for simultaneous scanning force and near-field optical microscopy, Prec. Eng. **26**, 199–203 (2002).

13 H.-U. Danzebrink, D. V. Kazantsev, C. Dal Savio, K. Pierz, and B. Güttler, Optical microscope with SNOM option for micro- and nanoanalytical investigations at low temperatures, Appl. Phys. A **76**, 889–892 (2003).

14 M. Tortonese, R. C. Barrett, and C. F. Quate, Atomic resolution with an atomic force microscope using piezoresistive detection, Appl. Phys. Lett. **62**, 834–836 (1993).

15 R. Jumpertz, J. Schelten, O. Ohlsson, and F. Saurenbach, Bridge configuration of piezoresistive devices for scanning force microscopes, Sensors Actuators A **70**, 88–91 (1998).

16 C. Dal Savio, Th. Dziomba, D. V. Kazantsev, and H.-U. Danzebrink, Entwicklung eines kombinierten Nahfeldmikroskopie- und -spektroskopiesystems, PTB-Bericht F-47, S. 1–94 (2003).

17 P. Güthner, U.Ch. Fischer, and K. Dransfeld, Scanning near-field acoustic microscope, Appl. Phys. B **48**, 89 (1989).

18 J. W.G. Tyrrell, D. V. Sokolov, and H.-U. Danzebrink, Development of a scanning probe microscope compact sensor head featuring a diamond probe mounted on a quartz tuning fork, Meas. Sci. Technol. **14**, 2139–2143 (2003).

19 H.-U. Danzebrink, J. W.G. Tyrrell, C. Dal Savio, and R. Krüger-Sehm, Combined optical and scanning probe microscopy, PTB-Bericht O-**68**, 112–123 (2003).

20 J. W.G. Tyrrell, C. Dal Savio, R. Krüger-Sehm, and H.-U. Danzebrink, Development of a combined interference microscope objective and scanning probe microscope, Rev. Sci. Instrum. **75,** 4, 1120–1126 (2004).

21 M. Bienias, S. Gao, K. Hasche, R. Seemann, and K. Thiele, A metrological scanning force microscope used for coating thickness and other topographical measurements, Appl. Phys. A **66**, 837–842 (1998).

22 K. Hasche, K. Herrmann, W. Mirandé, R. Seemann, L. Vitushkin, M. Xu, and G. Yu, Calibrated scanning force microscope with capabilities in the subnanometre range, Surf. Interface Anal. **33**, S. 71–74 (2002).

23 L. Koenders, et al., Comparison on nanometrology – NANO2: step height, Metrologia **40**, 04001 (2003).

24 K. Herrmann, W. Mirandé, K. Hasche, and F. Pohlenz, Investigations on gratings with period length in the nanometre range, in *Proceedings of the 5th Seminar on Quantitative Microscopy and 1st Seminar on Nanoscale Calibration Standards and Methods, Bergisch-Gladbach, November 2001,* PTB-Bericht F-44, S. 78–85 (2001).

25 P. Heydemann, Determination and correction of quadrature fringe measurement errors in interferometers, Appl. Opt. **20**, S. 3382–3384 (1981).

26 F. Meli and R. Thalmann, Long range AFM profiler used for accurate pitch measurements, Meas. Sci. Technol., Special issue on Dimensional Metrology **9**(7), S. 1087–1092 (1998).

27 G. Jäger, E. Manske, T. Hausotte, and H.-J. Büchner, Nanomessmaschine zur abbefehlerfreien Koordinatenmessung, tm-Technisches Messen **7-8**, S. 319–323 (2000).

28 G. Dai, F. Pohlenz, H.-U. Danzebrink, M. Xu, K. Hasche,an
d G. Wilkening, A metrological large range scanning probe microscope. Rev. Sci. Instrum. **75**, 4, 962–969 (2004).

29 G. Dai, F. Pohlenz, H.-U. Danzebrink, M. Xu, and K. Hasche, A novel metrological scanning probe microscope with a measurement range up to $(25\ \mathrm{mm})^2$, PTB-Bericht F-48 (2003), 175–182.

2
Nanometrology at the IMGC

M. Bisi, E. Massa, A. Pasquini, G. B. Picotto, and M. Pisani

Abstract

A survey of the nanometrology-related activities in progress at the Istituto di Metrologia "G. Colonnetti" (IMGC) is presented. Some special apparatus for critical measurements in the nanoscale range are described. The development of instrumentation and methods for quantitative scanning probe microscopy, optical diffractometry, and atomic scale displacement metrology by combined x-ray and optical interferometry is outlined. Focus is given on calibration and methods for traceable measurements, high-resolution positioning, and subnanometer displacements measurements.

2.1
Introduction

The continuous miniaturization of processes and products (top–down approach) as well as the fabrication of nanoscale systems by molecular assembly (bottom–up approach) have extended the needs for measurement and testing in the nanometrology [1, 2]. The development of instrumentation, standards and traceable measurement methods in the nanoscale should address these requirements of quantitative measurements of critical functions and dimensions, not only restricted to physical quantities and microscopic specimens.

In this contribution, some activities are briefly described at the IMGC in the fields of surface and atomic-scale metrology. A special apparatus (nanobalance) for the measurement of forces in the nanorange is also described. The IMGC is an Institute of the National Research Council (CNR) of Italy and carries out research to maintain and develop national measurements standards for thermal and mechanical metrology.

Nanoscale Calibration Standards and Methods: Dimensional and Related Measurements in the Micro- and Nanometer Range.
Edited by Gunter Wilkening, Ludger Koenders
ISBN: 3-527-40502-X

2.2
Surface Metrology

2.2.1
Scanning Probe Microscopy

Surface metrology of patterned, nanostructured, and functionalized surfaces in the submicrometer range is a key step in many processes of micro- and nanofabrication [3]. In this field, scanning probe microscopy (SPM) is a very useful metrological tool for high-resolution three-dimensional (3D) imaging of microtopography and local physical properties of surfaces of a wide range of materials. Quantitative SPM measurements of critical dimensions, pitch and step-height of patterned surfaces need of instruments with accurate and stable devices, which must use onboard laser interferometers or capacitive sensors to monitor and control tip/sample displacements. The use of laser interferometers is more complicated and expensive but provide direct traceability to the wavelength of light.

A probe microscope [3] in which particular attention has been paid to the traceability of surface geometry measurements has been made at IMGC to measure critical dimensions in regular structures (gratings, grids, and steps, etc.) and to observe critical parameters of irregular structures (granularity of evaporated films, surface roughness, etc.). The microscope has been used for intercomparisons on step-height standards, gratings and patterned grids [4].

The microscope (Figure 2.1) uses a flexible structure working either with tunneling or atomic force heads. The structure accommodates a sample-moving scanning device based on stacked *xy*- and *z*-stages operating in a working volume of $30 \times 30 \times 15$ μm with interferometer and capacitance-based controls of displacements. The *xy*-stage uses plane-mirror linear interferometers and fast phase meters to monitor and control the horizontal movements of precise ball-bearing stages driven by piezo flexure actuators.

The *z*-stage uses a novel design based on three pairs of capacitive sensors and PZT bimorph plates driving a kinematic sandwich-like assembling of two plates, the upper one supports the sample and can be easily removed and precisely repositioned for sample handling. The overall design and the kinematic arrangement allow a 3 degrees of freedom movements with a quasi independent electro-mechanic behavior of the three sensor-actuator pairs. The capacitive sensors have the double purpose to guarantee a pure parallel movement, namely *z* displacements free of pitch and roll tilts, and to deliver a measurement of the displacement itself.

The estimated error budget gives an uncertainty of $U_{95}/\text{nm} \sim Q[2, 1 \times 10^{-3} L]$ with planar dimensions L larger than 200 nm, and of $U_{95}/\text{nm} \sim Q[2, 2 \times 10^{-3} h]$ with step-height h larger than 100 nm. The quadratic notation $Q[a, b \cdot L]$ is the square root of quadratic sum of the two arguments a and $b \cdot L$.

Quantitative measurements of pitch, linewidth, step-height, and critical dimensions should include errors due to the tip shape, the finite sampling (number of

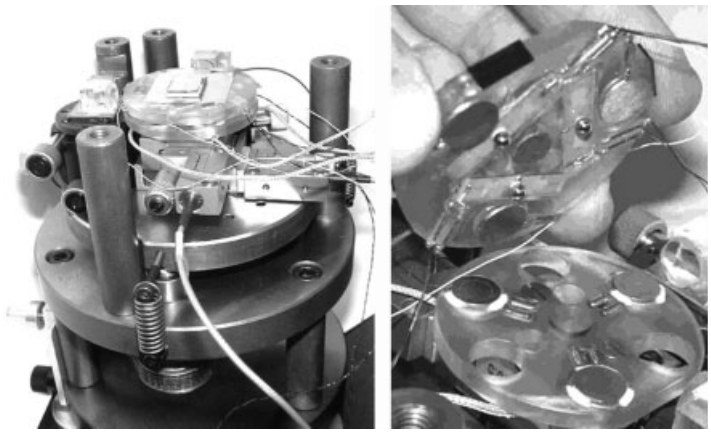

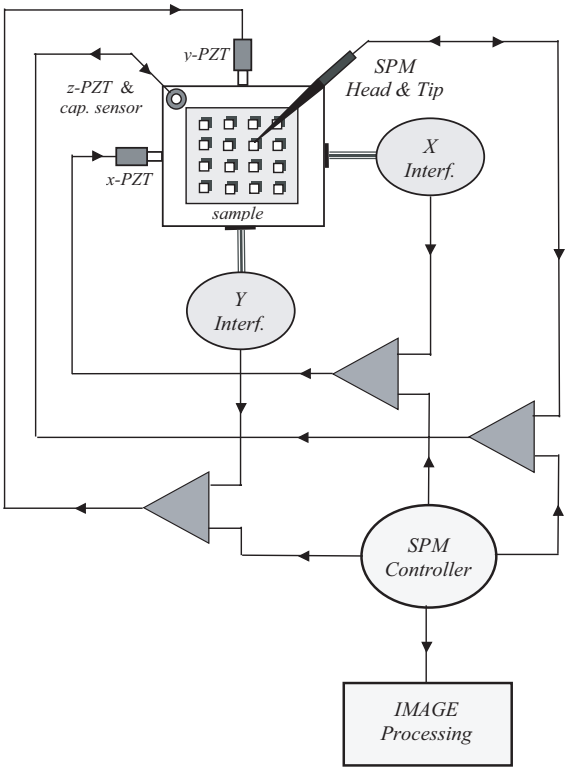

Fig. 2.1 Block diagram, scanning system and *z*-stage of the metrological SPM.

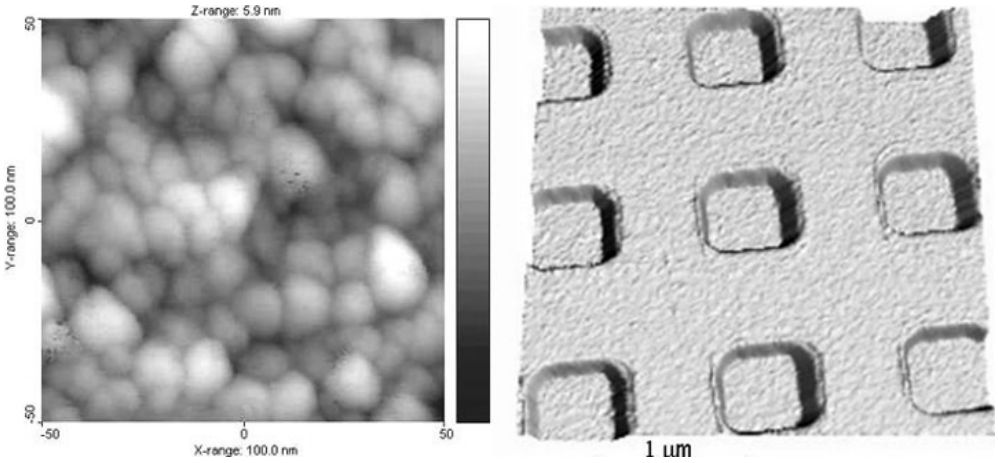

Fig. 2.2 STM images of a TiO_2 thin film (IMGC and UniTo) and of an *xy* grid standard.

sampling points and converters resolution) and numerical calculation (FFT, windowing, ...).

High sharpness of the tip may reduce reconstruction errors due to the finite tip size while imaging surfaces having high-aspect ratio features. A two-step electrochemical method has been developed for sharpening tunneling tungsten tips [5], and the feasibility of tips having carbon nanotubes at the apex is under a preliminary investigation. Carbon Nanotubes may represent ideal SPM probes due to their high-aspect ratio, provides faithful imaging of deep trenches, while good resolution is retained due to their nanometer-scale diameter.

2.2.2 Optical Diffractometry

Diffraction gratings and grids having pitch between few hundreds of nanometers and tens of micrometers are widely used as transfer standards for the calibration of microscopes (optic, probe or electronic). Optical diffractometry is by far the most accurate technique to calibrate this kind of standards.

A convenient way for measuring the grating pitch by means of the diffraction angle measurement is the "Littrow" (or "autocollimation") setup shown in Figure 2.3. The grating, mounted on a goniometric table is illuminated by a calibrated laser source and is rotated until the diffracted beams are parallel to the incoming beam (incident angle = diffracted angle = α), an optoelectronic device (a two-quadrant silicon photo-detector) reveals this null condition. Compared to other experimental configuration, the Littrow one offers the advantage of a fully symmetrical setup and only one angle to be measured. The diffraction angle can be measured either with respect to the normal reflection angle ($\alpha = 0$), or by measuring the difference between the two opposite diffraction angles thus minimizing

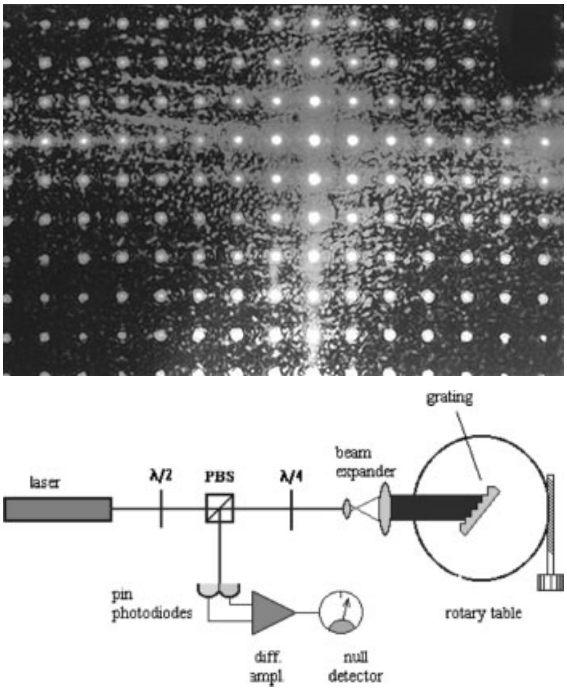

Fig. 2.3 Schematic of the diffractometer with the image of the pattern diffracted from a 2D grating.

systematic errors. When more than two diffracted beams are present, it can be advantageous to measure the higher orders because at greater angles the relative uncertainty of the goniometric table is less.

The IMGC diffractometer makes use of two He–Ne stabilized lasers (633 and 543 nm) whose wavelengths have been calibrated by comparison with the national length standard. The goniometric table angular resolution is 10″ and the optoelectronic circuit has a sensibility of 0.1″. A polarizing beam splitter (PBS) in combination with a quarter wave plate ($\lambda/4$) is used to direct the diffracted light toward the two-quadrant detector. A beam expander is used to expand the beam diameter in order to match the grating dimension. For pitches $p < \lambda/2$ there is no diffraction, thus the smallest measurable pitch is about 280 nm making the use of the green laser. The limit to the maximum measurable pitch is due to the visibility of the diffraction orders (which become closer and weaker for greater values). Gratings with pitches up to 100 μm have been measured.

With any of the n diffracted beams in the autocollimation condition, the grating pitch is

$$p = N\lambda/2 \sin \alpha \tag{2.1}$$

where λ is the laser wavelength, N is the diffraction order and α is the autocollimation angle. The main contribution to the uncertainty is given by the uncer-

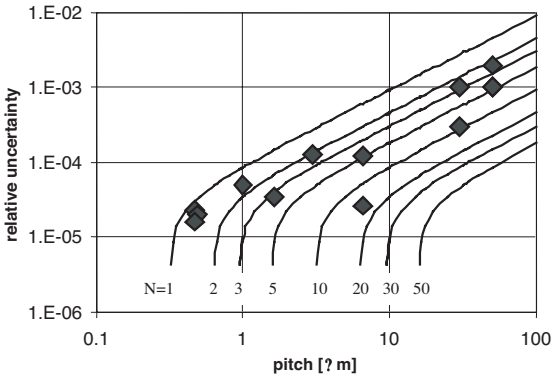

Fig. 2.4 Theoretical relative uncertainty (solid lines, for different values of *N*) and given experimental uncertainties (diamonds).

tainty of the measured angle α (the uncertainty of λ can be neglected). With some approximation, we obtain

$$\Delta p = \Delta\alpha(2p^2/N\lambda) \tag{2.2}$$

From the given estimation, it follows that the relative uncertainty is not constant but increases with the pitch (the smaller is the pitch, the better is the measurement). Meanwhile, the number of the visible orders N increases with the pitch ($N_{MAX} = \mathrm{INT}(2p/\lambda)$), thus leading to discrete jumps of the uncertainty to lower values.

The graphs of the relative uncertainty calculated for different values of the diffracted order N are shown in Figure 2.4. The diamonds represent the experimental uncertainties obtained in the calibration of gratings and grids. With larger pitches the uncertainty increases because it is limited by the maximum diffraction order N used for the measurement (indeed higher diffraction orders can be too weak to be measured).

The IMGC has taken part to the comparison CCL-S1 [6] on 1D gratings having nominal pitches of 290 and 700 nm. The uncertainties of the measurements carried out using optical diffractometers (OD) are comparable and the given values are compliant. Other techniques lead to much greater uncertainties.

2.2.3 Stylus Profilometry

A stylus-based profilometer is used at the IMGC for the calibration of step-height and groove-depth standards having wide rectangular steps and diamond-cutted grooves with flat or rounded trenches (type A – ISO 5436). The stylus makes the use of small tip–surface loads (10–100 μN) to record the profiles (Figure 2.5) of grooves/steps in the range from about 5 nm to 15 μm. The groove-depth/step-height h is given with an uncertainty $U_{95}/nm \sim Q[1, 4.7h]$ where h is expressed in micrometers. The given uncertainty is obtained by calibrating

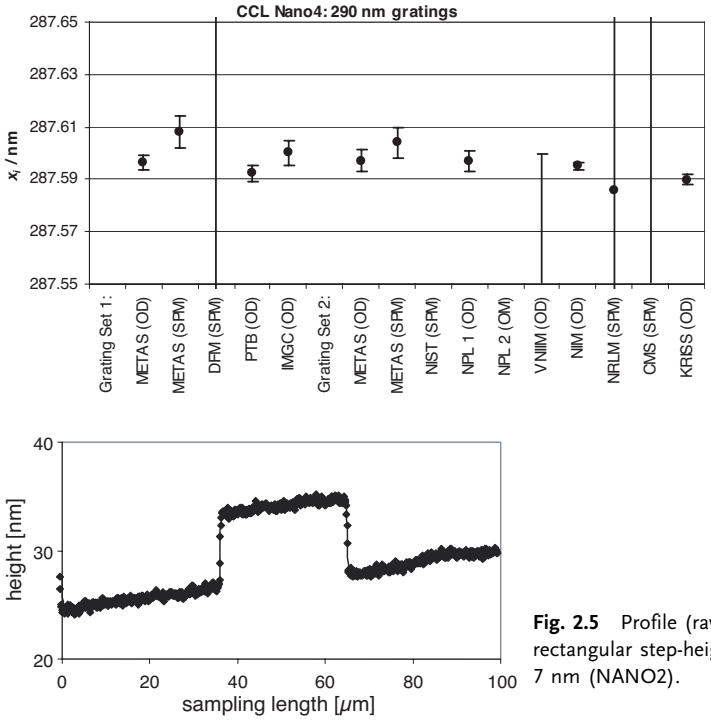

Fig. 2.5 Profile (raw data) of a rectangular step-height of about 7 nm (NANO2).

the displacement sensitivity of the stylus by means of a piezocapacitive displacement actuator, which in turn is calibrated using an interferometric setup [7]. In this way, a direct traceability to the length standard is obtained.

The displacement actuator is driven in such a way to realize rectangular displacement steps for calibrating the different magnifications of the instrument up to the full range of stylus displacements.

The profilometer has been used for the comparisons CCL-S2 (NANO2) on step-height standards, and EUROMET.L-S11 on roughness and groove standards type A2 [8, 9]. Results and uncertainties agree with the comparison reference values.

2.3 Atomic Scale Metrology

The activity is focused on the measurement of the (220) lattice plane spacing of silicon by means of combined x-ray and optical interferometry, which is one of the most advanced tool for atomic-scale displacement metrology. Our aim is to determine the spacing of the (220) lattice planes in silicon to within 5×10^{-9} relative uncertainty, about an order of magnitude lower than present uncertainty.

2.3.1
Lattice Parameter of Silicon

An x-ray interferometer is similar to a Mach-Zehnder interferometer in classical optics. As Figure 2.6 shows, it consists of three thin, flat, and parallel Si crystals cut in such a way that the (220) lattice planes are perpendicular to the surfaces of the three crystals. A crystal, called analyzer, is separated from the other two, so that it the can be moved in a direction orthogonal to the diffracting planes. Mono-energetic x rays (in Figure 2.6, the Mo Kα radiation from a conventional x-ray source) are split by Laue diffraction by the first crystal (splitter). The two beams are split again by the second crystal (mirror) and recombined by the analyzer. The lattice parameter of silicon is obtained from the number of (220) lattice planes in a crystal portion of known length. The measurement requires that the x-ray interferometer is combined, in vacuum, with an optical interferometer so as to have the same baseline, along which the analyzer is moved [10]. The polished front surface of the analyzer is itself a mirror ideally parallel to the (220) planes and its position and attitude are sensed by the optical interferometer.

The relevant measurement relation is $d_{220} = (m/n)\lambda/2$, where n is the number of x-ray fringes in m optical fringes of period $\lambda/2$. The (220) lattice plane spacing is related to the lattice parameter by $d_{220} = a_0/\sqrt{8}$. The definition of the quantity measured, ideally, the spacing of the (220) lattice planes, requires a careful examination. In fact, the x-ray interferometer performs an average of individual lattice spacing values and lattice strain, crystal bending and surface affect this average. If a relative uncertainty of 10^{-9} is required, these contributions to the measurement result must be carefully evaluated [11]. The development of long-range positioning devices having picometer resolution is crucial for the future of scanning x-ray interferometry. Successful operation of an x-ray interferometer is a difficult task. Particularly important are operation *in vacuo*, temperature control to within

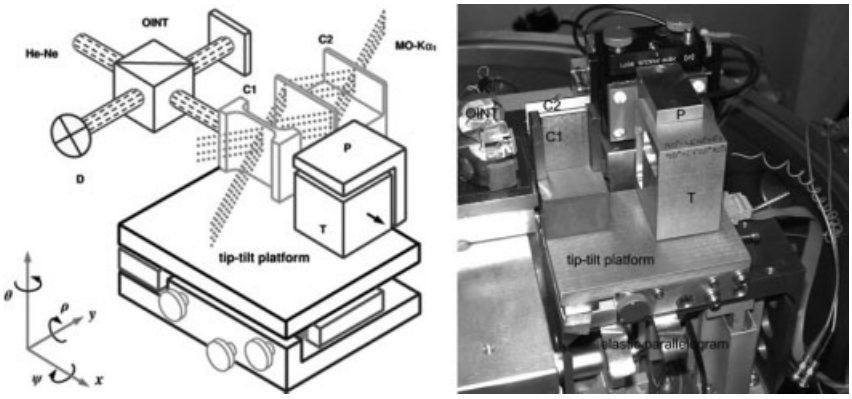

Fig. 2.6 A combined x-ray and optical interferometer. The laser interferometer senses the analyzer location at four points by means of a position-sensitive detector. Displacement, pitch, and yaw are thus simultaneously measured.

a few millikelvin, picometer positioning, vibration, and parasitic rotation control to within picometers and nanoradians, respectively. In a combined x-ray and optical interferometer, ultra-precision positioning and movement can be achieved by feeding back into the piezoelectric translator, the position error detected either by the x-ray interferometer or the laser interferometer. An elastic guide capable of displacements up to 2 mm, smooth to within 1 pm and with yawing and pitching to within 1 nrad, is described by Bergamin et al. [12]. It uses the feedback from the laser interferometer, which detects simultaneously the analyzer displacement position and parasitic rotation [13]. Not only prompt and accurate positioning was obtained, but vibrations were also compensated. For still longer displacements a slideway would be required, but, in order to compensate for relatively large guiding errors, it is necessary to have a mechanical interface seated atop and driven so as to compensate for parasitic rotations and for straightness errors. A solution is shown in Figure 2.6. It consists of two stacked platforms, which rest on piezoelectric elements [14]. The bottom platform compensates for lateral movement and yawing; the top one compensates for vertical movement and pitching. Two capacitive sensors, whose target plates are the top and side faces of a right parallelepiped, detect parasitic movements in order to render the displacements straight.

2.3.2
Combined Optical and X-Ray Interferometry (COXI)

The requirement is to measure displacements up to 1 mm with subnanometric accuracy. While in principle it is possible to measure a displacement of this magnitude using x-ray interferometry alone, the technological difficulties would be very great. X-ray beam intensities are such that, typically, x-ray displacement measurements are orders of magnitude slower than those made by optical interferometry; the slow scanning speed would make measurement times inconveniently long. Additionally, the longer measurement range would suggest the use of separate crystal x-ray interferometer with all its attendant problems of alignment and sensitivity to perturbations. These problems have been circumvented by limiting the range covered directly by the x-ray interferometer to 10 μm only, and by measuring the major part of the displacement by optical interferometry. COXI is based on coupling an optical interferometer and x-ray interferometer in such a way that the two interferometers supplement each other. The optical interferometer's fringe period is about 1648 times larger than the x-ray interferometer's fringe period, but is known with high accuracy (1 pm) (Figure 2.7). The objective of COXI is to provide a means whereby the transducer used for the nanometer range can be calibrated in terms of the national standards of length, that is to develop an instrument for the measurement of linear displacements with ultra high precision, ± 10 pm measurement uncertainty for displacement up to 10 μm, and ± 100 pm for displacement up to 1 mm [15, 16].

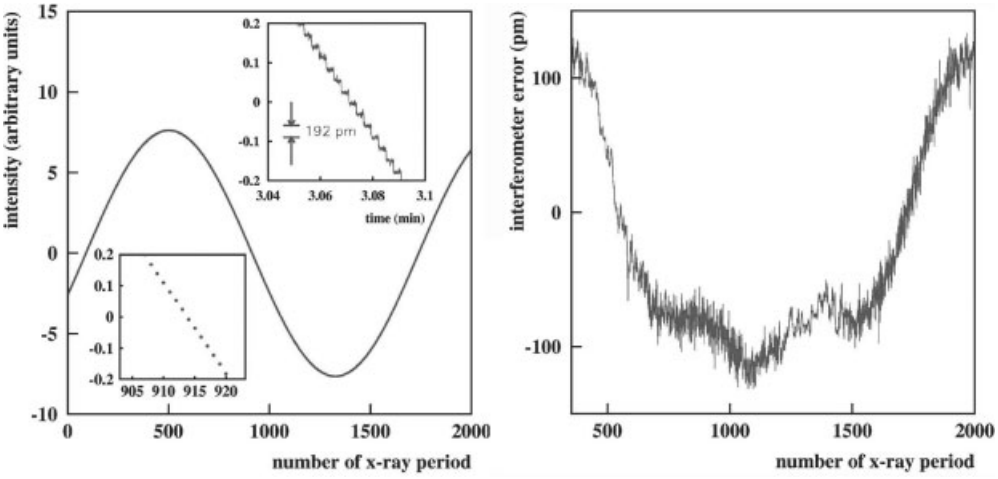

Fig. 2.7 Optical fringe interpolation by x-ray interferometry. The zoom shows the actual mirror displacement by increments of 192 pm. On the right, the residuals of a best fit sinusoidal model to data is shown.

2.4 Phase-Contrast Topograpy

X-ray interferometry makes it possible to apply phase-contrast imaging technique both to the investigation of crystal perfection and to the x-ray imaging.

2.4.1 Detection of Small Lattice Strain

In a triple Laue interferometer, the interference pattern is a moiré pattern formed by the superposition of the diffracting lattice plane of the crystals forming the interferometer. In other words, the phase delay of x rays along the two paths in the interferometer are $2\pi(s_A - s_2)/d_{220}$ and $2\pi(s_1 - s_S)/d_{220}$, where s_i are the components of the displacement vectors of the analyzer, splitter, and mirrors along a direction normal to the diffracting planes. The displacement vector is defined as the vector from an atom in the undeformed crystal to the very same atom in the deformed crystal. Therefore, s_i are small slowly varying functions describing the distortion of the (220) lattice planes [17]. Hence, fringes are created owing to x rays crossing through misplaced atoms; crystal defects and strains are visible in the interference pattern (Figure 2.8).

Since four sets of diffracting planes superimpose to form the moiré pattern, an identical deformation in all the crystals is unobservable. This technique gives no indication about the amount of strain in any individual crystal of the three. As shown in Figure 2.9, strain and rotations can easily be detected and mapped.

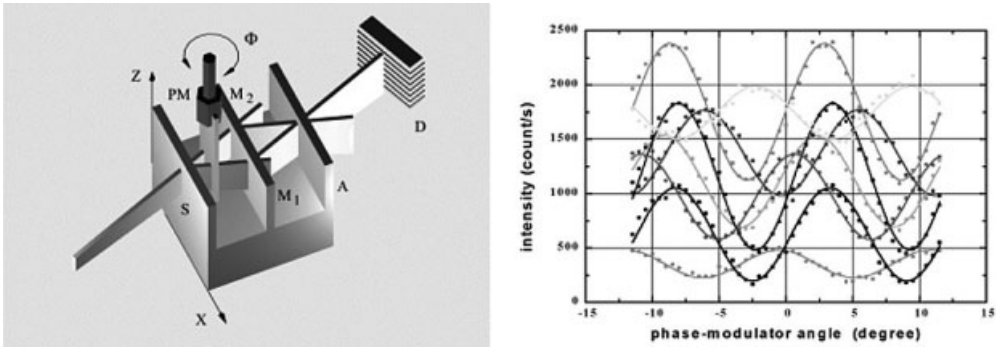

Fig. 2.8 Experimental setup: (PM) phase-modulator, (S) splitter, (M1 and M2) mirrors, (A) analyzer, and (D) multianode photo-multiplier with a pile of eight NaI(Tl) crystal. Set of eight traveling fringes obtained in a single scan of the phase-modulator.

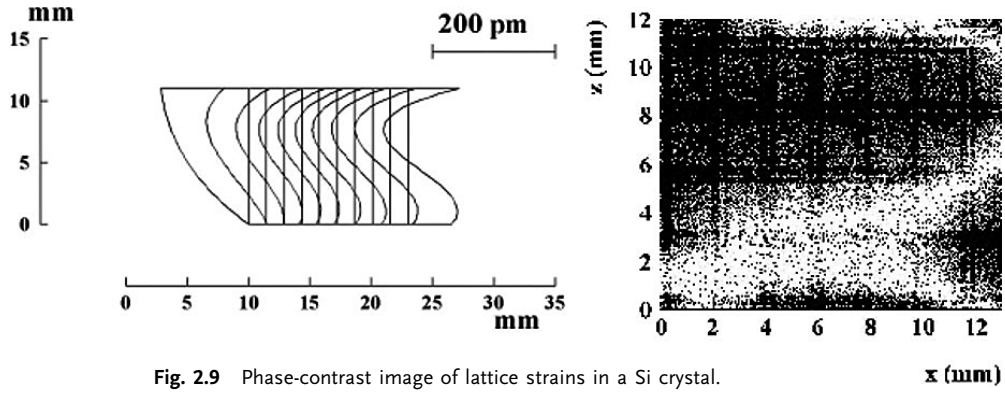

Fig. 2.9 Phase-contrast image of lattice strains in a Si crystal.

2.4.2
Phase-Contrast Imaging

X-ray imaging has remained unchanged since Roentgen's discovery and still relies on absorption. Absorption well differentiates heavy and light elements, but it is not so successful in distinguishing soft tissues, which are transparent to x-rays so that differences in density and composition have negligible effects on absorption. However, in the case of light elements and at typical x-ray energy of 20 keV, x-ray phase shifts can be up to a hundred times greater than absorption. The phase change is produced by the refraction index, as it is in optics. Therefore, it is possible to observe the sample "fingerprint" in the x-ray phase even when the corresponding shadow in a conventional intensity image is undetectable. A way to observe the phase fingerprint is by x-ray interferometry. A phase-shifting sample placed in either of the x-ray paths in the interferometer causes an inter-

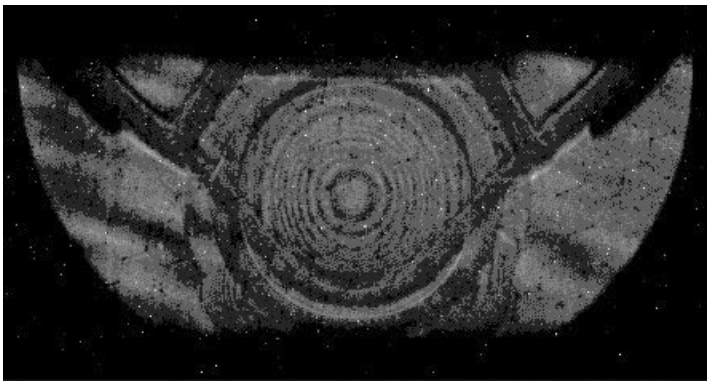

Fig. 2.10 Phase-contrast image (Newton's rings) of the lens focusing the laser beam in a compact disc reader. Lens diameter is 4 mm. The reflection plane of rays is in the vertical direction. The background interference pattern is due to lattice strains in the interferometer crystals. Remaining shadows are caused by the framework.

ference pattern encoding detailed information about the interior sample to be observed. Contrary to absorption, phase contrast does not display an immediately readable image: it is the electron-density contour map, where contour lines are the interference fringes. Fringe spacing is inversely proportional to the density gradient and when fringes become dense, they are hard to resolve. For this reason, x-ray interferometry is very satisfactory for almost flat phase profiles and is particularly suitable to detect small inhomogeneities. Figure 2.10 shows the interference pattern of the plastic lens that focuses the laser beam in a compact disc reader. That image has been obtained at the ELETTRA's SYRMEP beam-line. Symmetry makes the image particularly simple: dark and bright rings alternate from the center to the edge of the lens with increasing frequency. They are the equivalent of Newton's rings in optics and clearly evidence the lens shape. Fringe contrast is lost at the lens edge because of insufficient resolution. X-ray interferometry can reveal fine structures in biological samples, but limitations arise from the interferometer geometry: first, by absorption and, second, by loss of spatial resolution due to the Borrman broadening of x rays in the analyzer. This is evident in Figure 2.10, where fringe contrast is lost more quickly in the vertical than in the horizontal directions. The limit resolution, which can be overcome by reducing crystal thickness or by using Bragg geometry, is set by the width of the interferometer transfer function: this is a consequence of the uncertainty relationship between Fourier transform pairs.

2.5 Nanobalance

IMGC, Alenia Spazio, and Politecnico of Turin have designed and realized the *Nanobalance*, an instrument for the direct measurement of the magnitude and spectral density of thrust of ion micro-propulsor (field emission electric propulsion – FEEP) and gas micro-propulsor in the frequency band between 10^{-4} Hz and 5 Hz, with a (frequency-dependent) resolution between 10 nN and 1 μN. This type of micro-propulsor, characterized by a maximum thrust of 1 mN, will be used to control the attitude and to compensate for the atmospheric drag in some scientific missions such as GOCE (mapping of the Earth's geo-potential) and LISA (a Michelson interferometer for the detection of gravitational waves). *Nanobalance* is an innovative concept: it is an high-resolution instrument, used during the development phase of the micro-propulsors.

Nanobalance is an interferometric balance working in vacuum and consisting of a Fabry–Perot resonator whose length is modified by the action of the micro-propulsor. The instrument (Figure 2.11) is positioned on a circular plate, mechanically isolated by means of the vacuum chamber, which is mounted on a pneumatic damping system (Figure 2.12).

The micro-propulsor is mounted on a rigid pendulum connected to a Zerodur spacing by an elastic hinge. The other micro-propulsor (which in not used during the measurement) is mounted on another pendulum to balance the instrument. The two pendula have been manufactured in order to have the same mechanical characteristics (within manufacturing tolerances) in order to optimize the behavior of the instrument.

When the micro-propulsor is not powered, the pendula oscillate in phase (at about 13 Hz): every mechanical disturb (acoustical or seismic), which is propagated to the instrument, produces a common mode perturbation and does not impair the motion of the pendula. The rejection of the common mode disturbances cannot be completed eliminated because of the unavoidable small differences in

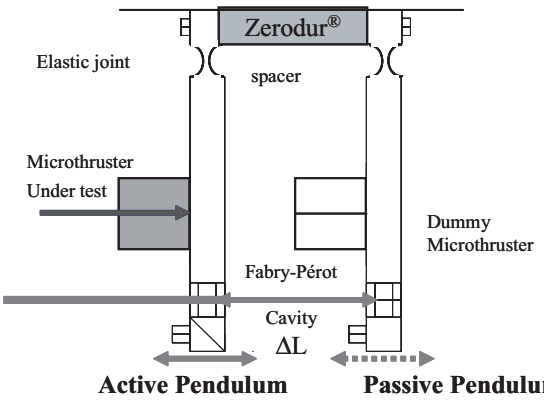

Fig. 2.11 Nanobalance concept.

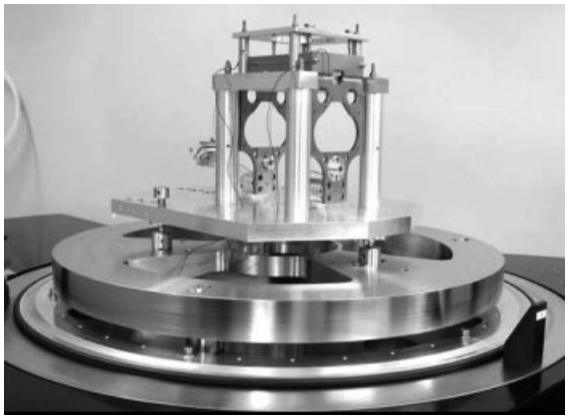

Fig. 2.12 Experimental apparatus.

the geometry of the two pendula. Anyway, the frequencies of the two pendula can be equalized to better than 0.1 Hz.

Two mirrors, mounted at the lower end of the pendula, realize a Fabry–Perot resonator. A Nd:YAG laser is locked to the FP resonance by means of the Pound–Drever technique [18] and of a digital control [19, 20]. Another laser is stabilized with respect to a transition of the iodine molecule, with a frequency stability better than 10^{-12} for 1 s integration time.

The beat frequency between the two lasers gives the information about the value of the thrust produced by the micro-propulsor. When the micro-propulsor is switched on, the FP resonator's length is modified and so is the beat frequency between the two lasers. The laser frequency (≈ 490 THz) is locked to the FP by means of a Digital Control Unity having a control bandwidth of about 200 Hz. Therefore, the laser frequency deviations represent the low-frequency response (< 2 Hz) of the instrument under the action of the micro-propulsor under test.

The calibration of the frequency-to-force conversion factor of the instrument is performed by applying a known force to one pendulum by means of a calibrated linear actuator.

2.6 Conclusions

Nanometrology at the IMGC aims to extend traceability and measurement capabilities in surface and atomic–scale metrology. A relevant activity is dedicated to the development of new apparatus for the measurements of physical quantities in the nanoscale.

Developments of the SPM metrological instrumentation are foreseen to extend sampling, working range, and measuring capabilities for the needs of critical dimension measurements. The optical diffractometer is used as well to investigate

the optical scatterometry, a promising technique for determining critical dimensions of periodic structures.

The future of x-ray interferometry is bounded by capabilities to comply with the accuracy requests in the fabrication of perfect-crystal x-ray optics and in the position and alignment controls of the separate crystals. One of the challenges is in the ability to extend the analyzer traverse over a distance of many centimeters. Such an extension must be based on the integration of long-range slideways, laser metrology, and control over 6 degrees of freedom commensurates with the requirement of picometer-scale displacements. Another is in the ability to extend the interferometer field of view and resolution of phase-contrast imaging.

The nanobalance is an innovative apparatus showing, to the authors' knowledge, the best resolution ever achieved for this kind of measurement. The characterization of one micro-propulsor has already been successfully performed; other micropopulsors will be characterized soon.

References

1 Position paper on The need for measurement and testing in nanotechnology, compiled by the High Level Expert Group (HLEG) on Measurement and Testing, EU (2001).

2 ITRS, Metrology 2003 Edition, http:/public.itrs.net.

3 G. B. Picotto and M. Pisani, A sample scanning system with nanometric accuracy for quantitative SPM measurements, Ultramicroscopy **86**(1–2), 247–254 (2001).

4 R. Breil et al., Intercomparison of scanning probe microscopes, Precision Engineering **26**(3), 296–305 (2002).

5 A. Pasquini, G. B. Picotto, and M. Pisani, STM tips fabrication for Critical Dimension Measurements, in *Proceedings of the NATO/ASI School and Conference: Scanning Probe Microscopy – Characterization, Nanofabrication and Device Application of Functional Materials* (Albunfeira, Portogallo, 1–13 October 2002) in press.

6 http://kcdb.bipm.org/AppendixB/appbresults/ccl-s1/ccl-s1.pdf.

7 A. Sacconi, G. B. Picotto, and V. Pasin, The IMGC calibration setup for microdisplacement actuators, IEEE Trans. Instrum. Meas. **48**(2), 483–487 (1999).

8 L. Koenders et al., Comparison on nanometrology: Nano2-Step height, Metrologia **40** (Technical Suppl.), 04001 (2003).

9 L. Koenders et al., Metrologia **41** (Technical Suppl.), 04001 (2004).

10 G. Basile, A. Bergamin, G. Cavagnero, G. Mana, E. Vittone, and G. Zosi, Measurement of the silicon (220) lattice spacing, Phys. Rev. Lett. **72**, 3133–3136 (1994).

11 G. Mana, C. Palmisano, and G. Zosi, Effects of analyzer deformation in scanning x-ray interferometry, Metrologia **41**, 238–245 (2004).

12 A. Bergamin et al., Scanning x-ray interferometry over a millimeter baseline, IEEE Trans. Instrum. Meas. **46**, 576–579 (1997).

13 A. Bergamin, G. Cavagnero, and G. Mana, A displacement and angle interferometer with subatomic resolution, Rev. Sci. Instrum. **64**, 3076–3081 (1993).

14 A. Bergamin, G. Cavagnero, G. Durando, G. Mana, and E. Massa, A two-axis tip–tilt platform for x-ray interferometry, Meas. Sci. Technol. **14**, 717–723.

15 A. Bergamin, G. Cavagnero, and G. Mana, Quantized positioning of an x-ray inter-

ferometer, Rev. Sci. Instrum. **68**, 17–22 (1997).

16 G. Basile, P. Becker, A. Bergamin, G. Cavagnero, A. Franks, K. Jackson, U. Kuetgengs, G. Mana, E. W. Palmer, C. J. Robbie, M. Stedmana, J. Stuempel, A. Yacoot, and G. Zosi, Combined optical and x-ray interferometry for high-precision dimensional metrology, Proc. R. Soc. Lond. A **456**, 701–729 (2000).

17 A. Bergamin, G. Cavagnero, G. Mana, E. Massa, and G. Zosi, Measuring small lattice distortions in Si-crystals by phase-contrast x-ray topography, J. Phys. D: Appl. Phys. **33**, 2678–2683 (2000).

18 R. W.P. Drever et al., Laser phase and frequency stabilization using an optical resonator, Appl. Phys. B **31**, 97–105 (1983).

19 E. Canuto, Active distance stabilization of large bodies using Fabry-Pérot interferometry, in *Proceedings of the 39th IEEE Conference on Decision and Control*, pp. 3957–3962 (2000).

20 E. Canuto et al., Digital control of the frequency of laser sources for fine metrology, in *Proceedings of the 2nd European Society of Precision Engineering International Conference*, pp. 314–317 (2001).

3
Metrological Applications of X-ray Interferometry

Andrew Yacoot

Abstract

In recent years there have been developments in the use of x-ray interferometry for dimensional metrology at the nanometre and sub-nanometre level. Examples of some applications are described in this paper.

3.1
Introduction

The technique of x-ray interferometry was first demonstrated by Bonse and Hart [1, 2]. A few years later Hart [3] showed that an x-ray interferometer could be used as a metrological instrument. Unlike most optical interferometers, the fringe spacing in an x-ray interferometer is independent of the wavelength of the incident radiation; it is determined by the spacing of diffraction planes in the crystal from which x-rays are diffracted. Silicon is the material normally used for an x-ray interferometer since it is readily available in a pure and defect free form with a known crystallographic orientation. Another major advantage for metrological applications is that the lattice parameter of silicon has been measured very accurately and is regarded as a traceable standard of length [4]. The fringe spacing in an x-ray interferometer is therefore not only several orders of magnitude smaller than that in an optical interferometer thereby obviating the need for fringe division as with optical interferometry, but is also traceable.

Figure 3.1 shows a schematic diagram of a monolithic x-ray interferometer and Figure 3.2 shows a photograph of a monolithic x-ray interferometer developed for the combined optical and x-ray interferometer (COXI) project described later. It was made from a single crystal of silicon. Three thin vertical equally spaced lamella were machined and a flexure stage was machined around the third lamella. The flexure stage has typically a range of a few micrometres and is driven by a piezoelectric transducer (pzt). X-rays are incident on the first lamellae, (B) at the Bragg angle and two diffracted beams are produced; the first lamella can

Nanoscale Calibration Standards and Methods: Dimensional and Related Measurements in the Micro- and Nanometer Range.
Edited by Gunter Wilkening, Ludger Koenders
ISBN: 3-527-40502-X

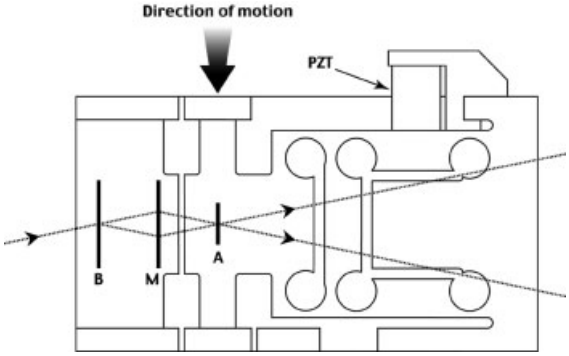

Fig. 3.1 Schematic diagram of an x-ray interferometer. The three lamellae B, M, and A are referred to as the beamsplitter, mirror and analyzer.

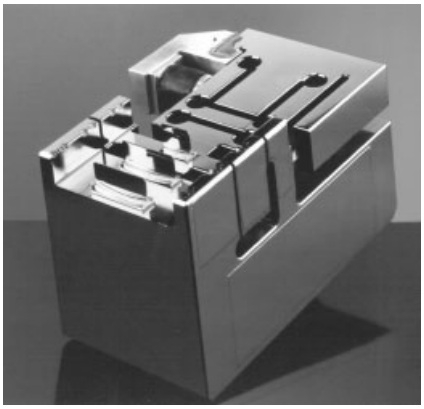

Fig. 3.2 Monolithic x-ray interferometer developed for COXI project.

be thought of being analogous to the beamsplitter in an optical interferometer. The two beams diffracted from the first lamella are incident on the second lamella (M) that can be thought of as being analogous to the two mirrors in a Michelson interferometer. Two more pairs of diffracted beams are produced and one beam from each pair converges on the third lamella (A). These two beams give rise to a fringe pattern whose period is equal to that of the lattice planes from which the x-rays were diffracted. For the (220) planes in silicon this is equal to 0.192 nm. The pattern would be too small to resolve individual fringes, however when the third lamella is translated parallel to the other two lamellae, a Moiré fringe pattern between the coincident beams and the third lamella is produced. Consequently, the intensity of the beams transmitted through the third lamella varies sinusoidally as the third lamella is translated. By measuring the intensity of one of these transmitted beams it is possible to measure the displacement of the third lamella. Since the displacements are traceable to the definition of the metre, the x-ray interferometer can be regarded either as a ruler with sub-nanometre divisions or as a translation stage that makes traceable displacements over a small range in sub-nanometre steps.

The major interest in x-ray interferometers has been directed towards coupling them with an optical interferometer for making more accurate measurements of the lattice parameter of silicon as part of the Avogadro project [5, 6]. The driving force for this work is a more accurate determination of the Avogadro constant, which could lead to the replacement of the kilogram mass standard artifact. The measurement of lattice parameter is achieved using a separated crystal x-ray interferometer in which the third lamella has been separated from the other two, i. e., the interferometer is no longer a monolith. This third lamella is mounted on a separate translation stage whose movement is measured using an optical interferometer. The stage has a greater measurement range than a monolithic x-ray interferometer. By counting the number of x-ray and optical fringes through which the third lamella is moved, it is possible to obtain the ratio of the lattice parameter of silicon to the wavelength of the radiation used in the optical interferometer and hence a traceable measurement of the silicon lattice parameter. Since the alignment of the two components of the x-ray interferometer must be maintained to sub-atomic tolerances great care is required. The value of the lattice parameter obtained from such experiments [7] is used in the other more practical applications of x-ray interferometry described below.

3.2 Measurement of Non-linearity in Optical Interferometers

Considerable effort has been made by metrology institutes towards developing x-ray interferometry into a practical tool for dimensional metrology. The displacements measured using an x-ray interferometer are free from the nonlinearity associated with optical interferometers [8]. X-ray interferometry is therefore an excellent tool for determining the non-linearity in an optical interferometer. The x-ray interferometer is used to make a known displacement that is measured using the optical interferometer under test. By servo controlling the piezoelectric transducer (pzt) used to move the third lamella is possible to either hold the third lamella in a fixed position or move it in discrete steps equal to one x-ray fringe period [9]. A comparison of the results obtained by the optical interferometer with the displacement of the interferometer yields the non-linearity in the optical interferometer. The non-linearity of the NPL designed Jamin interferometer and a Heidenhain encoder have both been measured using x-ray interferometery [10, 11]. In both cases cyclic errors with amplitudes of much less than 100 pm were observed once the Heydemann correction [12, 13] had been taken into account. Figure 3.3 shows results obtained for the Jamin interferometer when the x-ray interferometer was scanned through five optical fringes.

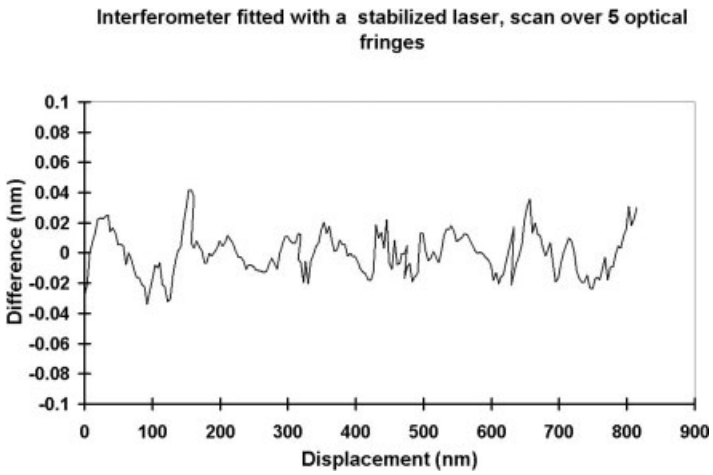

Fig. 3.3 Measurement of non-linearity in NPL Jamin interferometer.

3.3 Combined Optical and X-ray Interferometry

An obvious disadvantage of the x-ray interferometer is its limited range of a few micrometres. To overcome this problem the National Physical Laboratory (UK), Physikalisch-Technische Bundesanstalt (Germany) and Istituto di Metrolgia 'G. Colonnetti' (Italy), joined forces to develop a Combined Optical and X-ray Interferometer, COXI [14], as a facility for the calibration of displacement transducers. This instrument utilized the high resolution of the x-ray interferometer together with the long range of an optical interferometer to provide a calibration range of 1 mm. The x-ray interferometer developed for this project (see Figure 3.2) has on the side of the moving component an optical mirror that was coupled to an optical interferometer. Figure 3.4 shows a schematic diagram of the COXI instrument. The optical interferometer is a double differential system with one path measuring the displacement of the moving mirror on the x-ray interferometer with respect to the two fixed mirrors above the translation stage for a mirror in the optical interferometer. The other path measures the displacement of the mirror (M) moved by the translation stage with respect to the two fixed mirrors either side of the moving mirror on the x-ray interferometer. Both the x-ray and the optical interferometer are servo controlled. The x-ray interferometer moves in discrete x-ray fringes ($d_{220} = 0.192$ nm), the servo system for the optical interferometer registers this displacement and compensates by initiating a movement of the translation stage. If larger displacements are required, the x-ray interferometer can remain fixed and the translation stage of the optical interferometer can be moved through a discrete number of optical fringes. Consequently, the translation stage moves through displacements that correspond to a discrete number of

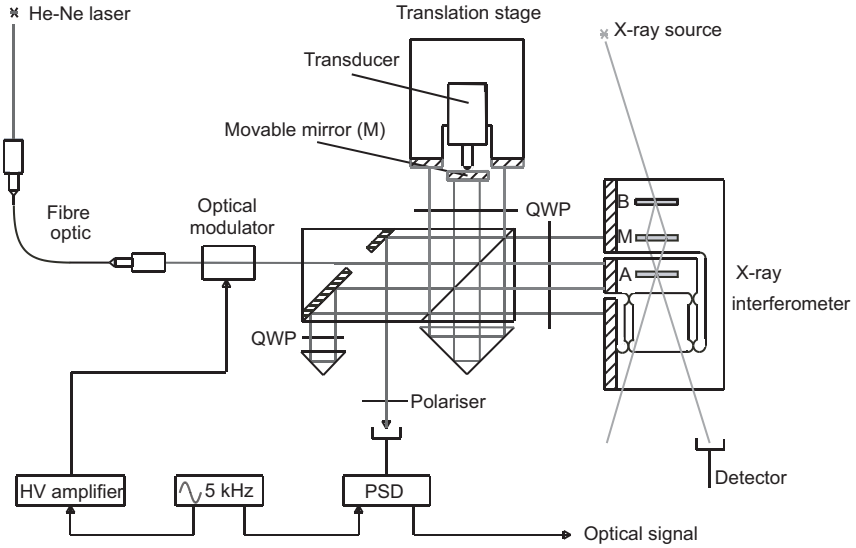

Fig. 3.4 Schematic diagram of COXI instrument. (QWP quarter wave plate, PSD phase sensitive detector).

optical or x-ray fringes, both of which are traceable. The transducer that is to be calibrated is referenced to the translation stage and its measured displacement is compared with the known displacements of the optical and the x-ray interferometer.

3.4 Measurement of Small Angles

Another interesting application of x-ray interferometry is the measurement of microradian angles with nanoradian resolution [15]. The monolithic x-ray interferometer used in this application had a somewhat different construction than that of the interferometer shown in Figure 3.2. The interferometer was skew symmetric with two 'M' Lamellae, one for each of the two beams diffracted by the first lamella. The flexure mechanism was such that the second two lamellae in the interferometer, i. e., one of the M lamellae and the analyzer (A) lamella could be rotated with respect to the first two lamellae. Calibration of the interferometer showed that one x-ray fringe corresponded to and angular rotation of about 10 nanoradians and the total range of the interferometer was 10 μradians.

3.5
X-ray Interferometry and Scanning Probe Microscopy

Since the x-ray interferometer is free from the nonlinearities associated with optical interferometry and its displacements are traceable to the metre it is an ideal translation stage for use with scanning probe microscopes. In one such configuration [16], a sample was placed on the moving component of the x-ray interferometer and a scanning tunneling microscope (STM) was placed above x-ray interferometer as shown in Figure 3.5. This configuration was used to measure the period of a 100 nm grating produced as a standard for SPMs and the period of an 80 nm grating. Similar work has been done using the COXI system in order to extend the scanning range. This time an atomic force microscope (AFM) was used instead of an STM. The grating under examination was placed on the optical interferometer translation stage and measurements of the grating period were made over a small range (up to 1 μm) by scanning the x-ray interferometer and simultaneously recording data with the AFM. A displacement was then made using the translation stage for the optical interferometer over a distance of several hundred micrometres followed by more measurements of the grating period using the x-ray interferometer and AFM [17]. Variations in the values of the local grating periods of a few nanometres were observed.

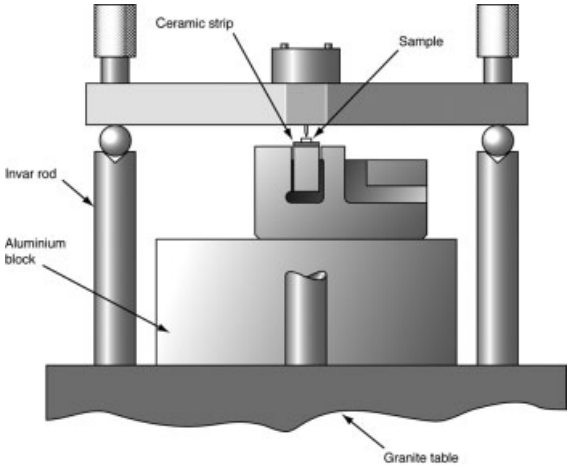

Fig. 3.5 Schematic diagram of scanning probe microscope combined with an x-ray interferometer. The STM sits on the three invar rods and is above the x-ray interferometer. Scanning direction is perpendicular to the plane of the paper.

3.6
Conclusions

X-ray interferometry offers the possibility of making traceable measurements at the sub-nanometre level and is free of the nonlinearities associated with optical interferometers. Since x-ray interferometry is a specialized technique requiring

extreme mechanical and thermal stability, it will probably remain mainly at national standards laboratories. However, its application allows the validation of other more conventional instruments that can be used in a wider variety of applications. With the increasing need to make dimensional measurements at the nanometre and sub-nanometre level, x-ray interferometry has a promising future.

References

1 U. Bonse and M. Hart, An x-ray interferometer, Appl. Phys. Lett. **6**, 155–156 (1965).

2 U. Bonse and M. Hart, Principles and design of Laue case x-ray interferometers, Z. Phys. **88** , 154–164 (1965b).

3 M. Hart, An Ångstrom ruler, Br. J. Appl. Phys. **1**, 1405–1408 (1968).

4 2000 Special issue on the 1998 CODATA internationally recommended values, Rev. Mod. Phys. **72.**

5 P. Seyfried, P. Becker, A. Kozdon, F. L. Èudicke, F. Spieweck, J. Stümpel, H. Wagenbreth„ D. Windisch, P. De Bi Áevre, H. H. Ku, L. Lenaers, T. J. Murphy, H. S. Peiser, S. Valkiers ‚A determination of the Avogadro constant, Z Phys., B **87**, 289–298 (1992).

6 D. Windisch and P. Becker, Silicon lattice parameters as an absolute scale of length for high precision measurements of fundamental constants, Phys. Status Solidi A **118**, 379–388 (1990).

7 J. Martin, U. Kuetgens, J. Stümpel, and P. Becker, The silicon lattice parameter – an invariant quantity of nature? Metrologia, **35**, 811–817 (1998).

8 N. Bobroff , Residual errors in laser interferometry from air turbulence and non-linearity, Appl. Optics **26**, 2676–2682 (1987).

9 A. Bergamin, G. Cavagnero, and G. Mana, Quantized positioning of x-ray interferometers, Rev. Sci. Instrum. **68**, 17–22 (1997).

10 A. Yacoot and M. J. Downs, The use of x-ray interferometry to investigate the linearity of the NPL differential plane mirror optical interferometer, Meas. Sci. Technol. **11**, 1126–1130 (2000).

11 A. Yacoot and C. Cross, Measurement of picometre non-linearity in an optical interferometer grating encoder using x-ray interferometry, Meas. Sci. Technol. **14**, 148–152 (2003).

12 P. L.M. Heydemann, Determination and correction of quadrature fringe measurement errors in interferometers, Appl. Opt. **20**, 3382–3384 (1981).

13 K. P. Birch, Optical fringe division with nanometric accuracy, Precis. Eng. **12**, 195–198 (1990).

14 G. Basile, P. Becker, A. Bergamin, G. Cavagnero, A. Franks, K. Jackson, U. Keutgens, G. Mana, E. W. Palmer, C. J. Robbie, M. Stedman, J. Stmpel, A. Yacoot, and G. Zosi, Combined optical and x-ray interferometer for high precision dimensional metrology, Proc. R. Soc. A **456**, 701–729 (2000).

15 U. Kuetgens and P. Becker, X-ray angle interferometry: a practical set-up for calibration in the microrad range with nanorad resolution, Meas. Sci. Technol. **9**, 1072–1075 (1998).

16 A. Yacoot, U. Kuetgens, L. Koenders, and T. Weimann, A combined scanning tunneling microscope and x-ray interferometer, Meas. Sci. Technol. **12**, 1660–1665 (2001).

17 A. Yacoot and L. Koenders, From nanometre to millimetre: a feasibility study of the combination of scanning probe microscopy and combined optical and x-ray interferometry, Meas. Sci. Technol. **14**, N59–N63 (2003).

Part II
Instrumentation – Long-range Scanning Probe Microscopes

Nanoscale Calibration Standards and Methods: Dimensional and Related Measurements in the Micro- and Nanometer Range.
Edited by Gunter Wilkening, Ludger Koenders
ISBN: 3-527-40502-X

4
Advances in Traceable Nanometrology with the Nanopositioning and Nanomeasuring Machine

Eberhard Manske, Rostislav Mastylo, Tino Hausotte, Norbert Hofmann, and Gerd Jäger

Abstract

Traceability at the nanometric scale is of significant importance for substantial progress in nanotechnology. At the Institute of Process Measurement and Sensor Technology of the TU Ilmenau, a nanopositioning and nanomeasuring machine (NPM machine) was developed, which achieves a measuring range up to 25 mm $\times$ 25 mm $\times$ 5 mm. The resolution of the three-dimensional laser-interferometric measurement is 0.1 nm and free from Abbe errors of first order in all axes. Design and operation of this NPM machine is described in this paper. Measurement results and opportunities of integration of both a high-precision focus probe and a scanning force sensor are presented as well.

4.1 Introduction

Current and future advanced technologies such as microelectronics, micromechanics, optics, molecular biology, and material engineering demand increasing ranges of motion, extreme precision, and high-positioning speeds. Nanopositioning and nanomeasuring machines (NPM machines) are technological means of positioning, measurement, scan, treatment and manipulation of objects with nanometer precision and can fullfill such demands for even smaller structures, being localized in increasingly large spatial areas.

According to the International Technology Roadmap for Semiconductors of 2003, the positioning ranges to be realized from 2010 to 2014 will cover an area of 450 mm $\times$ 450 mm. Furthermore, it will be necessary to measure and also to manufacture structure widths as small as about 35 nm with nanometer accuracy. Such extreme requirements are closely linked with technologies such as electron ray or X-ray lithography. However, also nanoimprinting lithography, which is a very promising new approach to the creation of nanostructures [1]

Nanoscale Calibration Standards and Methods: Dimensional and Related Measurements in the Micro- and Nanometer Range.
Edited by Gunter Wilkening, Ludger Koenders
ISBN: 3-527-40502-X

or self-organizing organic nanostructures, will also place great demands on measurement and positioning technology.

The following techniques and technologies are highly dependent on efficient measuring and positioning systems: mask and wafer inspection, circuit testing, large-area and high-speed scanning probe microscopy, genetic engineering, precision treatment and assembly, development and analysis of new materials, free-form surface characterization, and 3D-precision measurement of small parts (e. g., microlenses, microbenches, precision molds, and mechanical precision parts).

For a great number of scientific disciplines, mastering these new technologies and techniques means responding to enormous challenges. Also included are particularly the 3D-techniques for measuring and positioning objects and for sensing them. Only when these three components can meet highest demands and when they are optimally adapted to the positioning and measuring tasks, can the required new quality of measurement be achieved. Lastly, these measurement techniques require traceability at the nanometer scale over a large measurement range.

At the Institute of Process Measurement and Sensor Technology of the Technische Universität Ilmenau, an NPM machine (cf. Figure 4.4 and 4.10) with a positioning and measurement range of 25 mm × 25 mm × 5 mm, a resolution of 0.1 nm and positioning uncertainty of less than 10 nm has been developed and successfully tested [2], [3]. The outstanding precision has been obtained through the realization of the Abbe comparator principle in all the three measurement axes and applying a new concept for compensating systematic errors resulting from mechanical guide systems. These machines are manufactured by SIOS Messtechnik GmbH Ilmenau. Up to now, eight NPM machines have been built. They are operating successfully in several German and foreign research institutes.

4.2 Design and Operation

Conventional coordinate measuring machines realize three measurements in three perpendicular linear axes (cf. Figure 4.1). Eighteen axes (12 angular and 6 linear axes) are not considered or have to be calibrated. After calibration stochastic errors will especially influence the measurement uncertainty.

So called Abbe errors in two axes are cased by the large distances (a, b) between the axes of the measurement systems and the measurement point at the sample to be measured. These errors are calculated as follows:

$$\Delta l_x = a \cdot \sin \alpha \tag{4.1}$$

and

$$\Delta l_y = b \cdot \sin \beta \tag{4.2}$$

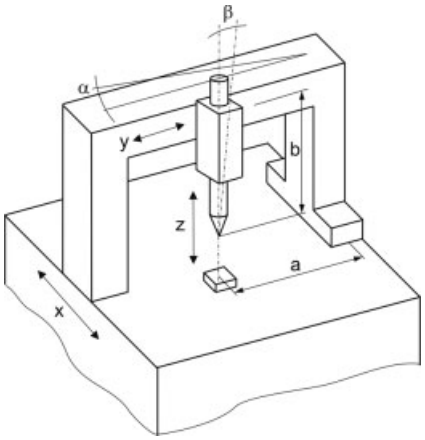

Fig. 4.1 Principle of a conventional CMM.

The small-scale coordinate measuring machine of NPL uses a six-axis heterodyne laser interferometer measurement system (Figure 4.2). The six interferometer axes measure the displacement and rotation of a set of three mutually orthogonal mirrors which are mounted on a frame, which itself is kinematically mounted on the *z*-axis of the commercial CMM [4].

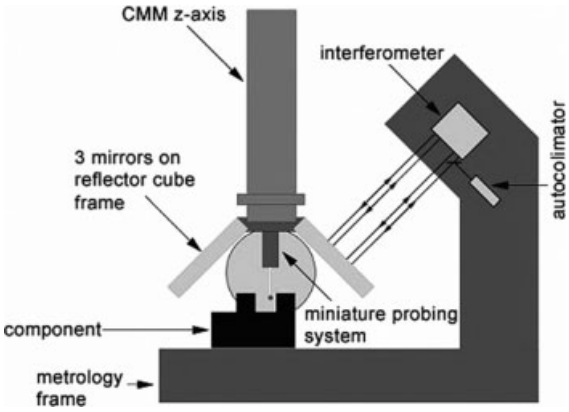

Fig. 4.2 Principle of the small-scale CMM of NPL.

The Abbe error occurs as well in two perpendicular axes by the same formulas (1) and (2). The advantages are:

- the amount of a and b is smaller than $\pm$ half of the measurement range
- the tilt (α and β) in both axes is measured.

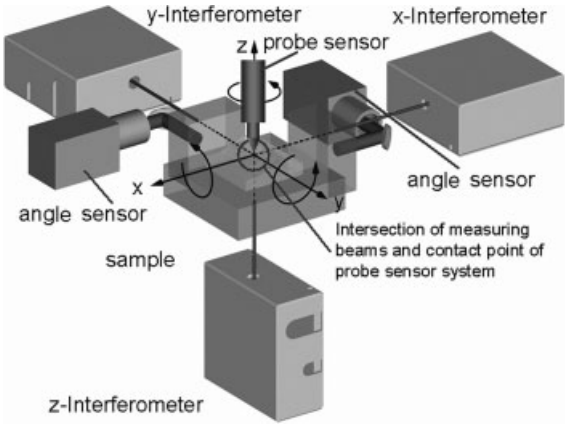

Fig. 4.3 Setup of an Abbe error free arrangement in three coordinates.

The approach of our NPM machine consists of a consequent realization of the Abbe comparator principle in all the three measurement axes at all times (Figure 4.3). This means that the axes of the three coordinates have to intersect together at the contact point of probe sensor system.

The essential advantage of the plane mirror interferometers, developed at the TU Ilmenau and produced for several years at SIOS Meßtechnik GmbH Ilmenau, is that only one laser beam on the mirror surface is used. All other known interferometers produce two laser spots on the mirror. Here, the measuring axis lies virtually in the middle of the two laser beams. In the SIOS interferometers, the measurement axis and the laser beam coincide ideally. Therefore, the intersection point can be determined by measurement means very precisely. Nevertheless, we have to assume a small eccentricity between the laser beam (representing the measuring axis) and probe tip (Figure 4.4).

A residual Abbe error is necessary a result of a slight tilt of the stage:

$$\Delta l = e \cdot \sin(\varphi) \tag{4.3}$$

In contrast to the arrangement of a conventional CMM and the SCMM the value e is much smaller than a and b (cf. formulas (1) and (2)) in the region of less than

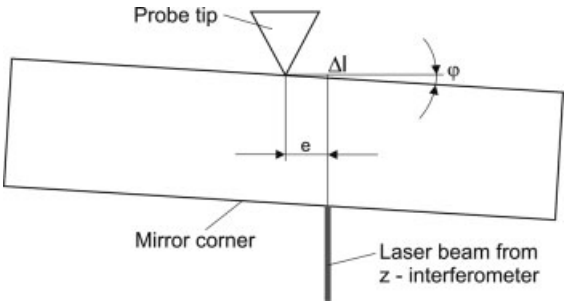

Fig. 4.4 Realization of the Abbe principle.

0.1 mm. To achieve an Abbe error of less than 1 nm, a tilt of less than 2 arcsec is allowed. This is a very difficult requirement for a positioning stage with a movement range of 25 mm. It can only be fulfilled with high-precision air bearings. In most cases such systems are very heavy. This leads to a worse dynamic behavior, a higher energy consumption and in the end to greater heat development.

Another disadvantage is the tendency of air bearings to vibrate in a range of 5 to 40 nm. Therefore, air bearings are less qualified for closed-loop operation to stabilize a positioning stage in one point with nanometer accuracy.

This leads to the use of ball bearing systems to minimize vibrations and weight – for the *x*- and *y*-axes one linear guiding system per axis; for the *z*-axis four cylindrical ball bearings. Precision ball bearings can achieve a tilt of < 30 arcsec. To eliminate the influence of this tilt it is necessary to extend the arrangement with two angular sensors (Figure 4.3) and correct this deviation by a closed-loop control with appropriate drive systems.

Therfore, fiber-coupled autocollimation sensors with a resolution of less than 0.001 arcsec were developed to measure tilt around all the three coordinate axes.

A number of different drive systems were investigated in the preliminary stages of the development of the NPM machine. Those drive systems should have a range of displacement of up to 25 mm and, at the same time, permit a positioning resolution of less than 1 nm. As conventional stepping and DC-motor drives do not achieve the required resolution, they were equipped with additional small-range precision actuators. Because of the permanent switching between coarse and fine positioning, it is not possible to achieve good dynamic behaviour.

Next, a number of piezoelectric stepping and vibration drives were investigated. Although those types of drives attain high displacement speeds of up to 300 mm/s, they do not provide the required resolution of 1 nm.

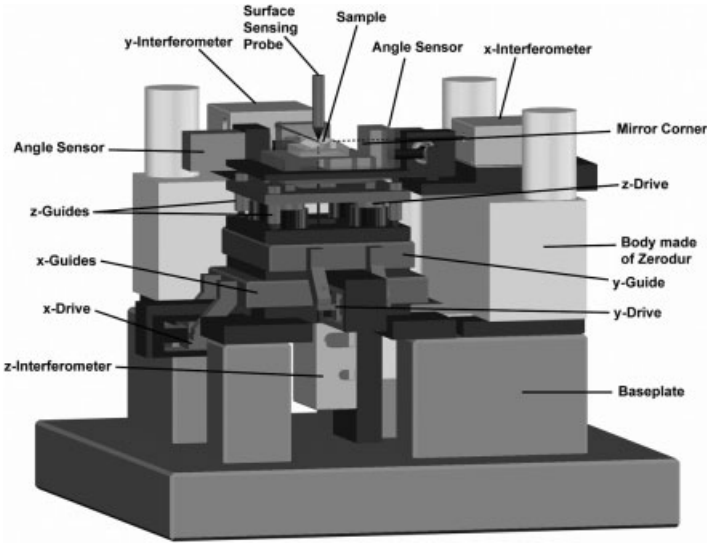

Fig. 4.5 Basic setup of the NPM machine.

For this reason, it was decided to employ electrodynamic drives in the NPM machine (cf. Figure. 4.3). These drives permit achieving displacement speeds of up to 50 mm/s within the entire positioning range and, at the same time, a positioning accuracy of 1 nm. As these drives are not self-locking, the permanent control of the position on the basis of the measurement values supplied by the interferometers is necessary. One drive system each has been employed for the x-axis and for the y-axis. The drive system of the z-axis consists of four individual drives, each of which is controlled individually. In this way, an influence also on the roll and pitch angles can be exerted. The uncertainty of the closed-loop control of these angles was determined to be < 0.05 arcsec.

The plane mirror interferometers of SIOS Messtechnik GmbH were improved to 0.1 nm resolution and upgraded with a symmetrical and thermally stable arrangement.

4.3 Uncertainty Budget

The next step was to estimate the uncertainty of the NPM machine. The contribution factors considered are described below:

- Wavelength of frequency stabilized He–Ne-Lasers
- Offset, amplitude, and phase deviations of analog interference signals (cyclic error)
- Quantization and rounding errors during demodulation of interference signals
- Uncertainty of reference coordinate system of the corner mirror
- Uncertainty of calculated refractive index of air
- Thermal expansion of metrology frame, interferometers and probe system
- Uncertainty of length by angular errors (Abbe offset and cosine errors)

Several measurement uncertainties have independent causes and can be summarized into a combined uncertainty of measurement:

$$u_c(l) = \sqrt{\sum_{i=1}^{7} (u_i(l))^2}$$

The combined uncertainty (without probe system) is 8 to 10 nm at the end of the measurement range.

The measurement arrangement is direct traceable to the laser wavelength of a stabilized He–Ne laser. Furthermore, the stabilized lasers of the NPM machine are attached to an iodine stabilized He–Ne laser in our institute, which is again attached to an iodine stabilized laser at the Physikalisch-Technische Bundesanstalt (PTB) Braunschweig by beat frequency measurement.

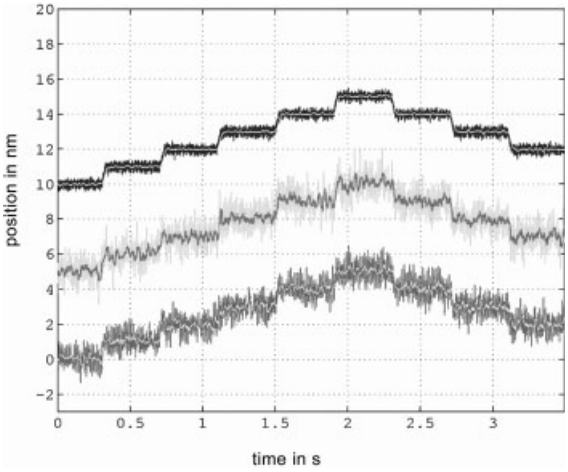

Fig. 4.6 Nanometer steps of the NPM machine.

The ability of the NPM machine to carry out nanometer steps was tested in all three axes (cf. Figure 4.6). The positioning noise in closed-loop operation is around 0.3 nm.

4.4 Focus Sensor

The most various sensor types can be used for scanning the samples. Compared with the mechanical scanning – for example by means of scanning force sensors – optical scanning presents several advantages. Therefore, an optical scanning sensor based on the autofocusing principle has been developed and integrated into the NPM machine.

The central part of the sensor is a so-called hologram laser unit (cf. Figure 4.7). It is comprised of a semiconductor laser diode (650 nm), the photodiodes for focusing error detection, and their pre-amplifiers. A small hologram arranged

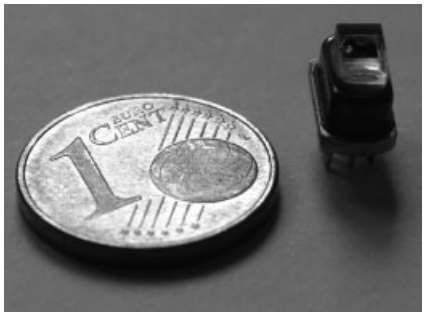

Fig. 4.7 Hologram Laser Unit.

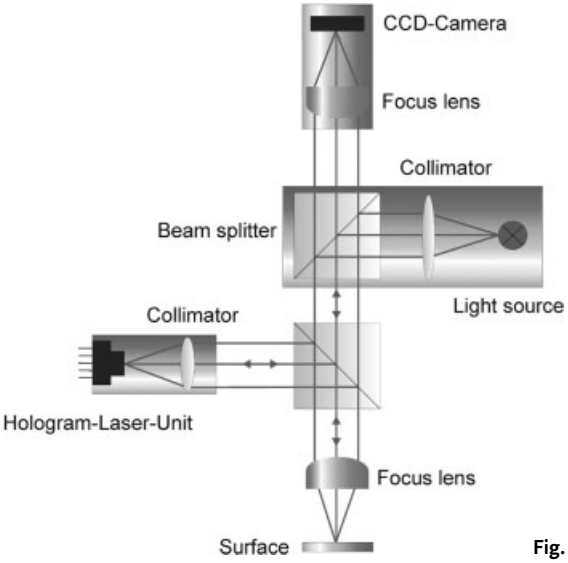

Fig. 4.8 Setup of focus sensor.

directly in front of the laser unit fulfills certain functions such as beam splitting, dividing and deflection. This multifunctional element has made the extreme miniaturization of the sensor possible.

The structure of the entire focus sensor is shown in Figure 4.8. The lateral resolution is about 0.8 μm. This is 30% better than conventional autofocus systems. The resolution depends on the laser wavelength and the focal aperture of the probe.

To be able to see the point of the optical scanning on the surface of the sample, the focus sensor has been combined with a CCD camera microscope, which allows the user to spot interesting regions on the sample surface and to find them repeatedly in a very comfortable manner.

The optical system has been dimensioned such that a measuring range of about $\pm$ 10 μm is achieved. Thus, a resolution of the zero point of $<$ 1 nm is made possible by the AD converter used.

The realized focus sensor (without microscope) is shown in Figure. 4.9, and the NPM machine with integrated focus sensor can be seen in Figure 4.10. The focus sensor is below the cover plate of the NPM machine and the microscope is above. The camera illumination is fed from an LED via optical fibrers so as to keep the heat penetration into the measuring machine minimal. The characteristics of the focus probe can be calibrated at any time using the laser interferometer of the NPM machine.

Five step-height standards from 7 nm to 780 nm were measured with the NPM machine in combination with the focus probe. The step-height standards have been calibrated at the PTB with an expanded uncertainty between 1 nm and 3.5 nm. The difference between the mean value measured by the PTB and our own results was less than $\pm$ 1.3 nm.

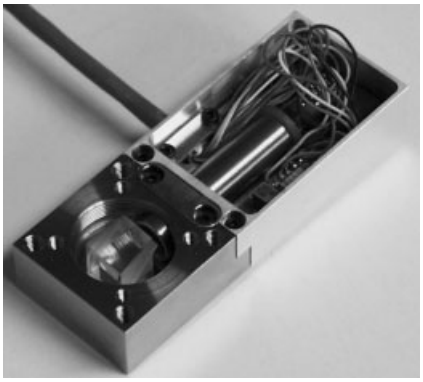

Fig. 4.9 Focus probe.

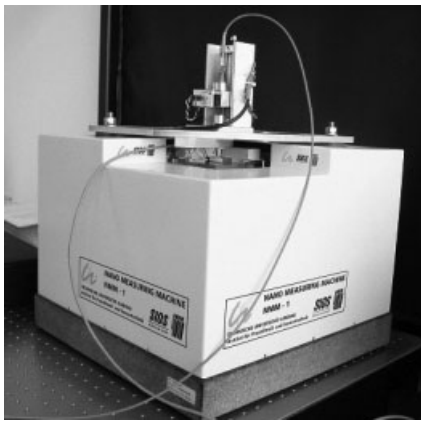

Fig. 4.10 NPM machine with focus probe.

Table 4.1 Comparison of step height measurements

Sample	PTB result H/(nm)	u/(nm)	TUI result H/(nm)	u/(nm)	Difference ΔH/(nm)
C26R18	7,4	1	7,8	0,7	0,4
C18R18	21,2	1,1	22,1	0,8	0,9
C17R27	69,1	1,2	68,4	0,8	–0,7
C19R26	294,2	2	294,7	1,1	0,5
C12R01	778,4	3,5	777,1	2	–1,3

4.5 Measuring Opportunities and Performance with Focus Sensor

The achievable scanning speed is of special interest with regard to large area scans. Scans with a velocity up to 500 μm/s have been carried out, without an observable increase of measurement uncertainty, which was about 0.8 nm. This provides the NPM machine with a large lateral scanning and measurement range of 25×25 mm^2 and a measurement height up to 5 mm with a resolution of 0.1 nm.

A large-area scan of a section of a rod lens in an area of 4×2 mm^2 with 160 000 data points was taken in 5 min (cf. Figure 4.11).

The focal probe has proven to be versatile in its opportunities for use. Different samples with varying geometric properties can be measured, for example, microlens arrays (cf. Figure 4.12), hardness indentations (cf. Figure 4.13) or harmonic drive gears (cf. Figure 4.14).

However, the lateral resolution is limited due to the spot size of the laser and diffraction effects.

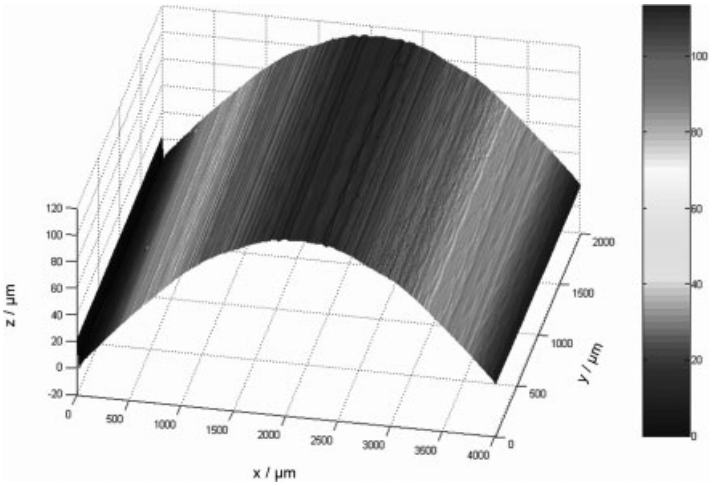

Fig. 4.11 Large area scan of a rod lens.

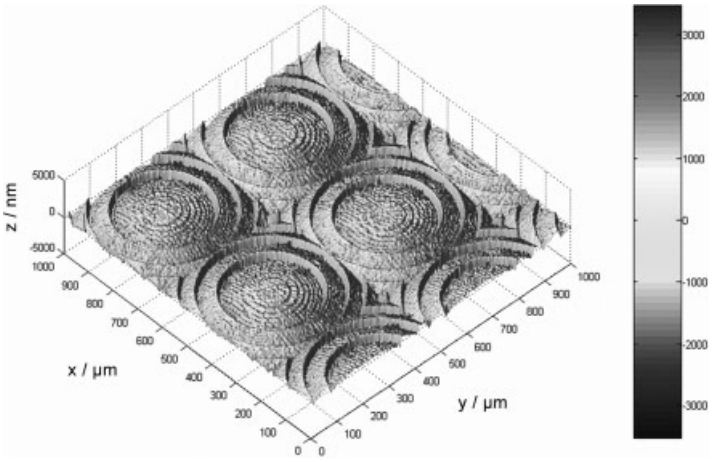

Fig. 4.12 Microlens array 1 × 1 mm^2.

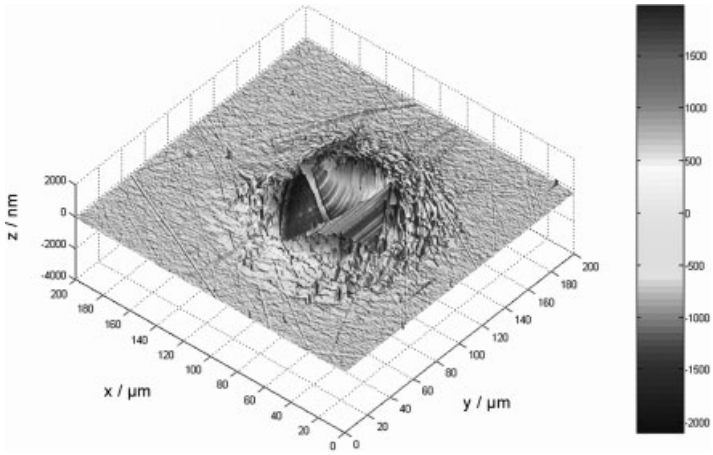

Fig. 4.13 Hardness indentation.

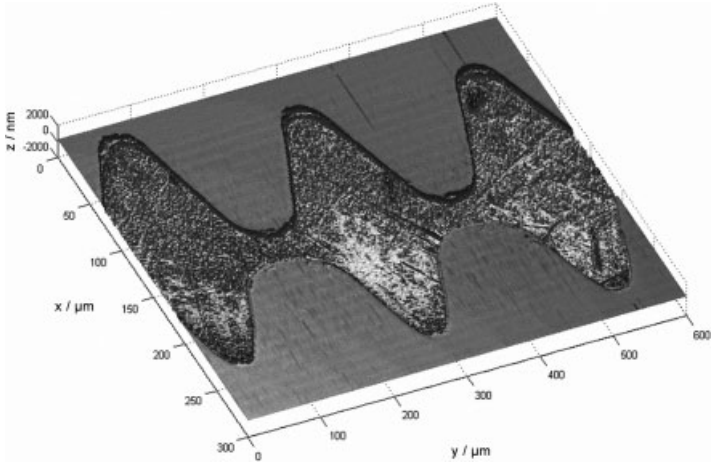

Fig. 4.14 Harmonic drive gear.

4.6
Focus Probe with SFM Cantilever

To improve the lateral resolution, a cantilever mount for the focus probe was designed. Therefore, the probe acts as a scanning force sensor. Due to an integrated piezotranslator, measurements in tapping mode as well as in contact mode are possible.

The 780 nm step height standard was measured once more (cf. Figure 4.15). An extended uncertainty of 0.4 nm ($k = 2$) was achieved. The deviation between the calibrated value by PTB and our own result was 0.64 nm. The scanning speed in tapping mode was 10 μm/s. Further improvements and the realization of accurate pitch measurements are among various planned investigations.

The opportunities of combination of several scanning force mircroscopes with the NPM machine such as large-area scanning without stitching (cf. Chapter 5) or high precision pitch and nanoroughness measurements (cf. Chapter 6) are also the object of further investigation in other research facilities.

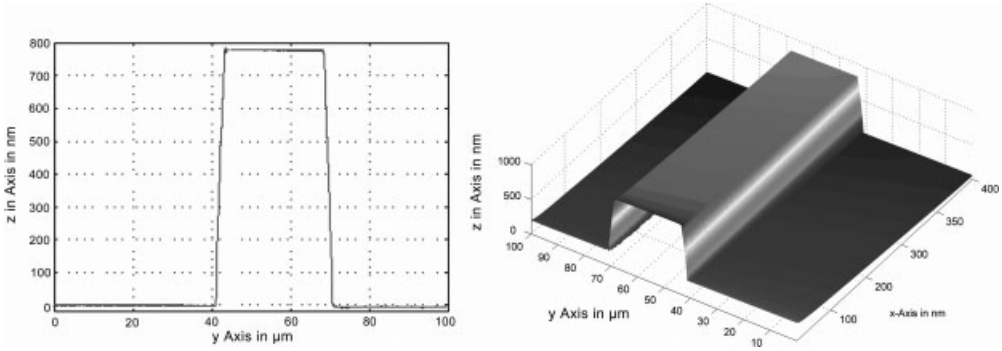

Fig. 4.15 Scan of a step height standard with SFM sensor.

4.7
Conclusion

In this document, an overview of a nanopositioning and nanomeasuring machine with a measurement range of 25 mm × 25 mm × 5 mm and a resolution of 0.1 nm in all measurement axes has been presented. The laser-interferometric measurement is free from Abbe errors of first order in all the three coordinates.

In combination with a focus probe, high-speed scanning up to 2 mm/s with uncertainties below 1 nm is possible. For scanning force microscopy the focus probe was supplemented with an SFM cantilever. Extended uncertainty of less than 1 nm was achieved in step height measurements.

Acknowledgements

The collaborative research centrer SFB 622 "Nanopositionier- und Nanomessmaschinen" is supported by the German Research Foundation (DFG) and the Thuringian Ministry of Science, Research and Arts. The authors wish to thank all those colleagues who have contributed to the developments described.

References

1 S. Zankoviych, T. Hoffmann, J. Seekamp, I. U. Bruch, and C. M. Sotomayor Torres, Nanoimprint lithography: challenges and prospects., Nanotechnology **12,** (2001). 91–95 (2001).

2 G. Jäger, E. Manske, and T. Hausotte, Nanomeasuring Machine., Invited Paper. MICRO. Ttec 2000., VDE World Microtechnologies Congress., Hannover., September 2000.

3 G. Jäger, E. Manske, T. Hausotte, H.-J. Büchner, R. Grünwald, and W. Schott, Nanomeasuring technology – nanomeasuring machine, in *The Sixteenth Annual Meeting, Crystal City, Arlington, Virgini*a (American Society for Precision Engineering, 10-15th November 2001), pp. 23–27.

4 G.N. Peggs, A.J. Lewis, and S. Oldfield, Design for a compact high-accuracy CMM, Ann. CIRP **48**, 417–420 (1999).

5
Coordinate Measurements in Microsystems by Using AFM-Probing: Problems and Solutions

Dorothee Hüser, Ralph Petersen, and Hendrik Rothe

Abstract

Facing the ongoing miniaturization in all fields of research, coordinate metrology needs alternative ways of positioning, probing, and measurement strategies. An instrument measuring in two and a half dimensions as any scanning probe microscope does and as well covering scan sizes of several millimeters without the necessity of stitching has been realized. A successful measurement of an area of 1000 μm × 100 μm on an electronics structure has been carried out with the prototype of the positioning system as presented in Manske et al.[1)] in combination with an atomic force microscope (AFM) head. Before an AFM head could be mounted onto the positioning system, the dynamic behavior of the system had been investigated. Measurements had been carried out, and in order to gain a deeper understanding simulations were performed in cooperation with the Institute for Mechatronics, Chemnitz.

5.1
Introduction

Traditional coordinate metrology has been developed in the field of production engineering concerning large engines. Work pieces of several ten or hundred millimeters are to be measured with a resolution of 1 or 10 μm. They are to be measure in full three dimensions. A direct miniaturization of those are instruments that use ball probes with diameters of 50 μm up to 100 μm. Such a probing sphere may either be fixed to a rigid silicon stylus [1–3], or connected to a fiber

1) Manske, R. Mastylo, T. Hausotte, N. Hofmann, and G. Jäger, Advances in traceable nanometrology with the nanopositioning and nanomeasuring machine, in *Proceedings of the 6th Seminar on Quantitative Microscopy and 2nd Seminar on Nanoscale Calibration Standards and Methods: Dimensional Measurements in the Micro- and Nanometer Range*, edited by K. Hasche, W. Mirandé, and G. Wilkening (Braunschweig 2004).

Nanoscale Calibration Standards and Methods: Dimensional and Related Measurements in the Micro- and Nanometer Range.
Edited by Gunter Wilkening, Ludger Koenders
ISBN: 3-527-40502-X

serving as wave guide to illuminate the sphere [4–6]. In the case of the rigid stylus, the deflection of that stylus is detected via a membrane. The alternative is detecting the sphere position with a camera system.

Many electronics systems and microsystems are produced in lithographic processes, therefore having two and a half dimensions. Their lateral size extends up to several millimeters with structure widths on the order of a hundred or several hundred nanometers. The vertical structures are not larger than a few micrometers and usually have heights of around 50 nm, 100 nm, or 250 nm. These are the objects typically inspected by optical systems working in the far field or in the case of investigating small areas in the near field by scanning probe microscopes, in particular tunneling, or atomic force microscopes. Nowadays a lot of work is being done with good success concentrating on the development for atomic force microscopy and as well on transducer development. The progress is very much pushed by microelectronics industry in the case of AFM and by mass storage system and wafer stepper industry in the case of transducers. The development in these fields promotes the development of CMMs of the microscopic world. There are two coordinate measuring machines worldwide covering a lateral measuring range of about 20 mm $\times$ 20 mm, resolving positions with 1.25 nm, showing a positioning uncertainty of a few ten nanometers without the necessity of stitching scans together. One of the CMMs has been developed in the USA in collaboration the University of North Carolina in Charlotte with the Massachusetts Institute of Technology MIT in Boston [8]. The other one is the German instrument presented in this chapter combining two OEM systems, a positioning system, and an atomic force microscope as probing system. The intention of the authors was to focus on measurement and calibration strategies rather than hardware development.

5.2 Realizing CMMs for Microsystems

The CMM regarded in this chapter employs a positioning system called Nanopositioning and Nanomeasuring Machine NMM. It has been developed in Ilmenau in cooperation of the University of Ilmenau and the company SIOS Messtechnik GmbH. The probe of the CMM is an AFM head developed by Surface Imaging Systems SIS GmbH, a company in Herzogenrath. The combination of these two systems has successfully been carried out after specific modifications have been made by the manufactures to prepare their systems for a CMM application (see Figures 5.1 and (5.2)).

The reason for choosing a modified *Ultra-Objectiv* of SIS is the fact that this AFM is a small, compact probing head. The Ultra-ObjectivE is as small as the lens system of a common optical microscope onto which it can easily be mounted. In order to be able to align the sample in the case of commercial Ultra-Objectives a lens system of the microscope's revolver is used and afterward the revolver is switched to the AFM head. For the CMM application SIS modified their AFM

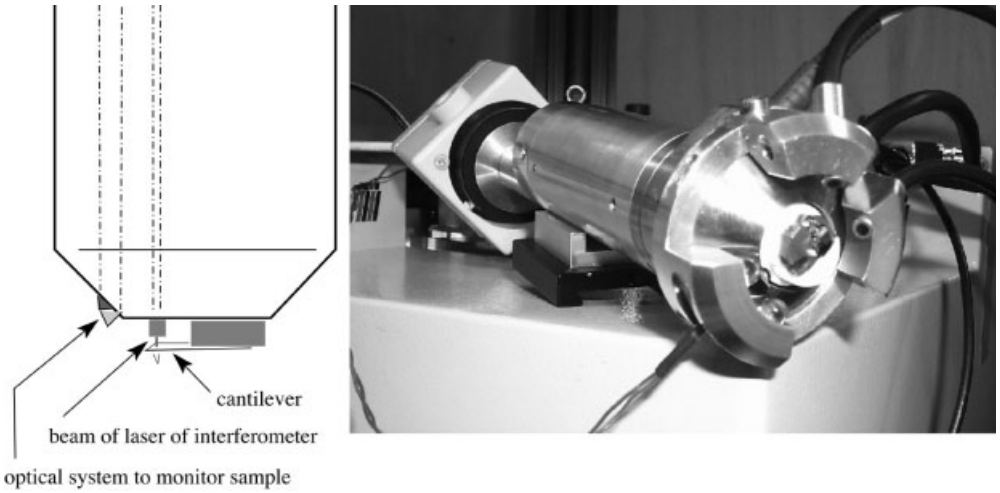

Fig. 5.1 An atomic microscope as probe head manufactured by Surface Imaging Systems SIS GmbH.

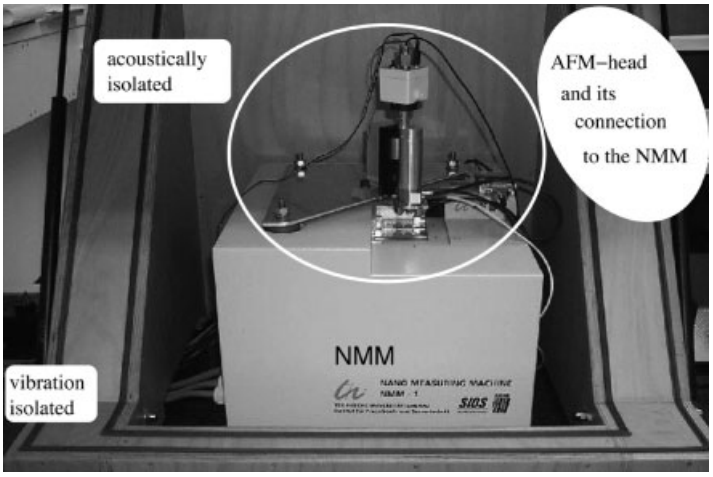

Fig. 5.2 The CMM for microsytems with a positioning system called Nanopositioning and Nanomeasuring Machine NMM developed in Ilmenau and the AFM head as probe.

in cooperation with Präzisionsoptik Gera GmbH, including a lens and camera system. This system has a cylindrical shape. It has a diameter of 35 mm and a length of approximately 120 mm. This AFM head includes no scanner for any lateral positioning since this job is done by the NMM. Its vertical axis is realized by a stack piezo driving up to 15 μm. The cantilever deflection is measured with a fiber optical laser interferometer.

The Ilmenau NMM is a universal ultra precision positioning stage designed for measuring and machining, i.e. one can mount a probe head to investigate a sample or one can mount a tool to perform manufacturing processes on a microsystem as work piece [8]. The advantage of the Ilmenau system is its kinematic design. By adjusting the probing point well the system measures without Abbe error. The NMM's control features were originally designed for singlepoint probing where the stage has to move quickly to a desired position without data taking, then slowly and precisely approaching the exact position and reading out the interferometer values. To prepare the system for the AFM head application the Ilmenau manufacturers included scanning features. Atomic force microscopes operate in a closed feedback loop after the sample and tip have been brought to the desired distance. The AFM control system drives the AFM piezo actuator following the topography of the sample such that either the tip deflection (in the case of contact mode) or the cantilever amplitude (in the case of oscillating mode) is kept constant. A scanner laterally moves either the sample or the tip with constant velocity and the elongation values of the piezo actuator are recorded as height distribution of the scanned profile.

The CMM application has been realized such that the vertical axis of the NMM is used to approach the sample to the tip until the AFM can operate in its feedback mode. For scanning, only the lateral axes of the NMM are involved and the vertical axis is supposed to keep its position constant. There are two reasons for not including the vertical NMM axis into the AFM feedback loop but using a piezo actuator, which has to carry nothing else than the cantilever and its tiny adapter piece. The vertical NMM axis is realized by four voice coils lifting a zerodur table of 800 g. Its movement is controlled via two sensors monitoring tilt errors and three position sensing interferometers. Since it is the third link of the kinematic chain, the zerodur table movement is influenced by the whole system. The piezo actuator, however, concentrates on just moving the cantilever to compensate for its deflection respectively its changing amplitude. It has far less weight and is not integrated in the complex control system of the whole positioning task of all slides. Therefore the piezo is able to react immediately. The second reason is that the positioning system and the AFM system are two independent products. The most simple interface then is to acquire a final probe head signal, which is the one proportional to the elongation of the piezo. This signal is fed to the DSP of the NMM. The DSP then reads out the AFM as well as the NMM sensors according to its internal triggering. All values are finally acquired by a data-taking computer via USB. The data-taking software is the NMM-CNC software manufactured by Zentrum für Bild- und Signalverarbeitung e.V. Ilmenau. The second reason that is based on the independent OEM products could easily be overcome by making a cooperation between manufacturers. Still the reason mentioned first has to be considered thoroughly.

5.3 Problems and Solutions

There are two principal problems accompanying the task to perform coordinate metrology on microsystems:

- the dynamic behavior of the whole system;
- the amount of data coming up with very large scans and high resolution.

The features playing the central role with regard to system dynamics are the shape of the acceleration trajectory and the choice of the controller parameters. To get an idea of the amount of data that can arise a scanned area of 1 mm × 0.1 mm and a scanning interval of 100 nm shall be regarded. This yields 10 000 × 1000 = 10^7 sampling points. If four coordinates, three of the NMM and one of the AFM, are recorded with 8 byte data resolution and if each scan line is taken in trace and retrace, then more than 610 MB have to be stored.

At first, theoretical evaluations in the form of computer simulations had been carried out to better understand which dynamical behavior can be expected from the positioning system moving masses of up to 4 kg. Before operating the positioning device with the AFM, experiments had been carried out to see the NMM performance using various acceleration limits and velocities [9]. Also the AFM was tested on a separate stage using a two-axis piezo translator to move the sample. The NMM and AFM have then been combined with interactively giving the commands to move the table in small steps in order to make a tip approach and thereafter measuring with scanning speeds of 80–100 μm/s. As first successful measurement of an area larger than a standard AFM can make it possible, an area of 200 μm × 200 μm was scanned [10]. An area of 1 mm × 0.1 mm with 100 nm step width has been scanned within 12 h [11]. Strategies have been designed to handle sample sizes of several millimeters and to investigate structures in steps of a few nanometers by selecting different regions with appropriate resolutions.

5.3.1 Dynamics of Positioning System

In principle, the dynamics may be described with mechanical differential equations, with differential equations representing the electrical part according to Kirchhoff's law and the equation representing the controller system. Approximating roughly the system with point masses, one can write

$$m\frac{\partial^2 x(t)}{\partial t^2} + k\frac{\partial x(t)}{\partial t} + cx(t) = k_M I(t) \tag{5.1}$$

with m = mass, k = damping factor, c = spring constant for a system obeying Hooke's law, and I = coil current. The coupling voice coil is the coupling of the electrical and mechanical part of the system, with the factor k_M being a function

of the position of the coil with respect to its core, i.e., it is a function of the transducer position x. In the case of the vertical axis, the slide has to be levitated in the field of earth's gravity:

$$m\frac{\partial^2 z(t)}{\partial t^2} + k\frac{\partial z(t)}{\partial t} + cz(t) = k_M I(t) - mg \tag{5.2}$$

Kirchhoff's law yields

$$RI(t) + L\frac{\partial I(t)}{\partial t} + k_M\frac{\partial x(t)}{\partial t} = U(t) \tag{5.3}$$

for the transducer and

$$U(t) = k_P\Delta(t) + k_I\int \Delta(t)\mathrm{d}t + k_D\frac{\partial \Delta(t)}{\partial t} \tag{5.4}$$

for the controller, which is equivalent to

$$\frac{\partial U(t)}{\partial t} = k_P\frac{\partial \Delta(t)}{\partial t} + k_I\Delta(t) + k_D\frac{\partial^2 \Delta(t)}{\partial t^2} \tag{5.5}$$

with R = Ohm's resistance, L = inductance of the coil, U = voltage, Δ = difference between the set and actual position and k_P, k_I, k_D for the gain factors of the PID-controller.

To simulate the positioning system as electromechanical multi body system in more detail in order to gain an insight into its performance influenced by parameters such as the friction of the bearings and the moments of inertia of the slides a numeric solver for all differential equations and all constraints has been applied. ALASKA, a software developed by the Institute of Mechatronics, Chemnitz, has been chosen for the evaluations. The name means **a**dvanced **la**grangian **s**olver in **k**inetic **a**nalysis. This software tool does not only carry out the calculations, but also supports the model design and makes it possible to export source code of the model equations that can be transfered to other computer systems.

The goal is to optimize the controller parameters of the positioning system such that no overshooting might damage the tip when a tip approach is made and that scans are possible with constant velocity and on straight lines. The gain factors k_P, k_I, k_D shall be optimized by minimizing the error functions e_0, e_1 defined by the difference between the desired and actual position Δ and the maximum overshooting:

$$J(k_P, k_I, k_D) = \mu_0 e_0(k_P, k_I, k_D) + \mu_1 e_1(k_P, k_I, k_D) \rightarrow \min \tag{5.6}$$

with μ_i = weight factors and e_i = error functions:

$$e_0(k_P, k_I, k_D) = \max_{t\in[0,T]}(\mid z(T) - z(t) \mid) \quad \text{and} \quad e_1(k_P, k_I, k_D) = \frac{1}{T}\int_0^T \vec{\Delta}^T\vec{\Delta} \tag{5.7}$$

The model equations exported from ALASKA have been used for the optimization evaluations on parallel computers at Edinburgh Parallel Computing Centre and at Helmut Schmidt University Hamburg [12]. Both relevant procedures, the "tip approach" and the "scanning mode", have been simulated. Figures 5.3 and 5.4 show the simulation results with the original values of k_P, k_I, k_D in comparison with the simulated path of the slides with optimized controller gain values.

Besides optimizing gain factors of all controller systems, the system of the NMM and that of the AFM, the trajectory needs to be chosen in such a way that position and velocity curves are continuous to avoid high frequency signals in the system's response. Figure 5.5 shows the trajectories in principle as well as the resulting position curve at the border of a scan line deviating from an ideal straight line. Since the NMM records the positions very precisely with a resolution of 1.25 nm the correct geometric information has to be included in data analysis.

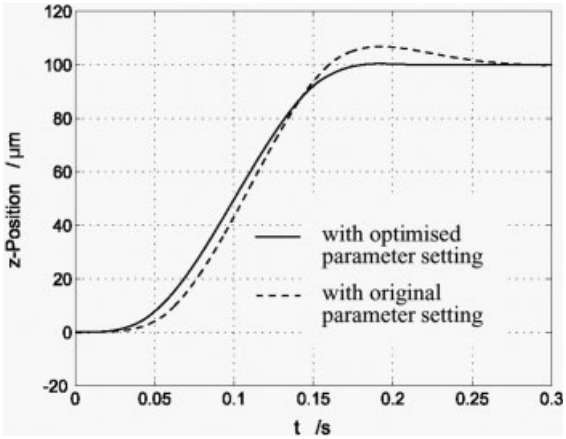

Fig. 5.3 Tip approach simulation before and after optimization of controller parameters.

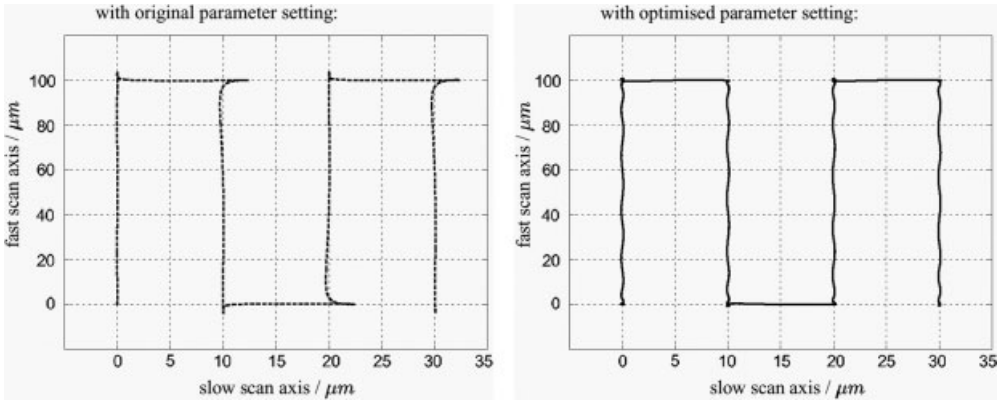

Fig. 5.4 Simulation of a scan before and after optimization of controller parameters.

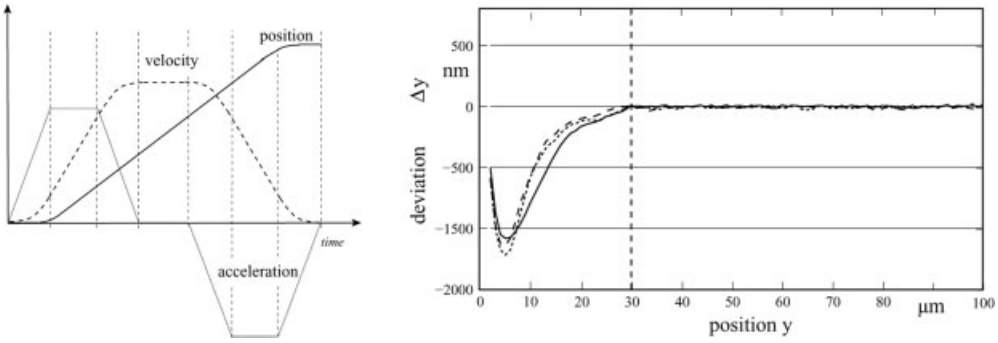

Fig. 5.5 Left: Trajectories in principle; right: position curve at the border of a scan line.

5.3.2
CMM: One-Millimeter Scan

Experiences with common commercial AFM performance have been helpful for bringing the CMM with AFM head to operation. In particular, experiences with the controller parameters, which are adjusted online for each sample resp. scan, have been fruitful for the development of the CMM. The criterion the user looks at is to compare trace and retrace of the same scan line. The profiles have to be the same. The adjustment does not only involve the controller gain factors but also the cantilever amplitude resp. deflection set point and the scanning speed. The feedback loop system very sensitively reacts at too high scanning speeds by causing instabilities. Velocities of around 50–200 μm/s, depending on the profile structure, give a safe, stable measurement. Up to 1000 μm/s might as well be possible. For scanning an area of 1 mm × 0.1 mm with the coordinate measuring machine for microsystems following limits of velocity, acceleration, and jerk were set for the trajectory generation [13]:

$$v_{\max} = 100\,\mu\mathrm{m/s},$$

$$a_{\max} = 100\,\mu\mathrm{m/s}^2,$$

$$j_{\max} = 1000\,\mu\mathrm{m/s}^3.$$

The whole procedure took 12 h. The CMM has been isolated from oscillations of the building and other environmental influences by placing it on a table standing on passive pneumatically isolating cylinders and placing it in an acoustically isolating box. The advantage of this box is that it does not only isolate sound but also the air flow from air conditioning. On the other hand, it as well isolates temperature so that the electronics and the motors inside heat up the system. After 12 h running temperature increased by 3 K. A known problem even with commercial well-tested AFMs and with measurements of around half an hour are controller instabilities that may cause bankrupt scan lines. This has also been the case with-

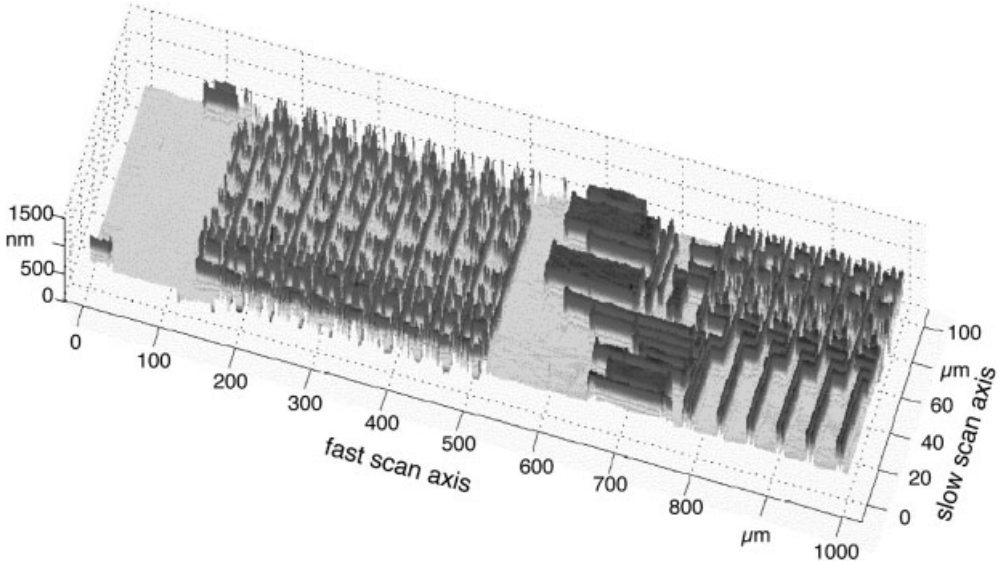

Fig. 5.6 The worldwide first 1-mm scan without stitching; with area: 1000 μm × 100 μm, sampling interval: 0.1 μm, duration of measurement: 12 h.

in the 12 h run. It may be stated that none of the instabilities increased such that the measurement had to be stopped and that the vast majority of data taken till the very end precisely show the topography of the sample and that the whole measurement could be successfully analyzed. Figures 5.6 and 5.7 show the whole scan. The tremendous lateral resolution of course cannot be made visible when displaying the scan in total. Therefore certain areas may be zoomed in to view them with different levels of detail. In particular, those data are selected that are used for further processing, such as edge detection, contour tracking, and geometry fitting [14]. Figure 5.8 shows cross sections of selected structures of the 1-mm scan to which edge finding algorithms may well be applied.

5.3.3 Measuring Strategies

Measuring strategies have to be designed with view to the results that are aimed at. In coordinate metrology the desired results are geometry parameters of the structures to be examined. In the case of, for instance, lithographically manufactured structures the geometrical shapes are two dimensional. They are mainly circles, elliptic bows, or straight lines for bars or polygons. The contours defining these shapes arise from edges separating two different height levels of, for example, silicon or chromium structures. Therefore data have to be taken in such a way that contours can be followed. To find one contour point a line perpendicular to the contour has to be scanned to which an edge detection algorithm can be

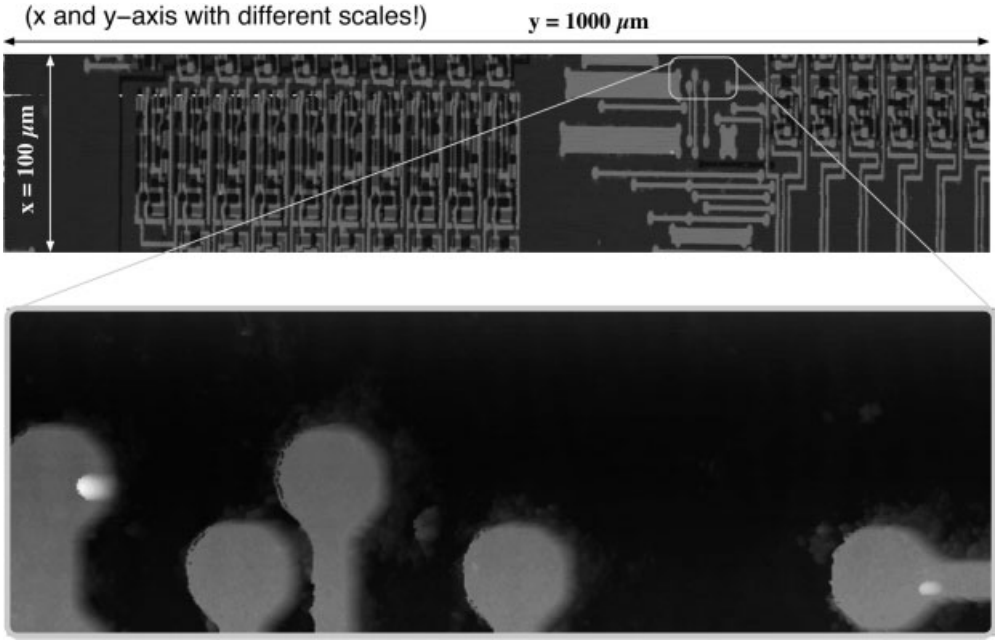

Fig. 5.7 The one 1-mm scan measured with a lateral resolution of 100 nm has to be analyzed with respect to different levels of detail.

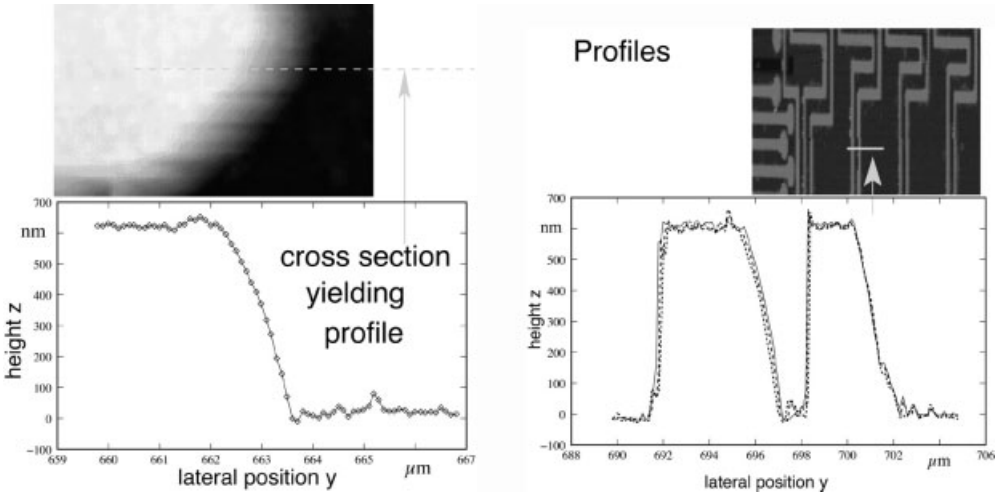

Fig. 5.8 Cross sections of selected structures of the 1-mm scan.

applied. Small structures may therefore be selected and scanned in a squared area with a grid of equidistant data points. This is exactly the procedure any scanning probe microscope performs. The decisive difference, however, is the ability of selecting a variety of such areas without any overlap and stitching, because the CMM keeps the metrologically correct relative positions of all areas. All scans are carried out within the same metrological frame. Furthermore, single straight lines that are much longer than 70–100 μm, which are common for piezo scanners of SPM, may easily be scanned with a CMM. One may, for example, investigate long bars on a structure by choosing several cross sections to obtain a set of contour points approximating the bar as indicated in Figure 5.9. Scanning across one bar each cross section yields two edges resulting in two contour points. One cross section represents a scan line with a sampling interval of a few nanometers, whereas the distance between such scan lines may be a tenth of a micrometer or even several micrometers.

Besides geometrical dimensions, roughness parameters of an object may as well be the focus of interest. So two-dimensional rms values may be evaluated from area scans or one-dimensional from single scan lines after considering the appropriate bandwidth [15–17]. Roughness as surface characterizing parameter very sensitively reacts on contamination, surface figures such as bows or waviness, and on measurement artifacts due to controller or piezo instabilities. The larger the chosen area the greater the contribution of surface figure. If data are not taken in sufficiently high resolution the measurement acts as low pass filter. The resolution is of greater importance if roughness parameters are regarded that do not just use the height values but also their dependence on

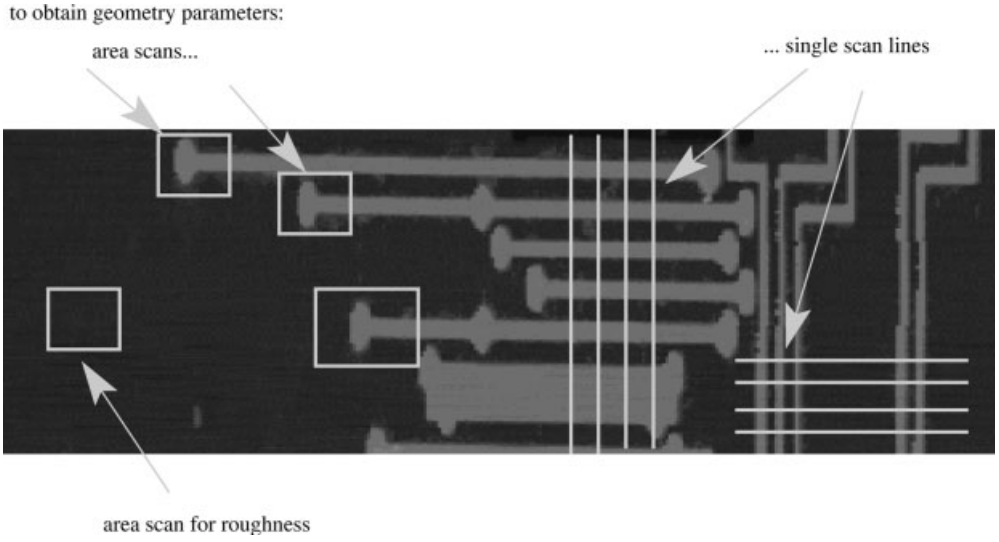

Fig. 5.9 Selecting specific areas or scan lines on a large structure with appropriate lateral resolutions.

the lateral position. Roughness parameters including the height distributions as a function of the lateral position are covariant and fractal in dimension.

Well-designed measuring strategies shall deliver a data set with all numbers necessary to process the desired parameters and no flood of redundant data just filling mass storage systems.

5.4 Conclusion and Outlook

This chapter has shown that it is possible to realize a coordinate measuring machine with an AFM for probing to scan along a millimeter with a step width of hundred nanometers. Problems with controlling the positioning slides as well as the probing AFM system have been discussed. They have been overcome by selecting the controller gain factors appropriately and in particular by taking care of scanning slow enough to give the AFM controller the chance to follow and fast enough to finish the measurement in a realistic time interval. Not only the scanning speed but also the acceleration and jerk have been limited such that the scan could be performed with sufficiently straight and stable scan lines. Finally, it has been pointed out that the choice of measurement strategies determines whether the data stream is manageable in a reasonable manner.

The successful realization of a prototype in a laboratory gives a promising view to CMMs for industry. Industrial application then demands for further developments of

- a sample holder,
- a safe and stable procedure for tip approach,
- user friendly CNC programming, and
- a data acquisition with checking of erroneous scanning.

The CNC software provided with the Ilmenau NMM is a comfortable script language enabling the user to control various probing, driving, and scanning procedures of the universal device that can employ all kinds of probe heads or machining tools. An industrial CNC programming for a CMM with AFM head will be specialized on that task. It will include the control of the AFM as well as the positioner in such a way that routine work may be carried out with it. Processes such as setting controller gain factors, performing a tip approach and changing a tip will be supported and automated by software and hardware. Safety mechanisms that protect the systems from damage are needed. Soon probing facilities will be a means for easily inspecting microsystems and electronics chips.

References

1 U. Brand, T. Kleine-Besten, and H. Schwenke, Development of a special CMM for dimensional metrology on microsystem components, in *ASPE Confonference, Scottsdale, AZ, USA, 22th-27th Oct. 2000*, pp. 542–546.

2 S. Bütefisch, S. Büttgenbach, T. Kleine-Besten, and U. Brand, Silicon three-axial tactile sensor for micromaterial characterization, J. Micro Syst. Technol. (2000).

3 P. Schellekens, 3D probe, CIRP Ann. **1** (50), 365–368 (2001).

4 E. Trapet (Inventor) and W. Messtechnik GmbH (Announcer), Taster zur Messung geometrischer Strukturen, German Patent: DE 197 24 739 A 1, 1998.

5 H. Schwenke, C. Weiskirch, and H. Kunzmann, Opto-taktiler Sensor für die 2D- und 3D-Messung kleiner Strukturen auf Koordinatenmegeräten, Technisches Messen **12** (1999).

6 K. Takamasu, M. Hiraki, K. Enami, and S. Ozono, Development of nano-CMM and parallel-CMM – CMM in the 21st century, in *International Dimensional Metrology Workshop, Tennessee, USA, May 1999*.

7 M. Holmes, R. Hocken, and D. Trumper, The long-range scanning stage: a novel platform for scanning-probe microscopy, *Precision Eng.* **24**, 191–209 (2000).

8 T. Hausotte, Nanopositionier- und Nanomessmaschine, Verlag ISLE, Diss., TU Ilmenau, 2002.

9 H. Rothe, D. Hüser, and R. Petersen, Simulation of the dynamic behaviour of a nanometer coordinate measuring machine, in *Proceedings of the 4th Seminar on Quantitative Microscopy: Dimensional Measurements in the Micro- and Nanometer Range*, PTB-Bericht, vol. PTB-F-39, edited by K. Hasche, W. Mirandé, and G. Wilkening, 2000.

10 R. Petersen, H. Rothe, and D. Hüser, Large area AFM-scans with the nanometer coordinate measuring machine, in *Proceedings of the 5th Seminar on Quantitative Microscopy: Dimensional Measurements in the Micro- and Nanometer Range*, PTB-Bericht, vol. PTB-F-44, edited by K. Hasche, W. Mirandé, and G. Wilkening (Bergisch Gladbach, Nov. 2001).

11 R. Petersen and H. Rothe, One way to accomplish the advanced requests of nanometrology: the nanometer coordinate measuring machine (NCMM), in *Advanced Characterization Techniques for Optics, Semiconductor, and Nanotechnologies*, Proc. SP/E, no. 5188–29, edited by A. Duparré and B. Singh, 2003.

12 A. Müller and H. Rothe, Optimization of controller parameter of a coordinate measuring machine, in *6th US National Congress on Computational Mechanics (USNCCM), Dearborn, Detroit*, August 2001.

13 R. Petersen, Theoretische und experimentelle Untersuchungen zur Koordinatenmesstechnik in der Nanometrologie, Shaker Verlag, Diss., Universität der Bundeswehr Hamburg, 2003.

14 D. Hüser, H. Rothe, and R. Petersen, Recognizing objects in dimensional micro-metrology, in *Proceedings of the 4th Seminar on Quantitative Microscopy: Dimensional Measurements in the Micro- and Nanometer Range*, PTB-Bericht, vol. PTB-F-39, edited by K. Hasche, W. Mirandé, and G. Wilkening, 2000.

15 D. Hüser and H. Rothe, Methods to recognize artefacts of AFM measurements as instrumental errors, in *Proceedings of the 3rd Seminar on Quantitative Microscopy: Geometrical Measurements in the Micro- and Nanometer Range with Far and Near Field Methods*, PTB-Bericht, no. PTB-F-34, edited by K. Hasche, W. Mirandé, and G. Wilkening, 1998.

16 H. Rothe, D. Hüser, A. Kasper, and T. Rinder, Investigations of smooth surfaces by measuring the BRDF with a stray light sensor in comparison with PSD curves evaluated from topography of large AFM scans, in *Surface Characterization for Computer Disks, Wafers, and Flat Panel Displays*, Proc. SPIE, no. 3619, edited by J. C. Stover, 1990.

17 D. Hüser and H. Rothe, AFM data analysis: separating surface microtopography from instrumental artifacts, in *Scattering and Surface Roughness III*, Proc. SPIE, no. 4100–20, edited by Z.-H. Gu and A. Maradudin, 2000.

6
Metrological Large Range Scanning Force Microscope Applicable for Traceable Calibration of Surface Textures

Gaoliang Dai, Frank Pohlenz, Hans-Ulrich Danzebrink, Min Xu, Klaus Hasche, Günter Wilkening

Abstract

PTB has set up a metrological large range scanning force microscope (LR-SFM) aiming for versatile traceable calibration of surface textures. The instrument is designed based on scanning sample principle with a fixed SFM head presently working in contact mode. Several special design aspects are carefully implemented in this instrument in order to enhance its performance: (1) A dual-stage positioning system is designed to scan samples. This dual-stage system consists of a stacked ball bearing mechanical stage, referred to as a nano measuring machine (NMM), and a compact *z*-axis piezoelectric positioning stage (compact *z*-stage). During measurements the compact *z*-stage, with its high mechanical resonance frequency (> 20 kHz), is responsible for the rapid motion while the NMM simultaneously makes slower movements over a larger motion range. In such a way, the LR-SFM can make measurements with both a high measurement speed (up to 50 μm/s) and a large measurement volume (25 mm $\times$ 25 mm $\times$ 5 mm along the *x*-, *y*-, and *z*-directions). (2) The design obeys the Abbe principle. The Abbe error, which is a dominant error source in most precision dimensional measurement instruments, is reduced to a minimum. (3) The direct traceability of the instrument is achieved by using interferometric position measurements. (4) Flexible measurement strategies are implemented in the software and hardware. The LR-SFM is able to perform large area imaging or profile scanning directly without stitching small scanned images. Selected measurement results obtained on a 2D grating and on a microroughness standard are presented.

Nanoscale Calibration Standards and Methods: Dimensional and Related Measurements in the Micro- and Nanometer Range.
Edited by Gunter Wilkening, Ludger Koenders
ISBN: 3-527-40502-X

6.1 Introduction

Scanning probe techniques have been rapidly developed since the invention of the scanning tunneling microscope in 1982 and the scanning force microscope (SFM) in 1986. At present, a large family of scanning probe microscopes (SPMs) is widely used for measuring surface textures. Compared to stylus and optical methods, the advantage of SPMs is that they are able to measure surfaces with both a very high vertical resolution (down to sub nanometer) and a high lateral resolution (<10 nm). In contrast, optical methods have limited lateral resolution due to the diffraction limit of light, whereas stylus methods have limited spatial resolution due to the large radius of the stylus tip (typically 2–5 μm). Additionally, scanning force microscopy methods are able to measure surfaces in a number of modes: contact, intermittent-contact, and noncontact. The force between the tip and the sample is low during the SFM measurement and, even in contact mode, reaches only a few nano-Newtons. This fact prevents scratching of the measured surface during SFM scanning procedure. In contrast, stylus profilers may cause scratches on soft material surfaces.

In the field of SPM techniques, some important aspects need further studies:

- *The calibration of SPMs*. Presently, most SPMs use capacitive sensors, linear variable differential transducers (LVDT), or strain gauges as position sensors [1]. These sensors have to be calibrated before they are capable of providing metrological values. This fact also holds true for other kinds of topography measurement instruments where the results cannot be traced directly to the meter definition, e. g., stylus profilers using either capacitive or inductive sensors as position sensors. For calibration purpose, some metrological SPMs are set up in some national metrology institutes worldwide [2–8]. They feature optical interferometers and thus enable their measurement results to be traced to the meter definition. These state-of-the-art metrological SPMs are able to measure micro- and nanostructures with nanometer or even subnanometer uncertainties. They make it possible to deliver precisely calibrated step-height and lateral standards for the subsequent calibration of other topography measurement instruments.
- *The limited scan speed*. Currently available SPMs have a relatively slow scan speed (typically < 20 μm/s), far less than that of stylus profilometers or optical methods. The bottlenecks are the limited dynamic properties of the servo control (especially along the *z*-axis) and the SFM tip wear.
- The limited scanning range, typically < 100 μm. This fact, which is mainly due to the mechanical structure of scanners and the properties of the piezoactuators, has limited the further application of SPMs, e. g., in the field of roughness measurements.

In order to expand the capabilities and applications of SFMs, the PTB has developed a new metrological large range scanning force microscope (LR-SFM). The instrument is capable of a measurement volume of 25 mm × 25 mm × 5 mm (*x*, *y*, and *z*). This chapter introduces the instrumentation as well as some selected measurement results in detail.

6.2 Instrumentation

6.2.1 Principle

The principle sketch of the LR-SFM is shown in Figure 6.1. It is a scanning sample system with a fixed SFM head working in contact mode. Unlike other commercial SFMs where a flexure-hinge stage is often used for moving samples, the LR-SFM described here moves samples using a novel dual-stage positioning system. This dual-stage system consists of a stacked ball bearing mechanical stage, referred to as a nano measuring machine (NMM) [9, 10], with a motion range of 25 mm × 25 mm × 5 mm along the *x*-, *y*-, and *z*-axes, and a compact *z*-axis piezoelectric positioning stage (compact *z*-stage) [11] with an extension range of 2 μm. The sample is magnetically coupled to the compact *z*-stage, which is in turn mechanically fixed on the NMM.

During operation, the sample is laterally scanned solely by the NMM. In the *z*-direction the sample is moved to keep the bending of the SFM cantilever at a constant value. Topographical information can thus be derived from the measured *z*-position of the sample. As one important feature of the instrument, the *z*-motion of the sample is achieved as a combined motion of the compact *z*-stage and the NMM by using a dual layer controller. This dual layer controller consists of a fast and a slow servo controller. The fast controller keeps the bending of the SFM cantilever at the constant set point value (S_0 in Figure 6.1) by moving the sample along the *z*-axis using the compact *z*-stage. The application of this fast servo control loop is aimed at enhancing the measurement speed, as the compact *z*-stage is specially designed and has a high mechanical resonance frequency larger than 20 kHz. The extension of the compact stage is measured by a capacitive sensor embedded in it. This extension of the compact *z*-stage is compared to a defined home position (S_1 in Figure 6.1) and yields a NMM motion target signal (S_3 in Figure 6.1). The S_3 signal is handled by the slow servo controller executed in the NMM controller to move the whole compact stage together with the sample along the *z*-axis. This slow servo controller is used to enlarge the measurement range, as the total motion of the sample is the sum of the motions from both the NMM and the compact *z*-stage. Since both servo controllers are executed in parallel, the slow servo controller will not limit the dynamic performance of the overall system. Therefore, by using this dual layer controller, both a large measurement range and a high measurement speed can be achieved. High scanning speeds

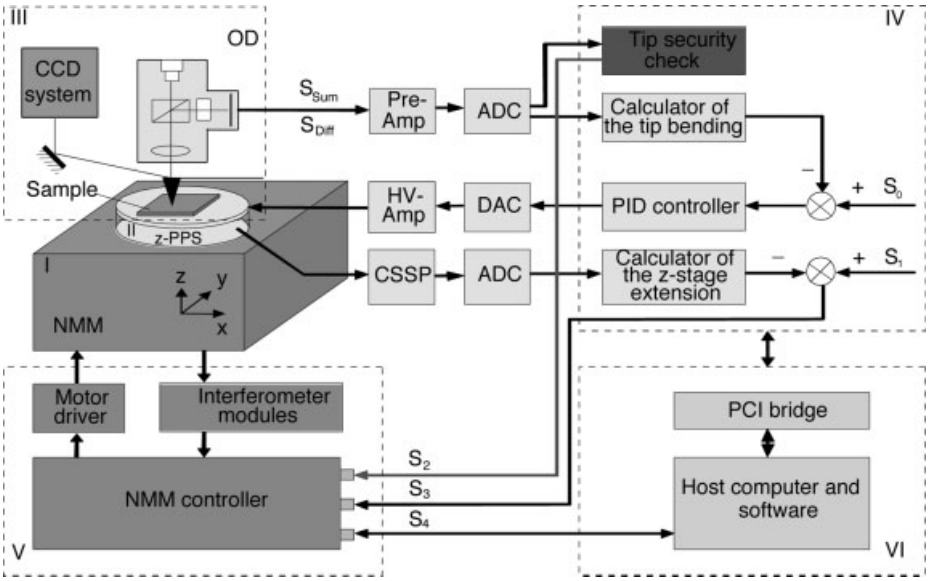

Fig. 6.1 The schematic diagram of the LR-SFM. The labels are defined as follows: OD, optical detector for measuring the bending of the cantilever; Pre-Amp, preamplifier for the electronic signal from the OD; ADC, analog to digital converter; DAC, digital to analog converter; HV-Amp, high voltage amplifier; CSSP, capacitive sensor signal processing unit; z-PPS, compact *z*-axis piezo positioning stage; S_0, the set point value of the cantilever bending; S_1, the target home position of the PPS; S_2, emergency signal to stop the NMM motion; S_3, the motion target of the NMM in the *z*-axis; S_4, commands, data, and configurations.

would not be possible if the NMM were operated alone due to its low resonance frequency, and the measurement range would be limited if only the compact *z*-stage were used for the motion along the *z*-axis due to its limited extension range.

The measurement setup is enclosed within an acoustic isolating box and placed on a vibration isolation table to attenuate vibrations from the ground and acoustic noise generated by external sources. Where possible, heat sources of the instrument are placed outside the acoustic isolating box to reduce the temperature increase inside the box. The complete instrument is located in a segment of the PTB's clean-room center. Its big advantage is the excellent temperature stability (better than ± 0.1 K) and cleanliness, therefore avoiding dust particle contamination of the measured sample.

6.2.2 Metrological Properties

The metrology related components of the instrument are depicted in Figures 6.2 and 6.3. As shown in Figure 6.2, the *x*-, *y*-, and *z*-coordinates of the motion stage

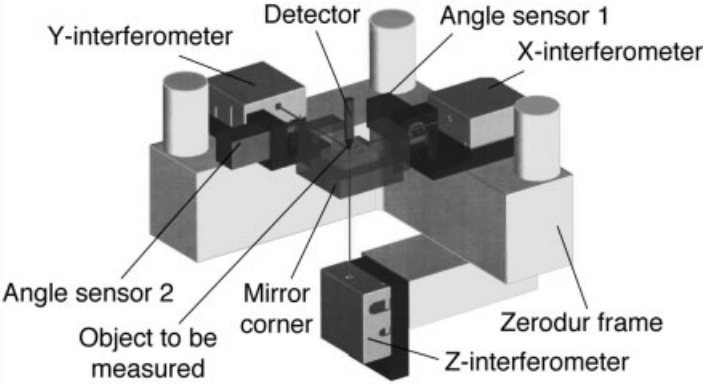

Fig. 6.2 The metrological principle of the NMM. For clarity the mechanical stages are omitted. The figure illustrates that the detection point of the detector coincides with the intersection point of three interferometer measurement beams orientated in the *x*, *y*, and *z* directions. This arrangement reduces the Abbe error to a minimum.

of the NMM are measured directly by three planar interferometers mounted on a Zerodur frame with a resolution of 0.08 nm and a noise level of 0.3 nm (RMS value, at the bandwidth of 6.25 kHz). The SFM probe point coincides with the intersection point of the three interferometer measurement beams orientated in the *x*-, *y*-, and *z*-directions. This arrangement reduces the Abbe error to a minimum.

The capacitive sensor located in the center of the compact *z*-stage is shown in Figure 6.3 [11]. This capacitive sensor measures the gap between the moving and the fixed part of the compact *z*-stage with subnanometer resolution. The important advantages of the *z*-stage are its compact size, the small mass, and the good dynamic performance. Since it has only 30 mm in diameter and 8 mm in thickness its mass is minimized to about 40 g. Therefore, when combined with the NMM the additional mass is small and the original dynamic performance

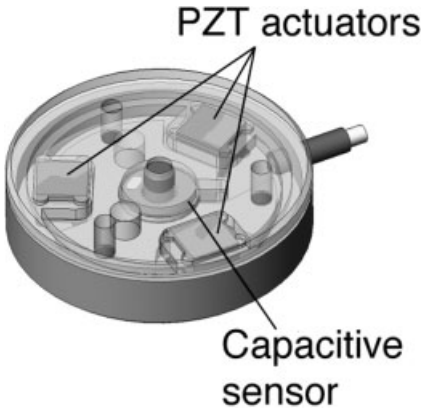

Fig. 6.3 The inner structure of the compact *z*-axis piezoelectric positioning stage. It consists of three parallel piezoelectric transducers located symmetrically around a central capacitive sensor.

of the NMM is maintained. Furthermore, because of the high stiffness of the PZTs, the small mass of the moving part and the carefully designed preload structure, the stage has a mechanical resonance frequency above 20 kHz. It should also be mentioned here that in the *z*-stage only one voltage value is applied to the three parallel PZTs. It is possible that this may cause unwanted jaw, pitch, and roll angle errors due to small physical differences between the three PZTs. However, these tilting angles are expected to be less than 0.2″ and no problems have been observed during our measurements so far. If required, the unwanted angle tilt can be compensated by applying different voltages to each PZT.

6.2.3 Traceability

The three He–Ne lasers used in the interferometers of the NMM are frequency-stabilized and have a frequency stability of better than 2×10^{-8} (calibrated by an iodine-stabilized laser). The interferometers operate in air. The refractive index of air is calculated and subsequently compensated in real time using Edlen's formula by measuring the air temperature, pressure, and humidity. In such a way, the measurement result of the NMM is directly traceable to the meter definition.

Because the sample is moved simultaneously along the *z*-axis by the rapid motion of the compact *z*-stage together with the relatively slow motion of the NMM during the measurement, topographic information must be derived from both the motion of the NMM in the z-direction and the extension of the compact *z*-stage. Although the motion of the NMM along the *z*-axis is measured traceably by interferometers, the extension of the compact *z*-stage is measured "only" by the embedded capacitive sensor. Therefore, to achieve traceable topographic measurements, the capacitive sensor in the compact *z*-stage has to be calibrated in advance.

For this purpose, an automatic procedure has been implemented to calibrate the capacitive sensor against the *z*-axis interferometer of the NMM in situ: After approaching the tip toward the sample, the fast servo loop is activated in the DSP so that bending of the cantilever is kept constant by the compact *z*-stage; the sample is then moved in the *z*-direction by the NMM by about 2 μm while keeping its *x*-, *y*-position unchanged; therefore, a fixed point on the sample is measured by the AFM tip and the sum value of the *z*-axis interferometer and the capacitive sensor should be constant. By recording simultaneously the value of the *z*-axis interferometer and the capacitive sensor, the capacitive sensor can be calibrated. This automatic calibration procedure does not need any other additional devices or changes in the experimental setup and can be executed easily within the software by a one-button click. As an example, one calibration result is given in Figure 6.4. The measurement bandwidth is 6.25 kHz. The nonlinear response of the interferometer (about 2 nm p-v) and the capacitive sensor, in addition to the overall noise of the system, contributes to the observed deviation from linearity.

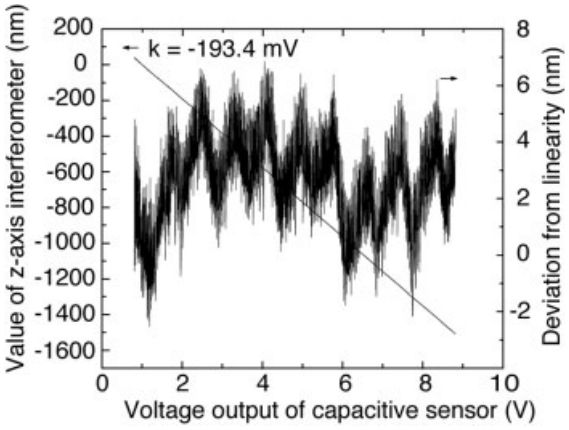

Fig. 6.4 Measurement data showing the calibration of the capacitive sensor embedded in the compact *z*-stage against the *z*-axis interferometer of the NMM. The calculated coefficient $k = -193.4$ nm/V is very close to the design value (–200 nm/V). The nonlinear response of the interferometer (about 2.5 nm p-v) and the capacitive sensor, in addition to the overall noise of the system, contributes to the observed deviation from linearity.

6.2.4 Specially Designed Features

The LR-SFM was developed with consideration of a set of special features facilitating its metrological applications:

a) The LR-SFM is capable of directly performing large area scanning up to the whole measurement volume without any stitching procedures. Compared to indirect methods where the long scanning profile or the large area scanning image is derived by stitching a series of SFM subimages [12, 13], this capability of the LR-SFM avoids several difficulties of the indirect methods: (1) The indirect methods have to determine some extra information required by the stitching procedures, e. g., the position information of the conjunction points between the neighboring images. For this purpose, either an additional positioning sensor or special software algorithms are often used. But the limited precision of these methods will directly influence the quality of the stitched result. (2) The typical bow shape of the xy plane of SFMs coupled in each scanned subimage will periodically appear in the stitched result and cause additional measurement errors. (3) If the scanned images have a certain overlay area, possible data conflicts may occur at these overlay areas and decrease the quality of the stitched result. (4) Since subimages are measured at different times, the drift of the

instrument, especially in the *z*-axis, will cause shifts at the border of neighboring profiles or images.

b) The measurement results of the LR-SFM are directly traceable to the meter definition by using optical interferometers for position measurements; whereas for other instruments, e. g., stylus profilometers, their position sensors must be calibrated by using a certain step-height or depth-setting standard. This feature of the LR-SFM avoids the measurement errors derived from both the standards (the uncertainties of the reference values, the quality of the standards, and so on) and the calibration procedure itself. In addition, since the calibrations can only be practically carried out on a limited number of calibration standards with each one representing one nominal value, probably the nonlinearity deviation of the position sensors under calibration could not be well corrected after calibration.

c) The LR-SFM is able to scan a profile or a measurement area with a large number of pixels only limited by the size of the physical memory of the computer. In contrast, most commercial SFMs have a limited number of pixels per scan line, e. g., 512 or 1024. This feature of the LR-SFM practically exploits the advantage of the high spatial resolution of SFM methods. As one can calculate, for scanning a profile with a length of 5.6 mm and a resolution of 10 nm, 560 001 data points would be received per scan line.

6.3 Measurement Result of a 2D-Grating Standard

A number of certified standard samples were investigated to characterize the metrological performance of the LR-SPM. Measurements of flatness standards, step-height standards, and nanoedge structures are given in an article [14]. Here, a detailed investigation of a 2D-grating standard is illustrated.

One- and two-dimensional gratings with calibrated pitch values are widely used to calibrate the magnification and to characterize image distortions of all types of high-resolution microscopes, optical microscopes as well as scanning probe and scanning electron microscopes.

6.3.1 Measurement Strategy

Following the traditional measurement strategy, gratings are scanned in one large rectangular area with nearly equidistant pixels. However, when the measurement area is enlarged in order to obtain a better statistic result, the necessary measure-

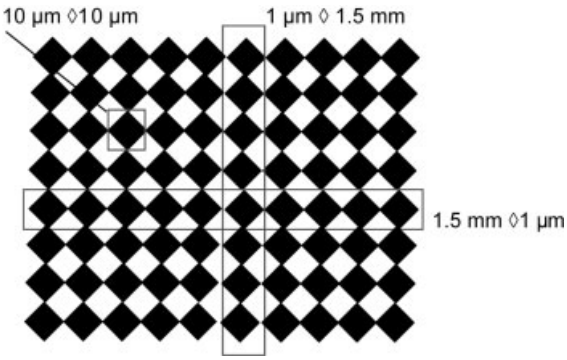

Fig. 6.5 A new measurement strategy is illustrated for measuring 2D gratings in the LR-SFM. The sample is scanned in three areas: one small square area for viewing structures in detail, and the other two narrow rectangular areas for calculating the mean pitch and the local pitch variation along the *x*- and *y*-axes, respectively. As an example, the marked measurement areas in the figure are used for measuring a lateral 2D standard.

ment time will be very long and the amount of the data collected will be very large. To avoid this difficulty, the LR-SFM features the capability of flexible measurement strategies. For measuring the 2D grating, a new measurement strategy is proposed and used in the LR-SFM, as shown in Figure 6.5.

By using this new measurement strategy, the size of the measurement areas is largely reduced, consequently the measurement time and the amount of the data can be reduced to a practically acceptable extent.

After the grating is inserted into the instrument and is coarsely aligned, there may exist angle deviations between its actual and ideal orientation in the *xy*, *xz*, and *yz* planes, respectively. These angle deviations may reach a few degrees and should be carefully reduced or compensated, since they will cause cosine error of the measurement results.

The angle deviation of the grating in the *xy* plane is reduced by selecting a proper fast scanning direction, as being achieved in following steps. (a) The grating is scanned in the direction along the *x*-axis. (b) The orientation angle of the grating in the *xy* plane is calculated from the shape of the measured profile. (c) The fast scan direction is set as the orientation of the grating in the *xy* plane, which is calculated in step (b). It is not necessary to rotate the grating in the *xy* plane for achieving the above-mentioned procedures. Therefore, they can be easily performed in a few minutes.

The influences of the angle deviations of the grating in the *xz* and *yz* planes are reduced using compensation method in the following three steps: (a) During the scanning, the measurement data are recorded without applying any kind of line fit or plan fit to the raw data. (b) After the measurement data have been taken, the angle deviations of the grating in the *xz* and *yz* planes are calculated from the plan fit result of the measurement data. (c) The orientation deviations calculated in step (b) are then used for compensating the cosine error during the calculation of the mean pitch and the local pitch variation.

6.3.2 Data Evaluation

Of the two narrow rectangular areas measured, one is used for calculating the mean pitch and local pitch variation along the *x*-axis and the other for the *y*-axis. The data evaluation task of the measurement data of each narrow rectangular area can be regarded as a same task for a one-dimensional grating.

A method based on a combined one-dimensional fast Fourier transformation (FFT) analysis and one-dimensional Fourier transformation analysis is designed for evaluating the data. Its schematic diagram is shown in Figure 6.6. The FFT analysis has the advantage of fast calculation speed; however, it has only a limited resolution. Therefore, the evaluation method uses FFT analysis for coarsely searching the approximated frequency (f_0) of the grating. The f_0 is then used as a starting data for precisely searching the final frequency of the grating using an iterated Fourier transformation analysis. In such a way, the resolution of the evaluation method is only determined by the desired smallest frequency step f_{res}. A very high calculation resolution can be achieved by selecting a small f_{res}. As an example, Figure 6.7 shows a FFT calculation result of a 2D sample (a lateral 2D standard with nominal pitch 1000 nm) for calculating the pitch value along the *x*-axis.

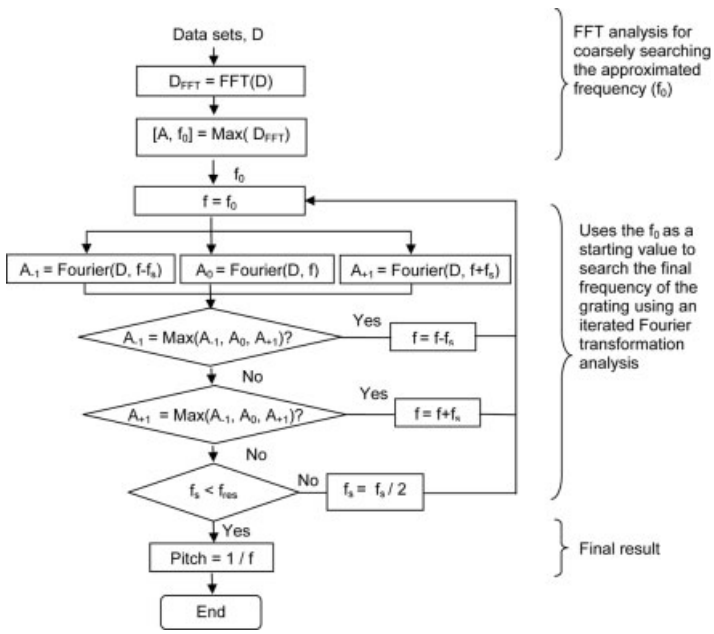

Fig. 6.6 Schematic diagram of the data evaluation method with combined fast Fourier transformation (FFT) analysis and Fourier transformation analysis.

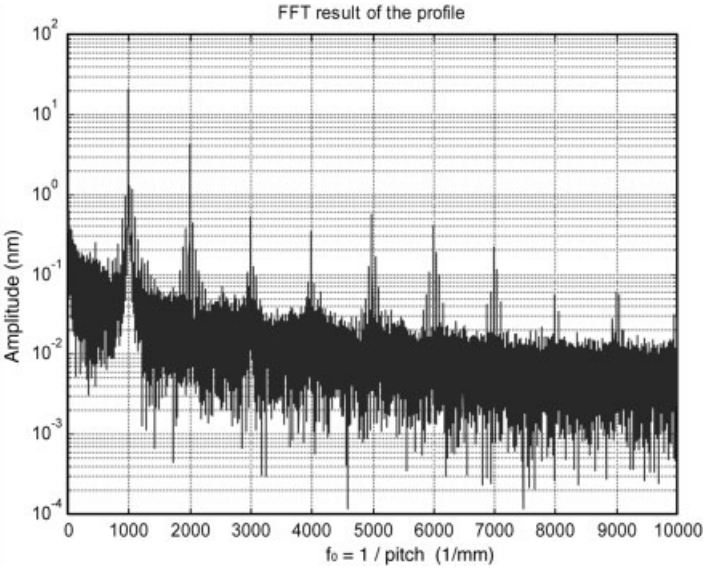

Fig. 6.7 A FFT calculation result of a 2D sample for calculating the pitch value along the *x*-axis. A frequency component at $f_0 = 1000$ (1/mm) can be seen with the largest amplitude peak in the spectrum.

6.3.3
Measurement Result of the Mean Pitch Value

A lateral standard (2D grating, Serial No. A00103), produced by means of a holographic method, was measured using the described measurement and evaluation method. The calibration surface of the standard has a size of 2 mm × 2 mm. It is measured within an area with a size of 1.5 mm × 1.5 mm at its center.

Its measured mean pitch value along the *x*- and *y*-axes is depicted in Figure 6.8(a) and (b), respectively. Both measurements are repeated more than 10 times (over more than 20 h) and a standard deviation of less than 2 pm is achieved.

6.3.4
Measurement of the Local Pitch Variation

For the purpose of characterizing lateral image distortions of other topographic instruments, it is also very important to know the local pitch variation. Although the optical diffraction method can also measure the pitch value of gratings, it can only provide a mean pitch value of the measured gratings in a large measurement area (mm size).

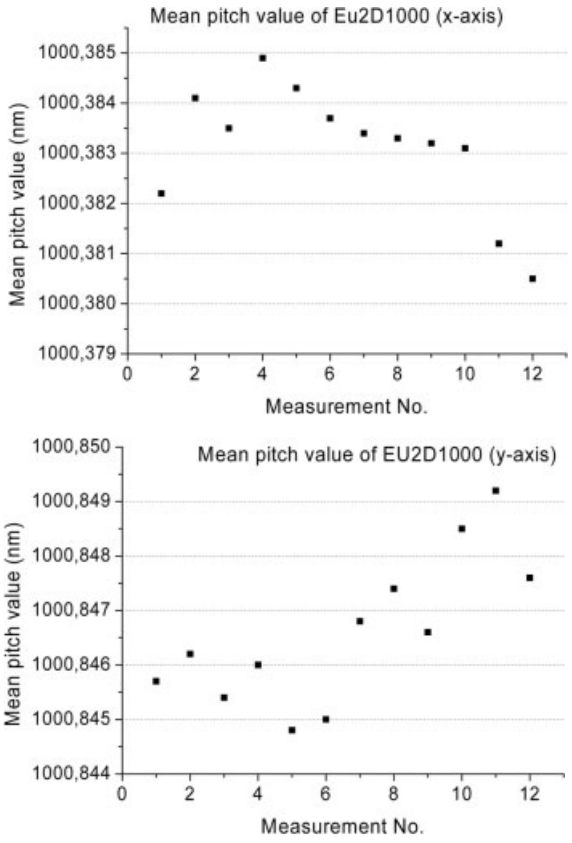

Fig. 6.8 The measured mean pitch value (along the *x*- and *y*-axes) of the lateral standard (Serial No. A00103) is shown in (a) and (b), respectively. These measurements are repeated more than 10 times (over more than 20 h) and have a standard deviation of less than 2 pm.

By using the calculated mean pitch value, the position deviation of individual structures on the 2D grating can be easily determined by calculating their phase shift using Fourier transformation. Figure 6.9(a) and (b) depicts the position deviation of the measured 2D grating along the *x*- and *y*-axes, respectively. The results have shown the following: (1) The deviations are less than 10 nm for the investigated measurement range of 1.5 mm. No irregularities are found. This result indicates the good homogeneity of the grating, which is manufactured using a holographic method. (2) Twelve repeated measurement results are depicted in Figure 6.9(a) and (b). The measured deviation of individual lines coincides well with each other, indicating good repeatability of the measurements.

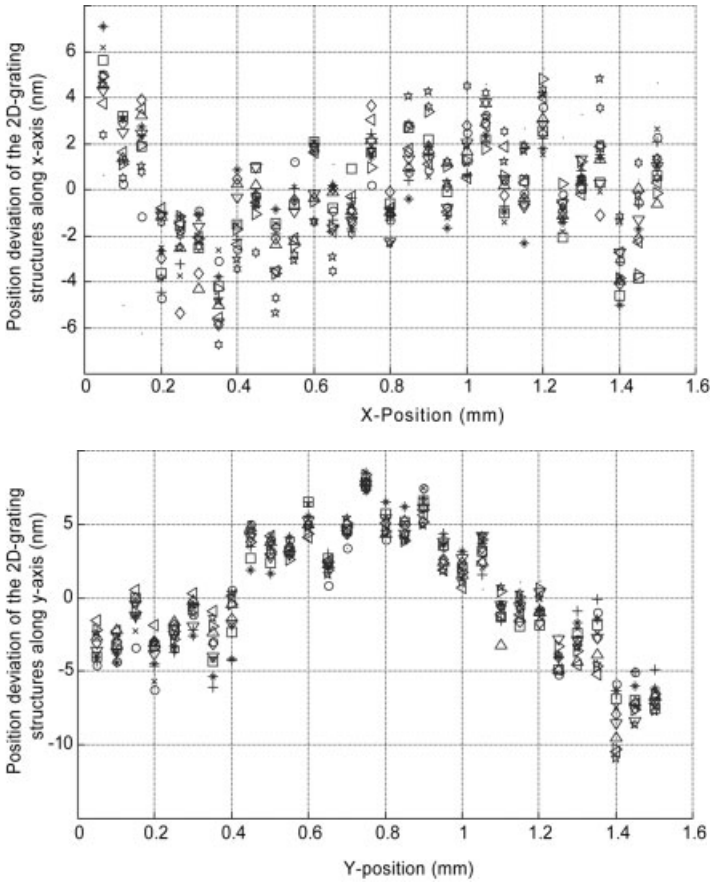

Fig. 6.9 The measured position deviation of individual structures on the European lateral standard (2D grating No. A00103) along the *x*- and *y*-axes, respectively. The deviation is less than 10 nm within the measurement range of 1.5 mm. No irregularities are found, indicating the good quality of the grating that was made by a holographic method. The figure depicts 12 repeated measurement results. These results also show good repeatability of the measured deviations.

6.4
A Selected Measurement Result of a Microroughness Standard

Although more and more AFM methods are used for measuring roughness, their measurement results cannot be compared with and linked to the results achieved using stylus profilers or interference microscope. This is mainly due to the fact that commercial AFMs have not the necessary scan range required by standard evaluation methods. For example, a scan range of $7 \times \lambda_c$ (λ_c is the cutoff wavelength, typically selected as 0.08–8 mm) is required for using the evaluation method ISO 4288 (1996) and phase correct profile filter according to ISO 11562

(1996). With its large range scanning capability, LR-SFM is a powerful tool for comparing and linking the roughness measurement results derived by using different methods.

A series of measurements and evaluations have been carried out in following sequence: (1) A new SFM tip is inserted into the LR-SFM and its geometrical shape is determined. (2) A flatness standard is measured by the LR-SFM in order to investigate the noise level of the instrument and its influence on the roughness measurement results. (3) A microroughness standard is measured by the LR-SFM with a profile length of 5.6 mm and a pixel distance of 100 nm; the measurements are repeated several times. (4) The same measurement area of the microroughness standard is measured by a PTB profilometer (Perthometer Concept, Mahr company) with a probe radius of 2 μm. (5) The profiles measured by both the LR-SFM and the stylus profilometer are evaluated by the same method. The roughness parameters are compared and discussed. (6) The SFM tip's geometrical shape is measured again in order to check the abrasion of the tip during the whole measurement.

6.4.1 Measurement Result of a Glass Flatness Standard

A PTB flatness standard with an "arithmetical mean deviation" $Ra < 1$ nm is measured by the LR-SFM. The derived roughness profile is depicted in Figure 6.10. This roughness profile is evaluated according to ISO 4288 (1996) and ISO 3274 (1996). The calculated Ra and the "average peak to valley height" Rz are 0.58 nm and 4.46 nm, respectively. This result illustrates that the influence of the overall noise level of the LR-SFM on the Ra value in microroughness measurements is less than 0.6 nm. It is worth mentioning that the dominant noise component with the amplitude of 2.5 nm (p-v) in Figure 6.10 is mainly caused by the nonlinearity of the *z*-axis interferometer of the LR-SFM. A sharp peak in Figure 6.10 is probably caused by a dust particle contamination.

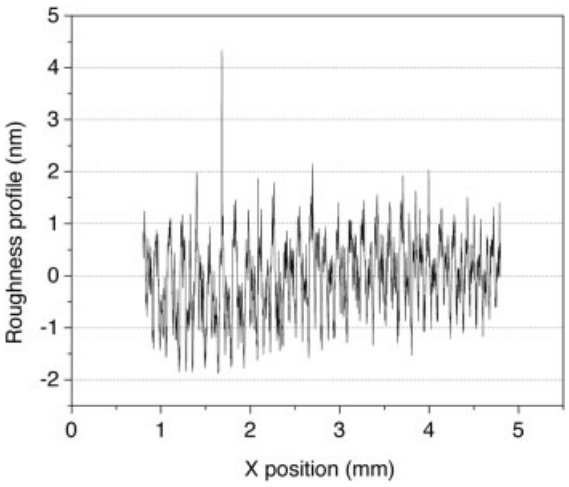

Fig. 6.10 The roughness profile of a measured PTB glass flatness standard, indicating that the influence of the overall noise of the LR-SPM on the roughness measurement is less than 0.6 nm (*Ra*).

6.4.2
Measurement of a PTB Microroughness Standard

A PTB microroughness standard (type D1, the standard has repeated structures in one direction) as shown in Figure 6.11 is measured by using the LR-SFM. The measurements are repeated 10 times within the measurement area. Figure 6.12(a) shows one of the measured profiles. Repeated roughness structures of the standard can be clearly discerned. Figure 6.12(b) shows a zoom-in figure that illustrates the same fractions of two measured profiles P1 and P2 with P1 shifted 500 nm upward. Similar details can be seen in different measured pro-

Fig. 6.11 The photo of the measured PTB micro roughness standard. Size: 40 mm (L) × 20 mm (W) × 10 mm (H).

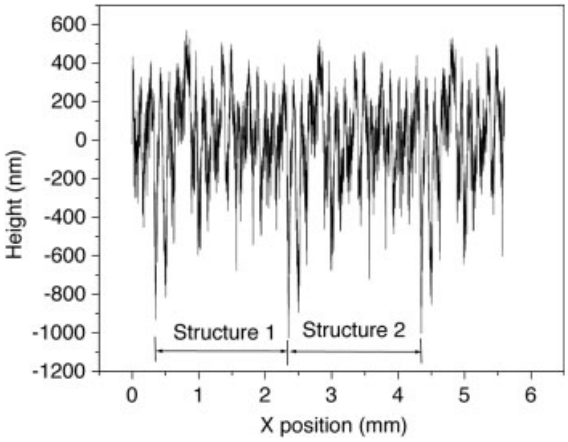

Fig. 6.12a The measurement results of a microroughness standard.

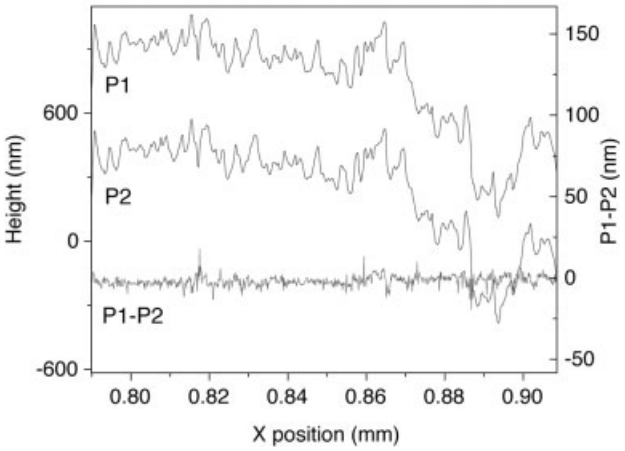

Fig. 6.12b The measurement results of a microroughness standard. Figure 5(a) shows one of the measured profiles of a microroughness standard. Fractions of two different measured profiles at the same location are zoomed in and shown in (b). Curve P1 is shifted 500 nm upward for clarity.

files. Curve P1 – P2, which is the difference between curves P1 and P2, has variation amplitude of mostly less than 10 nm, indicating the good measurement repeatability of the instrument. The derived roughness value will be presented and compared with that of the stylus method in the next section.

6.4.3
Comparison of the Roughness Measurement Results Derived from SFM and Stylus Instruments Using Gaussian Filter

For comparison purpose, the same measurement area of the microroughness standard is measured by a PTB profilometer (Perthometer Concept, Mahr company) with a nominal probe radius of 2.0 μm. This profilometer has a noise level of $Rz = 7$ nm (without λ_s filtering). All measured profiles from both instruments are phase correct filtered at the same $\lambda_c = 0.8$ mm and $\lambda_s = 2.5$ μm. Figure 6.13 shows the roughness profiles measured by both the stylus instrument and the SFM instrument. For ease of presentation, the profile data of the stylus method have been shifted 1000 nm upward. A good agreement in the profiles measured by the different instruments can be seen in the figure.

However, it can be seen in the marked circles in figure 6.13(b) that the valley structures of the measured profile determined by the SFM methods are wider and deeper than that measured by the stylus instrument. This result is caused by the fact that the radius and size of the SFM tip are much smaller than those of the stylus tip.

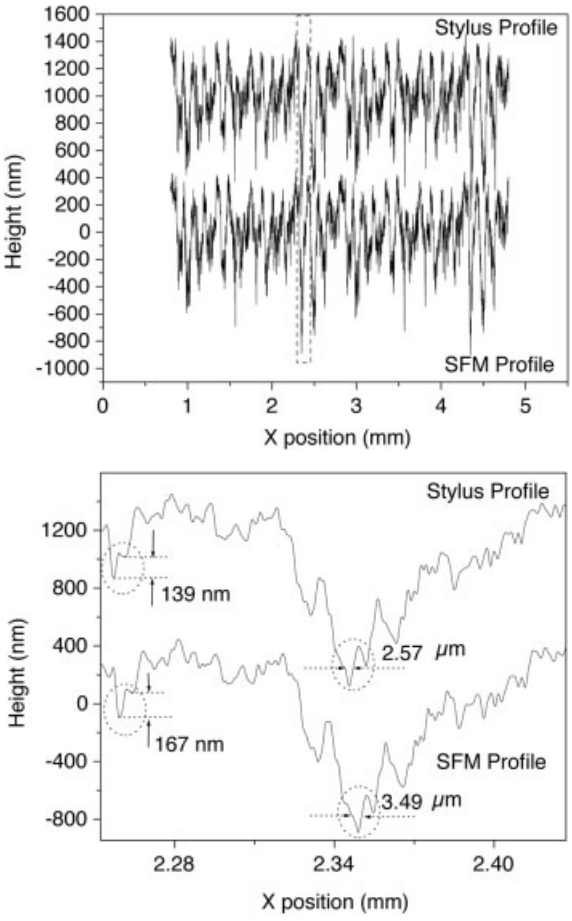

Fig. 6.13 The comparison between the measured SFM profile and the measured stylus profile is shown. (a) shows two roughness profiles derived by SFM and stylus instruments. Fractions of profiles (marked area) are zoomed in and shown in (b). The stylus profile is shifted 1000 nm upward for clarity.

6.4.4
Comparison Using Morphological Filters

Measured surfaces are dilated results of the real surfaces by sensor tips. They are closer to the real surfaces when the radii of the sensor tips are smaller, and reach the real surfaces only when the radii of the sensor tips become zero. In this sense, the profiles measured by the SFM method can be regarded as much closer to the real surface than those of the profilometer; and the profiles of the profilometer can be regarded as the dilated result of the SFM results by the used stylus tip.

In order to achieve a fair comparison between the SFM and the stylus result, raw profiles of the SFM method are dilated by a radius of 2.0 μm (this radius is selected to be the same as the nominal radius of used stylus tip; the true radius is not known). Figure 6.14 shows a dilated profile that is compared with the original SFM profile; parts of valley structures (circle marked area in Figure 6.14) are lost in the dilated profile.

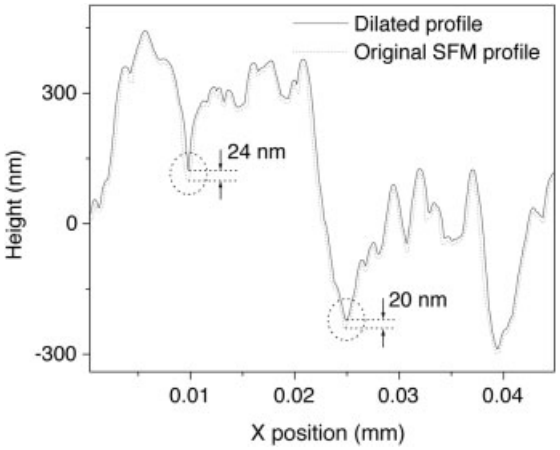

Fig. 6.14 Fractions of dilated and original SFM profiles are shown. The original SFM profile is dilated by a ball with a radius of 2.0 μm. The dilated profile is shifted downward so as to have a distance of 10 nm from the original profile for clarity.

6.4.5
Evaluation Results Using PTB Reference Software

The roughness profiles from stylus profilers, the original SFM profiles and the dilated SFM profiles are further evaluated by the PTB reference software, which is a standard from type F2 according to ISO 5436-2 (2000). The software calculates roughness parameters according to ISO 4287 (1997), ISO 4288 (1996), ISO 11562 (1996), and ISO 13565-1,2 (1996). The calculated roughness parameters are listed in Table 6.1. The definitions of these roughness parameters are referred to ISO 4287 (1997).

Table 6.1 The evaluated roughness parameters on profiles measured by the LR-SFM and the stylus profilometer are given. The data are evaluated according to ISO 4288 (1996) after phase correct filtering with $\lambda_c = 0.8$ mm and $\lambda_s = 2.5$ μm according to ISO 11562 (1996). D-SFM: the dilated SFM profiles, simulating the profilometer

Method	Rp (nm)	Rv (nm)	Rmax (nm)	Rz (nm)	Ra (nm)	Rq (nm)	Rt (nm)
Stylus	431.9±13.0	760.5±22.8	1366.8± 41.0	1200.4±60.0	176.9±5.3	222.6±13.0	1366.8±41.0
SFM	433.6	795.6	1346.8	1229.1	179.2	225.8	1348.8
D-SFM	431.1	789.1	1360.3	1220.3	177.0	223.4	1360.3

Regarding the results in Table 6.1, the following aspects can be discussed:

- The *Ra*, *Rq*, and *Rp* values of the dilated SFM profiles have an excellent agreement (difference < 1.0 nm) with that of the stylus profiles. This small difference may be due to the scaling error of the stylus instrument and the noise of both instruments.
- Compared to the results evaluated from the original SFM profiles, the results evaluated from the dilated SFM profiles have a better agreement with that of the stylus results. This fact coincides well with the theory, namely that the measured surfaces are dilated results of the real surfaces by sensor tips.
- The *Rp* value of the SFM profile is very close to that of the stylus profiles, but the *Rv* value is larger than that of the stylus method. This result also coincides well with the theory of morphological filters, namely that a valley structure will be lost if its radius is less than the radius of the dilation ball whereas peak structures will always be kept.
- The *Rv* value of the dilated SFM profiles still has a difference of 28.6 nm with that of the stylus profiles, although it is closer than that of original SFM profiles. The reason for this fact is that the stylus tip is assumed to be an ideal ball with a radius of 2.0 μm in the dilation calculation; however, its real shape has deviations, e. g., because of its abrasion. More careful investigations are to be done in future.

6.5 Outlook and Conclusion

We presented a large range scanning force microscope that has been designed to meet the demands of micro- and nanometrology on samples with up to millimeter sizes. The instrument is constructed in such a way that the Abbe error is minimized. Direct laser interferometric measurements allow for tracing the result to the meter definition. A dual-stage positioning system including a nano measuring machine and a compact *z*-stage is used for both aims–large measurement volume and high measurement speed. Furthermore, a user-friendly instrument interface was designed for flexible and easy operation. Measurement results of a 2D-grating standard and a microroughness standard have shown the very good metrological performance of the instrument.

In the near future, comparisons of the metrological LR-SFM with other instruments at PTB will be carried out to further verify the accuracy of the instrument. Error budgets will be calculated and the instrument will be prepared for calibration services.

To further improve the capabilities of the instrument various noncontact SFM modes should be implemented into the system. Other detection options, such as tuning fork sensors or piezoresistive cantilever sensors, are also considered to be

implemented into the instrument for a more versatile metrological capability. A micro probe, designed for the use with a 3D-micro-coordinate measuring machine will be combined with the instrument to extend the measurement capability for dimensional measurements of small parts with sizes of tens of millimeters, which is of great importance for the application field of precision mechanics, microelectronic mechanical systems (MEMS), and others. All different types of detection sensors will have identical mechanical, electrical, and software interfaces, so that they will be easily exchangeable and the instrument could rapidly switch between different measurement tasks.

References

1 O. Jusko, X. Zhao, H. Wolff, and G. Wilkening, Rev. Sci. Instrum. **65**, 2514 (1994).

2 S. Gonda, T. Doi, T. Kurosawa, et al., Rev. Sci. Instrum. **70**, 3362 (1999).

3 J. Haycocks and K. Jackson, in *Proc. of 2nd Euspen Conference, Torino, Italy* (2001), p. 392.

4 B. Picotto and M. Pisani, Ultramicroscopy **86**, 247 (2001).

5 M. Bienias, S. Gao, K. Hasche, R. Seemann, and K. Thiele, Appl. Phys. A **66**, 837 (1998).

6 R. Dixson, R. Köning, J. Fu, T. Vorburger, et al., *SPIE Metrology, Inspection, and Process Control for Microlithography, Santa Clara, CA, USA* (2000).

7 J. Garnaes, N. Kofod, A. Kühle, and C. Nielsen, Prec. Eng. **27**, 91 (2003).

8 F. Meli and R. Thalmann, Meas. Sci. Technol. **9**, 1087 (1998).

9 G. Jäger, E. Manske, T. Hausotte, et al., *Annual Meeting of ASPE, Crystal City,VA, USA* (2001).

10 SIOS Meßtechnik GmbH, Am Vogelherd 46, D-98693 Ilmenau, Germany. Web site: www.sios.de

11 Physik Instrumente (PI) GmbH, Auf der Roemerstrasse 1, D-76228 Karlsruhe, Germany. Web site: www.pi.ws

12 J. Condeco, L. H. Christensen, and S. F. Jorgensen, A comparative study of images stitching algorithms for surface topography measurements, in *Proc. of X International Colloquium on Surface, Chemnitz, Germany, Jan. 31st – Feb. 2nd* (2000), pp. 33–43.

13 J. C. Wyant and J. Schmit, Large field of view, high spatial resolution, surface measurement, in *7th Int. Conf. on Metrology and Properties of Engineering Surfaces* (1997), pp. 294–301.

14 G. Dai, F. Pohlenz, H.-U. Danzebrink, et al., Metrological large range scanning probe microscope, Rev. Sci. Instrum. **75**, 962–969 (2004).

15 G. Dai, L. Jung, F Pohlenz, et al., Measurement of micro roughness using a metrological large range scanning force microscope, Meas. Sci. Technol. 15, 2039–46 (2004).

Part III
Instrumentation – Development of SPM and Sensors

Nanoscale Calibration Standards and Methods: Dimensional and Related Measurements in the Micro- and Nanometer Range.
Edited by Gunter Wilkening, Ludger Koenders
ISBN: 3-527-40502-X

7
Traceable Probing with an AFM

K. Dirscherl and K. R. Koops

Abstract

The need for fast and accurate inspection of small sample features is eminent considering the developments in micro and nanotechnology. The atomic force microscope (AFM) offers extreme resolution and even accuracy when properly calibrated (R. Breil et al, Precision Engineering **26** (3) 296–305 (2002)), but the principle of operation results in inherently slow acquisition of the measurement data. At the Van Swinden Laboratorium of the Nederlands Meetinstituut in the Netherlands, we have constructed a traceable AFM using a stand alone AFM head, a 3D translation stage and an accurate 3D laser interferometer system. Nanometer measurement uncertainty is achieved in the entire scanning volume of 100 μm × 100 μm × 20 μm. Apart from providing direct traceability to the SI unit of length, we have added the possibility of probing the sample in arbitrary positions in contrast to an AFMs ordinary scanning process. Only the areas of interest are measured with maximum accuracy in this probing mode while the rest of the surface is ignored. This speeds up the acquisition of relevant data and enables the use of an AFM as a nanometer coordinate measuring machine. In order to achieve this freedom of positioning, a new control algorithm is developed that features feedforward–feedback control using the information of the laser interferometers. The measurement signals can be sampled at 50 kHz, which ensures control in real-time. This paper focuses on the key points of the AFM design as well as the control algorithm and shows first results.

7.1
Introduction

Since the invention of the scanning tunneling microscope (STM) in 1982 [1], an entire class of scanning probe instrumentation has been developed. The unprecedented resolution of these instruments is a result of the extremely small area of interaction between a tiny probe and the surface under study. In order to study an

Nanoscale Calibration Standards and Methods: Dimensional and Related Measurements in the Micro- and Nanometer Range.
Edited by Gunter Wilkening, Ludger Koenders
ISBN: 3-527-40502-X

area of the surface larger than the probe, the probe is scanned over the surface area and the resulting image is analyzed as a whole to extract the desired features. The measurement process is usually too slow for most industrial inspection applications. The (lack of) speed of these instruments is due to the imaging process that consists of serial acquisition of individual data points in a regular grid that spans the area of interest. In order to have sufficient spatial resolution the number of points on the acquisition grid is necessarily large, i. e., 512 × 512 or even more, resulting in proportionally long acquisition times. Additionally, because the acquisition is inherently slow the instrument itself can influence the measurement, for example by thermal or mechanical instabilities, which will ultimately affect the accuracy. Although the scanning mechanisms and data acquisition hardware have improved in speed over the years, faster scanning also results in loss of accuracy. Moreover, most of the information gathered in the scanning process is redundant and discarded in the end because often only a single quantity has to be extracted.

We describe a novel measurement approach in which the probe is controlled by positioning vectors. Using this strategy the measurement process can focus on accuracy, while maintaining speed because only the relevant data is captured. Similar to a 3D coordinate measuring machine (CMM), an arbitrary polygonal chain of movements provides the freedom to concentrate only on the feature characteristic that has to be extracted from the surface geometry like distance, height, pitch, line width or radius. The data analysis is therefore not based on an image of the entire surface but merely on data sets that contain only relevant data. This alternative measuring mode can significantly facilitate the implementation of faster measurement procedures as required in quality checks of a production line.

7.2 Setup

A commercial piezo table [2] with three independent translation axes is used. The table has a displacement volume (x, y, z) of 100 μm × 100 μm × 20 μm. A square aperture of 66 × 66 mm^2 in the center of the table provides space for interferometric positioning measurement along the z-axis. The pitch, roll, and yaw during translation along the axes are less than 2 arcseconds peak-to-peak for the whole range of motion. Moreover for a 3D movement, the rotations can simply be interpreted as a superposition caused by three individual 1D movements, as is proven by comparing a simulated superposition of two axes with the measurement, see Figure 7.1. The measured signal (bottom line) was obtained by simultaneously applying two identical sinusoidal waveforms in both the x- and y-axes while recording the roll of the table. The simulated signal (top line) was calculated as a linear superposition of individually measured roll when the same sinusoidal waveform was applied first along the x-axis, then to the y-axis. It is therefore possible to directly map the overall roll of the table via the time dependency of the waveform to the (x, y)-position on the table in both cases.

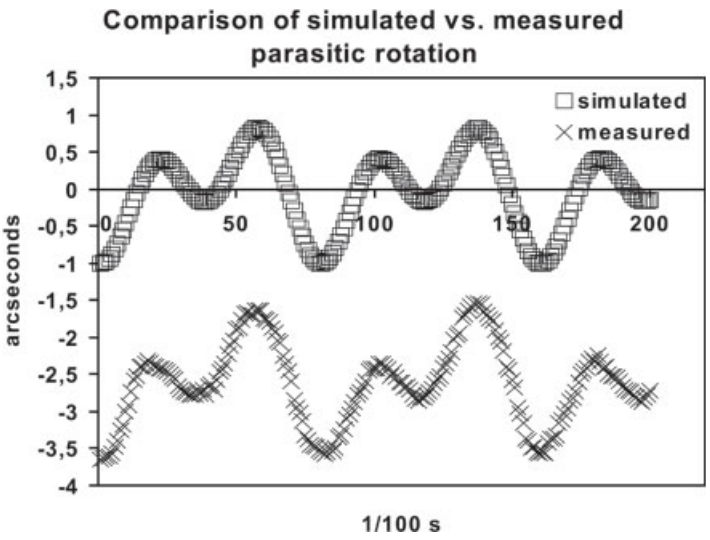

Fig. 7.1 The simulated roll (top) is the sum of the roll signals generated by individual translations along *x* and *y*. Simultaneous oscillations in *x* and *y* with different frequencies generate the measured roll (bottom). The datasets are shifted for better comparison.

A commercial interferometer system [3] is used to sample the 3D position of the scan table. The beam of a heterodyne laser is split into three beams, one for each axis. The interferometers are four-pass interferometers, allowing a resolution of $\lambda/4096$, which corresponds to approximately 0.16 nm. The four measurement beams of each interferometer form a square of about 12 mm side length. The 36-bit position signal provides a limit for maximum displacement of 11 m. For our purpose, 20 bit are sufficient. The optical quality of the laser and the interferometer optics has been determined. The ratio of the mixing of the two polarization states is 1:150 in the E-field, which results in a residual nonlinearity in the position of 0.7 nm peak-to-peak (measured) (see Figure 7.2). The optical components of the interferometer introduce a nonlinearity error of 1.4 nm peak-to-peak (calculated) to the measured position (see Figure 7.3).

A self-designed scan table with three perpendicular mirrors is attached to the piezo table (see Figure 7.4). In order to reduce environmental measurement errors caused by a long dead path, the interferometers are placed 1 mm from the mirrors. The achievable measurement uncertainty per axis is estimated to be better than 2 nm. The design of the feedback system and the scan table is chosen to ensure that the probing tip of the AFM rests in Abbe when scanning the sample.

An industrial PC with standard "Pentium IV" 1.5 GHz CPU controls the system of 3D piezo movement and position feedback. The PC is equipped with ISA-cards for digital input/output. PCI-cards would require the usage of additional driver software while only offering 3–4 times higher data throughput. A maximum sample rate of 50 kHz is realized with the ISA bus and is sufficient

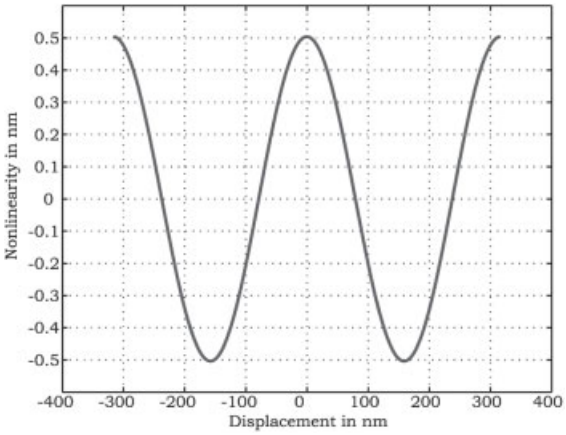

Fig. 7.2 The residual nonlinearity in the measured position is plotted versus the displacement from zero position. This measured signal is due to the mixing of the two polarization states of the laser source.

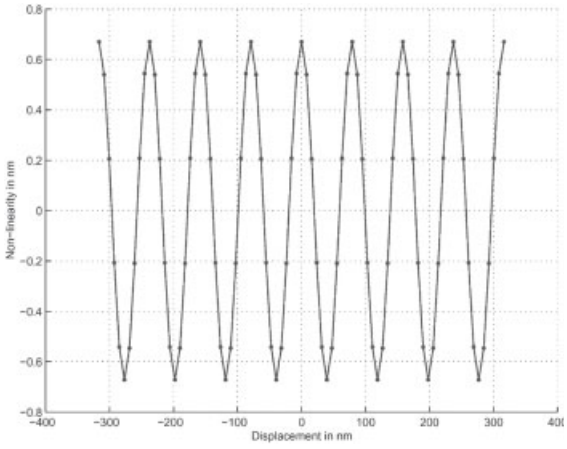

Fig. 7.3 The residual nonlinearity in the measured position is plotted versus the displacement from zero position. This calculated error signal is introduced by the optics of the interferometer.

for the 3D position and the signal of the AFM's photodiode. Still data aging must be taken into account if the four values are sampled in series. For a moderate line scan frequency of 0.5 Hz over a length of 100 μm, a time interval of 20 μs corresponds to a traveled distance of 2 nm. The first sampled value, say the x coordinate, will no longer correspond to the same position on the sample surface as the last sampled value, say the signal of the photodiode. Therefore, all four values are latched into buffers by a single one-byte write command to ensure simultaneity. These buffers are internal digital memory of the laser controller and the A/D converter for the signal of the photodiode. They can then be read in series without the need to compensate for data aging.

Three 20-bit DACs are used to send the calculated control voltages to the three piezos. A commercial high-voltage amplifier is interconnected between the DACs and the piezo table. The first sampled image as obtained by an ordinary periodic

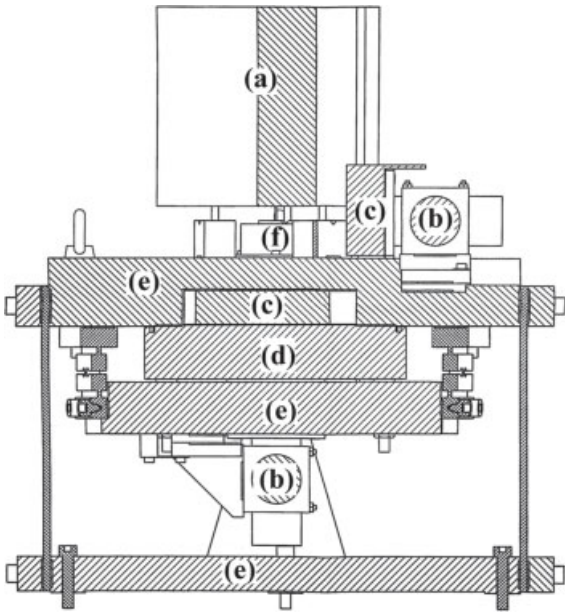

Fig. 7.4 Cross-section through the self-designed scan table. It consists of a metrological frame (e) which ensures that the sample table (f) remains in Abbe underneath the AFM head (a). To the metrological frame (e), the interferometers (b) are fixed. The only moving unit is formed by the mirror holders (c) and the sample table (f) which is displaced by the 3D piezo stage (d).

scan is shown in Figure 7.5. A "find-me" structure of a calibration grid was scanned over 35 μm × 35 μm and shows blocks with a height of about 400 nm. The sample frequency was 10 kHz, the scanning took 500 s. This corresponds to a lateral resolution of 5000 × 1000 samples. The tail-like structure in the upper center of the image results from the very beginning of the sampling process when the tip was not yet engaged and the z-feedback loop was not yet active.

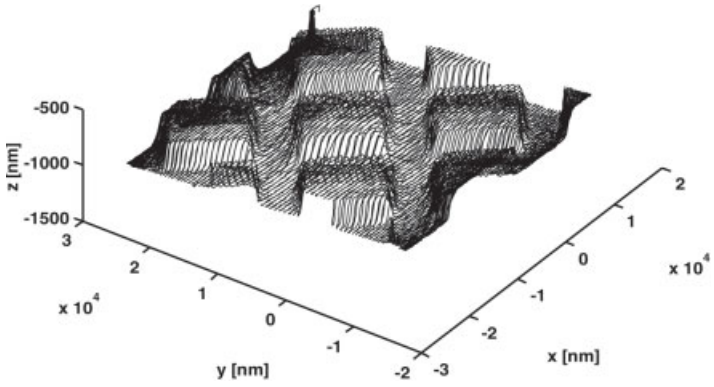

Fig. 7.5 A "find-me" structure of a calibration grid was scanned over 35 μm x 35 μm and shows blocks with a height of about 400 nm. A total of 5000 x 1000 samples are taken. The tail-like structure in the upper center results from sampling during the tip approach.

7.3 Correction for Piezo Nonlinearities

The hysteresis of a piezoscanner causes nonlinear deviation from an ideal linear movement. This error is typically on the order of 10–20 % of the range of motion. A simple feedback loop without compensation for hysteresis would require five iterations at least in order to reach an absolute positioning accuracy of 1 nm over a maximum displacement of 100 μm. Additionally, drift and cross talk between the displacement axes is also likely to increase the number of iterations per positioning task. Therefore, the controller software provides feedforward control that can correct in advance for nonlinear hysteresis and drift effects.

7.3.1 Hysteresis

A lot of effort has been undertaken to model the closed hysteresis loop of a periodic scan movement. The residual nonlinearity of the models range between 0.5 % and 5 %. The main disadvantage of most existing models for hysteresis is their applicability to the closed hysteresis loops of a periodic scan movement only. In [4] a model for hysteresis [5] was applied that simulates the hysteresis of a periodic movement of a piezoscanner to 0.2 % and better.

In addition, the model is flexible enough to describe arbitrary piezo movements. The model consists of an ordinary differential equation (ODE) (7.1)

$$\frac{\mathrm{d}x}{\mathrm{d}V} = \alpha \mathrm{sgn}\left(\dot{V}\right)(x - bV) + u, \tag{7.1}$$

where the parameters $b, u,$ and α are related to the piezoceramic material properties: its ideal linear electromechanical coupling b, the slope u of the virgin curve in the origin, and α a measure for its ferroelectric softness which is responsible for the hysteresis. In the case of a closed hysteresis loop, the voltage V oscillates for a periodic scan movement, say $V_{\min} \leq V \leq V_{\max}$, and the turning voltages $V_{\min}, V_{\max}$ define the appropriate boundary conditions for the differential equation. In order to use the model in a feedback control for arbitrary positioning purposes where the position x_0 is known at every voltage V_0, the ODE can be solved with the boundary condition $x(V_0) = x_0$. This yields the resulting position of the scanner after the application of a voltage V given a starting point (V_0, x_0):

$$x(V) = bV - \frac{b-u}{\alpha}\left(1 - \mathrm{e}^{-\alpha(V-V_0)}\right) + (x_0 - bV_0)\mathrm{e}^{-\alpha(V-V_0)}. \tag{7.2}$$

Note that in Eq. (7.2), the argument x can be replaced by y as well as by z in order to determine the control voltage along the movement of the lateral y-axis or even in the z-axis. The only difference is the usage of a new set of parameters

(b_y, u_y, α_y), (b_z, u_z, α_z), respectively, which is uniquely defined for the y-axis and z-axis.

Inverting (7.2), the desired control voltage $V(x) = x^{-1}(V)$ can be calculated which is necessary in order to go from a given piezo state (V_0, x_0) to a new position x.

$$V(x) = \frac{1}{b}\left(\frac{b-u}{\alpha}+x\right)+ \\ \frac{1}{\alpha}\text{Lambert } W\left[\alpha\left(V_0-\frac{1}{b}\left(\frac{b-u}{\alpha}+x_0\right)\right)e^{\alpha\left(V_0-\frac{1}{b}\left(\frac{b-u}{\alpha}+x_0\right)\right)-\frac{\alpha}{b}(x-x_0)}\right]. \tag{7.3}$$

The function Lambert W [6] is not implemented as a standard function in computer hardware, despite its importance for inverse exponential growth processes. For computational fast and accurate determination of its function values in Eq. (7.3), a Newton–Raphson iteration is applied. The value $w^* = \text{Lambert } W(v)$ is the root of the help function $h(w) := we^w - v$ so that $h(w^*) = 0$. It converges to an accuracy of 10^{-10} in typically less than six iterations. The inverse hysteresis model has been successfully applied as online control to a SPM [7].

The evaluation of (7.3) for the two coordinates x, y of the lateral 2D control takes 1200 CPU clock cycles, or roughly 800 ns on a 1.5GHz CPU.

In order to gain further computational speed, the nonlinear function can be linearly approximated for small displacements $|x-x_0|$, if the error is less than the required positioning accuracy:

$$V(x) \overset{|x-x_0| \text{ small}}{\cong} \frac{1}{b}\left(\frac{b-u}{\alpha}+x\right)+\frac{1}{\alpha}\left[\alpha\left(V_0-\frac{1}{b}\left(\frac{b-u}{\alpha}+x_0\right)\right)\left(1-\frac{\frac{\alpha}{b}(x-x_0)}{1+\alpha\left(V_0-\frac{1}{b}\left(\frac{b-u}{\alpha}+x_0\right)\right)}\right)\right]. \tag{7.4}$$

This approximation is linear in x and therefore facilitates speedy computations without the need for Newton–Raphson iterations. The application of the linear

Table 7.1 Runtime comparison of different control algorithms

Algorithm in SSE2 assembly code	CPU cycles	Time (µs) (P4 at 1.5 GHz)
Non-linear hysteresis control (2D lateral)	1200	0.80
Linearly approximated hysteresis (2D lateral)	200	0.13
Linear response model (2D lateral)	15	0.01
Drift fit (100 samples, 4 components) and χ^2-test	2000	1.33
For comparison: one sample at 50 kHz		20.00

Table 7.2 Decision making of the control algorithm

Use last measured 3D point as current 3D position		
Given the desired new 2D position, calculate new 2D control voltage:	IF displacement in x and $y < 5$ nm →	Linear response model for lateral axes
	IF displacement in x and $y < 100$ nm →	Approximate CH solution for lateral axes
	ELSE → nonlinear CH solution for lateral axes	
Apply new 2D control voltage		
Sample 3D position 100 times		
Calculate drift		

function is bounded by the values of the parameters (a, b, u) to $|x–x_0| < 50$ nm. The time of computation reduces to 200 CPU clock cycles, or roughly 135 ns on a 1.5 GHz CPU.

For $|x–x_0| < 5$ nm, correction for hysteresis is no longer applied, the piezo is treated as a displacement device with a linear response. Then the control algorithm reduces to a single multiplication with a gain value. Table 7.1 shows the time of calculation for the different control functions, coded in optimized SSE2 assembly (see Section 7.4 below).

Table 7.2 sums up the decision making during the feedforward algorithm for the lateral positioning.

7.3.2 Drift

While the hysteretic nonlinear contribution to the movement of a piezoscanner decreases with decreasing scan range, the drifting of the piezoceramic predominates the positioning errors for small scan ranges.

The bandwidth of the control loop is limited to about 500 Hz by the high-voltage amplifier and the stage itself, while the bandwidth of the sampling for 3D-position and tip-feedback is in the order of 50 kHz. This means that about 100 samples of the 3D-position (x, y, z) plus the signal of the photodiode p can be taken between two successive control signals. Each sampled quadruplet (x, y, z, p) is paired with the value of the internal CPU clock in order to provide an absolute time frame for the evaluation of the drift. Keeping track of the absolute time is important since modern multitasking operating systems do not allow real-time control.

After acquisition a line is fitted through each of the four components of the 100 samples. The slopes of the fitted lines indicate the drift of the measurement signals in the time interval between two successive control signals. In order to determine whether the calculated drift represents a significant drift or whether the

100 samples are dominated by random noise, the estimated displacement given by the product of the calculated drift and the time interval of the 100 samples is compared to the noise level of the samples given by the normalized χ^2 value of the fit. Only if the noise level is less than the estimated drift, drift correction will be included in the following loop of the control algorithm.

All these calculations, the linear fit for the four components as well as the χ^2-comparison of the noise level, are done within 2000 CPU clock cycles, or roughly 1.33 μs on a 1.5 GHz CPU, see Table 7.1. This corresponds to less than 1/10th of the time needed to take one single sample.

7.4 Real-Time Control Through SSE2 Assembly

Taking advantage of a recently introduced single-instruction-multiple-data (SIMD) extension to the x86 machine code, the control algorithm is applied simultaneously to values of both the *x*- and *y*-axes. The so-called SSE2 (Streaming SIMD Extension 2) [8] of the Pentium 4 processor now introduces vectorization of variables for the parallel processing of two double-precision or four single-precision real-valued numbers. This CPU feature is predestined for the purpose of controlling a two-dimensional movement in the lateral plane, because the same control algorithm can be applied simultaneously to both *x*- and *y*-coordinates. Double precision is required for sub-nanometer accuracy. Thus, each mathematical operation processes the two individual coordinates (*x, y*) in parallel. This is achieved by loading the two individual datasets of parameters (α_x, b_x, u_x) of the *x*-axis and (α_y, b_y, u_y) of the *y*-axis into memory. Notice that the scan direction $\mathrm{sgn}(\dot{V})$ as defined in (7.1) can be implemented as the sign of α. Therefore, flipping the sign-bit of α_x or α_y automatically sets the corresponding axis control to the desired direction.

The implementation of the linear fit for the drift is straightforward, together with the χ^2 comparison. Since double precision is not required for the determination of the drift, using only single-precision real values offers the possibility to process four individual coordinates simultaneously. Currently, the first three SSE2 components correspond to the three sample axes *x, y,* and *z*, while the fourth component is used for the feedback signal of the AFM scanning tip given by the photodiode.

Both corrections for hysteresis and drift have been hand-coded in SSE2 assembly exclusively, along with additional optimizations for speed. The performance of the drift code is shown in Table 7.1. The computation of both the nonlinear hysteresis control and the drift uses only 10 % of the time which is needed for a single sample.

In order to test the performance of the lateral positioning control, 10 simultaneous steps of 200 nm are applied in both the *x*- and the *y*-directions in order to simulate arbitrary probing. The points of probing lie along a straight line, the residual error being in the order of 20 nm peak-to-peak due to environmental

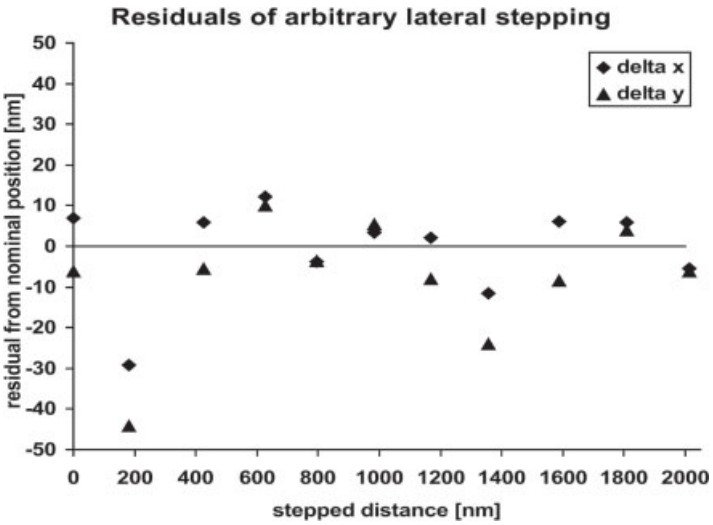

Fig. 7.6 Performance of the lateral control loop. 10 simultaneous steps are applied in both the *x* and the *y* direction to simulate arbitrary probing. The residual positioning errors along the line of stepping are in the order of 20 nm peak-to-peak. This coincides with the order of magnitude of environmental vibrations. The first outlier at 200 nm is due to the intertia of the stage.

vibrations, see Figure 7.6. These are in the same magnitude caused by the not yet optimized set-up. The first outlier at 200 nm is caused by the inertia of the stage. The control algorithm can be adjusted to cope with this initial effect during acceleration.

7.4 Implementation of the Measurement Controller

Conventional scanning results in an image of the surface under study as illustrated in Figure 7.7(a). In this process the operator defines the area of the scan as well as the number of points to be sampled. The resolution of the scan and therefore the accuracy of the analysis is mainly determined by these boundary conditions. If, for example, the pitch or line width of features on the surface has to be determined the only relevant information is located at the edges of the features. When the raster scan is processed to extract these features most information in the image is irrelevant and not used in the analysis. When we, however, only acquire data at the edges, see Figure 7.7(b), and ignore the rest of the surface, only the relevant information with maximum accuracy is obtained. The concept of probing described above requires the position control to correspond to any desired lateral movement. Therefore, a new command structure has been developed which allows the scanner to trace any lateral polygonal chain. The polygonal chain may consist of any pair of steps (Δx, Δy) in the *x*- and *y*-direction with a number

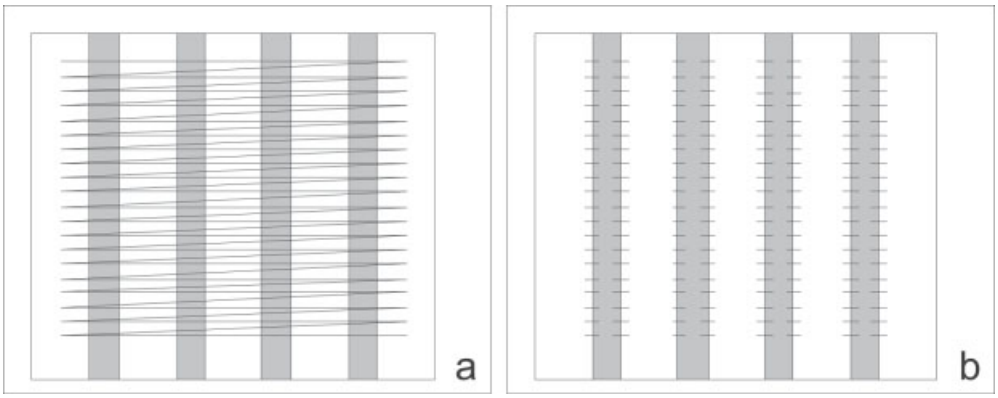

Fig. 7.7 Conventional scanning of a pitch or line width standard (a) results in redundant data and loss of accuracy while in (b) only the relevant data, at the edges, is probed with maximum accuracy.

n of repetitions of the step. A Boolean flag r determines whether or not to record while stepping n-times along $(\Delta x, \Delta y)$. Thereby the ith change of direction of the polygon chain is defined by $\begin{pmatrix} (\Delta x, \Delta y)_i \\ n_i \\ r_i \end{pmatrix}$. With this structure, any desired point within the 100 μm × 100 μm scan area can be reached and probed. Even the conventional rectangular scan along x and y is programmable.

A disadvantage of this method is that one needs a priori knowledge about where exactly to find the features of interest on the sample. This can easily be overcome by doing a low-resolution fast scan of the total sample surface and then marking the areas of interest.

7.6 Image Analysis

Since the measurement protocol as described above does not result in an image but in a set of coordinates, regular scanning probe image analysis software cannot be used to extract the required parameter values. The measurement has some similarities with measurements performed by a 3D CMM. However, the probe of a 3D CMM is calibrated and has a very well known shape while the probe of a SPM is usually only known approximately (see Figure 7.8). Even if the SPM probe is characterized very well before use, probe-surface interaction results in tear and wear during normal use that changes the characteristics of the probe. Therefore, when compared in relation to CMMs, a larger measurement uncertainty is to be expected when using CMM software algorithms. In this context it is important to identify valid sample points from those which have been recorded while the tip was not in a state of equilibrium at its set-point.

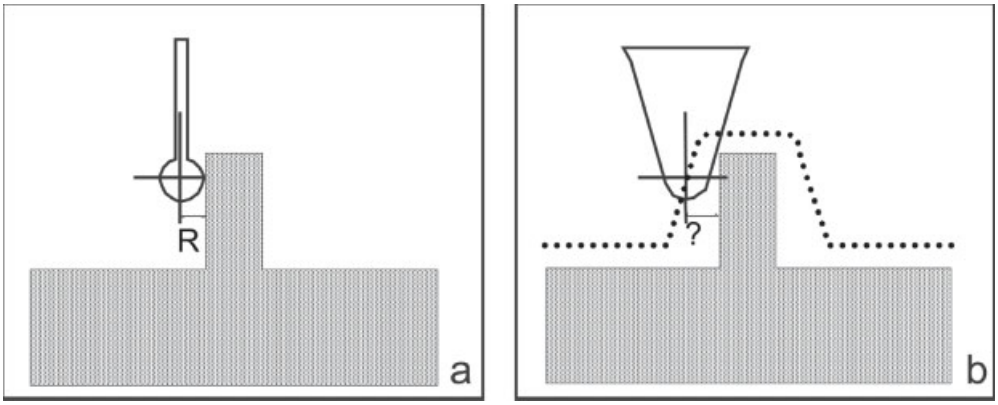

Fig. 7.8 In contrast to CMM measurements (a) where the probe is calibrated a SPM probe (b) is usually not well characterised resulting in additional measurement uncertainty.

Figure 7.10 shows the profile of a step. The rounded edges indicate a large settling time of the z piezo. The error signal from the photodiode clearly displays peaks at the edges. The cantilever is deflected and the tip is no longer at its equilibrium state of its set-point (see Figure 7.9). As a consequence, the sampled coordinates do not match the true topography of the surface. Therefore the edges should be marked as not being valid samples. With our probing algorithm it is possible to online identify these features during the process of sampling. The effect of a large settling time is immediately visible in the χ^2-analysis of the signal of the photodiode. An intelligent control algorithm can easily recognize this and either reduce the scan velocity until a stable tip signal is available again, or the samples can simply be discarded. Only those points are considered to be valid samples, when the signal of the photodiode constantly remains within a threshold around its set-point. The noise level of the photodiode signal is in the order of 0.1 nm (see Figure 7.10).

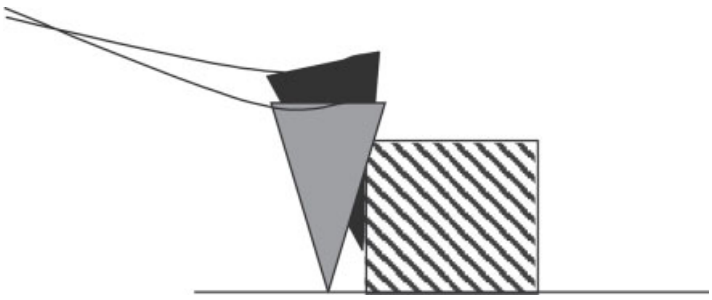

Fig. 7.9 At sharp edges, the cantilever is deflected (black tip) and the tip is no longer at its equilibrium state of its set-point (grey tip). The sampled data in this situation does not accurately match the topography of the sample.

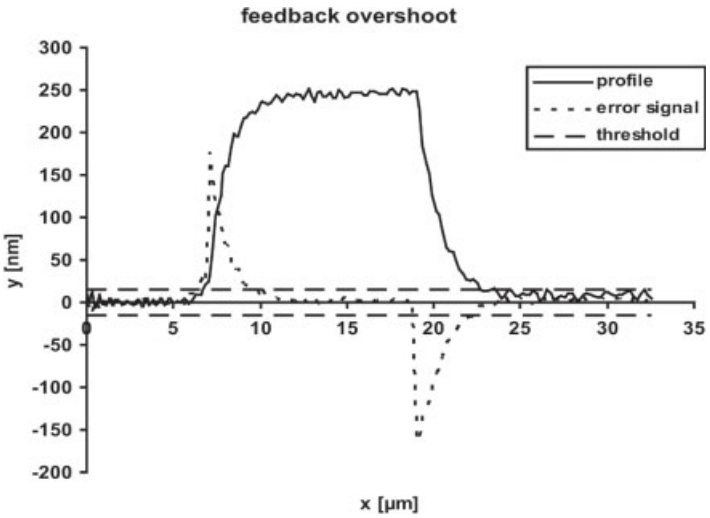

Fig. 7.10 The scanned profile over a step height (solid line) exhibits round edges which are caused by the large settling time of the *z* control. The error signal (dotted line) as recorded by the photodiode clearly shows the slow response of the feedback loop at steep edges. The dashed line indicates the threshold for the error signal. The corresponding part of the sampled profile can be treated as valid data if the error signal remains within its threshold. The noise of the photodiode signal is in the order of 0.1 nm.

7.7 Conclusions

We have established a 3D-controlled AFM with nanometer accuracy, which is directly traceable to the length standard. The position uncertainty is in the order of one nanometer. The advanced high-speed control software allows traditional scanning as well as isolated probing of metrologically interesting sample features only. Sources of uncertainty that evolve from data aging have been successfully tackled. In addition, a procedure is proposed to use the error signal of the photodiode online in order to identify the measurement quality of the sampled points. Upon the tip leaving its state of equilibrium, either the data can be discarded or the following measurement can be actively controlled in order to return the tip to its set-point. The machine coded control algorithm offers further possibilities to use the computational reserves for intelligent automated measurement control, such as automatic edge tracing.

Acknowledgments

We would like to thank Suzanne Cosijns from TU Eindhoven for the measurements on the nonlinearities of the laser and the optical component of the interferometers. The construction of the scan table to integrate the various parts of the traceable AFM was realized in close cooperation with the Department of Precision Mechanics of TNO TPD.

References

1 G. Binnig, H. Rohrer, Ch. Gerber, and E. Weibel, Physica **109** & **110** B, 2075–2077 (1982).
2 P-517.3 NanoPositioner, Physik Instrumente (PI), Karlsruhe, Germany.
3 ZMI 2000 3D interferometric system, Zygo Corporation, USA.
4 K. Dirscherl et al., Modeling the hysteresis of a scanning probe microscope, J. Vac. Sci. Technol. B **18**(2), (2000).
5 B. D. Coleman, M. L. Hodgdon, A constitutive relation for rate-independent hysteresis in ferromagnetically soft materials, Int. J. Eng. Sci. **24**(6), 897–919 (1986).
6 R. M. Coreless et al., On the Lambert W Function, Adv. Comput. Math. **5**(4), 329–359 (1996).
7 K. Dirscherl, Online correction of scanning probe microscopes with pixel accuracy, Ph. D. thesis, Technical University of Denmark, Lyngby, 2000.
8 Intel, IA-32 Intel Architecture Software Developer's, Vol. 1–3 (2002), order numbers 245470-006, 245471-006, 245472-006.

8
Scanning Probe Microscope Setup with Interferometric Drift Compensation

Andrzej Sikora, Dmitri V. Sokolov, and Hans U. Danzebrink

Abstract

Scanning probe microscopes (SPMs) are extremely sensitive instruments, which are strongly influenced by external environmental disturbances. The final quality of the picture depends on system stability as well as thermal, mechanical, and electrical noise immunity. Although one can isolate the SPM very carefully, but it is impossible to avoid any, e. g., thermal, drift in the system. We present an interferometric add-on system applied to a scanning probe microscope construction which allows us to monitor drifts of the scanning head and to reduce its influence on the measurement result.

8.1
Motivation

In a scanning probe microscope (SPM) we expect perfect mechanical stability of the scanning head. This is important since the *z*-piezo movement reflects the topography changes measured during the scanning process. If instabilities or drifts occur between the scanning head and the surface, the scanning *z*-piezo compensates these drifts resulting in artificial *z*-motions added to the sample's topography. As a consequence, the measurement result consists of both the topography and drift information. However, even if we would know about the presence of thermal drifts in the setup, we could not remove those artifacts from the imaging result alone because of their nonlinear and random behavior.

Some of our SPMs are designed as add-on systems, which are plugged into conventional optical microscopes [1, 2]. In these setups an optical microscope body from Zeiss ("AXIOTECH") was used as a base (Figure 8.1). Such constructions are not optimized for SPM applications and have a lot of elements that can introduce disturbances and artifacts because of thermal drift. Because of their geometry the most critical drift motion happens in vertical direction.

Nanoscale Calibration Standards and Methods: Dimensional and Related Measurements in the Micro- and Nanometer Range.
Edited by Gunter Wilkening, Ludger Koenders
ISBN: 3-527-40502-X

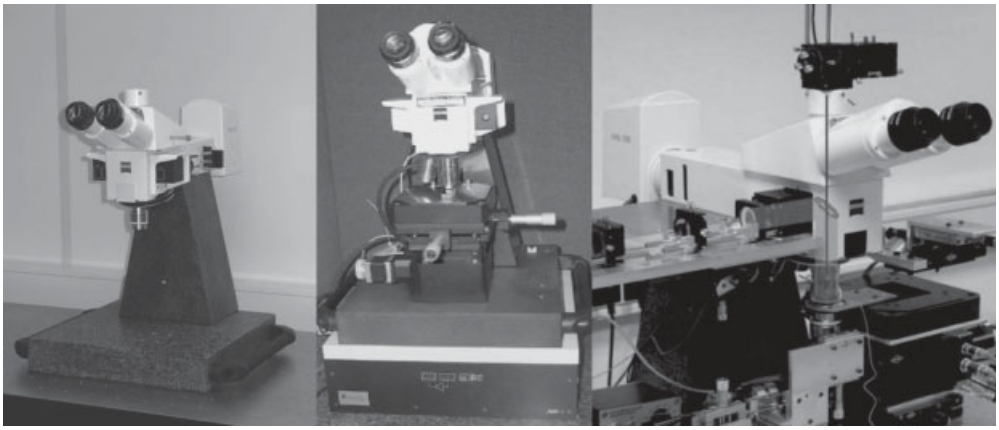

Fig. 8.1 Base construction of the optical microscope and some add-on SPM systems.

Typical artifacts caused by mechanical instabilities resulting in a nonsurface-related motions between the SPM and the surface are presented in Figure 8.2. Some software programs can do line wise filtering and most of such artifacts can be removed. Nevertheless, we do not have any quantitative information about this correction. Moreover, digital processing of the picture is not perfect and can introduce new artifacts. In addition, it must be noted that line wise filtering cannot remove every distortion caused by mechanical instabilities (including thermal drift), because some artifacts are also present in the fast scanning axis.

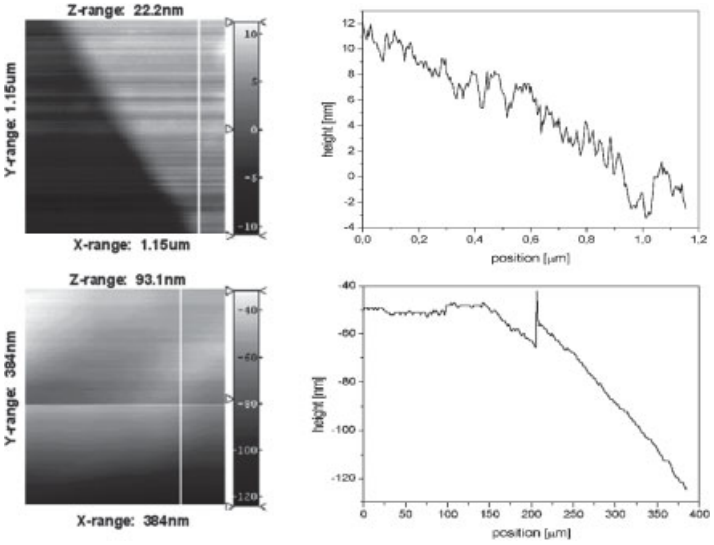

Fig. 8.2 Typical artifacts caused by mechanical instabilities of the setup of an SPM.

Simultaneous measurement of the instrument's drift would give a chance to remove its influence on the measurement result and to improve the final quality of the picture. Additionally, after investigation of the thermal behavior of the microscope, its construction may be improved with respect to this influence.

For the observation of thermal drift during measurement, an interferometric measurement system is proposed in this chapter. This method allows us to obtain high-resolution and high-accuracy measurements. A known and precisely defined wavelength can be used as a reference to quantitative and even traceable distance measurements.

8.2
Existing Setup – Without Drift Compensation

One of the best methods to avoid artifacts due to drift is to make the scanning head as small as possible using materials with the smallest possible thermal expansion coefficient. However, in some particular cases such a solution is impossible or uncomfortable.

The microscope – SPM solution shown in Figure 8.1 has a large "measurement circle" as illustrated in Figure 8.3(a). Therefore, several mechanical instability sources are present in this system. In order to improve the mechanical stability, the original iron cast stand was replaced by a granite base (Figure 8.1). It is not only the base of the microscope which introduces thermal drift, but also the *x*-, *y*-, *z*-coarse positioning stages, the SPM module, and the scanning piezo stage have also been taken into account. To reduce the influence of the number of possible drift sources a shortened "measurement circle" is proposed in this chapter (Figure 8.3(b)). This shortening is achieved by a direct measurement and compensation of the drift without significantly changing the scanning head construction.

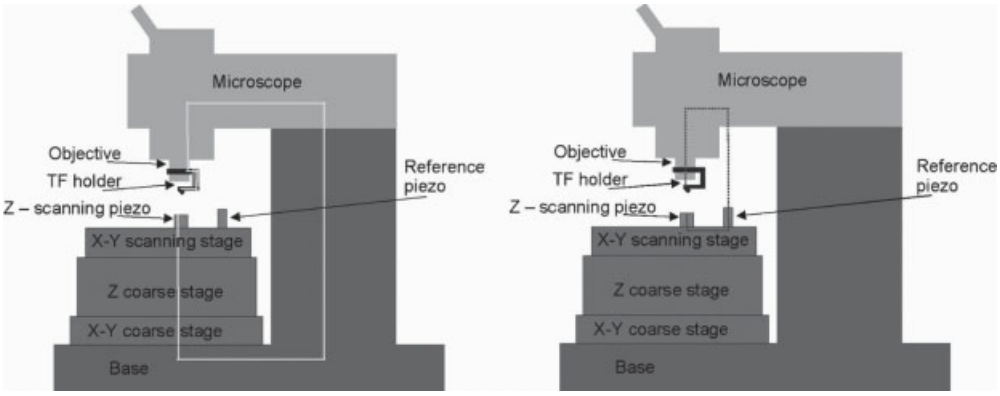

Fig. 8.3 (a) The large "measurement circle" of the uncompensated instrument and (b) the reduced "measurement circle" with interferometric drift compensation.

8.3 Measurement Method and Setup for Drift Compensation

In this realization, the SPM module is equipped with a quartz tuning fork (TF) used as the sensing element [3, 4]. To increase lateral resolution a specially commissioned whole diamond probe tip is mounted on the underside of the lower tineof the tuning fork [5]. This module is attached to the microscope objective using a ring adapter (see Figure 8.4).

To measure drifts in this system, with single-nanometer resolution, we introduced an optical interferometer into the measurement setup. This method allows us to obtain quantitative information about distance changes between the SPM head and the surface. Instead of a complicated interferometric fringe counting system, a control loop was established which tracks and holds a certain value of one interference fringe (see the following sections).

This interferometric setup was designed to be added to the existing SPM and optical microscope construction (Figure 8.4). Since the backside of the diamond tip is polished and orientated parallel to the sample surface, this plane is selected as the first mirror of our differential interferometer. The second mirror is placed next to the base for the scanning *z*-piezoactuator.

The motion to keep the tip–sample distance constant is performed by the sample stage, while the position of the tip remains the same (apart from its oscillating motion). For this reason, the distance between the SPM module and the reference mirror should be constant. Any movement, e. g., caused by a drift motion, is observed by this interferometer. We simulated the interferometer response on

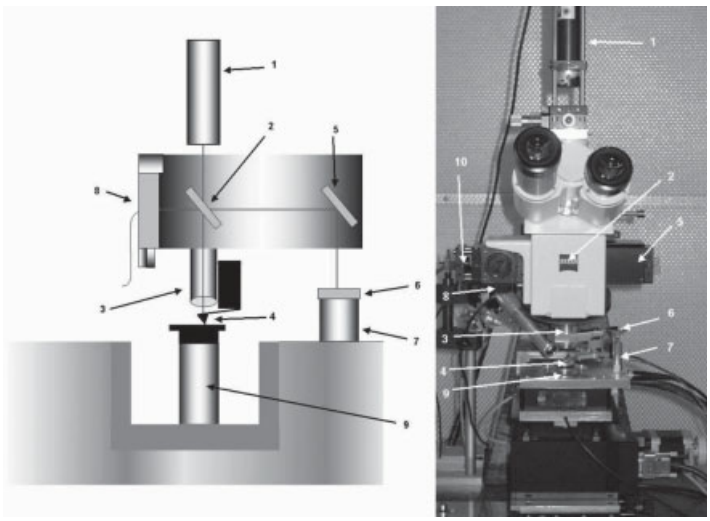

Fig. 8.4 Diagram and photo of the setup: (1) laser, (2) beam splitter, (3) objective, (4) scanning tip, (5) mirror, (6) reference mirror, (7) reference piezo, (8) photodiode, (9) scanning *z*-piezo, and (10) CCD camera.

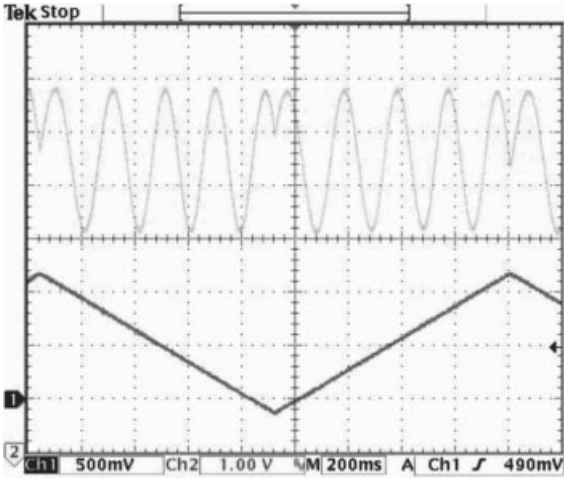

Fig. 8.5 Interferometric fringes (upper curve) and reference mirror driving voltage (lower curve). The scanning tip position was constant (no TF oscillation).

changes in this optical path by moving the reference mirror. The result is presented in Figure 8.5.

During the SPM operation the tuning fork (TF) is electrically driven at its resonance frequency (Figure 8.6). Consequently, the optical signal of the interferometer is also modulated due to the oscillating motion of the TF. For a reduction of noise a lock-in amplifier is used to measure the interferometer signal. When the average interferometer mirror distance is constant we expect a constant lock-in readout value. Otherwise we observe a readout change (amplitude and phase). An example of such an output signal is presented in Figure 8.7. We applied a typical excitation signal to the TF (oscillation amplitude: ca. 10 nm) and a triangle signal to the piezo with the reference mirror to simulate the scanning head drift (lower signal). The observed signal (amplitude multiplied by phase) is represented by upper curve.

Fig. 8.6 View of the SPM head: tuning fork holder with the tuning fork and its glued diamond tip.

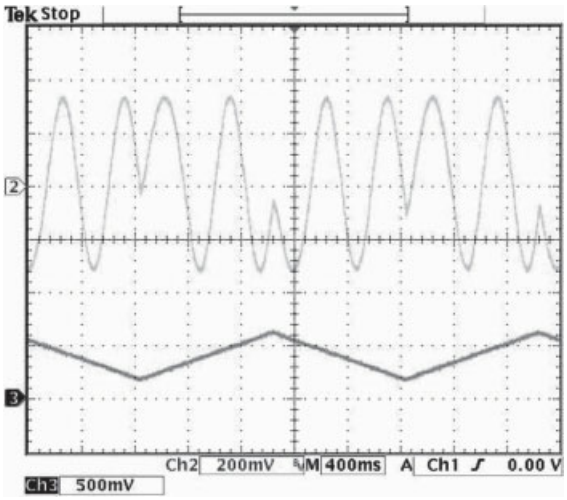

Fig. 8.7 Lock-in output signal (upper curve) and reference mirror driving voltage (lower curve). TF oscillation amplitude: 10 nm.

Since the lock-in output value represents a definite interferometer mirror distance, it is possible to track a certain value of an interference fringe and to use a feedback module to keep the lock-in response constant. This constant value is achieved by moving the reference mirror. The introduced motion compensates the drift motion and preserves the optical path length in the interferometer. Finally, the voltage applied to the reference piezo is recorded and used to monitor the mechanical drift of the scanning head.

The part of the signal processing unit which serves for the drift compensation includes a photodiode with preamplifier to detect the interference fringes, a lock-in amplifier, and a *PI* regulator with the possibility of changing amplification factors, as well as *P* and *I* parameters. Also an internal stable setpoint voltage source is implemented. For the analog drift compensation a simple subtracting module (with proportion 1:1) is added. The circuit also permits to add "artificial" drift signals to test the device (concerning control loop parameters, sensitivity, ...). Finally, three outputs allow us to observe and acquire each of the signals independently: topography signal (without compensation), thermal drift, and compensated topography signal.

The described signal processing unit was designed to be used as an add-on module for the existing setup to make the whole system more universal and reliable, and to avoid uncomfortable reconnection procedures. The complete electronic system is sketched in Figure 8.8.

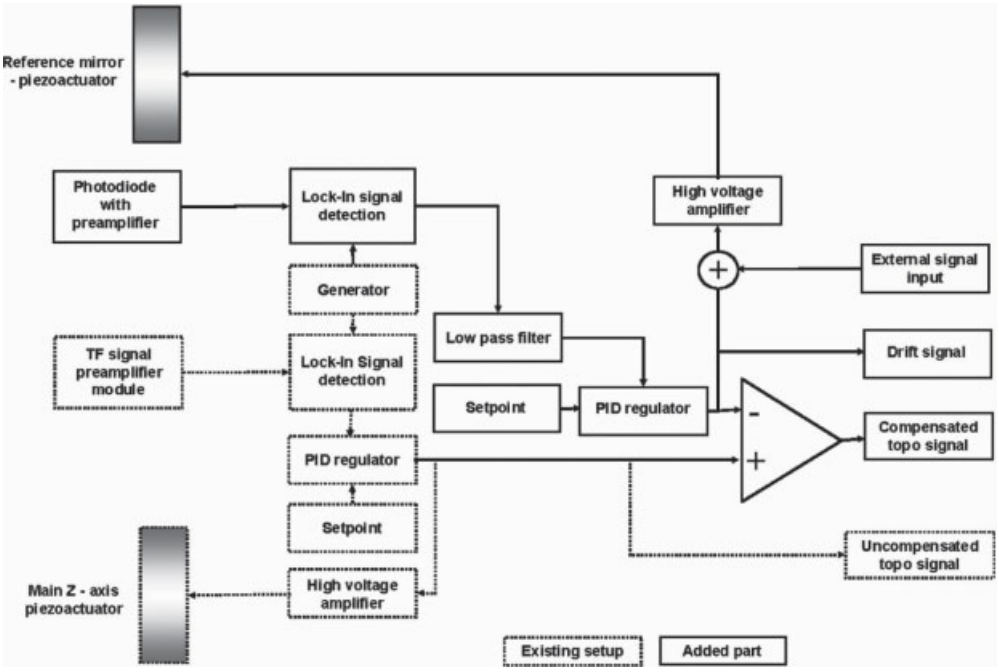

Fig. 8.8 Signal processing setup. The electronics include the laser interferometer readout ("photodiode with preamplifier") and the TF distance control ("TF signal preamplifier module", . . .," PID regulator").

8.4 Experiment and Results

Simultaneous measurements of sample topography and thermal drift were performed. To achieve real measurement conditions, especially concerning the thermal behavior, *x*-, *y*-scanning were also carried out instead of measuring the *z*-motion only and keeping the lateral position of the tip fixed. As the sample, a flat silicon surface was chosen. For this extremely flat and smooth sample the recorded uncompensated topography signal should be mainly due to the drift motion and not due to the sample's topography (see Figure 8.9).

The presented results from Figure 8.9 show a good agreement between the uncompensated topography signal and the thermal drift signal derived independently from the laser interferometer. Some artificial mechanical instabilities were simulated by adding a couple of nanometer shifts to the coarse *z*-stage. They are well visible in both pictures (positions: ca. 260 nm and 350 nm). Afterwards, the thermal drift is subtracted from the uncompensated topography signal using a data processing software. As a result, the *z*-range of the data is reduced from about 67 nm to 31 nm (Figure 8.10).

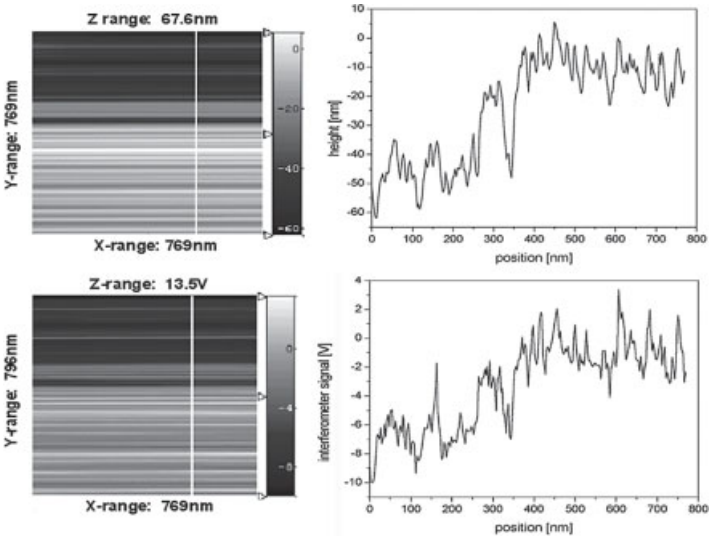

Fig. 8.9 Simultaneously recorded results of the uncompensated topography signal and the thermal drift signal. Upper part: uncompensated topography signal of a flat silicon surface, and lower part: corresponding drift signal from the interferometer (scanning speed: 1 line/s, environmental chamber: open).

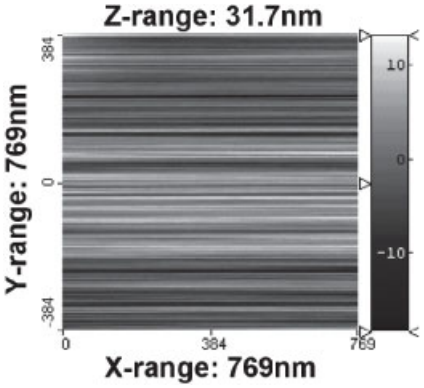

Fig. 8.10 Result of the subtraction between topography and drift data.

Because the thermal drift obviously depends on the ambient temperature stability, we compared drifts with opened and closed environmental chamber (Figure 8.11).

The instability of the microscope setup was reduced by a factor of 2 (deduced from the *z*-ranges) after closing the measurement chamber (about 150 nm *p–v* value with opened chamber and about 80 nm with closed chamber).

We also recorded the temperature changes in a 90 min time period (Figure 8.12). The room temperature was 21.3 °C. In the closed chamber the temperature was about 1.5 °C higher than outside. As expected, the warming-up process after closing the chamber is well visible in Figure 8.12 (curve in the middle).

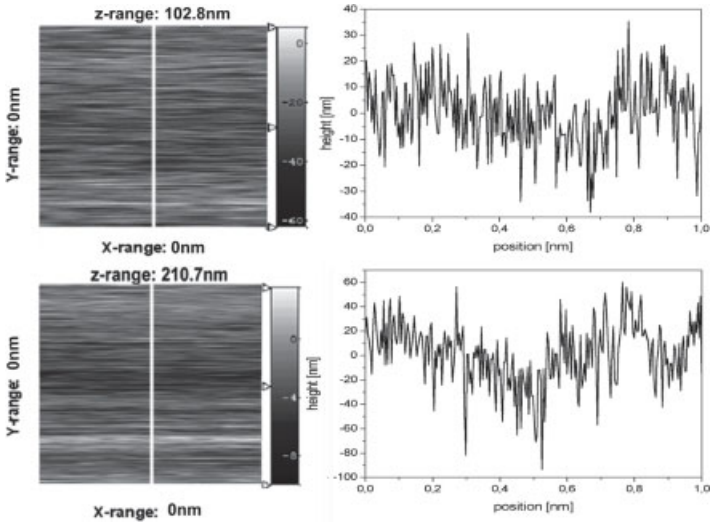

Fig. 8.11 Comparison of the setup's thermal drift: with closed chamber (above), and with opened chamber (below). Please note the different *z*-scale ranges.

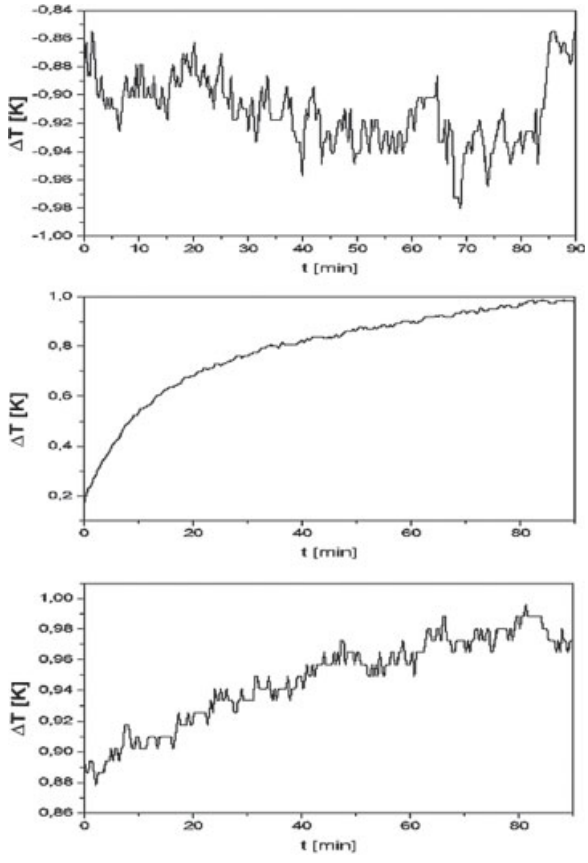

Fig. 8.12 Temperature changes in the microscope's environment, measured inside the chamber. Open chamber (upper curve), just after closing the chamber (in the middle), and a couple of hours after closing the chamber (lower curve).

8.5 Summary

The presented setup allows us to monitor thermal drifts of the SPM measurement system and to subtract the drift signal from the resulting "topography" image. The drift motion is measured by a Michelson interferometer, which is realized as an add-on module to the existing setup. The same interferometer allows us to obtain quantitative information about the oscillation amplitude of the scanning tip. Furthermore, by adding a fringe counting system it is possible to monitor the complete approach process of the SPM, including coarse and fine motion, very precisely.

References

1 C. Dal Savio, H. Wolff, T. Dziomba, H.-A. Fuß, and H.-U. Danzebrink, A compact sensor-head for simultaneous scanning force and near-field optical microscopy. Precision Eng. **26**, 199–203 (2002).

2 T. Dziomba, L. Koenders, H.-U. Danzebrink, and G. Wilkening, Lateral & vertical calibration of scanning probe microscopes and their measurement uncertainty, in *Proceedings of the XIth International Colloquium on Surfaces*, 2–3 February 2004 , edited by M. Dietzsch (Shaker Verlag, Aachen, 2004). ISBN 3-8322-2419-X.

3 P. Güthner, U.Ch. Fischer, and K. Dransfeld, Scanning near-field acoustic microscope. Appl. Phys. B **48**, 89 (1989).

4 K. Karrai and R. D. Grober, Piezoelectric tip–sample distance control for near field optical microscopes. Appl. Phys. Lett. **66**, 1842–1844 (1995).

5 J. W.G. Tyrrell, D. V. Sokolov, H.-U. Danzebrink, Development of a scanning probe microscope compact sensor head featuring a diamond probe mounted on a quartz tuning fork. Meas. Sci. Technol. **14**, 2139–2143 (2003).

9
DSP-Based Metrological Scanning Force Microscope with Direct Interferometric Position Measurement and Improved Measurement Speed

Gaoliang Dai, Frank Pohlenz, Hans-Ulrich Danzebrink, Klaus Hasche, and Günter Wilkening

Abstract

A digital signal processor (DSP)-based signal processing system is designed and implemented in an existing metrological scanning force microscope (M-SFM) of PTB named "Veritekt C"; hence the M-SFM is improved at two important aspects: (1) The DSP system is capable of processing the interferometer signals with online Heydemann corrections. This reduces the residual nonlinearity of interferometers from about 3.5 nm to less than 0.3 nm. As a result, the M-SFM is presently working with direct interferometric position measurement. (2) All sensors of the M-SFM, including the optical detector (for measuring the bending of the cantilever) and all interferometers, are sampled synchronously during scanning; therefore it is possible to derive the surface topography from the combined value of the result of the *z*-interferometer and the bending of the cantilever. As the benefit, the surface topography can be accurately measured during scanning even when the bending of the cantilever has some deviations from its setting value. Therefore the scanning speed of the M-SFM can be enhanced without any compromise of decreasing the measurement performance.

This chapter introduces the new design in detail and some measurement results are given to illustrate the effectiveness of this implementation.

9.1 Introduction

Measuring artifacts with a well-defined structure is a convenient and widely used method for the calibration of many kinds of microscopes and topographic measurement instruments, such as scanning force microscopes (SFMs), profilometers, and optical and scanning electron microscopes. Usually, one- or two-dimensional gratings are used for calibrating the *xy*-plane, and step-height standards for calibrating the *z*-axis. However, those standards have to be calibrated in

Nanoscale Calibration Standards and Methods: Dimensional and Related Measurements in the Micro- and Nanometer Range.
Edited by Gunter Wilkening, Ludger Koenders
ISBN: 3-527-40502-X

advance by higher accuracy methods, for instance, a metrological scanning force microscope (M-SFM). Compared to normal SFMs, a special feature of M-SFMs is that they are equipped with optical interferometers. In such a way, their measurement results can be directly traced to the meter definition.

Several M-SFMs aimed for a measurement uncertainty at the nanometer or sub-nanometer level are developed at national metrology institutes worldwide [1–6]. Based on the role of the optical interferometers used in the instruments, the operation mode of those M-SFMs can be classified into two groups. One group is using optical interferometers only for calibration purpose while capacitive sensors are still serving as position sensors during the measurement [1–3]. This is what we call "calibration mode" in this context. The other group is using optical interferometers for position readout or for direct position control [4–6]. It is called "direct measurement mode." Both modes have their own advantages and disadvantages. For example, the calibration mode can reduce the influence of inherent nonlinearities of optical interferometers by conducting the calibration at integral interference fringes that are perfectly equidistant. But, as a drawback, frequent calibration is needed. With the direct measurement mode, however, the resolution and nonlinearity of optical interferometers have to be carefully investigated and improved. The prevailing conditions in a system define the adequate operation mode.

In this chapter, a digital signal processor (DSP)-based signal processing system is realized for an existing M-SFM of PTB named "Veritekt C." By implementing this design, the Veritekt C is improved at two important aspects. Firstly, the interferometer signals processed with online Heydemann corrections result in a reduction of the nonlinearity of the interferometers from about 3.5 nm to less than 0.3 nm. This allows us to use the interferometers for direct position measurement, and thus change from the calibration mode to the direct measurement mode. Secondly, sensors of the M-SFM, including all interferometers and the optical detector of the cantilever, are sampled synchronously; as discussed below, this permits us to significantly increase the scanning speed of the M-SFM.

9.2 Instrument

9.2.1 Principle

A principle sketch of the M-SFM "Veritekt C" is shown in Figure 9.1. It is a scanning sample system with a stationary fixed cantilever probe. The 3D monolithic flexure-hinge stage with a scanning range of 70 μm × 15 μm × 15 μm along the *x*-, *y*-, and *z*-axes, respectively, is driven by piezoelectric translators (PZTs) equipped with capacitive sensors. The sample holder is fixed on the flexure-hinge stage. Its position is measured by three homodyne planar interferometers, which were designed in cooperation with SIOS Messtechnik GmbH and the Tech-

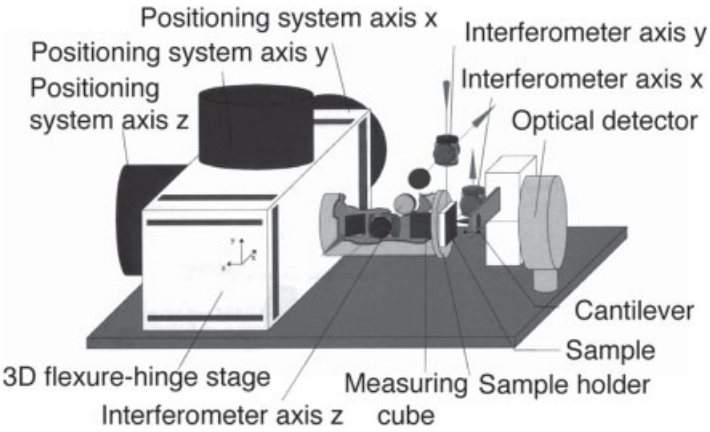

Fig. 9.1 Principle sketch of the M-SFM Veritekt C.

nical University of Ilmenau [7]. When the sample is mounted, its measurement point lies at the point of intersection of the three interferometer measurement beams so that the Abbe error can be minimized. For measurement, the sample is coarsely approached to the tip by a step motor (not shown in Figure 9.1), and is then scanned in contact mode. In this mode, the bending of the cantilever, measured by an optical detector, is kept constant. The base plate is made from Zerodur and the remaining structures are almost all made from super invar to enhance the thermal stability.

9.2.2 DSP-Based Signal Processing System

The "Veritekt C" is implemented with a newly designed DSP-based signal processing system. The signal flow chart of the instrument is depicted in Figure 9.2. It consists of four blocks. Block I is a DSP system that is the core of the whole signal processing system. During measurement, the DSP system runs with a servo loop at a bandwidth of 20 kHz. This servo loop deals with the following tasks:

a) It outputs a pair of analog signal that is fed to the block II (analog PZT controller) for scanning the sample along the *x*- and *y*-axes. This procedure is managed by the submodules "X-scanner" and "Y-scanner" in the DSP.
b) It latches and analog-to-digital converts the electrical signals of all interferometers, which are further demodulated in submodules "ISDU" of the DSP.
c) It latches and analog-to-digital converts the tip signal (sum and differential signal) from the optical detector for measuring the bending of the cantilever. The result is further fed

to a digital PID servo controller (DSC in Figure 9.2). The DSC outputs an analog signal to the block II for moving the sample along the *z*-axis. In such a way, the SFM tip bending is kept to a constant value ($Z_{Setting}$).

d) The demodulated sample position is monitored by a latch signal generator (LSG in Figure 9.2). Once the sample position has reached one of the desired measurement points, the LSG sends out a command to latch the measurement results, including both the sample position (the values of all interferometers) and the bending of the cantilever, into a data buffer. It should be stressed that the measurement results are sampled at a synchronization clock signal (SCLK in Figure 9.2).

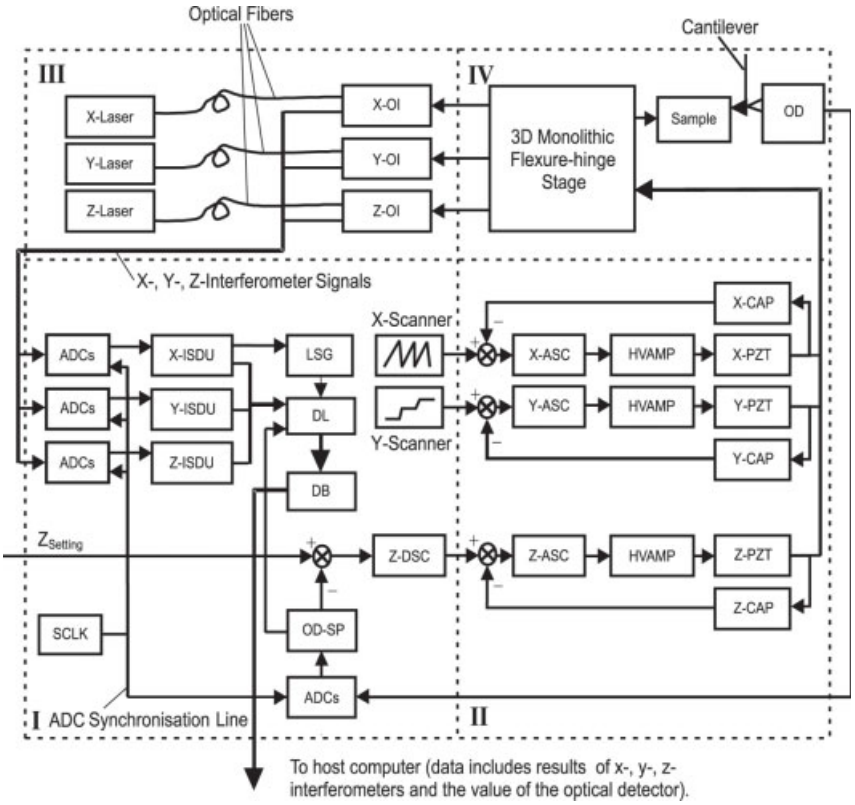

Fig. 9.2 The signal flow chart of the instrument. Legend in the figure are as follows: ASC, analog servo controller; DSC, digital servo controller; HVAMP, high voltage amplifier; CAP, capacitive sensor; PZT, piezoelectric transducer; OI, optical interferometers; ISDU, interferometer signal demodulation unit; OD, optical detector; OD-SP, signal processing unit for the optical detector; ADC, analog-to-digital converter; SCLK, synchronization clock; LSG, latch signal generator; DL, data latch; DB, data buffer; I, DSP system; II, analog PZT controller; III, optical interferometer system; IV, M-SFM body.

e) The measurement data will be transferred to host computer via a PCI bus after a line scan has been completed. Finally, the precise surface topography can be calculated from the combined value of the result of the *z*-interferometer and the bending of the cantilever at the host computer.

Block II is an analog PZT controller made by Queensgate company. It positions the sample along the *x*-, *y*-, and *z*-axes according to the applied voltages from block I. Block II is presently working in a closed loop using capacitive sensors for feeding back.

Block III is the optical interferometer system. In this block, the electronic signals of the interferometers have only been preamplified before they are fed to block I. Block IV represents the M-SFM body as shown in Figure 9.2.

9.2.3
Calibration of the Tip Signal for Traceably Measuring the Bending of the Cantilever

The bending of the cantilever has to be calibrated traceably since it is incorporated in the measurement results. For this purpose, an automatic procedure has been implemented to calibrate the tip signal against the *z*-axis interferometer in situ: After approaching the tip toward the sample, the sample is moved in the *z*-direction for about 50 nm while keeping its *x*-, *y*-position unchanged; therefore, a fixed point on the sample is measured by the SFM tip, and the sum value of the *z*-axis interferometer and the bending of the cantilever should be constant. By recording simultaneously the value of the *z*-axis interferometer and the tip signal, the tip signal can be calibrated. This automatic calibration procedure does not need any other additional devices or changes in the experimental setup and can be executed easily within the measurement software. As an example, one calibration result is shown in Figure 9.3.

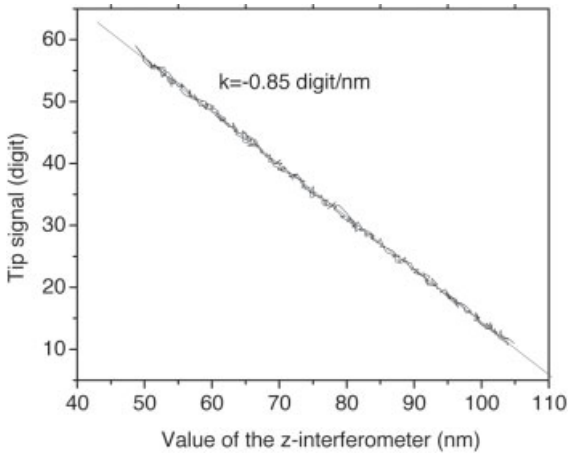

Fig. 9.3 Calibration result of the tip signal against the *z*-axis interferometer.

9.3
Correction of Nonlinearity of the Optical Interferometers in the M-SFM

9.3.1
Review of Nonlinearity Correction Methods

The ideal homodyne interferometer setup delivers a pair of electrical signals (u_1,u_2) with identical amplitude, zero offset, and exactly 90° phase difference for bidirectional counting and fringe subdivision. However, polarization mixing, laser power drift, laser beam misalignment, imperfection of electronic processing, and the error motion of the stage will cause the Lissajous trajectory of the two phase-quadrature signals to be distorted from the ideal circle. These distorted phase-quadrature signals (u_1^d, u_2^d) obtained by respective photodetectors can be expressed as follows:

$$\begin{aligned} u_1^d &= u_1 + p \\ u_2^d &= \frac{1}{r}(u_2 \cos\alpha - u_1 \sin\alpha) + q \end{aligned} \tag{9.1}$$

One possibility of correcting those distorted signals is published by Heydemann [8]. He used a least-squares ellipse fit to calculate the parameters p,q,r, and α. After that, the ideal vector (u_1, u_2) is recovered from the distorted vector (u_1^d, u_2^d). This method, which reduces the nonlinearity significantly, is widely used [9] and also known as *Heydemann correction*.

However, since the Heydemann correction needs complex computation, it is mainly used offline for postprocessing interferometric signals. As a compromise, the *gain/offset correction method*, which uses the parameters p, q, and r to recover the distorted vector by assuming $\alpha = 0$, is mostly adopted for real-time nonlinearity correction. It needs no time-consuming least-squares ellipse fit, and therefore, it is feasible to be realized by firmware in digital signal processors or pure hardware. There exist different methods to determine p, q, and r. The simplest way is to adjust the gain/offset potentiometers of the signal amplifier manually while monitoring its Lissajous trajectory to be a zero-centered circle. An alternative automatic way can be realized by adopting a pair of A/D converters, recording the peak values ($u_1^{\max}$, $u_1^{\min}$, $u_2^{\max}$, $u_2^{\min}$) of the conversion result while scanning the vector over several circles. Afterward, the parameters p, q, and r can be calculated as

$$\begin{aligned} p &= \frac{u_1^{\min} + u_1^{\max}}{2} \\ q &= \frac{u_2^{\min} + u_2^{\max}}{2} \\ r &= \frac{u_1^{\max} - u_1^{\min}}{u_2^{\max} - u_2^{\min}}. \end{aligned} \tag{9.2}$$

9.3.2
Adapted Heydemann Correction in a Fast Servo Control Loop

Nowadays M-SFMs are aiming at uncertainties in the sub-nanometer range following the increasing demands from industry. The Heydemann correction is the feasible solution for decreasing the nonlinearity of homodyne interferometer into sub-nanometer range. However, the least-squares ellipse fit of the Heydemann correction is quite time-consuming and cannot be realized online for sufficiently fast scanning speeds. To solve this problem, we use the Heydemann correction in an alternative way: calculate ellipse parameters at first, and then fix these parameters in the servo control process for a certain time (a few minutes or hours, depending on the stability). To use this method, two preconditions must be fulfilled: (1) The ellipse parameters must be stable over the whole servo control time; and (2) the ellipse parameters must be constant over all the movement range of the stage. It was confirmed experimentally that all interferometers of our SPM fulfill the above preconditions. As an example, the data of the *z*-axis are shown in Table 9.1. The maximum changes of these parameters are less than 0.1 %.

Table 9.1 Ellipse parameters calculated from measurements at different *z*-positions. Here, A_{u1} and A_{u2} are the amplitudes of signals u_1^d and u_2^d, respectively

Position (µm)	p/A_{u1} (%)	q/A_{u2} (%)	r	α (rad)
−8.1	−1.87	−1.17	1.0347	0.0212
−6.8	−1.88	−1.20	1.0347	0.0213
−5.5	−1.85	−1.18	1.0345	0.0214
−4.1	−1.91	−1.21	1.0347	0.0210
−2.7	−1.91	−1.21	1.0347	0.0210
−1.4	−1.91	−1.21	1.0350	0.0210
0	−1.88	−1.19	1.0348	0.0214
1.4	−1.89	−1.14	1.0346	0.0213
2.7	−1.89	−1.21	1.0351	0.0213
4.1	−1.90	−1.18	1.0347	0.0208
5.5	−1.89	−1.20	1.0349	0.0212
6.8	−1.92	−1.15	1.0347	0.0209
Maximum change	0.07	0.07	0.0006	0.0006

9.3.3
Performance of the Interferometers in the M-SFM Veritekt C

We experimentally measured the residual interferometer nonlinearity by using three different correction methods at different times. During the experiments, the stage is scanned in the z-direction by the respective piezoelectric actuator. The scan range is exactly 2λ, where λ is the optical wavelength of the laser light. The readouts of capacitive sensors and interferometers are recorded simultaneously. The results are depicted in Figure 9.4, showing the complete correlation curve and the deviation from linearity. Figure 9.4(a) shows the result when no correction method is applied. Figure 9.4(b) shows the result when the gain and offset correction method is applied. Figure 9.4(c) shows the result when the Heydemann correction method is used in real time.

Figure 9.4(a) shows first- and second-order residual nonlinearity with total peak-to-valley amplitude of about 3.5 nm, the first-order nonlinearity being the significant part. The first-order nonlinearity is the result of nonzero offset in the interferometer signals during demodulation. The second-order nonlinearity is caused by the fact that the signals are with unidentical amplitude and not exactly in quadrature. Figure 9.4(b) shows a residual nonlinearity including almost

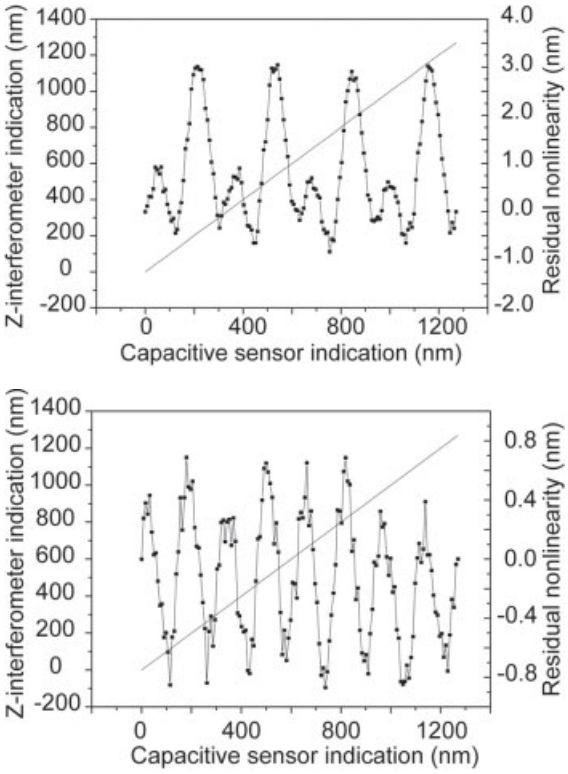

Fig. 9.4a, b Results of nonlinearity correction methods for homodyne interferometer in the M-SFM Veritekt C, with (a) manual electronic hardware adjustment, (b) the gain and offset correction.

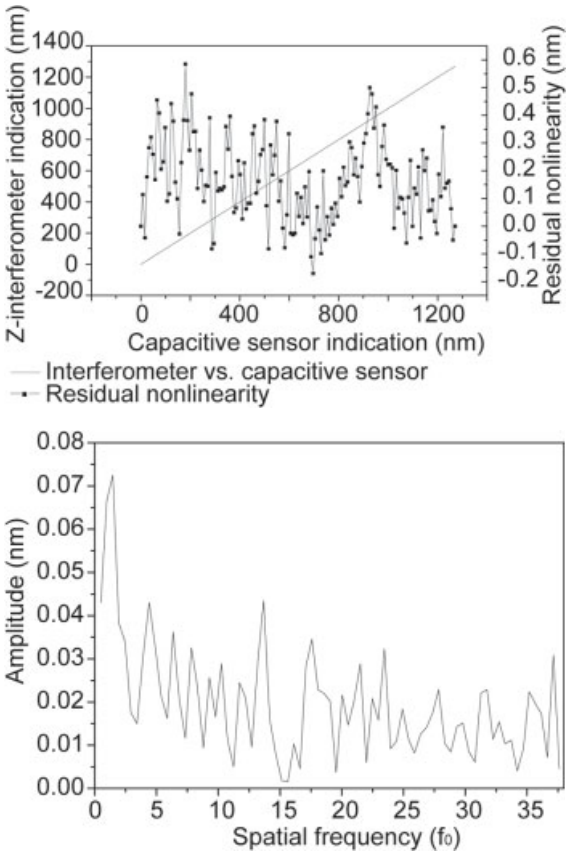

Fig. 9.4 Results of nonlinearity correction methods for homodyne interferometer in the M-SFM Veritekt C, with (c) the online Heydemann correction in real time; (d) represents the spectral analysis result of the residual nonlinearity signal of (c) $f_0 = 1/\lambda$, where λ is the optical wavelength of the laser light.

only second-order components with a peak-to-valley amplitude of about 1.5 nm. It indicates that the gain/offset correction method can remove the first-order nonlinearity but not completely the second-order nonlinearity. In Figure 9.4(c), no clear periodical nonlinearity is visible, indicating that the Heydemann correction removes both the first- and second-order nonlinearity significantly. This is also clearly demonstrated in the spectral analysis result shown in Figure 9.4(d). The remaining error is mostly caused by mechanical and electronic noise. We estimated the residual nonlinearity of interferometers after using the Heydemann correction to be less than 0.3 nm.

9.4 Improving the Measurement Speed

By using the newly designed DSP-based signal processing system, all sensors are sampled synchronously at each measurement point. The surface topography is calculated as the sum value of the result of the *z*-interferometer and the bending of the cantilever. As the benefit, the surface topography can be measured correctly even when the bending of the cantilever has a deviation from its setting value, because this deviation is also included in the *z*-interferometer at the same time and therefore can be compensated. In order to clarify this idea, a measurement result of a step-height sample is depicted in Figure 9.5 as an example. Curve 2 in the figure is only derived from the value of the *z*-interferometer, sharp peaks at the rising and falling edge of the profile can be seen. Compared to curve 2, curve 3 is calculated from both the value of the *z*-interferometer and the bending of the cantilever (curve 1 in the figure). It has no abnormal sharp peaks at the edge of the structure. It should be stressed here that exact synchronization is the important precondition for realizing this idea.

As the benefit of the above idea, the M-SFM is able to be operated with a nearly constant scanning speed. Compared to the former instrument where the positioning system has to set down at each measurement point by waiting a certain time, this capability can significantly improve the scanning speed.

The scanning speed of the MSPM is changeable by selecting different speed factors. Figure 9.6 depicts examples for measurements with different scanning

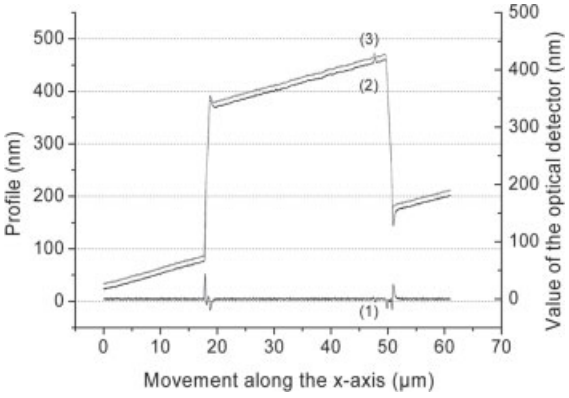

Fig. 9.5 Cross-sectional profiles of a 292-nm step-height structure measured at a scanning speed of 17.5 μm/s are depicted. Curve 1 represents the bending of the cantilever during the scanning. Curve 2 shows the profiler calculated using the *z*-interferometer value, and curve 3 is the profile calculated using the combined value of the *z*-interferometer and the bending of the cantilever. Curve 3 is shifted upward by 10 nm for clarity. This figure indicates that deviations occur at the edges of the structure if the profile is only calculated from the *z*-interferometer value; while the error can be compensated if the profile is calculated from both the *z*-interferometer and the bending of the cantilever.

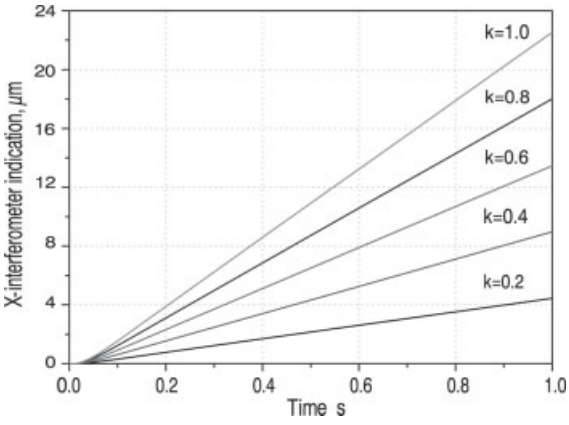

Fig. 9.6 Selecting the *x*-axis as the fast scan axis, the scan speed is determined by recording the *x*-interferometer indication in real time. The scanning speed can be increased up to 25 µm/s. The *k* is a speed factor, which can be selected in the measurement software.

speeds. The maximum scanning speed, up to now, is about 25 µm/s. However, the scanning speed should be properly selected according to the complexity of the surface structures to be measured. The more complex the surface structure is, the slower scanning speed should be selected to reduce the tip abrasion.

9.5 A Measurement Example of Step-Height Standard

In order to illustrate the achievable scanning quality of the improved instrument, a measurement result of a step-height standard (reference value of 290.9 nm) is shown in Figure 9.7. The measured results show a good agreement with the

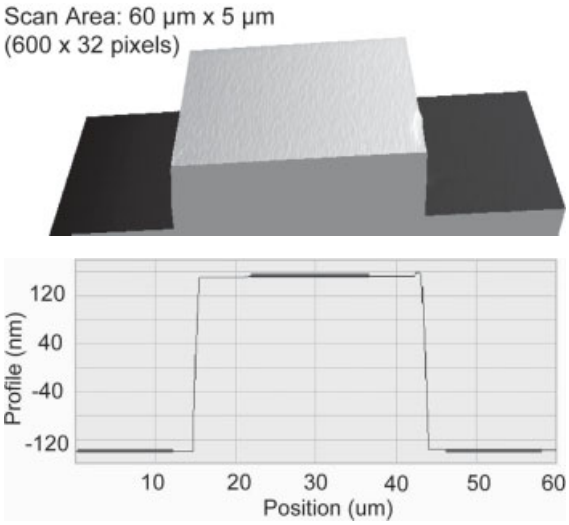

Fig. 9.7 Measurement results of a step-height standard with a reference step height of 290.9 nm is depicted as (a) a 3D view, (b) a cross-sectional profile, and (c) the mean value of the measurement results at different scanning speeds.

reference value, and they also illustrate the good repeatability at different measurement speeds. These measurements confirm that the improved scanning speed does not deteriorate the measurement performance.

References

1 J. Schneir, T. H. McWaid, J. Alexander, and B. P. Wilfley, Design of an atomic force microscope with interferometric position control, J. Vac. Sci. Technol. B **12**(6), 3561–3566 (1994).

2 M. Bienias, S. Gao, K. Hasche, R. Seemann, and K. Thiele, A metrological scanning force microscope used for coating thickness and other topographical measurements, Appl. Phys. A **66**, 837–842 (1998).

3 G. B. Picotto and M. Pisani, A sample scanning system with nanometric accuracy for quantitative SPM measurements, Ultramicroscopy **86**, 247–254 (2001).

4 S. Gonda, T. Doi, T. Kurosawa, Y. Tanimura, N. Hisata, T. Yamagishi, H. Fujimoto, and H. Yukawa, Real-time, interferometrically measuring atomic force microscope for direct calibration of standards, Rev. Sci. Instrum. **70**(8), 3362–3368 (1999).

5 J. Haycocks and K. Jackson, A metrological atomic force microscope for calibration of transfer standards, in *Proc. of the 2nd Euspen Conference, Turin, Italy, May 27th–31st* (2001) pp. 392–395.

6 K. R. Koops and K. Dirscherl, Nanometrology standards in the Netherlands: the traceable scanning probe microscope, in *Proc. of 3rd Euspen Conference, Eindhoven, the Netherlands* (2002), pp. 525–528.

7 G. Jaeger, Laser-based measurement to nanometer scale accuracy, *International Symposium on Laser Metrology for Precision Measurement and Inspection in Industry, Florianoplis, Brazil, October 13th–15th* (1999).

8 P. Heydemann, Determination and correction of quadrature fringe measurement errors in interferometers, Appl. Opt. **20**(19), 3382–3384 (1981).

9 K. P. Birch, Optical fringe subdivision with nanometric accuracy, Prec. Eng. **12**(4), 195–198 (1990).

10
Combined Confocal and Scanning Probe Sensor for Nano-Coordinate Metrology

Dmitri V. Sokolov, Dmitri V. Kazantsev, James W. G. Tyrrell, Tomasz Hasek, and Hans U. Danzebrink

Abstract

The development of a combined confocal–scanning probe microscope (SPM) sensor head is described. Wherein the SPM head is designed to be mounted with a ring adapter around a commercial microscope objective. In these studies, an SPM sensor based on a quartz tuning fork, equipped with a diamond tip, is applied. The advantages of the described system are as follows:

1. Distance control of the probe relative to the sample surface is realized on a self-sensing principle.
2. The diamond tip is robust enough for application in the complete range of dynamic modes: noncontact, intermittent, and nano-indentation.
3. Combination of an SPM and confocal objective allows the operation as an opto/tactile probing system.

To process the signals of the tuning fork sensor a custom current-to-voltage amplifier with a circuit for the compensation of the inherent capacitance of the tuning fork was designed. Furthermore, a quality factor control was implemented to improve the time-response characteristics of the sensor. The mechanical design has been realized to allow the positioning of the probe relative to the microscope objective and the swift exchange of the tuning fork sensors. Additionally, the design permits the rotation of the sensors, so that its orientation with respect to the sample surface may be changed.

The operation of the instrument has been established as a mechanical and optical profilometer. For the first time, the use of the confocal setup as an optical trigger during a two-step approach of the SPM probe has been demonstrated:

1. Quick and nondestructive "optically monitored" approach within millimeter distances from the surface.
2. The piezo stage (at lower approach speeds) is used for the final approach from a distance of a few micrometers from the surface until mechanical "contact" is achieved.

Nanoscale Calibration Standards and Methods: Dimensional and Related Measurements in the Micro- and Nanometer Range.
Edited by Gunter Wilkening, Ludger Koenders
ISBN: 3-527-40502-X

Moreover, the potential application of the tuning-fork-based sensor as a probe for nano-coordinate measuring machines (nano-CMMs) is further discussed.

10.1 Introduction

Combined methods of surface sensing, imaging, and profiling based on a variety of physical mechanisms of probe–sample interactions is of increasing interest in the field of material science [1, 2], biology [3], and medicine [4, 5]. A number of combined scanning electron microscopes (SEMs) with scanning probe microscopes (SPMs), and optical (conventional, confocal, and interference) microscopes with SPMs have been designed and some of them are even available commercially. The combination of "soft" optical or electron-beam probes with "hard" SPM probes provides the possibility of a comprehensive surface investigation and dimensional metrology. Contrary to SPM probes, the optical probes are considered as the ideal solution for a quick and nondestructive imaging of large samples. However, imaging with optical methods suffers from a number of factors: poor lateral resolution, diffraction artifacts, dependency on optical properties of the surfaces, etc. For SEMs the lateral resolution is high but the large depth of focus impedes surface profiling. Another restriction for SEMs is the necessity of placing the system in vacuum. However, these factors do not play a significant role for imaging with SPMs.

SPMs and optical profilometers are not only important for the use as imaging tools. Another quickly growing area of interest where the combination of different mechanisms of probe-to-sample interactions plays an important role is the field of nano-coordinate measuring machines (nano-CMMs). Standard and future applications of nano-CMMs are the topographical and geometrical analysis of microlenses, micro-electromechanical system (MEMS) or nano-electromechanical system (NEMS), and magnetic read/write heads for hard disk drives. These components are fabricated on a microscale, while nanoscale surface roughness and nanofabrication defects impact their performance strongly. With the measured dimensions approaching nanometer level the conventional methods of CMM touch trigger probes with micro-to-millimeter-sized probing tips and tip-to-sample forces in the mN range become critical from the point of view of the spatial resolution and tip-induced modification of nanostructures. Here, the combination of optical and mechanical probing in a low force, dynamic mode is promising for operations described above.

The main topic of this chapter is the development of a probing system based on an optical confocal sensor with the focus point placed several micrometers below the mechanical SPM probe. This combined system works in the following two modes:

1. Imaging mode based either on optical, confocal, or on SPM techniques (Section 10.3.1).
2. Single axis measurement mode with confocal or SPM "contact" sensors (Section 10.3.2).

10.2
Instrumentation and Experimental Details

Confocal laser microscopy is conventionally used in material science [6, 7], biology [8, 9], and medicine [10], but is still an actively evolving method. Confocal laser microscopy is utilized in these areas due to its superior lateral resolution and especially of its high sensitivity to axial displacements of the sample compared to conventional optical microscopy [11, 12]. Such a unique property of depth discrimination with nanometer resolution makes the optical tracking of surfaces in reflection mode as well as distance sensing, proposed earlier by Corle et al. [11], possible.

In the system, presented here, a commercial optical ZEISS microscope serves as a platform for the combined confocal–scanning probe microscope (Figure 10.1). The illumination and detection paths of the confocal setup are assembled from standard "Microbench" parts (LINOS GmbH) and attached to the upper outlet of the microscope. A laser beam ($\lambda = 632.8$ nm) is widened to fill the aperture of the objective and focused afterwards to a spot with a diameter close to the diffraction limit. The light which is reflected from the surface and passed through the microscope is focused to a mechanically fabricated 100 μm diameter pinhole by the focusing lens L2 ($F = 100$ mm). The total magnification of the confocal setup is dependent on the objective attached and could be up to 500 for a 100 $\times$ objective. Alignment of the reflected laser beam with respect to the pinhole is initially monitored by a CCD camera, and replaced by a photodiode for imaging. The pinhole serves as a spatial filter to collect only light coming from the focal plane of the objective. Depth discrimination in this setup is determined

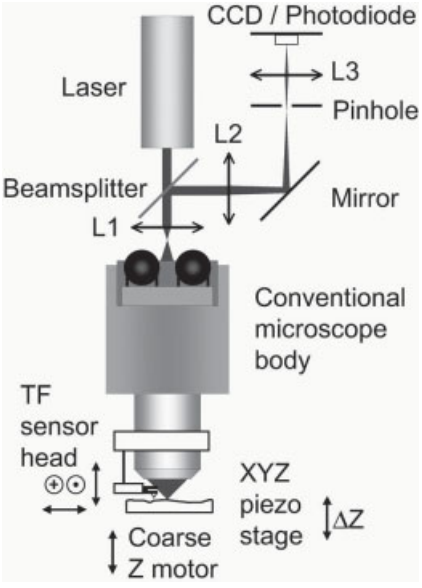

Fig. 10.1 Principal schematics of the conventional optical microscope with the integrated confocal setup, SPM head and *XYZ*-piezo stage mounted on a coarse *Z*-stepper motor.

by the numerical aperture (NA) of the objective and a combination of the total magnification of the system and effective diameter of the pinhole [12].

The high numerical aperture microscope objective with a large working distance is a key element in such a setup. Here, the high numerical aperture defines high resolution in the confocal measurements [11, 12], while a large working distance is needed for placing the SPM probe between the objective and the surface [13]. In the presented setup a microscope objective ZEISS Epiplan-NEOFLUAR 100×/0.75, with a working distance of about 4 mm (Figure 10.2(b)), serves as a base for the SPM probe holder (Figure 10.2(a)). Scanning of the sample is performed by an *XY*-piezo stage with an integrated capacitive position control (Physik Instrumente GmbH) with a range of 100 μm × 100 μm. The feedback loop, necessary for both the optical and SPM profiling, is based on a combination of an SR830 DSP lock-in amplifier (Stanford Research Systems Inc.) and an Easy-Scan controller (NanoSurf AG). The *Z*-motion is performed by a fast *Z*-piezo stage with integrated capacitive position control (Physik Instrumente GmbH),

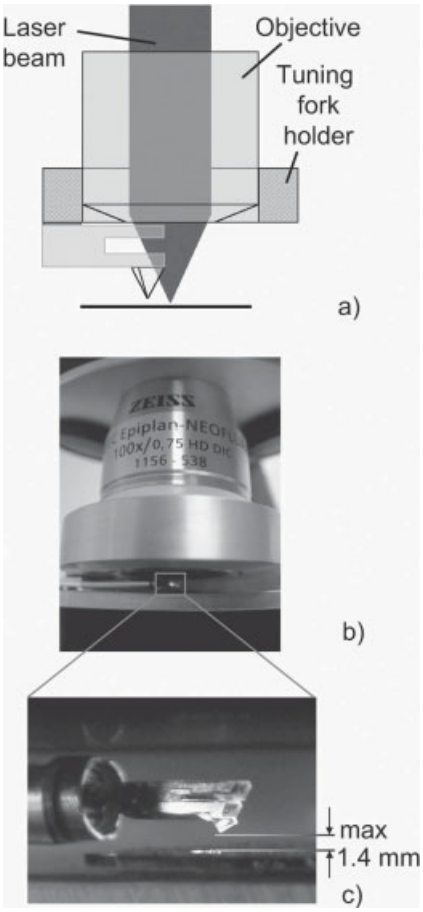

Fig. 10.2 Combined confocal–scanning probe microscope: (a) principal schematics of the combined confocal–SPM head, (b) ring-like mount of the tuning fork sensor arranged around the commercial ZEISS Epiplan-NEOFLUAR 100×/0.75 objective, and (c) tuning-fork-based sensor with 90° diamond tip. The maximum distance between the focal plane of the confocal objective and the apex of the tip is about 1.4 mm.

while a *Z*-stepper motor platform (OWIS GmbH) and an *XY*-manual microscrew positioning stage carries out the coarse motions.

The application of a self-sensing quartz tuning-fork-based probe eliminates additional alignment of optical elements in comparison to optical lever configurations. The piezoelectric effect of the quartz is used for both, driving the oscillations of the tuning fork near its resonance frequency with ac voltage applied, and simultaneously detecting the current induced by the tuning fork deflection. In such a way, the self-sensing of the tuning fork deflection is achieved by the detection of the current induced by the bending of the tuning fork.

The use of a diamond crystal as a tip attached to the tuning fork [13] allows for a measurement range of dynamic modes: noncontact, intermittent contact, and nano-indentation. The possibility of a quick and nondestructive investigation followed by surface modifications with nanometer precision is of increasing interest in material science [14] and is a promising tool for nanotechnology [3]. Two different diamond tips with full angles of 60° and 90° were constructed and tested.

To improve the performance of the tuning fork sensor system, a custom-made preamplifier is applied. Therein the compensation of the intrinsic capacitance of the tuning fork is realized while controlling the quality factor of the tuning fork assembly.

Both the confocal profilometer and SPM are very sensitive to mechanical vibrations. Therefore, placing the microscope on an actively damped antivibration table (HERZAN MOD-1) attenuates the seismic disturbances. Furthermore, the microscope is enclosed within an environmental chamber constructed from Perspex panels supported on an aluminum frame to minimize exposure to external acoustic and thermal noise, as well as to dust.

In order to perform optical profiling, lock-in detection methods are applied. The sample is oscillated by the *Z*-piezo with a frequency of about 1 kHz and an amplitude of a few tens of nanometers. This oscillation induces the ac component in the detected optical reflection signal, which is processed by the lock-in amplifier. The resulting dc component of the lock-in output is used as a feedback signal and sent to the *Z*-piezo actuator to keep the surface in the focal position.

Optical triggering based on the lock-in signals is realized by means of a custom-designed controller, which will be described in more details in a forthcoming chapter. The controller is mainly intended to control the sample-to-probe coarse approach speed independently for the optical and SPM probes. Furthermore, the controller stops the approach by a set of criteria's (trigger signals or thresholds), protects the SPM tip from crashing into the surface, and serves as an emergency switch. The interruption of the approach takes place when the combination of amplitude and in-phase signal for the confocal mode exceeds the pre-set threshold value, or the RMS value of the tuning fork oscillation amplitude drops below the corresponding pre-set threshold.

10.3 Results and Discussion

10.3.1 Imaging in the Confocal and SPM Mode

Figure 10.3 shows an optical image of a PTB test sample acquired in the confocal mode. The sample was manufactured at PTB using electron-beam lithography and contains Au/Pd test patterns on a silicon substrate. The image is taken at the highest possible scanning rate for this setup:

1. Scanning rate is software limited to 0.138 s per line ($\cong 0.58$ mm s^{-1} for 80 μm scans).
2. Data sampling rate of 256 × 256 pixels per image gives 310 nm per pixel that corresponds to 2 pixels for an optical resolution limit of 620 nm.

Such a combination of data sampling rate for the given scan size is limited by the data acquisition system for the SPM mode as well. In other words, imaging of the SPM areas exceeding 80 μm with such data acquisition parameters gives no considerable advantage compared to confocal microscopy, but instead suffers from scan speed limitations together with the danger of tip wear or sample surface modification.

However, the superior lateral resolution of an SPM can be achieved at smaller scan ranges. Figure 10.4 shows profiles of the same scan area of the PTB test sample. The profiles have been recorded in both the confocal profilometry and SPM mode. Here, artifacts associated with the confocal mode can be easily distinguished (multiple lines in the upper right corner in Figure 10.4(a)). These lines are not present in the high-resolution SPM images. FWHM of the features are in good agreement with each other and are about 1.2 μm for the bigger circles.

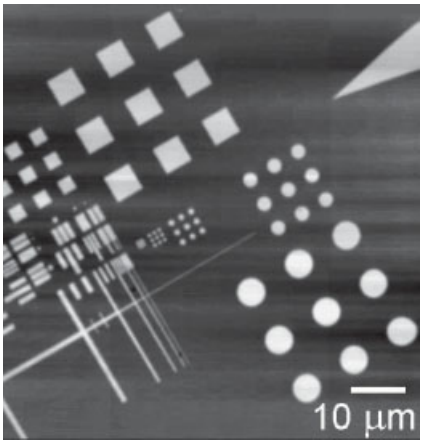

Fig. 10.3 Optical image of the PTB test sample taken in the confocal mode (scanning speed of 0.58 mm s^{-1}).

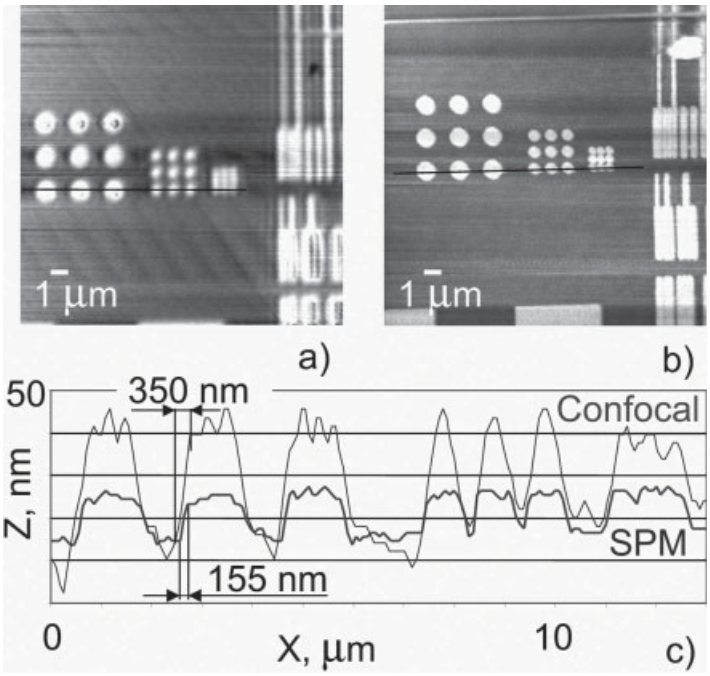

Fig. 10.4 Images of the PTB test sample recorded in the confocal and SPM mode. (a) Topography image recorded in the confocal tracking mode. Scan area of 20 µm × 20 µm, and a scanning speed of 20 µm·s^{-1}. (b) Topography image taken in the SPM mode. Scan area of 20 µm × 20 µm, and a scanning speed of 4 µm·s^{-1}. (c) Cross section of images (a) and (b).

All circular features have plateaus in the SPM profile and only the 1.2 µm features have plateaus in the confocal profile. Measurement of the slope width (10–90 % criterion) of the structures gives values of about 350 nm.

Figure 10.4 also gives an insight to a height artifact observed in the confocal mode when compared to the SPM mode: height values 30 nm versus 15 nm, respectively. Given the observed discrepancy in height values, a brief study was performed using a similar setup with a ZEISS Epiplan 50×/0.7 objective to investigate the optical tracking of thicker and wider chromium structures deposited on glass (photomask sample). An edge effect in confocal profiles is observed for setups with pinholes of diameters varying between 0.1 and 0.5 mm (Figure 10.5(a)). The step height deduced from the profiles is about 100 nm (after removing the edge effect) and is within a few nanometers close to the fabrication data of the structure. A confocal optical image taken simultaneously with the confocal profilometry measurement showed resolutions close to 600 nm (Figure 10.5(b)). In such a way, the increase in height of the confocal profile compared with the SPM profile (Figure 10.4(c)) can be explained in terms of the observed edge effect caused most likely by the diffraction processes on the edges of structures. In other words, if the lateral size of the feature is close to the resolution of the system, the

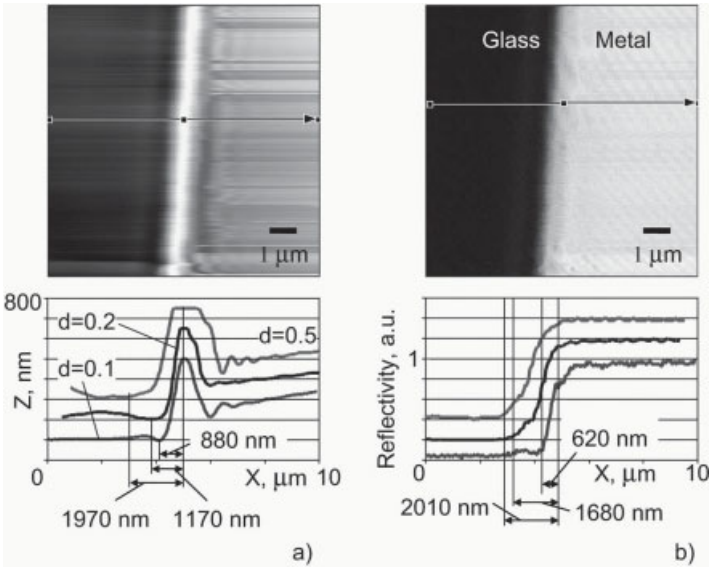

Fig. 10.5 Optical imaging and profiling of a 100 nm step Cr film on glass (photomask sample) in the confocal mode. (a) Top view of the 100 nm step profile for a pinhole diameter $d = 0.1$ mm and a series of profiles for $d = 0.1$, 0.2, and 0.5 mm. A plateau in the upper profile ($d = 0.5$ mm) is due to the limitations of the *Z*-piezo working range. (b) Reflectivity image of the sample surface taken simultaneously with the confocal profile ($d = 0.1$ mm) and reflectivity profiles for pinhole diameters 0.1, 0.2, and 0.5 mm.

appeared height of the feature is determined by the edge effect and exceeds the real value.

This study demonstrates the strong advantage of a combined sensor head arrangement. Once calibrated against a reference material (as discussed in [15]), the SPM module is able to verify step height values acquired using the optical methods.

In order to compare the tracking performance of the confocal setup with the noise measured in the SPM mode, measurements at 0 nm scan range were performed. The noise level for the confocal setup is about 1.5 nm (*p–v*) and is in good agreement with the values obtained with the SPM, which may indicate that the performance of the setup is limited by the mechanical stability of the setup and not by the measurement method.

10.3.2 One-Dimensional Optical and SPM Measurements

In this chapter, the sensor head is used for one-dimensional measurements normal to the surface. Two experiments have been performed to investigate the applicability of the optical focus signal as a trigger for a quick and nondestructive SPM probe approach to the sample surface, and to research the potential of the tuning-fork-based SPM probe as a probe for nano-CMMs.

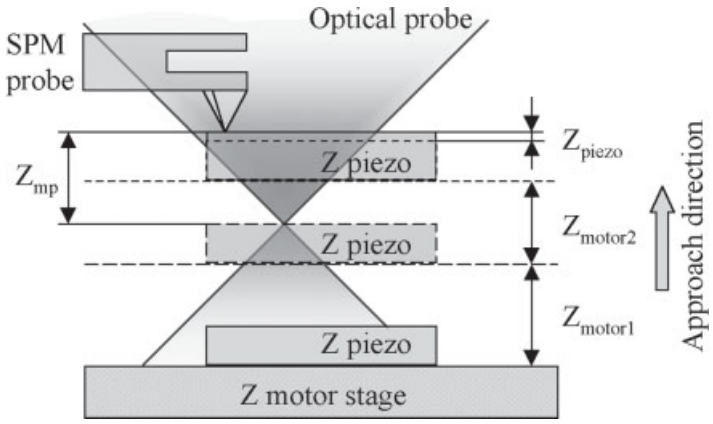

Fig. 10.6 Confocal/SPM probe approach procedure: (1) *Z* motor is driven for a distance of Z_{motor1} and stopped automatically with the sample surface in the focal plane of the confocal setup. (2) *Z* motor is driven for a distance of Z_{motor2} until the gap between the SPM tip and sample surface falls within the working range of the *Z*-piezo (2 μm). (3) Contact of the SPM probe and the surface is achieved by extending the *Z*-piezo.

During the first experiment, the sample is driven towards the tuning fork probe from a distance of a few millimeters as shown schematically in Figure 10.6. The approach is stopped when the sample surface meets the focal plane of the confocal setup. This corresponds to a travel for the *Z* motor of a distance Z_{motor1}. Then the motor is driven for the pre-set distance Z_{motor2} to place the diamond probe within the range of the *Z*-piezo stage (2 μm). Then the *Z*-piezo is engaged until contact is achieved between the SPM tip and the sample surface. At this point, the position of the *Z*-piezo stage is calculated from the displacement value acquired from the capacitance sensor of the piezo stage.

Figure 10.7 shows the results of the measurements of the distance $Z_{mp} = Z_{motor2} + Z_{piezo}$ between the focal plane of the confocal setup and the diamond tip.

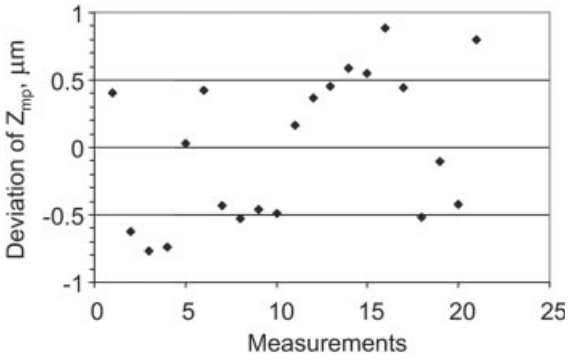

Fig. 10.7 Deviation from the average distance between the "confocal contact" and the "SPM contact" Z_{mp} (standard deviation of Z_{mp} is 0.54 μm).

Approach to the optical "contact" with the surface is performed with a speed of 16.5 μm · s^{-1}. Average Z_{mp} is 1.436 mm with an absolute deviation of 1.65 μm (p–v) and a standard deviation of 0.54 μm.

The precision of the sample positioning with respect to the optical probe's focal plane for the given approach speed is limited by the performance of the controller electronics and by the mechanical limitation of the coarse positioning system. A significant improvement of this precision is expected after the realization of a feedback control of the Z motor position by amplitude or in-phase signal from the lock-in amplifier.

The second experiment involved a series of measurements of the distance Z_{piezo} (see Figure 10.6) between the sample surface with Z-piezo fully withdrawn and the surface in contact with the diamond tip. In this case the Z motor position was fixed and only the Z-piezo was moved.

Figure 10.8 shows the results of the measurements. The approach to the mechanical "contact" with the surface is carried out with a speed of 0.78 μm · s^{-1}. The average distance, Z_{piezo}, is 1015.34 nm with an absolute deviation of 3.72 nm (p–v) and a standard deviation of 1.34 nm. These values are in good agreement with the data from vibration measurements performed with the SPM probe kept in contact with the surface. The achieved values with a standard deviation close to 1 nm confirm the potential of the diamond-based tuning fork probe as a probe for nanometer coordinate metrology.

The differences in the deviations of coarse (Figure 10.7) and fine (Figure 10.8) approaches can be explained due to different measurement conditions concerning mechanics and physical tip–surface interactions: (1) coarse movement of mechanical parts and confocal sensor focal depth (μm range) is large compared to (2) piezo stage motion and SPM tip–sample interaction region (nm range). Additionally, the approach speed for the confocal triggering was set 20 times faster compared to the SPM approach speed. The correlation of the standard deviation values (1.14×10^{-3} and 1.32×10^{-3} for the coarse and fine approach, correspondingly) given in relative units indicates close signal-to-noise levels for both modes. Future work will have to be performed in order to reduce or isolate the systems noise levels.

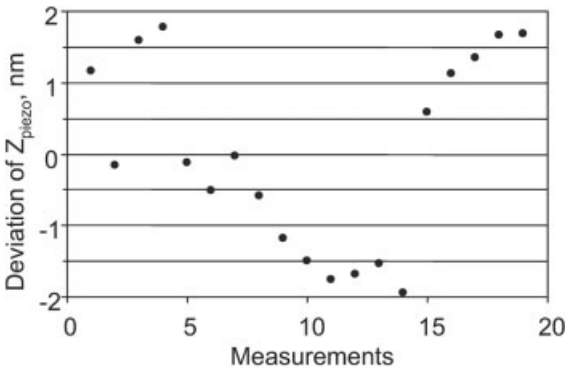

Fig. 10.8 Deviation from the average distance between the SPM tip and fully withdrawn sample surface Z_{piezo} (standard deviation of Z_{piezo} is 1.34 nm).

Although the operation of the setup with nanometer precision is demonstrated, further improvements of the measurement procedure in direction of an independent interferometric position control of the diamond tip and the sample surface is considered promising [16].

10.4 Summary and Conclusions

The key outcomes from this work can be summarized as follows:

- An SPM compact sensor head has been designed and constructed to be mounted around a conventional high numerical aperture microscope objective, making it compatible with commercial microscopes including an optional add-on home-built-integrated confocal microscope.
- The self-sensing mode of the operation of the tuning fork SPM sensor eliminates the need for additional optical components and accidental illumination of the surface.
- The natural diamond-tip-based tuning fork probe is robust for application in the complete range of dynamic modes: noncontact, intermittent contact, and nano-indentation.
- The combination of conventional optical microscope, confocal profilometer, and scanning probe microscope ensures the operation of the system in a number of modes: selection of the area of interest with respect to the optical and SPM probes, quick optical sampling of sub-millimeter areas with sub-micrometer resolution followed by nondestructive profiling in the confocal mode, and the precise imaging of micrometer-sized areas with SPM.
- Optical sensing of the surface is exploited as a trigger, whose values are directly used in the automatic approach of the SPM probe from millimeter distances.
- For the first time, the potential of the diamond-based tuning fork sensor as a probe for nano-coordinate measurements is demonstrated.
- In a future step a fiber-based confocal–tuning fork sensor head is to be built, based on the demonstrated principle and fixed to a mobile metrology arm of a CMM.

The authors foresee the role of the combined opto/tactile sensor as probing system in coordinate metrology. The goal is to bridge macro-, micro-, and nanoscales, and finally to measure nanostructured surfaces on even macroscopic samples. Furthermore, the authors envisage the instrument's use as a profilometer, 3D scanner of surface topography and nanoindentor to obtain material characteristics. The systems wide range of measurement capabilities could be of great value to many manufactures (e. g., optics, microelectronics [17], and computer

hard drive manufactures to name a few). However, this system is also of great interest to biologists, chemists, and medics who are, e. g., interested in 3D profiles of individual cells.

Acknowledgments

The authors would like to thank Matthias Kempe (PTB) for his expertise concerning mechanical construction and Dieter Schulz (PTB) for his valuable discussions and skill in realizing the electronics. Thanks are due to Dr. Anthony Grant (Cork Institute of Technology, Ireland) and Andrzej Sikora (Wroclaw University of Technology, Poland) for their valuable contributions to the project during their stay at PTB. We also would like to thank our partners Surface Imaging Systems GmbH (Dr. H.-A. Fuss) for their good cooperation. This work was financially supported by the Federal Ministry of Economics and Labour (BMWA project: VI A 2-05/02).

References

1 N Axelrod, A. Radko, A. Lewis, and N. Ben-Yosef, Topographic profiling and refractive-index analysis by use of differential interference contrast with bright-field intensity and atomic force imaging. Appl. Opt. **43**, 2272–2284 (2004).

2 H. S. Sands, F. Demangeot, E. Bonera, S. Webster, R. Bennett, I. P. Hayward, F. Marchi, D. A. Smith, and D. N. Batchelder, Development of a combined confocal and scanning near-field Raman microscope for deep UV laser excitation. J. Raman Spectrosc. **33**, 730–739 (2002).

3 P. Foubert, P. Vanoppen, M. Martin, T. Gensch, J. Hofkens, A. Helser, A. Seeger, R. M. Taylor, A. E. Rowan, R. J.M. Nolte, and F. C. de Schryver, Mechanical and optical manipulation of porphyrin rings at the submicrometre scale, Nanotechnology **11**, 16–23 (2000).

4 P. Lehenkari, G. Charras, S. Nesbitt, and M. Horton, New technologies in scanning probe microscopy for studying molecular interactions in cells. Expert Rev. Mol Med. March **2000**, 1–19 (2000).

5 M. Horton, G. Charras, C. Ballestrem, and P. Lehenkari, Single integration of atomic force and confocal microscopy. Single Mol. **1**, 135–137 (2000).

6 C.-H. Lee, H.-Y. Chiang, and H.-Y. Mong, Sub-diffraction-limit imaging based on the topographic contrast of differential confocal microscopy. Opt. Lett. **28**, 1772–1774 (2003).

7 M. Nakano and Y. Kawata, Compact confocal readout system for three-dimensional memories using a laser-feedback semiconductor laser. Opt. Lett. **28**, 1356–1358 (2003).

8 J. Novak, I. Georgakoudi, X. Wei, A. Prossin, and C. P. Lin, In vivo flow cytometer for real-time detection and quantification of circulating cells. Opt. Lett. **29**, 77–79 (2004).

9 P. Kitin, R. Funada, Y. Sano, and J. Ohtani, Analysis by confocal microscopy of the structure of cambium in the Hardwood Kalopanax Pictus. Ann. Bot. **86**, 1109–1117 (2000).

10 T. D. Wang, M. J. Mandella, C. H. Contag, and G. S. Kino, Dual-axis confocal microscope for high-resolution in vivo imaging. Opt. Lett. **28**, 414–416 (2003).

11 T. Corle, G. Chou, and G. Kino, Depth response of confocal optical microscope. Opt. Lett. **11**, 770 (1986).

12 D. R. Sandison, D. W. Piston, R. M. Williams, and W. W. Webb, Quantitative

comparison of background rejection, signal-to-noise ratio, and resolution in confocal and full-field laser scanning microscopes. Appl. Opt. **34**, 3576 (1995).

13 J. W.G. Tyrrell, D. V. Sokolov, and H. U. Danzebrink, Development of a scanning probe microscope compact sensor head featuring diamond probe mounted on a quartz tuning fork. Meas. Sci. Technol. **14**, 2139–2143 (2003).

14 D. V. Sokolov, Nanooxidation of *n*-$In_{0.53}Ga_{0.47}As$ with an atomic force microscope. Tech. Phys. **47**, 58–63 (2002).

15 J. W.G. Tyrrell, C. Dal Savio, R. Krüger-Sehm, and H.-U. Danzebrink. Development of a combined interference microscope objective and scanning probe microscope. Rev. Sci. Instrum. **75**, (2004).

16 A. Sikora, D. V. Sokolov, and H.-U, Danzebrink, Scanning probe microscope set-up with interferometric drift compensation, in these proceedings, pp. 109–118.

17 E. C. Teague, The National Institute of Standards and Technology molecular measuring machine project: metrology and precision engineering design. J. Vac. Sci. Technol. B **7**(6), 1898–1902 (1989).

11
Combined Shear Force–Tunneling Microscope with Interferometric Tip Oscillation Detection for Local Surface Investigation and Oxidation

Andrzej Sikora, Teodor Gotszalk, and Roman Szeloch

Abstract

In view of the rapid growth of interest in atomic force microscopes (AFMs) in the investigation of surface properties and local surface modification, the modular shear force/tunneling microscope is herein described. The presented setup is based on the fiber Fabry–Perot interferometer for the measurement of conductive microtip oscillation. An advantage of this system is that the quantitative measurements of tip vibration amplitude are easily performed. Moreover, the presented setup is extremely sensitive and compact.

Using the aforementioned measurement system, the quantitative measurement of probe dither motion with a resolution of 0.01 nm_{RMS} in a 100 Hz bandwidth is possible. The optical detection system allows one to apply voltage to the conductive microtip. In this case, the microtip can be used as an electron-beam (e-beam) source for nanolithography or as a collector of field emission current flowing between the surface and the microprobe. Some preliminary results of experiments will also be presented.

11.1
Introduction

Scanning force microscopy [1] is one of the many scanning probe techniques developed after the invention of scanning tunneling microscopy (STM) [2]. In atomic force microscopy (AFM) the force interaction observed between the microtip mounted on the cantilever and the investigated surface is utilized for the surface characterization. Several measurements techniques can be applied for the detection of force interactions acting on the microtip. One of them is the shear-force microscopy (SHFM). By this technique, the electrochemically etched tapered wire is mounted perpendicularly to the sample. This tip oscillates laterally to the surface near one of its mechanical resonant frequencies. At a distance of a few nanometers from the surface in question oscillations become dampened

Nanoscale Calibration Standards and Methods: Dimensional and Related Measurements in the Micro- and Nanometer Range.
Edited by Gunter Wilkening, Ludger Koenders
ISBN: 3-527-40502-X

out by shear forces. This may then be used for tip–sample distance regulation and may also be used as a basis for high-resolution topographical imaging. An accurate measurement of the true oscillation amplitude of the tip is crucial information, which allows us to use this tool with more confidence [3]. Moreover, for the purposes of high measurement sensitivity it is desirable to use as low an oscillation amplitude as possible for two reasons: in order not to lose the lateral resolution of surface measurements and in order to extend the lifetime of the microtip.

In parallel fundamental studies [3–7], several nanometer-scale devices such as single electron [8] and metal–oxide [9] transistors, quantum wires [10], high-density memory chips [3, 11], and Josephson junctions [12] have illustrated some of the nanoelectronic applications. Machining of silicon structures has also been demonstrated by an AFM oxidation [13]. Furthermore, local oxidation lithography is compatible with the operation of parallel tip arrays [14].

Because of an interest in the local electrical properties of the surface, different experimental setups were also proposed [15] as combined methods with the SPM [16–19]. Such methods can be used for correlating topography with certain electrical parameters of the surface.

11.2 Instrumentation

In our setup, a single-mode optic fiber is fixed at the distance of a few microns from the reflecting surface, whose deflection is monitored. The interference between the light reflected from the fiber–air interface and the backscattered light from the reflecting surface is monitored with an optical detector. In our interferometer design, we use the single-mode DFB pigtailed semiconductor laser (Mitsubishi) emitting 1313 nm wavelength with full width at half maximum (FWHM) –0.1 nm (Figure 11.1) as a light source.

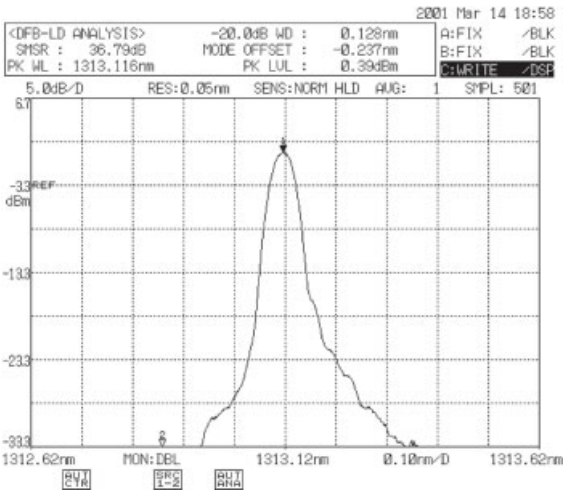

Fig. 11.1 Single-mode DFB semiconductor laser emission curve.

Because backscattered light from any junction in the optical fiber system can disturb the operation of the laser diode, we use the solid-state optical Faraday isolator (40 dB) to ensure the proper laser light emission. In our system, we utilize a built-in laser diode isolator, which accurately fits the wavelength of the light source and is insensitive to mechanical vibrations. One of the fiber ends of the bidirectional coupler (50 %/50 %) is connected directly with the optical isolator. The wire with the microtip is mounted close to the well-cleaved fiber end of the coupler (Figure 11.2(a)) and is excited to the point of oscillation with a piezoactuator (Figure 11.2(b)).

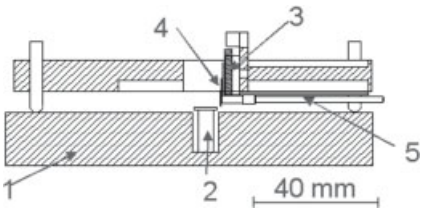

Fig. 11.2 Scanning head – scheme (a) and view (b) ((1) mainframe body, (2) piezotube, (3) piezoactuator, (4) scanning tip, and (5) optical fiber).

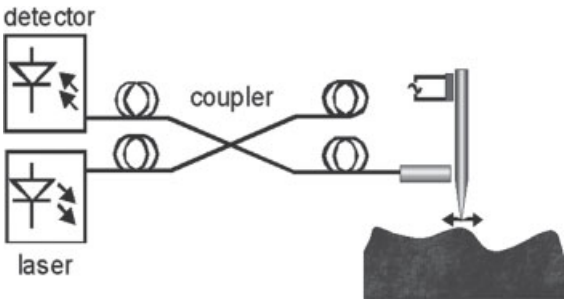

Fig. 11.3 Tip oscillation detection setup – optical fiber interferometer scheme and view.

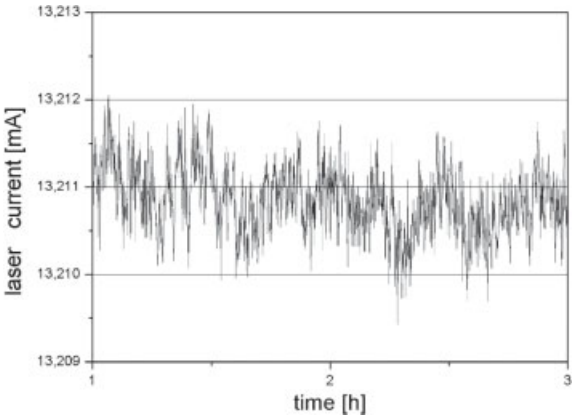

Fig. 11.4 Semiconductor laser current stability.

The signal photodiode (Figure 11.3) detects the interference of light reflected from the interferometer fiber end and microscope wire.

Because of high interferometer stability and external disturbance immunity the setup was placed on a granite plate and covered with an electromagnetic and thermal shield.

To obtain high-resolution and high-fringe stability the interferometer light source was supplied with a high-precision home-made current source, which ensures current supply stability in the range of ± 30 ppm (Figure 11.4). The temperature of the laser was controlled by a Peltier cooler with a stability of ± 5 mK (Figure 11.5). Results of laser stability measured with an optical spectral analyzer – Ando AQ-6315B – are shown in Figure 11.6. We tested the interferometer sensitivity by moving the wire away from and toward the interferometer fiber and simultaneously recording the interferometric fringes. If the amplitude of the wire movement was greater than $\lambda/4$ then we observed the pattern shown in Figure 11.7. In order to measure a single nanometer of the tip oscillation ampli-

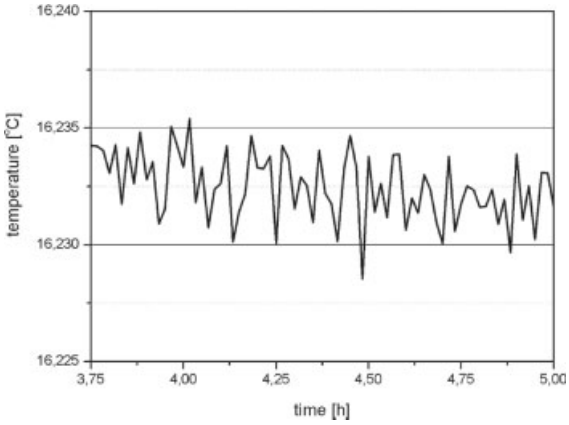

Fig. 11.5 Semiconductor laser temperature stability.

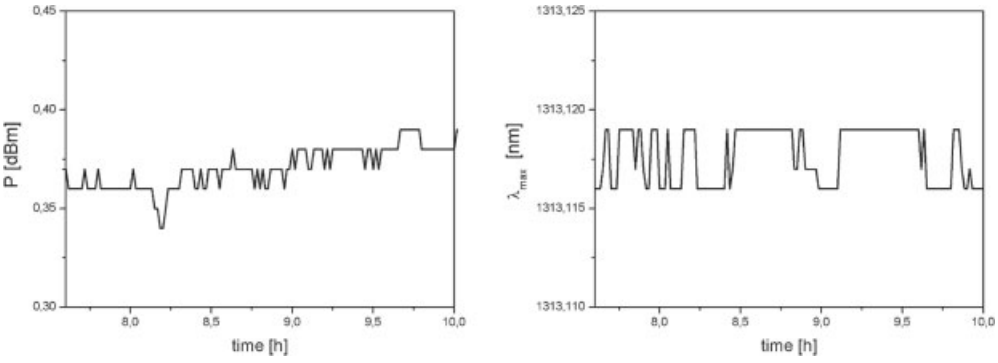

Fig. 11.6 Semiconductor laser output power and wavelength stability.

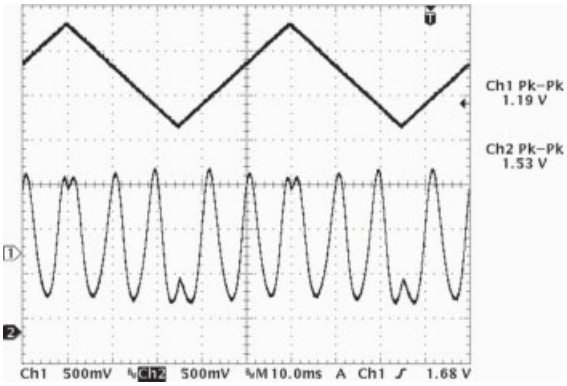

Fig. 11.7 Interferometric fringes (below) versus tip movement (above) and lock-in amplifier response versus tip oscillation amplitude dependence.

tude – on the slope of the interferometric fringe – dc voltage can be applied to the piezoactuator, which excites the scanning tip.

The sensitivity of the developed interferometer can be calculated on the slope of the recorded signal – in our design we obtain a sensitivity of 2 mV/nm. It should be noted that the distance between the interferometer fiber and the wire with a microtip must be adjusted with the piezoactuator so that the working point is placed on the linear part of the slope. A lock-in signal detection method with a sensitivity of 200 mV/nm and an output signal noise level of 2 mV_{RMS} (Figure 11.8) gives a resolution of 0.01 nm_{RMS} at a 100 Hz bandwidth.

The scanning tip is connected to the home-made I/U converter, which is placed next to the measuring head. As the main part of the converter precision, an electrically isolated operational amplifier OPA111 was used. The I/U converter is connected to the amplifying/biasing module, which can be controlled remotely (via scanning software) or manually. Module allows us to measure current with sensitivities from 100 pA/V to 100 nA/V. Internal PID loop allows us to work in constant voltage or constant current regime. The scanning tip is connected to the home-made I/U converter which is placed next to the measuring head. As

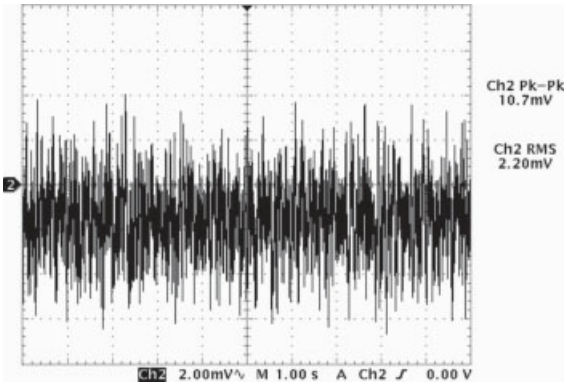

Fig. 11.8 Lock-in output signal noise.

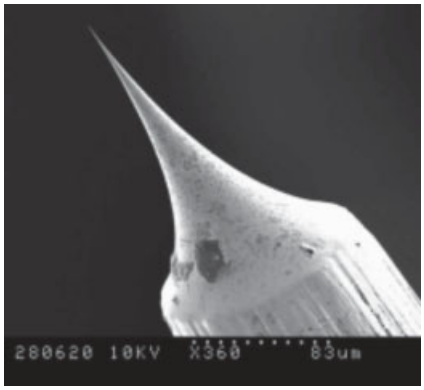

Fig. 11.9 SEM tungsten tip photo.

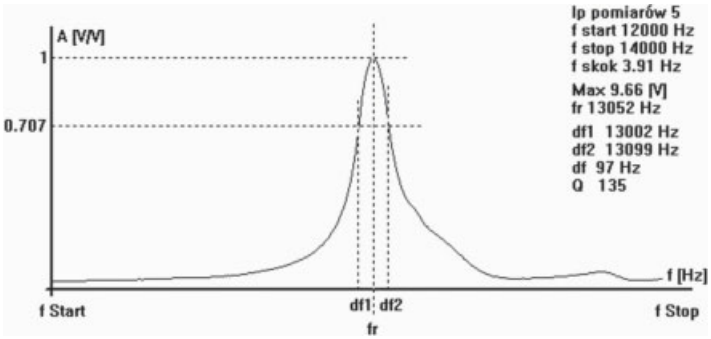

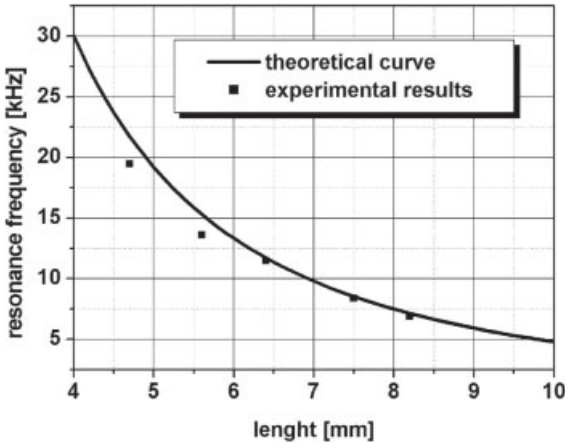

Fig. 11.10 Scanning tip resonance curve and resonance frequency versus wire length dependence.

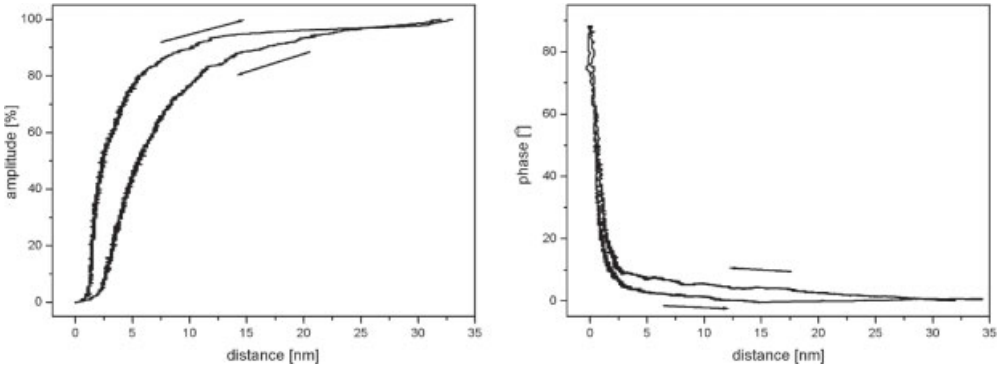

Fig. 11.11 Approach curves. A tip–sample distance equal to 0 nm was set arbitrarily.

main part of the converter precision, electrically isolated operational amplifier OPA111 was used. The *I*/*U* converter is connected to the amplifying/biasing module, which can be controlled either remotely (scanning software) or manually. The module enables one to measure the current with sensitivities from 100 pA/V to 100 nA/V. An internal PID loop makes it possible to work in either a constant voltage or constant current mode.

In our experiments, we used electrochemically etched tungsten wires (Figure 11.9). The diameter of the tungsten tip was 120 μm and the length varied from 5 to 7 mm, which corresponds with the wire spring constant in the range from 1 N/m up to 3 N/m. The typical length of the tungsten wire is 6 mm, which corresponds with a resonance frequency of 12 kHz (Figure 11.10).

The typical *Q*-factor of the wire resonance is 100–200.

The application of weaker wires enables the detection of smaller forces but the scanning process is more time consuming and sensitive to acoustical disturbances.

The tip–sample distance is controlled using the shear-force detection method. As the tip approaches the surface, the oscillation amplitude decreases and phase shift appears (Figure 11.11).

Tip–sample distance control with high accuracy is possible by using a lock-in signal detection from the interferometer.

The process is controlled by a PC with a plug-in A/D-D/A card – Keithley DAS 1702. The scanning process controlling the "Topo-Scan" program was developed at the Laboratory of Scanning Probe Microscopy, Nanostructures, and Nanometrology and allows one to control both 4 D/A and 6 A/D 12 bit converters. The simplified scheme of the setup and view is shown in Figure 11.12.

Environmental conditions are monitored with a compact integrated temperature/humidity digital sensor. The relative humidity in the measuring chamber can be changed from 1 % to 80 %.

For setup tests the HOPG sample was used. The topography and cross section is shown in Figure 11.13. The height of the monolayer is approximately 0.35 nm and corresponds with other results.

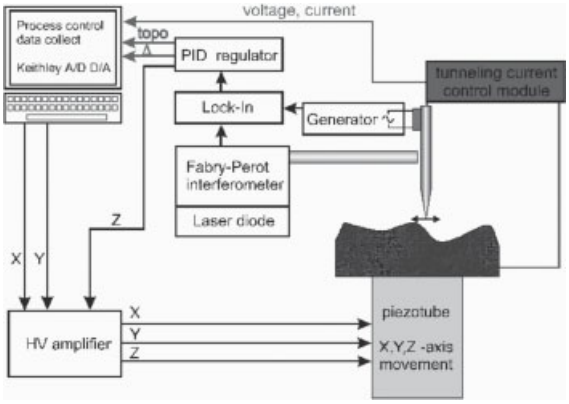

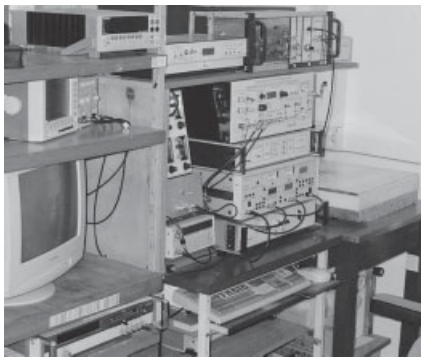

Fig. 11.12 Simplified scheme and view of the setup.

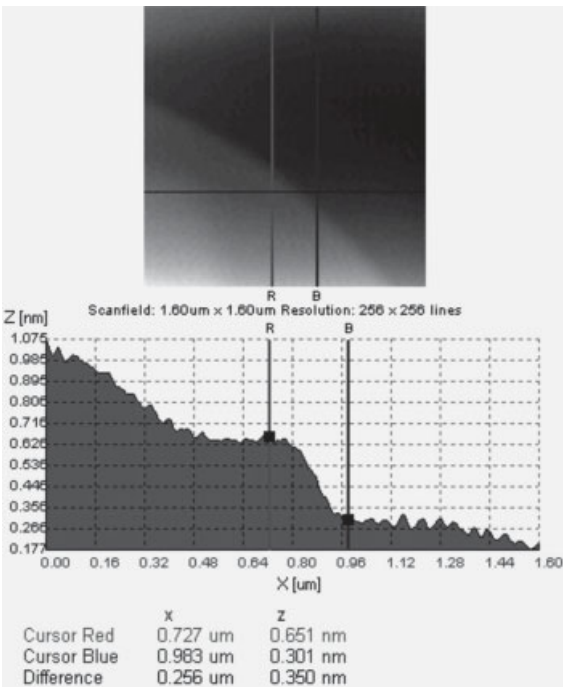

Fig. 11.13 HOPG surface and cross section.

11.3
Local Surface Electrical Properties Investigation

For tests of the emission current detection module the HOPG sample was scanned. The emission curve was measured for both bias polarizations (Figure 11.14). This setup opens up the possibility of researching local electrical material properties and correlating it with the topography of the surface [15].

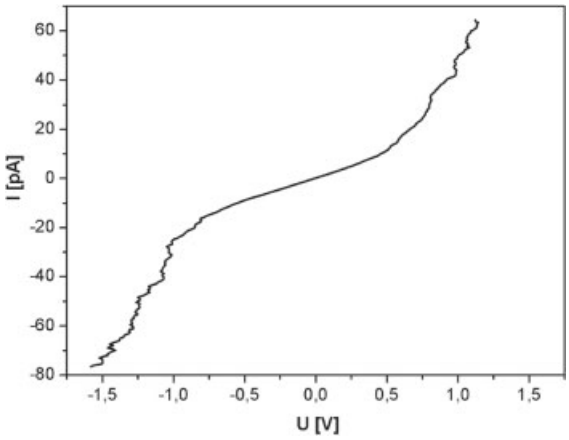

Fig. 11.14 Field emission current measured on the HOPG versus tip–sample voltage.

The emission current can be described as follows:

$$I = J \cdot A$$

$$J \approx \frac{C \cdot E^2}{\phi \cdot t^2(y)} \cdot \exp\left\{-\frac{B \cdot \phi^{3/2} \cdot \nu(y)}{E}\right\}$$

$$I = JA$$

$$J \approx \frac{CE^2}{\phi t^2(y)} \exp\left\{-\frac{B\phi^{3/2}\nu(y)}{E}\right\}$$

where A is the emitter area, E is the applied electric field, ϕ is the work function of the metal, B and C are the constants, and $\nu(y)$ as well as $t(y)$ are the functions which arise due to the inclusion of image charge effects.

11.4
Local Surface Oxidation

The oxidation procedure is an integral part of the "Topo-Scan" program. Process data are placed in a .txt file and can be easily modified using, for example, a standard word processor. The following parameters are available: X, Y are the start/stop point coordinates, t_1 is the in-point waiting time, t_2 is the tip moving time constant, and U is the tip applied voltage. Local oxidation was performed in con-

stant voltage mode. In distinction from pulse mode, in the presented case, the voltage was applied and the scanning tip was moved from the starting point to the stopping point.

A silicon surface for local anodization was used. The process was performed in ambient conditions (air temperature: 21°C, and RH: 42 %).

The experiment was performed in the following five steps:

- Scanning topography before the process (Figure 11.15).
- Process 1 (two lines: vertical and slanted line speed: 0.5 μm/s and 1.5 μm/s, respectively, applied voltage: 5V).
- Scanning topography after the first process step (Figure 11.16).

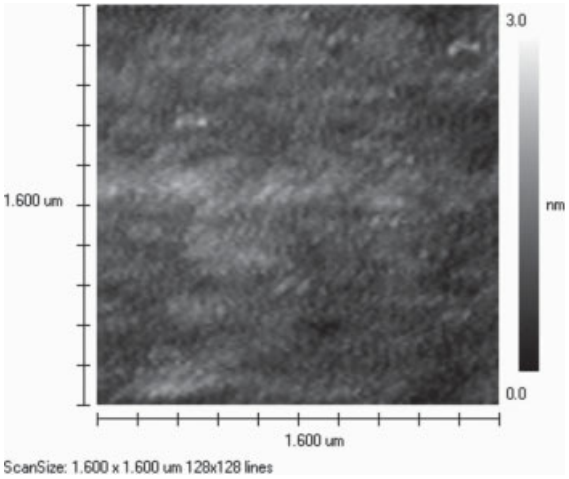

Fig. 11.15 Surface before process.

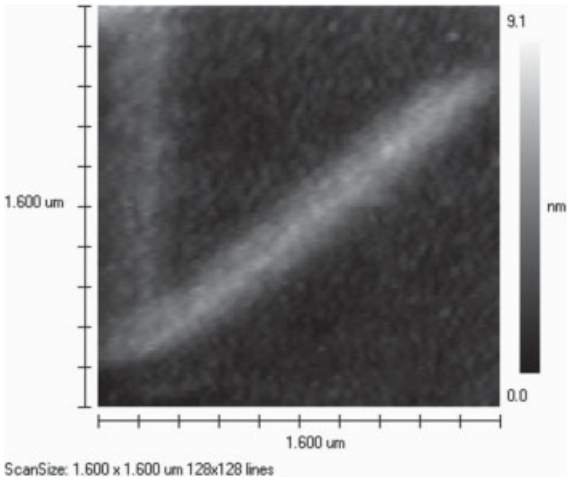

Fig. 11.16 Surface after process (step 1).

- Process 1 (two parallel, slanted lines speed: 1.5 μm/s, applied voltage: 5V).
- Scanning topography after the second process step (Figure 11.17).

Obtained structures are typically 160 nm full width at half maximum (FWHM) and 4 nm high.

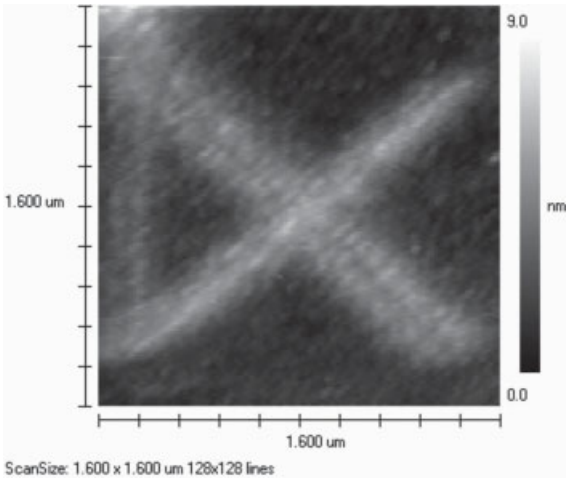

Fig. 11.17 Surface after process (step 2).

11.5 Summary

We presented experiments concerning the development and applications of SHFM measurement instrument based on the fiber Fabry–Perot interferometer for the measurement of the conductive microtip oscillation.

In order to obtain the high-fringe stability, the semiconductor laser work conditions were stabilized in a range of ±30 ppm/h for current and ±5 mK/h for temperature. As a result, we noted excellent power output and emitted wavelength stability.

The advantages of the presented setup are extreme sensitivity and a compact setup. Using the described measurement system, the quantitative measurement of probe dither motion with a resolution of 0.01 nm_{RMS} in a 100 Hz bandwidth is possible.

The presented setup can be used for local electrical surface properties investigation as well as for local surface oxidation.

Acknowledgements

We would like to thank our colleagues – Anna Sankowska, Jacek Radojewski, Pawel Janus, and Andrzej Marendziak for their collaboration. This work was partially sponsored by the State Committee for Scientific Research (KBN) project T11B 00224.

References

1 K. Karrai and R. D. Grober, Piezoelectric tip–sample distance control for near field optical microscopes, Appl. Phys. Lett. **66**, 1842 (1995).

2 G. Binnig, H. Rohrer, Ch. Gerber, and E. Weibel, Surface studies by scanning tunneling microscopy, Phys. Rev. Lett. **49**, 57 (1982).

3 J. U. Schmidt, H. Bergander, and L. M. Eng, Shear force interaction in the viscous damping regime studied at 100 pN force resolution, J. Appl. Phys. **87**, 3108 (2000).

4 R. Garcia, M. Calleja, and H. Rohrer, Patterning of silicon surfaces with non-contact atomic force microscopy: field induced formation of nanometer-size water bridges, Appl. Phys. **86**, 1898 (1999).

5 J. A. Dagata, T. Inoue, J. Itoh, K. Matsumoto, and H. Yokoyama, The role of space charge in scanned probe oxidation, J. Appl. Phys. **84**, 6891 (1998).

6 M. Calleja and R. Garcia, Nano-oxidation of silicon surfaces by non-contact atomic-force microscopy: size dependence on voltage and pulse duration, Appl. Phys. Lett. **76**, 3427 (2000).

7 M. Tello and R. Garcia, Nano-oxidation of silicon surfaces: comparison of non-contact and contact atomic-force microscopy methods, Appl. Phys. Lett. **79**, 424 (2001).

8 J. A. Dagata, F. Perez-Murano, G. Abadal, K. Morimoto, T. Inoue, J. Itoh, and H. Yokoyama, A predictive model for scanned probe oxidation kinetics, Appl. Phys. Lett. **76**, 2710 (2000).

9 K. Matsumoto, Y. Gotoh, T. Maeda, J. A. Dagata, and J. S. Harris, Room-temperature single-electron memory made by pulse-mode atomic force microscopy nano-oxidation process on an atomically flat α-alumina substrate, Appl. Phys. Lett. **76**, 239 (2000).

10 E. S. Snow, P. M. Campbell, F. A. Buot, D. Park, C. R.K. Marrian, and R. Magno, A metal/oxide tunneling transistor, Appl. Phys. Lett. **72**, 3071 (1998).

11 R. Held, T. Vancura, T. Heinzel, K. Ensslin, M. Holland, and W. Wegscheider, In-plane gates and nanostructures fabricated by direct oxidation of semiconductor heterostructures with an atomic force microscope, Appl. Phys. Lett. **73**, 262 (1998).

12 E. B. Cooper, S. R. Manalis, H. Fang, H. Dai, S. C. Minne, T. Hunt, and C. F. Quate, Terabit-per-square-inch data storage with the atomic force microscope, Appl. Phys. Lett. **75**, 3566 (1999).

13 V. Bouchiat, M. Faucher, C. Thirion, W. Wernsdorfer, T. Fournier, and B. Pannetier, Josephson junctions and superconducting quantum interference devices made by local oxidation of niobium ultrathin films, Appl. Phys. Lett. **79**, 123 (2001).

14 S. C. Minne, J. D. Adams, G. Yaralioglu, S. R. Manalis, A. Atalar, and C. F. Quate, Centimeter scale atomic force microscope imaging and lithography, Appl. Phys. Lett. **73**, 1742 (1998).

15 R. Watersa and B. Van Zeghbroeck, Fowler–Nordheim, Tunneling of holes through thermally grown SiO_2 on p+ 6H–SiC, Appl. Phys. Lett. **73**(25), 3692 (1998).

16 J. Planes, F. Houze, P. Chretien, and O. Schneegans, Conducting probe atomic

force microscopy applied to organic conducting blends, Appl. Phys. Lett. **79**(18), 2993 (2001).

17 D. W. van der Weide and P. Neuzil, The nanoscilloscope: combined topography and ac field probing with a micromachined tip, J. Vac. Sci. Technol. B **14**(6), 4144 (1996).

18 M. P. O'Boyle, T. T. Hwang, and H. K. Wickramasinghe, Atomic force microscopy of work functions on the nanometer scale, Appl. Phys. Lett. **74**(18), 2641 (1999).

19 A. Sikora, T. Gotszalk, R. Szeloch, A. Sankowska, and A. Marendziak, Modularny mikroskop tunelowy i sił atomowych do bada własności elektrycznych nanostruktur, in *Conference Materials "KKE Kołobrzeg 2003"* (2003) Vol.79.

12
Low Noise Piezoresistive Micro Force Sensor

L. Doering, E. Peiner, V. Nesterov, and U. Brand

12.1
Introduction

Stylus instruments are widely used for the measurement of surface roughness. These instruments allow us to adjust the static probing force typically within a range of 1 μN to 1 mN. For micro hardness measurements as well as for nondestructive probing of surfaces, the precise knowledge of the probing force becomes more and more important. Stylus instruments are calibrated by the manufacturer; however, accurate measurements require periodic recalibration of the probing force. The calibration can be obtained by using a suitable secondary standard, for example a calibrated micro balance or a micro force setting standard.

In this contribution, the development, production, and test of an *active* silicon sensor for the measurement and calibration of micro forces are described. The sensor can be used as micro force setting standard for the calibration of tactile probes such as nanoindenters and stylus instruments. Active sensor means that the force to be measured is directly proportional to the output voltage of a piezoresistive bridge. *Passive* sensors have already been described in detail in the past [1]. They are etched from a silicon chip without further electrical contacts. Several alignment labels are located on the sensor. Monocrystalline silicon was used for both types of sensors, because it exhibits a highly linear elastic response, shows no creep or aging behavior, and its dimensions and properties are only weakly influenced by temperature changes.

Commercially available cantilevers for atomic force microscopes with piezoresistive signal read-out are only applicable within limits for force calibration purposes [2]. Therefore we developed our own sensor based on a silicon cantilever with integrated tip and piezoresistive signal read-out. Because the exact position of the probing point must be well known, a special force ramp (the probing tip) is used. The same loading point is used for the calibration of the stiffness and the electrical sensitivity calibration as well as for the application as measurement standard. First measurements show a high signal-to-noise ratio and a good reproducibility.

Nanoscale Calibration Standards and Methods: Dimensional and Related Measurements in the Micro- and Nanometer Range.
Edited by Gunter Wilkening, Ludger Koenders
ISBN: 3-527-40502-X

12.2
Manufacturing of the Sensor

12.2.1
Computer Aided Design

In accordance with the requirements of the task a three-dimensional model of the prototype was created, which has approximately the same geometric dimensions, and investigated using a finite element analysis (FEM) analysis. More details are given in [3].

The following points were particularly examined:

- the resonance frequencies of the system,
- the estimated mechanical stiffness,
- definition and verification of the design, in particular the lateral position of the piezoresistive elements of the Wheatstone bridge (see Figure 12.1).

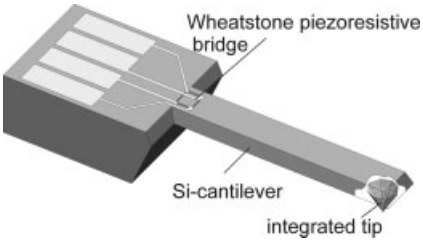

Fig. 12.1 Overview of the sensor design.

12.2.2
Manufacturing of the Sensor

The sensor is manufactured using conventional silicon processing technology such as wet chemical etching, oxidation, lithography, evaporation, and diffusion. The dimensions of the bending beam, which influence the mechanical properties and also the dimensions and doping profile of the piezoresistive strain gauges, which determine their electrical properties, can be varied in a wide range.

The seven process steps given in Figure 12.2 are necessary to manufacture the sensor.

The voltage supply U_0 and the signal read-out ΔU are contacted by pressing connector pins against the contact pads on the sensor (see Figure 12.3). Thus wire bonds can be avoided. The contact resistance is less than 2 Ω.

It is also possible to manufacture a truncated tip (see Figure 12.4), which is especially advantageous while calibrating a micro hardness detection device. In this case it is possible to use this flat area for probing with a sharp tip without increasing the measurement uncertainty significantly. Figure 12.5 shows the "normal" ordinary sharp tip.

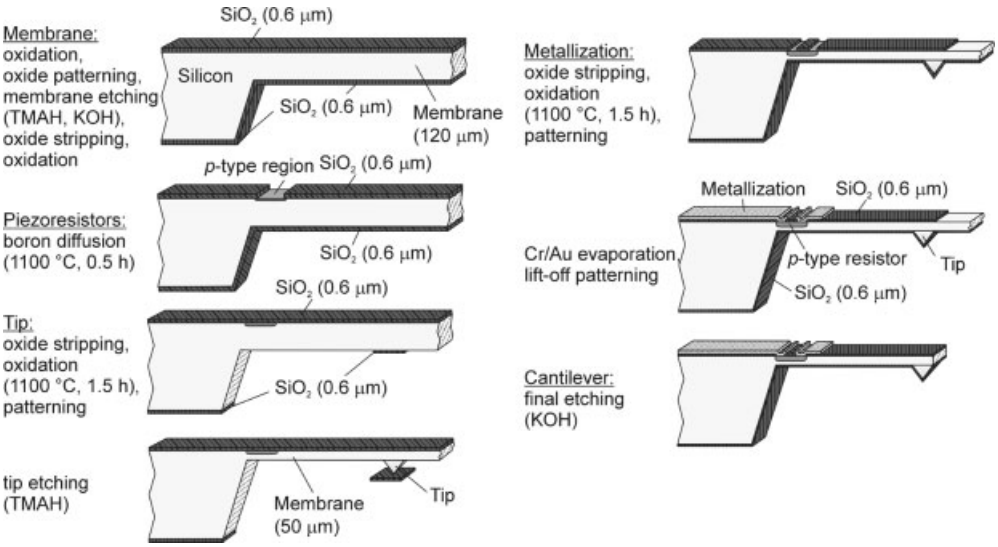

Fig. 12.2 Manufacturing of the sensor.

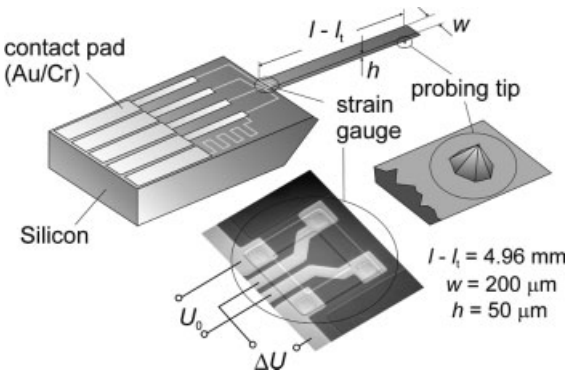

Fig. 12.3 Sketch of the micro force sensor and typical dimensions.

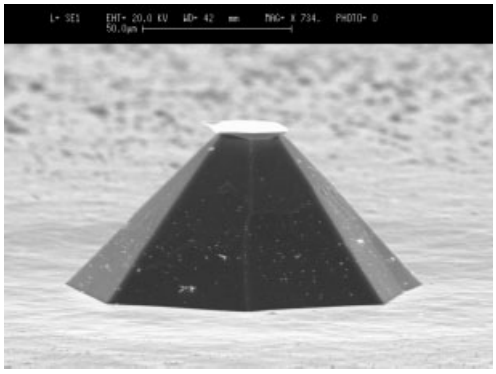

Fig. 12.4 Truncated tip.

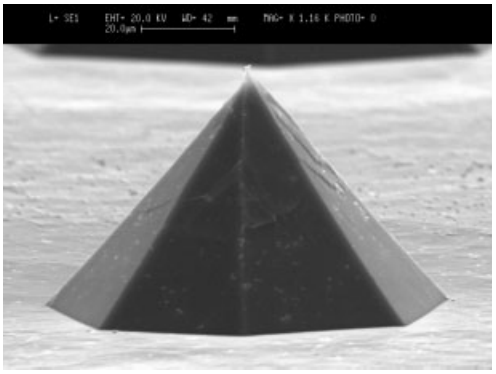

Fig. 12.5 Ordinary sharp tip.

The highlights of the manufactured sensor are as follows:

- the simple fabrication process, wet etching using TMAH (tetramethylammonium hydroxide) and KOH (potassium hydroxide), which allows the use of low-cost equipment and multi wafer processing;
- homogenous thickness of the beam is achieved by etching with TMAH as well as very smooth surfaces of cantilever and tip;
- doping using diffusion needs no toxic gases and does not lead to crystal damage;
- no packaging is required since the sensors can be directly connected to cables using pressed contacts, which therefore also allows a fast sensor replacement.

12.3 Sensor Properties

12.3.1 Doping Profile

While electronic circuits are still at the wafer state, there are many standard techniques to determine the doping concentration. For example, the SEM CL method [4] or the doping-induced contrast method in photoelectron emission microscopy may be used [5].

In an assembled state it is difficult to determine the doping profile of the piezoresistive elements. The aim of the work described in this chapter was to develop a simple, low-cost, and nondestructive method to determine the dopant profile accurately, which characterizes the quality of the manufacturing of the sensor. The dopant profile determines the electrical properties such as the sensor sensitivity and the temperature stability. The solution of this problem is based on the relation between the measured resistance and its temperature coefficient and the

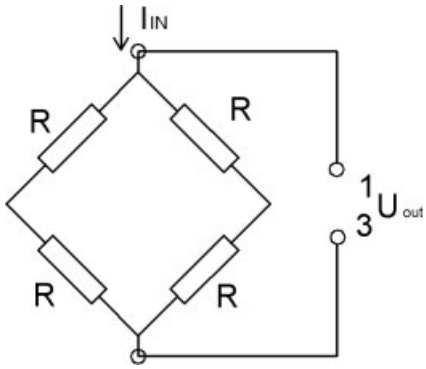

Fig. 12.6 Electrical schema for the measurement of the temperature coefficient.

geometrical dimensions of the resistor, the mobility of charge carriers, the doping concentration, and the depth of the doping profile.

Two steps are necessary. First, the temperature coefficient of the whole bridge and the resistance at 0 °C are unknown and have to be measured. The cantilever and a thermal resistor (Pt 100) are mounted in a well-isolated box. A heating device is used to increase the temperature to a certain level above room temperature. Then the heating device is switched off and the device is allowed to cool down to room temperature. The contacts 1 and 3 (see Figure 12.6) are connected to a constant current source and the voltage difference between the points 1 and 3 is measured by a high impedance voltmeter. While the temperature of the device decreases down to room temperature (Figure 12.7) the voltage (resistance) and the temperature are measured simultaneously. Because of the slow decrease of the temperature a very homogenous temperature distribution is expected. Figure 12.8 shows the observed resistance as a function of temperature. It shows a quite linear behavior. A linear fit is used to determine the value of the resistance at 0 °C and the linear (integral) temperature coefficient of the resistance, α, according to Eq. (12.1).

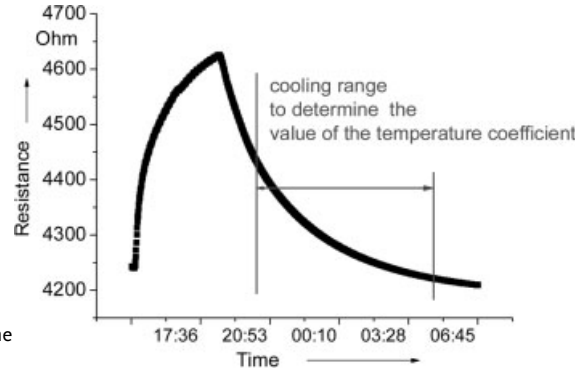

Fig. 12.7 Resistance over time while heating and cooling.

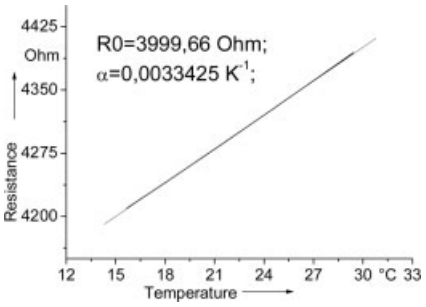

Fig. 12.8 A determined resistance and linear (integral) temperature coefficient using a linear fit.

$$R = R_0(1+\alpha^*T) \tag{12.1}$$

In a second step the doping concentration and its depth are evaluated using a Monte Carlo method. Assuming a Gaussian dependence $n(z)$ of the doping concentration on the depth z leads with doping concentration n_0 at the surface and w as the depth parameter in (12.3a) to formula (12.2). The resistance is described by [6]

$$R_c = \frac{L_R}{e \cdot b \cdot \int_0^{Z0} \frac{\mu(n(z))^*n(z)^*dz}{1+\alpha(n(z))^*T}} \tag{12.2}$$

$$z_0 = w \cdot \sqrt{ln\left(\frac{n_0}{n_{waf}}\right)} \tag{12.3}$$

$$n(z) = n_0 \cdot \exp\left(\frac{-z^2}{w^2}\right) \tag{12.3a}$$

where R_c is the computed resistance, L_R is the length of the resistor, μ is the mobility at 0 °C, $\alpha(n(z))$ is the local (differential) temperature coefficient of the resistance, b is the width of the resistor, e is the electrical elementary charge, n_{waf} is the doping concentration of the wafer, z_0 is the carrier density of dopand, which is equal to n_{waf}.

A self-written program adjusts the unknown values of n_0 (doping concentration) and w (depth of profile), so that the difference between the measured and calculated values of the resistance and its temperature coefficient become a minimum.

12.3.2
Spectroscopic Noise Analysis and Determination of the Hooge Constant

The measurements were performed at test structures. The goal of these investigations was to characterize the noise of piezoresistive bridge without the influence of further factors, e. g., air movements and thermal changes, which may excite the cantilever oscillations. For this purpose a special wafer was prepared. The steps mentioned in Section 12.2.2, which produce the membrane and the cantilever, were omitted. Therefore the influence of the membrane or cantilever contributions to the noise measurement is avoided. Thus the influence of the inevitable changes of temperature could be reduced as far as possible. The frequency analysis was carried out with a commercially available bridge amplifier [7], which allows us to measure the noise at different input voltages. Figure 12.9 shows the used electrical schema. All elements of the piezoresistive bridge generate the noise and all elements have the same temperature and the same characteristic. Other publications such as [8] are using other schemata including only one noise generator. This fact is considered in Eq. (12.5). Using DC the divisor is now 2 in place of 1 [9]. Both lead to higher sensitivity and higher accuracy.

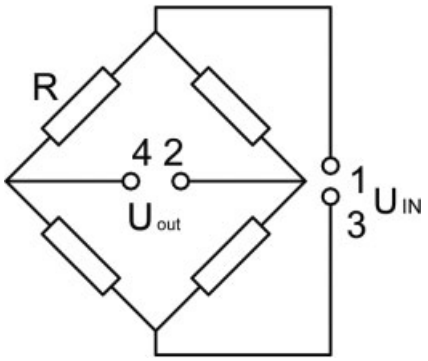

Fig. 12.9 Electrical schema for noise measurement.

The frequency range was selected from 7 μHz up to 1 kHz. The whole range was divided into four measurement ranges in order to reduce the duration of measurement.

According to the Wiener–Khintchine theorem (Eq. (12.4)) the variance of the values of the power spectrum is scaled.

The amplifier noise has to be considered as well. The measured values of the noise consist always of the noise contribution of the amplifier and the noise contribution of the measuring bridge. For this reason the amplifier used should have a noise level much lower than the measuring signal that is expected. The lower curve in Figure 12.11 shows the noise of a pure Ohmic bridge (special wire layout with low inductivity or carbon resistor), which means that the detected noise is caused by the amplifier only. The upper curve shows the result of a noise analysis

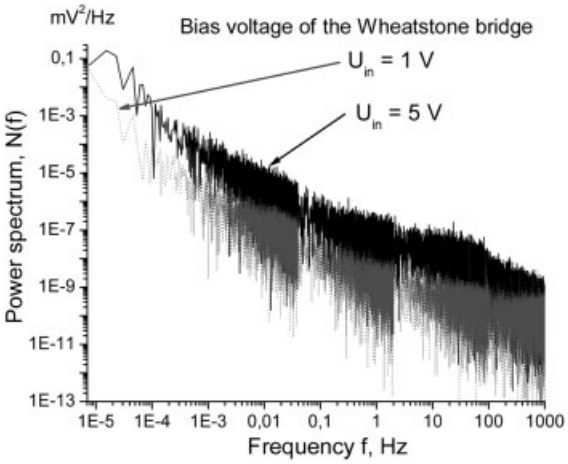

Fig. 12.10 Power spectrum at different bias voltages U_{in}.

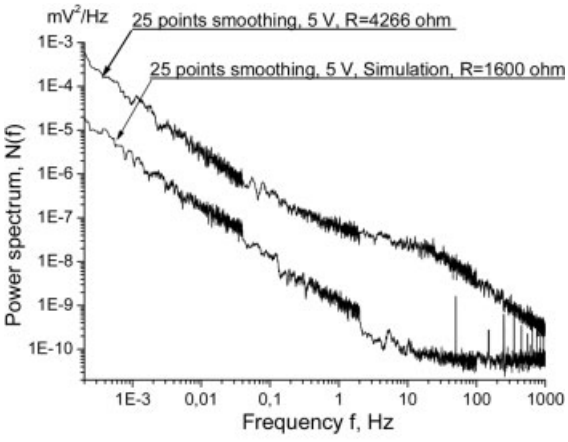

Fig. 12.11 Power spectrum of a piezoresistive bridge and an Ohmic bridge (lower curve).

of a real piezoresistive bridge. The noise contribution of the amplifier is more than 500 times lower than the noise contribution of the piezoresistive bridge.

Figure 12.12 represents a magnified view from Figure 12.10. In this frequency range the logarithm of the power spectrum shows a linear dependence on the logarithmic frequency. The parameters A and B obtained by a linear fit are used to characterize the power spectrum and to calculate the Hooge constant. The value for the slope B is used in Eq. (12.5) for the bias voltage in DC mode (important!) and describes the Hooge function. In the ideal case the slope B should be –1.0. However, the measured value of ≈ -1.05 is very close to the ideal value. The intercept A is used in Eq. (12.7).

$$\sigma^2 = \int_0^{f_m} \mathrm{N(f)df}; \tag{12.4}$$

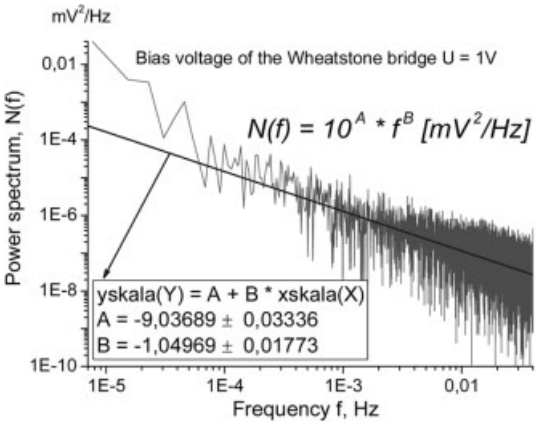

Fig. 12.12 Determination of important factors to compute the Hooge constant.

$$N(f) = \frac{\alpha_{H^*}\, U^2}{2 \cdot N_0 \cdot f^{-B}}; \tag{12.5}$$

$$N_0 = \frac{\sqrt{\pi}}{2} \cdot n_0 \cdot L_R \cdot b \cdot w; \tag{12.6}$$

$$\alpha_H = \frac{2 \cdot 10^A \cdot N_0}{U^2} \tag{12.7}$$

The total number N_0 of carriers is calculated by inserting the values for the geometrical data for width and length and the equivalent depth in Eq. (12.6). With U as the bias voltage of the Wheatstone bridge (1000 mV), N_0 the total number of carriers, L_R the length = 107 μm, b the width = 15 μm, w the depth of the profile = 0.96 μm, A the coefficient (from Figure 12.12) = −9.04, it follows that

$$\alpha_H = 2.6 * 10^{-6} \tag{12.8}$$

Compared with other publications such as [10] where the minimal achieved value of the Hooge factor is close to 1×10^{-6}, here a very good piezoresistor with very low Hooge noise was obtained.

12.3.3 Force Calibration and Electrical Calibration

If the sensor is to be used as a micro force setting standard, it has to be calibrated. A detailed description of the calibration setup (see Figure 12.13) and the calibration procedure used here has already been published in [11].

For the calibration procedure a nano force calibration device consisting of

- a high precision translation stage (resolution 1 nm, reproducibility ±5 nm [12]),

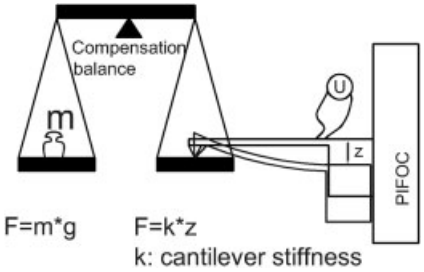

Fig. 12.13 Calibration setup.

- a high precision compensation balance [13] (resolution of 0.1 μg), and
- a measuring amplifier [7] for the acquisition of the electrical signals

was used.

Two sensors were calibrated. The first one showed a mechanical stiffness of 8.6 N/m (numbered as D4D, cantilever thickness 50 μm), and the second showed a mechanical stiffness of 4.3 N/m (numbered as i490, cantilever thickness 40 μm). The electrical values for the sensitivity are 85.7 μN/mV (i490) and 93.4 μN/mV (D4D).

Figure 12.14 shows a typical curve with small residuals of the linear fit of ± 16 nN. The electrical sensitivity is plotted in Figure 12.15. The residuals of the linear fit are within ±0.320 μN. Repeated (44) measurements over a period of 2 days in a well-controlled temperature environment (20.19 ± 0.044 °C and ± 0.008 K/h) show a low scatter of the stiffness values (within ± 0.01 %) and of the output signal (within ± 0.23 %).

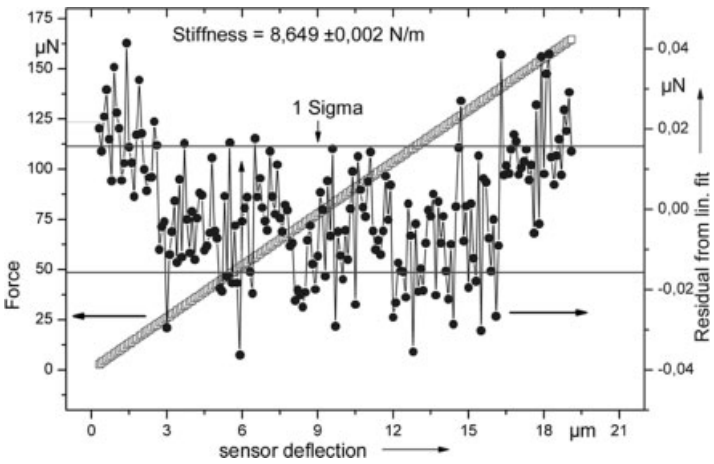

Fig. 12.14 Mechanical stiffness with residuals from linear fit.

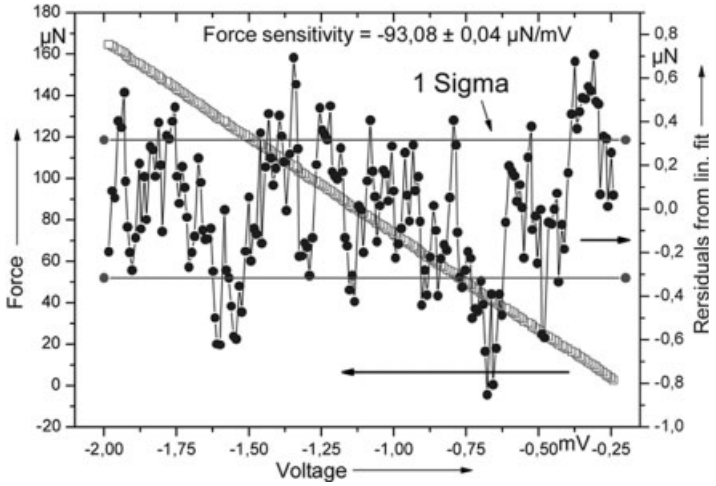

Fig. 12.15 Force versus output voltage with residuals of linear fit.

12.4 Application: Force Calibration of a Stylus Instrument

The calibrated sensors were applied to measure the probing force of a stylus instrument [14]. The evaluation with two different methods, using the piezoresistive signal and the stylus instrument profile was tested. Both measurement procedures are based on scanning the cantilever surface. The conventional evaluation of the stylus instrument profile suffers from several problems, essentially tilt and roughness of the etched sensor surface. These problems can be avoided using the

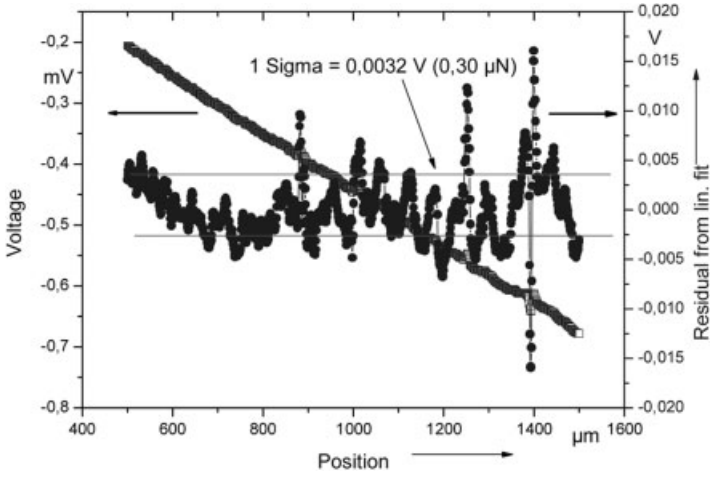

Fig. 12.16 Electric output signal while scanning the standard.

methods in [1]. The electrically measured deflection of the new active micro force setting standard can be evaluated in a much simpler way.

Figure 12.16 shows the voltage signal of the piezoresistive bridge while scanning. The curve is not influenced by tilt and roughness of the etched cantilever surface. The residuals of a linear fit show that the vibration near the clamped end (left) has only minor amplitude. These vibrations decrease with decreasing nominal probing force while the influence of noise is increasing.

Four measurements were carried out with standard no. i490 and three measurements with standard no. D4D, each of which is repeated once (Table 12.1). The probing force was obtained by simply multiplying the measured slope with the distance of the probing point from the clamped end and multiplying with the sensitivity obtained from the slope from calibration. The deviation in the last column shows a good agreement of the measured value with the target force value.

Table 12.1 Calculation of the probing force of a stylus instrument with the sensors D4D and i490

Calculation of probing forces (sensor i490)					**with probing point at**	**4930 µm**	
Meas #	**Target Value**	**Target force**	**slope measured**	**Volt. at prob. Point**	**slope from calibration**	**force measured**	**meas./ target force**
1	20,0 mg	196,2 µN	−4,73E-04 V/µm	−2,3324 V	−85,737 µN/V	200,0 µN	102 %
2	20,0 mg	196,2 µN	−4,76E-04 V/µm	−2,3463 V	−85,737 µN/V	201,2 µN	103 %
3	5,0 mg	49,1 µN	−1,20E-04 V/µm	−0,5913 V	−85,737 µN/V	50,7 µN	103 %
4	5,0 mg	49,1 µN	−1,20E-04 V/µm	−0,5902 V	−85,737 µN/V	50,6 µN	103 %
5	1,0 mg	9,8 µN	−2,46E-05 V/µm	−0,1215 V	−85,737 µN/V	10,4 µN	106 %
6	1,0 mg	9,8 µN	−2,51E-05 V/µm	−0,1237 V	−85,737 µN/V	10,6 µN	108 %
7	0,1 mg	1,0 µN	no value	no value	no value	no value	no value
8	0,1 mg	1,0 µN	−2,15E-06 V/µm	−0,0106 V	−85,737 µN/V	0,9 µN	93 %
Calculation of probing forces (sensor D4D)					**with probing point at**	**4930 µm**	
Meas #	**Target Value**	**Target force**	**slope measured**	**Volt. at prob. Point**	**slope from calibration**	**force measured**	**meas./ target force**
1	20,0 mg	196,2 µN	−4,61E-04 V/µm	−2,2747 V	−93,409 µN/V	212,4 µN	108 %
2	20,0 mg	196,2 µN	−4,55E-04 V/µm	−2,2438 V	−93,409 µN/V	209,6 µN	107 %
3	1,0 mg	9,8 µN	−2,22E-05 V/µm	−0,1092 V	−93,409 µN/V	10,2 µN	104 %
4	1,0 mg	9,8 µN	−2,32E-05 V/µm	−0,1143 V	−93,409 µN/V	10,7 µN	109 %
5	0,1 mg	1,0 µN	−3,32E-06 V/µm	−0,0163 V	−93,409 µN/V	1,5 µN	156 %
6	0,1 mg	1,0 µN	−2,95E-06 V/µm	−0,0146 V	−93,409 µN/V	1,4 µN	139 %

The measured force values of 209.6/212.4 μN and 200.0/201.2 μN differ from the nominal force of 196.2 μN. This deviation of the two measurement results must be further examined. A better judgment can be made once the measurements have been repeated.

The standard i490 has lower mechanical stiffness (half value) than the standard D4D and especially the measured value for the small force of 1 μN is more comparable to the target value. This is due to the larger (double) deflection at the same force, which can be measured more accurately. The calculated deflection using the sensor i490 loaded with a probing force of 1 μN leads to the very small deflection value of 0.2 μm at the load point. Using the sensor D4D loaded with the same force leads to the very small deflection value of 0.11 μm. The measured deviation of 150 % is equal to a deflection variation of 65 nm.

12.5 Conclusions

A piezoresistive cantilever sensor for the determination of micro forces was developed to serve as a portable force setting standard. The manufacturing of the standard is based on micromachining of silicon bulk material. A finite element analysis was applied in the design of the cantilever and has proven to be very useful to locate the position of increased internal stress. A self-written software tool was used to determine the essential electrical properties of the sensor post its fabrication such as the doping concentration and the profile depth. The noise measurements were performed at structures comparable to the real sensor layout. The spectroscopic noise analysis and the determination of the Hooge constant revealed that the contribution of the piezoresistive elements to the total sensor noise is very small and that there are other influences. They have to be considered at the total noise budget and dominate the achievable sensitivity of the sensor. For the mechanical and the electrical calibration a calibration setup with low measuring uncertainty has been used. The probing forces of a stylus instrument were calibrated. Small forces of a few μN are resolved.

References

1 Lutz Doering, Uwe Brand, Erwin Peiner, et al., Development of micro force setting standards for stylus instruments, in Proc. of Euspen International Topical Conference on Precision Engineering, Micro Technology, Measurement Techniques and Equipment, edited by Verlag Rhiem Voerde (Aachen, 2003), Vol. 2, pp. 407–410.

2 Lutz Doering and Uwe Brand, Si-cantilevers with integrated piezo resistive elements as micro force transfer standards, in Proc. of Nanoscale 2001, edited by PTB-Bericht (2001), pp. 185–192.

3 Björn Herold, Entwicklung eines Transferkraftnormals mit piezoresistiver Messbrücke, Diploma thesis, TU Braunschweig, 2002.

4 Colin Warwick, Defects in Czochralski-grown InP and GaAs, a dissertation submitted for the degree of Doctor of Philosophy, University of Oxford, 1983.

5 V. W. Ballarotto, K. Siegrist, R. J. Phaneuf, et al., Model for doping-induced contrast in photoelectron emission microscopy, J. Appl. Phys, **91**, 469 (2002).

6 Ingolf Ruge, Hermann Mader, Walter Heywang, et al. (Eds.), *Halbleiter-Technologie* (Halbleiter-Elektronik Bd. 4, 1991), 287

7 Hottinger, Amplifier ML10B, HBM Mess- und Systemtechnik, Postfach 10 01 51, D-64201 Darmstadt, Germany.

8 M. Gel and I. Shimoyama, Force sensing submicrometer thick cantilevers with ultra-thin piezoresistors by rapid thermal diffusion, J. Micromech. Microeng. 423–428 14, (2004).

9 F. N. Hooge, Discussion of recent experiments on 1/*f* noise, Physica **60**, 130–144 (1976).

10 Jonah A. Harley, Advances in piezoresistive probes for atomic force microscopy, Dissertation, Stanford University, 2000.

11 Lutz Doering, Joachim Frühauf, and Uwe Brand, Micro force transfer standards, in Proc. of IMEKO, the International Conference on Force, Mass, Torque, Hardness and Civil Engineering Metrology in the Age of Globalization (VDI-Berichte, Celle, 2002), Vol. 1685, pp. 83–88.

12 Pifoc, P 721 with digital controller E 750 Physik Instrumente (PI) GmbH & Co. KG 76228 Karlsruhe, Germany.

13 Sartorius, Compensation balance type SC2 37075 Göttingen, Germany.

14 Tencor, Stylus instrument P11, Tencor Corp., 3231 Scott Blo., Santa Clara, CA 95054, USA.

Part IV
Calibration – Overview

Nanoscale Calibration Standards and Methods: Dimensional and Related Measurements in the Micro- and Nanometer Range.
Edited by Gunter Wilkening, Ludger Koenders
ISBN: 3-527-40502-X

13
Towards a Guideline for SPM Calibration

T. Dziomba, L. Koenders, and G. Wilkening

Abstract

In the course of the evolution of many high technologies such as microelectronics, micromechanics, and also biotechnology, the size of technical structures is being decreased continuously. In many technical applications, the feature size has already reached the submicron scale and often needs to be measured with an uncertainty in the nanometer range. Scanning probe microscopes (SPMs) are therefore increasingly used today as quantitative measurement instruments. Consequently, the demand for standardized calibration routines for these types of instruments rises. A number of transfer standards suited for SPMs have already been developed for this purpose and are commercially available. While detailed knowledge of the standards' properties is a prerequisite for their practical application, the calibration procedure itself also deserves careful consideration. Up to now, there is no generally accepted guideline on how to perform SPM calibrations. This chapter therefore discusses a possible calibration scheme and focuses on several critical aspects of SPM characterization, e. g., the determination of the static and dynamic physical properties of the instrument and its ultimate limits, the influence factors that need to be considered when plotting a scheme for the calibration of its scan axes, and the possible error sources that need to be checked to ensure that all uncertainty contributions are taken into account on calculation of the measurement uncertainty according to *Guide to the Expression of Uncertainty in Measurements* (GUM).

13.1
Introduction

Scanning probe microscopy (SPM) is increasingly used today not only in research and development but also in many fields of industrial fabrication and inspection. Growing importance is therefore attached to the *quantitative* information these instruments provide. Consequently, there is an increasing need to check the accu-

Nanoscale Calibration Standards and Methods: Dimensional and Related Measurements in the Micro- and Nanometer Range.
Edited by Gunter Wilkening, Ludger Koenders
ISBN: 3-527-40502-X

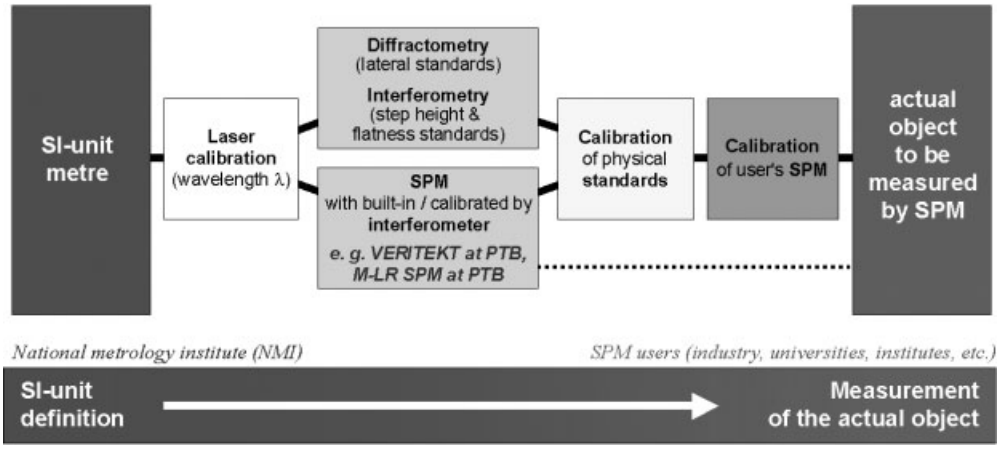

Fig. 13.1 Traceability chain for SPM.

racy of the SPM used in a similar way as it is already routinely practiced with coordinate-measuring instruments used for larger scale measurements and to make sure that those measurements are traceable to the SI unit (see Figure 13.1).

However, except for a few specially designed setups mainly at national metrology institutes, measurements made with these instruments usually lack traceability to the meter definition. In an attempt to fill this gap, several commercial companies and research institutes have developed a number of transfer standards in recent years that are especially suited for the needs of SPMs [1, 2]. They may be divided into those for the actual calibration and others for the verification of the instrument (Figure 13.2).

The first types of standards consist of regular structures of well-known geometry with calibrated dimension(s) in lateral and/or vertical direction and are thus meant to allow the calibration of SPMs, e. g., single axis x, y, or z, to look for rectangularity of the axes, etc.

Calibration	Verification of properties
• x- and y-axes • z-axis • Angle errors of axes (yaw, pitch, roll) • Rectangularity of the axes	• Influence of external mechanical and acoustic vibrations, electrical noise, air flow • Noise of the instrument • Thermal drift • Internal noise • Scanner guidance properties • Tip characteristics

The other types of standards or samples are needed to verify the behavior of the instrument at its location respectively in its environment such as its susceptibility toward ambient conditions (noise, drift) and to determine its internal properties

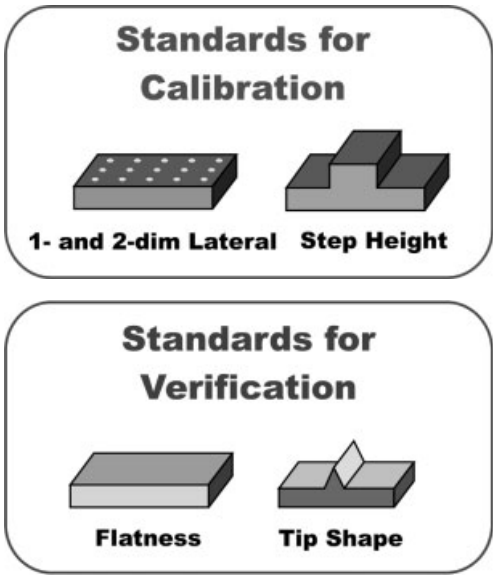

Fig. 13.2 Calibration of SPM and verification of properties.

such as warm-up characteristics and the shape of the tip used. While tip problems may be solved easily by changing the probe, most of the other properties can be measured, but many of them often cannot be adjusted by simple means. For example, the noise of the instrument may usually be recorded easily, while it typically takes a considerable effort to reduce the noise level, particularly when changes to the laboratory turn out to be inevitable.

A guideline should therefore help the user to determine the right calibration strategy with respect to his or her instrument type, to define an agreeable characterization/correction effort according to his or her actual needs and available resources, to perform the necessary calibration steps in the right way, and to draw the correct conclusions. Consequently, the aims of such a guideline for SPM are as follows:

- the definition of metrological terms, symbols, procedures, and standards
- minimal requirements for the calibration of an instrument
- criteria to determine the degree to which an instrument can be calibrated reasonably
- determination of the uncertainty of measurements
- the improvement of the comparability of measurements of geometrical properties

13.2 General

13.2.1 Schematic Description of SPMs

Figure 13.3 shows the schematics of an SPM with the main components as used in the chapter.

The main components of SPMs are as follows (Figure 13.3):

x–*y* scanner	element to displace the probe (scanning probe microscope) or alternatively the sample (scanning sample microscope) usually in equidistant steps or continuously at constant speed
z actuator	element to keep the probe under constant conditions (usually at a constant value of the interaction used for control) while scanning the sample surface
Probe	fine tip for the investigation of the sample properties
Sample	object to be investigated by SPM
Feedback sensor	element that allows us to detect small changes of the tip or cantilever properties (i. e., of the interaction exploited)
x–*y* coarse positioning	elements to position and align the sample to bring the region of interest of the sample into the reach of the *x*–*y* scanner
z coarse approach	element to decrease the displacement between the sample and the probe to a value that allows the *z* actuator to bring the probe and the sample into interaction

The SPM can be understood as a small coordinate measurement machine in which the probe is moved in all three directions, but with smaller ranges. Therefore the probe and the scanning system have all degrees of freedom. In three dimensions, this amounts to 21 degrees (see Figure 13.4): 3 positioning errors (*xpx, ypy, zpz*), 6 straightness errors (*ytx, xty, ztx, zty, xtz, ytz*), 9 rotational errors (*xrx, yry, zrz, xry, yrx, zrx, zry, xrz, yrz*), and 3 squareness errors (*xwy, xwz, ywz*).

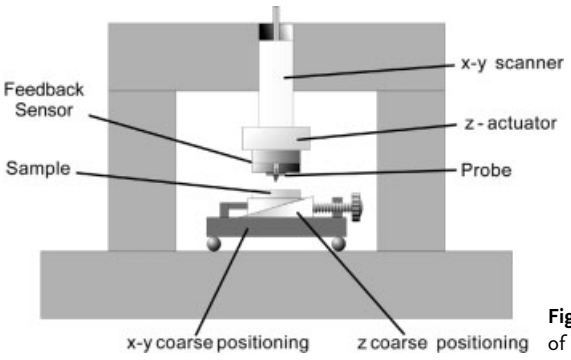

Fig. 13.3 Schematic description of the components of an SPM.

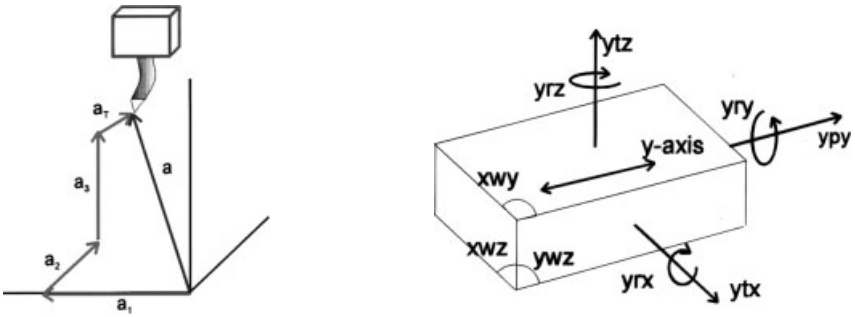

Fig. 13.4 (a) Vector **a** describing the movement of the tip in 3D. (b) Schematic description of the translation rotation axes and axes between the axes.

13.2.2
Metrological Classification of SPMs

If an SPM is not only expected to yield qualitative information but also intended for quantitative measurements, the traceability to the SI unit of length has to be realized. Before a calibration routine is plotted, it is therefore essential to consider how traceability is actually realized in the SPM system to be calibrated respectively how a traceability chain might be established.

Consequently, existing types of SPMs may – according to their properties – be divided into the following three categories with respect to the quality of their position measurements:

A Reference SPMs with integrated laser interferometers, traceability directly via the wavelength of the laser used is possible (often called "metrological SPM").

B SPMs with position monitoring by integrated position sensors, e. g., capacitive sensors, inductive sensors, strain gauges, encoders calibrated either by temporarily attaching laser interferometers to the scan system or by using high-quality physical transfer standards. This category comprises both SPMs with active position control (i. e., with a feedback circuit: so-called closed-loop SPMs) and without (open-loop SPMs with integrated position sensors for monitoring only).

C SPMs with positioning by simply using the voltage applied to the scanner (x & y) respectively with positions deduced from the voltage applied to the scanner (z), usually calibrated by using physical transfer standards.

As a consequence of this definition of categories, certain SPM systems may not be assigned to one category as a whole, as the equipment of each of its three axes might differ. In such a case, each axis needs to be treated individually.

The category is a first important criterion for the planning of the calibration routine, as both the focus of the calibration procedure and the extent of the calibration effort largely depend on the metrological properties of the SPM. For instance, it is generally not advisable to purchase a set of very precise and thus rather expensive standards, e. g., of the uncertainty class 10^{-5} for the calibration of an SPM of category C. In such a case, a standard with an uncertainty of 10^{-3} will most likely prove sufficient.

13.2.3 Calibration Intervals

Another general classification describes the appropriate repetition rate of calibration. This depends both on the class of instrument and its stability and on the accuracy the user aims to maintain for the specific measurement purposes. As calibrations are usually quite time-consuming and thereby cost-intensive, a compromise is to be found between necessary calibration effort and tolerable uncertainty.

Especially when starting the operation of a new (or substantially modified) SPM system or changing its ambient conditions, frequent recalibrations are advisable in the initial phase. In order to find the best-suited strategy, experience needs to be gained for the particular SPM system to assess its behavior and deduce criteria for recalibration. The following schemes of calibrations (A) and measurements (B) may prove reasonable:

ABB... ABB...	instrument with a high medium-term stability: calibration necessary only in regular time intervals, e. g., weekly, monthly, annually
AB, AB, ...	instrument with sufficient short-time stability, but lacking satisfying long-time stability: calibration necessary before each measurement
ABA, ABA, ...	calibration before and after the measurement to exploit the maximum accuracy of the system; or the system shows poor stability–drift of the system's properties taken into account as closely as possible

13.3 Verification of Properties of Instrument, Tip and Environment

As a first step to develop a calibration procedure for SPM, all possible error sources that may influence the performance of the scan system need to be identified and assessed. Then, in a second step, suitable calibration routines have to be established. Examples for this procedure are given in the following.

13.3.1
Ambient Conditions

Temperature changes, turbulences, vibrations, dust, and dirt as well as the presence of staff are ambient factors that deserve consideration before the SPM system is implemented. Sometimes the SPM is isolated from the environment by using an acoustic chamber. The drawback of such an acoustic chamber is that it might also act as thermal insulator. The heat sources and the time constants of the temperature change need to be determined to take appropriate counter measures. At least they should be taken into account when operation guidelines are plotted. Such a temperature dependence can be avoided – or at least minimized – in the course of the construction of an SPM system by taking great care of the measuring circle, i. e., the mechanical construction that links the probe with the sample. The basic idea is to construct the measuring circle in such a way that the probe's position relative to the sample does not change at all or at least not in all three directions. This is usually achieved by selecting materials with a low thermal expansion coefficient and designing the measurement circle to be as small as possible.

In order to avoid misleading conclusions and to reduce the calibration effort to the level actually required, the physical properties of the SPM system need to be taken into account when determining the best-suited strategy for the SPM's calibration. Especially the degree of reproducibility is decisive for the necessary and reasonable calibration effort.

13.3.2
Flatness Measurements and Signal Noise

Guidance errors and the noise in the measured signal are key figures of an SPM's principal mechanical and electronic limits. They set the ultimate limit for the necessary calibration effort reasonable for the particular SPM system. It is therefore advisable to determine these values before making a thorough calibration plan for the individual SPM system (see Table 13.1).

A first assessment of guidance errors is accomplished by measurement of a flatness standard, i. e., a sample with a well-defined reference area that has been calibrated by interference microscopy. Subtraction of these reference data from the actual SPM measurement data yields the out-of-z-plane movement across the lateral scan range of the measuring system (Figure 13.5).

By repeating such measurements, a distinction can be made between deviations from the z plane of temporary, initial nature (e. g., remaining temperature drift, creep of piezos), and permanent cross-talk in the z-direction by lateral movement in the x and y (e. g., scanner bow, detection/feedback errors).

In order to check the signal noise, measurements can be recorded without (i. e., lateral scanning disabled) and while scanning a small section, e. g., of a flatness standard [1]. The detected oscillations may be caused by mechanical or electronic influences.

Table 13.1 Instrument properties and their quantitative determination

Properties		
Drift	Vertical	Flatness standard or sample with flat regions. Measurements of a 2D grid with small height and looking for differences. Variation of environmental conditions. Opening of chamber. Switching on/off of instruments
	Lateral	Sample with straight edge or line with small step height parallel or perpendicular to the scan direction. Measurements of a 2D grid with small height and for differences
Guidance errors	Cross-talk *xtz*, *ytz*	Flatness standard
	Cross-talk *xty*, *ytx*	2D lateral standard or line respectively groove perpendicular to the fast and parallel to the slow scan direction.
z –noise	Static: without moving in the *x*- or y-direction	After stabilization of the instrument. Measurement on a flat sample region without structure while any movement is disabled. Additionally, variation of environment conditions, e. g., mechanical damping, acoustic vibrations, etc.
	Dynamic: scanning in the *x*- or *y*-direction	After stabilization of the instrument. Fast recording of two or more measurement lines on a flat sample region without any structure. The differences should give the dynamical noise.
x–*y* noise	Static	After stabilization of the instrument. Sample with straight edge or line with small step height parallel or perpendicular to the scan direction.

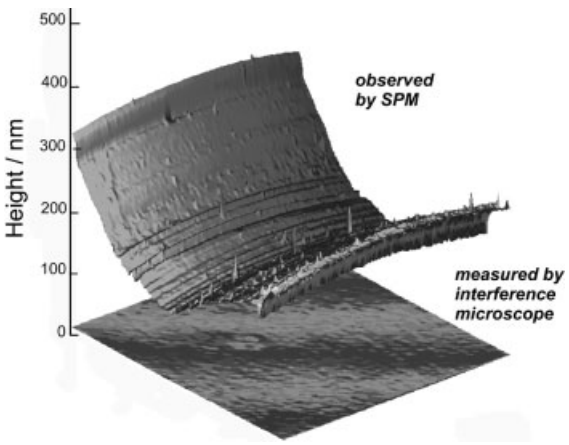

Fig. 13.5 Use of a flatness standard to determine out-of-*z*-plane movement of an SPM. *Lower plane*: surface of the flatness standard measured by interference microscopy as reference 100 μm × 100 μm, *upper plane*: the same region as observed by an SPM with a typical tube piezo scanner. By subtraction of the interferometrically measured plane, the flatness errors of the SPM can be determined, e. g., "scanner bow," drift, noise, and errors in the *z*-feedback control (here: spikes).

Mechanically induced vibrations may consequently be reduced by passive means (e. g., a more massive support of the instrument, a better acoustic shielding/damping or, if possible, by alterations to the geometry of the instrument), or by active means (e. g., a closed-loop antivibration table).

Electronic oscillations may be caused by ambient interference or the feedback control settings. In the first case, a better electromagnetic shielding of the electronics might help, in the latter case a variation of the control parameters.

13.3.3 Repeatability and Noise

To illustrate repeatability and noise investigations, measurements of the stability and the noise of an STM equipped with capacitive transducers (SPM of category B) are discussed as a practical example. The same line was scanned several times without changing the *y*-position, first on a flat part of a sample, later in a structured region with holes 100 nm in depth and 1500 nm in width (see Figure 13.6).

Scanning lines under the same conditions on a structured region yields the results shown in Figure 13.7(a). To better illustrate the details, some successive lines are plotted in Figure 13.7(b). Here the sharp edges of the structure can be used to guide the eye. The fine structures at the tops and at the bottoms look very similar. The difference between the profiles obtained in two successive lines is shown in Figure 13.7(c). The maximum deviations are now in the range of ± 5 nm. The positions at which these large differences occur clearly

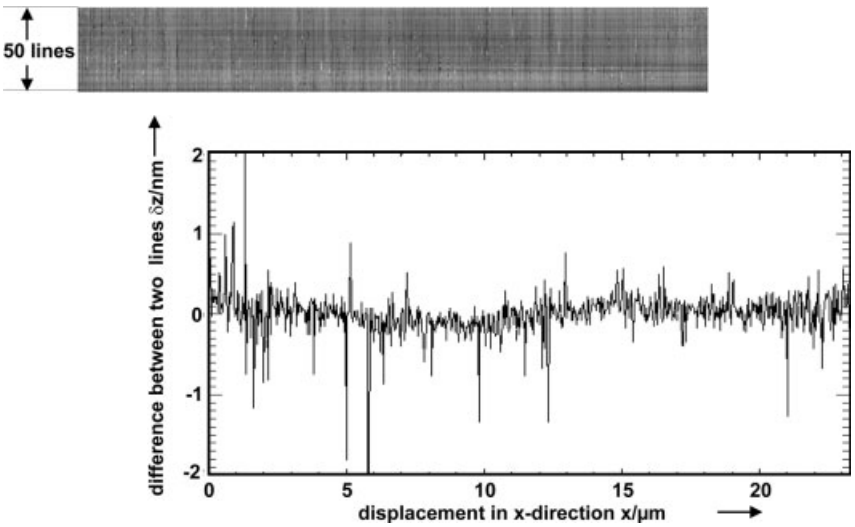

Fig. 13.6 STM with capacitive transducers [3], which was located in the PTB clean room center. (a) Image obtained in the flat area. No significant changes of the profile occur within these 50 scans. (b) The difference between two successive measured lines is displayed. The difference is clearly smaller than 0.5 nm (except for some spikes).

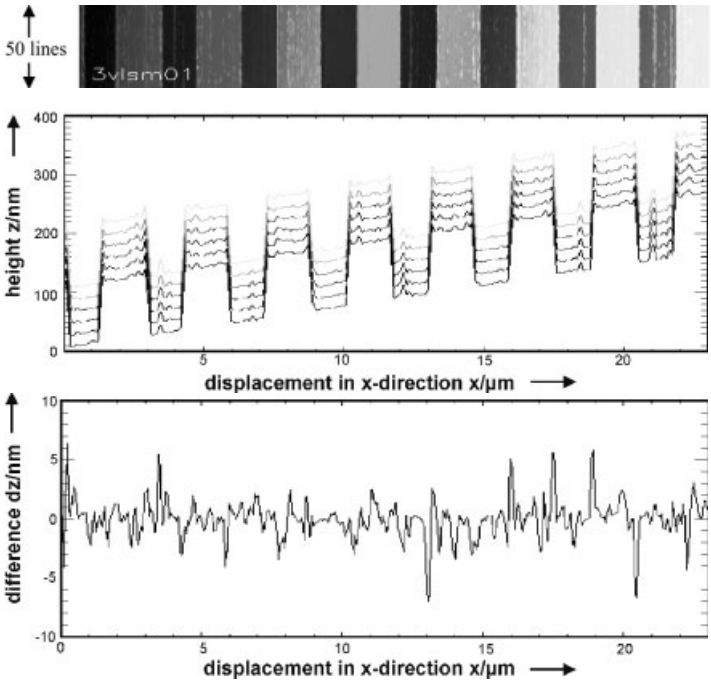

Fig. 13.7 (a) Repeatability of the STM discussed while scanning a structured region. (b) Profile lines taken from the data in (a). (c) Differences between two successive profile lines reveal a maximum deviation of 5 nm at the edges of the lines.

show that this happens at the transitions upward or downward. This behavior can be explained by small changes of the tip positions and by the sharp edges of the structure; as the tip and also the sample step edges are not ideal, e. g., as there is some roughness, small changes in the relative position between the tip and the sample lead to a change of the points at which the interaction happens.

13.3.4 Tip Shape

The SPM image can basically be understood as a convolution or a dilation of the actual surface features with the shape of the tip used for probing the sample [4]. To characterize the tip shape, various methods implying different evaluation algorithms can be applied [5].

Direct tip imaging methods allow us to read the tip shape from the SPM image [6]. Suitable specimens are upright tips or cylindrical features with (nearly) vertical edges. Straight edges allow us to deduce the cross-section of the tip body in one direction. The very first nanometers of a probe may also be characterized by gold particles (typical diameter: 5–30 nm) on a flat substrate.

Test samples with sharp edges of random orientation such as TipCheck and NioProbe [7] may be applied for an indirect tip shape determination: The so-called blind reconstruction method [8] is an algorithm that calculates the "sharpness" of the tip necessary to obtain the actual image. The most critical aspect of this method is how to eliminate noise prior to the tip reconstruction calculation [9].

Apart from tip characterization in the SPM itself, scanning electron microscopy is usually a good means to study the probe.

13.4 Calibration of the Scanner Axes

13.4.1 Lateral Calibration

The lateral calibration of B- and C-type SPM systems is usually performed by a set of measurements at appropriate physical standards that should be chosen according to the actual needs (Figure 13.8). Such lateral standards with regular periodic structures of well-known dimension in one [10, 11] or two lateral directions [12] are meant to determine individual correction factors for the *x*- and *y*-axes. To reduce the influence of *z*-movements, the height of the structures should be as small as possible.

Before a decision is taken that which standards are actually to be used for the calibration, not only the pitch values including their uncertainties, the material

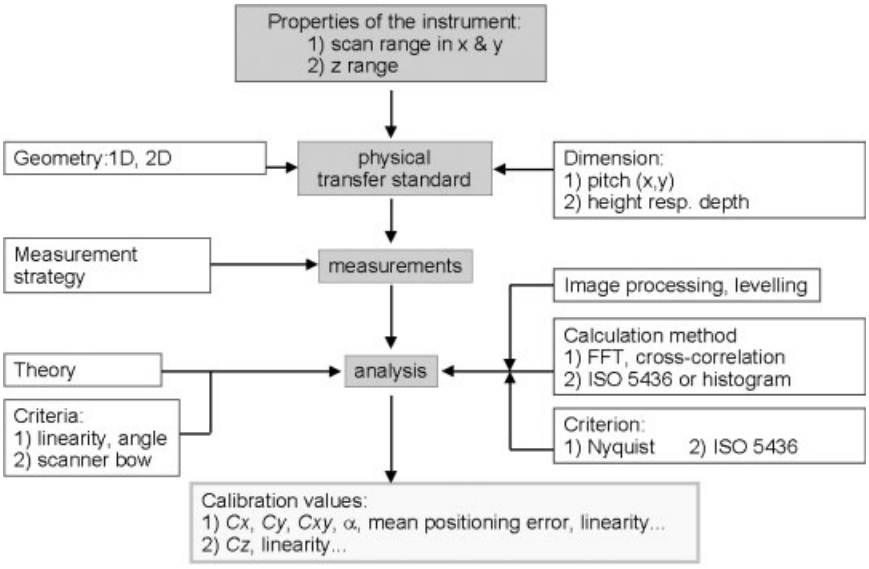

Fig. 13.8 Calibration scheme for (1) lateral calibration and (2) vertical calibration [13].

composition, the structures' geometry respectively arrangement should be considered, but also the practicability of the standards, e. g., whether the size of the standard is suited for mounting and whether the standard allows sufficiently easy positioning in the apparatus (e. g., by orientation marks that guide the user to the reference field) to make sure that the certified area is found.

Another very important criterion often neglected is the homogeneity of the structures: Irregularities within the reference field such as possible gradual variations of the pitch value or significant periodic or occasional deviations [14] from the mean pitch–e. g., due to stitching errors of the lithography tools used to generate the structures–are, moreover, often not to be found in the documentation delivered with the standard or even not yet known at all. Especially when aiming at a high-quality calibration of SPMs of category B, such "hidden" irregularities may unnecessarily lead to a wrong calibration.

With the present evolution of large-range metrology SPMs, it is to be hoped that more knowledge of nanostandard irregularities will be gathered in the next years and consequently be included in the product descriptions and calibration certificates of nanostandards.

Investigations of a structured sample in different orientations 0°, 90°, 180°, and 270° provide information on the rectangularity of the *x*–*y* scanner system. The analysis can relate the *x*- and *y*-axes of the scanner to the **a** and **b** vectors of the surface unit cell. This analysis can be done by instruments or additional commercial software (see Figure 13.9).

A linear transformation (Figure 13.10) of the scanned and uncorrected image into a corrected image can be defined by a set of correction parameters *Cx*, *Cy* for the *x*- respectively *y*-axis and *Cxy* for the coupling between these two axes. Such transformations are integrated in some software packages to allow the user to correct scanner properties easily. The observed image is considered as linear, as the residual nonlinearity of the image is much less than one pixel for the actual measurement conditions.

To obtain information about the rectangularity of the *x*–*z* or *y*–*z* plane it is necessary to carefully investigate samples with well-defined topographical structures with finite slope. The analysis is described by Garnaes [16].

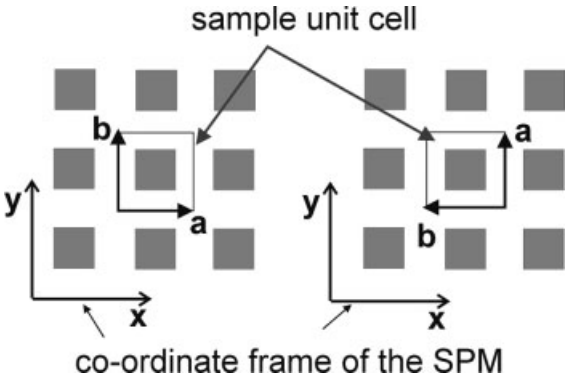

Fig. 13.9 Rectangularity within the *x*–*y* scanning plane can be obtained from at least two successive measurements with intermediate rotation of the test sample [12].

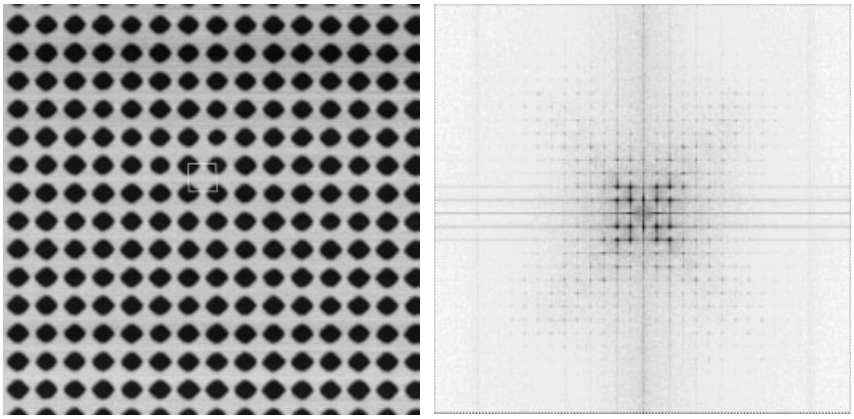

Fig. 13.10 SPM image of a 2D 1000 standard (14.67 μm × 14.48 μm) and the 2D FFT to determine the unit cell vectors and the angle ∡ (**a**,**b**) using SPIP [15].

Furthermore, lateral standards allow distortions in the measured image to be determined, i. e., positioning, straightness, squareness, and rotational errors of the scan system used (Figure 13.11). Depending on their origin, these errors are either temporary, permanent, or of a dynamic nature.

Temporary distortions might be caused by drifts due to temperature changes of the mechanical components, by initial piezo drifts or by the warm-up of electronic components. Such initial effects are to be avoided by making sure that the system is allowed a sufficient idle time to reach its equilibrium.

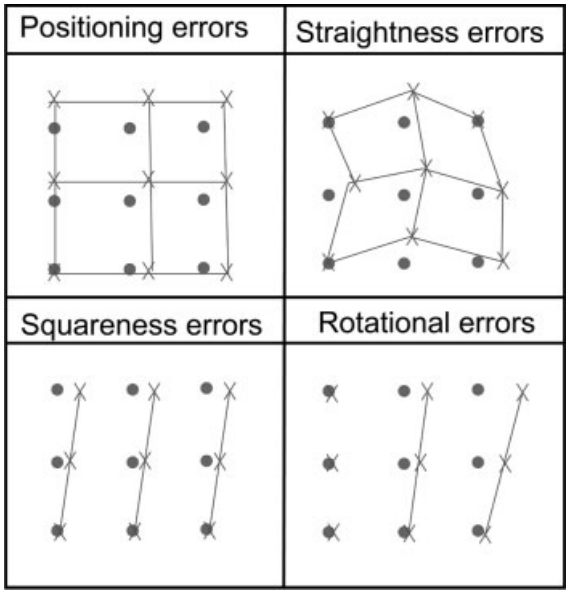

Fig. 13.11 Different types of image distortions. The small circles indicate the reference positions in the ideal two-dimensional grid; the crosses indicate the measured positions.

Permanent distortions are mainly due to a nonideal design of the instrument such as a nonrectangular arrangement of the scan units, an insufficient mass balance inducing torque and mechanical stress, nonuniform guidance, etc. These effects need to be studied in order to check whether they can be taken into account systematically.

The notorious piezo hysteresis is, unless corrected by a closed-loop position control circuit, a permanent cause of image distortions, but strongly depends on the scan speed and scan range and is thereby of dynamic nature. Other dynamic error sources are a consequence of the frequency transmission functions of the various mechanical and electronic components, resulting in a low-pass-type retardation of the actual scan position to the desired position when the scan speed is set too high.

Some of the above-mentioned errors depend systematically on the actual scan parameters such as scan size and scan speed; consequently, calibration measurements usually need to be performed for several settings of these parameters.

By recording a series of calibration measurements at various scan sizes, a set of correction factors is acquired for these scan sizes that may serve as the basis to calculate a scan-size-dependent correction function. With the help of this function, images of any size may be corrected by an appropriate correction factor. It has to be taken into account, however, that such a correction function is usually based on only a few data points (usually 5–10) and therefore not very exact.

In many cases it proves reasonable to also take the dynamic behavior of the scan system into account when performing a lateral calibration. Moreover, the correction factors respectively image correction functions, which then need to be applied, often turn out to be more influenced by the dynamic behavior of the scan system than by the selection of the scan range.

Even in the case of a closed-loop position-controlled scanstage, scan-speed-dependent distortions are distinguishable [17]. Such a systematic influence of the scan speed allows one to calculate individual mathematic functions to correct the image distortions. Furthermore, depending on the actual system used, it is anyway often advisable to determine lateral correction factors for different scan speeds.

Further boundary conditions to be considered are the digital resolution (bit depth), electronic noise, and the number of pixels in an SPM image.

13.4.2 Calibration of the Vertical Axis

In many respects the calibration procedure for the vertical axis (z-axis) is comparable to that for the lateral axes. The calibration effort is therefore quite similar.

Like the lateral axes, also the movements along the vertical axis might show a nonlinear behavior and be affected by distortions. Moreover, as the vertical movements are often much faster, in order to follow the object's topography, than in the lateral scan directions, dynamic properties of the z-axis play an even larger role than in the case of the lateral axes. Consequently, much attention is to be

paid to them. Furthermore, the parameters of the feedback control system (e. g., proportional factor *P* and integration time constant *I*) directly influence the dynamic behavior of the SPM in the *z*-direction and need to be adjusted carefully for the actual measurement, e. g., by monitoring the error signal and subsequently minimizing it.

Depending on the design of the instrument and the accuracy achievable respectively desirable, various strategies might be followed to characterize the *z*-axis. Two of them will be discussed in the following: direct laser-interferometric calibration and calibration by measurements at a set of transfer step-height standards.

Using Laser Interferometers

The elongation of the *z*-piezo can, at least in principle, be directly measured by laser-interferometry: In the case when the probe is moved in the *z*-direction, a small mirror is attached to the probe holder that serves as reflector for the laser beam. A deflection prism (or mirror) on the sample holder directs the laser beam from the vertical to the lateral direction and thus back to the interferometer. In the case when the sample is scanned in the z-direction, the mirror is placed on the sample holder and a small deflection prism is attached to the probe holder, respectively [18–20].

With this auxiliary measurement setup, the voltage externally applied to the *z*-actuator and the interferometer signal can be recorded simultaneously. In case the *z*-position is monitored by a sensor, this signal is recorded parallel to the interferometer reading. The particular advantage of this method is that it is ultimately versatile because the SPM user is – by choosing the shape of the voltage curve – free to simulate any "artificial topography" to study the system's response. Furthermore, a more direct traceability to the meter definition is achieved by using a possibly stabilized laser of calibrated wavelength.

For instance, the voltage might be increased from the minimum to the maximum allowed level in equal steps; this method allows us to determine the nonlinearity along the *z* scan range in a similar way as a pitch standard across the lateral scan directions. Based on these data, a correction function can be calculated. Secondly, the time constant of the stage's response can be read directly from the interferometer signal at any voltage step.

The dynamics of the *z* scan system can easily be assessed by varying the duration of the voltage steps. As piezo creep and hysteresis might be significant, it might be advisable in some cases to calculate a set of correction functions for the *z*-values for different speeds of the voltage ramp depending on the particular SPM system.

It has to be noted, however, that this method works "without load," i. e., the system is not in active distance control feedback. Switching to feedback control will consequently change the time constants of the system's response depending on the *P* and *I* parameter settings of the PI feedback system.

Using Transfer Standards

While not every SPM user has a laser-interferometer at his or her disposal and the geometry of many SPM systems does not allow the integration of an optical interferometer, physical transfer standards are often used. They are easier to handle and can be used in any SPM system. The disadvantage is, however, that the traceability chain is longer than for the laser-interferometric method: The uncertainty of the transfer standard adds to the overall uncertainty of the SPM calibration. The advantage is that the transfer standards are measured under the same conditions as in the experiments later (i. e., in active probe feedback).

In order to take the nonlinearity of the z scan system into account, a set of standards of different step height should be used. In a first calibration approach, the z offset may be adjusted, if possible, in such a way that the z actuator operates in the middle of its range, i. e., symmetrically around 50 % of its maximal elongation during each of the calibration measurements (Figure 13.12). Provided that all future measurements of the actual measurement objects will adhere to this rule, satisfactory results will most likely be achieved in this way. If this is not possible, the same calibration procedure may be repeated around other mean elongations, e. g., around the 10 %, 30 %, 70 %, and 90 % threshold of maximum piezo span as depicted in Figure 13.12.

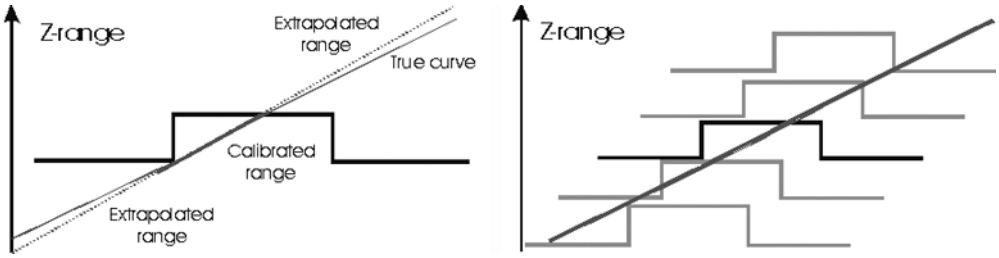

Fig. 13.12 Calibration of the z-axis using transfer standards. (a) single-point and (b) multiple-point calibration.

Evaluation of Step Height

Two methods of data analysis have proven to be suited for the determination of the correction factor for the z-axis: the histogram method (Figure 13.13) and ISO 5436 (Figure 13.14). Both methods yield similar results that usually agree within the uncertainty limits.

A precondition for the successful application of the histogram method is that the sample tilt has already been subtracted. In many cases a first-order plane correction will not be sufficient. It is therefore advisable to start with a measurement at a flatness standard prior to the height measurements in order to be able to subtract the flatness error from the step-height images. The histogram method itself comprises a plot of the height value distribution, the identification of the two peaks corresponding to the two height levels, the determination of the center

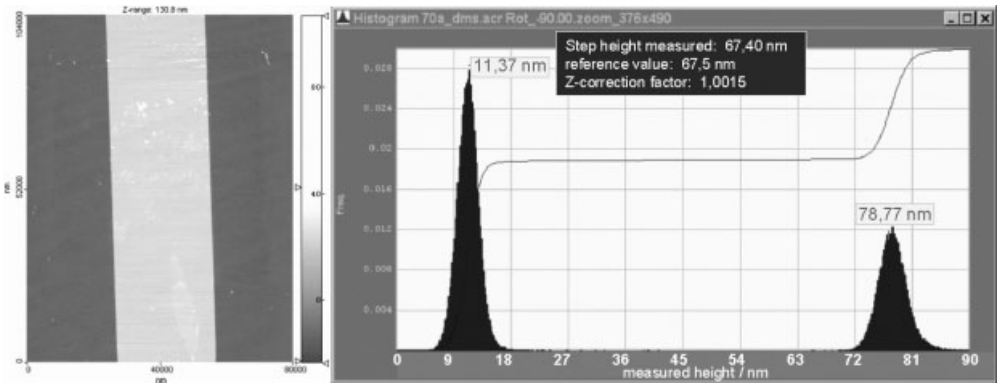

Fig. 13.13 Measurement (80 μm × 104 μm) at a step-height standard and corresponding histogram plot.

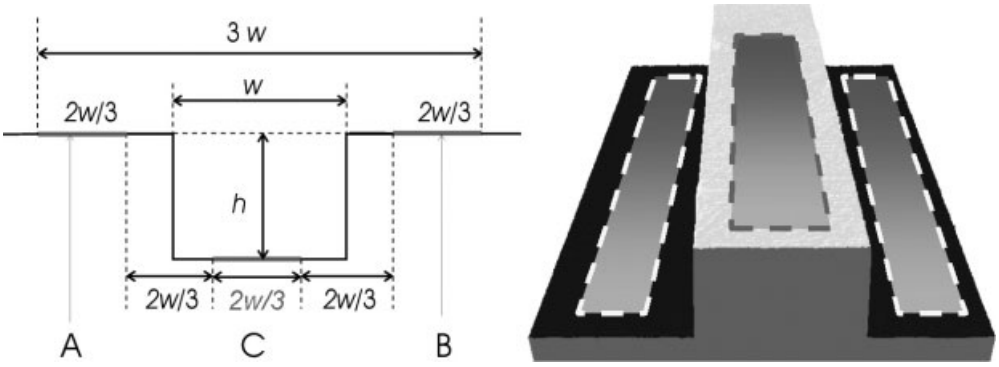

Fig. 13.14 Illustration of step-height determination according to ISO 5436: The central part of a one-dimensional structure (here 2/3 of its width, C) and two sections A & B of the same size as C and equally spaced from the edges are taken into account, whereas the edge region is left out of consideration.

of gravity in each of these two peaks, and calculating their difference (Figure 13.13).

The principle of ISO 5436 is illustrated in Figure 13.14: The central part of a positive or negative bar is chosen to fit a line through these values. As reference, two equally sized sections on both sides of the 1D structure are selected with equal spacing to the edges of the bar, and a line is also fitted through these values. The height value of the bar is defined as the normal distance of both fit lines. ISO 5436 may be applied either for a single scan line only or subsequently for several lines respectively the whole scan image–with the latter allowing us to determine variations in the height values measured along the 1D structures.

In this way, the edges themselves are not taken into consideration, which is a practical advantage of ISO 5436: Apart from the fact that edges often suffer from contamination and corner rounding, feedback errors are usually much larger at

edge transitions than on the flat areas. Furthermore, optical techniques for the cantilever bending/oscillation detection such as the commonly used beam deflection or the focus sensor often not only detect the measuring beam reflected from the probe as desired, but also unwanted reflections from the sample surface that consequently spoil the signal used for the feedback and thereby height measurement; ISO 5436 reduces the influence of this parasite signal as such effects occur especially at edges.

A key problem in using transfer step-height standards is how to deal with contaminations—no matter whether the histogram method or ISO 5436 is applied. Unfortunately, especially smaller dust and dirt particles can often not be removed from the standards completely.

13.5 Uncertainty of Measurements

The uncertainty has to be calculated for the measurements following the rules of the *Guide to the Expression of Uncertainty in Measurement* (GUM) [21]. For this, the properties of the instrument and of the experimental setup have to be taken into account as well as the properties of the standard and the sample. Here we will give an example for the calibration of a step height on an unknown sample by a single measurement. Repetition of this measurement would reduce uncertainty contributions that are based on random errors, but not reduce systematic deviations.

The instrument has been calibrated by a given certified standard of height h_c together with the expanded uncertainty U_{95} using a coverage factor of $k = 2$. The standard used should have a height $h_{c,}$ which is close to that of the unknown sample h_x. For the calculation of the uncertainty, a model has to be set up. In our case the model is given by

$$h_x = \frac{h_c}{h_{cm}} h_{xm} + \sum \delta h_i$$

where h_x is the value of the step height of the unknown sample, h_c is the value of the step height of the standard given in the certificate, h_{cm} is the measured value on the standard, h_{xm} is the measured value on the unknown sample, and δh_i are other contributions to the measurement uncertainty.

The other contributions are related to errors due to stability and quality of the standard, remaining nonlinearity of the scanner, cross-talk between the x–y and z-axis, roughness and homogeneity of the standard and the sample, type of evaluation method, drift effects in the scanner during the measurement, and so on. Below heights of 1 μm a correction of the step height due to deviations from 20°C is negligible for standard materials.

The standard uncertainty $u_c(h_x)$ calculated from the above model is given by

$$u_c^2(h_x) = u^2(h_c) + u^2(h_{cm}) + u^2(h_{xm}) + u^2(\delta h_{non\text{–}lin}) + u^2(\delta h_{cross\text{–}talk}) + u^2(\delta h_{eva.}) + \cdots$$

Here we considered a case in which $h_c \sim h_{cm} \sim h_{xm}$. The expanded uncertainty U_{95} has to be calculated from $u_c(h_x)$ using a coverage factor of $k = 2$. For more detailed calculations a greater knowledge of the instrument is necessary.

For more information about uncertainty budget calculation for pitch and step height, see [10, 11, 18–20].

Acknowledgments

We would like to thank the members of the former "SPMet—European Network on the Calibration of SPMs" that prepared a sound basis for present-day activities toward a calibration guideline for SPM. One of these current activities is the discussion group of the VDI-GMA FG 3.43; we especially appreciate the valuable discussions with its members M. Flemming, P. van Schendel, T. Sulzbach, and J. Schöbel. Last but not least thanks are due to our PTB colleagues G. Dai, H.-U. Danzebrink, and S. Czerkas.

References

1 J. Garnaes, N. Kofod, A. Kühle, P. Besmens, O. Ohlson, J. B. Rasmussen, G. Wilkening, L. Koenders, W. Mirande, K. Hasche, J. Haycocks, J. Nunn, and M. Stedman, in *Proceedings & Posters Xth Int'l Colloq on Surfaces, Chemnitz, Germany,* edited by M. Dietsch and H. Trumpold (Shaker-Verlag, Aachen, Germany, 2000), pp. 277–287.

2 L. Koenders and G. Wilkening, Review on available calibration artefacts, in *Proceedings of the 5th Seminar on Quantitative Microscopy and 1st Seminar on Nanoscale Calibration Standards and Methods, Braunschweig, Germany,* PTB-F-44 (Braunschweig, 2001), pp. 50–60. An updated version of this list is also available from the authors upon request (see also http://www.ptb.de/de/org/5/51/514/index.htm

3 X. Zhao, PTB-report F-20, Wirtschaftsverlag NW, Bremerhaven, Germany, 1995.

4 T. Machleid, R. Kästner, and K.-H. Franke, Reconstruction and geometric assessment of AFM tips, *these proceedings.*

5 J. S. Villarrubia, Algorithms for scanned probe microscope image simulation, surface reconstruction, and tip estimation, J. Res. Natl. Inst. Stand. Technol. **102,** 425–454 (1997).

6 S. Czerkas, T. Dziomba, and H. Bosse, Comparison of different methods of SFM tip shape determination for various characterisation structures and types of tip, *these proceedings.*

7 TipCheck and NioProbe, Aurora NanoDevices Inc., Edmonton/AB, Canada.

8 P. M. Williams, K. M. Shakesheff, M. C. Davies, D. E. Jackson, C. J. Roberts, and S. J.B. Tendler, Blind reconstruction of scanning probe image data, J. Vac. Sci. Technol. B 14, 1557–1562 (1996).

9 P. M. Williams, M. C. Davies, C. J. Roberts, and S. J.B. Tendler, Noise-compliant tip-shape derivation, Appl. Phys. A **66,** S911–S914 (1998).

10 F. Meli, International comparison in the field of nanometrology, pitch of 1D grating (NANO4), *2nd Int'l. Conf. Euspen, Torino, Italy* (2001), p. 358.

11 I. Misumi, S. Gonda, T. Kurosawa, and K. Takamasu, Uncertainty in pitch measurements of one-dimensional grating standard using nanometrological atomic

force microscope, Meas. Sci. Technol. **14**, 463 (2003).

12 J. Joergensen, J. Jensen, and J. Garnaes, Lateral metrology using scanning probe microscopes, 2D pitch standards & image processing, Appl. Phys. A **66**, 847–852 (1998).

13 N. Kofod, Validation and industrial application of AFM, Ph. D. thesis, Technical University of Denmark, Lyngby, 2002.

14 T. Dziomba, W. Häßler-Grohne, H. Bosse, H.-U. Danzebrink, and G. Wilkening, Influence of nanostandard properties on calibration procedures of SPMs, in *Proceedings of Euspen Int'l Topical Conference, Aachen, Germany*, edited by M. Weck and H. Kunzmann (Verlag Rhiem, Voerde, Germany, 2003), pp. 491–494.

15 Scanning Probe Image Processor software (SPIP), Image Metrology AS, Lyngby, Denmark.

16 J. Garnaes et al., *these proceedings*.

17 T. Dziomba, L. Koenders, H.-U. Danzebrink, and G. Wilkening, Lateral & vertical calibration of scanning probe microscopes and their measurement uncertainty, in *Proceeding of the XIth Int'l Colloq on Surfaces, Chemnitz, Germany*, edited by M. Dietzsch (Shaker Verlag, Aachen, Germany, 2004), pp. 117–128.

18 F. Meli, Z calibration of a metrology AFM scanner using an interferometer and a filtering device together with a linear displacement stage, in *Proceedings of 3rd Seminar on Quantitative Microscopy, Lyngby, Denmark*, PTB-report F-34 (Wirtschaftsverlag NW, Bremerhaven, Germany, 1998), pp. 61–67.

19 H. Edwards, J. Joergensen, J. Dagata, Y. Strausser, and J. Schneir, Influence of data analysis and other factors on the short-term stability of vertical scanning probe microscope calibration measurements, J. Vac. Sci. Technol. B **16**, 633–644 (1998).

20 L. Koenders et al., Comparison on nanometrology NANO2: step height, Metrologia **40**, 04001 (2003).

21 *Guide to the Expression of Uncertainty in Measurements (GUM)*, BSI, London. ISBN 0580 234827 (1995).

14
True Three-Dimensional Calibration of Closed Loop Scanning Probe Microscopes

J. Garnaes, A. Kühle, L. Nielsen, and F. Borsetto

Abstract

There is an increasing demand for accurate and traceable measurements with atomic force microscopes (AFMs) within many fields, such as micro optics where the functionality of components is directly and critically related to the absolute dimensions. In particular, true three-dimensional measurements of deep structures, that is, structures with a dept larger than the width, are a challenge. This chapter is a contribution to setting up guidelines for the three-dimensional calibration of so-called closed loop atomic force microscopes, where distance sensors such as capacitive sensors measure the movement of the tip. In earlier published works, the calibration along the axes has been derived but often the coupling between the horizontal and vertical movements, which has to be known in order to make a true three-dimensional measurement, has not been assessed. In this chapter, a thorough analysis describes the "true" metric x-, y-, and z-coordinates of an imaged surface as a linear function of the observed x'-, y'-, and z'-coordinates, taking into account the coupling between the horizontal and vertical movements. Based on series of measurements on triangularly shaped ridges, an analytical model function for the two coefficients describing this coupling is given. The misalignment of the vertical axes relative to the horizontal axes was found to be 1.0(0.2)° and 2.7(0.2)° for the investigated closed loop AFM. Ignoring the influence of the tip shape, it is now possible with our setup to correct any image of a three-dimensional surface. An example of estimating the technological important sidewall angle α of a grating wall with an uncertainty of $u(\alpha) \approx 0.3°$ is given.

14.1
Introduction

For many years, atomic force microscopy (AFM) has been used almost exclusively to examine rather flat structures or surfaces where only the horizontal or the vertical components were important or significant. Examples are step heights, rough-

Nanoscale Calibration Standards and Methods: Dimensional and Related Measurements in the Micro- and Nanometer Range.
Edited by Gunter Wilkening, Ludger Koenders
ISBN: 3-527-40502-X

ness structures, or atomic lattices. However, to enlarge the scope of the AFM, it is desirable to image also true three-dimensional structures like deep structures, where the depth is larger than the width. The technological importance of deep structures is increasing within fields such as micro optics and micro mechanics. For some applications, the functionality of an optical grating depends critically on the sidewall angle as well as on the roughness and the shape of the sidewall. In micro mechanics, many structures have vertical sidewalls and the angle and roughness of the sidewalls can be critical if, for example, the sidewalls on two different parts shall fit together to form a robust three-dimensional structure.

For measurements involving a larger length scale, guidelines for the verification of coordinate measuring machines (CMMs), taking into account the coupling between the motions in the different directions, are available [1]. Such a verification is often done by interferometers, which are not suitable for AFMs.

For the estimation of the three-dimensional surface structure, the coupling between the horizontal and vertical motions has to be known. Indeed, for our state-of-the-art AFM, which is equipped with capacitive distance sensors and a close loop x-, y-, and z-stage, the coupling is significant and has to be corrected for. In general, many microscope systems are often constructed with an almost symmetric device producing the horizontal x, y motions but with a different device producing the vertical z motion with a much smaller dynamic range. This can lead to a significant misalignment of the vertical motion relative to the horizontal motion.

14.2 Model of the Measurement System

The physical model of the measurement process used here is that the microscope samples the surface height in an approximately orthogonal raster pattern. The sampled coordinates – that is, the recorded image – are functions of the environmental conditions, such as temperature T, and humidity H. These environmental conditions influence the mechanical connection between the probe and the sample as well as the sensitivity of the (capacitive) distance sensors.

For a system with (capacitive) distance sensors, mechanical creep and hysteresis are often insignificant. This means that the corrected coordinates $r = (x, y, z)$ are single valued[1)] functions of the observed coordinates and the environmental parameters. This can be written as

1) A "single-valued function" is normally just referred to as a "function" but the phrase "single-valued" is used here to point out the difference to a "multi-valued function". For a piezo electrical scanning system exhibiting hysteresis and creep, the position of the tip as a function of the control signal (typical the voltage applied to the piezo scanner) is a multi-valued function, as there are several possible positions for a given control signal, depending on the history of the control signal applied and the time since the application of the voltage started (creep).

$$\begin{aligned} x &= x(x',y',z',T,H) \\ y &= y(x',y',z',T,H) \\ z &= z(x',y',z',T,H) \end{aligned} \tag{14.1}$$

In general, the model function of x, y and z is a nonlinear function of the input quantities.

The calibration (including a nonlinear correction) along the three metric axis, $x = x(x')$, $y = y(y')$, and $z = z(z')$ has been derived based on gratings with known period [2–4] or steps with known height [5, 6]. The influence of the environment and Abbé offset, that is $x = x(T, H, \ldots)$, is included in the uncertainty evaluation discussed in [2–6]. The coupling between the x and y motion, that is $y = y(x', y')$, has been addressed using a two-dimensional grating with known angle, see [2]. The image bow, that is $z = z(x'^2, z')$ and $z = z(y'^2, z')$, has been addressed using a flat reference plane [6]. However, the coupling between the vertical and horizontal motion, that is $z = z(x', z')$ and $z = z(y', z')$ is often not discussed thoroughly.

The goal of this chapter is to

1. estimate and correct for the coupling between the z motion and the x and y motion;
2. integrate the correction for the coupling into a 3×3 correction matrix transforming the observed coordinates $r' = (x', y', z')$ into corrected coordinates $r = (x, y, z)$.

14.3 The Correction Matrix

The unit vectors in the microscope's coordinate system ($\underline{e}_{x'}$, $\underline{e}_{y'}$, $\underline{e}_{z'}$) are the directions and distances that the microscopes tip is moving for a change in indication of one unit of length in the fast scanning direction $\underline{e}_{x'}$, in the slow scanning direction $\underline{e}_{y'}$, and in the height direction $\underline{e}_{z'}$ (see Figure 14.1). The metric coordinate system ($\underline{e}_x$, $\underline{e}_y$, $\underline{e}_z$) is an orthogonal coordinate system, in which the length of each of the three unit vectors is expressed in terms of the SI unit for length. The matrix elements $c_{xz'}$ and $c_{zz'}$ are the coordinates of the projection of $\underline{e}_{z'}$ on the plane spanned by $\underline{e}_x$ and $\underline{e}_z$. Similarly, the matrix elements $c_{yz'}$ and $c_{zz'}$ are the coordinates of the projection of $\underline{e}_{z'}$ on the plane spanned by $\underline{e}_y$ and $\underline{e}_z$.

Ignoring the effect of the environment, a linear transformation between the observed positions $\underline{r}' = (x', y', z')$ and the equivalent values in a metric coordinate system can be approximated as

$$\begin{pmatrix} x \\ y \\ z \end{pmatrix} \cong \begin{pmatrix} \left.\frac{\partial x}{\partial x'}\right|_{r'=(0,0,0)} & \left.\frac{\partial y}{\partial x'}\right|_{r'=(0,0,0)} & \left.\frac{\partial z}{\partial x'}\right|_{r'=(0,0,0)} \\ 0 & \left.\frac{\partial y}{\partial y'}\right|_{r'=(0,0,0)} & \left.\frac{\partial z}{\partial y'}\right|_{r'=(0,0,0)} \\ 0 & 0 & \left.\frac{\partial z}{\partial z'}\right|_{r'=(0,0,0)} \end{pmatrix} \begin{pmatrix} x' \\ y' \\ z' \end{pmatrix} = \begin{pmatrix} c_{xx'} & c_{xy'} & c_{xz'} \\ 0 & c_{yy'} & c_{yz'} \\ 0 & 0 & c_{zz'} \end{pmatrix} \begin{pmatrix} x' \\ y' \\ z' \end{pmatrix}. \tag{14.2}$$

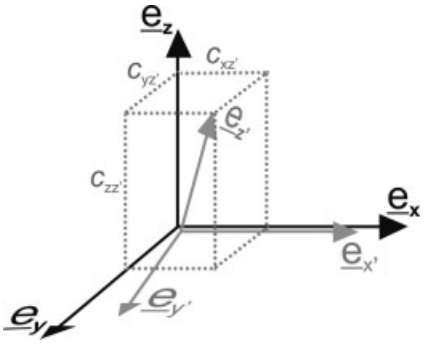

Fig. 14.1 The unit vectors in the microscopes coordinate system ($\underline{e}_{x'}$, $\underline{e}_{y'}$, $\underline{e}_{z'}$) are the direction and distance the tip is moving for a change in indication of one unit length in the fast scanning direction $\underline{e}_{x'}$, the slow scanning direction $\underline{e}_{y'}$, and the height direction $\underline{e}_{z'}$. The metric coordinate system ($\underline{e}_x$, $\underline{e}_y$, $\underline{e}_z$) is an orthogonal coordinate system where the length of the three unit vectors is expressed in terms of the SI unit for length. The matrix elements $c_{xz'}$ and $c_{zz'}$ is the projection of $\underline{e}_{z'}$ on the plane spanned by $\underline{e}_x$ and $\underline{e}_z$. The matrix elements $c_{yz'}$ is the projection of $\underline{e}_{z'}$ on the plane spanned by $\underline{e}_y$ and $\underline{e}_z$.

In general, the partial derivatives will depend on x', y', and z' in a nonlinear way, and the point of evaluation $\underline{r} = (x'_0, y'_0, z'_0)$ for the partial derivative has to be specified; we have selected $\underline{r}' = (0, 0, 0)$. Note that the matrix transformation is an approximation to first order of the Taylor series for each coordinate. Higher order terms in x', y', and z', and other input quantities, such as the humidity H and temperature T, are not included in the discussion of this chapter. The matrix elements $c_{xx'}$, $c_{yy'}$, and $c_{zz'}$ correct the (linear) scales, whereas $c_{yx'}$ corrects for the coupling in the horizontal plane between x and y. These matrix elements have been estimated traceable to the SI units by other measurements, see [2–6]. The matrix elements $c_{yz'}$ and $c_{xz'}$ correct for the coupling between the vertical and the horizontal planes and will be discussed and estimated in this chapter.

As we choose the unit vector $\underline{e}_x$ in the x-direction of the metric coordinate system to be parallel to the unit vector $\underline{e}_{x'}$ and the unit vector $\underline{e}_y$ in the y-direction of the metric coordinate system to be in the plane spanned by $\underline{e}_{x'}$ and $\underline{e}_{y'}$, three matrix elements in Eq. (14.2) become 0.

14.4 Theory for Estimating the Vertical Skew

When the metric coordinate system (x, y, z) is chosen to have the x-axis parallel to the actual scanning x'-axis of the microscope and the y-axis in-plane with the x'–y' plane, the coupling can be interpreted solely as a skew along the x'- and y'-axes as illustrated in Figure 14.2. In this figure, the solid line represents a true structure on the surface of the sample. The dashed line illustrates the actual recorded profile due to the coupling between the z'- and the x'-axes in the case where the sample plane is parallel to the x'-axis.

The skew can be characterized by a misalignment angle, $\varphi_{xz'}$ (see Figure 14.2). This angle can be determined by measuring an artifact consisting of structures with sides having well-defined side angles.

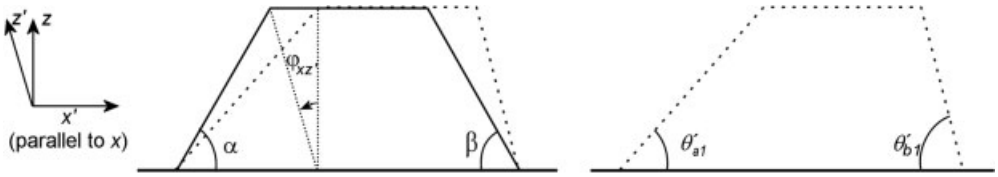

Fig. 14.2 Solid line: sketch of the cross section of a rhombic feature on the surface in the case where the sample surface is parallel to the x'-axis. Dashed line: illustration of the recorded profile when the x' and the z'-axes are misaligned by an angle, $\varphi_{xz'}$. The physical side angles of the structure are named α and β. The recorded angles of sides of the structure are named θ'_{a1} and θ'_{b1}, respectively.

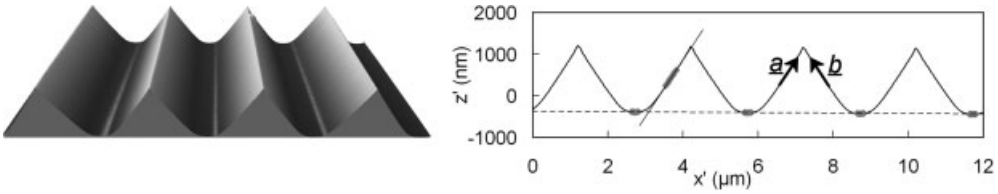

Fig. 14.3 Left: AFM image (12 μm × 6 μm) of the triangular grating shown in 3D projection. Right: average profile with indication of linear fit to the side of the ridge (indicated in gray). The side vectors, $\underline{a}$ and $\underline{b}$ are also indicated.

A sample consisting of parallel ridges with triangular profiles, see Figure 14.3, has been used. The image shown and other investigations indicate that the quality and uniformity of the sidewalls is adequate. The analysis is performed on one pair of axes at a time, which reduces the problem to two dimensions. When the coupling between the x'- and z'-axes is investigated, the ridges of the sample are aligned with the y'-axis. Similarly, the ridges are aligned with the x'-axis, when the coupling between the y'- and z'-axes is investigated. Each side of the triangular ridges is characterized by a vector, which points up along the side toward the top of the ridge and lies in a plane vertical to the ridges. After the image has been corrected for axis misalignments, the angle between the vectors of each side of the ridge should be conserved no matter how the standard is oriented during measurement. The coupling between, for example, the x'- and z'-axes can therefore be measured by comparing two images taken with the ridges parallel to the y'-axis, but with the sample rotated 180° around a vertical axis between the measurements.

Let the side vectors determined from the raw image (see Figure 14.4) be denoted by a'_n and b'_n where the subscript $n = 1, 2$ refers to the two measurements performed with different sample orientation, that is one before and one after the sample is rotated 180° within the lateral plane. The coordinates of the side vectors in the uncorrected (x', y', z') coordinate system of the microscope are expressed as functions of the observed side angles $\theta'_{a1}, \theta'_{b1}, \theta'_{a2}, \theta'_{b2}$, that is

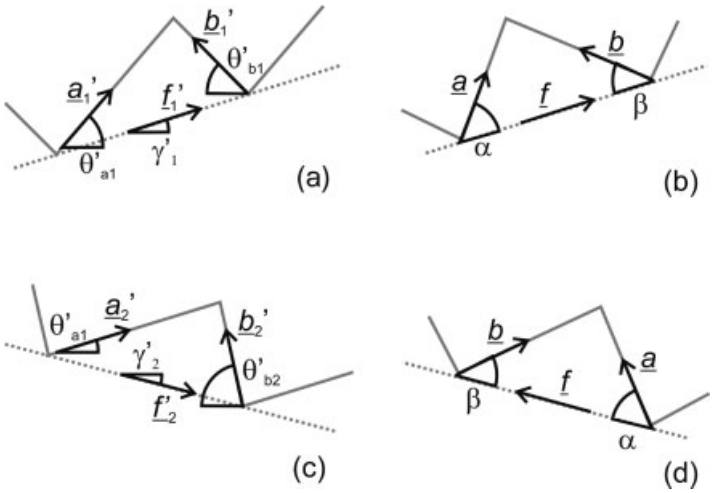

Fig. 14.4 Drawing of profiles of the pyramid form ridges: (a) and (c) are a drawing of the measured profile; both profiles have been skewed by the same amount in the *same* direction; (b) and (d) are the actual profile of the physical grating for the measured profiles. In (d) the physical grating has been turned 180° within the lateral plane, and the slope of the physical side angle α is now related to the measured sidewall vector $\underline{b}'_2$.

$$\underline{a}'_1 = \begin{pmatrix} \cot\theta'_{a1} \\ 1 \end{pmatrix}, \quad \underline{b}'_1 = \begin{pmatrix} -\cot\theta'_{b1} \\ 1 \end{pmatrix}, \quad \underline{a}'_2 = \begin{pmatrix} \cot\theta'_{a2} \\ 1 \end{pmatrix}, \quad \underline{b}'_2 = \begin{pmatrix} -\cot\theta'_{b2} \\ 1 \end{pmatrix}. \tag{14.3}$$

The base line vector $\underline{f}'_n$ is a vector along the bottom (or the top point) of the grooves given by the observed slope γ'_1 and γ'_2 as

$$f'_1 = \begin{pmatrix} 1 \\ \tan\gamma'_1 \end{pmatrix}, \quad f'_2 = \begin{pmatrix} 1 \\ \tan\gamma'_2 \end{pmatrix}. \tag{14.4}$$

The corrected side vectors can be obtained from the measured side vectors using the transformation given in Eq. (14.2). In the two-dimensional analysis described here, the transformation to first order, $\underline{\underline{T}}$, is given by

$$\underline{\underline{T}} = \begin{pmatrix} c_{xx'} & c_{xz'} \\ 0 & c_{zz'} \end{pmatrix} \quad \text{or} \quad \underline{\underline{T}} = \begin{pmatrix} c_{yy'} & c_{yz'} \\ 0 & c_{zz'} \end{pmatrix}. \tag{14.5}$$

In the metric coordinate system, the corrected side vectors are denoted by $\underline{a}_n$ and $\underline{b}_n$ where again the subscript $n = 1, 2$ refers to the two measurements performed with different sample orientation. They are given by

$$\underline{a}_1 = \underline{\underline{T}}\underline{a}'_1, \quad \underline{b}_1 = \underline{\underline{T}}\underline{b}'_1, \quad \underline{a}_2 = \underline{\underline{T}}\underline{b}'_2, \quad \underline{b}_2 = \underline{\underline{T}}\underline{a}'_2, \quad f_1 = \underline{\underline{T}}f'_1, \quad f_2 = -\underline{\underline{T}}f'_2. \tag{14.6}$$

The side vectors $\underline{a_2}$ and $\underline{b_2}$ denote the left- and right-hand sides of the triangle, respectively, but because the sample has been rotated 180°, $\underline{a_2}$ and $\underline{b_2}$ are the transformation of the original $\underline{b}$ and $\underline{a}$ side of the sample (see Figure 14.4). If both side vectors $\underline{a}$ and $\underline{b}$ are measured, two constraints can be written, reflecting that the two corrected measurements of the same physical angles α or β of the ridges should be the same in the metric coordinate system:

$$\cot\alpha = \frac{a_1 \cdot f_1}{a_1 \cdot \hat{f}_1} = \frac{a_2 \cdot f_2}{a_2 \cdot \hat{f}_2} \tag{14.7}$$

$$\cot\beta = -\frac{b_1 \cdot f_1}{b_1 \cdot \hat{f}_1} = -\frac{b_2 \cdot f_2}{b_2 \cdot \hat{f}_2} \tag{14.8}$$

where the caret (∧) is used to indicate cross vectors, that is if $r = (x, y)$ then $\hat{r} = (-y, x)$. By inserting expressions (14.3)–(14.6) into (14.7) and (14.8), we obtain two equations, each of which can be solved for $c_{xz'}$, assuming that $c_{xx'}$ and $c_{zz'}$ are known a priori. In general, the two equations have different solutions for $c_{xz'}$, which could be combined to a single solution by averaging. Alternatively, by subtracting the two constraints (14.7) and (14.8), they can be combined into a single constraint for the difference $\cot(\alpha) - \cot(\beta)$, which then provides an equation that can be solved with respect to $c_{xz'}$:

$$c_{xz'} = c_{xz'}(\theta'_{a1}, \theta'_{b1}, \theta'_{a2}, \theta'_{b2}, \gamma'_1, \gamma'_2, c_{xx'}, c_{zz'}). \tag{14.9}$$

Similarly, the coupling coefficient $c_{yz'}$ can be determined as

$$c_{yz'} = c_{yz'}(\theta'_{a1}, \theta'_{b1}, \theta'_{a2}, \theta'_{b2}, \gamma'_1, \gamma'_2, c_{yy'}, c_{zz'}). \tag{14.10}$$

The analytical expression is given in the appendix.

In the ideal case, where the physical angles between the base vectors $\underline{f_1}$ and $\underline{f_2}$ of the standard and the x'-axis of the microscope is 0, that is $\gamma'_1 = \gamma'_2 = 0 \cdots$, the solution for the misalignment angle reduces to the simple expression

$$c_{xz'} = \frac{c_{xx'}}{4}(\cot\theta'_{a1} - \cot\theta'_{b1} + \cot\theta'_{b2} - \cot\theta'_{a2}), \tag{14.11}$$

as shown in the appendix.

Let the unit vector $\underline{e_{z'}}$ in the coordinate system of the microscope be projected on the plane spanned by $\underline{e_x}$ and $\underline{e_z}$. The angle between this vector and the metric z-axis along $\underline{e_z}$ is defined as the misalignment angle $\varphi_{xz'}$ of the x'- and z'-axes; the misalignment angle $\varphi_{yz'}$ is defined similarly for the y'- and z'-axes. That is,

$$\tan(\varphi_{xz'}) \equiv -\frac{c_{xz'}}{c_{zz'}}, \quad \tan\left(\varphi_{yz'}\right) \equiv -\frac{c_{yz'}}{c_{zz'}}. \tag{14.12}$$

This implies that all sets of coordinates (x', z') appear to have been skewed an amount $z' \tan(\varphi_{xz'})$ along the x'-axis. In order to correct for this, all coordinates (x', z') have to be skewed by an equal amount in the opposite direction which is why the matrix element $c_{xz'}$ should be assigned the value $c_{xz'} = -\tan(\varphi_{xz'})c_{zz'}$. The same principle applies for the coupling between the y'- and z'-axes, where the corresponding correction element is denoted by $c_{yz'}$.

The misalignment angle can now be expressed as

$$\varphi_{xz'} = \arctan\left(\frac{c_{xx'}}{4c_{zz'}}(\cot\theta'_{a1} - \cot\theta'_{b1} + \cot\theta'_{b2} - \cot\theta'_{a2})\right). \tag{14.13}$$

If the angles γ'_1 and γ'_2 between the base line vectors and the x'-axis of the microscope is sufficiently small, the following approximations are valid:

$$c_{xz'} \cong \frac{c_{xx'}}{4}(\cot(\theta'_{a1} - \gamma'_1) - \cot(\theta'_{b1} + \gamma'_1) + \cot(\theta'_{b2} - \gamma'_2) - \cot(\theta'_{a2} + \gamma'_2)). \tag{14.14}$$

$$\varphi_{xz'} \cong \arctan\left(\frac{c_{xx'}}{4c_{zz'}}(\cot(\theta'_{a1} - \gamma'_1) - \cot(\theta'_{b1} + \gamma'_1) + \cot(\theta'_{b2} - \gamma'_2) - \cot(\theta'_{a2} + \gamma'_2))\right). \tag{14.15}$$

14.5 Experimental Results and Discussion

A metrological AFM with a scan volume of 70 μm × 70 μm × 6 μm, equipped with capacitive distance sensors [7], was used for the investigation. All measurements were done in dynamic resonant mode using silicon cantilevers [8]. Image processing and measurements from images were done with SPIP [9]. A specially developed plug-in was used to apply the correction given in Eq. (14.2) and to resample the image into a square pattern suitable for further measurements and display.

In order to determine the misalignment angle for each of the x'- and y'-axes, we have used a line standard with triangular line profiles [10]. The profile is nominally symmetric with side angles of 55°, period of 3000 nm and a height of 1800 nm. The sample is placed with the ridges perpendicular to the axis of investigation (x' or y'). The axis of investigation should be made the fast scanning axis during the measurement in order to reduce the influence of thermal drift and other ambient factors. In order to obtain a reliable image of the sides of the ridges, the AFM tip used should have effective half cone angles along the investigated axis of less than $90° - 55° = 35°$, including the incidence angle of the tip. Several standard AFM tips [8] facilitate this. An AFM image recorded along the nominal x'-axis of the microscope is shown in Figure 14.3. An average profile along the x'-direction is calculated, and from this the side angles are determined by fitting straight lines to the central part of the ridge sides. The measured angles have to be corrected for the tilt of the sample relative to the microscope's x-axis,

Table 14.1 Example of values determined for the misalignment of the x'- and z'-axes. The physical angles of the sample are $\alpha = 53.3(0.2)°$ and $\beta = 53.5(0.2)°$. The hypothesis that the ridges are symmetric thus cannot be rejected at a confidence level of 95 %. The top of the ridge has an opening angle of 73.2(0.3)°; the manufacture has specified an opening angle of 70° but no associated uncertainty is given

Sample rotation	Observed sidewall angle α	β	Slope of base line	$\varphi_{xz'}$	$c_{xz'}$
0	$\theta'_{a1}=53.72°$	$\theta'_{b1}=53.36°$	$\gamma'_1=-0.35°$	$-0.97°$	0.017
180	$\theta'_{b2}=52.14°$	$\theta'_{a2}=54.36°$	$\gamma'_2=0.39°$		

that is the x'-axis. We determine the tilt angle by fitting a line to the lowest 8 points of each valley in the average x'-profile of the image. The results from such calibrations performed for both the x'-axis and the y'-axis are shown in Table 14.1. The misalignment angle determined for the x'-axis is $-0.97°$. Performing the same analysis for the microscopes y'-axis we find a misalignment of 2.72°. Both misalignment angles are significantly higher than expected for our microscope, which stresses the importance of correcting this error.

We estimate the total uncertainty of the found misalignment angles to be 0.1–0.2°. The contribution from alignment of the standard is insignificant, since with the ridges parallel to the slow scanning axis, an alignment error of about 0.5° results in an error of only $\sim$0.001°. The uncertainty when fitting 1 order polynomials to the sides in order to determine the side angles (averaged over more than 100 scan lines) is about 0.1° estimated from the spread in many measurements. The uncertainty related to sample homogeneity has not been assessed quantitatively, but our experience so far is that this contribution is small and less than 0.1°.

Figure 14.5(a) shows an average profile from an AFM image of an optical grating with a nominal pitch of about 2.7 μm. The image has been recorded with the grating lines parallel to the microscope's slow scanning axis (in this case the x'-axis). The profile results from averaging all fast scan lines in the nominally square image. During imaging the grating was tilted approximately 15° in order for the tip to be able to image the sidewalls. The observed angle between the sidewalls and the plateaus is 92.3°. Figure 14.5(b) shows the average profile *after* the image has been corrected according to Eq. (14.2). The inside angle between the surface plateau and the sidewall for a grating line is now observed to 89.9°. It is thus clear that accurate 3D form measurements can be performed with the AFM if (and for our microscope *only if*) the images, in addition to the corrections for nonlinearity (in z') and scaling errors, are also corrected for the misalignment between the z'-axis and the (x', y') plane.

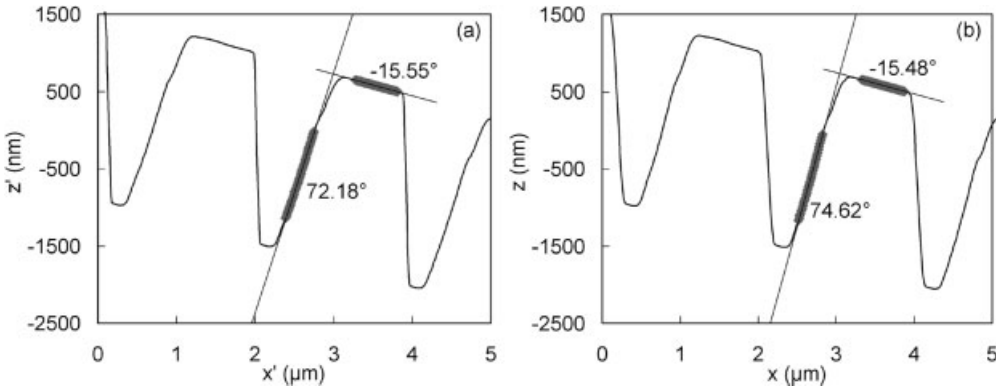

Fig. 14.5 Average profiles from AFM image of an optical grating. Linear fits (indicated in gray) have been performed on the top plateau and on the sidewall of one crest in order to estimate the surface angle relative to horizontal. (a) Profile before correction for the misalignment of the x'- and z'-axes and (b) after correction. In the uncorrected image, the inside angle between the sidewall and the plateau is 92.3°; after correction the angle is determined to 89.9°.

14.6 Conclusion

Based on a series of measurements on triangular-shaped ridges, the matrix elements c_{xz} and c_{yz} describing the coupling was calculated. The calibration of c_{xz} and c_{yz} requires that the other coefficients in the matrix transformation (14.2) are estimated, but the estimation of c_{xz} and c_{yz} does *not* require that the angle on the reference sample with triangular-shaped ridges are known. The misalignment of the vertical axes relative to the horizontal axes was found to be 1.0(0.2)° and 2.7(0.2)° for the closed loop AFM used in our investigation. With our setup, and ignoring the influence of the tip shape, it is now possible to correct any images of a three-dimensional surface. An example of estimating the technological important sidewall angle α of a grating wall with an uncertainty of $u(\alpha) \approx 0.3°$ was given.

Acknowledgements

We would like to acknowledge useful discussions with Jan Hald and Jan Conrad Petersen and financial support from CEMOST 2002-603/4001-97/55118.

Appendix

The full analytical solution for $c_{xz'}$ is given by

$$c_{xz'} = -\frac{2C}{B + \sqrt{B^2 - 4AC}} \tag{14.16}$$

where

$$A = \frac{1}{c_{xx'}}\left(\frac{\tan\gamma'_1}{1-k_1} + \frac{\tan\gamma'_1}{1+k_2} + \frac{\tan\gamma'_2}{1-k_3} + \frac{\tan\gamma'_2}{1+k_4}\right), \tag{14.17}$$

$$B = \left(\frac{1+k_1}{1-k_1} + \frac{1-k_2}{1+k_2} + \frac{1+k_3}{1-k_3} + \frac{1-k_4}{1+k_4}\right), \tag{14.18}$$

$$C = c_{zz'}^2 A + c_{xx'}\left(\frac{\cot\theta'_{a1}}{1-k_1} - \frac{\cot\theta'_{b1}}{1+k_2} + \frac{\cot\theta'_{a2}}{1-k_3} - \frac{\cot\theta'_{b2}}{1+k_4}\right), \tag{14.19}$$

and

$$k_1 = \tan\gamma'_1\cot\theta'_{a1}, \qquad k_2 = \tan\gamma'_1\cot\theta'_{b1}, \qquad k_3 = \tan\gamma'_2\cot\theta'_{a2}, \qquad k_4 = \tan\gamma'_2\cot\theta'_{b2}.$$

If it is assumed that $\gamma'_1 = \gamma'_2 = 0\cdots$, then $k_1 = k_2 = k_3 = k_4 = 0$, which implies that

$$A = 0, \qquad B = 4, \qquad C = c_{xx'}(\cot\theta'_{a1} - \cot\theta'_{b1} + \cot\theta'_{b2} - \cot\theta'_{a2}). \tag{14.21}$$

In that case (14.16) reduces to

$$c_{xz'} = \frac{c_{xx'}}{4}(\cot\theta'_{a1} - \cot\theta'_{b1} + \cot\theta'_{b2} - \cot\theta'_{a2}). \tag{14.22}$$

References

1 For example VDI/VDE 2617-3 Components of Measurement Deviation of the CMM.

2 N. Kofod, J. Garnaes, and J. F. Jørgensen, Methods for lateral calibration of scanning probe microscopes based on two-dimensional transfer standards, in *Proceedings of the 4th Seminar on Quantitative Microscopy QM 2000 Dimensional Measurements in the Micro- and Nanometre Range, Semmering, Austria, 12–14 January 2000*, edited by K. Hasche, W. Mirandé, and G. Wilkening (PTB-Bericht, 2000) pp. 36–43.

3 J. Garnaes, L. Nielsen, K. Dirscherl, J. F. Jørgensen, J. B. Rasmussen, P. E. Lindelof, and C. B. Sørensen, Two-dimensional nanometer scale calibration based on one-dimensional gratings, Appl. Phys. A **66**, 831–835 (1998) (DFM-97-R22).

4 J. F. Jørgensen, C. P. Jensen, and J. Garnaes, Lateral metrology using scanning probe microscopes, 2D pitch standards and image processing, Appl. Phys. A **66**, 847–852 (1998).

5 F. Meli et al., Z-calibration of a metrology AFM scanner using an interferometer and a tilting device with a linear stage, in *Proceedings of the Third Seminar on Quantitative Microscopy* (Lyngby, Denmark, PTB-F-34, November 1998) pp. 61–67 (1998).

6 J. Garnaes, N. Kofod, A. Kühle, C. Nielsen, K. Dirscherl, and L. Blunt, Calibration of step heights and roughness measurements with atomic force microscopes, Precision Eng. **27**, 91–98 (2003).

7 Dimension 3100 SPM with Metrology AFM Head, Digital Instrument, USA.

8 OMCL-AC160TS Probe, Olympus, Japan.

9 The Scanning Probe Image Processor (SPIP), Image Metrology, Denmark (www.imagemet.com).

10 Grating TGG01, MikroMasch, Estonia.

15
Height and Pitch at Nanoscale – How Traceable is Nanometrology?

L. Koenders and F. Meli

Abstract

Three international comparisons (NANO2, NANO3, and NANO4) were performed in the field of nanometrology between 1999 and 2002. Two of them, NANO2 (step height) and NANO4 (1D pitch), included scanning probe microscopes (SPM) for the first time. It was therefore important for the SPMs to perform successfully in order to show their full potential for dimensional metrology. Other techniques used in the comparisons were optical diffraction and optical microscopy for pitch measurements and stylus instruments and interference microscopes for step-height measurements. We present results of these two comparisons and compare the results and the uncertainties obtained by SPM with those of the other techniques. Both comparisons showed that most of the participants were able to make reasonable estimates of measurement uncertainties. The ranges of uncertainties estimated were in a small range for step-height measurements whereas they varied by a factor of 660 for the pitch measurements.

15.1
Introduction

The ability to measure small dimensions is of vital interest in micro- and nanotechnology. Contact stylus instruments, optical instruments, and scanning probe microscopes (SPMs) are all capable of making high-resolution dimensional measurements of small surface structures. More and more users of such instruments also require traceability of their lateral and vertical measurements. Traceability means that a measured result can be related to stated references, usually national or international standards, through an unbroken chain of comparisons, that all have stated uncertainties. The traceability can be realized by calibration of the instruments using lateral (pitch) and vertical (step height or groove depth) standards [1]. For the calibration of such standards it is essential to establish traceability to the SI unit of length. This is done in National Metrology Institutes

Nanoscale Calibration Standards and Methods: Dimensional and Related Measurements in the Micro- and Nanometer Range.
Edited by Gunter Wilkening, Ludger Koenders
ISBN: 3-527-40502-X

(NMIs) worldwide. Independent proof of traceability of the applied measurement methods and the proof of consistency of the results are most effectively given by international comparisons. Consequently for a new method such as the scanning probe microscopy, it is important to participate successfully in such comparisons.

The working group for dimensional metrology (WGDM7) of the Consultative Committee for Length (CCL) decided in 1998 to start a series of five preliminary key comparisons among National Metrology Institutes. Since then three of these international comparisons in the field of nanometrology have taken place: NANO4 (1D gratings) [2], NANO3 (line scales) [3], and NANO2 (step height) [4]. SPMs together with some other techniques were used in the NANO2 and NANO4 comparisons to measure vertical and lateral dimensions. In NANO4, the pitch of 1D gratings with nominal values of 290 nm and 700 nm was measured by SPMs, light diffraction techniques, and optical microscopes. In NANO2, step-height standards with a line width of 30 μm were chosen so that its heights could not only be measured by SPMs but also by contact stylus instruments and interference microscopes. These comparisons are comprehensive tests of the reliability of the instruments and their suitability for traceable measurements.

In the following the results of these comparisons will be presented and discussed. The chapter has two parts corresponding to the two comparisons NANO2 and NANO4. In each part we present the standards used, the measurement methods applied, and the results that were obtained. Finally, we will compare the SPM results to those obtained by other techniques and discuss the advantages and disadvantages of the methods.

15.2
Comparison on One-Dimensional Pitch Standards (NANO 4)

This first international comparison in the field of nanometrology started in February 1999 and was finished roughly one year later. The Swiss Federal Office of Metrology and Accreditation (METAS) acted as the pilot laboratory.

15.2.1
Standards and Measurand

Two holographic gratings, manufactured by Moxtek [5], with pitches of nominally 290 nm and 700 nm were used as the transfer standards. The gratings consist of a structured polymer resist material on a silicon surface that is coated with a tungsten layer. The ribs with heights of about 200 nm have a somewhat rounded, rather than completely flat top surface. The standards were mounted onto steel disks for an easy use in all instruments. Engraved on the steel disk were the identification and the measurement direction ($\rightarrow x$). The measurand for this comparison was defined to be the average pitch over the central surface of 1 mm $\times$ 1 mm at 20 °C. The direction of the pitch was defined to be orthogonal to the ribs of the

grating. As the first set of standards was severely damaged during the comparison it was necessary to replace it by a second set.

15.2.2 Participants and Measurement Methods

Twelve institutes located in different countries all over the world participated in this comparison (Table 15.1). Three different methods were applied to measure the pitch. The main methods used were optical diffraction (OD) and scanning probe microscopy (SPM). One institute used also an optical microscope (OM) to measure the pitch of the 700-nm sample. Two institutes have supplied results for two independent methods.

All but one of the used optical diffraction instruments was based on the Littrow configuration in combination with a laser light source, a precision rotary table, and a photodetector or CMOS array detector. Most of the SPMs were unique instruments built by the individual laboratories using commercially available components such as flexure displacement stages, laser interferometers, and capacitive sensors. Two SPMs were commercially available standard systems. Table 15.1 also gives a brief overview of the applied methods.

Table 15.1 Participants and measurement methods for Nano4

Institute	Principle	Instruments and Traceability
DFM	SPM	Commercial AFM with capacitive position sensors (DI metrology head). Calibration of AFM head with an IBSEN grating traceable to NPL. A special calibration software was used (SPIP). Image size typ. 50 μm × 6.5 μm
PTB	OD	Good Littrow diffraction approximation, Ar-laser with three wavelengths (W. R. Benett, Atomic gas laser transition data, IFI/Plenum), precision angle encoder (Heidenhain RON 255), CMOS array detector at 4 m distance
IMGC	OD	Littrow diffraction, red and green He–Ne laser, goniometric table, two-quadrant photodetector
NIST	SPM	NIST C-AFM with heterodyne laser interferometer (laser NIST traceable), closed loop control of the lateral sample position. Image size 1.5–3.5 μm
NPL1	OD	Littrow diffraction, green He–Ne laser, manual angle table with two reading heads, optical screen
NPL2	OM	Optical microscope, linear translation stage with laser interferometer (laser NPL traceable). For 700 nm grating only
VNIIM	OD	Laser interference diffractometer with reference line scale (comparator). Line scale (5 μm) traceable to VNIIM Argon laser with two wavelengths (R. J. Pressley (Ed.), *Handbook of Lasers*, Chemical Rubber Company, Cleveland, 1971)

Table 15.1 (continued)

Institute	Principle	Instruments and traceability
NIM	OD	Littrow diffraction based, green He–Ne laser, precision angle encoder (inductosyn), two-quadrant photodetector
NRLM (now NMIJ)	SPM	NRLM AFM with three-axis laser interferometer (laser NRLM traceable), line scans of 10–17.5 μm and 5500–8000 data points
CMS	SPM	Commercial AFM with capacitive position sensors (DI metrology head). Calibration of AFM head with Moxtek grating and factory certificate. Image analysis with SPIP software. Image size 3 μm and 7 μm
KRISS	OD	Littrow diffraction, argon laser at 487.986 nm (*Handbook of Laser Wavelengths*, CRC, 1999, p. 308), calibrated angle encoder (Heidenhain ERO 725), four-quadrant photodetector
OFMET1 (now METAS)	OD	Littrow diffraction, red and green He–Ne laser (METAS traceable), rotary table with air bearings, friction wheel drive and piezo fine adjustment, calibrated precision angle encoder (Heidenhain RON 905), four-quadrant photodetector
OFMET2 (now METAS)	SPM	METAS AFM profiler with interferometric long-range linear displacement stage (laser METAS traceable). Linescans 288 μm and 350 μm, local ridge detection

15.2.3 Results

To ensure that the standards remained stable during the comparison, control measurements were performed at METAS before and after the comparison for each of the two sets of gratings, see Table 15.2. The pitch change measured with laser diffraction was well below the measurement uncertainty and it is therefore concluded that the standards were stable during the time of comparison.

Because of the already mentioned damage, the first set of gratings was replaced after the first loop by a second set. The two sets of gratings were compared to each other at METAS. From all the measurements made at METAS, i. e., OD initial and final and the AFM measurements at the beginning, weighted mean values for the pitch of the gratings of set 1 and set 2 were calculated. The pitch difference between the two G-300 gratings is well below one standard uncertainty and for the G-700 gratings it is 1.4 standard uncertainties. It was therefore assumed that the corresponding gratings of the two sets have identical pitch values. This allowed an easy comparison of all measurements made by the different laboratories without taking into account any pitch difference.

The participants were asked to deliver in their report the average pitch values with the standard uncertainty u_c and the degree of freedom ν_{eff}. Figures 15.1 and 15.2 show the results for the G-300 and G-700 gratings, respectively.

Table 15.2 Pitch difference final-initial and its combined standard uncertainty measured at METAS with optical diffraction

Grating	G-300	G-700
1 (set 1)	0.003 ± 0.005) nm	(0.000 ± 0.014) nm
3 (set 2)	(0.000 ± 0.005) nm	(0.003 ± 0.007) nm

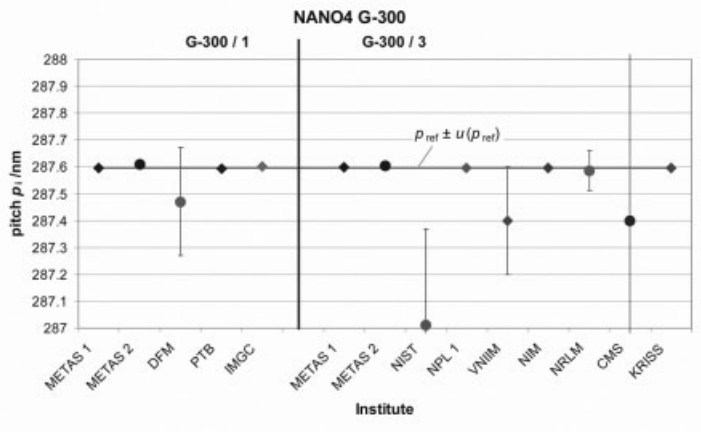

Fig. 15.1 Measurement results for the G-300 gratings. The error bars show the standard measurement uncertainty $u_c(x_i)$. Diamonds are used for OD, circles for SPM.

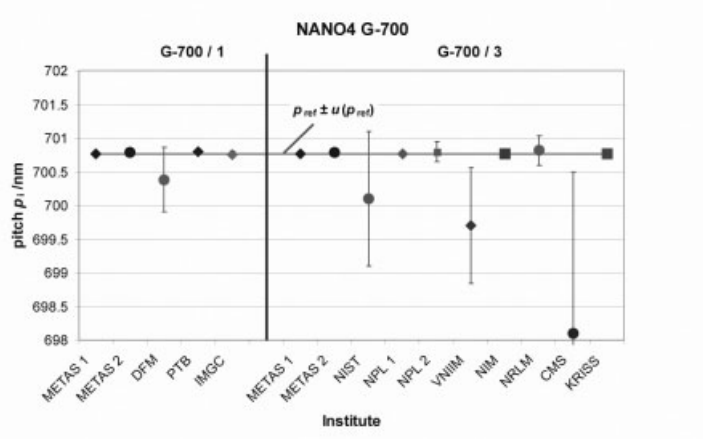

Fig. 15.2 Measurement results for the G-700 gratings. The error bars show the standard uncertainty $u_c(x_i)$. Diamonds are used for OD, squares for the OM, and circles for SPM.

Table 15.3 The comparison reference value p_{ref}, the combined standard uncertainty u_c, the resulting degree of freedom ν_{eff}, and the expanded uncertainty U_{95} obtained from all measurements with $En \leq 1$

Gratings:	**G-300**	**G-700**
p_{ref}	287.5961 nm	700.7607 nm
u_c	0.0011 nm	0.0023 nm
ν_{eff}	146	159
U_{95}	0.0021 nm	0.0046 nm

The reference value (x_{ref}) for this comparison was calculated as the weighted mean of all measurements (x_i). The weights used were $u^{-2}(x_i)$. With the given combined uncertainties $u^{-2}(x_i)$ and their effective degree of freedom $\nu_{eff}(x_i)$ the $En(x_i)$ values with a confidence value of 95 % were determined. Measurements with *En* values larger than 1 were omitted one by one for the calculation of the reference value. Finally, all values contributing to the reference value had *En* values ≤ 1. For the calculation of the comparison reference values only 2 of the total 29 measurements had to be omitted. For the results finally included in the calculation of the reference value the average *En* values were 0.36 and 0.40 for the G-300 and G-700 gratings, respectively. The reference values are given in Table 15.3.

15.2.4 Uncertainty

The participants were asked to deliver an uncertainty estimation according to the *ISO Guide to the Expression of Uncertainty in Measurement (GUM)* [6]. In order to achieve a better comparability some possible influence parameters were already mentioned in the instructions. The participating laboratories were encouraged to use all known influence parameters for their applied method. However, due to the various methods used the contributions considered in the uncertainty budgets were quite different. Most laboratories included the following contributions in the uncertainty budget:

- Repeatability
- Vacuum laser wavelength
- Refraction index of the air
- Angle uncertainty (OD)
- Interferometer alignment (SPM, OM)
- Sample alignment (SPM, OM)
- Local pitch variations within the central 1 mm^2 (SPM, OM)
- Angular motion of translation stages and Abbe offsets (SPM, OM)

Individual contributions included by some labs that should be considered also by others were

- Influence of mechanical clamping forces (bending)
- Grating temperature deviation from the reference temperature of 20 °C
- Expansion coefficient uncertainty
- Detector calibration
- Interferometer nonlinearity (SPM, OM)
- Interferometer resolution (SPM, OM)
- Single line definition (SPM, OM)
- Variation of different diffraction orders (OD)
- Variation for different diffraction orientations 0° and 180° (OD)

The uncertainties for the pitch measurements estimated by the participants covered a wide range. A factor of 660 is estimated between the smallest and the largest uncertainty.

The degrees of freedom were estimated quite differently by the participants, especially for the type B contributions. If the effective degree of freedom was estimated too high, the correct expanded uncertainty could be considerably larger and the corresponding En_{95} value therefore smaller.

15.2.5 Discussion

Table 15.4 shows the mean values for the two measurement methods OD and SPM separately. The largest difference between the corresponding mean values is only 0.028 nm. The standard deviation for the OD methods is three times smaller than for SPM methods. The optical diffraction methods proved to be very successful for the lateral pitch calibration. Their advantage is that they directly deliver the average pitch over the central measurement surface. Local probing methods, on the other hand, require many sites within this area to be measured and averaged. Their advantage is that they can deliver information about local pitch variations, nonlinearities, and stitching effects [7, 8].

Table 15.4 Weighted mean values with uncertainty and standard deviation for the results of each measurement method separately. OD = optical diffraction, SPM = scanning probe microscopy

Grating:	G-300			G-700		
	p (nm)	u_c (nm)	SD (nm)	p (nm)	u_c (nm)	SD (nm)
OD	287.5954	0.0011	0.0742	700.7598	0.0023	0.3565
SPM	287.6060	0.0042	0.2297	700.7878	0.0126	1.0502
Both	287.5961	0.0011	0.1642	700.7607	0.0023	0.7265

15.3
Comparison on Step Height (NANO4)

This comparison started in September 2000 and lasted 2 years. The PTB was the pilot laboratory.

15.3.1
Standards

A set of five step-height standards manufactured by the Fraunhofer Institute of Microelectronics in Stuttgart for the PTB was used for this comparison (see Figure 15.3). The nominal step heights of the standards were 7 nm, 20 nm, 70 nm, 300 nm, and 800 nm. The silicon chips of 5 mm × 5 mm are glued onto a thin steel disk with a diameter of 12 mm. The lateral size of the structures of the step-height standards was chosen such that the height could be measured by different types of instruments, such as interference microscopes, stylus instruments, and scanning probe microscopes.

Although the step height h is defined in analogy with ISO 5436, the restriction of the measuring range of some SPMs had to be taken into account, and the scan length A and B had been shortened compared to ISO standards (see Figure 15.4).

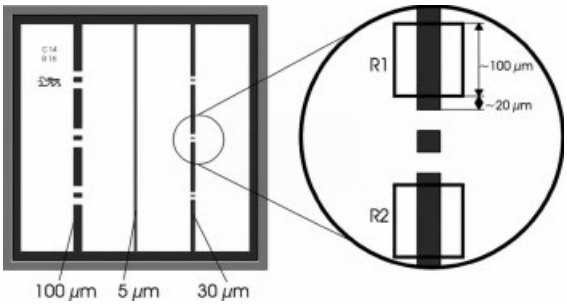

Fig. 15.3 Layout of the step-height standard. The substrate is silicon, the lines are SiO_2, and the whole sample is covered by a chromium layer of approximately 100 nm thickness. There are three lines with widths of 5 µm, 30 µm, and 100 µm. The line used for the comparison has a width of 30 µm and is located on the right-hand side. The field R1 used for the measurements is shown on the right drawing.

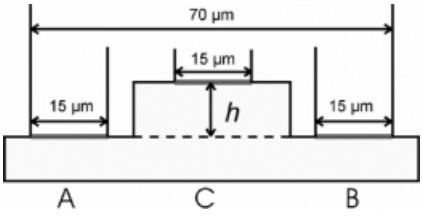

Fig. 15.4 Definition of step height h used in the comparison. This definition is similar to those in ISO 5436-1, but with a smaller base length of 70 µm instead of 90 µm normally required for a 30-µm wide step.

15.3.2 Measurement Methods

Fourteen national institutes worldwide participated in this comparison. Table 15.5 shows the various methods used to measure the step heights: Stylus profilers (5 instruments), interference microscopes (6), laser heterodyne interferometer (1), and scanning probe microscopes (8).

The stability of the standards was monitored by different calibrations performed by the pilot laboratory during the comparison. Stylus and interference microscope calibrations were made in Sept. 2000, Sept. 2001, and May 2002. The results showed that with the exception of the first measurement by interference microscope of SH070 at PTB, no significant change in the step height occurred.

Table 15.5 Participants and measurement methods for Nano2

Institute	Principle	Instrument	Traceability
CEM	IM	Interferential microscope MicroXAM-Ex from Phase Shift Technology	Calibrated using several steps/ grooves with certified values (NIST, NMi-VSL)
	ST	Stylus profiler Dektak^3 ST from Veeco	Calibrated using several steps/ grooves with certified values (NIST, NMi-VSL)
CMS	SPM	Commercial AFM with capacitive position sensors (DI metrology head). Image analysis with SPIP software	Step-height reference standards from VLSI Standards Incorporated (STS2-1800S) (traceable to NIST)
DFM	SPM	Commercial AFM with capacitive position sensors (DI metrology head). A special calibration software was used (SPIP)	Step-height standard H800 from Nanosensors calibrated at PTB
GUM	IM	Linnik-type micro-interferometer (type MII-4)	Green light ($\lambda = 536.6$ nm)
IMGC	ST	Stylus profilometer (Talystep 1, Taylor Hobson- RTH)	Displacement piezoactuators with capacitve transducers (DPT-10 from Queensgate) that have been calibrated using a heterodyne interferometer
KRISS	ST	Stylus instrument (Nanostep 2, Taylor Hobson Ltd, UK)	Gauge block calibrated by interferometer at KRISS
METAS	SPM	METAS AFM profiler with interferometric long-range linear displacement stage. AFM with DI metrology head	Laser traceable to METAS standards

Table 15.5 (continued)

Institute	Principle	Instrument	Traceability
NMIJ	IM	Interferometric microscope with a Mirau-type interferometric objective	Laser interferometer
	SPM	AFM with three-axis laser interferometer	Laser traceable to NMIJ standards
NMi-VSL	IM	Zeiss Interphako interference microscope with phase modulator and digital readout of the phase adjustments	546.23 nm line of a mercury discharge lamp
NIM	SPM	AFM VERITEKT 3 with integrated laser interferometer	Laser traceable to NIM standards
NIST	SPM	NIST C-AFM with heterodyne laser interferometer, closed loop control of the lateral sample positioning system	633 nm wavelength of the I_2-stabilized He–Ne laser
	ST	Talystep stylus instrument	Interferometrically measured step
NPL	SPM	NPL metrological atomic force microscope (MAFM) with integrated laser interferometers in three axes	Laser traceable to NPL standards
PTB	IM	Zeiss interference microscope with CCD-system	Thallium lamp ($\lambda = 535$ nm)
	SPM	Veritekt B with integrated laser interferometers in x, y, and z	Lasers traceable to PTB standards
	ST	Nanostep (Taylor-Hobson) stylus instrument	Step gauges calibrated by interference microscope
VNIIM	LHI	Laser heterodyne interferometer with a single-frequency He–Ne laser and acousto-optical modulators	Laser traceable to VNIIM standards
	μI	Michelson micro interferometer illuminated by the light of Ar or He–Ne lasers	Lasers traceable to VNIIM standards

15.3.3 Results

Figures 15.5 and 15.6 show the results obtained on the 7 nm and 800 nm step-height standard. The reference value h_{ref} for each standard was calculated as the weighted mean of all measurements h_i. The weights were $1/u^2(h_i)$. The expanded uncertainty U was calculated using a coverage factor of $k = 2$ [4]. Measure-

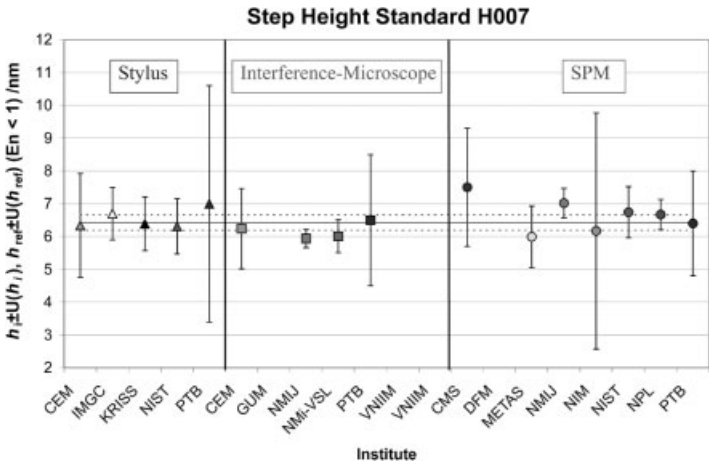

Fig. 15.5 Step heights measured on the SH007 standard grouped for the different instruments and the calculated reference value h_{ref} (full line) and its uncertainty U_{95} (dashed lines).

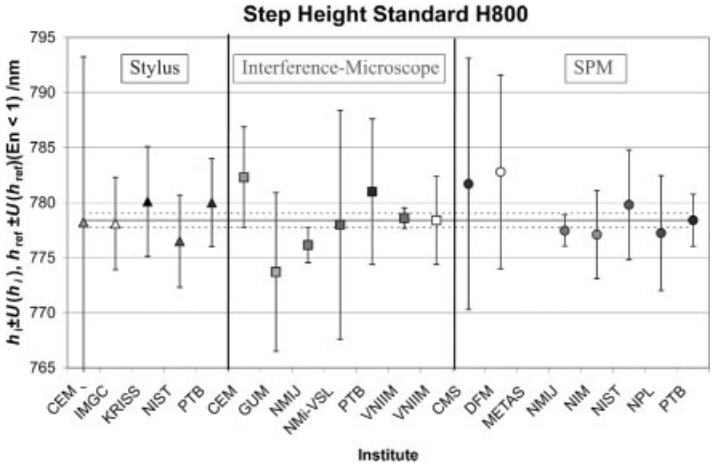

Fig. 15.6 Step heights measured on the SH800 standard grouped for the different instruments and the calculated reference value h_{ref} (full line) and its uncertainty U_{95} (dashed lines).

ments with the *En* value greater than 1 were omitted as described above for Nano4. One institute withdrew two values due to problems of the instrument at larger step heights. Only four measurements from over 90 did not fulfill the *En* criteria. This small number shows that the performance of the most instruments was excellent. The reference values are listed in Table 15.6.

The comparison Nano2 shows that today step heights on samples can be measured with uncertainties in the sub-nanometer range. Differences in the calcula-

Table 15.6 Reference value h_{ref}, uncertainty $u(h_{ref})$, expanded uncertainty $U(h_{ref}, k = 2)$, degree of freedom ν_{eff}, and number of measurements n for each standard

Standard	h_{ref} (nm)	$u(h_{ref})$ (nm)	$U(h_{ref}, k=2)$ (nm)	ν_{eff}
SH007	6.42	0.12	0.23	61
SH020	20.70	0.07	0.15	157
SH070	67.53	0.13	0.26	82
SH300	291.30	0.23	0.45	79
SH800	778.39	0.32	0.64	164

tion of the uncertainty depend on the type of instruments and on the laboratory. For SPMs it would be helpful to have a more standardized model.

15.3.4 Uncertainties

The uncertainty components should be divided into components associated with the realization of the object compared, and those associated with the comparison method. Contributions to the uncertainty budgets depend on the method and the instrument used:

1. *Calibration*
- vacuum wavelengths of lasers
- refraction index of the air
- interferometer alignment
- uncertainty of calibrated standards used
- nonlinearity of the instrument
- angular motion of translation stages
- Abbe offset

2. *Measurement*
- sample alignment
- noise of instrument
- repeatability

3. *Evaluation*
- roughness of the standard
- out of plane motion
- temperature of the standard

15.3.5 Discussion

As the step heights were measured by three different methods it was interesting to check the results for possible systematic differences between them. The mean step height value was calculated for each group of instruments and for each standard and was then plotted as a function of the values obtained by the stylus instruments.

A least-squares fit of the values for optical instruments, h_{IM}, and scanning probe microscope, h_{SPM}, to those of the stylus h_{ST} gave $h_{IM} = 1.0049 \cdot h_{ST} - 0.05$ nm and $h_{SPM} = 1.00076 \cdot h_{ST} - 0.12$ nm, respectively. The small deviation of the slope from 1.0 and the small offset values show that there is a very good agreement between the different types of instruments and there is no systematic difference between them. In Figure 15.7 the residuals of the least-squares fit for the IM and SPM methods are plotted as a function of the height obtained by stylus instruments to visualize possible nonlinearities of the scales.

The individual diagrams for each standard such as Figures 15.5 and 15.6 give an overview of the instruments and their measurement uncertainty. As the range of step heights was from 7 nm to 800 nm it was possible to evaluate offset and linearity for each instrument. We analyzed the linearity m_i and the offset b_i of each instrument with respect to the calculated reference values using linear least-squares fits. The linearity of the most instruments for step heights up to 800 nm is better than 1 %, the linearity of six instruments is better than 1‰, and that of one instrument is even better than 0.1‰. The offsets b_i calculated from the fits are shown in Figure 15.8. A few offset values b_i were even smaller than 0.2 nm. These offsets may indicate deviations or systematic differences for each instru-

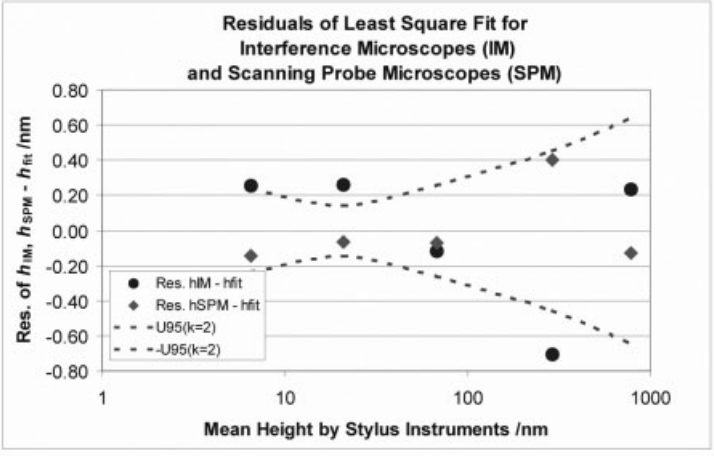

Fig. 15.7 Residuals of the fit of mean heights for optical and scanning probe microscopes to those of the stylus. The dashed lines give the band of the expanded uncertainty for the reference values of the standards.

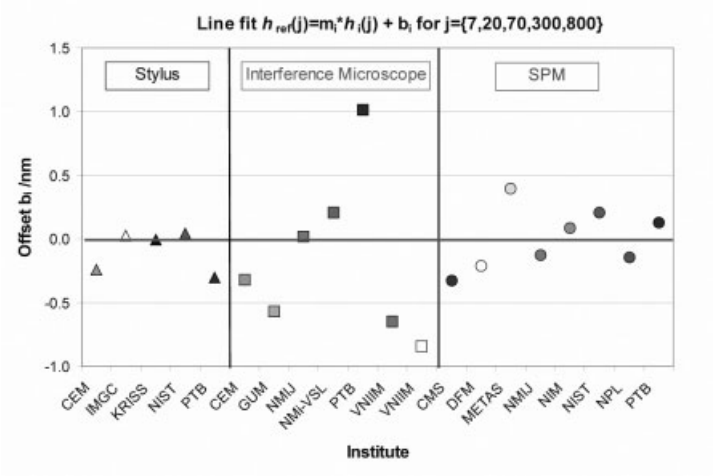

Fig. 15.8 Offset of the instruments m_i calculated from the measured data on each standard j using a least-squares fit of $h_{ref}(j) = m_i\ h_i(j) + b_i$.

ment, and could be helpful for the participants if compared to their uncertainty budget.

15.4 Conclusions

Although these two comparisons were made for the first time in the field of nanometrology they were very successful. Many of the used instruments were only recently developed and did not have a long working history. The participating laboratories were also able to estimate the measurement uncertainty correctly in most cases. Only a few measurements were outliers. On the basis of this comparison the participants are now able to validate their instruments or to improve them. As some of the instruments are under constant improvement regular comparisons in the future will help them maintain their validation.

Acknowledgment

Andrew Yacoot from National Physical Laboratory in particular is thanked for carefully reading of the paper.

References

1 Review of Standards, see www.ptb.de/5/51/514/index.htm

2 F. Meli, International comparison in the field of nanometrology: pitch of 1D gratings (Nano4), in *Proc. of 2nd Euspen Int. Conf., Turin, May 27th–31st* (2001), Vol. 1, p. 358.

3 H. Bosse, W. Häßler-Grohne, J. Flügge, and R. Köning, Final report on CCL-S3 supplementary line scale comparison Nano3, *Metrologia* **40**(Technical Supplement), 04002 (2003).

4 L. Koenders, R. Bergmans, J. Garnaes, J. Haycocks, N. Korolev, T. Kurosawa, F. Meli, B. C. Park, G. S. Peng, G. B. Picotto, E. Prieto, S. Gao, B. Smereczynska, T. Vorburger, and G. Wilkening, Comparison on nanometrology: Nano 2–Step-height, *Metrologia* **40**(Technical Supplement), 04001 (2003).

5 Moxtek, www. moxtek.com

6 *Guide to the Expression of Uncertainty in Measurement (GUM)*, ISO, 1995.

7 F. Meli and R. Thalmann, Long-range AFM profiler used for accurate pitch measurements, Meas. Sci. Technol. **9**, 1087–1092 (1998).

8 Th. Dziomba, W. Häßler-Grohne, H. Bosse, H.-U. Danzebrink, and G. Wilkening, Influence of nanostandard properties on calibration procedures of SPMs, in *Proc. 4th International Euspen Conference* (2003), Vol. 2, pp. 491–494.

16
The Behavior of Piezoelectric Actuators and the Effect on Step-Height Measurement with Scanning Force Microscopes

A. Grant, L. McDonnell, and E. M. Gil Romero

Abstract

A recent study has shown that frequent calibration is essential if height measurements are to be accurately made using a scanning force microscope (SFM) that is not equipped with positional control of the *Z* actuator. This study showed that the greatest uncertainty in measuring step heights was the behavior of the *Z* actuator. In the present work we have studied the behavior of the *Z* actuators for two scanning force microscopes – a commercial instrument with a separate *Z* actuator and an in-house instrument with a monolithic tube *XYZ* scanner – and the effect on step-height measurements. It is clear that the sensitivity of open-loop *Z* actuators in SFMs varies considerably with the amplitude of the applied voltage sweep. Therefore, in order to improve the accuracy of step-height measurements, open-loop *Z* actuators in SFMs should be calibrated for different height ranges (as is generally the case for open-loop *XY* actuators) rather than for their full dynamic range. Further additional calibration uncertainties arise if the *Z* actuator is not operated around its mid-position. Users need to be aware that offsetting the *Z* actuator deliberately, or as a consequence of sample tilt or form, may affect the accuracy of height measurements. For the two SFMs studied, the actuator offset resulting from scanner curvature does not introduce any significant height measurement errors.

16.1 Introduction

Since its invention in 1986 [1], the scanning force microscope (SFM) has been used to image surface topography for a wide range of sample types, materials, and applications. The reasons for the rapid popularity of scanning force microscopy are manifold: the potential for spatial resolution at the atomic scale; a lateral range that encompasses those of optical microscopy and scanning electron microscopy; the ability to image in air, liquid, or vacuum; and the absence of any

Nanoscale Calibration Standards and Methods: Dimensional and Related Measurements in the Micro- and Nanometer Range.
Edited by Gunter Wilkening, Ludger Koenders
ISBN: 3-527-40502-X

general technique-specific sample preparation requirements. Moreover, contrast in SFM images is derived from direct measurements of surface topography and thus three-dimensional measurements can be readily extracted from SFM images. Despite this intrinsic quantitative ability, many SFMs have been designed to visualize, rather than measure, surface topography and therefore considerable care is needed if valid measurements are to be derived from SFM images.

One of the core technologies underpinning scanning probe microscopy is piezoelectric actuation. Piezoelectric materials are extremely frugal – hardly moving for significant voltage inputs – and thus are well suited to actuation at the microscale and the nanoscale. Unfortunately, piezoelectric materials suffer from creep, aging, nonlinearity, and hysteresis and hence are far from ideal as actuators. The first generation of SFMs used piezoelectric actuators in open loop and these instruments are fully exposed to the inadequacies of the actuators. Nevertheless, knowledge of how open-loop actuators behave allows off-line [2] and on-line [3, 4] corrections to be made for nonlinearity, hysteresis, and creep. Second generation SFMs use closed-loop positional control of the *X*, *Y*, and *Z* movements [5] to counteract the deficiencies of the piezoelectric actuators and this has helped the SFM to evolve into a more quantitative instrument. However, it should be noted that closed-loop control of SFM actuators has its limitations and is prone to uncertainties that arise from the behavior of the position sensors, the signal conditioning circuits, and the control loop characteristics.

The principle of operation of the SFM is straightforward; a sharp tip on a soft cantilever is scanned across a surface to image its topography. Thus, image contrast in the SFM derives directly from height (*Z*) measurements made at specified lateral (*XY*) positions. However, uncertainties in height measurement arise from a number of sources that include (i) the interaction between the SFM tip and the sample [6,7], (ii) the response of the *Z* control loop [8], and (iii) the behavior of the *Z* actuator. Recently, Roe et al. [9] identified the variation over time of the sensitivity of the *Z* actuator of a first generation SFM as being the greatest contributor to the error in step-height measurement. Nevertheless, these authors showed that the uncertainties introduced by such actuator behavior could be minimized by very frequent calibration.

Indeed, Senoner et al. [10] identified calibration deficiencies as being the most important reason for the measurement deviations of the 41 SFMs used in an interlaboratory comparison of nanometric step heights. Their study revealed that whilst 20 % of the participants measured step heights to within 2 % of the true value, a similar percentage deviated by more than 10 % from the true value. Interestingly, the latter study showed that first generation instruments performed as well as second-generation instruments. Thus, it appears that the user may have a significant influence on the quantitative performance of an SFM. Clearly, this is an unsatisfactory situation as the instrument per se should be the limiting factor. Users of SFMs need to know how often to calibrate their instruments and this, in turn, requires knowledge on how the piezoelectric actuators within their instruments behave.

In general, there are two types of SFM designs: the scanned sample type [1] and the more complex scanned cantilever type [11, 12]. Within these instrument types, two methods of piezoelectric actuation are in use: the tube scanner [13] and the tripod scanner [14, 15]. A number of authors have carried out studies of the behavior of piezoelectric actuators. Some of these studies have concentrated on the *XY* behavior of the scanners [16–18], others on the *Z* behavior [19, 20]. Several studies have been made on tube scanners [21–23] with others on tripod scanners [24, 25]. Heyde et al. [26] have made a particularly intensive study of the behavior of the *Z* actuation of the tripod scanner and the tube scanner of a commercial SFM. From the prior work, it is clear that the calibration of open-loop *Z* actuators of SFMs is affected by a number of factors. Firstly, the sensitivity of a given actuator increases with increasing voltage sweep. Secondly, the amount of hysteresis increases with increasing voltage sweep. Furthermore, the movement of an actuator and its repeatability depend on the history of the actuator. A particularly important aspect of Heyde et al.'s work was the effect of applying a voltage offset to the *Z* actuator; the sensitivity of the actuator changed with the voltage offset and these authors pointed out the implications of such behavior for height measurements.

In our work, we characterized the displacement behavior of the *Z* actuators of two SFMs: the tripod scanner (TR) of a commercial scanned cantilever SFM and the tube scanner (TS) of an in-house scanned sample SFM. The behavior of the *Z* actuators was determined by measuring their displacements with a commercial optical-fiber displacement sensor and by analyzing the step heights in SFM images of commercial calibration artifacts for different actuator settings. This has enabled us to determine the effect of *Z* actuator offset on the accuracy of step-height measurements. We also examined the implications of sample tilt and scanner curvature for step-height measurements.

16.2 Experimental

16.2.1 Scanning Force Microscopes

Two SFMs were used in this study: a commercial instrument (Explorer™ model, Veeco Instruments, Santa Barbara, CA, USA) and an in-house instrument that has been described elsewhere [27]. The Explorer™ SFM is a scanned cantilever instrument that was configured for this work with a long-range tripod scanner (TR: *XY* range of 150 μm by 150 μm; *Z* range of 5.7 μm). The in-house SFM was configured for this work as a medium range tube scanner (TS: *XY* range of 50 μm by 50 μm). Both instruments were operated in contact mode in air. The Explorer™ SFM was operated with triangular silicon UltraSharp™ cantilevers (type CSC21/3, MikroMasch, Tallinn, Estonia). The cantilevers had the following characteristics (manufacturer's specifications): resonant frequency 15 kHz;

spring constant 0.03–0.30 N m^{-1}. The in-house SFM was operated with rectangular contact mode silicon Pointprobe™ cantilevers (Nanosensors, Wetzlar, Germany). The cantilevers had the following characteristics (manufacturer's specifications): resonant frequency 14–18 kHz; spring constant 0.18–0.45 N m^{-1}. Linescan rates during contact mode imaging were typically in the range 0.67–1 Hz.

16.2.2
Z Calibration with Step-Height Standards

Step-height standards (Series TGZ0x, Silicon-MDT Co., Moscow, Russia) were placed either onto the manual *XY* sample translation stage or the computer-controlled *XY* sample translation stage supplied with the SFM. Unless stated otherwise, the SFM was adjusted to be at a certain level, i. e., the tilt in the image was less than 1° in the *X* and *Y* directions, thereby ensuring that the error in step-height measurement due to sample tilt was less than +0.1 % [9]. Unless stated otherwise, feedback was engaged with the *Z* actuators of both SFMs at their mid-positions.

The image pixel resolution was selected to maximize the accuracy of the step-height measurement and to minimize the image acquisition time. All images were planar leveled using the three-point planar leveling algorithm within the SPMLab 3.06.06 software (Veeco Instruments, Santa Barbara, CA, USA) provided with the Explorer™ SFM. This leveling algorithm has been confirmed as being free of any artifacts that affect the accuracy of subsequent step-height measurements [9]. Heights within the SFM images were analyzed using software written in Matlab (Release 12, The Mathworks, Natick, MA, USA).

16.2.3
Z Calibration with Fiber-Optic Displacement Sensor

Heyde et al. [26] have shown that a relatively low-cost fiber-optic displacement sensor can be used to study the behavior of piezoelectric actuators and to calibrate them. In the work reported here, the performance of the *Z* actuator was studied using such a displacement sensor (Model D20-A1H1, Philtec, Annapolis, MD, USA). AC displacement measurements were obtained by applying oscillations to the piezoelectric actuator and connecting the output of the displacement sensor to a lock-in amplifier (Model PAR 5210, EG&G Instruments, Wokingham, England).

16.3 Results

16.3.1 Effect of Voltage Sweep

Hysteresis curves of the TS *Z* actuator were obtained using the optical displacement sensor for different voltage sweeps about the mid-position of the actuator. These curves are shown in Figure 16.1(a), where it is clear that decreasing the symmetric voltage sweep decreases the average sensitivity of the actuator, the latter being the slope of the straight line joining the two extremes of the hysteresis curve. The variation of average sensitivity with voltage sweep is shown in Figure 16.1(b) and is in agreement with van de Leemput et al. [19] and Hudlet et al. [22]. Often, open-loop *Z* actuators are calibrated using the average sensitivity obtained for a symmetric voltage sweep across the full dynamic range. As a result, the actuator will increasingly overestimate heights as the voltage sweep is reduced. From the data shown in Figure 16.1, an error of about +12 % occurs if the TS1 actuator is calibrated at its full dynamic range and then swept through 20 % of that range. The data in Figure 16.1 were obtained for symmetric voltage sweeps about the mid-range position of the *Z* actuator, the position in which feedback

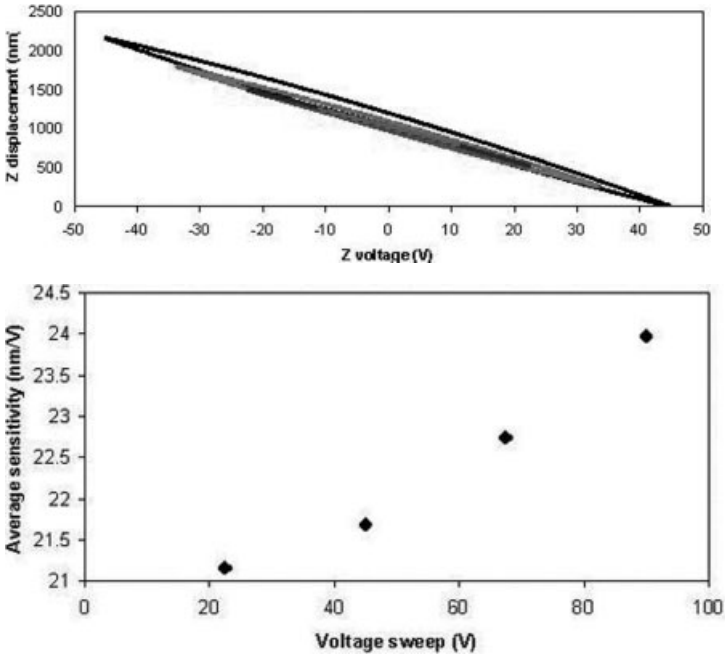

Fig. 16.1 (a) Hysteresis curves for the TS *Z* actuator obtained for different symmetric voltage sweeps. (b) The average sensitivity of the TS *Z* actuator versus the amplitude of the symmetric voltage sweep.

is normally engaged in the SFM. As discussed in the next section, this is not always the case.

16.3.2
Effect of Z Actuator Offset

As noted above, *Z* actuators are normally operated so that the SFM goes into feedback with the actuator in its mid-range position, thereby providing equal dynamic range for positive and negative *Z* measurements. However, with many samples the topography results in a completely asymmetric voltage sweep. For example, with a step-height artefact, the *Z* actuator goes into feedback on either the top or bottom of the step, as there is in effect no mid-position available, and an asymmetric topography ensues. Furthermore, many SFMs allow the user to apply a *Z* actuator offset for operational reasons, such as coping with large-scale asymmetric topographies or offsetting sample tilt and/or surface form. Figure 16.2(a) shows hysteresis curves obtained with the TS *Z* actuator for two different voltage sweeps and three different actuator offsets. In agreement with Hudlet et al., the principal effect is to shift the hysteresis curve. Within their experimental error, Hudlet et al. did not detect any effect of actuator offset on the average sen-

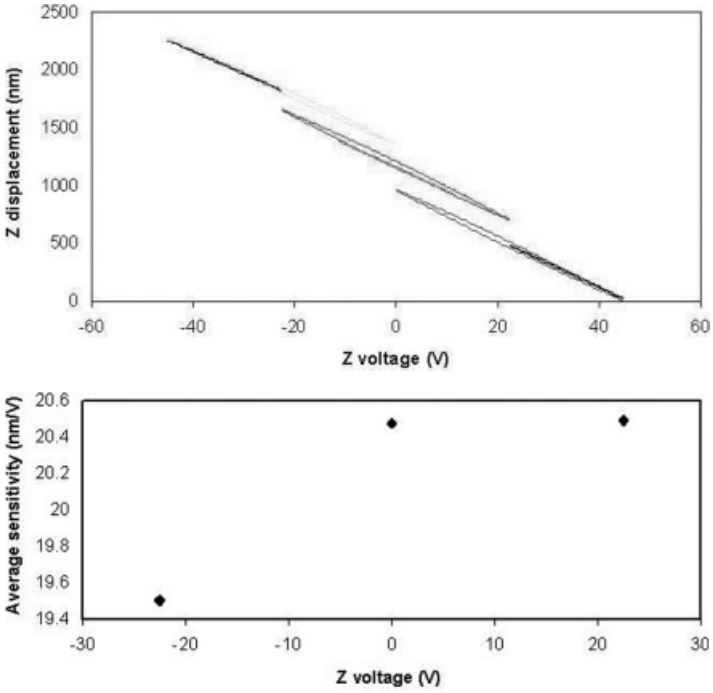

Fig. 16.2 (a) Hysteresis curves for the TS *Z* actuator obtained for two different sweep amplitudes and three different actuator offsets. (b) The average sensitivity of the TS *Z* actuator versus the actuator offset.

sitivity of the actuator. However, as Figure 16.2(b) reveals, our work shows a reduction in average sensitivity as the offset is changed from actuator contraction to actuator extension, in general agreement with van de Leemput et al.

In order to investigate the effect of *Z* actuator offset, a 512 nm step-height standard was imaged at different offsets with the TR *Z* actuator. The step heights measured from these images are plotted against the *Z* actuator voltage in Figure 16.3(a). The data shown were obtained as the *Z* actuator was contracted over 50 % of its full dynamic range (the latter being 100 V), which corresponded to a contraction of 2.9 μm. The effect of changing the offset of the TS *Z* actuator was determined by measuring the AC response of the actuator using the fiber-optic displacement sensor. For these measurements, a 1 kHz sinusoidal AC signal, corresponding to a displacement amplitude of 109 nm, was applied to the TS

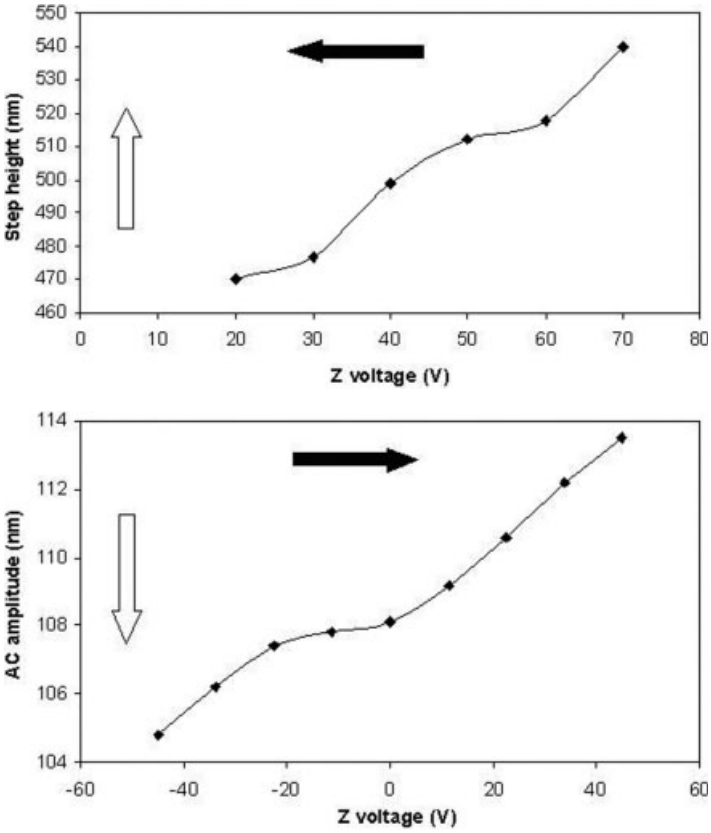

Fig. 16.3 (a) The variation in the measurement of a 512 nm step height due to changes in the *Z* voltage of the TR *Z* actuator (50 V corresponds to no offset). (b) The variation in the AC amplitude measured by the optical displacement sensor due to changes in the *Z* voltage of the TS *Z* actuator (0 V corresponds to no offset). *Note*: for both graphs, the white arrow indicates the direction of increasing step-height measurements whilst the black arrow indicates the direction of actuator contraction.

Z actuator and various DC voltage offsets were applied. It is clear from Figure 16.3(b) that the sensitivity of the actuator is changing as the offset changes. The data shown were obtained as the *Z* actuator was contracted over 100 % of its dynamic range (the latter being 90 V), which corresponded to a contraction of 2.1 μm.

Now, when an SFM is in feedback, a reduction in the sensitivity of the *Z* actuator means that more voltage is needed for a given step height and thus the SFM will overestimate the height. Therefore, to allow a direct comparison of the behavior of the TR and TS actuators, the data in Figure 16.3(b) have to be inverted to emulate actual step-height measurements. Nevertheless, it is evident from Figures 16.3(a) and (b) that the qualitative behavior of both *Z* actuators is similar. It can also be seen that changing the offset by 20 % of the actuator's full dynamic range can lead to step-height measurement errors of 7 % for the TR *Z* actuator and 2 % for the TS *Z* actuator.

16.3.3
Implications of Actuator Offset for Sample Tilt

The data presented above were obtained for a level sample (see Section 16.2.2). When the sample is tilted, or contains significant slopes in topography or form, the *Z* actuator experiences variations in offset during the lateral scan. This effect has been assessed by SFM imaging (50 μm by 50 μm) a 512 nm step-height grating, tilted by 3° in the *X* direction, with the TR *Z* actuator. Prior to SFM imaging, feedback is established in one corner of the area to be imaged and thus the other *X*-axis corner will experience maximum offset. For the above example, the *Z* displacement between the two *X*-axis corners is 2.8 μm. Analysis of the step heights at such corners for both level and tilted SFM images revealed errors that were consistent with the data shown in Figure 16.3(a), the tilt angle and the movement made by the *Z* actuator to reach the diagonally opposite corner. Clearly, excessive tilt of the sample can introduce significant actuator offsets with consequent height measurement errors.

16.3.4
Implications of Actuator Offset for Scanner Curvature

The *Z* trajectories of the two SFMs used in this study have been determined from large-area SFM images of flat surfaces (data not shown). For the TS *Z* actuator, a maximum *Z* displacement of 32 nm was measured for a lateral scan of 50 μm. For the TR *Z* actuator, a maximum *Z* displacement of 8 nm was measured for a lateral scan of 50 μm. Although the *Z* displacement is four times greater for TS than for TR, the values for both actuators are so small that the maximum offset experienced during wide area (50 μm by 50 μm) images does not produce any significant measurement error.

16.4 Conclusions

It is clear that the sensitivity of open-loop *Z* actuators in SFMs varies considerably with the amplitude of the applied voltage sweep. Therefore, in order to improve the accuracy of step-height measurements, open-loop *Z* actuators in SFMs should be calibrated for different height ranges (as is generally the case for open-loop *XY* actuators) rather than for their full dynamic range. Further additional calibration uncertainties arise if the *Z* actuator is not operated around its mid-position. Users need to be aware that offsetting the *Z* actuator deliberately, or as a consequence of sample tilt or form, may affect the accuracy of height measurements. For the two SFM scanners studied the actuator offset resulting from scanner curvature does not introduce any significant height measurement errors.

Acknowledgments

This work was carried out with support from the Technological Sector Research Programme of the Department of Education and Science under the National Development Plan 2000-2006.

References

1 G. Binnig, C. F. Quate, and C. Gerber, Phys. Rev. Lett. **49**, 57 (1986).
2 H. Kaizuka, Rev. Sci. Instrum. **60**, 3119 (1989).
3 H. Jung, J. Y. Shim, and D.-G. Gweon, Rev. Sci. Instrum. **71**, 3436 (2000).
4 J. F. Joergensen, K. Carneiro, L. L. Madsen, and K. Conradsen, J. Vac. Sci. Technol. B **12**, 1702 (1994).
5 R. C. Barrett and C. F. Quate, Rev. Sci. Instrum. **62**, 1393 (1991).
6 F. Moreno-Herrero, J. Colchero, and A. M. Baro, Ultramicroscopy **96**, 167 (2003).
7 A. N. Round and M. J. Miles, Nanotechnology **15**, S176 (2004).
8 G. Schitter, F. Allgower, and A. Stemmer, Nanotechnology **15**, 108 (2004).
9 G. Roe, L. McDonnell, and A. Ghanem, Ultramicroscopy **100**, 319–329 (2004).
10 M. Senoner, L. Koenders, W. Unger, and G. Wilkening, in *Proceedings of the 5th Seminar on Quantitative Microscopy and 1st Seminar on Nanoscale Calibration Standards and Methods (NanoScale 2001)*; PTB-Bericht F-44 (Physikalisch-Technische Bundesanstalt, Braunschweig, 2002), p. 70.
11 M. Hipp, H. Bielefeldt, J. Colchero, O. Marti, and J. Mlynek, Ultramicroscopy **42–44**, 1498 (1992).
12 R. C.Gamble and P. E.West, United States Patent 5,319,960 (1994).
13 G. Binnig and D. P.E. Smith, Rev. Sci. Instrum. **57**, 1688 (1986).
14 R. Young, J. Ward, and F. Scire, Rev. Sci. Instrum. **43**, 999 (1972).
15 G. Binnig, H. Rohrer, C. Gerber, and E. Weibel, Phys. Rev. Lett. **49**, 57 (1982).
16 C. J. Chen, Ultramicroscopy **42–44**, 1653–1658 (1992).
17 C. J. Chen, Appl. Phys. Lett. **60**, 132–134 (1992).
18 J. F. Joergensen, L. L.Madsen, J. Garnaes, K. Carneiro, and K. Schaumburg, J. Vac. Sci. Technol. B **12**, 1698 (1994).

19 L. E.C. van de Leemput, P. H.H. Rongen, B. H. Timmerman, and H. van Kempen, Rev. Sci. Instrum. **62**, 989 (1991).
20 M. E. Taylor, Rev. Sci. Instrum. **64**, 154–158 (1993).
21 C. Wei, H. Zhang, L. Tao, W. Li, and H. Shi, Rev. Sci. Instrum. **67**, 3594 (1996).
22 S. Hudlet, M. Saint Jean, D. Royer, J. Berger, and C. Guthmann, Rev. Sci. Instrum. 66, 2848 (1995).
23 S. Yang and W. Huang, Rev. Sci. Instrum. **69**, 226 (1998).
24 E. P. Stoll, Ultramicroscopy **42-44**, 1585 (1992).
25 U. Heider and O. Weis, Rev. Sci. Instrum. **64**, 3534 (1993).
26 M. Heyde, H. Sturm, and K. Rademann, Surf. Interface Anal. **27**, 291 (1999).
27 A. Grant and L. McDonnell, Ultramicroscopy **97**, 177 (2003).

17
An Approach to the Development of Tolerance Systems for Micro- and Nanotechnology

J. Schöbel and E. Westkämper

Abstract

Production processes with an accuracy in the range down to the nanometer scale gain growing importance in industry. A crucial requirement for their economical application are capable and controlled processes. These in turn are dependent on suitable measurement devices and strategies. Though measurement devices with the required precision are available, strategies and tolerance systems in the considered dimensions do not exist. In this chapter an approach to the development of tolerance systems for features in micro- and nanotechnology is presented as the examples micromilling and sputtering as production processes as well as atomic force microscopy as a measurement process.

17.1
Introduction

To ensure the function of a part tolerances are designated to dimensions. With the specification of tolerances additional influences resulting from the production and measurement processes have to be taken into account. At the moment, however, tolerance systems for features in the micro- and nanometer scale are not available. For that reason the designer is largely dependent on his or her own experience. A mere extrapolation of existing tolerance systems seems not to be appropriate because with shrinking dimensions effects have to be considered that are negligible in the macroscopic world. A strict distinction between roughness and shape, for example, can no longer be maintained. Furthermore, measurement instruments such as scanning probe microscopes are used to which existing standards can only be applied with substantial limitations [1].

An approach to the development of tolerance systems for micromachined parts will be presented and exemplarily introduced for the production processes, micromilling and sputtering, and for the measurement process, atomic force microscopy. To develop new tolerance systems for micro- and nanotechnology the influ-

Nanoscale Calibration Standards and Methods: Dimensional and Related Measurements in the Micro- and Nanometer Range.
Edited by Gunter Wilkening, Ludger Koenders
ISBN: 3-527-40502-X

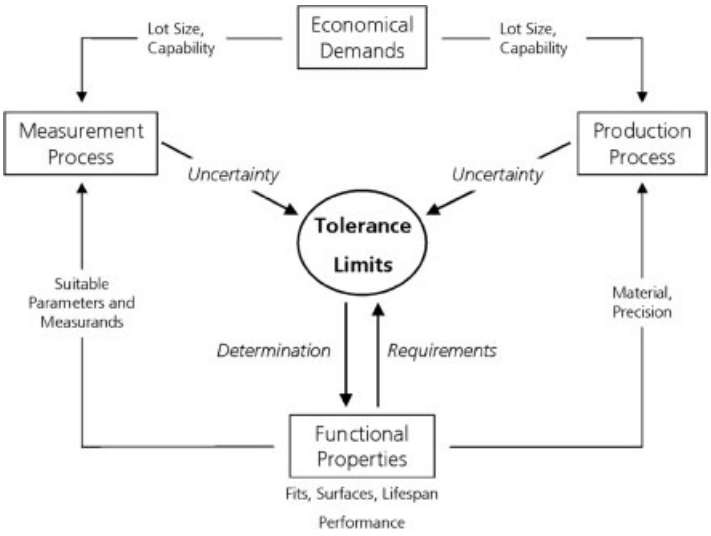

Fig. 17.1 Influences on the determination of tolerances.

encing factors of the tolerances have to be identified first. Primarily these are the variations in the production processes and the uncertainties of the measurement processes [2]. In general, these influences act as a constraint on the desired functional properties and have to be balanced with economical requirements (Figure 17.1). The influences have then to be quantified in systematical analysis. Here the uncertainties of microroughness measurements with an atomic force microscope (AFM) are determined by a measurement systems analysis. The achievable surface roughness of the production processes, micromilling and sputtering, and their variations are determined through test series. The surface properties are measured with an AFM to avoid the limited spatial resolution of optical or stylus instruments.

17.2
Tolerancing and Standards

The framework for geometrical tolerancing is set up in ISO/TR 14638 "geometrical product specifications (GPS)" [3]. The GPS is organized in four groups of standards–fundamental, global, general, and complementary. The general standards are represented as a matrix model with the geometrical properties arranged in its rows. The rows form chains in whose links the standards for the definitions of the nominal and actual characteristics of the features, the definition of tolerances, and requirements for measurement equipment and its calibration are collected. The complementary standards contain chains for specific manufacturing processes and machine elements.

Whereas the fundamental and global standards can generally be applied to micro- and nanotechnology as well, the situation is different for the general and complementary standards. Tolerance grades, for example, are not defined for nominal sizes below 3 mm. Novel manufacturing processes such as LIGA and measurement instruments such as SPM or white light interferometers have neither found their consideration in the GPS. The increasing dissemination of these instruments in industry, however, requires that accepted standards for their calibration and application are developed. Only then reproducible and comparable results can be obtained, which allow a decision over the conformance of a product with its specification.

The current state can thus be summarized that in none of the GPS chain links satisfying solutions for applications in the micro- and nanometer range exist. Standards in this field are currently specific to industrial sectors and their organizations. New tolerance systems for micro- and nanotechnology, however, are likely to be generally accepted only if they can be seamlessly integrated into the GPS.

17.2.1 Measurement Systems Analysis

To determine the uncertainties of microroughness measurements with an AFM, repeatability studies with step-height standards and a roughness standard were carried out. A *Digital Instruments Dimension 3100* AFM was used for the measurements. All AFM measurements were evaluated with the software *SPIP* by *Image Metrology A/S* [4].

17.2.2 Step-Height Measurements

For the step-height measurements three different line gratings with nominal heights of 26 nm, 104 nm, and 530 nm were used. The AFM images were acquired in contact mode as the 530 nm steps were insufficiently mapped in tapping mode. Besides imaging artifacts appeared at the step edges, which obstruct the evaluation of the images. On each standard 10 arbitrarily chosen spots were measured twice.

To take the influence of the evaluation method into account the height values were determined by two different methods. Firstly, the height values were directly measured in the histogram of the images [4]. The second method is described in ISO 5436-1 [5]. Here lines are fitted into the inner third of the ridge and valley plateaus of a profile by least-squares fits and the distance between the lines is determined. The height value of the measured area is calculated as the mean of the profiles.

In Figure 17.2 the expanded standard deviation of all 20 measurements of each standard with a coverage factor of $k = 3$ is shown. Also the standard deviations of the differences of the height values measured in the two consecutive images

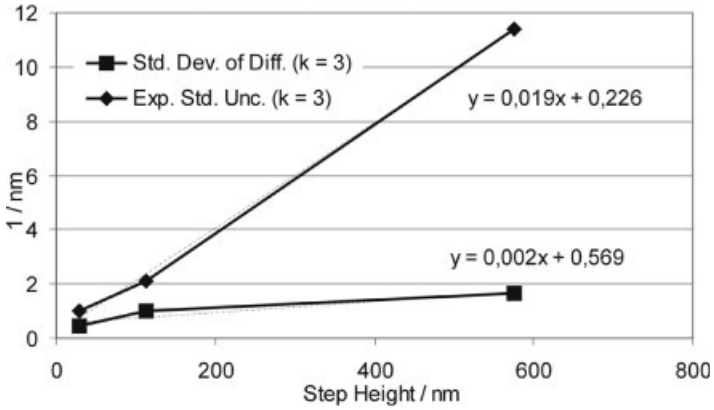

Fig. 17.2 Expanded standard deviation and standard deviation of differences of step-height measurements.

acquired at the same spot of the standard were calculated. The coverage factor $k = 3$ was applied likewise.

The significantly higher values of the standard deviation with respect to the standard deviation of the differences can partly be attributed to the uncertainty of the step-height standards. A further influence arises from the nonlinearity of the piezoactuators, because the absolute position of the z-piezo varies between the different measurement spots.

The difference between the two evaluation methods was found to be very small with slightly higher uncertainties in the histogram method (Table 17.1). This may be attributed to the discretization of the height classes in the histogram.

Table 17.1 Differences between step-height evaluation methods (all values in nm)

Step height	Expanded SD ($k = 3$)		SD of differences ($k = 3$)	
	Histogram	ISO 5436	Histogram	ISO 5436
26	1.19	1.02	0.54	0.45
104	2.95	2.13	1.79	1.00
530	11.44	11.41	2.59	1.67

17.2.3 Microroughness

Because the standardization process for microroughness and three-dimensional surface measurements is still in an early stage no generally accepted guidelines for these measurements are available. Calibration specimens for microroughness measurements are developed and evaluated in [6] but were not available for the presented work yet.

Here the measurements were carried out with a DKD (German Calibration Service) roughness standard that is intended for the calibration of stylus instruments. The nominal values for the standard are $R_a = 0.233$ μm, $R_z = 1.56$ μm, and $R_t = 1.79$ μm at a cutoff wavelength of $\lambda_c = 0.8$ mm. Comparable results from AFM measurements cannot be expected because the transmission bands of the instruments have just little overlap. The measured values can only be regarded as a basis of comparison for the machining experiments. On the standard 17 arbitrarily chosen spots were measured twice with a scan range of 80 μm.

Firstly, suitable filter parameters for the AFM measurements had to be identified. The approach was to minimize the standard deviation of the roughness parameters related to the actual values to achieve an optimum separation from the waviness profile. In Figure 17.3 the relative standard deviations of S_a and S_q are displayed with respect to the cutoff wavelength of the applied two-dimensional Gaussian filter. S_a shows a minimum at $\lambda_c = 11.4$ μm, which is 1/7 of the scan range.

Table 17.2 shows the results of the microroughness measurements. The standard deviation of the differences was calculated as noted in the previous section.

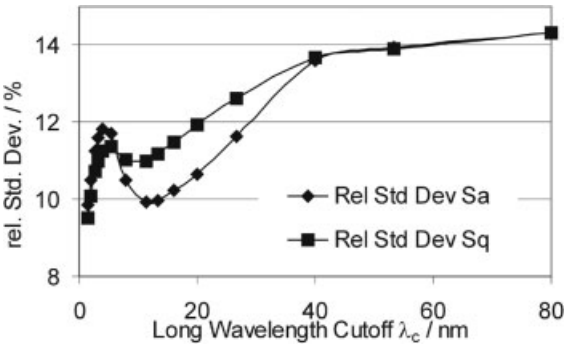

Fig. 17.3 Relative standard deviation of microroughness measurements ($n = 34$ measurements, scan size = 80 μm) with respect to the filter wavelength.

Table 17.2 Result of microroughness measurement with DKD roughness standard (all values in nm, coverage factor $k = 3$)

Parameter	S_a	S_q	S_z	S_k	S_{pk}	S_{vk}
Mean	61.5	78.2	524.3	184.4	86.3	80.1
Expanded SD	18.3	25.8	266.4	63.6	65.0	72.1
SD of differences	0.6	0.9	34.3	3.1	3.4	2.7

The high standard deviations of the parameters can be attributed to the rather inappropriate standard and show that specific standards for microroughness measurements are required.

17.3 Machining Experiments

17.3.1 Micromilling

The machining experiments were carried out on a *Kugler Microgantry GU2* micromachinig-center. The positioning accuracy of the machine is specified with 0.3 μm for the *X*- and *Y*-axes as well as 0.5 μm for the *Z*-axis. The machining spindle allows rotational speeds of up to 160 000 rpm. Two-flute end mills with 0.5 mm diameter of the type Magafor were used as tools. Because of their good machining properties brass ($CuZn_{39}Pb_2$) and aluminum (AlCuMnPb) were chosen as sample materials.

To achieve even reference planes the experiments were carried out on prepared matrix structures with rectangular elements of 1.5 mm by 15 mm in size. On the longer sides of the rectangles single paths were milled with combinations and intermediate values of the parameters shown in Table 17.3. Overall 480 paths were milled but for the evaluation only the brass samples were used because the aluminum samples tended to burr and impeded the measurements with the AFM.

Three-dimensional surface parameters are described in [7]. Here a subset of these parameters was used. Additionally the three parameters R_k, R_{pk}, and R_{vk} described in ISO 13565-2 [8], extended to three-dimensional measurements, were used.

The influence of the machining parameters on the surface properties was determined by a regression analysis. For each combination of the roughness and machining parameters the significance of the dependency was calculated as the quotient of the test value of the regression and the critical value of the *t*-distribution at a significance level of $\alpha = 99\,\%$ (Table 17.4).

Values larger than 1 indicate a significant influence. Table 17.4 shows that the feed per tooth has the highest influence on the surface characteristics followed by

Table 17.3 Machining parameters for milling experiments

Parameter		Minimum	Maximum
Cutting speed	v_c (m/min)	157	236
Feed rate	f_z (μm)	0.5	2.25
Depth of cut	a_p (μm)	1	100
Width of cut	a_e (mm)	0.25	0.45

Table 17.4 Significance of the influence of cutting parameters on surface parameters (brass sample)

Parameter		a_p	v_c	f_z	Parameter		a_p	v_c	f_z
Roughness average	S_a (nm)	0.3	1.4	1.9	Root mean square slope	S_{dq} (1/nm)	0.2	1.2	1.9
Root mean square	S_q (nm)	0.3	1.4	2.0	Surface bearing index	S_{bi}	0.5	0.2	1.2
Surface skewness	S_{sk}	0.1	0.4	1.1	Core fluid retention index	S_{ci}	0.4	0.1	1.3
Surface kurtosis	S_{ku}	0.3	0.0	0.9	Valley fluid retention index	S_{vi}	0.0	0.0	0.8
Peak to peak height	S_y (nm)	0.4	0.9	2.3	Core roughness depth	S_k (nm)	0.2	1.2	1.7
Ten-point height	S_z (nm)	0.4	0.9	2.3	Reduced summit height	S_{pk} (nm)	0.7	1.6	1.6
Mean summit curvature	S_{sc} (1/nm)	0.4	1.1	1.2	Reduced valley depth	S_{vk} (nm)	0.3	1.1	2.2

the cutting speed. The depth of cut shows no significant influence on the microroughness of the surface. The amplitude parameters S_a, S_q, S_y, and S_z correlate better with the machining parameters than the functional parameters but their significance to functional properties of a manufactured part is inferior. For the determination of process capabilities, however, an investigation of the tool life and the degradation of the tool during its lifespan are necessary. Figure 17.4 shows the dependency of S_z on the feed per tooth.

Two AFM images of the milled surfaces are shown in Figure 17.5. The dominating influence of the feed per tooth is clearly visible. The left sample was milled with $f_z = 2.25$ µm and the right sample with $f_z = 0.75$ µm. The ten-point heights are $S_z = 115$ nm and $S_z = 317$ nm, respectively.

The standard deviations of the measured roughness parameters lie far above the values that were determined with the step-height standards. These values, however, are not directly comparable. To separate the influences of the production and the measurement process, suitable roughness standards with nominal values in the range of the machined surfaces and comparable wavelengths are necessary.

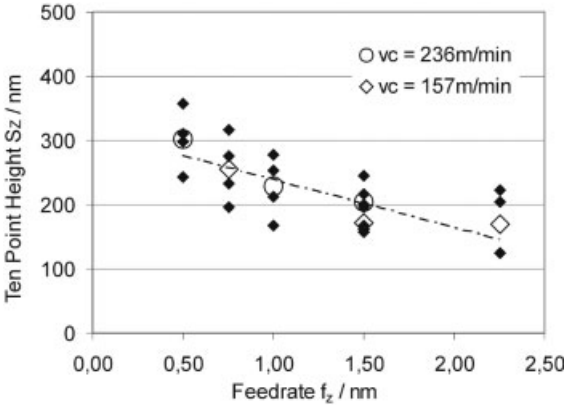

Fig. 17.4 Influence of the feed f_z on ten-point height S_z (variable cutting speed and depth of cut).

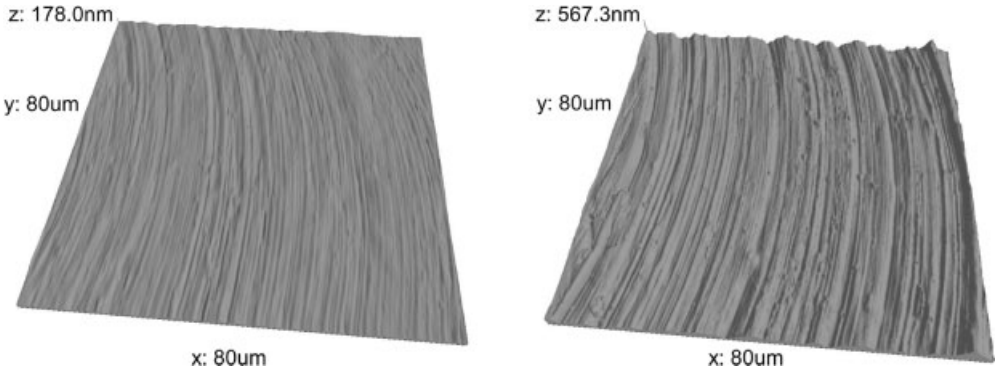

Fig. 17.5 AFM images of micromilled brass surfaces. Left: $f_z = 2.25$ μm. Right: $f_z = 0.75$ μm; $V_c = 157$ m/min in both images.

17.3.2 Sputtering

To determine the uncertainties of the deposition process Cu was sputtered on Si [111] substrate. The process parameters for the different samples are shown in Table 17.5. Three samples for each parameter set were sputtered. The surface roughness and the layer thickness were measured with the AFM at several different areas of the samples. Two samples of the surfaces are shown in Figure 17.6.

The roughness values as described in the above section were determined at a scan range of 1 μm and a Gaussian filter with a cutoff wavelength of $\lambda = 143$ nm was applied. To measure the layer thickness a part of the Cu layer was removed and the step height was evaluated as the distance between the peaks in the histogram of the AFM images. The results of the measurements for the ten-point height S_z and the thickness are shown in Figure 17.7. The expanded standard deviation of the thickness measurements is 9% of the step height. For the ten-point height an expanded standard deviation of 3.0 nm was observed.

Table 17.5 Parameters for sputtering experiments

Set No.	Pressure (mbar)	Time (s)
1	0.0100	60.0000
2	0.0075	60.0000
3	0.0050	60.0000
4	0.0075	300.0000
5	0.0050	300.0000
6	0.0050	900.0000

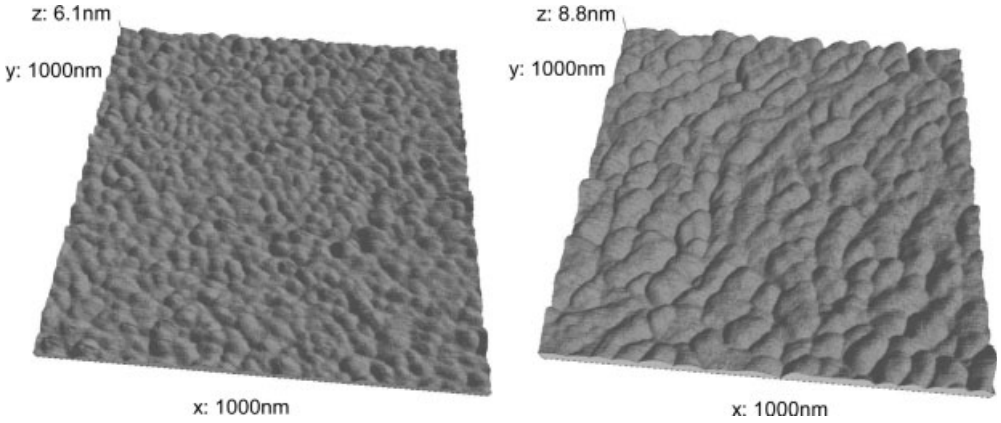

Fig. 17.6 AFM images of sputtered surfaces. Left: $t = 60$ s. Right: $t = 300$ s; $p = 0.005$ mbar, $P = 200$ W in both images.

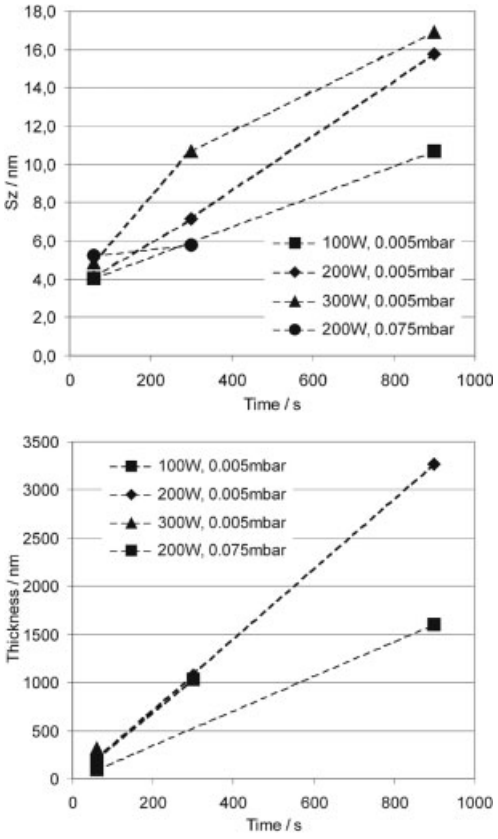

Fig. 17.7 Results of roughness (left) and thickness (right) measurements of sputtered surfaces with respect to the sputtering time.

Table 17.6 shows the significance of the influence of the sputtering parameters on the surface roughness. The significance was calculated as described for the milling experiments. Again a value larger than 1 indicates a significant influence. Whereas the amplitude parameters S_a, S_q, S_y, and S_z show a good correlation with the sputtering time the standard deviations at short sputtering times are high and vary between the different samples. A stabilization of the process can be observed with increasing sputtering times.

Table 17.6 Significance of the influence of sputtering parameters on surface parameters

Surface parameter		Significance		
		Power	Time	Pressure
Roughness average	S_a (nm)	1.0	8.0	1.4
Root mean square	S_q (nm)	1.0	8.1	1.3
Surface skewness	S_{sk} (nm)	0.9	3.4	3.4
Surface kurtosis	S_{ku} (nm)	0.3	1.7	3.7
Peak to peak height	S_y (nm)	0.9	7.1	1.0
Ten-point height	S_z (nm)	1.0	7.5	1.1
Density if summits	S_{ds} (1/um^2)	0.8	3.5	0.5
Mean summit curvature	S_{sc} (1/nm)	0.7	3.5	1.2
Texture index	S_{ti}	0.1	0.9	0.3
Root mean square slope	S_{dq} (1/nm)	0.4	5.4	2.0
Surface area ratio	S_{dr} (%)	0.4	4.9	1.6
Surface bearing index	S_{bi}	1.2	3.1	1.3
Core fluid retention index	S_{ci}	1.1	3.5	1.8
Valley fluid retention index	S_{vi}	1.2	3.5	1.6
Core roughness depth	S_k (nm)	0.9	7.7	1.5
Reduced summit height	S_{pk} (nm)	0.6	5.9	0.4
Reduced valley depth	S_{vk} (nm)	1.3	6.4	1.3
Texture direction	S_{td} (deg)	0.4	0.3	0.1
Texture direction index	S_{tdi}	1.6	1.9	0.2
Dom. rad. Wavelength	S_{rw} (nm)	0.1	0.0	0.8
Radial wave index	S_{rwi}	1.5	1.8	0.1
Mean half wavelength	S_{hw} (nm)	0.6	1.3	0.6

17.4 Conclusions

Among others the functional properties of a product are determined by its geometry and surface characteristics. The designer has to choose the parameters that reflect these properties as good as possible and has to assign limits to these parameters that must not be exceeded to ensure the function of the part. Based on the functional requirements production and measurement processes have to be chosen that are capable to comply with the requirements. Standards for these processes can be developed either for general geometrical properties, for specific machine elements, or for a specific manufacturing process.

The results of the step-height and microroughness measurements suggest that the observed uncertainties are highly dependent on the availability of calibration standards and procedures as the differences between the standard deviations and the standard deviations of the differences show. A definition of tolerance grades is therefore only reasonable when standards at the chain links five (measurement equipment requirements) and six (calibration requirements–measurement standards) in the GPS matrix are available.

The capability of a production process is dependent on the spread of the process and also on the uncertainty of the measurement process. The higher the measurement uncertainty is the narrower the spread of the production process has to be to maintain a specified tolerance. A tolerance system has to take both sources of uncertainty into account. The results of the conducted experiments show that some of the surface characteristics of the examined processes correlate well with machining parameters. A correlation of the results with functional properties of manufactured parts will allow a direct toleration of these properties [9]. The combined uncertainties of the measurement and production process determine boundaries of achievable manufacturing results and determine minimum tolerances that can be assigned to dimensions. Systematical analysis of production and measurement processes in which uncertainties and their sources are investigated can then be developed into a tolerancing scheme.

References

1 H. N. Hansen et al., Calibration and industrial application of instruments for surface mapping based on AFM, Ann. CIRP **51** (1), 471–474 (2002).

2 E. Westkämper and M. H.R. Kraus, Functional and depth oriented characterisation of technical surfaces, in *Proceedings of the 1st Euspen Topical Conference on Fabrication and Metrology in Nanotechnolgy, Copenhagen, May 28–30, 2000* (Center for Geometrical Metrology, Lyngby, DK, 2000).

3 ISO/TR 14638, Geometrical Product Specifications (GPS)–Masterplan, 1995.

4 SPIP–The Scanning Probe Image Processor, Image Metrology ApS, Lyngby, Denmark, http://www.imagemet.com.

5 ISO 5436-1, Geometrical Product Specifications (GPS)–Surface texture: Profile method; Measurement standards–Part 1: Material measures, 2000.

6 R. Krüger-Sehm et al., Judgement of the profile of nano-roughness standard specimens by different contacting and non contacting methods, in *Proceedings of the NanoScale 2004, Braunschweig, Germany, March 25–26, 2004.*

7 K. Carneiro et al., Roughness parameters of surfaces by atomic force microscopy, Ann. CIRP **44** (1), 517–522 (1995).

8 ISO 13565-2, Geometrical Product Specifications (GPS)–Surface texture: Profile method; Surfaces having stratified functional properties–Part 2: Height Characterization using the linear material ratio curve, 1996.

9 E. Westkämper and H.-W. Hoffmeister, Function-oriented lapping and polishing of ceramic rolling elements through characterization of the workpiece surface, Ann. CIRP **45** (1), 529–532 (1996).

Part V
Calibration – Standards for Nanometrology

Nanoscale Calibration Standards and Methods: Dimensional and Related Measurements in the Micro- and Nanometer Range.
Edited by Gunter Wilkening, Ludger Koenders
ISBN: 3-527-40502-X

18
Standards for the Calibration of Instruments for Dimensional Nanometrology

L. Koenders, T. Dziomba, P. Thomsen-Schmidt, and G. Wilkening

18.1
Introduction

Geometrical quantities of nanostructures are determined with scanning probe microscopes (SPM) and scanning electron microscopes (SEM). Whereas the latter usually furnish only two-dimensional information, SPMs allow three-dimensional structures to be measured. In national metrology institutes, high-precision scanning probe microscopes are equipped with laser interferometers, which allow the measurement results to be traced back directly to the unit of length "metre" [1]. In commercial devices used in research and application in industry and institutes, capacitive or inductive sensors or strain gauges help the deficiencies of the piezoelectric control elements normally used (e. g., drift and hysteresis) to be minimized. These must be compared with the SI unit of length on the basis of a calibration. For this purpose, standards of known properties are used. The design of the standards is adapted to the proper measurement purpose and to the manufacturing method.

In addition to geometrical quantities, it is important for nanometrology to determine – i. e., to prove and resolve – material differences on a scale of a few nanometres. This refers to layer thickness and depth profiles as well as to the lateral distribution of different materials on the surface. Typical devices for the determination of the layer thickness are X-ray reflectometers and ellipsometers. For the material analysis of small lateral structures, high-resolution electron microscopes (HREM), Auger electron spectrometers (AES), and secondary ion mass spectrometers (SIMS) are used in particular. Standards for these techniques are described elsewhere [2].

Nanoscale Calibration Standards and Methods: Dimensional and Related Measurements in the Micro- and Nanometer Range.
Edited by Gunter Wilkening, Ludger Koenders
ISBN: 3-527-40502-X

18.2
Standards for Scanning Probe Microscopy

For the calibration of the lateral properties of the scanning unit of scanning probe microscopes, one-dimensional or two-dimensional gratings exist with structures in the range 10 μm down to a few nanometres. To avoid disturbing effects on the lateral calibration by too large deflections in the vertical direction, the structures are kept quite flat, i. e., only in a few cases they are suitable to simultaneously calibrate the vertical axis. For this purpose, special step-height standards are used which show individual two-dimensional or three-dimensional arrangements. The structures of some standards are clearly below the wavelengths of the visible light (<400 nm). Their manufacture with electron beam lithography procedures requires high technical effort.

In addition, there are some test samples available that show the functional efficiency of measuring set-up and probe. In scanning probe microscopes, the probe is moved over the scanning range by piezo-actuators while the tip follows the sample topography. Although the measuring ranges are very small – typical are 70 μm x 70 μm – such systems show clear deviations from an ideal guide. Moreover, external influences (temperature, mechanical and acoustical oscillations as well as impact sound) are acting on the device during the measuring time.

In the image process of structures, the probe with its fine tip is a very critical element. Here it is important that their imaging quality can be checked. For this purpose, a large variety of tip characterizers are used. However, they cannot be used to perform a "calibration" of the "true" dimensions of the tip, it can at least be verified whether the tip has been changed by the measuring process or not.

In the past few years, different standards for the verification and calibration of scanning probe microscopes have been developed by Physikalisch-Technische Bundesanstalt (PTB) in cooperation with partners. In addition to a flatness standard, six step-height standards (8 nm to 2400 nm) and five lateral standards (100–10.000 nm) were developed [3]. After that, additional prototypes for lateral standards with structural periods of 30 and 50 nm have been further developed and investigated. Depending on the resolution and area of application, these standards can, of course, also be used for calibration by other high-resolution devices. In addition, samples of other offerers (see tables and Ref. [4]) can be used for calibration. In the course of quality assurance, an unbroken chain of the traceability of the measurand must, however, be ensured.

18.2.1
Flatness Standard

Figure 18.1 shows the overall layout of a flatness standard with adjusting aids and reference field in the center. In the case of these standards, chromium layers have been structured on high-quality glass substrates (5 mm x 7 mm x 2 mm). The

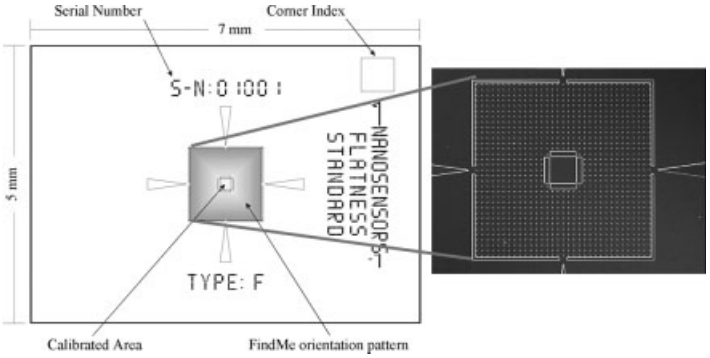

Fig. 18.1 a) Layout of the flatness standard with optically marked orientation marks, orientation guides for scanning probe microscopy and central reference field.

reference area in the center was calibrated with an interference microscope. The peak-to-valley (P–V) value is indicated as characteristic of the flatness. For these standards, this value is clearly smaller than 10 nm (typical are 6 nm).

Such flat surfaces allow the quality of the scanning unit of scanning probe microscopes and their environment to be checked (Figure 18.2). Deviations by "scanner bow" problems of the zero detector, drift effects due to temperature changes and disturbances by mechanical and acoustical oscillations can be clearly seen sometimes [5]. External influences are generally easy to recognize and can be eliminated, for example, by an improved insulation against acoustical and mechanical oscillations. Intrinsic disturbances, as for example the "scanner bow" in the case of tube scanners, drift effects due to temperature changes or disturbing interferences on the quadrant diode by undesired reflections on the sample, are more difficult to detect and eliminate. Both effects can well be proved on flat surfaces of low roughness.

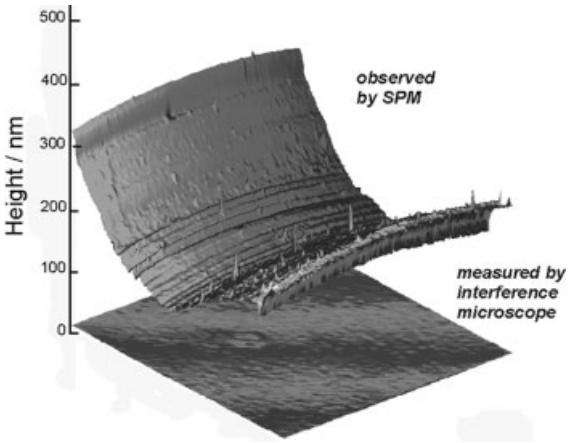

Fig. 18.2 The lower plain face shows the range of the flatness standard recorded with an interference microscope (100 μm x 100 μm). The upper face shows the range recorded at the same place with the SPM. In the direction of the X axis (rapid axis of motion), the slight curvature shows the influence of the scanner face which is not ideal. Larger deviations due to drift, disturbing interferences and the like can be clearly seen along the slower axis.

18.2.2
Tip Characterizers

When fine structures with sharp tips are imaged, the result is a convolution – better: a morphological dilatation – of the surface topography with the tip shape (without taking interacting influences into account). Here, sharp and stable structures are often used to control the tip shape. This allows qualitative tests to be performed before and after important measurements. Only in the case of a known tip geometry could it be possible to obtain a "true" or a better approximated topography reconstruction. For this purpose, mathematical methods (fast Fourier transform (FFT), Legendre transformation [6], and morphological methods [7]) are used which allow statements on the tip shape to be made on the basis of measured images and topographies. The known procedure of the blind reconstruction [8] is based on morphological procedures (erosion, dilatation) and calculates the bluntest tip with which the image could be measured.

In a joint project of PTB, Institut für Physikalische Hochtechnologie Jena (IPHT) and Nanosensors (now Nanoworld), line structures with very sharp tran-

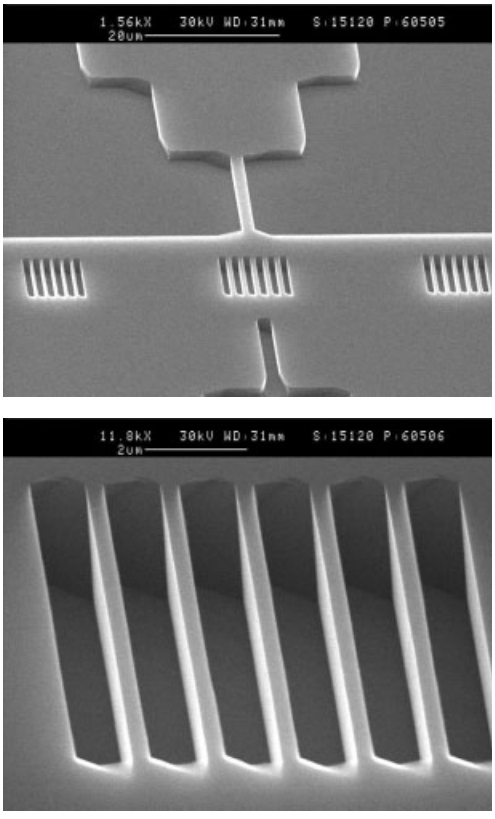

Fig. 18.3 SPM-mapping at the tip characterizer.
Map of the test structures recorded with the scanning electron microscope for determination of the tip shape. The larger structures are optical orientation guides. For determination, three fields of different width with identical structure depths may be used (source: IPHT, Jena).
a) REM-mapping of the central range with finding structures.
b) A group of lines for determination of the tip parameter. Specified: width and distance of the lines.

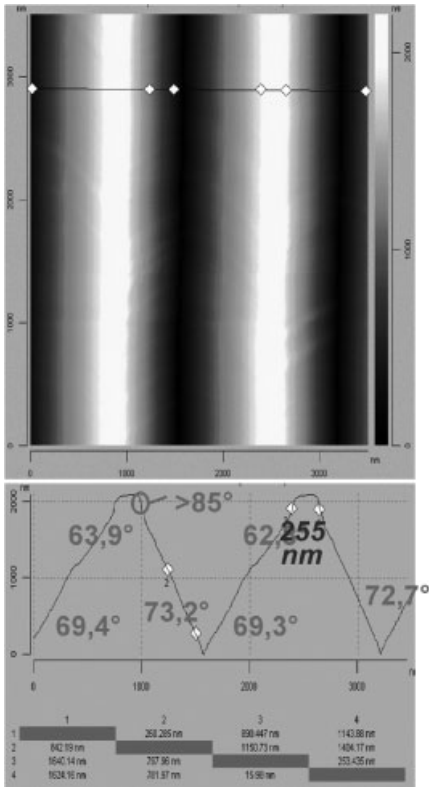

Fig. 18.4 AFM-mapping of a range of tip characterizers (upper part). Profiles and evaluation of the parameters "included angle" and "tip radius" (lower part).

sitions were manufactured for the preparation of special samples [9]. Figure 18.3 shows such a structure and Figure 18.4 the profiles recorded on it. The width of the lines of the test structure have been measured very exactly with well-proven optical measuring methods to obtain a very low uncertainty. By special sharpening procedures, the edges have been finished to show a very small curvature radius. This allows the geometry of the shaft to be determined with larger accuracy.

Investigations of Meli [10] showed that there is a difference of a few nanometres between the geometrical shape of the tip (manufacturer's datasheet) and the tip shape derived from very careful investigations performed on undercutted structures. This can be attributed to interactions occurring between tip and sample when the surface is scanned. This aspect is very important for nanometrology and has to be further investigated in future.

18.2.3
Lateral Standards

For these standards, different manufacturing and calibration procedures are used. Spacings above 300 nm can be realized by optical means. The standards with mean spacings between 1 μm and 10 μm, which are used to calibrate large scanning ranges, are produced with the aid of holographic methods. Below 300 nm, electron beam writers are used. In research projects, gratings were also prepared with atomic-optic lithography with spacings of ≈212.7 nm [11]. Figure 18.5 shows a holographically manufactured two-dimensional standard with a pitch size of 1 μm in both directions. These standards are characterized by very good homogeneity and rectangularity of the structures. Figure 18.6 shows another two-dimensional standard with spacings of 300 nm manufactured by electron beam lithography. The structures are directly etched into the silicon.

The somewhat larger spacings are usually calibrated by optical diffraction methods in which averaging is performed over the whole reference area. An advantage of this method is that very small uncertainties can be realized with short measuring times. Although structures with spacings of 300 nm can still be calibrated by

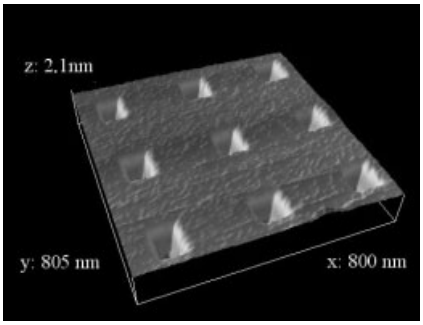

Fig. 18.5 Range of the 2D300 standard imaged with the metrological Veritekt scanning force microscope. Here, the small pyramid-shaped depressions which were directly etched into the silicon by anisotropic procedures can be clearly seen.

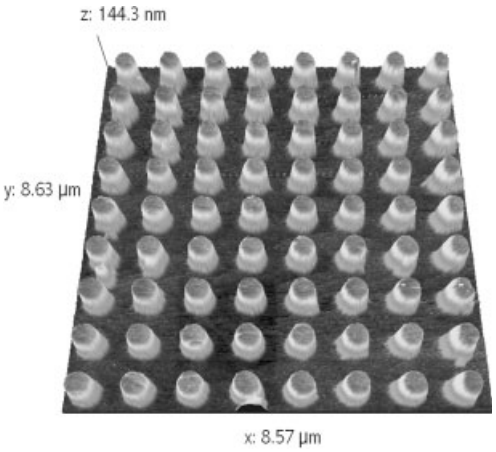

Fig. 18.6 Image of the 2D1000 standard in 3D representation recorded with the scanning force microscope with vertical exaggeration of the topography in the z-direction. After analysis of the data set, the values certified for the distance of the structures can be used to calibrate the axes of the scanning force microscope in the x or z-direction.

diffraction methods, these structures manufactured by electron beam lithography clearly demonstrate the disadvantage of a global calibration method. In subsequent investigations performed with scanning force microscopes it turned out that jumps in the grating spacings of up to 20 nm occur [12] between adjacent structures. These are due to the limited positioning accuracy of the electron beam for the stitching process. If such effects are avoided and averaging is performed over a sufficiently high number of structures, a close approximation of the value determined by the light optics can be achieved. Lateral standards with structural spacings of less than 300 nm can at present be calibrated only with metrological scanning probe microscopes [1].

Standards with even smaller spacings can be realized by "structuring" of semiconductor heterostructures [13, 14]. Molecular beam epitaxy (MBE) or other techniques, like metal organic chemical vapor deposition (MOCVD) allow epitaxial growth of very thin single-crystal layers with changing material compositions. The proper structure for calibration of the scanning force microscopes is obtained by wafer cleaving and subsequent anisotropic etching of the layer system laid open on the cleaved surface (Figure 18.7). The small topography contrast of 2–5 nm is sufficient to image structures with the scanning force microscope. At PTB, structures of 30 and 50 nm period were manufactured and special importance was attached to traceability of the calibration. It turned out that $Ga_{30}Al_{70}As$/GaAs heterostructure layer systems can well be investigated and calibrated by means of X-ray reflectometry (XRR). Complementing investigations with neutron reflectometry and transmission electron microscopy (TEM) showed very good agreement. For an improved topography contrast, it is also possible to apply ion beam techniques for preparation. At present, investigations into the long-term stability of such standards are carried out.

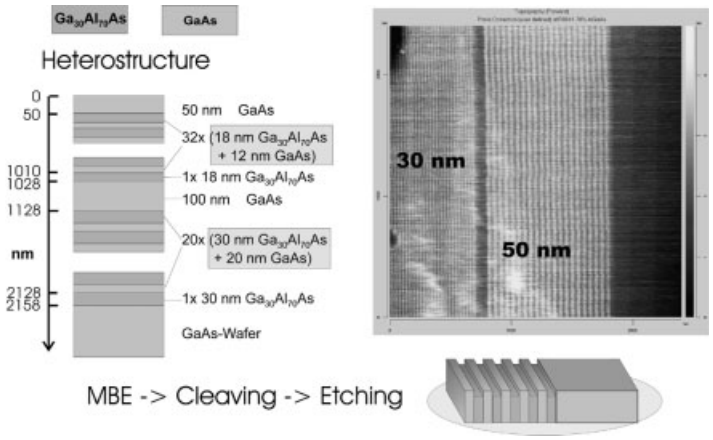

Fig. 18.7 a) Stack of the $Ga_{30}Al_{70}$/GaAs heterostructure with two different periods of 30 and 50 nm. b) Range of the layer system excavated by splitting of the waver imaged with the scanning force microscope before etching. By natural oxidation, the $Ga_{30}Al_{70}$ layers are somewhat increased.

18.2.4 Step-Height Standards

In addition to the lateral dimensions, the height or depth is also an important quantity in surface topography. Whereas the lateral *x*- or *y*-positions are specified by the device, the tip of the topography must very well follow the surface topography in the *z*-direction. Different strategies are followed to determine the behavior in the *z*-direction. The calibration can be performed on a standard with a single line, a field with many identically high structures or several standards of different heights. In most cases, calibration is carried out on a single line, which is positioned in the center of the *x*–*y* scanning range and of the *z*-deflection range of the piezo. Deflection in this direction is, however, performed via a control loop and a control variable (tunnel current in the case of scanning tunneling microscopes (STM) and force in the case of the scanning force microscopes (SFM)); the probe is adequately tracked. Compared with a calibration of the *z*-displacement sensor only, a calibration by measurement with the cantilever on standards has the advantage that potential deviations of the cantilever's positional controller are included [15].

Step-height standards are often made of silicon. Figure 18.8 shows a detail of such a standard. The proper reference structure in the center of the sample is a two-dimensional arrangement of holes with as flat a bottom as possible and nominally identical depths on a surface of 240 μm x 240 μm. The hole pattern represents a height standard with a certified mean step height *h*. The surrounding quadrants show horizontal and vertical lines as well as two-dimensional hole patterns with different spacings.

Figure 18.9 shows an image taken with the scanning force microscope on a single line on a SiO_2 layer thickness standard [16]. Here, lines of different widths 5 μm, 30 μm, and 100 μm can be found on the silicon substrate. Such standards are calibrated with interference microscopes or with metrological scanning probe microscopes. Expanded uncertainties of $U\ (k = 2) \sim 1$ nm are realized. These very small uncertainties have been confirmed by the international intercomparison NANO2 [17].

The limit for step-height standards can be seen in atomically high steps on crystalline surfaces as, for example, silicon. The step height, i. e., the spacing between the two crystal planes on the surface, derived from volume data of silicon, amounts to 0.13 nm for the (001) surface. In most cases, these surfaces can, however, be measured only under ultrahigh vacuum conditions. When exposed to air, adsorption of water films or bio-compatible films occur in addition to oxidation and contamination. These can considerably change the arrangement of the surface atoms. In view of the symmetry of the arrangement of atoms, crystalline surfaces would be ideal samples for angle measurements in small sections (rectangularity etc.). Atomically plane single-crystal surfaces over areas of a few millimetres could be ideal samples for form measurement techniques for microstructures [18].

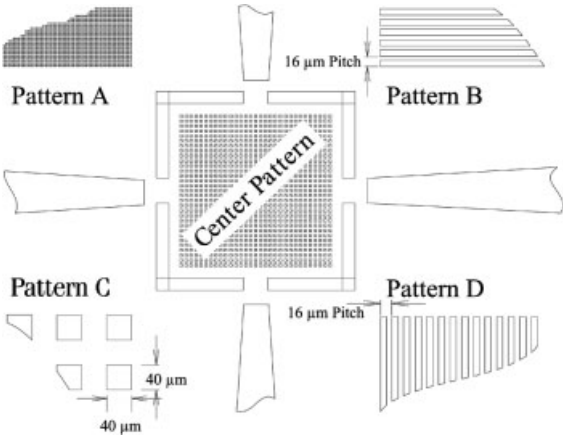

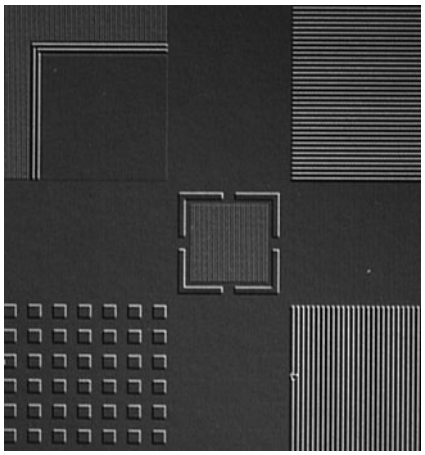

Fig. 18.8 a) Layout of the central area of the step-height standard with the reference field (4x4 µm cavities with 8 µm period). The areas A, B, C and D show other patterns. b) Image of the central range recorded with an optical microscope.

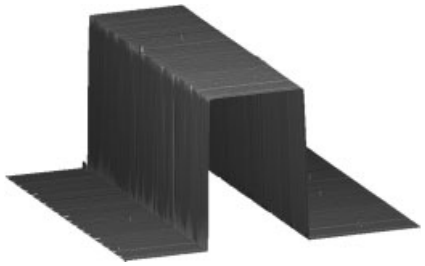

Fig. 18.9 The image recorded with the scanning electron microscope shows a section of 60 µm x 10 µm with a step 1 µm in height on a SiO_2 layer thickness standard.

18.2.5
Nanoroughness Standards

In addition to these standards with simple geometrical structures, PTB is also working on a nanoroughness standards in cooperation with the IMT (Hannover University) and Nanosensors [19]. This standard is manufactured with the aid of nanogrinding and is to show values of Rz 30 and 80 nm. Figure 18.10 shows images of such a sample taken with the scanning probe microscope. These standards could fill the gap between superfine roughness standards (150 nm $\leq$ *Rz* $\leq$ 450 nm) and plane glass surfaces (*Rz* $\sim$ 2 nm) and serve as a bridge between conventional roughness measurements with contact stylus instruments and metrology with scanning probe instruments.

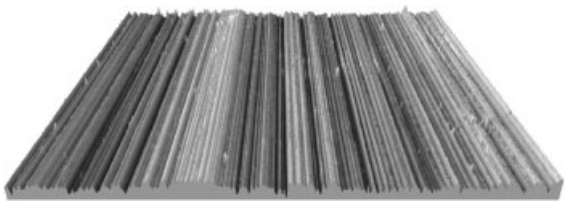

Fig. 18.10 Image of a nano-roughness standard recorded with a scanning probe microscope. The range has a size of approx. 72 μm x 70 μm, the grey gamut represents a vertical range of 80 nm. The roughness characteristics are: Sa $\sim$ 8.5 nm.

18.3
Film Thickness Standards

Thin films are important components in the field of nanotechnology. They are used as gate oxides in MOSFETs as protective coatings, storage media in optical or magnetic drives and reflectors for synchrotron radiation. Here, precise thickness control plays a decisive role. X-ray mirrors, for example, are made of a large number of single layers on a curved substrate and show film thickness values less than 1 nm. To achieve that such a mirror meets the required specifications and functionality, the film thicknesses calculated before must exactly complied with for substrates of up to 100 mm in length.

Within the scope of a BMBF project, material measures were manufactured and metrologically characterized for the nanometre range [20]. Calibration procedures were developed and tested under conditions related to practice. Two different types of material measures were manufactured for different film thickness standards. One set of film thickness standards is intended for the field of X-ray reflectometry, X-ray fluorescence analysis, and electron beam microanalysis, the other set is tailored to ellipsometry. For the first-mentioned fields, the thinnest metal layers of platinum and nickel on a quartz glass substrate are used (Figure 18.11). The substrates are polished by an ion beam technique before Pt or Ni

Fig. 18.11 Quartz glass with 10 nm platinum coating (60 mm x 20 mm x 10 mm).

is deposited. The platinum films are directly deposited on the quartz substrate by the laser pulsed technique, whereas the nickel films are embedded between two thin protective carbon layers. These additional layers should prevent oxidation of the nickel and diffusion of nickel into the substrate. The nominal thickness values of the metal layers lie between 10 nm and 50 nm. These standards were calibrated by X-ray reflectometry at PTB in Berlin. Proof of stability and resistance to aging was furnished at the Bundesanstalt für Materialforschung und -prüfung (BAM). Subsequent investigations at PTB, manufacturer, and different users showed very good agreement with the calibrated values.

For the calibration of ellipsometers, thermal SiO_2 layers were grown on silicon wafers (Figure 18.12). The nominal values of the standards manufactured were: 6, 70, 160, 400, and 1000 nm. Calibration was also performed at BESSY II by X-ray reflectometry (XRR) at an optimized beam energy of 1841 eV [21]. The boundaries of the layers were investigated by TEM. The SiO_2 standards were additionally provided with a lithographically prepared microstructure to make the layer thickness

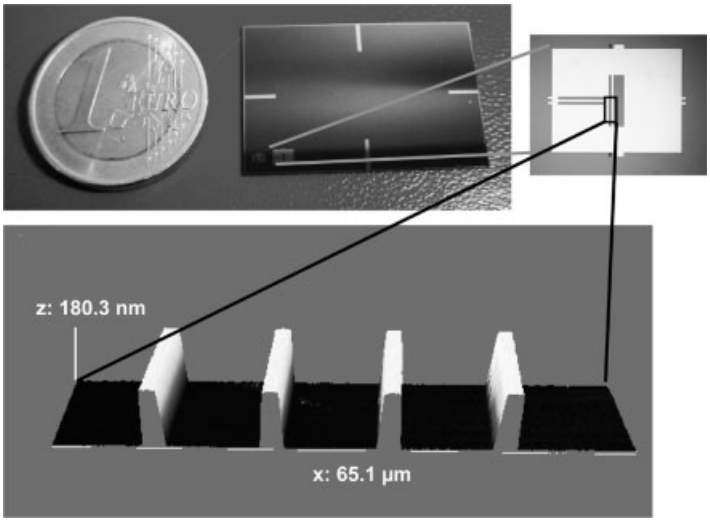

Fig. 18.12 SiO_2/Si layer thickness standard for the field of application "ellipsometry". The general survey (view from above) is shown on the upper left. On the right above, the structure for the topographic measurement with the SFM can be seen. The lower image shows SPM-mapping of the four lines of this range.

accessible for measurements with a scanning probe microscope. Comparisons between the results obtained on these structures with a metrological scanning force microscope (SFM) and results from XRR investigations in the center of the sample furnished excellent agreement of the procedures within the scope of the uncertainty. In comparison to XRR results, ellipsometric thickness values based on a simple computation model were systematically too thick. A least square fit showed a constant offset of 1 nm and a linear deviation of 1 %. This systematic effect can be corrected by a calibration of the ellipsometers using the XRR calibrated SiO_2 layer thickness standards. This could impressively be demonstrated by investigations on the two calibrated sets and another SiO_2 standard [22].

18.4 Outlook

The above survey shows that a large number of different standards is available for the range of scanning probe microscopy. In future, they will have to be selectively used for the calibration of scanning probe devices. Due to this the VDI/VDE-GMA Committee 3.43 "Standards for Nanometrology" [23] has started to draw up directives, which are to support users in the testing and calibration of their devices. Almost the same applies to the use of nanometre layer thickness standards for X-ray reflectometry and ellipsometry. In the case of the standards for scanning probe microscopy, the next objective is to link atomic plane single-crystal surfaces up with the SI unit of length "metre." For this, X-ray interferometry could serve as the required metrological basis [24]. For a further reduction of measurement uncertainties for scanning probe microscopy, it is necessary to investigate the interaction between sample and probe more exactly. As the processes that take place upon probing and scanning and the occurring interactions are not yet exactly known, quantifiable statements cannot be made. This lack of knowledge leads to measurement uncertainties whose sum may lie in the upper sub-nanometre range.

Acknowledgments

The authors wish to express their gratitude to all persons involved from BAM, Berlin, PTB Braunschweig and Berlin, who in the course of the past few years have actively participated in the two projects and have thus contributed to their success. Special thanks are due to our numerous partners from industry (NanoWorld Services GmbH/Nanosensors GmbH, Wetzlar; Ibsen S/A, Farum, Denmark; Image Metrology APS, Lyngby, Denmark; Präzisionsoptik, Gera; Bruker AXS, Karlsruhe; Seifert, Ahrensburg; GKSS FZ, Geesthacht; OTB, Berlin; LOT-Oriel GmbH, Darmstadt; SOPRA, Bois Colombes, France), Fraunhofer Institute as well as to institutes inside and outside universities (Institut für Werkstoff

und Strahltechnik (IWS), Dresden; Leibniz – Institut für Oberflächenmodifizierung e. V. (IOM), Leipzig; Institut für Mikroelektronik, Stuttgart University; Institut für Mikrotechnologie (imt), Hannover University and Institut für Halbleitertechnik, TU Braunschweig) and other national metrology institutes (National Physical Laboratory (NPL), Danish Institute of Fundamental Metrology (DFM)). The SPM transfer standards have been developed within the scope of the EU project SMT4-CT95-2018 "Transfer Standards for SPM." The heterostructure standards were investigated within the scope of a feasibility study of the German Nanotechnology Competence Center "Nanoanalysis." The nanometre layer thickness standards, the samples for tip characterization and the nanoroughness standards were developed and tested within the scope of the programme "Nanoscale Standards" promoted by the BMBF.

References

1 H.-U. Danzebrink et al.: Metrologische Rastersondenmikroskope – Messgeräte für die dimensionelle Nanometrologie (Metrological Scanning Probe Microscopes – Instruments for Dimensional Nanometrology), *these proceedings*.

2 M. Senoner et al., Testing the lateral resolution in the nanometre range with a new type of certified reference material, *these proceedings*.

3 J. Garnaes, N. Kofod, J. F. Jørgensen, A. Kühle, P. Besmens, O. Ohlsson, J. B. Rasmussen, P. E. Lindelof, G. Wilkening, L. Koenders, W. Mirandé, K. Hasche, J. Haycocks, J. Nunn, and M. Stedman, Nanometre scale transfer standards, in *Proceedings for Euspen 1st International Conference and General Meeting of the European Society for Precision Engineering and Nanotechnology*, edited by: P. McKeown, J. Corbett et al., on May 31st–June 4th 1999, Congress Center Bremen, Germany, Vol. 2, (1999) pp. 134–137.

4 Updated lists of commercially available standards can be found on the PTB website http://www.ptb.de/de/org/5/51/514/index.htm.

5 T. Dziomba et al., Towards a guideline for SPM calibration, *these proceedings*.

6 D. Keller, Reconstruction of STM and AFM images distorted by finite-size tips, Surf. Sci. **253**, 353 (1991).

7 P. M. Williams, K. M. Shakesheff, M. C. Davies, D. E. Jackson, and C. J. Roberts Blind reconstruction of scanning probe image data, JVST B **14**(2), 1557–62 (1996).

8 J. S. Villarrubia, Algorithms for scanned probe microscope, image simulation, surface reconstruction and tip estimation, J. Nat. Inst. Stand. Technol. **102**, 435–454 (1997), see also http://ois.nist.gov/jres/102/4/j24vil.pdf.

9 U. Hübner, W. Morgenroth, H. G. Meyer, Th. Sulzbach, B. Brendel, and W. Mirandé, Downwards to metrology in nanoscale: determination of the AFM tip shape with well-known sharp-edged calibration structures. Appl. Phys. A **76**, 913–917 (2003).

10 F. Meli, Critical dimension (CD) measurements using a metrology AFM profiler, in *Proceedings of the 4th Seminar on Quantitative Microscopy QM 2000 Dimensional Measurements in the Micro- and Nanometre Range, Semmering, Austria* (January 12–14 2000, PTB Report F-39 (2000)), pp. 58–65, edited by Klaus Hasche, Werner Mirandé, and Günter Wilkening.

11 M. Oberthaler, Präzisionslineale auf Nanometerskala, Machbarkeitsstudie Kompetenzzentrum "NanoClub Lateral" (Precision Straight Edges on Nanometre Scale, Feasibility Study Competence Center "NanoClub Lateral," Konstanz University, 2001.

12 Th. Dziomba, W. Häßler-Grohne, H. Bosse, H.-U. Danzebrink, and G. Wilkening, Influence of nanostandard properties on calibration procedures of SPMs, Proc. 4th International Euspen Conference **2**, 491–494 (2003).

13 D. Wüllner, H.-H. Wehmann, P. Bönsch, A. Schlachetzki, and R. Lacmann, III/V Semiconductor calibration standards for atomic-force microscopy, *in Proceedings of the 2nd Seminar on Quantitative Microscopy: Geometrical Measurements in the Micro- and Nanometre Range with Far and Near Ffield Methods,* , Wien, Austria (November 6–7 1997, PTB Report F-30 (1997)), pp. 154–157, edited by Klaus Hasche, Werner Mirandé, and Günter Wilkening.

14 L. Koenders, Heterostrukturnormale für die Kalibrierung von Rastersondenmikroskopen, Machbarkeitsstudie Kompetenzzentrum "Nanoanalytik" (Heterostructures for the Calibration of Scanning Probe Microscopes, Feasibility Study Competence Center "Nanoanalysis," Hamburg, (2002).

15 J. Kwon, J. Hong, Y.-S. Kim, D.-Y. Lee, K. Lee, S.-M. Lee, and Sang-il Park, Atomic force microscope with improved scan accuracy, scan speed, and optical vision, Rev. Sci. Instrum. **74**, 4378 (2003).

16 K. Herrmann, L. Koenders, H.-U. Danzebrink, K. Hasche, G. Wilkening, F. Pohlenz, and K.-P. Hoffmann, Dimensional metrology using scanning probe microscopy, Lecture Sino-German Symposium on Micro Systems and Nano Technology, 5–7 September 2001, Braunschweig.

17 L. Koenders et al., Height and pitch at nanoscale – how traceable is nanometrology, *these proceedings.*

18 S. Gröger et al., "Atomic flat" silicon surface for the calibration of stylus instruments, *these proceedings.*

19 R. Krüger-Sehm, T. Dziomba, and G. Dai, Profile Assessment of Nano Roughness Standards by Contact and Non-Contact Methods. XI. Int. Oberflächenkolloquium Chemnitz, 2–3. February 2004, Chemnitz, Verlag Shaker, p. 31.

20 P. Thomsen-Schmidt, K. Hasche, G. Ulm, K. Herrmann, M. Krumrey, G. Ade, J. Stümpel, I. Busch, S. Schädlich, A. Schindler, W. Frank, D. Hirsch, M. Procop, and U. Beck, Realization and metrological characterization of thickness standards below 100 nm, Appl. Phys. A, DOI:10.1007/s00339-003-2273-7.

21 M. Krumrey, M. Hoffmann, G. Ulm, K. Hasche, and P. Thomsen-Schmidt Thickness determination for SiO_2 films on Si with X-ray reflectometry at the Si K edge, Thin Solid Films, *in press.*

22 P. Thomsen-Schmidt, Consistent standards for nanometrology or step height versus film thickness measurement, Proc. XI. Oberflächenkolloquium Chemnitz, 2–3. 2004, Chemnitz, Verlag Shaker, 2004, p. 108.

23 VDI/VDE-Gesellschaft Mess- und Automatisierungstechnik, see http://www.vdi.de or (http://www.vdi.de/vdi/organisation/schnellauswahl/fgkf/gma/index.php).

24 A. Yacoot, U. Kütgens, L. Koenders, and T. Weimann, A combined scanning tunneling microscope and X-Ray interferometer, Meas. Sci. Technol. **12**, 1660–1665 (2001).

19
"Atomic Flat" Silicon Surface for the Calibration of Stylus Instruments

S. Gröger and M. Dietzsch

Abstract

For the calibration of stylus instruments the extraction of the total profile defined in DIN EN ISO 3274:1998 takes place with a surface flatness standard. The total profile is the digital profile of the traced profile relative to the reference profile. The shape of the reference profile is the practical realization of the theoretical exact profile. Its deviations depend on the deviations of the guide as well as the external and internal disturbances. The total profile is the result of the reference profile and the deviations of the standard.

For calibration an ideal smooth and flat surface (flatness standard) should be used for the extraction of the total profile. Commonly used optical flats have flatness deviations above 40 nm. Flats without geometrical deviations lead to the total profile as reference profile. Single crystal silicon develops "atomic flat" surfaces (facets) during crystal growing. The grown facets with the size of 15 mm by 40 mm have been tested with a modified stylus instrument. The reduction of the disturbances from the environment and the internal influences produced a total profile of less than 20 nm on the length of 30 mm.

19.1
Calibration of Stylus Instruments

For the reduction of measurement uncertainty measurement instruments have to be developed. The characteristics of these measurement instruments are evaluated through calibration. The approach discussed in this paper is the improvement of stylus instruments through calibration with a new calibration standard for the measurement in the range of a few nanometers.

Nanoscale Calibration Standards and Methods: Dimensional and Related Measurements in the Micro- and Nanometer Range.
Edited by Gunter Wilkening, Ludger Koenders
ISBN: 3-527-40502-X

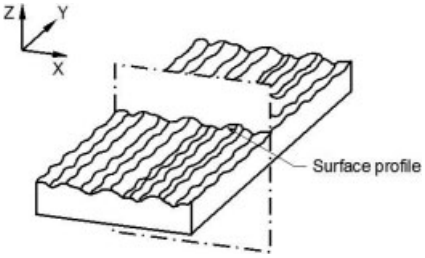

Fig. 19.1 Surface profile [1].

Stylus instruments scan surfaces with a stylus and detect deviations which are presented in a surface profile (Figure 19.1). The surface profile is defined in DIN EN ISO 4287:1998 as

the profile that results from the intersection of the real surface by a specified plane [1].

The calibration of stylus instruments takes place among other standards with a surface flatness standard [2]. The result of tracing the flatness standard is the *residual profile*. It is defined in DIN EN ISO 3274:1998 as

the primary profile obtained by tracing a ideally smooth and flat surface (optical flat) [3].

The *primary profile* is defined in the same standard as

the total profile after the application of the short wavelength filter, λ_s. It is the basis for digital profile processing [3].

The filter for short wavelength λ_s, which is applied in the primary profile causes problems for the evaluating of profiles in the range of a few nanometers. Filtering with λ_s leads to a reduction of amplitudes according to the filter characteristic. The identification of the effects influencing the profile can only be achieved with a profile without filtering.

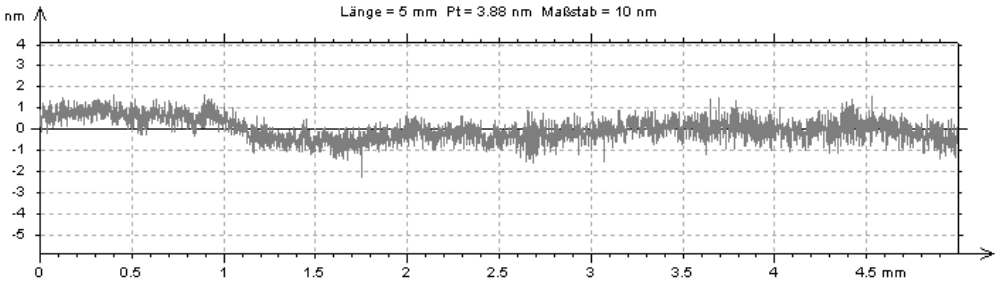

Fig. 19.2 Primary profile (total height 3.8 nm).

For the evaluation of the characteristics of a stylus instrument two new approaches have to be considered.

1. The total profile as an unfiltered profile is the closest realisation of the traced profile.
2. The traced profile as the center line of the stylus tip causes false reproduction of the real surface. Equidistant irregularities on the traced surface are not detectable without the determination of the real surface.

The traced profile is defined in DIN EN ISO 3274:1998 as

the locus of the center of a stylus tip as it traverses the surface within the intersection plane [3].

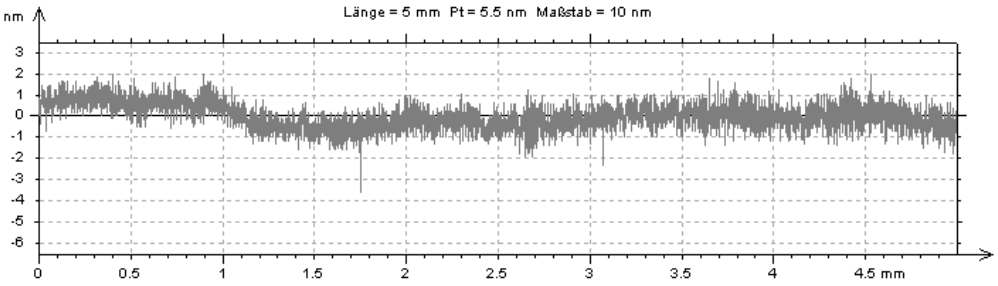

Fig. 19.3 Total profile (total height 5.5 nm).

Defined in DIN EN ISO 3274:1998 the *total profile* is

the digital profile of the traced profile relative to the reference profile. The shape of the reference profile is the practical realization of the theoretical exact profile. Its deviations depend on the deviations of the guide as well as the external and internal disturbances [3].

The total profile is the result of the reference profile, the deviations of the standard and the external and internal disturbances. The closest profile to the real profile for the calibration of stylus instruments is total profile. The real profile for the measurement with a stylus instrument is the boundary between the contact probe and the surface of the standard.

The real profile is part of the real surface. The real surfaces of workpieces have different functional meanings. Depending on the physical interaction in the atomic structures different functions lead to different real surface. The "mechanical and the electro-mechanic" are two different real surfaces [4]. The functional surface for the calibration of stylus instruments is the "mechanical surface" as

surface limiting the body and separating it from the surrounding medium [1].

The "mechanical" real surface of a workpiece is defined in ISO/DTS 14406-1 as

"mechanical" *boundary of the erosion, by a spherical ball of the radius r, of the locus of the center of an ideal tactile sphere, also with the radius r, rolled over the real surface of a workpiece [4].*

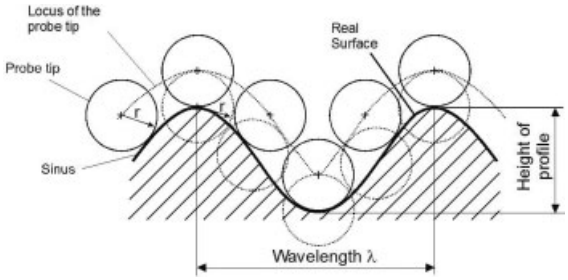

Fig. 19.4 Operations for the determination of the "mechanical" surface.

The result of the application of a circle disk instead of a spherical ball for the determination of the real surface is the real profile. The application of the circle disk produces a two dimensional profile. The development of the mechanical surface is still correct because profiles are also a two dimensional information as a result of a trace in an intersection plane. The connection of the profiles is schematically presented in Figure 19.5.

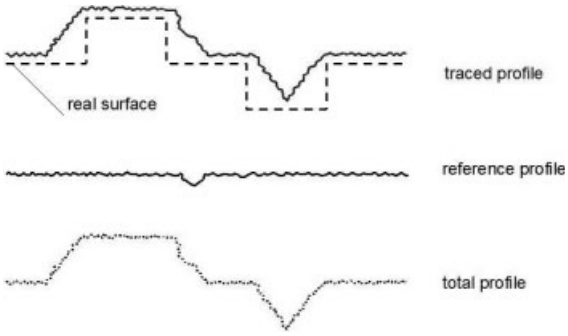

Fig. 19.5 Excessively magnified profiles defined in DIN EN ISO 3274:1998 [3].

Today flatness standards are optical flats with deviations above 40 nm. Considering the development of stylus instruments guide deviations below 40 nm have to be achieved. With the deviations of the optical flat and the deviations of the guide in the same dimension the deviations of the guide can not be separated explicit from the deviations of the optical flat. This thesis is demonstrated in Figure 19.6. For the separation an ideal smooth and flat surface (flatness standard) should be used for calibration. Flats without geometrical deviations would lead to the total profile as reference profile.

Fig. 19.6 Reference profile and traced profile with the same dimension of deviations.

19.2 "Atomic Flat" Silicon as Calibration Standard

Most flatness standards are made of glass. There are also developments in the area of SPM where standards are made of silicon. Standards for the calibration of the vertical measuring range and standards with different profiles like trapezoidal, triangular, rectangular and arched are also made of silicon with different micro technological processes [5, 6]. The usage of silicon as material for standards seems to be beneficial. Therefore the etching of flats has been examined. The resulting deficits are the limits of the dimensions of the wafer and the deviations resulting from the etching process [7].

Silicon can grow also flats during the pulling of single crystal cylinders from the melt by the Czochralski process for the production of wafers. These flats are {111} facets with a theoretical flatness < 1 nm. These facets are therefore called "atomic flat" [8]. The sizes of the facets depend on the diameter of the cylinder and the axial gradient of the diameter change [7]. Figure 19.7 is a picture of a silicon cone with four facets. For the research work discussed in this paper facets with sizes of about 15 mm by 40 mm have been selected.

Until today the verification of the theoretical "atomic flatness" as characteristic of a mechanical surface has not been proved through measurement.

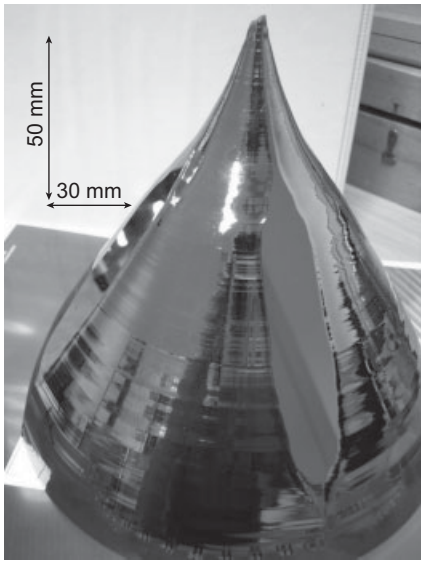

Fig. 19.7 Silicon cone with "atomic flat" facet.

19.3 Selection of the Measurement Instrument for the Assessment of Flatness

A flat surface can be extracted by three-dimensional measurements or by the mathematical combination of two-dimensional profiles to a three-dimensional object [9].

For the evaluation of "atomic flat" surfaces on silicon cones the following characteristics are required:

- application range depending on the silicon cone height
- planar measurement range of at least 600 mm^2 (facet size 15 mm by 40 mm)
- vertical resolution 1 % of expected deviations, the expected deviations are < 1 nm, consequently a resolution of 10 pm is required
- a measurement uncertainty of 100 nm (10 % of the expected deviations (< 1 nm)) is also required

The sensitive part of these requirements is the vertical resolution. With 3D coordinate measurement machines and form measuring instruments this vertical resolution is not attainable. AFM have a high vertical resolution but a small application range and measurement range. Stylus instruments meet the requirements for the evaluating of the silicon facets.

A stylus instrument, ME 10, with an air bearing reference guide of 100 mm with deviations below 0.1 μm/100 mm and a resolution of 1 nm of the probe had been developed 30 years ago by the company Carl Zeiss in Jena [11].

At the Institute of Production Measuring Technology and Quality Assurance at the Chemnitz University of Technology, these ME 10 measurement instruments have been under investigations for many years. With the addition of an A/D converter a resolution of 3 pm of the probe has been achieved [12].

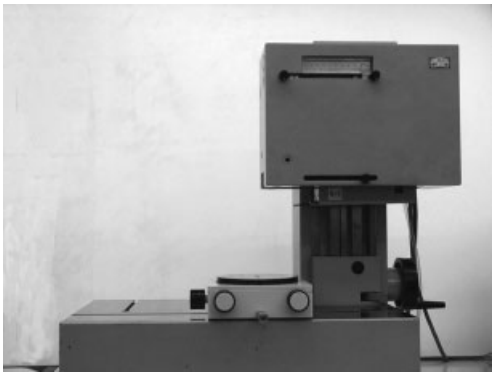

Fig. 19.8 Stylus instrument ME 10 by Carl Zeiss Jena.

19.4
Calibration of the Stylus Instrument ME 10

The ME 10 had been calibrated with a traceable optical flat with a flatness deviation of 0.069 μm. The result of the calibration was a total profile with an obvious influence from vibrations. With a frequency analysis the frequency of 50 Hz had been identified as a source for natural frequency of the measurement unit. For the elimination of this influence the drive unit inside the measurement unit has been replaced by a second stylus instrument in a tandem assembly. With locating the instruments on different tables the vibrations from the drive unit are eliminated from the measurement process. A schema of the tandem assembly is demonstrated in Figure 19.9.

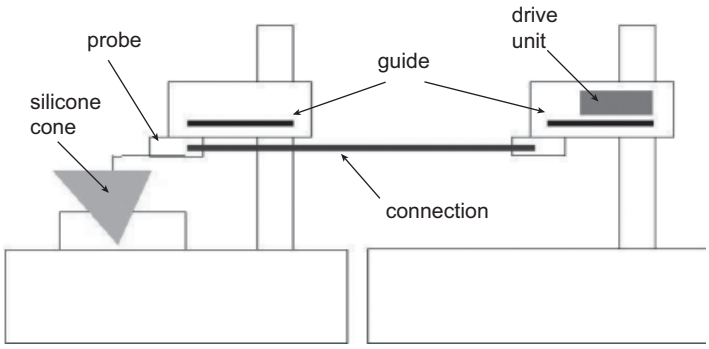

Fig. 19.9 Tandem assembly of two stylus instruments.

After this modification a silicon facet on a cone was used as standard. Profiles extracted with a silicon facet as standard are reference profiles under the assumption that the silicon facets are "atomic flat." The deviations from the silicon falsify the profile at a maximum in the range of the accepted measurement uncertainty. The reference profile still includes the deviations of the guide as well as the external and internal influences. With a step by step change of the environmental and the measurement system conditions the reference profile shows only the deviations of the guide.

Intense temperature gradients during the measurement lead to profiles which represent the temperature change and not the surface. Step one was the elimination of temperature change effects. A repetition of a measurement in the same intersection plane of a facet produced two totally different profiles. Figure 19.10 is a profile with the influence of temperature.

With the covering of the whole tandem assembly with isolation material the heat radiation of the operator during the recording of the measurement data in front of the measurement instrument had been reduced (Figure 19.11).

The location of the measurement instrument in an air-conditioned room is not sufficient to transport the inserted heat from the manual alignment inside the

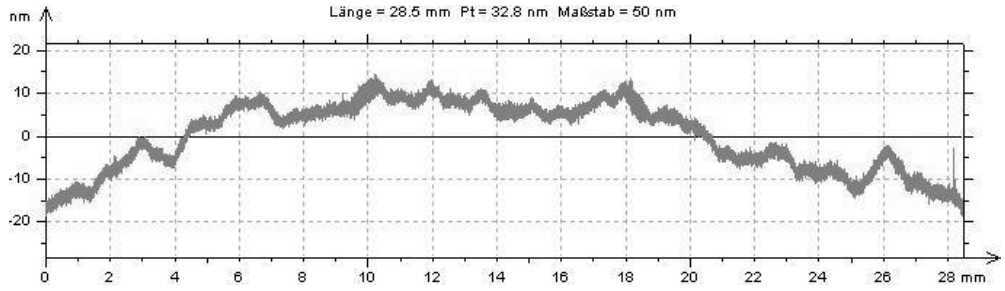

Fig. 19.10 Reference profile with the influence of temperature changes.

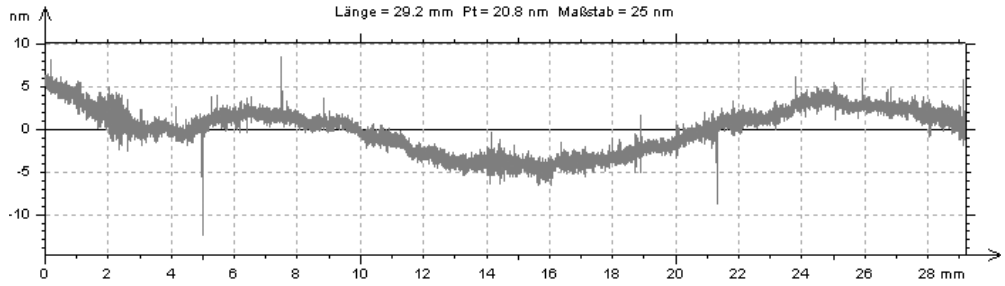

Fig. 19.11 Reference profile after the reduction of the influence of temperature.

cover. To achieve traceable and repeatable results a minimum of 12 h conditioning time has to be allowed.

After the reduction of the influence of temperature a second step was the testing of different locations for the reduction of vibrations from the environment. Different places at the University and in a cellar of a castle with natural-grown ground analysed with the stylus instrument produced interesting and expected results. Placing the measurement instrument on natural-grown ground the deviations resulting from vibrations can be reduced to half.

A calibrated PTB superfine roughness standard mentioned in DIN EN ISO 5436 Type D was included in the calibration procedures. The results of this calibration confirmed the traceability of the measurement instrument characteristics. The characteristics after the reduction of the influences from the environment and the internal disturbances are the content of the next paragraph.

19.5
Characteristics of the Measurement Instrument After Modification

The Figure 19.12 is the reference profile of a facet. The total height of the profile is 17.6 nm over a length of 29.2 mm.

The form of the profile in Figure 19.12 can be compared to the form of the profile in Figure 19.14. The profile was extracted in the same intersection plane of the reversed facet with a total height of 20.8 nm over the same length of 29.2 mm. 3.8 x 13.3 mm) Figure 19.13 is the schema of the error separation method through reversal to detect the influence of temperature and guide deviations [10]. Author: Ref. [10] is not in sequence. Please check.

The resulting deviations are still a superposition of the effects of temperature changes and guide deviations. The marked outliers are a reason for further investigations about the real surface of the silicon facets.

Without the knowledge of the origin of the outliers it is necessary to evaluate further on the unfiltered profiles.

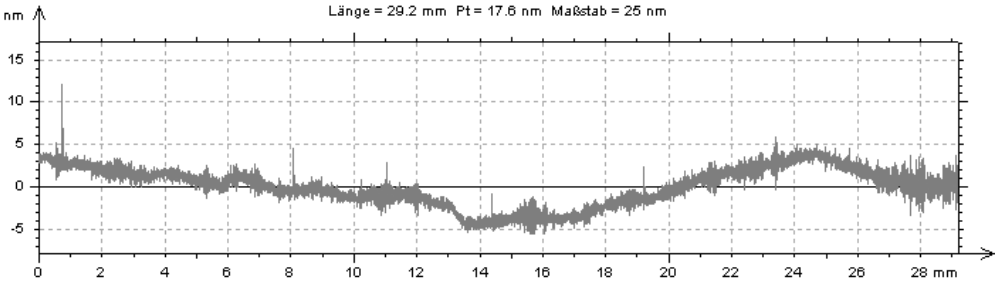

Fig. 19.12 Reference profile, 0°.

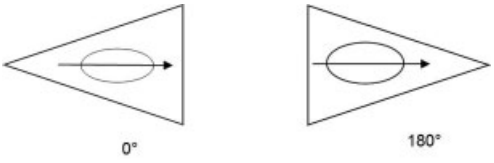

Fig. 19.13 Schema of a silicon cone with a facet and the tracing direction.

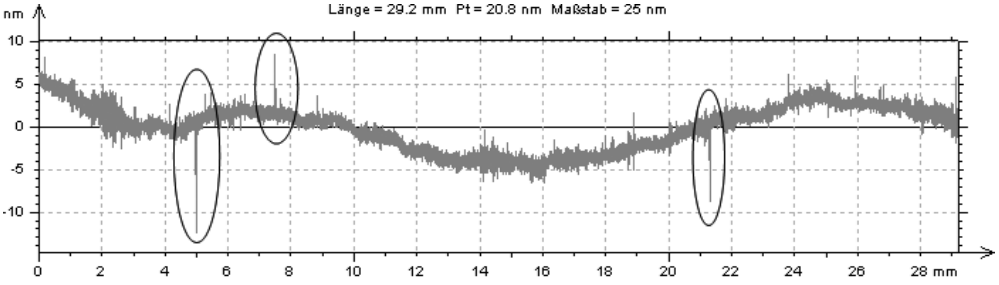

Fig. 19.14 Reference profile, 180°.

19.6 Conclusions and Outlook

The flatness of the "atomic flat" facets can not be proved without the modification of a measurement instrument. Using the silicon facets as standard during modification external and internal influences like temperature changes and vibrations are detectable. The results show that a standard without geometrical deviations is a great improvement for the calibration of stylus instruments for the measurement in the range of a few nanometers.

The proof of the "atomic flatness" requires a further development of the stylus instrument. The combination of profiles to a three dimensional object is possible with different mathematical procedures. The selection of the procedure depends on the ability of the measurement instrument and will be a subject for further investigation. The use of the facets as calibration standards is also the topic of a planned research project. The separation of the facets to smaller pieces to be applied in other measurement instruments without changing the characteristics of the facet will be the main subject of research.

References

1 DIN EN ISO 12179: 2000, Geometrische Produktspezifikation (GPS). Oberflächenbeschaffenheit: Tastschnittverfahren, Kalibrierung von Tastschnittgeräten.

2 DIN EN ISO 4287: 1998, Geometrische Produktspezifikation (GPS) Oberflächenbeschaffenheit: Tastschnittverfahren; Benennungen, Definitionen und Kenngrößen der Oberflächenbeschaffenheit.

3 DIN EN ISO 3274: 1998, Geometrische Produktspezifikation (GPS). Oberflächenbeschaffenheit: Tastschnittverfahren, Nenneigenschaften von Tastschnittgeräten.

4 ISO DTS 14406 (E): 2003, Geometrical Product Specifications (GPS) – Extraction

5 J. Frühauf, S. Krönert, and U. Brand, Tiefen- und Längennormale aus Silizium. tm -Technisches Messen **68**, 7–8 (2001).

6 J. Frühauf, S. Krönert, Linear silicon gratings with different profiles: Trapezoidal, triangular, rectangular, arched, in X. International Colloquium on Surfaces, Proceedings Chemnitz University of Technology (2004).

7 J. Frühauf, Charakterisierung von Ebenheit und Rauheit gewachsener Silizium-{111}-Facetten, Laborbericht 07/01, Technische Universität Chemnitz.

8 K.-T. Wilke, Kristallzüchtung, Deutscher Verlag des Wissens, Berlin, 1988.

9 ISO/TS 12781-2: 2003-12, Geometrische Produktspezifikation (GPS) – Ebenheit – Teil 2: Spezifikationsoperatoren

10 C. Evans, Keynote paper: Self-calibration, reversal, redundancy, error separation, and absolute testing, Annals CIRP **45**(2), 1996.

11 Manual of the ME 10 by Carl Zeiss Jena, 1972.

12 Th. Walter, Bewerten von Silizium Oberflächen mit modifizierten Tastschnittgeräten. student research paper, 2003.

20
Investigations of Nanoroughness Standards by Scanning Force Microscopes and Interference Microscope

R. Krüger-Sehm, T. Dziomba, and G. Dai

Abstract

Roughness standards are needed to calibrate scanning force microscopes (SFMs) for the use in surface metrology. As a further development beyond the existing standards like the well-known "Halle"-roughness standard specimens and the diamond-turned superfine roughness standards, specimens generated by a new manufacturing technique were investigated. The so-called "Nanogrinding" process was used to generate specimens with roughness areas turning out a random surface profile in one direction and uniform profile in the other. Like the other roughness standard specimens, the aim is the repetition of the profile. Its roughness amplitudes are between 20 nm and 100 nm. This chapter describes the surface characteristics of the standards, using the results of the SFM and optical topography evaluation techniques. Statistical methods like the correlation function are used to describe the degree of similarity between the areas of profile repetition. Derived from these results, conclusions are drawn for further development.

20.1
Introduction

Scanning force microscopes (SFMs) have proven their capabiliy to yield comparable measurement results on a lot of calibration specimens [1] that are available for the calibration of horizontal and vertical axes as well as for the determination of flatness, straightness, and angular deviations of the scanners. However, specimens and procedures for the calibration of roughness in the range between 10 nm and 100 nm – a range particularly relevant for the SFM – are not yet available. The comparability of their measurements to those of the well-established contact stylus instruments is consequently still a challenge. To close this gap, the National Metrological Institute of Germany, the PTB, joined with the Institute for Microtechnology (IMT) in Hannover, in a project funded by the German Ministry of Education and Research (BMBF). The aim was to develop a new kind of Nano-

Nanoscale Calibration Standards and Methods: Dimensional and Related Measurements in the Micro- and Nanometer Range.
Edited by Gunter Wilkening, Ludger Koenders
ISBN: 3-527-40502-X

roughness calibration standard. This chapter reports on the measurement results gathered on different instruments and gives an insight into the interactions between instrument features, standardization, and manufacturing aspects.

20.2 Standardization Aspects

In the field of contact stylus instruments the matrix of geometric products specifications (GPS) standardization covers all applications feasible with these instruments. This concerns

- filtering wavelengths and scan range on the long wavelength side,
- short wavelength filter cutoff and sampling density in the horizontal direction on the short wavelength side,
- measurement conditions dependent on the type and amplitudes of the topography,
- calibration standards and adequate calibration procedures, and
- roughness standards to characterize the behavior of the whole measurement systems as reaction to dynamic inputs.

By the standard ISO 4288 [2] conditions for the measurement with contact stylus instruments are given in dependence of the surface roughness. An excerpt is shown in Table 20.1.

For a calibration standard of types D1 [2] and D2 according to ISO 5436-1 [3] intended for the use with a profile filter cutoff length of $\lambda_c = 0.25$ mm, the length of the profile has to be at least five times of λ_c, that means 1.25 mm. The roughness standard specimens introduced in 1995 [4] contain such features. In Figure 20.1, a specimen is shown where the profile repetition can be recognized. During its use a set of traces is measured at agreed positions as shown below. The measured traces also have a length of five times λ_c. So the extraction of information from the surface remains constant, even if the arrangement of the traces deviates from the agreed position. For the comparison with interference microscopes, the

Table 20.1 Measurement conditions for contact stylus instruments according to ISO 4288

Periodic profile *RSm* (mm)	Aperiodic profile *Rz* (µm)	*Ra* (µm)	Profile filter wavelength λ_c (mm)	Evaluation length l_m (mm)
0.01–0.04	<0.1	<0.02	0.08	0.40
0.04–0.13	0.1–0.5	0.02–0.1	0.25	1.25
0.13–0.4	0.5–10	0.1–2	0.8	4.0
0.4–1.3	10–50	2–10	2.5	12.5
1.3–4	>50	>10	8	40

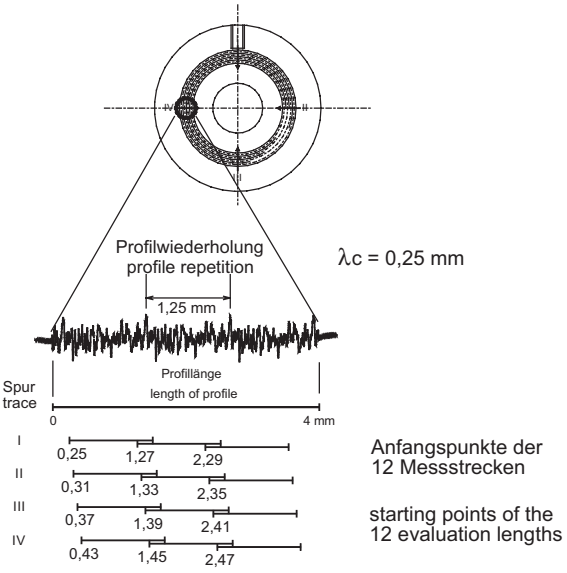

Fig. 20.1 Roughness calibration standard with measurement scheme for $\lambda_c = 0.25$ mm. The starting points of the evaluation lengths are noted below the profile, referring to the outer beginning of the profile.

measurement over this profile length takes already some efforts because of the limited measurement field of view of interference microscopes (typically 100–700 μm). In [5], the conditions for the microscope are defined by several measurement fields with a certain amount of displacement and overlap between them.

20.3 Manufacturing of Calibration Specimens

20.3.1 Conditions for Smaller Roughness

This measurement strategy is transferred now into the next finer roughness range noted in the first line of Table 20.1, thus setting the manufacturing conditions for the Nanoroughness standards.

By a look into this table two problems arise: the measurement conditions in the first line have an open lower end, and furthermore, they do not fit to the specifications of most of the SFMs. This means in detail:

- The rules for roughness values below 100 nm leave the lower roughness limit open, where the next finer cutoff (in an assumed extrapolation for $\lambda_c = 25$ μm) should start.
- A waviness cutoff wavelength of 80 μm has to be applied. Following the rules for the roughness calibration specimens described in Chapter 2, a roughness field with a width of 400 μm has to be manufactured and repeated after that length. However,

compared with the typical scan ranges of the SFMs that are usually limited to 100 μm or even less (typically only 20 μm), it is obvious that it would usually take too much effort to measure this complete length of profile and even much more effort to measure the profile repetition. The practical consequence is that the rules for measurements with the SFMs need to be modified. The modifications are determined by the "natural" waviness cutoff wavelength being the double of the scan range, i. e., for instance about 40 μm for a 20 μm scanner. Taking into account the edge influence of modern profile filters only about 15 μm profile length is useable from a typical scan range of 20 μm. This leads to a cutoff of 30 μm and a profile length of about 150 μm, which is consequently to be manufactured and repeated.

20.3.2 Manufacturing Process

The manufacturing process was designed according to these conditions. A modified process of "Nanogrinding" [6] was used. The usual "Nanogrinding" is a lapping process with the specimen holder rotating around its (usually vertical) axis independent of the rotation of the lapping disc.

In the special realization by IMT the grinding grain is embedded in a matrix of a tin disc. Roughness values below $Ra = 1$ nm with an irregular nature in both lateral directions are feasible. For the manufacturing process of roughness calibration specimens the blanks are fixed in their lapping holder, thus avoiding their rotation. The result is a uniform smooth profile in the lapping direction of the circumference and an irregular profile in the radial direction. To demonstrate the feasibility of this technique, specimens of silicon and Sapphire were manufactured with dimensions of 5 mm × 9 mm, having no structure but roughness. As to be seen in Figure 20.2, arbitrarily arranged measurements yielded roughness values in *Rz* of about 40 nm with a considerable amount of variation over the length of the specimens and rather uniform behavior in the grinding direction.

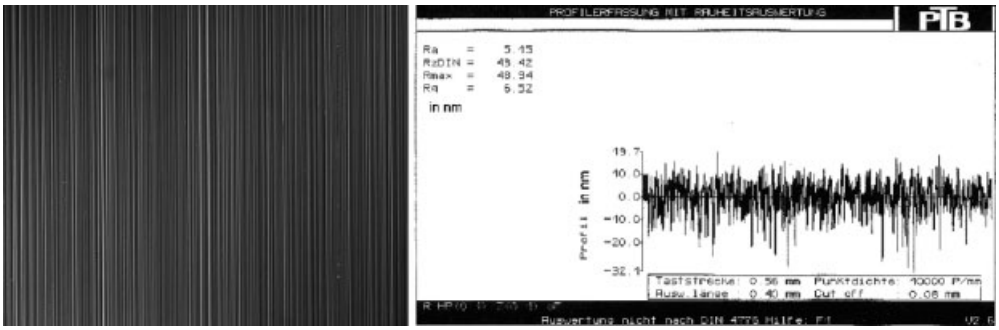

Fig. 20.2 Specimen with a uniform rough surface.

20.3.3
Profile Repetition

For the generation of a rough profile and its repetition according to the conditions developed in Chapter 3.1, the extension of the grinding area must be limited and the blank must be moved laterally in relation to the "table mountains" between consecutive grinding steps. The working principle is shown in Figure 20.3.

By this principle, a plain contact is kept between the tool and the blank, thereby preserving the flattening behavior of the lapping process. Another advantage is that a big number of specimens is manufactured in one step. In order to investigate the features of the repeated profile sections, the separation of the grinding traces was chosen in a way that there was no overlap. In order to identify definite measurement areas, an additional array of sectioning lines nearly perpendicular to the grinding direction was added by a wafer saw. The result is shown in Figure 20.4 with different magnifications.

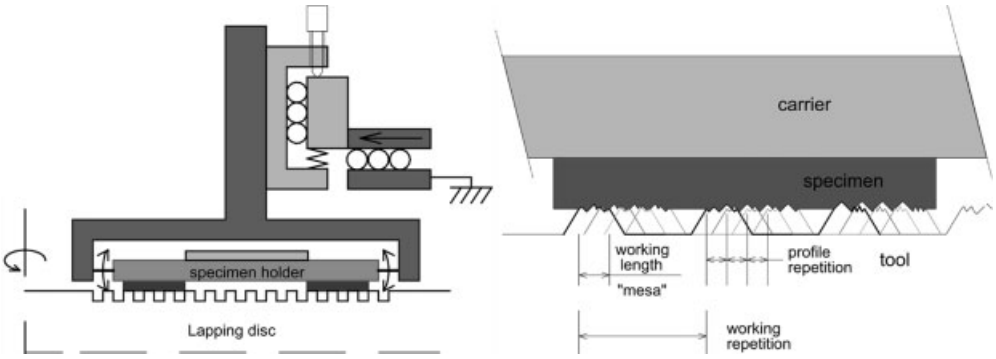

Fig. 20.3 Working principle for profile repetition overview (left) and detail.

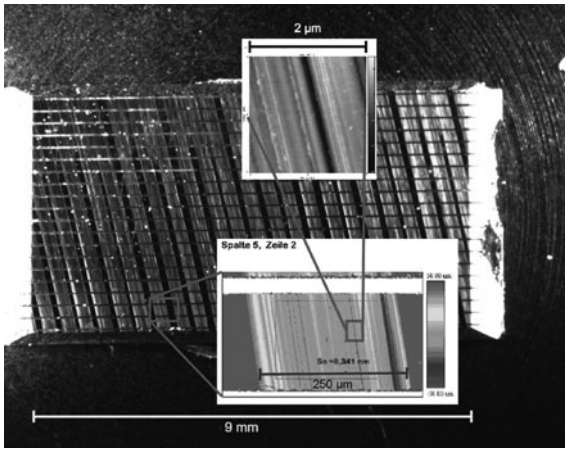

Fig. 20.4 Surface on a silicon specimen after the "Nano-grinding" process; total view by dark field illumination (horizontal lines: sectioning lines cut by a wafer saw), intermediate view by interference microscope with 20× magnification, detail view by SFM.

The small angle of the grinding traces is intended to provide roughness profiles with a lateral offset between the lines of the rectangular scan fields, as it would be necessary for a measurement scheme corresponding to Figure 20.1.

20.4 Measurements

20.4.1 Identification of the Fields of Interest

For the identification of columns containing nominally the same profile, an overview with white light interference fringes was set up. As a result, the columns of interest could be numbered for further measurements.

As Figure 20.5 shows, the columns have a trough-shaped profile, though the tool is an inverse table mountain. For this reason, it was agreed to subtract a cylinder from the raw profile data for all further measurements. This method makes sure that one does not run into problems when the usual filtering technique is applied later. Further on, for the measurement positions of the instruments it was agreed that the centers of their measurement fields are to be adjusted to the center of the dedicated roughness fields, marked by row and column numbers.

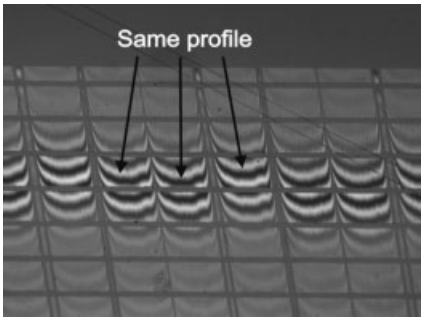

Fig. 20.5 Identification of roughness columns with repeated profiles.

20.4.2 Correlation of Fields

In order to quantify the degree of similarity between different roughness fields the correlation function was calculated. Compared with roughness parameter according to ISO 4287 [7] this parameter is mathematically independent from different interpretations of roughness evaluation software. Moreover, the maximum of the correlation not only quantify the degree of similarity between the measurement fields, but also the displacement between them. This gives a value for the accuracy of the positioning facility, with which the roughness fields are moved to the measurement position.

20.4.3
Measurements with Interference Microscope

For this investigation an interference microscope "Micromap" was used in white light mode with an objective 50×, having a field of view of 160 μm × 120 μm. The sampling density is 0.26 μm in that case. Because of the known short wavelength cutoff of about 2 μm, this instrument can only deliver the agreement for the coarser structures, but offers a fast and easy handling. In Figure 20.6, the measured fields of three columns of row 10 on the specimen NRN6 are to be seen in false color coding, showing the same structure. The evaluation of the normalized correlation function between these fields is to be seen below in Figure 20.6. The correlation to the next but one column increases. The value of the maximum of about 0.8 gives an outlook on the maximum achievable standard deviation of roughness parameters, if measurements would be carried out on both fields. A standard deviation of 20 % of the measured value can therefore be expected.

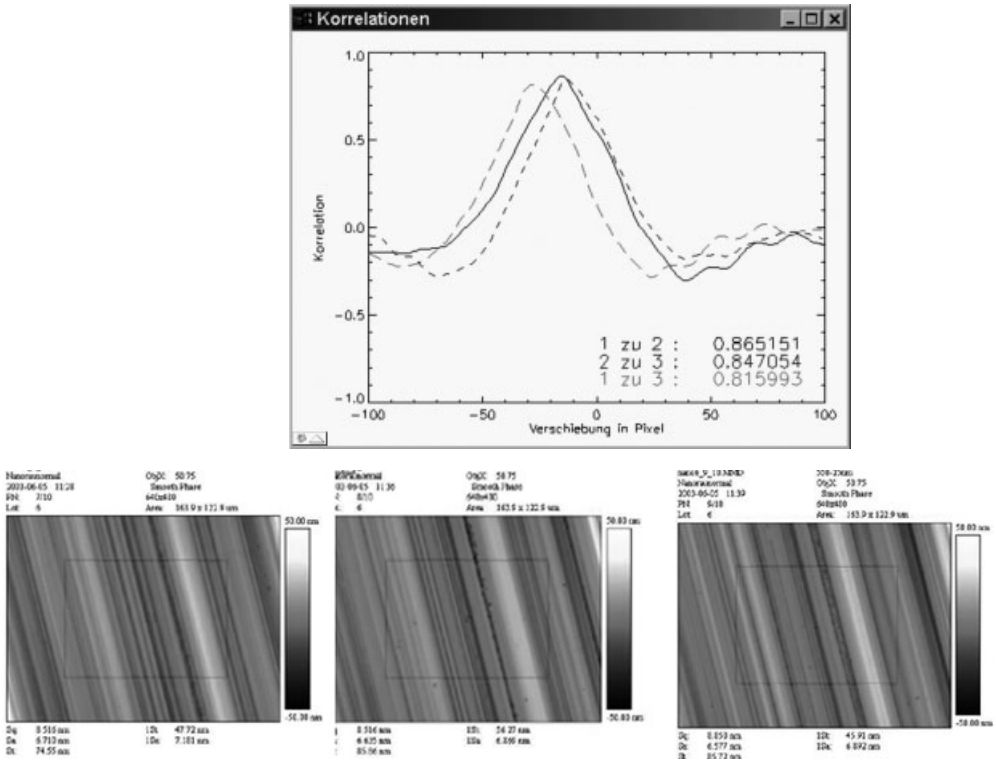

Fig. 20.6 Topography (by "Micromap" interference microscope) and correlations between fields of row 10 in column 7 (number 1), column 8 (number 2) and column 9 (number 3) on specimen NRN6. The displacement due to nonidentical positioning of the fields can be recognized.

20.4.4
Scanning Force Microscope Measurements

In order to get a more detailed view of the surface, an SFM from SIS (Herzogenrath, Germany) was used with a scan length of about 100 μm in one axis and 50 μm in the other. It was used in contacting mode with a silicon tip at a sampling density of 0.1 μm. Because of the better resolution, determined by the 10 nm tip radius, here it was reasonable to calculate roughness parameters without filtering.

With the evaluation software "SPIP" [8] the correlation was also calculated. The correlation between different fields is expressed as a length and therefore values must be normalized to the maximum of the autocorrelation function measured within one field, as it is shown in Figure 20.7.

These results indicate that the correlation between the fields decreased compared to the interferometric measurements. The reason is that the deviations between the ground columns are hidden in the details of the topography and consequently not taken into account when calculating the correlation between interference microscope images, while they are detected well by the higher resolution of the SFM–tip (Figure 20.8).

The evaluation for roughness parameters of four repeated measurements are listed in Table 20.2. The evaluation of the Abbot–Firestone curve yields a smooth curved shape (Figure 20.9), which confirms that the amplitude distribution is ideal for a roughness calibration standard.

The data shown here only represents a very small fraction of the measurement results obtained on these roughness specimens at PTB. For the control of tip wear in the SIS instrument, the tip was examined by using a tip characterizing specimen before and after all measurements. Little degradation of the tip was to be detected, but too small to influence the results significantly.

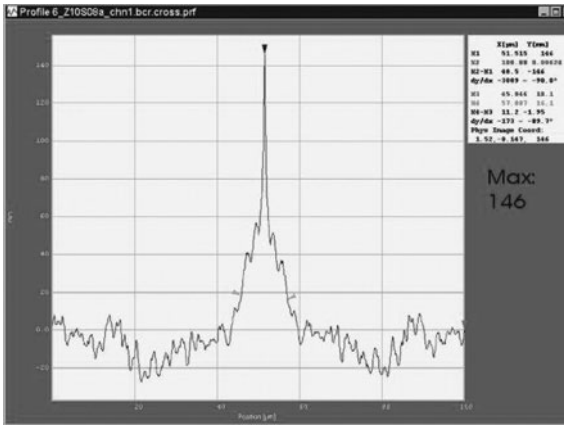

Fig. 20.7 Autocorrelation of the SFM image recorded in field row 10, column 8, maximum 146 nm.

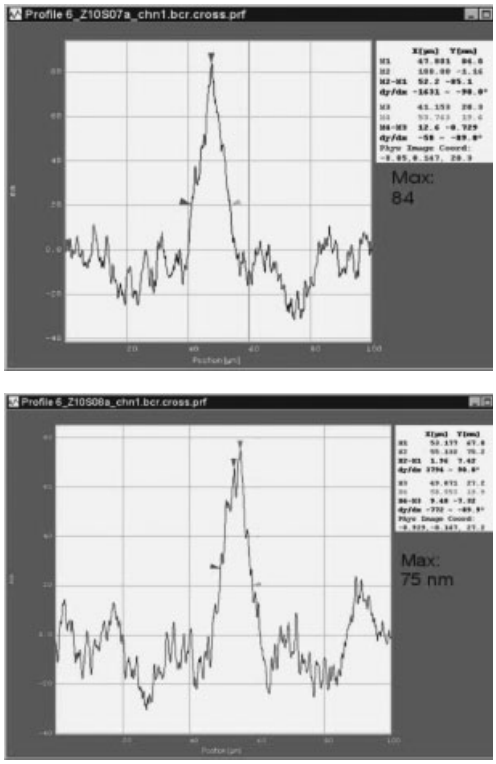

Fig. 20.8 Correlation of SFM images in row 10; in the upper: between columns 7 and 8, maximum 84 nm; in the lower: between columns 8 and 9, maximum 75 nm. Related to the maximum value of correlation of Fig. 20.7, the maximum of correlation is in the upper 0.58, respectively, 0.51 in the lower.

Table 20.2 Results of some roughness parameters derived from SFM measurements

	Average (nm)	**Standard deviation (%)**
Sa	8.3	1.7
Sq	10.8	1.4
Sz	103	18
Spk	11.3	5.3
Sk	23.9	2.6
Svk	13.3	2.6

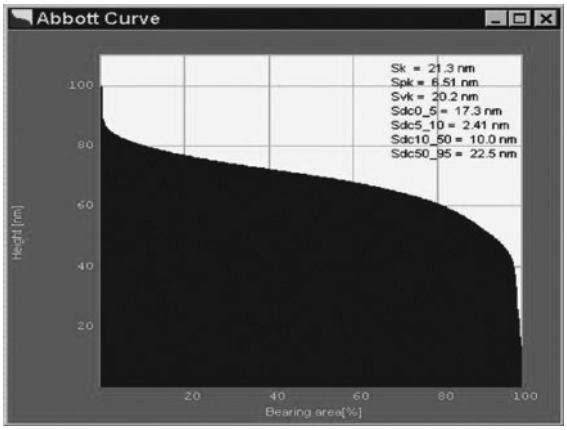

Fig. 20.9 Abbot–Firestone curve of an SFM image.

20.4.5
Long Range SFM Measurements

In the next step, a new long range SFM was used by Dai et al. [9]. Because of its large scanning capability, the measurements and evaluations could be proceeded closer to the rules of ISO 3274 and ISO 4288. The measurement length was 200 μm, the sampling interval 0.1 μm. The profile was divided into five evaluation lengths of 40 μm as it would be for a λ_c of 40 μm. The waviness filtering was approximated by a third-order polynomial fit for a better comparison with the other measurements. The measurements were carried out on specimen NRN5, which is from the same manufacturing set as NRN6, showing a rather agreeable stability of the manufacturing process. The remaining waviness especially at the ends of the profile indicates, however, that the subtraction of a polynomium is not the best choice.

The evaluation of a scanned area of 200 μm × 100 μm delivered the results in Table 20.3.

It should be mentioned here that these measurements are just a first estimation of the measurement capabilities of the long range SFM on nanoroughness standards (Figure 20.10). Therefore, no statistics or reliable uncertainty estimations are available until more detailed comparison measurements are carried out.

Table 20.3 Roughness parameters for NRN5 using long range SFM

Sa	Sq	Sz	Spk	Sk	Svk
13.1	17.1	19.1	19.5	39.2	22.7

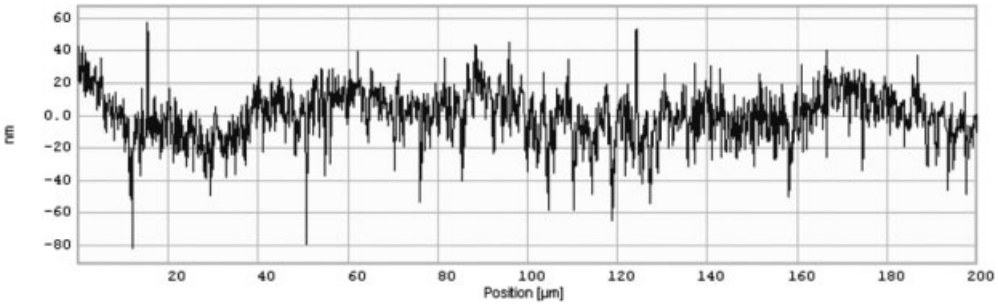

Fig. 20.10 Profile measured on NRN5 with long range SFM.

20.4.6
Relation to Proven Roughness Standards

The correlation function gives an expressive description of the homogeneity of the roughness as an important feature for a roughness calibration standard. For a valuation of the degree of correlation obtained here the correlation of the profile repetition of a classical roughness calibration standard was determined. A maximum value of about 0.95 was achieved. With such calibration standards following a measuring scheme as in Figure 20.1 a standard deviation of about 5 % of the measured parameters is proved.

20.5
Conclusions and Outlook

As a result of the relations between the correlation functions discussed above, the following conclusion is drawn: the degree of correlation between consecutive profiles found here cannot improve the stability of data extraction, which is usually carried out by a set of laterally displaced measurement traces. Nevertheless, the "Nanogrinding" surfaces will be used further on, because they have a lot of useful features, as it was demonstrated here:

- range of *Rz* roughness between 30 nm and 80 nm,
- uniform roughness over complete specimen,
- unidirectional profile,
- wide spectrum of spatial frequencies,
- amplitude distribution is symmetrical, without holes or turning points, and
- dimension of specimen fits to usual instruments holder.

However, another strategy must be established that fits better to the measuring capabilities of commonly available SFMs. In contrast to the stylus instruments, they have a better defined measurement position. They may therefore be easily

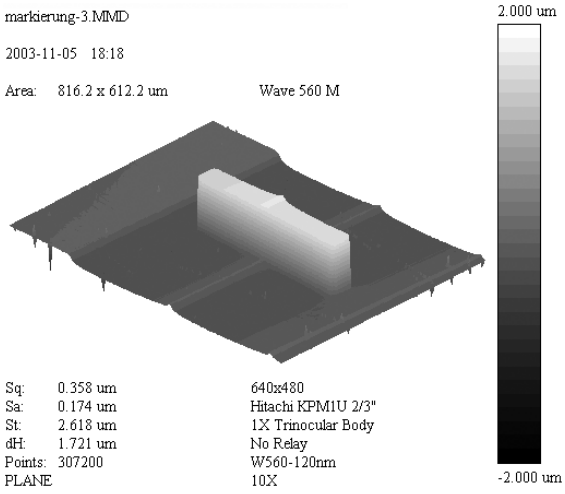

Fig. 20.11 Topograpy of a "measurement island" in a roughness field, about 40 μm × 400 μm.

guided to well-defined (e. g., marked) measurement areas of roughness without any major effort. The idea of marking the measurement field is shown in Figure 20.11 as a first attempt: table mountains are generated by removing the surrounding material, in this case by about 1 or 2 μm. The removing process was ion-beam etching. The remaining of the surface topography as to be recognized in Figure 20.11 is an accompaniment, which is not necessary for the function. Even when a layer with a thickness of, e. g., 0.5 μm is taken away, the residual plateaux can be easily identified visually and by the measuring signal of the instruments. Thus, the fields can be measured definitely by the instruments in the calibration chain.

The design in Figure 20.12 shows a set of frames to be etched in this way, containing some orientation marks (details not shown here). The length of the fields for different cutoffs is between $\lambda_c = 5$ μm and $\lambda_c = 80$ μm with a step factor of 2.

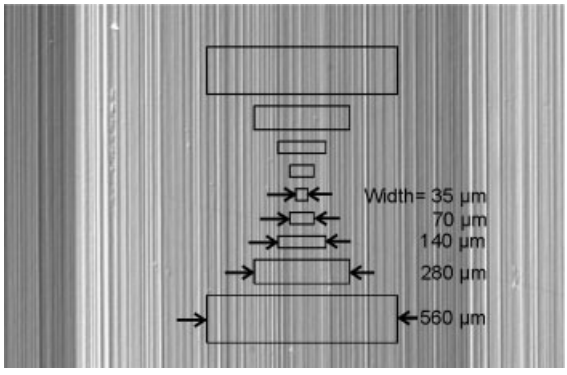

Fig. 20.12 Design for an array of definition marks for fields with scanning lengths between 35 μm and 560 μm.

The homogeneity in grinding direction allows the measurement of similar roughness areas under different conditions.

One advantage of this concept for the calibration procedure should be pointed out: even though these extensive experiments did not really degrade the tip, this principle of table mountains is less burdening for the tip than the originally intended array of measurement fields.

Acknowledgments

The manufacturing of the specimens was carried out by Christos Kourouklis at the IMT, whom the authors owe thanks and appreciation for his respectable work that was a valuable contribution to this development. The authors express their thanks to their colleagues, especially Lutz Jusko for his careful microscopic photos measurements and evaluations, and Ludger Koenders for helpful discussions.

References

1 L. Koenders and G. Wilkening, in *International Comparison on Nanometrology: Step Height (NANO 2) Proceedings of XI International Colloquium on Surfaces* (Chemnitz, 2–3 February 2004), pp. 139–145.

2 DIN EN ISO 4288, *Rules and Procedures for the Assessment of Surface Texture* (1998).

3 ISO 5436-1, *Geometrical Product Specifications (GPS) – Surface Texture: Profile Method; Measurement Standards – Part 1: Material Measures.*

4 W. Hillmann et al., *Superfeine Raunormale (Superfine Roughness Standards). Qualität und Zuverlässigkeit* (Carl Hanser Verlag, München 1997), Vol. 42.

5 R. Krüger-Sehm and J. A. Luna Perez, Proposal for a guideline to calibrate interference microscopes for use in roughness measurement, Int. J. Mach. Tools Manuf. **41**, 2123–2138 (2001).

6 H. H. Gatzen and J.C Maetzig, *Nanogrinding. Precision Engineering* (Elsevier, Oxford, September–December 1997), Vol. 21, pp. 134–139 (Engl.).

7 ISO 4287, *Geometrical Product Specifications (GPS) – Surface Texture: Profile Method – Terms, Definitions and Surface Texture Parameters.*

8 "SPIP": Trademark of Evaluation Software by J. F. Joergensen, Image Metrology, Denmark, www.imagemet.com.

9 G. Dai, F. Pohlenz, H.-U. Danzebrink, R. Krüger-Sehm, and K. Hasche, Metrological scanning force microscopy applicable for surface evaluations, in *Proceedings of XI. International Colloquium on Surfaces, Chemnitz* (Part II, 2–3 February 2004), pp. 1–10.

21
Testing the Lateral Resolution in the Nanometre Range with a New Type of Certified Reference Material

M. Senoner, Th. Wirth, W. Unger, W. Österle, I. Kaiander, R. L. Sellin, and D. Bimberg

Abstract

A new type of test sample for the determination of lateral resolution in surface analysis is presented. The certified reference material BAM-L002 "Nanoscale strip pattern for the length calibration and testing of lateral resolution" is an embedded cross section of epitaxially grown layers of $Al_xGa_{1-x}As$ and $In_xGa_{1-x}As$ on GaAs substrate. The surface of the sample provides a flat pattern with strip widths ranging from 0.4 to 500 nm. The combination of gratings, isolated narrow strips, and sharp edges of wide strips offers improved possibilities for the calibration of length scale, the determination of lateral resolution and the real-time optimization of instrument settings. Numerical simulations of the imaging process illustrate the determination of lateral resolution and give the relation between different parameters used to describe the lateral resolution of instruments in surface chemical analysis.

21.1
Introduction

The lateral resolution of instruments is a key point for the accuracy of imaging in the nanometer range. Correspondingly, the determination of lateral resolution is of great importance for the application of methods of surface analysis and the comparability of results. But in most of the cases, there is only limited information on lateral resolution of instruments. This deficiency is mainly due to the lack of appropriate reference materials.

In the area of surface chemical analysis the lateral resolution is defined as "distance measured either in the plane of the sample surface or in a plane at right angles to the axis of the image-forming optics over which changes in composition can be separately established with confidence" [1]. Note 2 to this definition gives two measures of lateral resolution.

Nanoscale Calibration Standards and Methods: Dimensional and Related Measurements in the Micro- and Nanometer Range.
Edited by Gunter Wilkening, Ludger Koenders
ISBN: 3-527-40502-X

"In practice, the lateral resolution may be realized as either (i) the full width at half maximum (FWHM) of the intensity distribution from a very small emitting point on the sample or (ii) the distance between the 12 % and 88 % intensity points in a line scan across a part of the sample containing a well-defined step function for the signal relating to the property being resolved. These two values are equivalent for a Gaussian intensity distribution. For other distributions, other parameters may be more appropriately chosen. Often, for a step function, the distance between the 20 % and 80 % intensity points or the 16 % and 84 % intensity points in the line scan are used. The latter pair gives the two sigma width for a Gaussian resolution function" [1].

The definition of lateral resolution is based on the smallest distance that can be resolved with confidence. This definition enables a direct estimation of lateral resolution by imaging of gratings with different periods. This method works without any numerical analysis and therefore it is particularly suitable for the "real-time" adjustment of instruments and the optimization of instrument settings. For an exact determination of lateral resolution note 2 of the definition gives two measures. The determination of these measures demands well-defined structures: a very small area or a straight edge (step transition).

At the time, different test samples with geometric and/or material patterns were available. In surface chemical analysis straight edges, mesh bars of copper grids, and gold islands were used for the determination of lateral resolution, but no samples with regular structures with dimensions between lithographic patterns (> 100 nm) and the crystal lattice (< 1 nm) are available. For this reason, BAM developed a new type of test sample: the certified reference material BAM-L002 "nanoscale strip pattern for length calibration and testing of lateral resolution".

21.2 Description of the Reference Material

The strip pattern (Figure 21.1) can be used for the calibration of a length scale and the determination of such instrument parameters as lateral resolution and beam diameter. It is applicable to all measurement methods which are able to differentiate between the materials forming the semiconductor strip pattern. This includes an analysis using electrons, ions, photons or scanned probes. The application of BAM-L002 in scanning electron microscopy (SEM, Figure 21.2), secondary ion mass spectroscopy (SIMS, Figure 21.3), and x-ray photoelectron spectroscopy (XPS) [2] was successfully tested.

The sample is an embedded cross section of a multilayer stack of GaAs, $Al_{0.65}Ga_{0.35}As$, and $In_{0.33}Ga_{0.67}As$ layers on a GaAs substrate. The multilayer stack was grown by metalorganic chemical vapor deposition (MOCVD). The coated 2 inch wafer was sawed into 5×5 mm platelets. A coated GaAs platelet and an uncoated GaAs platelet were brought into close contact and embedded together in conducting epoxy. After curing the epoxy block was ground and

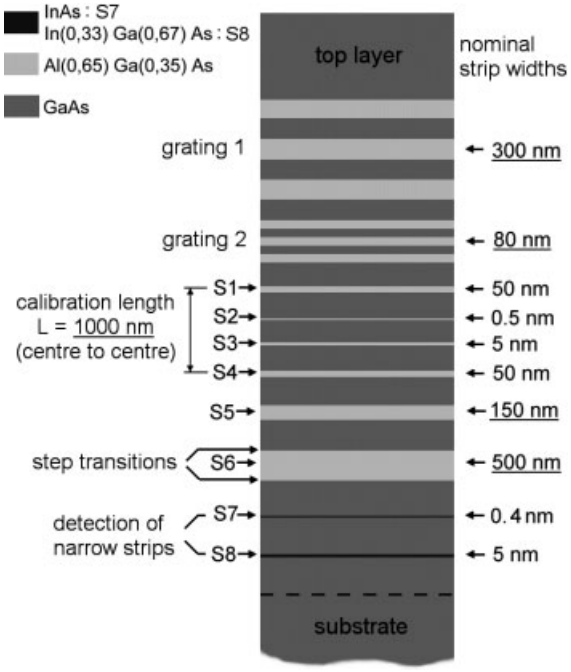

Fig. 21.1 Scheme of the strip pattern. Only the underlined nominal values are certified. The exact values are given in the certificate.

polished perpendicular to the plane of the two embedded platelets. As a result, the surface of the block shows a cross section of the multilayer stack (Figure 21.2). The strip pattern is solely caused by elemental composition and the flat surface shows no substantial three-dimensional structure. Correspondingly, shadowing and edge enhancement like that observed in Auger microscopy at the edges of layers [3] do not appear in imaging of BAM-L002. The calibration length and four strip widths (underlined in Figure 21.1) were certified by transmission electron microscopy (TEM).

Figure 21.3 shows an example of application. BAM-L002 was imaged with a time of flight secondary ion mass spectrometer (TOF–SIMS IV, IONTOF GmbH, Germany). The element mapping for aluminum shows that grating 1 with its 300 nm strips is clearly resolved and grating 2 with the 80 nm strips is at the limit of resolution. The convolution of the strip pattern with a 150 nm wide Gaussian yields a profile (top) that is very similar to that through the measured aluminum distribution (bottom).

21.3
Modeling of Lateral Resolution

Based on the definition of lateral resolution in surface chemical analysis (see above [1]), there are three methods to determine the lateral resolution of imaging

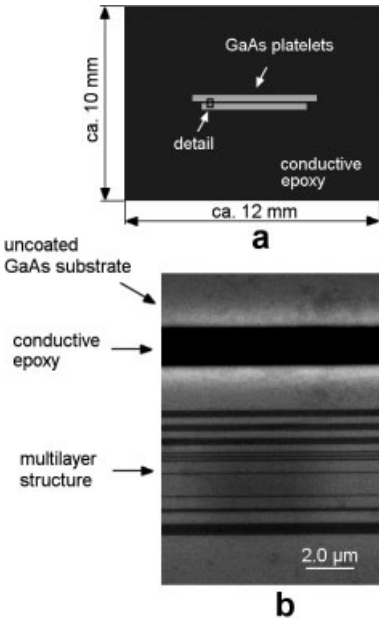

Fig. 21.2 (a) Scheme of the whole sample and (b) the SEM image of the detail marked in Figure 2(a).

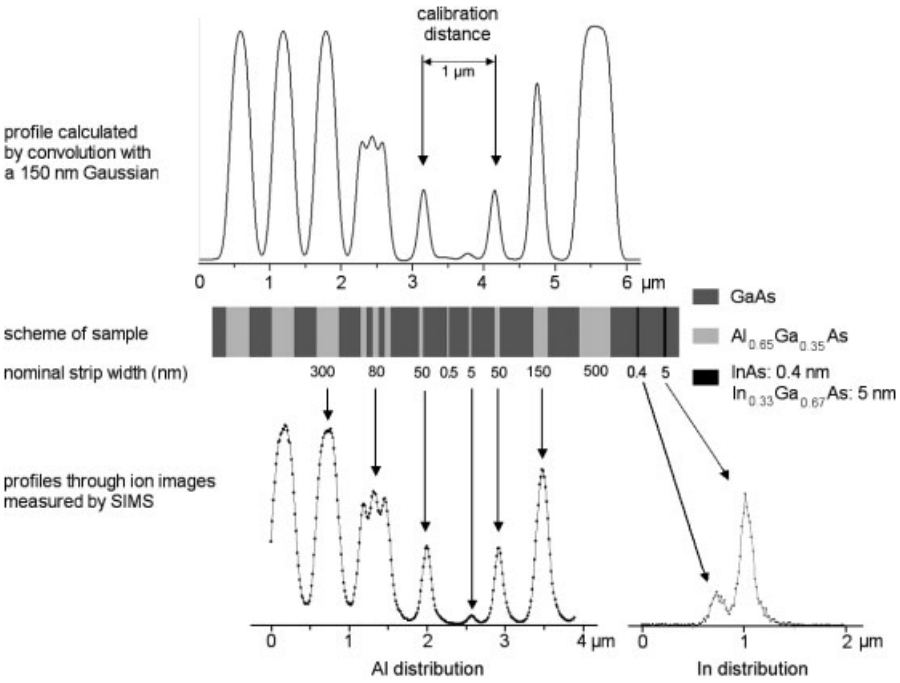

Fig. 21.3 Calculated intensity profile (top) and ToF–SIMS analysis (bottom) of BAM-L002. The measured profiles are accumulated from 256 horizontal line scans. The points are measured values (scan points).

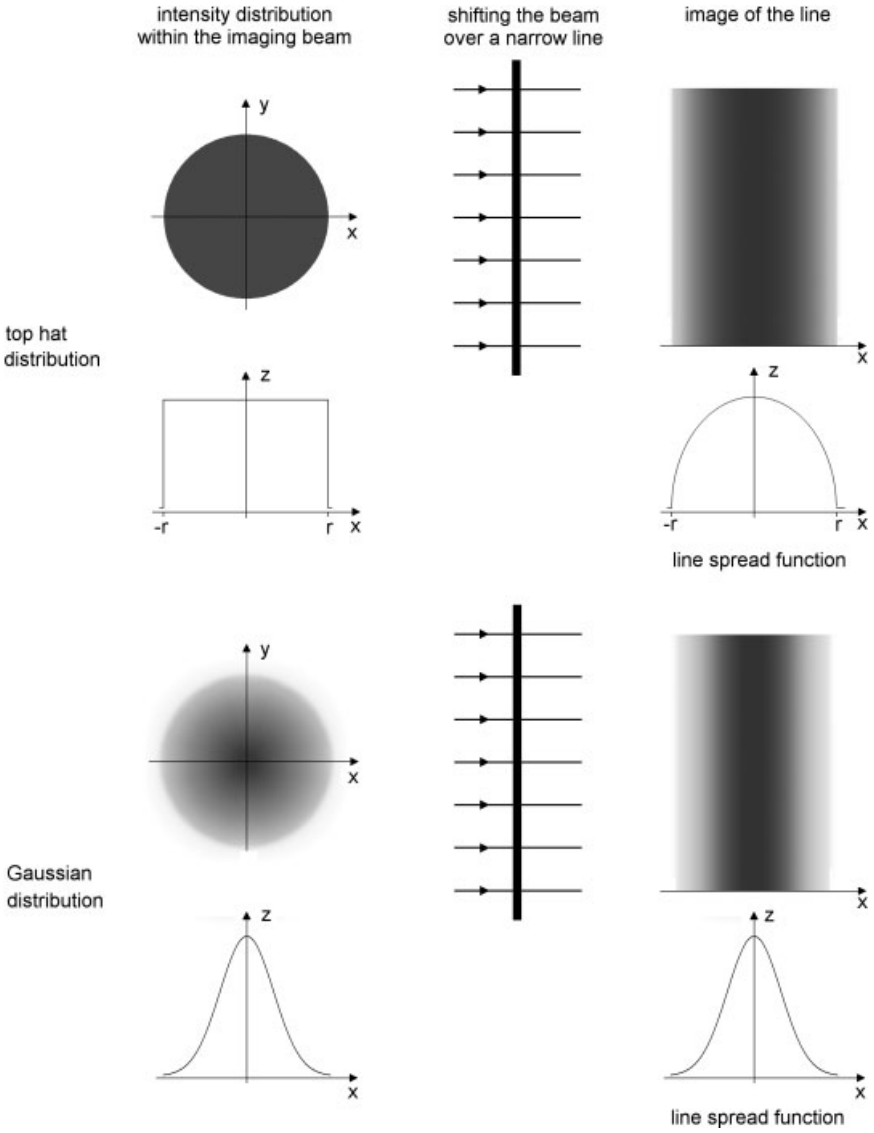

Fig. 21.4 Determination of the line spread function (LSF) for scanned beam instruments demonstrated for two different intensity distributions of incident particles. The *z* values corresponds to the intensity of incident particles and the signal intensity within the image, respectively.

instruments: the imaging of straight edges (step transitions), small areas (points or narrow strips), and gratings. The strip pattern of BAM-L002 enables all these methods. The advantages and limitations of the different methods will be demonstrated by numerical simulations of the imaging process.

Imaging of an object can be simulated by a convolution of the object pattern with the instrumental function of the imaging instrument. Instrumental functions can be represented by the image of a small point (point spread function (PSF)) or a cross section through the image of a narrow line (line spread function (LSF), see Figure 21.4). The latter one is restricted to one dimension, but its determination is more practicable. Imaging of a narrow line is easier than imaging of a small point, because the extended dimension of a line gives higher signal intensities and correspondingly an improved signal-to-noise ratio.

For instruments using scanned beams the PSF corresponds to the two-dimensional intensity distribution of incident particles on the sample surface[1)]. Shifting of this intensity distribution over a narrow line yields the LSF (see Figure 21.4). Mathematically, this corresponds to the integration of the two-dimensional intensity distribution $I(x, y)$ along the direction of the narrow line:

$$\mathrm{LSF}(x) = \int_{-\infty}^{+\infty} I(x,y)\,\mathrm{d}y. \tag{21.1}$$

The LSF is in general different from a cross section through the two-dimensional distribution of intensity on the sample surface [5]. In Figure 21.4, this is demonstrated for the top hat distribution. Only in the case of the two-dimensional Gaussian distribution, which is often used to describe the intensity distribution in light and particle beams, the line spread function is identical to the corresponding one-dimensional distribution:

$$I(x) = \frac{I_0}{\sigma\sqrt{2\pi}} \exp(-x^2/2\sigma^2). \tag{21.2}$$

Therefore, we used the one-dimensional Gaussian distribution for our model calculations. The second model function used is the Lorentzian distribution:

$$I(x) = \frac{I_0 \times b}{\pi(x^2 + b^2)}. \tag{21.3}$$

It has broader tails (Figure 21.5) and may be used to describe strongly blurred spots. The corresponding line spread function is unknown because the integration over the two-dimensional Lorentzian distribution according to Eq. (21.1) yields no analytical expression. For the sake of simplicity, we used the one-dimensional Lorentzian distribution given in Eq. (21.3). The Lorentzian distribution is a borderline case of intensity distribution because of its extremely extended tails. In practice, a weighted sum of Gaussian and Lorentzian functions, the pseudo-Voigt function, is more convenient to describe blurred spots.

1) The scanning step width does not influence the PSF if it is chosen sufficiently small. For electron beam methods the image is caused by primary and backscattered electrons, but the contribution of backscattered electrons is small compared to that of primary electrons [3, 4]. Correspondingly, for scanning methods the PSF is mainly determined by the distribution of particles within the incident beam.

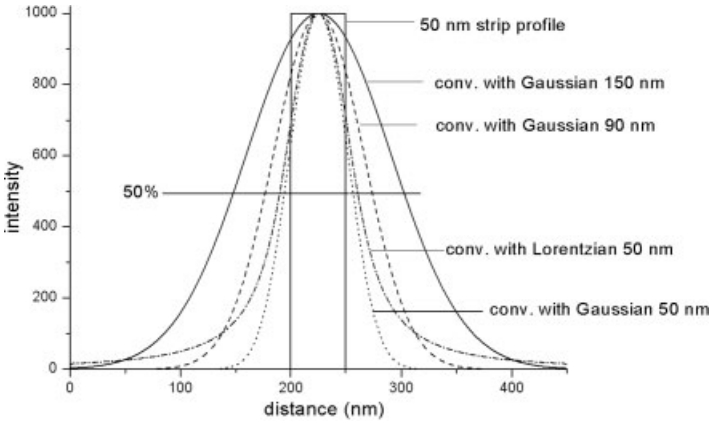

Fig. 21.5 Convolution of a 50 nm wide strip with different beam profiles. The calculated curves are normalized to the same height. The given values are the full widths at half maximum of the beam profiles.

For all beam methods the lateral resolution is determined by the size and shape of the incident beam (scanning methods) or the characteristics of the lens system. For both cases, the LSF can be used to describe the lateral resolution of the imaging system. Beam profiles and LSF are characterized by their full width at half maximum (FWHM).

21.3.1 Analysis of a Narrow Strip

The analysis of narrow strips was not used for the determination of lateral resolution in the submicron range because no samples with sufficient narrow strips were available. The strip pattern of BAM-L002 includes $Al_{0.65}Ga_{0.35}As$ strips of 50 nm, 5 nm, and 0.5 nm, respectively. The TEM image of the strip pattern shows the 50 nm and the 5 nm strips with sharp edges. The 0.4 nm InAs strip S7 (Figure 21.1) was detected with SIMS (Figure 21.3). The ratio of the peak areas of the strips S7 and S8 (note the different indium concentration) in the measured indium profile confirms the width of 0.4 nm.

In general, the image of a pattern is the convolution of the pattern with an instrumental function. Two borderline cases are of interest. If the beam FWHM is small compared to the smallest details of the imaged pattern, then the convolution yields an image that is very similar to the original pattern. If the beam FWHM is large compared to the width of an imaged strip, then the convolution yields the line spread function (Figure 21.4). The latter case is that needed for a simple determination of the line spread function without a deconvolution procedure.

But what means the beam FWHM is large compared to the strip width? Figure 21.5 shows that the convolutions of a 50 nm wide strip with 50 nm wide Gaussian

Table 21.1 Determination of beam FWHM by imaging of a 50 nm strip. Deviation of the image FWHM from the true beam FWHM for Gaussian and Lorentzian beam profiles

Beam halfwidth		Convolution of a 50 nm strip with different beam profiles			
		Gaussian		Lorentzian	
FWHM (nm)	FWHM/W_{strip}	FWHM of convolution (nm)	Deviation from true beam FWHM (%)	FWHM of convolution (nm)	Deviation from true beam FWHM (%)
50	1	62	24.0	70	40.0
70	1.4	78	11.4	86	22.9
90	1.8	96	6.7	102	13.3
120	2.4	124	3.3	130	8.3
150	3	153	2.0	158	5.3
200	4	202	1.0	206	3.0

and Lorentzian profiles have a FWHM of more than 50 nm. The deviation of the image FWHM (calculated by the convolution) from the true beam FWHM is given in Table 21.1 for Gaussian and Lorentzian distributions of different FWHMs. The deviation from the true beam FWHM is smaller than 2 % for Gaussian beam profiles and 5 % for Lorentzian beam profiles, respectively, if the strip FWHM is at least three times smaller than the beam FWHM. From this condition, it follows that the 0.5 nm and 5 nm strips of BAM-L002 enables the analysis of beam profiles down to FWHMs of 1.5 nm and 15 nm, respectively.

A further necessary condition for the analysis of beam profiles is that the narrow strip is separated from other structures in the samples surface. The superposition of images induces a broadening of features in the image and correspondingly a broadening of the measured beam profiles (see below Section 21.3.3). The distance to the next structure must be at least equal to the FWHM of the beam for Gaussian profiles and more than the FWHM in the case of long-tailed distributions like Lorentzian profiles.

21.3.2
Analysis of a Straight Edge

The most commonly used method to determine the lateral resolution is the imaging of a straight edge. The straight edge is a sufficiently sharp chemical gradient between two constant levels of concentration of a chemical constituent, a so-called "chemical edge". For our calculations, we used the ideal case of a straight edge: the step transition. The area of constant levels on both sides of the edge must be large compared to the lateral resolution of the imaging system, because the image of the step transition must show two areas of constant intensity. Figure

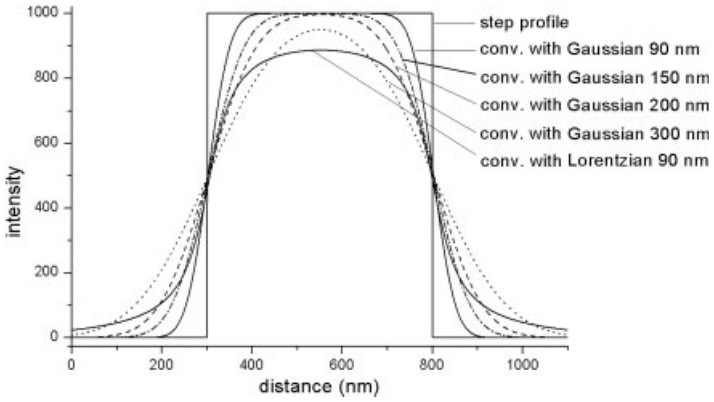

Fig. 21.6 Convolution of a 500 nm wide strip with different beam profiles. The given values are the full widths at half maximum of the beam profiles.

21.6 shows the convolution of different beam profiles with a 500 nm wide strip, representing S6 of BAM-L002 (see Figure 21.1). The convolutions with Gaussian profiles of 200 nm FWHM and more have no level of constant intensity and therefore such profiles cannot be analyzed with a 500 nm wide strip. From this it follows that for the analysis of Gaussian beams the strip width of a step transition W_{strip} must be at least three times larger than the FWHM of the beam profile: $W_{strip} \geq 3 \times W_{FWHM}$. For beam profiles with longer tails the minimum strip width for the determination of lateral resolution is much larger. The convolution of a 90 nm wide Lorentzian with a 500 nm wide strip yields no level of constant intensity (Figure 21.6) and, therefore, it is not possible to determine the beam profile from an image of this strip.

The profile measured at the step transition corresponds to the integral of the line spread function over x (the direction perpendicular to the edge of the step transition, see Figure 21.4) and correspondingly the first derivative of this profile yields the line spread function. But the profile of a step transition may yield also information on lateral resolution without differentiating. In accordance with note 2 of the definition of lateral resolution (see above [1]), the distance between points of well-defined intensity is taken as a measure of lateral resolution. For Gaussian beams the distance between the 12 % and 88 % intensity points (indicated in Figure 21.7) corresponds to the FWHM of the beam profile. For Lorentzian beams and other profiles with extended tails the 12–88 % distance is much larger than the FWHM of the beam profile (Figure 21.7). The 12–88 % distance of 237 nm for the convolution of the step transition with the 90 nm Lorentzian is shorter than the correct value because the strip width of 1000 nm taken for the calculation of Figure 21.7 is not wide enough to reach the 100 % level. The relation of the different parameters for Gaussian and Lorentzian distributions is given in Table 21.2.

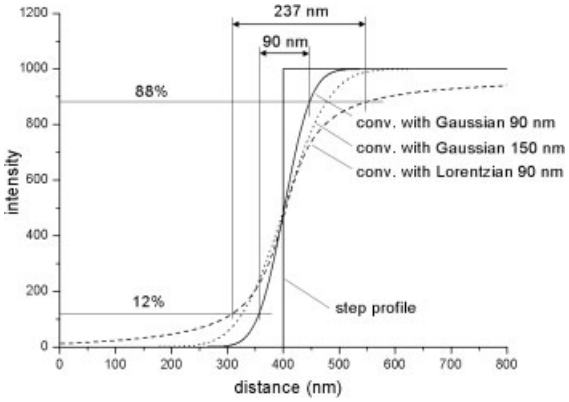

Fig. 21.7 Convolution of different beam profiles with a step transition between two 1000 nm strips. The given values are the full widths at half maximum of the beam profiles. The 12–88 % distance is given for the 90 nm Gaussian and the 90 nm Lorentzian.

Table 21.2 Relation between the rise of intensity in the image of a step transition and the parameters of the profiles used for imaging (after [5]). For the meaning of σ and b see Eqs. (21.2) and (21.3), respectively

Rise at a step transition (%)	Gaussian		Lorentzian	
	σ	FWHM	b	FWHM
12–88	2.35σ	1 × FWHM	$5.07b$	2.54 × FWHM
16–84	2σ	0.85 × FWHM	$3.67b$	1.84 × FWHM
20–80	1.68σ	0.72 × FWHM	$2.75b$	1.38 × FWHM

21.3.3 Analysis of Gratings

The imaging of gratings gives a direct impression of lateral resolution without any further mathematical analysis and therefore this procedure is in particular suitable for the "real-time" adjustment and parameter optimization of imaging instruments. Furthermore, it enables the determination of the modulation transfer function (MTF). The modulation describes the contrast of objects and images and is defined as

$$m=(I_{\max}-I_{\min})/(I_{\max}+I_{\min}), \tag{21.4}$$

where $I_{\max}$ is the maximum value of a periodic structure (object or image) and $I_{\min}$ is the minimum value between two maxima (see Figure 21.10). The maximum value of modulation $m = 1$ is reached if the intensity between two maxima drops to zero ($I_{\min} = 0$). The modulation transfer function is defined as

$$\mathrm{MTF}(k) = m_\mathrm{i}/m_\mathrm{o}. \tag{21.5}$$

This function describes the transfer of the object modulation m_o to the image modulation m_i as a function of spatial frequency k (reciprocal of the spatial period of the grating). The ideal imaging instrument is characterized by $m_\mathrm{i} = m_\mathrm{o}$ and correspondingly MTF = 1. With decreasing strip width of a grating the image modulation m_i and therewith MTF decreases. Correspondingly, the MTF reflects the lateral resolution of an imaging instrument.

According to the definition (see above [1]), the lateral resolution is the "distance … over which changes in composition can be *separately established with confidence*". An objective criterion for "separately established with confidence" gives the Rayleigh criterion

$$m \geq 0.152, \tag{21.6}$$

which corresponds to a dip of about 26 % between two maxima in the image of a periodic structure. Although this criterion is derived from diffraction optics it is commonly used also to describe the resolution of instruments in surface chemical analysis [4].

The strip pattern of BAM-L002 includes two gratings of 600 nm and 160 nm period, respectively. To analyze the relation of lateral resolution and beam FWHM, we calculated the image of a 160 nm grating by convolution with different beam profiles. Figure 21.8 shows some examples. The convolutions with 120 nm and 150 nm FWHM Gaussian and Lorentzian beam profiles, respectively, show well-pronounced dips between the strips of the grating. The convolutions with a 180 nm FWHM beam yield a dip only for the Lorentzian beam profile. The general relation between modulation of the image m_i (see Eq. (21.4)) and a normalized beam FWHM is given in Figure 21.9. The Rayleigh criterion for resolution is fulfilled up to a beam FWHM that is about 75 % of the grating period. The cutoff beam FWHM is about 110 % and 130 % of the grating period for Gaussian and Lorentzian beam profiles, respectively. The real limit of resolution de-

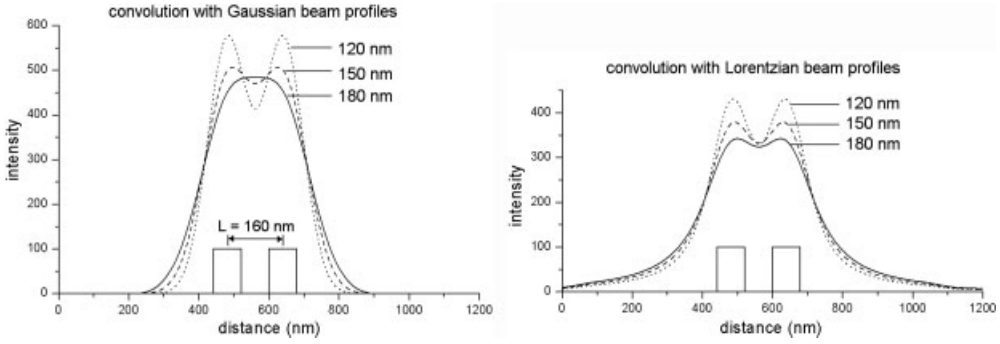

Fig. 21.8 The convolution of a 160 nm grating with different beam profiles. The inserted values are the FWHM of the beam profiles.

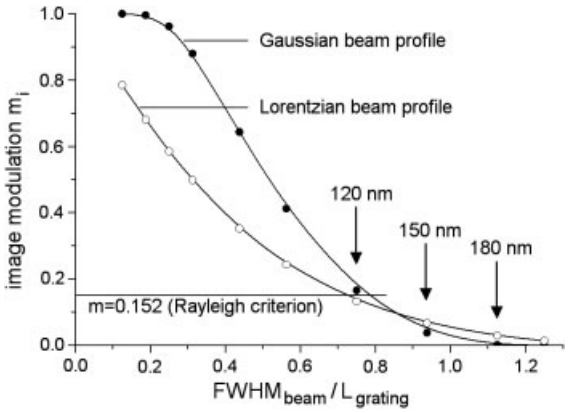

Fig. 21.9 Relation between image modulation m_i and the ratio of beam FWHM to grating period. The arrows indicate the values taken from the convolutions given in Figure 21.8.

pends on the signal-to-noise ratio of the measurements and lies between Rayleigh criterion and modulation cutoff.

The lateral resolution demonstrated in Figures 21.8 and 21.9 is valid only for a grating with 100 % material contrast ($m_o = 1$). The image contrast depends on the lateral resolution of the instrument as well as on the material contrast between the strips of the grating with respect to the method of analysis applied. The material contrast between the $Al_{0.65}Ga_{0.35}As$ and GaAs strips of BAM-L002 is much greater in the SIMS image (Figure 21.3) than in the REM image (Figure 21.2). A reduced material contrast of the grating also reduces contrast and lateral resolutions of the image. Figure 21.10 shows the effect of decreased material contrast on the contrast in the image. The reduction of the materials contrast from 100 % to 60 %, which corresponds to a reduction of the object modulation m_o from 1.0 to 0.43, decreases the image modulation m_i by the same ratio. As a consequence, the Rayleigh criterion $m_i \geq 0.152$ is not fulfilled and in this sense the grating is not

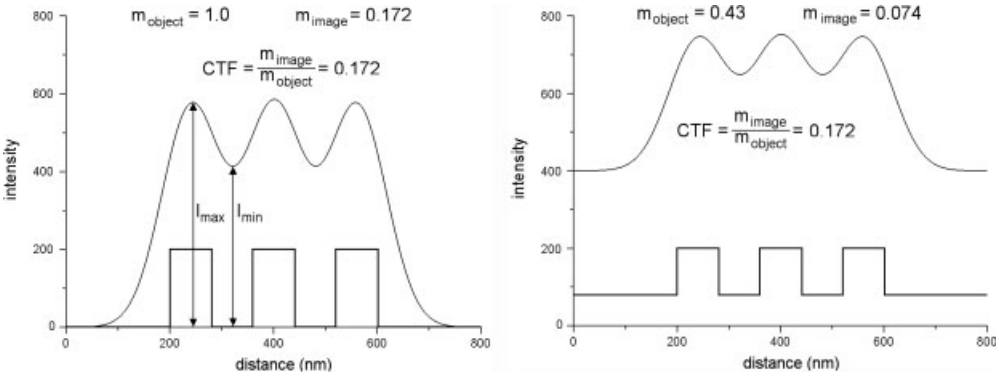

Fig. 21.10 The convolution of two 160 nm gratings with different material contrast with a 120 nm FWHM Gaussian.

resolved. If the lateral resolution for a certain sample should be estimated, the modulation transfer function, determined by the properties of the instrument, must be multiplied by the object modulation.

21.4 Conclusions

The certified reference material BAM-L002 is a new type of test sample for the determination of lateral resolution in surface analysis. Its flat semiconductor strip pattern provides chemical contrast without any substantial three-dimensional topography. For the first time, regular structures with dimensions between 0.4 and 100 nm are available for the determination of lateral resolution. The combination of gratings, isolated narrow strips, and sharp edges of wide strips offers improved possibilities for the calibration of a length scale, the determination of instrument parameters and the "real-time" optimization of instrument settings. The numerical simulation of the imaging process illustrates the determination of lateral resolution and gives the relation between the different parameters used to describe the lateral resolution of instruments in surface chemical analysis.

Acknowledgments

The authors would like to thank S. Benemann (BAM) for the metallographic preparation of samples, H. Rooch (BAM) for TEM investigations, and B. Strauss (BAM) for SEM investigations. This work was supported by the Federal Ministry of Education and Research under contract 13 N 7698 and advised by VDI Technologiezentrum Physikalische Technologien.

References

1 ISO 18115: 2001 – *Surface Chemical Analysis – Vocabulary* (ISO, Geneva, 2001).

2 D. Funnemann, P. Bernhard, M. Escher, F. Forster, B. Krömker, M. Merkel, F. Reinert, S. Schmidt, G. Schönhense, J. Westermann, and C. Ziethen, NanoESCA: imaging XPS with resolution below 200 nm, *BESSY Annual Report* 2002, pp. 350–351, www.bessy.de/publications/05.annual_reports/files/AnnualReport2002.pdf.

3 M. M. El Gomati, M. Prutton, B. Lamb, and C. G. Tuppen, Edge effect and image contrast in scanning Auger microscopy: a theory/experiment comparison, Surf. Interf. Anal. **11**, 251–265 (1988).

4 J. Cazaux, Minimum detectable dimension, resolving power and quantification of scanning Auger microscopy at high lateral resolution, Surf. Interf. Anal. **14**, 354–366 (1989).

5 M. P. Seah, Resolution parameters for model functions used in surface analysis, Surf. Interf. Anal. **33**, 950–953 (2002).

Part VI
Calibration – Tip shape

Nanoscale Calibration Standards and Methods: Dimensional and Related Measurements in the Micro- and Nanometer Range.
Edited by Gunter Wilkening, Ludger Koenders
ISBN: 3-527-40502-X

22
Reconstruction and Geometric Assessment of AFM Tips

Torsten Machleidt, Ralf Kästner, and Karl-Heinz Franke

Abstract

At present, many researchers are working on different tasks to turn tactile scanning microscopy from a pure "Imaging tool" into a precision measuring instrument. Furthermore, the semiconductor industry requires larger and larger measuring ranges at a resolution below some nanometers. At the Ilmenau Technical University, these new requirements were taken into account, and a novel measuring machine for nanometer resolution was developed in cooperation with the SIOS Meßtechnik GmbH and the Zentrum für Bild- und Signalverarbeitung e. V. This machine already possesses a measuring volume of $25 \times 25 \times 5$ mm^3 ($W \times L \times H$), which is a million times more than that of conventional atomic force microscopes (AFMs). Furthermore, a resolution of 0.1 nm can be achieved. Because of the enormous requirements, a normal atomic force microscope is used for scanning the sample surface. If a metrological evaluation of the AFM data is to be carried out, the shape and the position of the AFM–tip has to be known. Its characteristics are not static but are changing dynamically due to physical effects (e. g., friction) and normal attrition. Procedures for the reconstruction of the tip on the basis of the AFM measurement data are necessary to evaluate these changes. In the technical literature, there are different approaches for determining the tip geometry, which were all investigated and assessed in detail. Based on these procedures the evaluation of the AFM–tip can be realized. Proceeding on the determined tip shape, procedures for extensive interpretation and quantitative characterization of the tip geometry will be introduced. Several approaches will be presented, which realize the transformation of topological data into geometrical primitives. As a result their properties allow the assessment of quality and position of the AFM–tip and the involved physical effects. In the outlook, it will be focused on the usage of the procedures to prove the physical influences between tip and sample. In what way will the geometry and position of the "reconstructed AFM–tip" change under different measurement conditions (measurement velocity, normal power, and measurement direction)?

Nanoscale Calibration Standards and Methods: Dimensional and Related Measurements in the Micro- and Nanometer Range.
Edited by Gunter Wilkening, Ludger Koenders
ISBN: 3-527-40502-X

22.1 Introduction

The research team "*Nanomeasuring technology*", headed by Prof. Jäger from the Ilmenau Technical University and comprising scientists of various disciplines, have developed a novel nanopositioning and measuring method [1]. This method permits for the very first time the Abbe error-free coordinate measurement in three coordinates simultaneously. Thus, the fundamental accuracy limitations of already existing solutions can be overcome. In addition, another decisive drawback of already existing solutions is removed, namely, the inevitable errors of mechanical guiding systems which influence the measuring result negatively. These guiding errors are nearly completely compensated by an intelligent control concept offered by this new method. Thus, the bases have been created permitting the user to really penetrate the nanometer and subnanometer ranges also in large measuring volumes.

On the basis of this novel concept, a nanopositioning and measuring machine (NPM) has been realized (Figure 22.1) which, in the case of large measuring and positioning ranges ($25 \times 25 \times 5$ mm^3) and a high traveling dynamics (up to 50 mm/s), permits measurements and positioning exact to the nanometer (resolution of 0.1 nm and error tolerances of < 5 nm).

If a certain resolution requirement to be met by the scanning force measurement is exceeded, then the insufficiently narrow shape of the tactile tip (radius about 10 nm) will result in extremely inexact measurements. Thus, for example, it is not possible to record particularly abrupt changes of the topology as the geometry of the probe does not allow it to penetrate the structure completely. On the other hand, steep slopes and edges appear to be slanted and gentle due to the conical or pyramidal shape of the tip. Figure 22.2 clearly illustrates this problem.

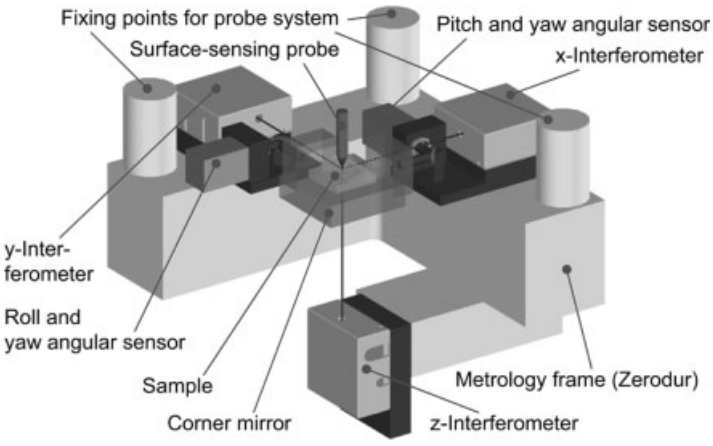

Fig. 22.1 Nanopositioning and nanomeasuring machine realized at the Ilmenau Technical University.

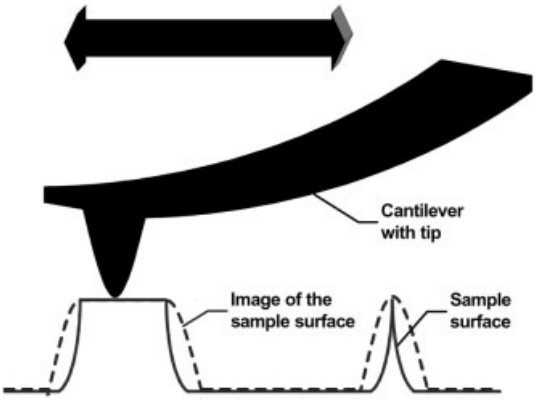

Fig. 22.2 Imaging errors.

Formally, the imaging function of a tip P (mirrored in all coordinates) and a sample S on an image I corresponds to a morphological operation and can therefore be described as dilatation in the following way:

$$I = S \oplus P.$$

Consequently, after performing an erosion – the mathematical reversal of the dilatation[1)] – the reconstructed surface S_r, which is identical to the imaged sample in an ideal case, results according to the following equation:

$$S_r = I \ominus P.$$

This idea constitutes the basis for a reconstruction of the measuring data, but it requires to know the shape of the tip. In what follows, three fundamental approaches are described by means of which the geometry of the tactile tip can be determined.

22.2
Reconstruction of the Tactile Tip

22.2.1
Imaging the Tip Using Scanning Electron Microscopy

The tip assessment can be realized by applying scanning electron microscopy. The line-by-line sampling process using a beam of electrons solely generates two-dimensional information describing the perspectively projected structure

1) The erosion is only an approximation of the mathematical reversal of the dilatation!

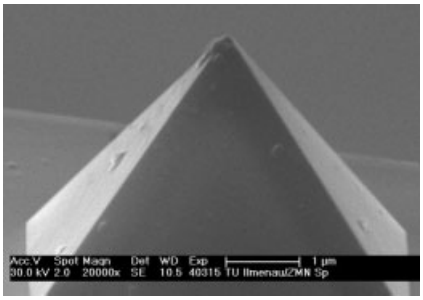

Fig. 22.3 Tip scanned by SEM.

(Figure 22.3). Because of the expensive tip preparation and the fact that the probe might probably be destroyed during the measurement, this method is not intended for practical use. Its purpose restricts to experimental fields.

22.2.2
Reconstruction by Known Sample Structure

The image recorded shows the superposition of the sample and the tactile tip. If the geometry of the sample is exactly known, it is possible to determine the shape of the probe from the measuring data. Therefore, calibration normals are used whose surfaces present exactly determined structures in the form of pyramids, waves, or blocks. An example of such a normal is shown in Figure 22.4.

As the reliable reconstruction of a topological image always requires to know the tip (the tip, however, can greatly change during the measuring process under certain circumstances), such calibration normals must be employed relatively often in an ideal case. Also, they are relatively expensive and have a limited service life only. Therefore, some more flexible methods for the reconstruction of the tactile tip were developed [3].

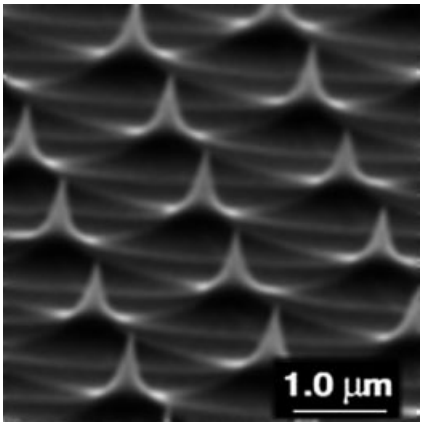

Fig. 22.4 Calibration normal TGT01.

Furthermore, these calibration normals describe the tactile tip only "macroscopically" because of the size of the structures. A description in the subnanometer range would require very small, highly exact structures [2].

22.2.3
Blind Tip Estimation

The blind tip estimation determines the potential geometry of the probe without using more exact information about the sample used for the characterization. The basic approach is based on the assumption that the image of the shape of the tip – as explained above – is always a component part of the topological maps of a sample that can be generated by means of dilatation. An iterative algorithm, as presented in [3], is thus able to permit an estimation of the maximum dilation of the probe (Figure 22.5).

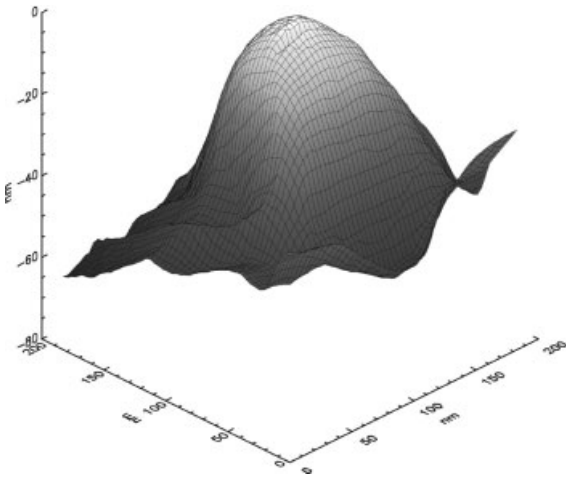

Fig. 22.5 Tip estimation resulting from the blind tip estimation.

22.2.4
Motivation

Having a closer look to an upper-bound estimation for the tip provided by the blind reconstruction method leads to a first, qualitative impression of its geometric properties. Since investigating the tip and reconstruction quality include the task of comparing results originating from several measurements, a quantitative characterization approach has to be found. Motivated by the idea of being able to prove various effects on the tip, e. g., wear or lateral and deformation forces, a solution should provide flexibility as well as robustness. The characterization results then can be used to determine strategies for choosing parameters, which optimize the reconstruction process.

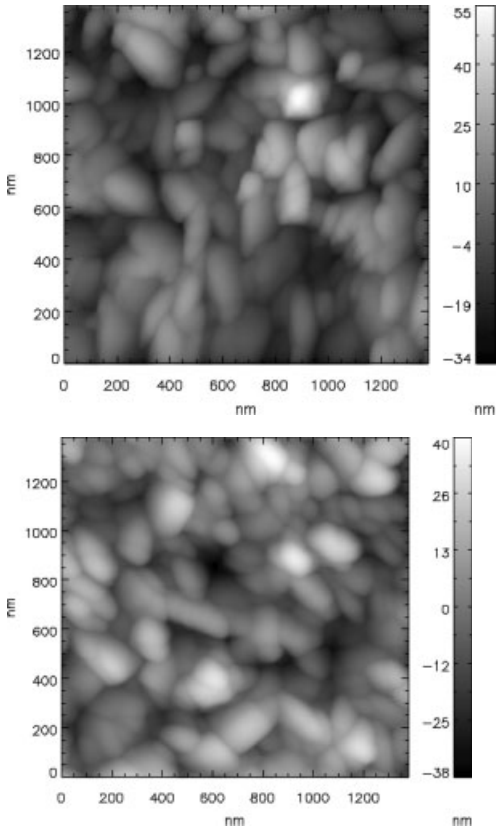

Fig. 22.6 A titanium object is scanned using a new (top) and a worn (bottom) tip.

Figure 22.6 gives an impression of the manifold quality demands the reconstruction method has to meet. Whilst the influence of tip wear on the measurement results seems to be absolutely obvious, proving physical interaction effects are much more challenging.

22.2.5 Tip Assessment

22.2.5.1 Two-Dimensional Characterization

A modest approach for characterizing and analyzing tip shapes is the geometrical interpretation of slices resulting from a cut through the tip structure. Although the loss of information in the consequence of the dimensional reduction should not be underestimated, a variety of simple algorithms allow the determination of angle and curvation parameters in an efficient and robust way.

Let the topological function of the tip image defined at the sample points (x_i, y_j) for $i=1,\ldots,i_{max}$ and $j=1,\ldots,j_{max}$ be denoted as

$$z_{i,j} = f(x_i, y_j).$$

Choosing the location of the cutting plane takes place without any relevant previous knowledge about the tip structure. Only the maximum of the three-dimensional function describing the probe is assumed to be contained in the slice. The approach introduced defines a cut $g_k(x_i)$ parallel to the (x,z)-plane of the Cartesian coordinate system and thus can be described as follows:

$$z_i^s = g_k(x_i) = f(x_i,k)|\max\{f(x_i,y_j)\} \in f(x_i,k).$$

22.2.5.2 Geometrical Interpretation

Figure 22.7 shows a sample tip as well as the location of the cutting plane on which the analysis and assessment of the probe is based. Hereby, a geometrical interpretation can be made under several aspects.

Since the mechanical sensing device is manufactured with a conical, tetrahedral, or pyramidal shape, the microscopic slice mostly looks similar to the one illustrated below. That's why a keen interest focuses on the angle enclosed by the function intervals to the left and the right of the maximum.

Whilst the microscopic scale makes the tip look sharp, the profiles appear rounded near the maximum in the nanometer scale, as shown in Figure 22.8. If those effects are not based on the filtering mechanisms used during the measurement or the reconstruction process, the rounding can be considered as real, quantitative characteristic of the probe resulting from the manufacturing process, repulsive interaction forces or simply wear. Thus, a geometrical interpretation can be given using a semicircle defined by its radius or by determining the curvation of a second-order polynomial approximating the profile.

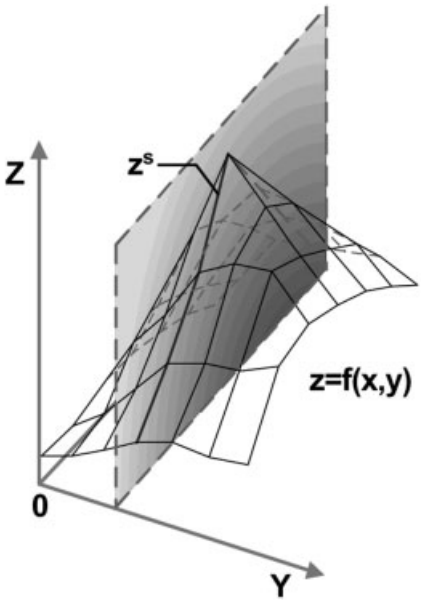

Fig. 22.7 Tip slice.

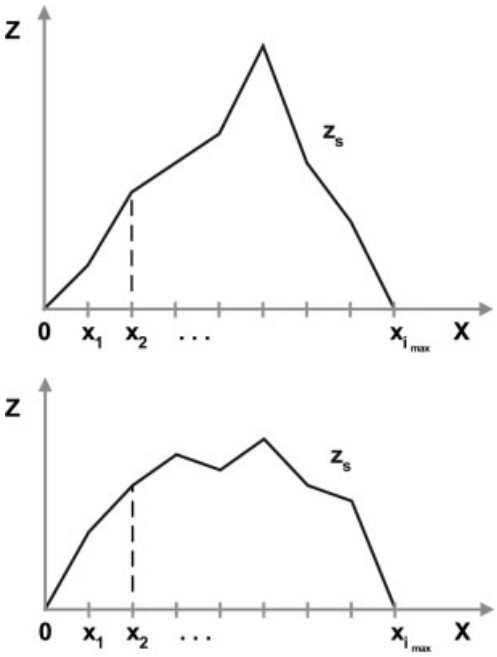

Fig. 22.8 Microscopic (top) and nanoscopic (bottom) tip slice.

22.2.5.3 **Tip Angle**

The determination of the angle α enclosed by the function intervals to the left and the right of the tip's maximum x_{max} is based on the principle of simple linear regression. For that reason let the points defining the tip are denoted as

$$z_i^l = g_k^l(x_i) = g_k(x_i) | x_i \leq x_{max} \quad \text{and} \quad z_i^r = g_k^r(x_i) = g_k(x_i) | x_i \geq x_{max}.$$

Thus, finding two straight lines $\hat{z}_l(x) = m_l x + n_l$ and $\hat{z}_r(x) = m_r x + n_r$ approximating the slice geometry by nearly matching those points means minimizing their summed up squared distances to the profile:

$$E_l(m_l, n_l) = \sum_{i=1}^{max} (z_i^l - \hat{z}_l(x_i))^2 \quad \text{respective} \quad E_r(m_r, n_r) = \sum_{j=max}^{i_{max}} (z_i^r - \hat{z}_r(x_i))^2.$$

The wanted angle α can then be determined by calculating:

$$\alpha = \pi - \gamma_l - (\pi - \gamma_r) = \gamma_r - \gamma_l = \arctan(m_r) - \arctan(m_l).$$

22.2.5.4 Tip Radius

Determining the tip radius r means finding the semicircle that approximates the given slice best. Similar to the simple linear regression procedure, hereby the summed up squared distances between the sample points and the estimated geometry have to be minimized. Fixing one of the three possible degrees of freedom by assuming the semicircle's center $M(x_c,z_c)$ to be placed somewhere on a parallel to the abscissa, the approximating function can be denoted as

$$(x-x_c)^2+(z-z_c)^2=r^2.$$

Thus, the summed up error results in

$$E(x_c,z_c,r)=\sum_{i=1}^{i_{max}}(L_i-r)^2, \quad \text{with} \quad L_i=\sqrt{(x_i-x_c)^2+(z_i-z_c)^2}.$$

A feasible approach for minimizing the error term is the fixed point Iteration derived from the gradient-based Newton's algorithm.

22.2.5.5 Tip Curvation

The determination of the tip curvation k is based on approximating the profile to a second-order polynomial, generally denoted as

$$\hat{z}_s(x)=a_0+a_1x+a_2x^2.$$

This leads to the following error term:

$$E(a_0,a_1,a_2)=\sum_{i=1}^{i_{max}}(z_i^s-\hat{z}_s(x_i))^2.$$

Given the fitting polynomial the curvation is defined as

$$k(x)=\frac{\hat{z}_s''(x)}{(1+\hat{z}_s'(x)^2)^{\frac{3}{2}}}, \quad \text{with} \quad \hat{z}_s'(x)=\frac{\partial\hat{z}_s}{\partial x}=a_1+2a_2x, \quad \hat{z}_s''(x)=\frac{\partial^2\hat{z}_s}{\partial x^2}=2a_2.$$

Setting x to the maximum's position $\hat{x}_{max}$ leads to the simple expression:

$$k=k(\hat{x}_{max})=2a_2.$$

The curvation can also be considered as the angle enclosed by two tangents on the endpoints of an infinitesimal small interval of the polynomial. Furthermore, the so-called curvation radius can be determined by $\varrho=k^{-1}$. Because of the fact that the curvation at a function's maximum is always negative, k is generally supposed to be contained in $(0,-\infty]$. While flat second-order polynomials have a k near zero, the values decrease with a strengthened rounding. The reader should note that in

contrast to the radius, which gives a good absolute impression of the tip geometry, the curvation is more or less expected to be the basis for relative characterizations.

22.2.5.6 **Review**

Figure 22.9 shows a geometrical interpretation of the approaches presented above. In general, all methods presented realize a fast and robust two-dimensional tip characterization. Solely, the reliability of the quantitative results is nearly unpredictable due to the missing knowledge about the three-dimensional geometry of the probe. Thus, the estimation depends roughly on the cutting plane's orientation and it seems uncertain that the chosen tip slice is really representative for the whole structure. Due to this an extended approach considering the complete tip geometry is introduced.

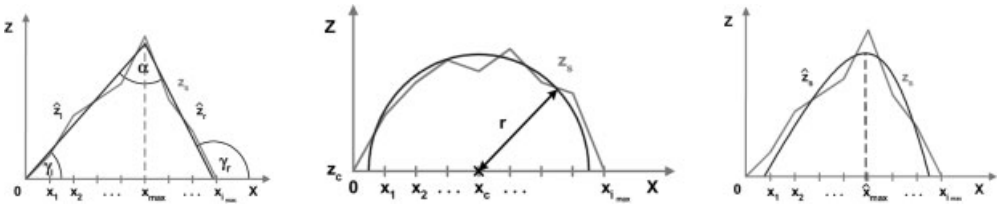

Fig. 22.9 Determination of tip angle (left), radius (middle), and curvation (right).

22.2.6 **Three-Dimensional Characterization**

The characterization of the three-dimensional tip structure requires its approximation to spatial geometric primitives. Because of the fact that this process is generally based on nonlinear and nonsteady error functions, specialized optimization algorithms are needed. Those algorithms mainly feature a minimum search which is not gradient-driven and thus need no first-order derivatives.

22.2.6.1 **Geometrical Interpretation**

Since tips are manufactured in various ways resulting in different shapes, concentrating exclusively on one primitive makes very little sense. The introduced method for defining geometric shapes in a flexible way assumes probe structures which appear convex along the spatial z-axis. It should be noted that the blind reconstruction algorithm indeed exactly generates this kind of topological functions describing an upper-bound estimation for the real tip.

The main idea of this approach is to define primitive shapes by determining parameters for a set $S_F = \{A_1, \ldots, A_m\}$ of analytical second-order surfaces forming its facets. Because of the convex appearance of the tip the function describing the primitive can be described generally as follows:

$$\hat{z} = \min_{1 \le k \le m} \{A_k \in S_F\}.$$

For example, let the idea in [4] be seized, where the tip shape is assumed to be pyramidal (Figure 22.10). Thus, the primitive can be defined using four planes and five degrees of freedom. Whilst the pyramid's apex should be fixed exactly at the maximum of the estimated topological function, the angles enclosed by the perpendicular raised through the apex and the bounding planes, denoted as α_1, α_2, α_3 respective α_4, and a rotation angle φ, which allows rotating the whole primitive around the perpendicular, distinctly define its geometry. Further, assuming other shapes means parameterizing corresponding second-order surfaces. In this way, all kinds of tips are quantitatively characterizable as, e. g., tetrahedron, cone, etc., and wear can be detected by considering may be hemispherical structures or pyramidal stubs.

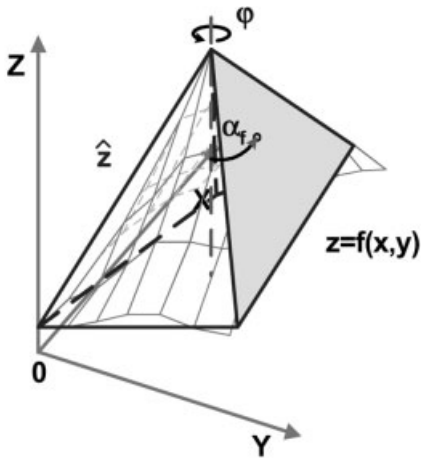

Fig. 22.10 Characterization of a pyramidal tip.

22.2.6.2 **Simulated Annealing Algorithm**

An optimization approach satisfying the requirements stated above is the simulated annealing algorithm, which is derived from the principle of liquid annealing in physics. Thus, its main idea is motivated by the fact that cooling down liquid matter at a low rate leads to optimal energetic configurations resulting in grid structures. Besides providing an exclusively error-driven minimum search, this randomized uphill–downhill method owns the ability to differentiate between a local and a global extremum. For a detailed introduction in simulated annealing please see [5].

Referring to the example drafted above, a parameter vector defining the geometry to be approximated and used for the optimization might be denoted as

$$\vec{c} = (\alpha_1 \; \alpha_2 \; \alpha_3 \; \alpha_4 \; \varphi)^T.$$

Next, an error function $E(\vec{c}_t)$ quantifying the approximation quality for the iteration t and motivating the minimum search is needed. Defining a measure $d(P_{i,j},\hat{z}_t)$ for the distance between a point $P_{i,j}(x_i,y_j,z_{i,j}=f(x_i,y_j))$ of the estimated tip and the approximated geometry $\hat{z}_t(x,y)$, the overall error can be described as

$$E(\vec{c}_t)=\sqrt{\frac{1}{i_{max}j_{max}}\sum_{i=1}^{i_{max}}\sum_{j=1}^{j_{max}}d(P_{i,j},\hat{z}_t)^2}.$$

In the context of this approach, two possible distance measures have been defined and implemented. A highly efficient method simply determines the difference of the function values provided by the estimation $f(x_i,y_j)$ and the approximation $\hat{z}_t(x_i,y_j)$. Alternatively, orthogonal distances might be computed (Figure 22.11).

Furthermore, the annealing mechanism controlling the system's temperature $T(t)$ itself has to be chosen. A modest approach assumes a constant loss of energy at a rate t_v, $0<t_v<1$, which simply leads to exponentially decreasing annealing steps denoted as

$$T(t)=T_0 t_v^t.$$

The parameter T_0 states the starting temperature in a feasible way. Last but not the least, a random generator applying various changes to the optimization parameters has to be defined.

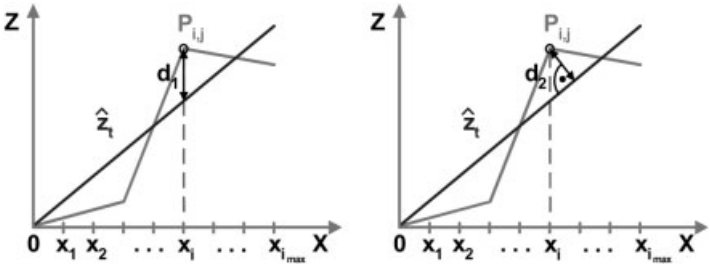

Fig. 22.11 Distance measures: difference of the functions (left) and orthogonal distances (right).

22.2.6.3 **Convergence**

Following a good evolutionary strategy for finding the global optimum, the convergence of the algorithm is very likely but not certain under all circumstances. This mainly addresses the choice of primitives, which strongly differ from the estimated tip structure. However, in general, the approach introduced above reaches a useful optimization result after three- to four-thousand iteration steps. Applying the orthogonal distance measure to the error term slightly accelerates the convergence. Unfortunately, the speedup in time remains insignificant due to the higher computing complexity of this method.

22.2.7
Experimental Results

Figure 22.6 shows measurements realized by using differently worn tips. A solely visual inspection of the sample data does not lead to a clear proof of the probe's states. Exclusively massive worn might be identified without quantitatively characterizing the tips using the Blind Reconstruction method.

Figure 22.12 illustrates the results obtained by applying this procedure. The estimated tips can be characterized and compared using the presented methods. Assuming a hemispherical geometry, radii of 81 nm and 94 nm have been calculated for the new respective worn tip.

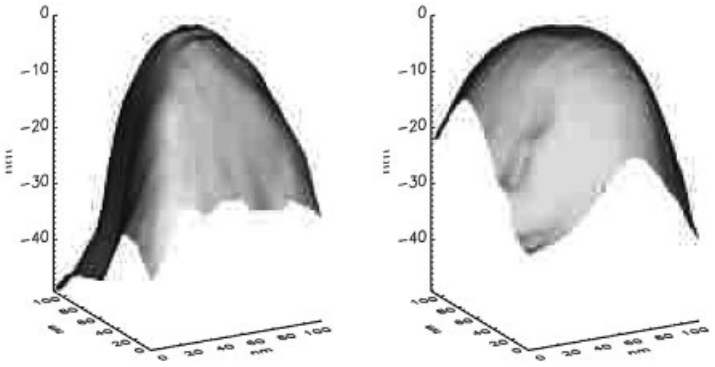

Fig. 22.12 New (left) and worn (right) tip reconstructed using the blind tip estimation.

22.3
Summary and Outlook

At the Ilmenau Technical University, a new generation of nanopositioning and measuring devices has been developed. The extremely high resolution of the systems requires an exact investigation of the imaging process. It was shown that imaging errors result from the dilatation of the tactile tip. These errors can be eliminated partly by means of morphological methods. For this, it is necessary to have exact knowledge of the shape of the tactile tip which can be determined via the known tip characterization and the blind tip estimation.

However, the practical demands include the assessment of the probe considering wear and other artifacts. The approach presented introduced two-dimensional and three-dimensional methods that allow a quantitative parameterization of the tip's geometry, thus realizing its comparability. Because of the fact that the three-dimensional characterization process is not based on a dimensional reduction of the tip data, the spatial approach showed important advantages.

In the future, work is going to face the modification of reconstruction methods to yield better results concerning disturbances. Furthermore, the approach presented is going to be applied for the analysis of physical tip–sample interaction. Changes of the measurement parameters should result in changes of the physical effects, thus causing different characterization parameters. In that way, the influence of tip–sample interaction on the measured data can be determined.

References

1 G. Jäger, E. Manske, T. Hausotte, and H. Büchner, *Nanomessmaschine zur abbefehlerfreien Koordinatenmessung*, tm 7-8/2000, S. 271–278.

2 H. Hübner, W. Morgenroth, H. G. Meyer, Th. Sulzbach, B. Brendel, and W. Mirandé, Downwards to metrology in nanoscale: determination of the AFM tip-shape with well-known sharp-edged calibration structures, Appl. Phys. A, **76 (6), 913–917 (2003).**

3 J. S. Villarrubia, Algorithms for scanned probe microscope image simulation, surface reconstruction, and tip estimation, J. Res. Natl. Inst. Standards Technol. **102**, 425 (1997).

4 M. Lucas, Rekonstruktion von SPM-Spitzen aus SPM-Bildern und deren Analyse, Diplomarbeit im Fachbereich Physik, UNI Münster (1997).

5 S. Kirkpatrick, C. D. Gelatt Jr., and M. P. Vecchi, *Optim. Simul. Annealing*, **220** (4598), 671–681 (1983).

23
Comparison of Different Methods of SFM Tip Shape Determination for Various Characterisation Structures and Types of Tip

S. Czerkas, T. Dziomba, and H. Bosse

Abstract

Recently scanning force microscopy (SFM) has become a very important tool for measurement of the widths of small features (e. g., critical dimension or CD metrology). Contrary to pitch measurements however, knowledge of the exact tip shape is needed for absolute linewidth measurements. For this reason we analyze the possibility of determining tip width and shape based on SFM images recorded at different samples. Our investigation takes different tip types into account. The SFM measurements were performed on different well-known silicon structures with sharp edges, gold nanospheres, and also unknown sharp features. All samples were investigated with standard silicon tips; additionally some of them were also imaged with sharp e-beam deposited (EBD) carbon needle tips. Depending on the sample features, either blind tip reconstruction or erosion of the image was used, with latter requiring knowledge of the sample shape. We could observe differences in calculated tip shape obtained with different calibration samples. In our chapter we try to explain these discrepancies.

23.1
Introduction

The determination of the width of small artificially fabricated nanostructures (CD metrology) is directly influenced by the tip shape. As shown in Figure 23.1 the conventional SFM gives no information about the actual sidewalls. The sidewalls appearing in an SFM image at a location of a steep sample slope are indeed an image of the probe and not the sample. There is no information about the area under the edges. Even when using very sharp conventional tips (Figure 23.1(b)) the situation remains the same at least at 90° and undercut structures. Just the uncertainty in the profile becomes smaller. For this reason only the determination of the width of top plateau (top CD) makes sense for conventional tip shapes, provided that the tip is either sufficiently sharp or that its own end plateau width is

Nanoscale Calibration Standards and Methods: Dimensional and Related Measurements in the Micro- and Nanometer Range.
Edited by Gunter Wilkening, Ludger Koenders
ISBN: 3-527-40502-X

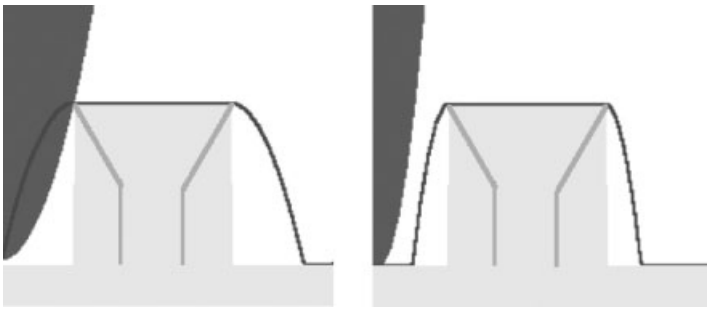

Fig. 23.1 Real geometry (rectangular sample and with sidewall undercut) and SFM image for a dull (a) and a sharp probe (b).

known so that the measured top width can be corrected accordingly to determine the real top CD. A bottom or middle CD does not yield any additional information about the sample, and furthermore the influence of the probe shape (i. e., finite probe diameter) is larger than that for the top CD.

The problem of dilation of image features by the SPM tip is known already for several years. There were many suggestions on how to solve this problem [1–3]. In the following a number of samples were proposed in order to estimate tip shape [4–6]. In order to evaluate their practical applicability for CD metrology, we compare the results obtained with several of these different tip shape estimation and characterization techniques in this chapter.

23.2 Instrumentation

All the investigations presented in this chapter were performed with a modified commercial SFM system based on the Nanostation (SIS GmbH, Herzogenrath, Germany)[1)]. The change in cantilever deflection is measured by a glassfiber interferometer in this system. Lateral scanning is performed with a piezo scanstage equipped with capacitive sensors for active position control (Physik Instrumente, Germany). The SFM is calibrated in regular intervals either by physical transfer standards or by temporarily attaching laser interferometers. All measurements were done in noncontact mode. The tip–sample distance was controlled by keeping the damping of the tip oscillation amplitude at a constant value. All tip shapes shown in this chapter were calculated from measurements conducted with the same tip (unless other stated).

1) Certain commercial equipment is identified in this report in order to describe the experimental procedure adequately. Such identification does not imply recommendation or endorsement by the Physikalisch-Technische Bundesanstalt, nor does it imply that the equipment identified is necessarily the best available for the purpose.

23.3
Results and Discussion

23.3.1
Needs of CD Metrology

As a typical example of CD measurement by SFM, Figure 23.2 shows a section of an SFM image of a chromium line on a quartz substrate and the corresponding line profile (also marked by the white line in the SFM image). As the profile depicts, the plateau surface is not imaged perfectly flat, which is due to the imperfections of the structure itself (i. e., surface roughness), instrument noise, etc. Consequently, it is not possible to determine conveniently the width of the top plateau. A possible solution of this problem is to define top CD as the cross-section between the line profile and a horizontal line a few nanometer below the middle height of the top plateau. These few nanometers need to be determined in such a way that the distance from the top is just large enough to overcome the problems with surface roughness, noise, etc., while on the other hand, it needs to be kept as small as possible to reduce the influence of the probe diameter to a minimum. The proper value of this height difference can vary from sample to sample. Typically, 3 nm prove enough at most samples. If different specimens are to be compared, a uniform and therefore usually larger value of, e. g., 8 nm should be chosen. Top CD defined in this way is very easily measurable and good reproducible. In order to eliminate the influence of tip shape on such determined CD, just the knowledge of the tip diameter at a chosen height from the tip end is needed.

A very important issue in CD metrology is tip wear. If the tip wears off during the measurement, reproducible results cannot be achieved. The tip wear can be quantified by characterizing the tip before and after the CD measurement. Alternatively, repeated CD measurements are a good means to check for tip wear by monitoring as they yield the same CD value as long as there is no wear of the tip. Figure 23.3 shows an example of such repeated typical CD measurements. There is no trend in these four consecutive measurements; it can therefore be concluded that there was no tip wear during these measurements. As seen

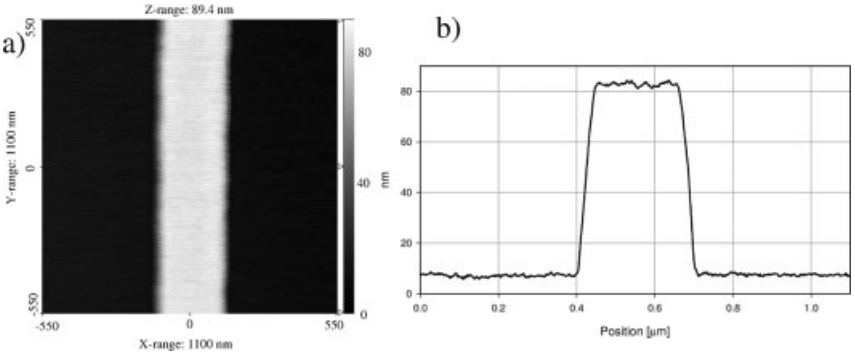

Fig. 23.2 SFM image of a chromium line on quartz (a) and a corresponding line profile (b).

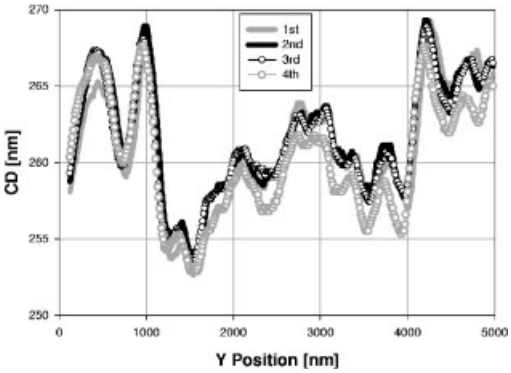

Fig. 23.3 Linewidth distribution along the Y axis for four consecutive measurements.

from this figure the repeatability of the CD value is in the range of 2 nm. Any changes of the tip diameter to values greater than these 2 nm in the course of measurements would be visible in the graph and could thus be identified easily. As the changes of tip shape thereby can be monitored very easily during the actual CD measurements, just one additional measurement on a special tip characterizer sample is required at any time in order to obtain the absolute value of the tip diameter. In most cases tip wear occurs predominantly with new tips; in general, the speed of tip wear decreases with the duration of its use so that the tip finally remains stable over many measurements. Consequently, it is advisable to perform some initial prescans to make sure that the tip reaches a sufficiently stable shape before the actual valid measurements are recorded.

23.3.2 Tip Shape Determination

We investigated the possibility of determining the absolute value of the tip diameter on many different samples that appear suited for such a characterization. First we used three different silicon test structures: triangular, rectangular, and with undercut sidewall.

Figure 23.4 shows a typical SFM image of rectangular silicon structure with 90° sidewalls. This sample with very well-defined structures and only very few irregularities has already been described by Hübner et al. [4]. With this kind of structures the determination of the edge position (the highest point in the case of profile shown in Figure 23.4) is – similar to CD metrology – somehow arbitrary, which may lead to a large error in the calculated tip shape. Provided that the topographic profile of the trench is actually perfectly rectangular as assumed, the tip shape equals the imaged profile of the 90° sidewall (Figure 23.4 (right)). Four profiles are shown, the two in the middle are typical ones, while the other ones are examples of extreme profiles (thick gray and black lines) that can be observed at different locations within the same image. As these profiles are each well repeatable, they can be assigned to sample irregularities. The widest curve (thick black line) can be explained by a location at the trench, where the corner

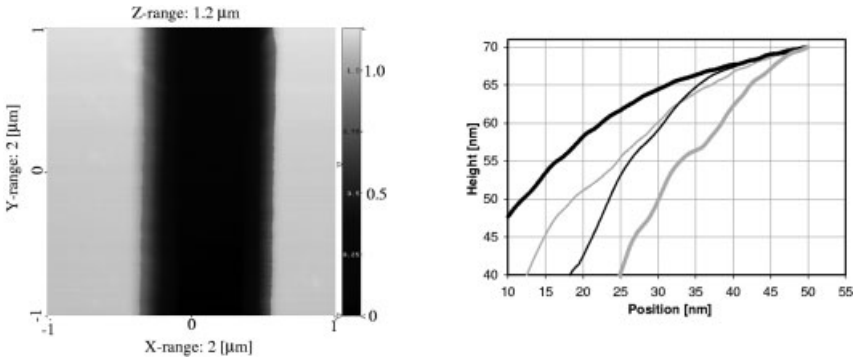

Fig. 23.4 SFM image of a rectangular tip characterization sample (left) and selected sidewall profiles (right).

roundness is larger than in average. The very sharp profiles (thick gray line), however, do not necessarily represent sharper corners of the trench, but appear where an artifact is visible on the top plateau. This means that due to actually unwanted artifacts on a sample, the effective corner roundness becomes smaller. As these sites are more or less accidentally distributed over the sample, they are not well suited for repeatable characterization of the probe.

As can be seen in Figure 23.1, no differences between the SFM images of samples with rectangular shape and those with undercut sidewall are to be expected as long as only the geometrical factors are considered. In experiment, however, significant differences can often be identified between such pairs of SFM images, which are to be attributed to differences in the physical interactions (tip bending, differences in the force field above the sample, material contrast, etc.) in both cases. Meli [7], for example, showed that there is a difference of up to some nanometers between the geometrical shape of the tip and tip shape calculated from measurements on samples with sidewall undercuts. Figure 23.5 therefore compares experimental line profiles from such a sample and one with rectangular edges. While the gray profile (rectangular sample) has a form clearly different from the profile for sample with undercut (black line with empty circles) and is furthermore also much wider, the black line (for the same rectangular sample as the gray curve) actually depicts the same behavior as the blue one although the measured widths under the top plateau differ. The measured sidewall profile equals the probe shape if a perfect rectangular structure is assumed (see Figure 23.5 (left)). If a finite corner rounding is assumed one has to deconvolute the image in order to determine the shape of the tip. In this chapter we adhere to the worst case scenario (i. e., the dullest tip that would yield the observed image of the assumed surface) and calculate the tip shape using the mathematical approach presented by Villarubia [8]. Figure 23.5 (right) presents tip shapes deduced from respective line profiles in the right image of this figure. For a rectangular sample a corner rounding of 4 nm and for a sample with undercut sidewalls a perfect edge was assumed. As Figure 23.5 demonstrates, a very good agreement (within 2–3 nm) between the tip shapes deduced from these two samples is

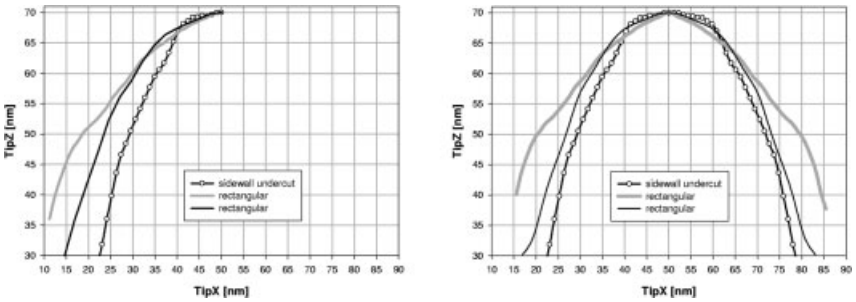

Fig. 23.5 Tip shape profiles calculated from line profiles measured at a rectangular sample (assumptions: perfect edges in the left image and 4 nm corner rounding in the right image) and with undercut sidewall (assumed perfect edges in both images). Measurements on these samples were conducted with two different Si tips of the same type. Profiles in the left image were mirrored for visualization purposes.

already reached if we introduce a small assumed corner roundness. It can be concluded that we see no evidence for any deviations from the simple geometrical model in the case of these two investigated samples. This means that no sample-specific tip bending or similar can be distinguished with ordinary pyramidal silicon tips.

Figure 23.6 shows a typical SFM image of a triangular silicon structure, and also an example line profile and a plot of the structure width determined 8 nm below the edge along the *Y* axis for forward and backward scan. With the instrument used here, the repeatability of typical CD measurements is in the range of 2 nm. Until now the smallest width obtained with an ordinary Si tip and sharp EBD tip are 17 nm and 10 nm, respectively. These values were not obtained at the same positions. In the case of triangular samples, interaction between probe and sample can lead to effective tip radii that are different from those for rectangular CD structures. The advantage of a triangular shape is that it allows an easy and unambiguous determination of the edge position.

Figure 23.7 shows a typical overview SFM image of gold nanospheres with a nominal diameter of 30 nm on mica. In this image both isolated spheres and also groups consisting of up to 10 spheres are visible. Only the isolated spheres

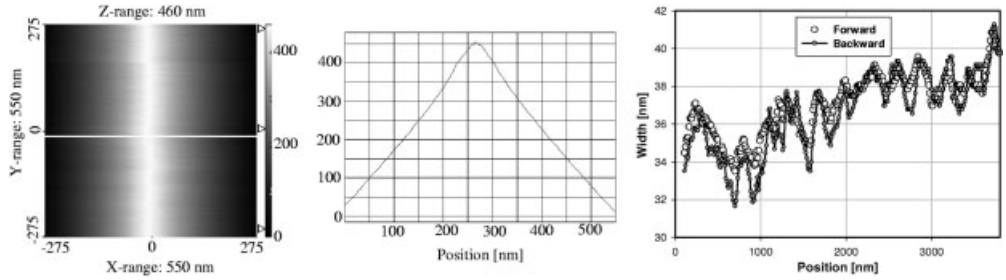

Fig. 23.6 Triangular silicon sample: SFM image (left), line profile (middle), and variation along the Y axis of linewidth 8 nm below the edge.

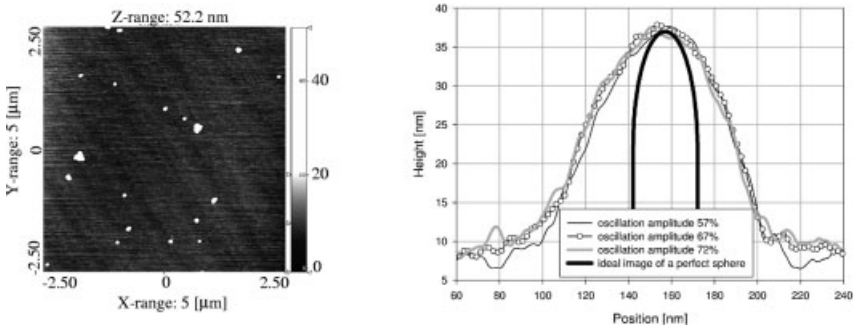

Fig. 23.7 Gold nanospheres on mica: AFM image (left) and line profiles for different remaining oscillation amplitudes (right).

are taken into account for tip shape characterization. Measurements done here aimed to check the influence of the scanning parameters on the imaged specimen shape. Figure 23.7 depicts some example line profiles through the middle of a gold sphere for different remaining cantilever oscillation amplitudes in the range of 40–72 % of the free amplitude. There are no significant differences in these profiles, i. e., the imaged profile does not depend on the sample-probe force in the investigated range. These results are in good agreement with Vesenka et al., who did not observe any compressibility for gold nanospheres with diameters of 5–20 nm either [6]. In Figure 23.8, SFM profiles through the middle of a gold nanosphere are compared for ordinary Si and EBD tips.

The figure underlines that the EBD tip images the upper half of the sphere almost perfectly, which means that these nanospheres are not suited for the characterization of such ultrasharp tips. As the sphere is imaged perfectly it is not possible to distinguish any differences between different EBD tips until they are too dull to follow the sphere's shape. Furthermore, a difference can be recognized in the profiles taken on two different gold nanospheres with two ordinary tips. For a tip evaluation knowledge of the specimen geometry is needed. As the forces acting on a Au particle bounded on the substrate are not symmetric, but highly anisotropic, it is probable that the shape of Au particles on the substrate is not spherical. For this reason Vesenka et al. [6] assumed a hemispherical shape of

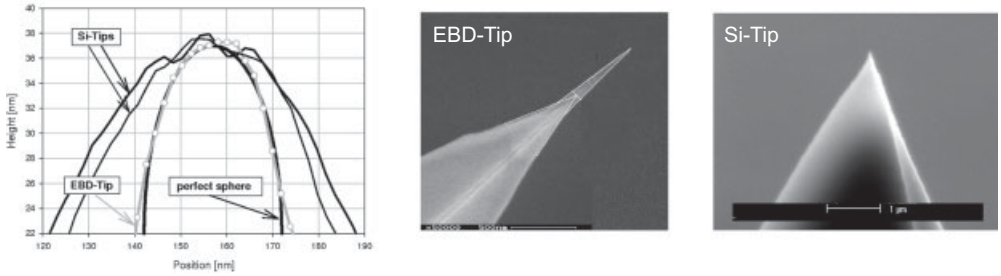

Fig. 23.8 Gold nanosphere on mica. AFM line profiles for ordinary Si and sharp EBD tips and SEM images of such typical tips. SEM image of EBD tip by courtesy of NanoTools GmbH.

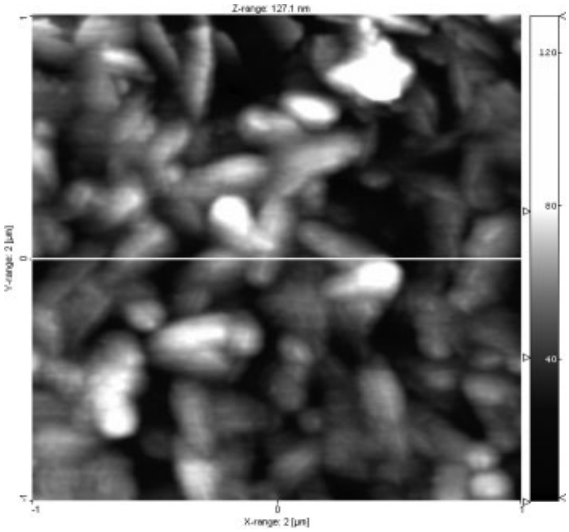

Fig. 23.9 SFM image of the TipCheck sample for complete blind tip reconstruction.

the specimen. In this work a spherical shape is assumed, and as seen in the SFM profile recorded with an EBD tip, any shape duller than a sphere is excluded (at least in the upper half of a gold particle). Because the diameter of gold spheres varies a lot from the value specified by the vendor, for every sphere an individual diameter equal to its height is used.

Completely blind reconstruction was applied in the case of the TipCheck sample from Aurora Nanodevices (see Figure 23.9). The difficulties arising in the use of this method are the comparatively high risk of tip wear at the sharp features of this sample and the extreme sensitivity of this evaluation technique on noise and feedback errors.

Furthermore, the sample structure is very complicated and thus the force field varies in an unpredictable way across this rough surface contrary to the much better defined conditions at well-defined CD structures. For this reason special attention needs to be devoted to the scan control parameters. They need to be adjusted carefully in order to get the best possible image. If the simple geometrical interaction model does not satisfactorily explain the tip–sample interaction, the calibration of the tip used for CD metrology by means of such a sample can yield a wrong effective tip radius. The SFM image shown in Figure 23.9 is a good example of potential problems when using such a sample: In the upper part of the image the structures are clearly sharper than in the lower half, which indicates that the tip suffered from wear during the scan process and that the tip apex thus became larger.

23.3.3 Conclusions

Figure 23.10 compares the tip shapes derived from the measurements on different samples with SEM images of a new tip of the same type. For rectangular sam-

ples a 4-nm corner rounding, for Au particles a perfect spherical shape, and for triangle structure a perfect triangle with 40° apex angle were assumed. In all cases a worst case tip is shown. In the left image a good agreement between the SEM imaged tip and that calculated from SFM measurement of rectangular structures is visible. In the middle picture an SEM image with greater magnification and tip shapes calculated from measurements of all samples investigated in this chapter are shown. Also in this picture a good qualitative agreement is visible, although the quality of the SEM image does not allow any precise conclusions about the differences between the SEM and the SFM results. In order to visualize the differences between the tip shapes extracted from SFM measurements of different samples a graph is shown on the right side of Figure 23.10. Tip shapes determined on gold nanospheres and TipCheck (completely blind reconstruction) have an angle of about 40–50°, when measured about 20 nm from the tip end. For all other samples, the tip angle has a value of about 60–70°. For rectangular structures the angle value reaches always about 70° not later than 40 nm below the tip end. The angle values obtained at gold nanospheres and TipCheck are clearly lower than those determined by scanning artificially etched silicon structures. The possible reason is a lack of high angled features on these samples that are a prerequisite for the characterization of these parts of the tips.

As stated already in the introduction, for linewidth metrology (more precisely, for top CD determination) the width of the tip at a certain distance from its end (e. g., 8 nm as in the example discussed above) is needed. The values of this tip width determined on different samples (see Figure 23.10) vary between 17 nm and 35 nm with the mean of 26 nm. Differences in obtained tip shapes may be caused by the fact that worst case tips were calculated, i. e., the real tip shape might be sharper than those determined at some of the samples here. More investigations with tips that have smaller and bigger tip radii are needed to achieve a better understanding to what extent the tip shapes calculated on the basis of SFM data recorded at different test samples differ and how these discrepancies can be taken into account accordingly to allow us to state reliable absolute values (including their uncertainties) for the tip shape.

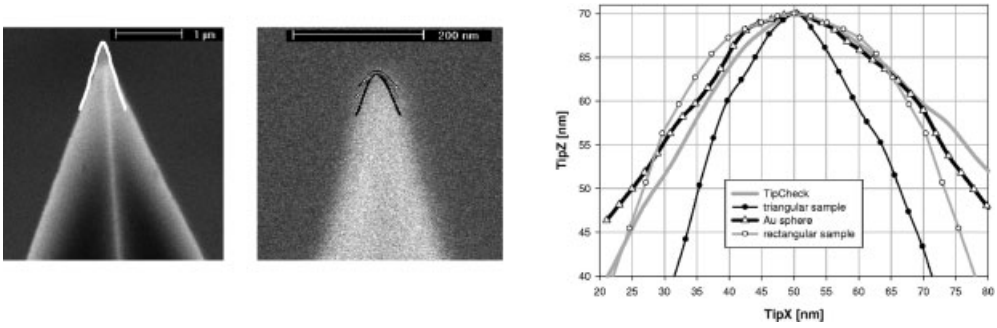

Fig. 23.10 Tip shapes calculated from SFM images of different samples and SEM images of a Si tip. See the text for details.

23.4 Summary

The possibility of determining tip shape from SFM images of different samples were analyzed. The silicon rectangular structures show the valuable advantage that they are very similar to the actual measurement object, i. e., CD structures: For both samples the probe has the same effective radius, even if there are very strong deviations from the simple geometrical model. The disadvantage of these samples is the difficulty in determining an adequate edge position contrary to the triangular silicon structures that allow us to determine the edge position unambiguously. The lack of sharp high-angled features on gold nanospheres makes it impossible to characterize sharp tips on these samples. The method of a completely blind reconstruction (used for the TipCheck sample) is very sensitive to noise, as one cannot distinguish easily between sample features and noise, because the sample shape is unknown.

For the tip width of about 8 nm from the tip end, values determined on the basis of measurement data of different samples such as various etched silicon structures or gold nanospheres vary by about ± 10 nm. It was shown that the introduction of an assumed very small corner roundness in the order of usually a few nanometers leads to a very good agreement between the tip shapes deduced from images recorded at samples with rectangular and undercut features. More investigations are needed in order to show if the differences in calculated tip shapes are due to imperfections of the used samples or whether they stem from physical effects. Furthermore, we did not succeed in repeating the whole measurement series with the same tip. The reasons were tip wear and inability to find the same measurement position on some of the samples. The tip characterization for the same tip over many repeated measurements were made for selected samples pairs. Another important aspect that deserves much more attention is the contribution of material contrast to image formation and consequently to which extent this effect needs to be taken into account when characterising tips. Furthermore, different interaction detection systems are likely to influence the tip charachterisation results as their sensitivity towards the different tip bending motions varies.

References

1 G. Reiss, F. Schneider, J. Vancea, and H. Hoffman, Appl. Phys. Lett. **57**, 867 (1990).

2 D. Keller, Surf. Sci. **253**, 353 (1991).

3 J. Vesenka, R. Miller, and E. Henderson, Rev. Sci. Instrum. **65**, 2249 (1994).

4 U. Hübner, W. Morgenroth, H. G. Meyer, T. Sulzbach, B. Brendel, and W. Mirande, Appl. Phys. A **76**, 913 (2003).

5 K. M. Edenfeld, K. F. Jarausch, T. J. Stark, D. P. Griffis, and P. E. Russel, J. Vac. Sci. Technol. B **12**, 3571 (1994).

6 J. Vesenka, S. Manne, R. Gibson, T. Marsh, and E. Henderson, Biophys. J. **65**, 992 (1993).

7 F. Meli, in *Proceedings of the 4th Seminar on Quantitative Microscopy QM 2000*, PTB-Report F-39, 2000, p. 58.

8 J. S. Villarubia, J. Natl. Inst. Stand. Technol. **102**, 435 (1997).

Part VII
Calibration – Optical Methods

Nanoscale Calibration Standards and Methods: Dimensional and Related Measurements in the Micro- and Nanometer Range.
Edited by Gunter Wilkening, Ludger Koenders
ISBN: 3-527-40502-X

24
Double Tilt Imaging Method for Measuring Aperture Correction Factor

Yen-Liang Chen, Chao-Jung Chen, and Gwo-Sheng Peng

Abstract

This study presents a method for measuring the correction factor of numerical aperture in phase measurement by an interference microscope. The numerical aperture affects the spacing of the fringes in measuring surface topographies, meaning the height value needs to be corrected after measurement. In this study, a double tilt imaging (DTI) method is used to determine this factor. A reflected mirror with $\lambda/10$ flatness is fixed on the top surface of a square gauge block positioned on the sample stage of the interference microscope with quasi-monochromatic light source. The straight fringe pattern of the reflected mirror is formed after adjusting the focal position and the inclination of the sample stage. An autocollimator is positioned adjacent to the square gauge block to measure the tilt angle of its lateral surface. After tilting the sample stage in positive and negative inclines separately, both images of the fringe patterns are recorded. The spatial frequency of the fringe images is then calculated by the sine curve fitting algorithm. The value of the wavelength and the difference both in angle and in spatial frequency between positive and negative tilts provides sufficient information to allow the determination of the aperture correction factor directly. An experimental setup of an interference microscope with a 10× Mirau-type objective lens is utilized to measure the aperture correction factor by adopting the DTImethod. The result yields a traceable average value of 1.01936 for the correction factor with a relative standard uncertainty of 5.7×10^{-4}.

24.1
Introduction

Surface profilers are popular tools for measuring small features on semiconductor chips or MEMS devices with high vertical and lateral resolution. These measurements are performed by stylus instruments [1], scanning probe microscopes (SPM) [2], or optical methods such as confocal and interference microscopes

Nanoscale Calibration Standards and Methods: Dimensional and Related Measurements in the Micro- and Nanometer Range.
Edited by Gunter Wilkening, Ludger Koenders
ISBN: 3-527-40502-X

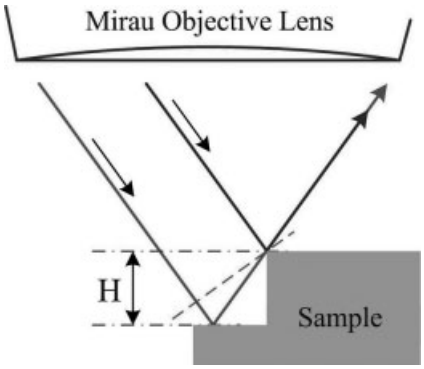

Fig. 24.1 Optical path difference with height difference.

(IMs). For determining or comparing the performance of these instruments, step-height or depth-setting standards are popular for vertical scale calibration [3].

An interference microscope is an efficient and powerful tool for measuring surface textures with high sensitivity and vertical resolution of below 1 nm [4]. In IMs such as Michelson, Mirau, or Linnik types, the optical path differences of positions on sample surfaces are not equal to twice the difference in height because of the focus by objective lens [5]. Figure 24.1 illustrates the measurement between different heights of the sample surface; the height H is not equal to half of the optical path difference unless the incident light is perpendicular to the surface. Hence, the effective numerical aperture (NA) of the system affects the spacing of the fringes and the height value needs to be corrected after measurement.

This investigation presents a double tilt imaging (DTI) method for measuring the correction factor of NA in phase measurement by an IM. A reflected mirror, a square gauge block, and an autocollimator are used to measure the correction factor of the microscope with a 10× Mirau-type objective lens. Using this simple method, the experimental result yields a traceable correction factor of 1.01936 with a relative standard uncertainty of 5.7×10^{-4}.

24.2 Traceability of Step Height

A traceable interference microscope (TIM) has been established to calibrate the step-height standards at the National Measurement Laboratory (NML) in Taiwan. It consists of a commercial IM, a stabilized helium–neon laser, and a ground glass. The light source of the IM is replaced by a stabilized laser. To eliminate the sparkle noise during the optical fiber transmission, the laser passes through a rotated ground glass before the interference. By analyzing the fringe interval in the interference image, the height value of the standard would be calculated and traced to the definition of meter via the stabilized laser.

Figure 24.2 shows the traceability of step height. For SPMs, Ims, or stylus instruments, users usually need the step-height standard to periodically calibrate

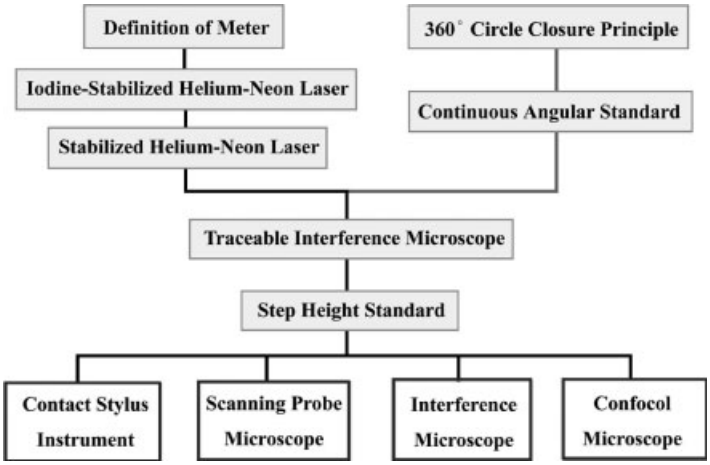

Fig. 24.2 Traceability of step height.

the displacement sensors. The step-height standard can be calibrated by our TIM with stabilized laser to be traced to the length standard. On the other hand, the DTI method is used to measure the NA correction factor. In this method, two tilted angles are measured by an autocollimator, which is calibrated by angular standard and traced to the circle closure principle.

24.3 Working Principle of DIT method

Figure 24.3 reveals the relationship between the spatial wavelength L (or pitch) of interference fringes and the height difference. When the incident light is perpendicular to the sample surface, the height difference between single fringe interval is $\lambda/2$, where λ is the light wavelength. Because of the effect of focus by objective lens, the height difference has to be corrected by multiplying by a factor k, which is called the NA correction factor. Thus, the inclined angle $\bar{\theta}$ can be expressed by trigonometric function as

$$\bar{\theta} = \tan^{-1}\frac{k\cdot\lambda/2}{L} \cong \frac{k\cdot\lambda/2}{L}.$$

Using our proposed DTI method, we measured a flat surface twice at different inclined angles (θ_1 and θ_2). Simultaneously, we also measured two spatial frequencies (ω_1 and ω_2) of the fringe patterns. The spatial wavelengths would be regarded as $L_1 = 2\pi/\omega_1$ and $L_2 = 2\pi/\omega_2$. Therefore, we get $\theta_1 \cong \frac{k\cdot\lambda/2}{L_1} = \frac{k\cdot\lambda\cdot\omega_1}{4\pi}$

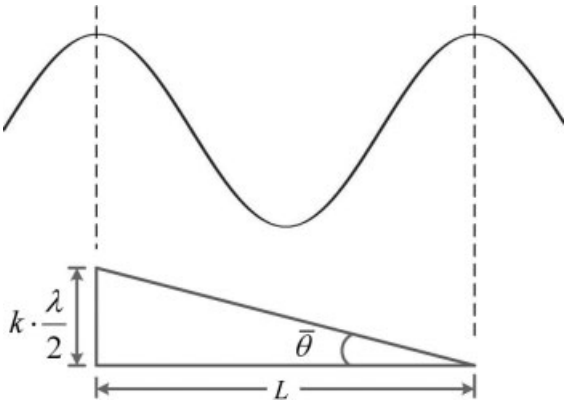

Fig. 24.3 Fringes interval with height difference.

and $\theta_2 \cong \frac{k \cdot \lambda \cdot \omega_2}{4\pi}$. Assuming that $\theta = \theta_1 + \theta_2$ and $\omega = \omega_1 + \omega_2$, the NA correction factor can be obtained:

$$k = \frac{4\pi \cdot \theta}{\lambda \cdot \omega}.$$

Here the values of θ and λ must be traced to the circle closure principle and the definition of the meter respectively, and ω can be obtained by the sine curve fitting algorithm [6].

24.4 Experimental Setup

Figure 24.4 illustrates the experimental setup for measuring the NA correction factor. The stabilized laser beams (1) are separated by beam splitter (2) and then focused by Mirau-type objective lens (3). A reflected mirror with $\lambda/10$ flatness is fixed on the upper surface of square gauge block (5) positioned on the sample stage of the IM. An autocollimator (6) is positioned adjacent to measure the inclined angle of the lateral surface of the square gauge block. After tilting the sample stage in positive (7) and negative (8) inclines separately, both images of the fringe patterns are recorded.

Figure 24.5 shows the straight fringe image of the reflected mirror (9), which is recorded by the CCD camera (4), after adjusting the focal position and the inclination of the sample stage. The image size of the field of view must be calibrated by microscale before measurement. The spatial frequency of the fringe images is then calculated by the sine curve fitting algorithm. The value of the wavelength and the difference both in angle and in spatial frequency between positive and negative tilts reveal sufficient information to allow for the determination of the NA correction factor directly.

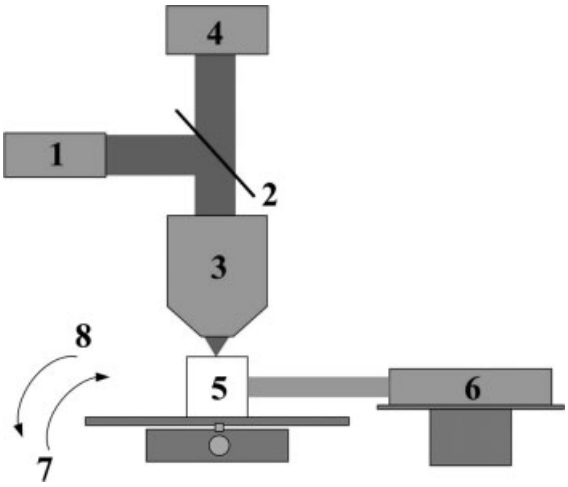

Fig. 24.4 DTI method for measuring NA correction factor.

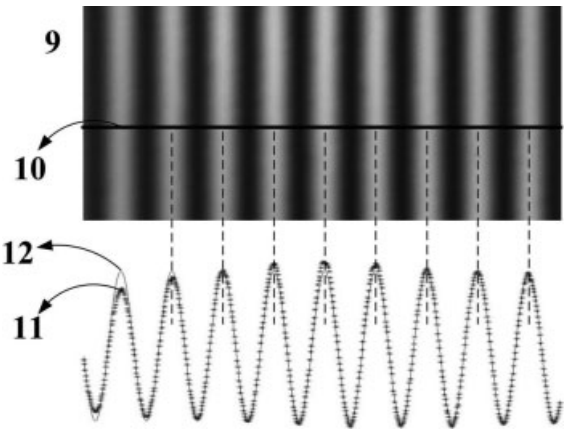

Fig. 24.5 Sine fitting to obtain the spatial frequency from fringe pattern.

Table 24.1 lists the 20 repeat measurements of the NA correction factor of a 10× Mirau objective lens by the DTI method. The average value is 1.01936 and the standard deviation is 5.6×10^{-4}.

Table 24.1 Twenty repeat measurements of NA correction factor

1	1.01829	6	1.01950	11	1.01956	16	1.01985
2	1.02008	7	1.01926	12	1.01948	17	1.01977
3	1.01985	8	1.01968	13	1.01945	18	1.01896
4	1.01923	9	1.01820	14	1.01895	19	1.01912
5	1.01912	10	1.02043	15	1.01874	20	1.01971

24.5 Relative Standard Uncertainty of Numerical Aperture Correction Factor

From the equation of the numerical aperture correction factor (k), the relative standard uncertainty can be expressed as

$$u_{\mathrm{rel}}^2(k)=u_{\mathrm{rel}}^2(\theta)+u_{\mathrm{rel}}^2(\lambda)+u_{\mathrm{rel}}^2(\omega).$$

1. Relative standard uncertainty of angle measurements by autocollimator, $u_{\mathrm{rel}}(\theta)$:
   The summation of positive and negative tilted angles is $\theta=\theta_1+\theta_2$, where θ_1 and θ_2 are measured by autocollimator (ELCOMAT 2000/244). The error sources of angle measurement are (1) traceability, $u(\theta')$ (2) repeatability, $u(\theta'')$; and (3) resolution, $u(\theta''')$.
   (1) *Traceability:* The autocollimator was calibrated by PTB of Germany. The standard uncertainty of traceability is $u(\theta')=0.15''/2=0.075''$, and the degree of freedom is evaluated as 50.
   (2) *Repeatability:* Every value of angle is the average value of 250 repeat measurements, and the standard deviation of these measurements does not exceed 0.2″. Therefore, the standard uncertainty of repeatability is evaluated as $u(\theta'')=0.2''/\sqrt{250}=0.013''$, and the degree of freedom is 249.
   (3) *Resolution:* The resolution of the autocollimator is 0.05″, the standard uncertainty is evaluated as $u(\theta''')=0.05''/2\sqrt{3}=0.014''$, and the degree of freedom is evaluated as 12.5.
   The standard uncertainty of the summation angle is $u^2(\theta)=u^2(\theta_1')+u^2(\theta_1'')+u^2(\theta_1''')+u^2(\theta_2')+u^2(\theta_2'')+u^2(\theta_2''')=2\times[u^2(\theta')+u^2(\theta'')+u^2(\theta''')]$, therefore $u(\theta)=0.11''$ and the combined degree of freedom is $\nu(\theta)=115$. Assuming the measured angle is about 800″, the relative standard uncertainty of angle is evaluated as $u_{\mathrm{rel}}(\theta)=0.11''/2\times 800''=6.9\times10^{-5}$.
2. Relative standard uncertainty of laser wavelength, $u_{\mathrm{rel}}(\lambda)$:
   A stabilized helium–neon laser ($\lambda = 0.632991$ μm) is used as the light source. The uncertainty of the light wavelength would not exceed 0.01 nm, which is sufficient to serve as the light source. The relative standard uncertainty of laser wavelength is $u_{\mathrm{rel}}(\lambda)=0.01/632.99=1.6\times10^{-5}$, and the degree of freedom is evaluated as 50.
3. Relative standard uncertainty of spatial frequency, $u_{\mathrm{rel}}(\omega)$:
   The spatial frequency, obtained by the "four-parameter fitting

of sine" algorithm, is the sum of two spatial frequencies of the fringe images ($\omega = \omega_1 + \omega_2$). The error sources that would affect sine fitting are (1) theory limitation, $u(\omega')$, and (2) optical quality, $u(\omega'')$.

(1) *Theory limitation:* From the limitation of the sine fitting algorithm, $\Delta\omega'/\omega' < \sqrt{2}/\pi \cdot 2^{N+2}$, where $\Delta\omega'$ is the range of frequency varied, ω' is the fitted frequency value, and N is the digital resolution of the bit number. Although the bit number of CCD is 8, we assume that $N = 7$ to take into account the occurrence of lower visibility. Assuming that $\omega' \approx 0.084 = \mu m^{-1}$ for the angle of 800″, we then get $\Delta\omega' < 7.4 \times 10^{-5}$ μm^{-1}. The standard uncertainty of theory limitation $u(\omega') = 7.4 \times 10^{-5}/2\sqrt{3} = 2.14 \times 10^{-5}$ μm^{-1} and the degree of freedom is evaluated as 12.5.

(2) *Optical quality:* The frequency values of fitting lines across sections of the fringe image were not the same due to the optical quality. The maximum difference between any two values $\Delta\omega''$ did not exceed 2.2×10^{-4} μm^{-1}. The standard uncertainty is $u(\omega'') = 2.2 \times 10^{-4}/2\sqrt{3} = 6.4 \times 10^{-5}$ μm^{-1} and the degree of freedom is 12.5.

The standard uncertainty of the sum of two spatial frequencies is $u^2(\omega) = u^2(\omega_1') + u^2(\omega_1'') + u^2(\omega_2') + u^2(\omega_2'') = 2 \times [u^2(\omega') + u^2(\omega'')]$ therefore $u(\omega) = 9.5 \times 10^{-5}$ μm^{-1} and degree of freedom is 60. After normalizing the evaluated value of ω ($2 \times 0.084 = 0.168$ μm^{-1}), the relative standard uncertainty of spatial frequency is shown as $u_{rel}(\omega) = 9.5 \times 10^{-5}/0.168 = 5.7 \times 10^{-4}$.

Thus, the relative standard uncertainty of the numerical aperture correction factor would be shown as $u_{rel}(k) = \sqrt{(6.9 \times 10^{-5})^2 + (1.6 \times 10^{-5})^2 + (5.7 \times 10^{-4})^2} \cong 5.7 \times 10^{-4}$ and the combined degree of freedom is 61.

24.6
Uncertainty Analysis of the Numerical Aperture Correction Factor

Table 24.2 illustrates the uncertainty budget of NA correction factor. We can see that the optical quality caused by the defocus error makes the largest contribution.

24.7
Conclusion

The double tilt imaging method was used for measuring the correction factor of numerical aperture in the phase measurement of an interference microscope

Table 24.2 Uncertainty budget of NA correction factor

Quantity	Estimate	Type	Dist.	Std. Uncertainty	Rel. Uncertainty	υ_i
k	1.01936	–	–	–	5.74×10^{-4}	61
θ	1600″	–	–	0.11″	6.9×10^{-5}	115
$\theta_{1\ \text{Traceability}}$		B	N	0.075″		50
$\theta_{1\ \text{Repeatability}}$		A	t	0.013″		249
$\theta_{1\ \text{Resolution}}$		B	R	0.014″		12.5
$\theta_{2\ \text{Traceability}}$		B	N	0.075″		50
$\theta_{2\ \text{Repeatability}}$		A	t	0.013″		249
$\theta_{2\ \text{Resolution}}$		B	R	0.014″		12.5
λ	632.991 nm	B	–	0.01 nm	1.6×10^{-5}	50
ω	0.168 μm^{-1}	–	–	9.5×10^{-5} μm^{-1}	5.7×10^{-4}	60
$\omega_{1\ \text{Theory limit.}}$		B	R	2.14×10^{-5} μm^{-1}		12.5
$\omega_{1\ \text{Optical qual.}}$		B	R	6.4×10^{-5} μm^{-1}		12.5
$\omega_{2\ \text{Theory limit.}}$		B	R	2.14×10^{-5} μm^{-1}		12.5
$\omega_{2\ \text{Optical qual.}}$		B	R	6.4×10^{-5} μm^{-1}		12.5

with a 10× Mirau-type objective lens. The error sources such as angle measurement, wavelength of light source, and fitting spatial frequency are considered for evaluating the relative standard uncertainty of the numerical aperture correction factor, k. This method shows that the average value for k is 1.01936 with a relative standard uncertainty of 5.7×10^{-4}, which is also traceable to both the definition of meter and angle standard.

References

1 J. F. Song and T. V. Vorburger, Standard reference specimens in quality control of engineering surfaces, J. Res. NIST **96**, 271–289 (1991).

2 J. M. Bennett, V. Eling, and K. Kjoller, Recent developments in profiling optical surface, Appl. Opt. **32**, 3442–3447 (1993).

3 U. Brand and W. Hillmann, Calibration of step-height standards for nanometrology using interference microscopy and stylus profilometry, Prec. Eng. **17**, 22–33 (1995).

4 B. Bhushan, J. C. Wyant, and C. L. Koliopoulos, Measurement of surface topography of magnetic tapes by Mirau interferometry, Appl. Opt. **24**, 1489–1497 (1985).

5 G. Schulz and K. E. Elssner, Errors in phase-measurement interferometry with numerical apertures, Appl. Opt. **30**, 4500–4506 (1991).

6 T. Z. Bilau, T. Megyeri, A. Sárhegyi, J. Márkus, and I. Kollár, Four-parameter fitting of sine wave testing results: iteration and convergence, Comput. Stand. Interfaces **26**(1), 51–56 (2003).

25
How Statistical Noise Limits the Accuracy of Optical Interferometry for Nanometrology

Victor Nascov

Abstract

Our chapter states out the highest degree of accuracy that one can actually get by measuring lengths and wavelengths using optical interferometry followed by processing interference fringes that are digitally recorded and affected by statistical noise. It is substantially based on some of our previous papers concerning with statistical processing of elementary fringe patterns. Here only theoretical results are presented. However, they may be applicable to design real life interferometers when using the best optical components, just in the case of the highest demand of accuracy.

25.1
Introduction

Optical interferometry is a classical method in metrology, commonly used for measurement and testing with micrometer accuracy. Even in nanometrology, optical interferometry is nowadays a main tool for measurement and testing, but in order to increase the sensitivity and accuracy, one uses phase-shift interferometry or multiple wavelength interferometry and, of course, advanced means for detection and information processing [1]. Other new methods of interferometry have been developed recently in order to perform measurements at nanoscale: combined optical and X-ray interferometry [2], homodyne interferometry [3], heterodyne interferometry [4].

In any case, the accuracy on measuring lengths or wavelengths depends on the accuracy with which one can determine the fringe spacing and the fringe position. Many authors report in their papers statements like this: "We get the fringe spacing with a relative accuracy of 1/1000" without any justification. We have analyzed in more detail just this problem of establishing the accuracy of measuring digitized fringes.

Nanoscale Calibration Standards and Methods: Dimensional and Related Measurements in the Micro- and Nanometer Range.
Edited by Gunter Wilkening, Ludger Koenders
ISBN: 3-527-40502-X

There are two main kinds of factors affecting the accuracy of optical metrology. The first kind consists of a lot of uncorrelated disturbances that produce statistical noise, for example, electronic and quantum noise in the CCD detector. In our analysis we have taken into account only these random error sources, which can be globally described by a Gaussian distribution function. The other class of error sources includes deformation of wavefronts due to optical components, imperfections in the CCD detector, mechanical instability of the optical components, temperature instability, etc. Unlike the statistical noise of the first kind, all these error sources have a deterministic nature and our analysis does not take them into account.

25.2
Optical Interferometry Overview

25.2.1
Two Waves Interferometry

Most interferometers divide an incident light beam into two secondary waves, which can be regarded as originating from pointlike sources located at certain positions $S_1(x_1, y_1, z_1)$; $S_2(x_2, y_2, z_2)$, of course neglecting astigmatism. Their complex amplitudes are

$$\begin{aligned} &u_1(x,y,z)=a_1\cdot e^{i\Phi_1(x,y,z)}, \qquad u_2(x,y,z)=a_2\cdot e^{i\Phi_2(x,y,z)},\\ &\Phi_1(x,y,z)=\frac{2\pi}{\lambda}\sqrt{(x-x_1)^2+(y-y_1)^2+(z-z_1)^2},\\ &\Phi_2(x,y,z)=\frac{2\pi}{\lambda}\sqrt{(x-x_2)^2+(y-y_2)^2+(z-z_2)^2}. \end{aligned} \tag{25.1}$$

We give more importance to the phase functions of the complex amplitudes; that is why we set their real amplitudes to be constant. One obtains plane waves as the limit case when the point sources are located at infinity. The fringe pattern of two-wave interference has a harmonic intensity distribution:

$$I(x,y,z)\sim|u_1+u_2|^2=I_0+I_1\cdot\cos(\Delta\Phi),\quad I_0=a_1^2+a_2^2,\quad I_1=2a_1a_2,\quad \Delta\Phi=\Phi_2-\Phi_1 \tag{25.2}$$

where I_0 is the background intensity and I_1 is the intensity of the fundamental harmonic. Regardless of their specific setup, all interferometric devices can be characterized by only a set of a few parameters: the position of each secondary point source relative to the screen (x_1, y_1, z_1); (x_2, y_2, z_2) and the size of the screen $L_x \times L_y$. The fringe pattern depends only on these geometrical parameters, regardless of the fact that the secondary point sources are real or virtual.

There are two types of well-known elementary fringe patterns: Young's fringes and Newton's rings.

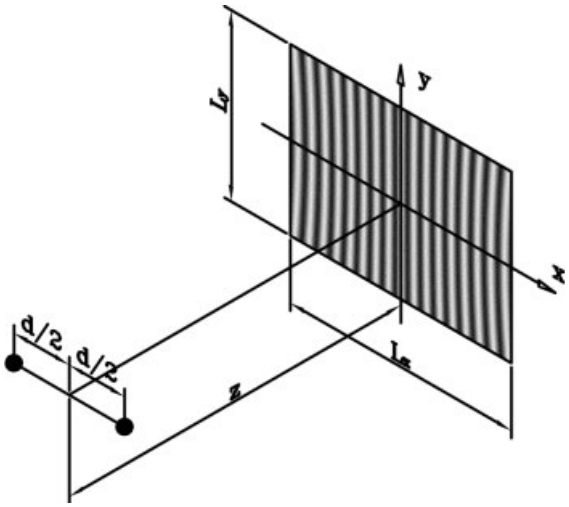

Fig. 25.1 Young's fringes interferometer setup.

Young's fringes occur when the two secondary point sources are located on a direction parallel to the screen. Let their positions be: $S_1(-d/2,0,0)$, $S_2(d/2,0,0)$, as in Figure 25.1. The phase difference function becomes the following third-order series development:

$$\Delta\Phi(x,y)=2\pi\cdot\frac{d}{\lambda}\cdot\frac{x}{z}-\pi\cdot\frac{d}{\lambda}\cdot\frac{x^2+y^2}{z^2}\cdot\frac{x}{z}. \tag{25.3}$$

The first term belongs to a fringe pattern with straight equispaced fringes and a spatial frequency of $d/\lambda z$. This is the dominant component of the fringe pattern while the other term estimates the systematic phase error that we may do when considering such a fringe pattern to have perfect straight and equispaced fringes.

Such an interferometric setup outlines the spatial coherence feature of the light, which is a common feature of all light sources, i. e., any light source is able to produce Young's fringes (at large distance from the point source).

We will use the discrete version of the phase function, with $N_x \times N_y$ samples:

$$\Delta\Phi_{mn}=\Delta\Phi(m\delta_x,n\delta_y)=\frac{2\pi}{N_x}N_{fx}\cdot m-\frac{2\pi}{N_x}N_{fx}\cdot\frac{1}{2}\cdot\frac{L_x^2}{z^2}\cdot\frac{m^2+\gamma^2n^2}{N_x^2}\cdot m,$$
$$N_{fx}=\frac{d}{\lambda}\cdot\frac{L_x}{z},\quad \gamma=\frac{\delta_y}{\delta_x}\quad m=0,1,\ldots,N_x-1,\quad n=0,1,\ldots,N_y-1, \tag{25.4}$$

where N_{fx} denotes the number of fringes along the x direction, and δx and δy denote the sampling steps on the two orthogonal directions x and y.

Newton's rings occur when the two secondary point sources are located on a direction perpendicular to the screen. Let their positions be: $S_1(0,0,-d/2)$ and $S_2(0,0,d/2)$, as in Figure 25.2. The phase difference function becomes the following fourth-order series development:

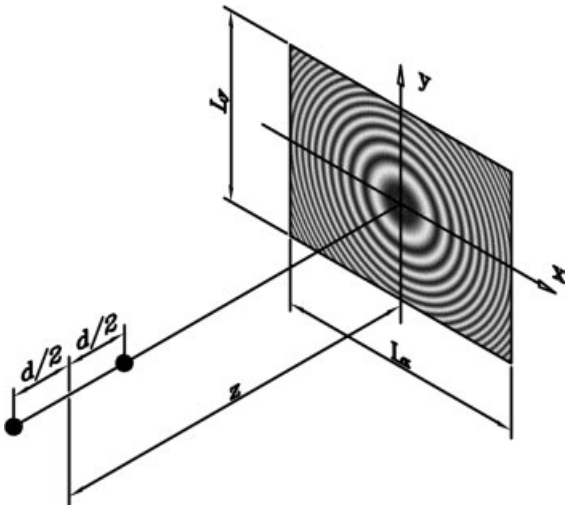

Fig. 25.2 Newton's rings interferometer setup.

$$\Delta\Phi(x,y)=2\pi\cdot\frac{d}{\lambda}-\pi\cdot\frac{d}{\lambda}\cdot\frac{x^2+y^2}{z^2}+\frac{3\pi}{4}\cdot\frac{d}{\lambda}\cdot\left(\frac{x^2+y^2}{z^2}\right)^2. \tag{25.5}$$

The first two terms are commonly used to describe Newton's rings, with their characteristic quadratic dependence of the ring's radius with respect to the interference order. This is correct if the interfering waves are not spherical, but parabolic. The last term gives more precision and may serve to estimate the systematic error done by considering such a fringe pattern to have perfect quadratic dependence of the ring's radius with respect to the interference order.

This interferometric setup outlines the temporal coherence feature of the light. Since this is not a common feature of all light sources, only high coherence light sources (with coherence length greater than d) are able to produce such fringes.

The most convenient discrete version of the phase function with $N_x \times N_y$ samples is

$$\begin{aligned}
&\Delta\Phi_{mn}=\Delta\Phi(m\delta_x,n\delta_y)=\varphi-\frac{8\pi}{N_x^2+\gamma^2N_y^2}\cdot N_f(m^2+\gamma^2n^2)+48\pi\cdot N_f^2\cdot\frac{\lambda}{d}\cdot\left(\frac{m^2+\gamma^2n^2}{N_x^2+\gamma^2N_y^2}\right)^2,\\
&\varphi=2\pi\cdot\frac{d}{\lambda}\bmod 2\pi,\quad N_f=\frac{d}{\lambda}\cdot\frac{L_x^2}{8z^2}(1+\varepsilon^2\gamma^2),\quad \varepsilon=\frac{N_y}{N_x},\quad \gamma=\frac{\delta_y}{\delta_x},\\
&m=-\frac{N_x}{2},\ldots,\frac{N_x}{2}-1,\quad n=-\frac{N_y}{2},\ldots,\frac{N_y}{2}-1.
\end{aligned} \tag{25.6}$$

If the two secondary point sources are located on a direction that is neither normal nor parallel to the screen (Figure 25.3), the fringe pattern becomes a mixture of Young's fringes and Newton's rings.

Let us analyze the fringe pattern of the Michelson interferometer, which has two plane mirrors designed to be perpendicular to each other (Figure 25.5). Be-

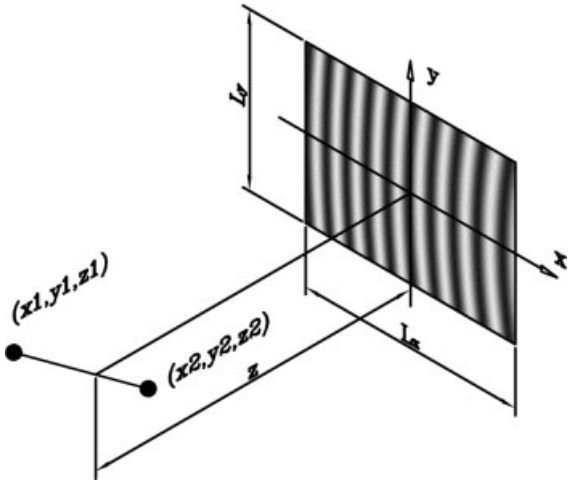

Fig. 25.3 General setup of two point sources interferometer.

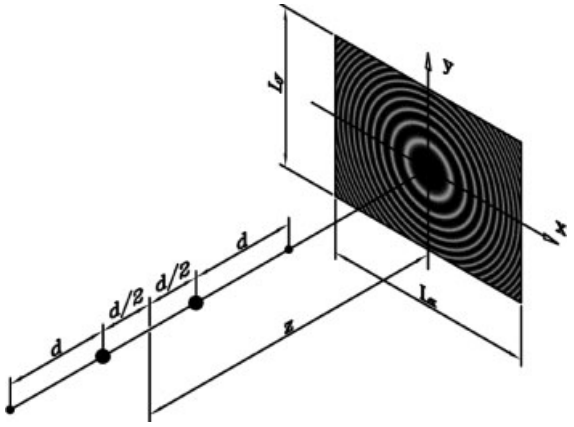

Fig. 25.4 Multiple point sources interferometer in a Newton's rings setup.

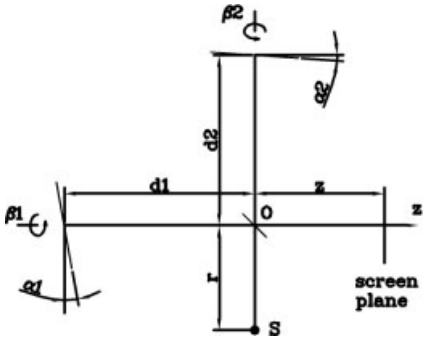

Fig. 25.5 Michelson interferometer.

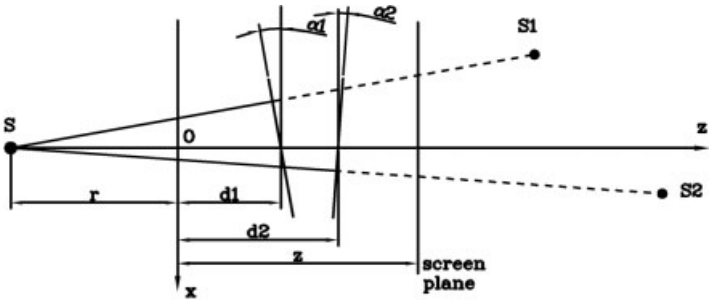

Fig. 25.6 Geometry that generally describes interferometers having two reflecting surfaces.

cause of various reasons, these mirrors may have some tilts relative to their normal position. Figure 25.6 shows the basic geometry of the sources relative to the mirrors and screen, as the two arms of the interferometer were aligned to the same direction. The primary source is located at S and the two secondary sources are located at S_1 and S_2, being the virtual images of the primary source trough the mirrors.

Generally each of the two reflecting surfaces has two degrees of freedom: a tilt angle α and an azimuth β, so that the two secondary point sources are located at

$$S_1(-(r+d_1)\sin 2\alpha_1 \cos\beta_1, -(r+d_1)\sin 2\alpha_1 \sin\beta_1, (r+d_1)\cos 2\alpha_1), \tag{25.7}$$

$$S_2(-(r+d_2)\sin 2\alpha_2 \cos\beta_2, -(r+d_2)\sin 2\alpha_2 \sin\beta_2, (r+d_2)\cos 2\alpha_2). \tag{25.8}$$

Therefore, the phase function has the following third-order series development:

$$\begin{aligned}
\Delta\Phi(x,y) = {} & 4\pi\frac{d_2-d_1}{\lambda} \\
& +4\pi\cdot\left[\frac{\alpha_2\cos\beta_2-\alpha_1\cos\beta_1}{\lambda}\cdot\left(1+\frac{z}{r}+\frac{z^2}{r^2}\right)\right]\cdot x + 4\pi\cdot\left[\frac{\alpha_2\sin\beta_2-\alpha_1\sin\beta_1}{\lambda}\cdot\left(1+\frac{z}{r}+\frac{z^2}{r^2}\right)\right]\cdot y \\
& -2\pi\cdot\left(\frac{d_2-d_1}{\lambda}+\frac{\alpha_2\sin\beta_2-\alpha_1\sin\beta_1}{\lambda}\cdot y\right)\cdot\frac{x^2}{r^2} - 2\pi\cdot\left(\frac{d_2-d_1}{\lambda}+\frac{\alpha_2\cos\beta_2-\alpha_1\cos\beta_1}{\lambda}\cdot x\right)\cdot\frac{y^2}{r^2} \\
& +4\pi\cdot\left[-\frac{d_2\alpha_2\cos\beta_2-d_1\alpha_1\cos\beta_1}{\lambda r}\cdot\left(1+3\frac{z}{r}\right)+2\frac{d_2^2\alpha_2\cos\beta_2-d_1^2\alpha_1\cos\beta_1}{\lambda r^2}\right]\cdot x \\
& +4\pi\cdot\left[-\frac{d_2\alpha_2\sin\beta_2-d_1\alpha_1\sin\beta_1}{\lambda r}\cdot\left(1+3\frac{z}{r}\right)+2\frac{d_2^2\alpha_2\sin\beta_2-d_1^2\alpha_1\sin\beta_1}{\lambda r^2}\right]\cdot y.
\end{aligned} \tag{25.9}$$

The expression above contains a mixture of straight, equidistant fringe patterns and Newton's rings, which generally are not circular. This geometry and expression (25.9) describe, as well, any other interferometric device with two reflecting surfaces: Twyman-Green, Fabry Perot, Murty, optical wedge, etc.

25.2.2
Multiple Waves Interferometry

When interfering waves originating from N_S sources of the form $u_k = a_k e^{ik\Delta\Phi}, k=0,\ldots,N_S-1$, the fringe pattern becomes N_S-2 higher harmonic terms, besides the fundamental harmonic:

$$\begin{aligned} &I = I_0 + I_1 \cdot \cos(\Delta\Phi) + I_2 \cdot \cos(2\Delta\Phi) + \cdots + I_{NS-1} \cdot \cos((N_S-1)\Delta\Phi) \\ &I_0 = \sum_{k=0}^{N_S-1} a_k^2, \quad I_l = 2\sum_{k=0}^{N_S-l-1} a_k a_{k+l}, \quad l=1,\ldots,N_S-1. \end{aligned} \tag{25.10}$$

This is the case of interferometric devices with high reflectivity surfaces. More than two secondary point sources are virtually produced due to multiple reflections and all of them are situated equidistantly on the same direction (Figure 25.4).

There is also another reason why the fringe patterns may have high-order harmonics: By acquiring data with a nonlinear device the output signal becomes higher order harmonics. In such cases the acquired signal is often related to the fringe intensity by raising it to a power

$$I = J_0[1 + V\cos(\Delta\Phi)]^{\gamma}, \qquad \gamma = 0.5 \div 2.5, \quad V = -1 \div 1, \tag{25.11}$$

where V is the fringe contrast. This signal has the following cosine Fourier series:

$$\begin{aligned} &I = I_0 + I_1 \cdot \cos(\Delta\Phi) + I_2 \cdot \cos(2\Delta\Phi) + \cdots + I_{N-1} \cdot \cos((N-1)\Delta\Phi) \\ &I_0 = J_0 \cdot \left[1 + \sum_{k=1}^{\infty} \left(\frac{V}{2}\right)^{2k} \cdot \frac{\gamma \cdot (\gamma-1)\cdots(\gamma-2k+1)}{(k!)^2}\right], \\ &I_l = 2J_0 \cdot \left(\frac{V}{2}\right)^{l} \cdot \sum_{k=1}^{\infty} \left(\frac{V}{2}\right)^{2k} \cdot \frac{\gamma \cdot (\gamma-1)\cdots(\gamma-2k-l+1)}{k!(k+l)!}, \quad l=1,\ldots,N-1. \end{aligned} \tag{25.12}$$

25.3
Statistical Errors on Processing Elementary Fringe Patterns

Some of our previous papers are concerned just with statistical processing of these two elementary types of fringe patterns: straight equispaced fringes and Newton's rings [5–9]. For this purpose we commonly use least-squares fitting (LSF) routines to compute the basic parameters of the fringe patterns as statistical quantities.

Straight equispaced fringes are often regarded to have a harmonic distribution of intensity along a direction x or over a plane (x, y):

1D fringe pattern:

$$I(x)=I_0+I_1\cdot\cos(2\pi\nu x+\varphi) \tag{25.13a}$$

2D fringe pattern:

$$I(x,y)=I_0+I_1\cdot\cos\left(2\pi(\nu_x\cdot x+\nu_y\cdot y)+\varphi\right), \tag{25.13b}$$

where ν is the spatial frequency of the fringes having two components for the 2D fringe pattern and φ is a phase parameter that specifies the global positioning of the fringe pattern.

Fringe pattern acquisition by a CCD leads to a set of sampled and quantized values of the intensity distribution:

1D:

$$I_k=I(k\cdot\delta x)=I_0+I_1\cdot\cos\left(\frac{2\pi}{N}N_f k+\varphi\right);\quad N_f=N\cdot\nu\cdot\delta x,\quad k=0,1,\ldots,N-1 \tag{25.14a}$$

2D:

$$I_{mn}=I(m\cdot\delta x,n\cdot\delta y)=I_0+I_1\cdot\cos\left(2\pi\cdot\left(m\cdot\frac{N_{fx}}{N_x}+n\cdot\frac{N_{fy}}{N_y}\right)+\varphi\right); \tag{25.14b}$$
$$N_{fx}=N_x\cdot\nu_x\cdot\delta x,\quad N_{fy}=N_y\cdot\nu_y\cdot\delta y,\quad m=0,1,\ldots,N_x-1,\quad n=0,1,\ldots,N_y-1$$

where δx and δy denote the sampling steps, which are the spacing between two adjacent CCD pixels, on the two orthogonal directions x and y. Instead of the spatial frequency ν it is more convenient to use the adimensional parameter N_f, that is the number of fringes in the fringe pattern. It has also two components in the case of 2D fringe pattern.

Compare relations (25.14a) and (25.14b) with (25.4) to find out the relationship between the interferometric device parameters (d, z, L, λ) and the fringe pattern parameters (N_f, φ).

We have found by analytical calculus [6, 7] that, when applying a LSF computer routine to process such a fringe pattern, the fringe parameters can be determined with the following statistical uncertainties (standard deviations):

1D:

$$\mathbf{A}=[\,I_0\quad I_1\quad N_f\quad \varphi\,],\quad \sigma_{\mathbf{A}}=\frac{1}{\sqrt{N}}\cdot\left[\,\sigma_I\quad \sqrt{2}\sigma_I\quad \frac{\sqrt{6}}{\pi}\frac{\sigma_I}{I_1}\quad 2\sqrt{2}\frac{\sigma_I}{I_1}\,\right] \tag{25.15a}$$

2D:

$$\mathbf{A}=[\,I_0\quad I_1\quad N_{fx}\quad N_{fy}\quad \varphi\,],\quad \sigma_{\mathbf{A}}=\frac{1}{\sqrt{N}}\cdot\left[\,\sigma_I\quad \sqrt{2}\sigma_I\quad \frac{\sqrt{6}}{\pi}\frac{\sigma_I}{I_1}\quad \frac{\sqrt{6}}{\pi}\frac{\sigma_I}{I_1}\quad \sqrt{14}\frac{\sigma_I}{I_1}\,\right] \tag{25.15b}$$

assuming that there are additive Gaussian noise with 0 mean and σ_I^2 variance in the image of the fringe pattern ($\sigma_I = \sqrt{\sigma_I^2}$).

Moreover, if the intensity fluctuations of all the pixels in the fringe pattern are statistically independent and each of them has Gaussian distribution, then the statistical fluctuations of **A** are Gaussian too (multivariate normal distribution).

We created computer programs for fringe processing based on LSF or discrete Fourier analysis [6, 7]. We proved the theoretical results (25.15) by statistically processing the results of a lot of simulated fringe patterns ($> 10\,000$) and concluded that these formulae estimate well the actual uncertainties in fringe processing if the fringe pattern contains at least three sine fringes or 15–20 not harmonic fringes (Fabry Perot), which may have as well not uniform contrast. The statistical errors (25.15) do not depend on the number of fringes if the sampling does not go lower than eight samples for fringe spacing.

Newton's rings patterns have the following distribution of intensity:

1D fringe pattern:

$$I(x) = I_0 + I_1 \cdot \cos\left(\frac{\pi d}{\lambda z^2} \cdot (x - x_0)^2 - \frac{2\pi d}{\lambda}\right) \tag{25.16a}$$

2D fringe pattern:

$$I(x,y) = I_0 + I_1 \cdot \cos\left(\frac{\pi d}{\lambda z^2} \cdot ((x - x_0)^2 + (y - y_0)^2) - \frac{2\pi d}{\lambda}\right) \tag{25.16b}$$

(x_0, y_0) being the center of the rings. The most convenient digitized form of the Newton's rings has been proved to be

1D:

$$I_k = I(k \cdot \delta x) = I_0 + I_1 \cdot \cos\left(\frac{8\pi}{N^2} \cdot N_f \cdot (k - C_x \cdot N)^2 + \varphi\right), \quad k = -\frac{N}{2}, \ldots, \frac{N}{2} - 1, \quad C_x = \frac{x_0}{L_x} \tag{25.17a}$$

2D:

$$I_{mn} = I(m \cdot \delta x, n \cdot \delta y) = I_0 + I_1 \cdot \cos\left(\frac{8\pi}{N_x^2 + \gamma^2 N_y^2} \cdot N_f \cdot (m^2 + \gamma^2 n^2) + \varphi\right),$$
$$m = -\frac{N_x}{2}, \ldots, \frac{N_x}{2} - 1, \quad n = -\frac{N_y}{2}, \ldots, \frac{N_y}{2} - 1, \quad \gamma = \frac{N_y}{N_x}. \tag{25.17b}$$

For simplicity, 2D Newton's rings were regarded here to be centered, but see paper [6] for further details in the general case. We have found by analytical calculus [9] that, when applying a LSF computer routine to process such a fringe pattern, the fringe parameters can be determined with the following statistical uncertainties (standard deviations):

1D:

$$\mathbf{A}=[\,I_0 \quad I_1 \quad N_f \quad \varphi \quad C_x\,],$$
$$\sigma_{\mathbf{A}}=\frac{1}{\sqrt{N}}\cdot\left[\sigma_I \quad \sqrt{2}\sigma_I \quad \frac{3\sqrt{5}}{2\sqrt{2}\pi}\frac{\sigma_I}{I_1} \quad \frac{3}{2}\sqrt{2(80C_x^4-8C_x^2+1)}\frac{\sigma_I}{I_1} \quad \frac{\sqrt{2}}{8\pi N_f}\sqrt{3(1+60C_x^2)}\frac{\sigma_I}{I_1}\right] \tag{25.18a}$$

2D:

$$\mathbf{A}=[\,I_0 \quad I_1 \quad N_f \quad \varphi\,],$$
$$\sigma_{\mathbf{A}}=\frac{1}{\sqrt{N\gamma}}\cdot\left[\sigma_I \quad \sqrt{2}\sigma_I \quad \frac{3(1+\varepsilon^2\gamma^2)}{2\pi}\sqrt{\frac{5}{2(1+\varepsilon^4\gamma^4)}}\frac{\sigma_I}{I_1} \quad \sqrt{\frac{9+10\varepsilon^2\gamma^2+9\varepsilon^4\gamma^4}{2(1+\varepsilon^4\gamma^4)}}\frac{\sigma_I}{I_1}\right], \tag{25.18b}$$
$$N=N_xN_y, \quad \varepsilon=N_y/N_x, \quad \gamma=\delta_y/\delta_x$$

assuming that there are additive Gaussian noise with 0 mean and σ_I^2 variance in the image of the fringe pattern. See reference [9] for more details about these statistical errors.

25.4
Wavelengths and Displacements Measurement

Let us design an interferometer for measuring wavelengths or relative displacements with a relative accuracy of 10^{-11}, which being the accuracy of specifying the international etalon of meter nowadays. We choose a Murty interferometer in a setup that provides straight equispaced fringe pattern: a few minutes optical wedge whose faces make up an optical path d (referring to Figure 25.6, $d = d_2–d_1$). The light beam should be collimated (primary source S located at infinity).

Applying a computer LSF routine to the digital fringe pattern we get the fringe parameters (N_f, φ) with the statistical uncertainties (σ_{N_f},σ_φ), theoretically estimated by (25.15). The high-order terms in (25.9) can be used to determine the systematical phase error due to various reasons (the beam may be not very well collimated, the reflecting surfaces may be misaligned, etc.). The systematical errors have to be compared with the statistical ones, which critically depend on the CCD resolution (number of samples N).

Determining the number of fringes N_f we can get the wavelength λ relative to a reference wavelength λ_0 of an etalon source that makes a fringe pattern with N_{f0} fringes. The accuracy achieved by now is not so good, but it can be improved in a next step, using the information contained in the phase parameter , as well and designing the interferometer to work at high interference order (thickness d as large as possible). Firstly, we get a coarse value λ^* of the wavelength based on the proportionality between fringe spacing and wavelength. Then we compute the interference order k and at last we get the wavelength λ with increased accuracy:

$$\lambda^* = \lambda_0 \cdot \frac{N_{f0}}{N_f}, \quad k = [d/\lambda^*], \quad \lambda = \frac{2\pi d}{2k\pi + \varphi}, \quad \frac{\sigma_\lambda}{\lambda} \approx \frac{\sigma_\varphi}{2k\pi}. \tag{25.19}$$

Hence, the larger the interference order k is, the better the accuracy of the distance measurement will be. However, the interference order k cannot be increased indefinitely, but as much as it can be determined with an accuracy of one unit, using the fringe number N_f:

$$\sigma_k = k\frac{\sigma_{N_f}}{N_f} < 1 \quad \Rightarrow \quad k < \frac{N_f}{\sigma_{N_f}} = N_f\sqrt{N}\frac{\pi}{\sqrt{6}} \cdot \frac{I_1}{\sigma_I} \tag{25.20}$$

The thickness d should not exceed a maximal value given by $d < k_{max}\lambda$. Thus, we find out the accuracy limit on measuring the wavelength using the whole information contained in the straight equispaced fringe pattern with N samples:

$$\sigma_k < 1 \quad \Rightarrow \quad \frac{\sigma_\lambda}{\lambda} > \frac{\sigma_\varphi}{2\pi} \cdot \frac{\sigma_{N_f}}{N_f} = \frac{\sqrt{21}}{\pi^2 N N_f} \cdot \frac{\sigma_I^2}{I_1^2}. \tag{25.21}$$

Relations (25.20) and (25.21) were established by using formulae (25.15*b*).

If the thickness d is set to 0 (i. e., interference order k is 0 too), the interferometric device is equivalent with the setup in Figure 25.1, for producing Young's fringes. Such a setup cannot be used for precise measurements, since the accuracy is limited to the accuracy of N_f because the phase parameter becomes useless. This case is like measuring with a caliper without vernier. Such an interferometer cannot reach nanometric accuracy since the accuracy of N_f is typically of about 10^{-4} (assuming $N = 10^6$ pixels and $\sigma_I/I_1 = 0.1$).

Assuming a 1024 × 1024 pixels CCD and a relative noise of 5 % ($\sigma_I/I_1 = 0.05$), the wavelength can be measured with a relative accuracy of 10^{-11} if the fringe pattern has about 110 fringes. In this case the sampling rate would be of about 9 pixels/fringe spacing. Note that the sampling rate should not go less than 8 pixels/fringe spacing.

The same interferometer can also measure relative displacements with the same relative accuracy, but only using the parameter because the number of fringes N_f gives no information about displacements (it depends only on the wedge angle). Only by fringe counting one can measure large displacements, but this is a lengthy task, strongly affected by various disturbances. This case is like measuring with a caliper that has a vernier but the coarse scale is missing.

25.5
Absolute Distance Measurement

We have found the expression *absolute distance measurement* in reference [10] with the following meaning: precise distance measurement by two-wave optical interferometry, without need of relative displacements and fringe counting. In that

reference the method used was phase shift interferometry, but now we will check if absolute distance measurement is possible as well, by statistically processing a single fringe pattern instead of using phase shifting.

Let us think about the interferometer setup in Figure 25.2. The device parameters (λ, z, L) should be kept precisely constant, while d is the variable to be measured. Based on the fringe pattern parameters (N_f,) computed by a LSF routine with the statistical uncertainties (σ_{N_f},σ_φ), theoretically estimated by (18), the distance d can be measured in two steps: Firstly, we get a coarse value d^* based on the proportionality between this quantity and the number of rings N_f in the fringe pattern. Then we compute the interference order k and at last we get the distance d with increased accuracy:

$$d^*=N_f\cdot\frac{8z^2}{L_x^2(1+\varepsilon^2\gamma^2)}\cdot\lambda,\quad k=[d^*/\lambda],\quad d=\left(k+\frac{\varphi}{2\pi}\right)\cdot\lambda,\quad \sigma_d=\lambda\cdot\frac{\sigma_\varphi}{2\pi},\quad \frac{\sigma_d}{d}\approx\frac{\sigma_\varphi}{2k\pi}. \tag{25.22}$$

Hence, the larger the interference order k is, the better the accuracy of the distance measurement will be. However, the interference order k cannot be increased indefinitely, but as much as it can be determined with an accuracy of one unit, using the fringe number N_f:

$$\sigma_k=k\cdot\frac{\sigma_{N_f}}{N_f}<1\quad\Rightarrow\quad k<\frac{N_f}{\sigma_{N_f}}=N_f\sqrt{N}\frac{2\pi}{3\sqrt{5}}\cdot\frac{I_1}{\sigma_I}. \tag{25.23}$$

The maximal distance d that can be measured is given by $d<k_{max}\lambda$. Thus we find out the accuracy limit on absolute distance measuring, using the whole information contained in the Newton's rings pattern with N samples:

$$\sigma_k<1\Rightarrow\frac{\sigma_d}{d}>\frac{\sigma_\varphi}{2\pi}\cdot\frac{\sigma_{N_f}}{N_f}=\frac{3\sqrt{35}}{4\pi^2N\cdot N_f}\cdot\frac{\sigma_I^2}{I_1^2}. \tag{25.24}$$

We established relations (25.23) and (25.24) by using formulae (25.18*b*) and supposing quadratic pixels ($\delta_x=\delta_y$) and CCD area ($N_x=N_y$).

Note that all these measurements depend on a reference wavelength and the parameters of the device, which are length quantities too. Thus, the distances can be measured only relatively to a reference length. The interferometric device has to be calibrated using a very precise reference distance d_0. The reference distance d_0 should also be measured relative to the wavelength of the source used. For this purpose the interferometric device absolutely requires a moving part to continuously modify the distance d_0 in the range from 0 to an upper limit. During this movement one needs to count the fringes. Only by this way it is possible to calibrate the interferometric device relative to a reference wavelength, as the nowadays metrological standards state. Once calibrated, we can further use the interferometric device to measure fixed distances (not relative displacements, i. e., absolute distance measurement).

As a light source we should use the best-stabilized He–Ne laser (λ = 632.99139822 nm), which is one of the radiation sources recommended by the "Bureau International des Poids et Measures" (Paris) to be used as maximum precision etalon [11].

The same interferometric device can be designed to measure wavelengths, having the same relative accuracy like in the case of measuring distances:

$$\frac{\sigma_\lambda}{\lambda} > \frac{\sigma_\varphi}{2\pi} \cdot \frac{\sigma_{N_f}}{N_f} = \frac{3\sqrt{35}}{4\pi^2 N \cdot N_f} \cdot \frac{\sigma_I^2}{I_1^2} \tag{25.25}$$

Also the measuring result depends on the device's parameters, which has to be calibrated so that all the measurements can be expressed relatively to a reference wavelength, accordingly to the international metrological statements. (The meter etalon itself is expressed as a multiple of a reference wavelength.)

25.6 Conclusions

We were concerned with establishing theoretically the accuracy limit of optical interferometry and concluded that it is possible to reach nanometric accuracy on measuring lengths and wavelengths when processing digitized fringe patterns with a number of samples of about 1 Mpixel. We have found that both straight equispaced fringe patterns and Newton's rings can be used for measuring wavelengths and relative displacements with the same level of accuracy, when they have the same number of samples.

The possibility for *absolute distance measurement* was discussed by statistically processing a single fringe pattern of Newton's rings type, instead of applying phase shifting as presented in [10].

Although the overall error budget for the real life optical interferometers includes more other terms than the Gaussian statistical errors, these theoretical results approach the accuracy limit of the best manufactured optical interferometers, working in the best conditions when all deterministic errors are minimized.

References

1 R. Schödel and G. Bönsch, Interferometric measurements of thermal expansion, length, stability and compressibility of glass ceramics, in *Proc. of the 3rd Euspen International Conference, Eindhoven, The Netherlands, May 26th–30th* (2002).

2 G. Basile, P. Becker, A. Bergamin, G. Cavagnero, A. Franks, K. Jackson, U. Kuetgens, G. Mana, E. W. Palmer, C. J. Robbie, M. Stedman, J. Stümpel, A. Yacoot, and G. Zosi, Combined optical and X-ray interferometry for high-precision dimensional metrology, Proc. R. Soc. London A **456**, 701–729 (2000).

3 Taeho Keem, Satoshi Gonda, Ichiko Misumi, Qiangxian Huang, and Tomizo Kurosawa, Removing nonlinearity of a homodyne interferometer by adjusting the gains of its quadrature detector systems, Appl. Opt. **43**(12), 2443–2448 (2004).

4 Chien-ming Wu, Heterodyne interferometric system with subnanometer accuracy for measurement of straightness, Appl. Opt. **43**(19), 3812–3816 (2004).

5 Adrian Dobroiu, Adrian Alexandrescu, Dan Apostol, Victor Nascov, and Victor Damian, Improved method for processing Newton's rings fringe patterns, *6th Symposium on Optoelectronics (SIOEL '99)*, Proc. SPIE **4068**, 342–347 (2000).

6 Victor Nascov, Adrian Dobroiu, Dan Apostol, and Victor Damian, Statistical processing of elementary fringe patterns, Proc. SPIE **5227**, 43–50 (2002).

7 Victor Nascov, Adrian Dobroiu, Dan Apostol, and Victor Damian, Statistical processing of straight equispaced fringe patterns using the discrete Fourier analysis, Proc. SPIE **5144**, 96–104 (2003).

8 Victor Nascov, Adrian Dobroiu, Dan Apostol, and Victor Damian, Automatic digital processing of Newton's rings fringe pattern, Proc. SPIE **4430**, 835–841 (2001).

9 Victor Nascov, Adrian Dobroiu, Dan Apostol, and Victor Damian, Statistical errors on Newton fringe pattern digital processing, *7th Conference in Optics (Romopto 2003)*, to be published in Proc. SPIE.

10 Hyug-Gyo Rhee and Seung-Woo Kim, Absolute distance measurement by two-point diffraction interferometry, Appl. Opt. **41**(28), 5921–5928 (2002).

11 www.bipm.org, website of the Bureau International des Poids et Mesures.

26
Uncertainty Analysis of the PTB Measuring Equipment for the Investigation of Laser Interferometers

G. Sparrer and A. Abou-Zeid

Abstract

A measuring facility of the highest precision for the calibration of the complete laser interferometers (LI) for length measurements is described. During calibration a shifting comparison with a standard LI is made. So-called Abbe errors are thus avoided. The comparator is situated in a measuring chamber wherein temperature, and later air pressure, too, can be measurably varied. The calibration facility also includes a highly accurate weather station and temperature gauge with which the absolute refractive index, respectively, thermal expansion can be determined and compensated. Uncertainty budgets for the two main components of the calibration facility, the mechanics/optics of the comparator and the standard LI with compensators are being compiled according to GUM. The measurement uncertainties for a number of variants and eventually the expanded uncertainties for the entire unique facility are given.

26.1
Introduction

Laser interferometers for length measurements (in the following called "LI") range are among the most precise means of length measurement. Their in principle high accuracy can, however, be impaired by numerous influencing quantities and components (e. g., laser head, interferometer optics, measuring electronics, air and body sensors, weather station resp. compensator, software, and, if applicable, associated air refractometer, etc.) [1–3, 7, 10]. This disadvantage can be compensated by calibrating the LI. There are two basic methods to calibrate an LI which can at times be combined:

1. Calibation of all individual components of the LI.
2. Calibration of the entire LI with interaction of all components in a shifting comparision preferably with a standard LI on a comparator.

Nanoscale Calibration Standards and Methods: Dimensional and Related Measurements in the Micro- and Nanometer Range.
Edited by Gunter Wilkening, Ludger Koenders
ISBN: 3-527-40502-X

Fig. 26.1 Comparator for the calibration of complete LIs with measuring chamber.

At PTB a shifting comparator for the calibration of LIs has been put on stream which mainly operates according to method 2 [3–9] (Figure 26.1). The aim is to determine the resulting average systematic length-dependent measurement deviation and the measurement uncertainty of the LI to be calibrated. If these calibration values are used for the correction of the measurement result, the accuracy of an LI can be increased by approx. one order of magnitude. However, precondition is the most accurate knowledge of the measurement uncertainty of the standard measuring equipment. Therefore, the main part of the work is to describe and analyze the measurement uncertainties of the most important characteristics of this unique equipment to which belong the comparator, three standard LI, and a standard weather station.

26.2 The Calibration Facility

In the calibration procedure applied, comparison measurements are carried out between the complete laser interferometer to be calibrated and a PTB standard LI. The lengths of the two measurement beams are varied by the same amount and free of so-called Abbe errors. This is achieved by a comparator with a specific optical measuring setup (Figure 26.2). The main component thereof is a large

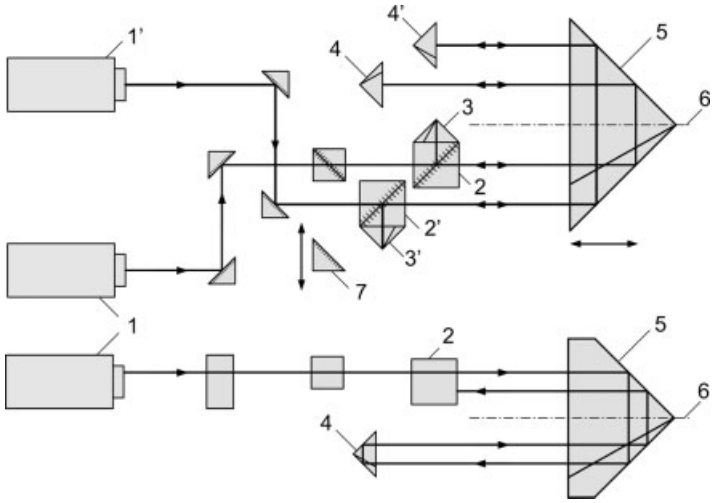

Fig. 26.2 Optical principle of the comparator with a large triple mirror (schematically); standard-LI: 1 – laser, 2 – beam splitter, 3 – reference triple prism, 4 – measuring triple prism – to be calibrated LI: the same numbers as standard LI but with apostrophe; 5 – large triple mirror, 6 – measuring axis, 7 – deviating prism (top and side view).

triple mirror mounted on a measuring carriage [3–9] (straightness deviation of the guide < 30 μm, angle deviation $< 1'$). The triple mirror consists of three wrung zerodur plates each with an optical layer which practically does not influence the polarization condition of the impinging laser beams (beam deviation $< 5''$, straightness of surface $< \lambda/20$). The dead paths in Figure 26.2 amount to a maximum of some 100 mm, are showing, however, for both measuring beams the same amount so that their effect is self-erasing so that the correction of the dead stretches can be abandoned.

The two measurement beams are so adjusted that they touch this triple mirror parallel to each other (beam distance 26.5 mm), are then reflected antiparallel to their respective measurement triple prisms 4 and 4' (these are usually movable but in this case fixed), and are then directed back via the triple mirror to the respective detectors of the LIs. The avoidance of the so-called Abbe error is achieved by the use of the large triple mirror. This mirror effects self-centering of the two measuring axes (each one being the symmetry line between outgoing measurement beam and returning measurement beam) of the LIs to be compared, i. e., these axes always agree ideally.

The measuring setup also guarantees that the two measurement beams to be compared are more or less located in the same beam corridor and in the same measurement circle and that, as a result, the same refractive index and the same thermal expansion influence act on the two LIs.

The calibration equipment also includes calibrated precision measuring devices for the determination of the air parameters (temperature, pressure, humidity, and

CO_2 content) and of the body temperature. The traceability of the standard measurement installation (hence also of the wavelength of the radiation of the used standard LI, and, if necessary, also of the LIs to be calibrated by frequency comparison with the primary standard of length, the $^{127}J_2$ stabilized He–Ne laser) is guaranteed by PTB calibrations and measurement comparisons.

A high accuracy of the calibrations is further achieved by arranging the LI, except for the laser heads, within a thermostated and to the exterior well-insulated measuring chamber. The interior of the chamber is of aluminum. Because of the good thermal conduction and the thermal short circuit thus induced, very small air temperature gradients, spatially and temporally stable, prevail in the chamber (< 20 mK/m resp. < 10 mK/h even during movement of the triple mirror. The temperature changes of the body temperature sensors for specimen and standard, which are arranged in the same spot, are smaller than 1 mK/h). With the aid of thermostats it is possible to keep the temperature constant or to vary it in the range of 20 °C ± 5 K. The measuring chamber is constructed as a manostat so that within a foreseeable time a variation of the air pressure can be created.

26.3 Measurement Procedure

The measured values are recorded at fixed positions in a working range of about 2 m and in steps of predominantly 80 mm. The respective results of counts of the two LIs (uncorrected increments of fractions of the laser wavelength of the standard LI as well as corrected metric measurement values for the LI to be examined, obtained by the compensation unit of the LI to be calibrated) were recorded synchronously by means of external trigger pulses. In the same way, the air parameters assigned to the calibration device and the body temperature were recorded. With these synchronously measured air parameters, the current absolute refractive index of air is determined according to [11], and the thermal expansion is ascertained from the registered body temperatures and the linear expansion coefficient α, both for each measurement interval. The corrected length values measured with the standard LI are calculated from the calibrated vacuum wavelength, the number of measured increments, the respective refractive index of air, and the thermal expansion.

i measurement points in j measurement sequences and k measurement series are recorded at different air parameters. From the measured value pairs for the corrected lengths L_{Pijk} and L_{Nijk} of the LI to be tested resp. of the standard LI, all individual measurement deviations ΔL_{ijk} were calculated as follows:

$$\Delta L_{ijk} = L_{Pijk} - L_{Nijk}, \tag{26.1}$$

e. g., with $1 \leq i \leq 26$, $1 \leq j \leq 10$ and $1 \leq k \leq 7$.

The average length-dependent systematic measurement deviation ΔL of the LI to be calibrated was calculated from all value pairs [L_{Nijk}; ΔL_{ijk}] by linear regression:

$$\Delta L = a + bL_N. \tag{26.2}$$

On the calibration certificate, the respective length-depending correction value and the expanded measurement uncertainties of the calibrated LI calculated according to GUM [12, 13], with and without the use of the stated correction, will be shown. For the calculation of these measurement uncertainties, it is necessary to determine the measurement uncertainty of the complete calibration facility. The systematic measurement deviations of the sensors of the specimen and their measurement uncertainties are also determined.

26.4 The Uncertainty of the Complete Calibration Facility

The calibration facility consists of two main components:

1. mechanics/optics of the comparator,
2. standard LI with the measuring facilities for determining the refractive index of air (the so-called weather station) and the thermal expansion (depending on the task, also without the latter).

In the following, a measurement uncertainty budget according to GUM [12, 13] is drawn up resp. calculated for each of the two components. The calculating rule given therein will only be outlined here. Between the overall uncertainty $u(y)$ of the estimated value y of the result quantity Y, the individual uncertainty contributions $u_i(y)$ of the estimated values x_i of the result quantities X_i, the standard measurement uncertainties $u(x_i)$, and the sensitivity coefficient c_i, the following applies:

$$u^2(y) = \sum u_i^2(y) \tag{26.3}$$

$$u_i(y) = c_i u_i(x) \tag{26.4}$$

$$c_i = \frac{\partial f}{\partial X_i}. \tag{26.5}$$

The model function f must be differentiated partially each time according to X_i. In the uncertainty budgets, a distinction is made between length-independent and length-dependent components.

26.4.1 The Measurement Uncertainty of the Comparator

For the investigation of the so-called “comparator error”, two high-quality standard LIs with calibrated vacuum wavelengths were first of all compared to each other according to Figure 26.2. In principle, the influences of the refractive

index of air and of the thermal expansion cancel out each other. During further investigations, the measurement setup with a biaxial LI could be used which is metrologically more advantageous. Here, both measurement axes are operated with one and the same laser source (in Figure 26.2, beam deflector 7 is then inserted according to the arrow direction).

The advantage of this setup is that the uncertainties of the two separate wavelengths as above no longer occur and that the uncertainty of the one wavelength is even compensated. Thus, only those deviations remain which are caused by the mechanics/optics of the comparator provided that any possible differences between the measurement electronics assigned to the two axes have previously been ruled out by exchange.

The differences ΔL_{Kijk} of the corrected lengths L_{N1ijk} und L_{N2ijk} measured in both axes and the regression line of the comparator ΔL_{K} from the value pairs $[L_{\mathrm{N1ijk}};\ \Delta L_{\mathrm{Kijk}}]$ result – analogous to (26.1) and (26.2) – as follows:

$$\Delta L_{\mathrm{Kijk}} = L_{\mathrm{N2ijk}} - L_{\mathrm{N1ijk}} \tag{26.6}$$

$$\Delta L_{\mathrm{K}} = a + b L_{\mathrm{N1}}. \tag{26.7}$$

Instead of the value zero which had been expected, slope b showed +88 nm/m on average, which means that in the exterior axis 2, it had – compared to the interior axis 1 – always been measured too long by the amount mentioned. The investigations with regard to the exact reasons for this deviation have not been concluded yet. It was found that the value of b remained quasi constant over months, despite interim readjustments. The precondition for this was that by means of an adjustment shields, always the same points had been set for the measuring beams to touch the triple mirror. The standard uncertainties of b were only a few nm/m. Thus, with opposite signs, the determined systematic measurement deviation of the comparator can be used for correction. This correction is also valid during calibration of an LI if one lets the measuring beam of this LI touch the large triple mirror with the same coordinates as previously the measuring beam of axis 2 of the standard LI. A further precondition for the constancy of b is that the measuring beam of axis 1 remains in the original position, too.

The high linearity and reproducibility of the measurements can be seen in Figure 26.3. The figure shows the differences of the individual measurements between the two axes of a biaxial LI in a working range of approx. 2 m in relation to the regression line. The differences of the mean values of the individual measurements relative to the regression line show a maximum nonlinearity of only 7 nm. The standard measurement uncertainties of the individual measurements were a maximum of 3 nm. The result of nonlinearity arises through superposition. Therefore, it is here not determinable whether a genuine interpolation error of one or both LIs is concerned, or whether other influences, e. g., the straightness deviation of the carriage guide show an impact. Through special investigations it could be proven that in this case the measurement result was mainly affected by the quality of the guide.

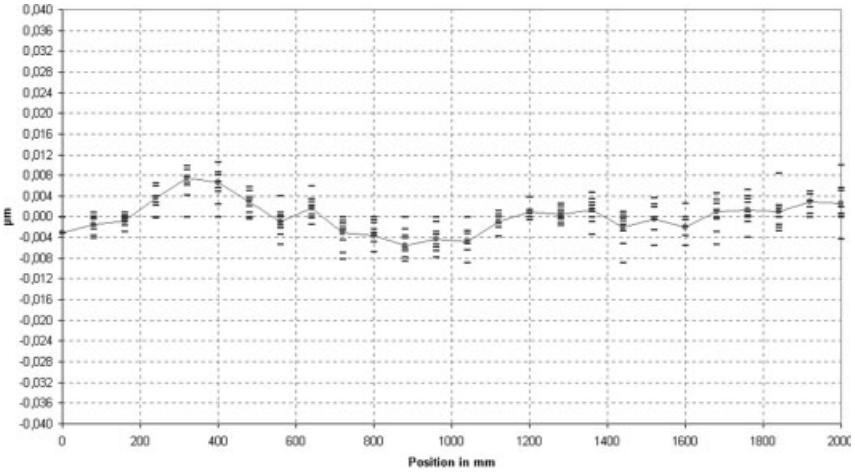

Fig. 26.3 Differences between the two axes of the standard LI to the regression line (single measurements).

In the following, the model equations needed for the measurement uncertainty budget (Table 26.1) of the mechanics/optics of the comparator are shown (see signs and symbols at the end of the chapter, Δ-values are correction values, δ-values are standard uncertainties):

$$\Delta L_K = \Delta L_{KR} + \delta l_{KR} + \delta l_{KB} \tag{26.8}$$

$$\Delta L_{KR} = a + bL \tag{26.9}$$

$$\begin{aligned}\delta l_{KR} = {} & \delta l_{KRa2} + \delta\delta l_{KRa2} + \delta l_{KRE} + \delta\delta l_{KRE} + \delta l_{SRa1} + \delta\delta l_{SRa1} + \delta l_{SRa2} + \delta\delta l_{SRa2} + \\ & \cdots + \delta l_{SRE} + \delta\delta l_{SRE} + (\delta l_{KRb2} + \delta\delta l_{KRb2} + \delta l_{SRb1} + \delta\delta l_{SRb1} + \delta l_{SRb2} + \delta\delta l_{SRb2})L\end{aligned} \tag{26.10}$$

$$\delta l_{KB} = L_{N2} - L_{N1} \tag{26.11}$$

$$L_{N2} = (Z_{EN2} - Z_{AN2}) \cos\varepsilon_2 \frac{\lambda_{0N}}{q} \frac{1}{n_{tpfxN}} \frac{1}{(1+\alpha(t_{KN} - 20^\circ\mathrm{C}))} \tag{26.12}$$

$$\varepsilon_2 = \arctan\frac{S_2}{V} \tag{26.13}$$

$$S_2 = \sqrt{(S_{2h})^2 + (S_{2v})^2} \tag{26.14}$$

$$L_{N1} = (Z_{EN1} - Z_{AN1}) \cos\varepsilon_1 \frac{\lambda_{0N}}{q} \frac{1}{n_{tpfxN}} \frac{1}{(1+\alpha(t_{KN} - 20^\circ\mathrm{C}))} \tag{26.15}$$

$$\varepsilon_1 = \arctan\frac{S_1}{V} \tag{26.16}$$

$$S_1 = \sqrt{(S_{1h})^2 + (S_{1v})^2} \tag{26.17}$$

Usually the Edlén equations according to [11] are used for the correction of the lengths. In this case, they are omitted because in the following uncertainty budget, they do not make any contributions (Table 26.1).

The measurement uncertainty u_{Kt1} of the mechanics/optics of the comparator for the temperature range $t_1 = 20\,°C \pm 1$ K is

$$u_{Kt1} = \sqrt{(5.5\,\text{nm})^2 + (2.6 \cdot 10^{-9} L)^2}. \tag{26.18}$$

The measurement uncertainty u_{Kt} of the mechanics/optics of the comparator for the temperature range $t_2 = 20\,°C \pm 5$ K is

$$u_{Kt2} = \sqrt{(8.5\,\text{nm})^2 + (5.0 \cdot 10^{-9} L)^2} \tag{26.19}$$

26.4.2
The Measurement Uncertainty of the Standard Laser Interferometer Taking Into Account the Refractive Index of Air and the Thermal Expansion

In the following, the model equations needed for the measurement uncertainty budget (Table 26.2) of the standard LI are shown (see signs and symbols at the end of the chapter):

Model equations:

$$L_N = (Z_{EN} - Z_{AN}) \cos\varepsilon_N \frac{\lambda_{0N}}{q} \frac{1}{n_{tpfxN}} \frac{1}{(1 + \alpha(t_{KN} - 20^{\circ}C))} \tag{26.20}$$

$$t_{KN} = \frac{t_{K1N} + t_{K2N}}{2} \tag{26.21}$$

$$\varepsilon_N = \arctan\frac{S_N}{V} \tag{26.22}$$

$$S_N = \sqrt{(S_{hN})^2 + (S_{vN})^2} \tag{26.23}$$

with [11]:

$$n_{tpfxN} = n_{tpxN} - \Delta n_{fN} + \delta n_E \tag{26.24}$$

$$n_{Ntpx} = 1 + (n_{xN} - 1) \frac{p_N}{93214.60} \frac{(1 + 10^{-8}(0.5953 - 0.009876 t_{LN}) p_N)}{1 + 0.0036610 t_{LN}} \tag{26.25}$$

Table 26.1 Uncertainty budget of mechanics/optics of the comparator for the temperature range $t_1 = 20\,°C \pm 1$ K

Quantity	Value	Standard uncertainty	Sensitivity coefficient	Uncertainty not length depending (nm)	Uncertainty length depending (nm/m)
a	2.72 nm	0.40 nm	1	0.4	
b	87.53 nm/m	1.80 nm/m	1		1.8
δl_{Kra2}	0 nm	0.54 nm	1	0.5	
$\delta\delta l_{\mathrm{Kra2}}$	0 nm	0.05 nm	1	0.1	
δl_{KRE}	0 nm	4.42 nm	1	4.4	
$\delta\delta l_{\mathrm{KRE}}$	0 nm	0.39 nm	1	0.4	
δl_{Sra1}	0 nm	1.46 nm	1	1.5	
$\delta\delta l_{\mathrm{Sra1}}$	0 nm	0.25 nm	1	0.3	
δl_{Sra2}	0 nm	0.34 nm	1	0.3	
$\delta\delta l_{\mathrm{Sra2}}$	0 nm	0.54 nm	1	0.5	
δl_{SRE}	0 nm	0.88 nm	1	0.9	
$\delta\delta l_{\mathrm{SRE}}$	0 nm	0.18 nm	1	0.2	
δl_{KRb2}	0 nm/m	0.44 nm/m	1		0.4
$\delta\delta l_{\mathrm{KRb2}}$	0 nm/m	0.05 nm/m	1		0.1
δl_{SRb1}	0 nm/m	1.50 nm/m	1		1.5
$\delta\delta l_{\mathrm{SRb1}}$	0 nm/m	0.63 nm/m	1		0.6
δl_{SRb2}	0 nm/m	0.26 nm/m	1		0.3
$\delta\delta l_{\mathrm{SRb2}}$	0 nm/m	0.54 nm/m	1		0.5
$Z_{2\mathrm{EN}}$	809 165 272	1	1.2 nm	1.2	
$Z_{2\mathrm{AN}}$	0	1	−1.2 nm	−1.2	
$\lambda_{0\mathrm{N}}$	632.991486 nm	$4 \cdot 10^{-6}$ nm	0		0.0
T_{KN}	20 °C	$2.5 \cdot 10^{-3}$ K	0		0.0
$S_{2\mathrm{h}}$	200 µm/m	11.5 µm/m	$-13 \cdot 10^{-6}$ m/µm		−0.1
$S_{2\mathrm{v}}$	200 µm/m	11.5 µm/m	$-13 \cdot 10^{-6}$ m/µm		−0.1
$Z_{1\mathrm{EN}}$	809 165 272	1	−1.2 nm	−1.2	
$Z_{1\mathrm{AN}}$	0	1	1.2 nm	1.2	
$S_{1\mathrm{h}}$	200 µm/m	11.5 µm/m	$13 \cdot 10^{-6}$ m/µm		0.1
$S_{1\mathrm{v}}$	200 µm/m	11.5 µm/m	$13 \cdot 10^{-6}$ m/µm		0.1
δn	0	$1.4 \cdot 10^{-8}$	0		0.0

$$p_N = \frac{p_{1N} + p_{2N}}{2} \tag{26.26}$$

$$n_N = 1 + (n_{SN} - 1)(1 + 0.5327 \cdot 10^{-6}(x_N - 400)) \tag{26.27}$$

$$n_{SN} = 1 + \left(8091.37 + \frac{2\,333\,983}{130 - (\lambda_{0N})^{-2}} + \frac{15\,518}{38.9 - (\lambda_{0N})^{-2}}\right) \cdot 10^{-8} \tag{26.28}$$

$$\Delta n_{fN} = \frac{rf_N}{100}\, e^{E}\left(3.8020 - 0.0384\frac{1}{\lambda_{0N}^2}\right) \cdot 10^{-10} \tag{26.29}$$

$$rf_N = \frac{rf_{1N} + rf_{2N}}{2} \tag{26.30}$$

$$E = A(t_{LN} + t_0)^2 + B(t_{LN} + t_0) + C + D(t_{LN} + t_0)^{-1}. \tag{26.31}$$

The measurement uncertainty $u_{N\alpha 1}$ for the standard LI with correction of the refractive index and thermal expansion for $\alpha_1 = 11.5 \cdot 10^{-6}\ K^{-1}$ (steel) is

Table 26.2 Uncertainty budget for the standard LI with correction of refractive index and thermal expansion for $\alpha_1 = 11.5 \cdot 10^{-6}\ K^{-1}$

Quantity	Value	Standard uncertainty	Sensitivity coefficient	Uncertainty not length depending (nm)	Uncertainty length depending (nm/m)
Z_{EN}	809 165 272	1.4	1.2 nm	1.7	
Z_{AN}	0	1.4	−1.2 nm	−1.7	
λ_{0N}	632.991486 nm	$4 \cdot 10^{-6}$ nm	$1.6 \cdot 10^{6}$		6.4
t_{K1N}	20 °C	$2.5 \cdot 10^{-3}$ K	$-5.8\ K^{-1}$		−14.0
t_{K2N}	20 °C	$2.5 \cdot 10^{-3}$ K	$-5.8\ K^{-1}$		−14.0
S_{hN}	200 µm/m	11.5 µm/m	$-13 \cdot 10^{-6}$ m/µm		−0.1
S_{vN}	200 µm/m	11.5 µm/m	$-13 \cdot 10^{-6}$ m/µm		−0.1
δn_{EN}	0	10^{-8}	$-1.0 \cdot 10^{6}$		−10.0
p_{1N}	10^5 Pa	2.6 Pa	$-1.3 \cdot 10^{-3}\ Pa^{-1}$		−3.5
p_{2N}	10^5 Pa	4.0 Pa	$-1.3 \cdot 10^{-3}\ Pa^{-1}$		−5.3
T_{LN}	20 °C	$7.8 \cdot 10^{-3}$ K	$0.94\ K^{-1}$		7.4
X_N	400 ppm	10 ppm	$-1.40 \cdot 10^{-4}$		−1.4
rf_{2N}	50 %	0.5 %	$4.3 \cdot 10^{-3}$		2.2
rf_{1N}	50 %	0.5 %	$4.3 \cdot 10^{-3}$		2.2

$$u_{N\alpha 1} = \sqrt{(2.5\,\text{nm})^2 + (25.4 \cdot 10^{-9} L)^2}. \tag{26.32}$$

The measurement uncertainty $u_{N\alpha 0}$ for the standard LI with correction of the refractive index but without the thermal expansion having been taken into account ($\alpha_0 = 0\ \text{K}^{-1}$) is

$$u_{N\alpha 0} = \sqrt{(2.5\,\text{nm})^2 + (15.5 \cdot 10^{-9} L)^2}. \tag{26.33}$$

26.4.3
The Expanded Measurement Uncertainty of the Entire Calibration Facility

The expanded measurement uncertainty U of the entire measuring facility for calibration of an LI for length measurements is calculated from the measurement uncertainties u_N and u_K of their two main components standard LI and comparator. With the expansion factor $k = 2$

$$U = 2\sqrt{u_N^2 + u_K^2}. \tag{26.34}$$

Accordingly, by combination of pairs of the calculated measurement uncertainties (Eqs. (26.18), (26.19), (26.32), and (26.33)) with the above-mentioned linear expansion coefficient $\alpha_1 = 11.5 \cdot 10^{-6}\ \text{K}^{-1}$ or $\alpha_0 = 0\ \text{K}^{-1}$, the two temperature areas $t_1 = 20\,°\text{C} \pm 1\ \text{K}$ and $t_2 = 20\,°\text{C} \pm 5\ \text{K}$ and $k = 2$, the four expanded measurement uncertainties for the entire calibration facility is with (26.18) and (26.32):

$$U_{\alpha 1 t1} = \sqrt{(12\,\text{nm})^2 + (51 \cdot 10^{-9} L)^2}, \tag{26.35}$$

with (26.18) and (26.33):

$$U_{\alpha 0 t1} = \sqrt{(12\,\text{nm})^2 + (31 \cdot 10^{-9} L)^2}, \tag{26.36}$$

with (26.19) and (26.32):

$$U_{\alpha 1 t2} = \sqrt{(18\,\text{nm})^2 + (52 \cdot 10^{-9} L)^2}, \tag{26.37}$$

with (26.19) and (26.33):

$$U_{\alpha 0 t2} = \sqrt{(18\,\text{nm})^2 + (32 \cdot 10^{-9} L)^2}. \tag{26.38}$$

Signs and Symbols of the Model Equations and the Uncertainty Budgets:

u: standard uncertainty (general); $\boldsymbol{\Delta L_K}$: measuring deviation of the comparator for calibration of LI; $\boldsymbol{\Delta L_{KR}}$: regression line of all length differences ΔL_{ijk} measured between the two axes of the standard LI depending on the length measured with axis 1; $\boldsymbol{\delta l_{KR}}$: u in connection with the regression line ΔL_{KR}; $\boldsymbol{\delta l_{KB}}$: u in connection with the calculation of the length differences between the two axes; $\boldsymbol{a}$: distance on y-axis of regression line ΔL_{KR}; $\boldsymbol{b}$: slope of regression line ΔL_{KR}; $\boldsymbol{L}$: nominal length; $\boldsymbol{\delta l_{KRa2}}$: u of distance a of regression line ΔL_{KR} of a series of measurements; $\boldsymbol{\delta\delta l_{KRa2}}$: u of the mean value of all δl_{KRa2} (of all series of measurements); $\boldsymbol{\delta l_{KRE}}$: u of all measuring deviations ΔL_{ij} in relation to regression line ΔL_{KR} of a series of measurements; $\boldsymbol{\delta\delta l_{KRE}}$: u of the mean value of all δl_{KRE}; $\boldsymbol{\delta l_{Sra1}}$: distance a of regression line ΔL_{SR} (of standard uncertainties depending on length) on the y-axis of a series of measurements; $\boldsymbol{\delta\delta l_{Sra1}}$: u of the mean value of all δl_{SRa1}; $\boldsymbol{\delta l_{SRa2}}$: u of distance a of regression line ΔL_{SR} on the y-axis of a series of measurements; $\boldsymbol{\delta\delta l_{Sra2}}$: u of the mean value of all δl_{SRa2}; $\boldsymbol{\delta l_{SRE}}$: u of all measuring deviations ΔL_{ij} in relation to regression line ΔL_{KR} of a series of measurements; $\boldsymbol{\delta\delta l_{SRE}}$: of the mean value of all δl_{SRE}; $\boldsymbol{\delta l_{KRb2}}$: u of slope b of regression line ΔL_{KR} of a series of measurements; $\boldsymbol{\delta\delta l_{KRb2}}$: u of the mean value of all δl_{KRb2}; $\boldsymbol{\delta l_{SRb1}}$: u of slope b of the regression line ΔL_{SR} (of standard uncertainties depending on length) of a series of measurements; $\boldsymbol{\delta\delta l_{SRb1}}$: u of mean value of all δl_{SRb1}; $\boldsymbol{\delta l_{SRb2}}$: u of the mean value of all ΔL_{SR} of a series of measurements; $\boldsymbol{\delta\delta l_{SRb2}}$: u of the mean value of all δl_{SRb2}; $\boldsymbol{L_{N2}}$ ($\boldsymbol{L_{N1}}$): length corrected is measured by standard LI, axis 2; $\boldsymbol{N}$: measured by the standard LI resp. by the standard weather station (index); $\boldsymbol{Z_{EN2}}$ ($\boldsymbol{Z_{EN1}}$): increments measured with standard LI in measuring axis 2 (1) at the end of the measurement (standard deviation of the limits contains "digit errors"); $\boldsymbol{Z_{AN2}}$ ($\boldsymbol{Z_{AN1}}$): increments measured with standard LI in measuring axis 2 (1) at the start of the measurement (standard deviation of the limits contains "digit errors"); ε_2 (ε_1): angle deviation from the parallelism between the beam direction of axis 2 (1) to the axis of movement; $\boldsymbol{\lambda_{0N}}$: vacuum wavelength of standard LI for both measuring axes; $\boldsymbol{q}$: interpolation factor (resolution of standard LI); $\boldsymbol{n_{tpfxN}}$: refractive index of air dependent on temperature, pressure, humidity, CO_2 content; α: linear thermal expansion coefficient; $\boldsymbol{t_{KN}}$: body temperature; $\boldsymbol{S_2}$ ($\boldsymbol{S_1}$): resultant beam displacement particular to the measuring axis 2 (1) of a LI after displacement V, measured with a position-sensitive detector; $\boldsymbol{V}$: effective displacement of the laser beam by beam folding (4 m); $\boldsymbol{S_{2h}}$ ($\boldsymbol{S_{1h}}$): horizontal component of S_2 (S_1); $\boldsymbol{S_{2v}}$ ($\boldsymbol{S_{1v}}$): vertical component of S_2 (S_1); $\boldsymbol{L_N}$: corrected length measured by standard LI; $\boldsymbol{n_{tpxN}}$: refractive index of dry air dependent from temperature, pressure, and CO_2 content; $\boldsymbol{\Delta n_{fN}}$: refractivity of air through influence of the relative humidity; $\boldsymbol{\delta n_E}$: u of the Edlén equation [11], $\boldsymbol{n_{xN}}$: refractive index of dry air under standard conditions dependent on CO_2 content; $\boldsymbol{p_N}$: air pressure; $\boldsymbol{t_{LN}}$: air temperature; $\boldsymbol{n_{SN}}$: refractive index of dry air under standard conditions dependent on the vacuum wavelength; $\boldsymbol{x_N}$: CO_2 content of air; $\boldsymbol{rf_N}$: relative humidity; $\boldsymbol{t_0}$: 273.16 K; $\boldsymbol{A}$: $12.378847 \cdot 10^{-6}$ K^{-2}; $\boldsymbol{B}$: -0.019121316 K^{-1}; $\boldsymbol{C}$: 33.93711047; $\boldsymbol{D}$: -6643.1645 K.

References

1 N. Bobroff, Recent advances in displacement measuring interferometry, Meas. Sci. Technol. **4**, 907–926 (1993).

2 VDI-Bericht 750: Dokumentation und Genauigkeit von Laserinterferometer-Systemen. Zusammengestellt und herausgegeben vom VDI/VDE-GMA-Ausschuß 7.4 "Grundlagen der Längen und Winkelmessung" (Obmann Dr.-Ing. Hans-H. Schüssler, Düsseldorf, April 1989).

3 G. Sparrer, Anordnung zum direkten Vergleich und zur Kalibrierung von Laserinterferometern. Offenlegungsschrift vom 08.04.1993, G 01 B 9/02 DE 4208189 A 1.

4 G. Sparrer, Anordnung zum direkten Vergleich sowie zur Kalibrierung von Laserinterferometern und zur Präzisionsmessung mit einem Laserinterferometer. Offenlegungsschrift vom 18.11.1993, G 01 B 9/02 DE 4236993 A 1.

5 K. Herrmann, G. Sparrer, and G. Wilkening, Testing of laser measuring systems, especially laser interferometers in the PTB – state-of-the-art and perspectives. *PTB-Bericht F-15, Calibration and Testing of Laser Interferometers* (Euromet-Workshop, Berlin, 11–12 March 1992) pp. 30–41.

6 K. Herrmann, G. Sparrer, F. Pohlenz, and J. Hannemann, Investigation and calibration of laser measuring systems, in *VDI Berichte 1118 of IMEKO-Symposium Laser Metrology for Precision Measurement and Inspection in Industry* (Heidelberg, 21–22 March 1994).

7 G. Sparrer, Meßanordnungen zur Kalibrierung kompletter Laserinterferometer. Microtecnic 3/1994, 27-32 (English translation obtainable from the author).

8 A. Kuhn, M. Frenzel, and G. Sparrer, *Kalibriereinrichtung für Laserinterferometer* (Jahresbericht der Physikalisch-Technischen Bundesanstalt, 1997) pp. 155–156.

9 G. Sparrer, T. Meyer, H. Lindemann, and A. Abou-Zeid, Die Kalibrierung von Laserinterferometern für Längenmessungen und Bestimmung ihrer Messunsicherheiten in der PTB, in *Presentation at 47th Internationalen Wissenschaftlichen Kolloquium der Technischen Universität Ilmenau* (23–26 September 2002) (English translation obtainable from the author).

10 J. Stone, M. Schroeck, and M. Stocker, *Testing Displacement-Measuring Interferometer Systems* (Internal work report of Precision Engineering Division, National Institute of Standard and Technology, 1998).

11 G. Bönsch and E. Potulski, Measurement of the refractive index of air and comparison with modified Edlén's formulae, Metrologia **35**, 133–139 (1998).

12 Guide to the Expression of Uncertainty in Measurement (1993), 1st ed., corrected and reprinted 1995, International Organisation for Standardization (Geneva, Switzerland), German translation in DIN: Leitfaden zur Angabe der Unsicherheit beim Messen. 1. Edition 1995, (Beuth–Verlag–GmbH, Berlin–Wien–Zürich).

13 Windows-Programme "GUM Workbench" of Metrodata GmbH, Grenzach.

Part VIII
Application – Lateral Structures

Nanoscale Calibration Standards and Methods: Dimensional and Related Measurements in the Micro- and Nanometer Range.
Edited by Gunter Wilkening, Ludger Koenders
ISBN: 3-527-40502-X

27
Lateral and Vertical Diameter Measurements on Polymer Particles with a Metrology AFM

F. Meli

Abstract

Particle counters measure particle size distributions and therefore they must not only be able to count the particles correctly but also to determine the particle sizes precisely. For the calibration of particle counters typically monodisperse reference particles such as gold colloids or polymer spheres with various sizes are used. The diameter of the reference particles themselves can be determined in a traceable way with a metrology atomic force microscope (AFM). There are two different methods of calibrating particles by an AFM measurement. Firstly, the height of individual particles spread out on an atomically flat mica surface can be measured. The height corresponds to the particle diameter if the interaction distance of the AFM tip is the same on the particle and on the flat reference surface and if no particle embedding in a possible surface layer occurs. Secondly, for a close-packed particle monolayer on a mica surface one can determine the particle diameter from the lateral distance of the particles. A metrology AFM with interferometrically calibrated capacitive position sensors was used in tapping mode to acquire the particle image data. A specially made image evaluation software helped us evaluate data from hundreds of particles. Results of lateral and vertical diameter measurements on polymer and gold particles are shown and compared. Some fundamental properties of AFM tapping mode height measurements are discussed.

27.1
Introduction

Particle counters are widely used to characterize medical and industrial clean rooms. Quality control systems require regular calibrations of the instruments applied in these fields. Also an increasing demand for accurate particle measurements is expected in relation with environmental particle monitoring and for characterization measurements of exhaust gases from furnaces, turbines, and

Nanoscale Calibration Standards and Methods: Dimensional and Related Measurements in the Micro- and Nanometer Range.
Edited by Gunter Wilkening, Ludger Koenders
ISBN: 3-527-40502-X

combustion engines. Especially exhaust gases of diesel engines contain submicron carbon particles that are themselves agglomerates of about 20 nm small carbon globules. Accurate particle measurement procedures will help us enforce quality systems and legal regulations for environmental protection.

Because particle counters typically determine a particle size distribution they need to be able to classify the particles in diameter ranges. Correct diameter determination and correct counting are important. There are many different particle counters using different measurement principles on the market. Often particle transportation properties in gases or liquids are used to determine the particle size, e. g., by sedimentation, differential mobility analysis [1], laser Doppler velocimetry, etc. As these methods are indirect methods most counters need to be calibrated with well-known reference particles of various sizes.

The diameter of monodisperse reference particles such as gold colloids or polymer spheres can be measured in a traceable way by various microscopy techniques [2]. For the microscopic observation the particles must be deposited on sample carriers in order to measure their size or height. Besides scanning electron microscopy (SEM) and transmission electron microscopy (TEM), atomic force microscopy (AFM) provides an easy, nondestructive measurement under ambient condition. For accurate measurements the metrological performance and the calibration of the AFM scanner are essential. A powerful image evaluation method is also necessary as many particles on many images have to be analyzed to obtain a meaningful size distribution and the average diameter or the more robust median.

With an AFM, particle diameters can be calibrated using height or lateral measurements. Ideally the height of individual particles on an atomically flat surface should correspond to the particle diameter; however, a few questions remain with respect to the surface interaction of the AFM tip and the embedding of the particle in a possible surface layer. On the other hand, it is possible with certain particle surface combinations to deposit a close-packed monolayer of particles. In this situation it is possible to determine the particle diameter from the lateral distance of the particles. This distance is not influenced by the AFM tip shape or the surface interaction (Figure 27.1).

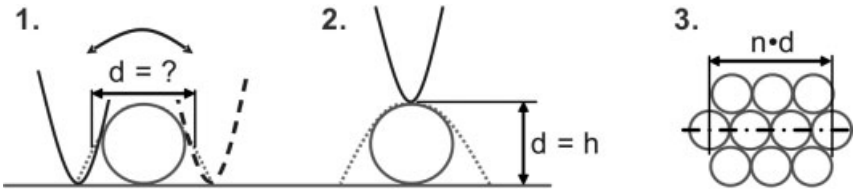

Fig. 27.1 Possible ways to determine a particle diameter with an AFM. (1) A lateral diameter measurement on a single particle is strongly influenced by the AFM tip. (2) Particle diameter measurement using its height. (3) Diameter determination using the lateral distance of a close-packed particle surface layer.

In this chapter, a comparison of lateral and vertical diameter measurements is made with a metrology AFM on gold colloid and polymer particles with sizes in the range from 4 nm to 194 nm.

27.2 Experimental Setup

The AFM system used to acquire the particle images consists of a commercial metrology AFM head (Digital Instruments) and a linear sample displacement stage with a laser interferometer. The AFM head includes a parallelogram-type scanner with an x–y–z range of 70 μm × 70 μm × 7 μm. The x–y–z displacements are measured with capacitive position sensors. A reference cube located close to the tip acts as the counter electrode. The x–y sensors are used in feedback loops to linearize the x–y motion while the z-sensor signal is recorded. Because of the linear behavior of the sensors and the low pitch, roll and yaw of the AFM scanner a high level of accuracy is achieved.

Below this stand-alone metrology AFM head there is a sample displacement stage with monolithic flexures forming a double parallelogram. This piezo actuated stage provides a linear motion over 380 μm. Its displacement is simultaneously measured by a capacitive transducer and a laser interferometer (Figure 27.2). The stage with the interferometer is used to calibrate the capacitive position sensors of the AFM head. In order to calibrate also the z-axis sensor, which is important for the particle height measurements, a mirror was attached to the z-scanner below the AFM tip and a 90°-deflection prism was used to deflect the two horizontal laser beams of the differential double pass plane mirror interferometer into the vertical direction.

The linear long-range displacement stage is similar to a construction made earlier at the PTB [3]. It was fabricated out of a single piece of a 22-mm-thick hardened aluminum alloy containing 4.7% Zn, 3.1% Mg and 0.6% Cu. After a rough preshaping, the work piece was again heat treated to regain good and homogeneous mechanical properties. The critical holes, which define the position and the thickness of the flexures [4], were grinded on a precision grinding machine. Position and diameter were measured to be within a tolerance of 2 μm. The stage is actuated by a 150 V piezo with a nominal stroke of 70 μm. A lever amplifies the motion by a factor of 6 to provide a linear displacement over 380 μm.

Small errors of motion are, together with a small Abbe offset, the basis for an accurate displacement measurement. Pitch and yaw of the linear stage motion were measured with an autocollimator. They are roughly linear with the displacement and smaller than 0.7 arcsec over the full stroke. With an Abbe offset <1 mm this results in an error of less than 3 nm.

The position of the linear displacement stage is measured by a capacitive position sensor (Queensgate) and a double pass differential plane mirror HeNe-laser interferometer of the Jamin type developed at the NPL [5]. Both the capacitive and

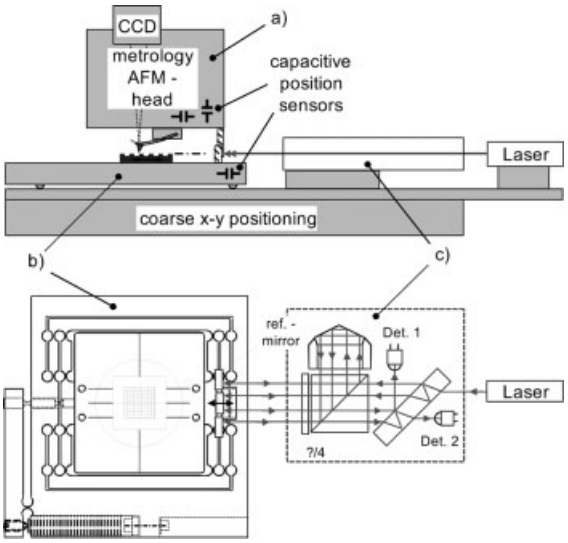

Fig. 27.2 General setup of the metrology AFM system. (a) Metrology AFM head including a video microscope, (b) piezo actuated linear long-range displacement stage with monolithic flexures forming a double parallelogram, and (c) schematic of the differential double pass plane mirror interferometer with HeNe laser.

the interferometric measuring systems have subnanometer resolution capability. The capacitive sensor signal is used in a PID feedback loop to control the piezo with a DSP controller having 21-bit AD converter. The differential interferometer measures the displacement of the sample with respect to the fixed part of the AFM head where the reference mirror is attached. Therefore relative drift of the stage frame with respect to the AFM head is cancelled. The moving mirror and the reference mirror are located in the same plane in order to avoid a dead path for the laser beam. The two detectors of the interferometer provide two sinusoidal signals in phase quadrature with a periodicity of 158 nm ($\lambda/4$) for the fringe counter board. Preamplifiers before the A/D conversion allow software adjustments of gain and offset of the interferometer signals. To obtain a linear phase interpolation down to subnanometer accuracy and to correct for any phase mixing a numerical method described by Heydemann [6] is applied.

The AFM head supports various modes, such as contact mode, tapping mode, and lateral force mode. Only a few measurements were made in contact mode because particle removals were observed frequently. On the other hand, tapping mode [7] proved to be very reliable with very little particle removals. With this mode, the cantilever with the tip is vibrated at its resonance frequency around 300 kHz with an amplitude of approx. 15 nm. During scanning, the damping of the oscillation amplitude due to the proximity of the tip to the sample surface is held at a constant value (setpoint). This mode gives very reproducible measurements because of the intermittent contact and the therefore negligible lateral forces.

An optical zoom video microscope and a coarse *x*–*y* table allow for easy positioning of the sample below the tip. The control of the interferometer and of the piezo HV amplifier as well as the acquisition of the capacitive sensor signal

from the displacement stage and from the AFM head is programmed in LabView. More details about this system and about accurate pitch, step height, structure width (CD), and roughness measurements were published earlier [8–12].

27.3 Measurement Results and Discussion

The two possible methods of calibrating particle diameters with an AFM by lateral or height measurements have both their advantages and drawbacks. Height measurements are possible for most types of particles as they require only that a few particles stick somewhere on a flat surface. Lateral measurements require that at least islands of single layer of close-packed particles are formed on a surface. While the determination of the particle diameter from lateral measurements is straightforward, this is not the case for the height measurements as the apparent height can be influenced by the surface interaction of the AFM tip and the particle embedding on the surface. The following two sets of measurements on gold colloids and polymer spheres clarify the degree of equivalence of both methods.

27.3.1 Height Measurements on Gold Colloids

Gold colloids of five different nominal sizes were deposited on cleaved mica surfaces. The cleaved mica provides atomically flat surface regions, which are necessary as a reference plane for the particle height determination. A pretreatment with poly-l-lysine is needed to adjust the surface charges and therefore to enhance the adhesion of the particles. The colloid solutions were diluted with ultrapure water to obtain a suitable particle density. All solutions and the mica carriers were obtained from Pelco as a "Gold calibration Kit" (Ted Pella Inc., Redding, CA). Surface regions of about 50 particles were imaged with AFM scan sizes between 600 nm and 1.4 μm. Most AFM measurements were performed in tapping mode using Pointprobe silicon AFM tips from Nanosensors (now Nanoworld, Neuchâtel, Switzerland).

A METAS designed image evaluation software was used to determine the particle heights in a few simple steps (Figure 27.3):

1. The image background is flattened line by line using a second- or third-order polynomial fit. Only background data points are used for this fit. The particles are discriminated using an appropriate height threshold (Figure 27.3(b)).
2. In the flattened image all possible particles are first recognized and then the particle multiples are discarded on the basis of their larger surface area. Also all particles on the border of the image are discarded (Figure 27.3(c)).
3. The remaining single particles with clear surrounding are further analyzed. The three highest pixels are averaged to

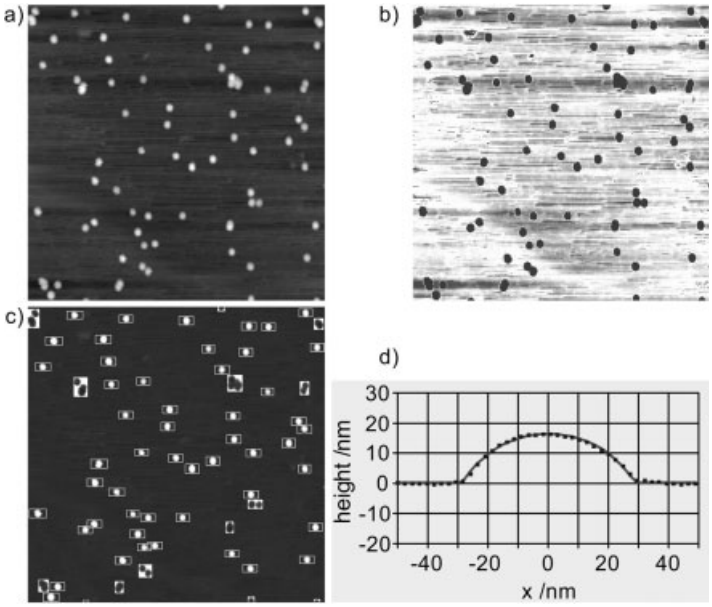

Fig. 27.3 Steps of the AFM image evaluation: (a) original AFM data 2 μm × 2 μm with 16 nm gold colloids, (b) background selection for image flattening using a height threshold, (c) selecting valid particles for height estimation, and (d) particle height and AFM tip radius evaluation by fitting a circle segment to the measured points of the particle bump ($r_{part} = 16$ nm, $r_{tip} = 29$ nm).

give the height (diameter) of a single particle. Alternatively, a circular fit can be applied to each individual particle bump. In this way also the AFM tip radius can be estimated (Figure 27.3(d)).

4. Based on the analysis of all particles in the image the mean and the median particle diameters as well as the standard deviation are calculated.

By analyzing a few images taken from the same sample, particle data are accumulated and the size distribution can be determined. Figure 27.4 shows the particle size distribution of the 8.3 nm gold colloids. Evaluating 391 particle diameters the standard deviation was 0.7 nm resulting in a standard deviation of the mean of only 0.03 nm (i. e., 0.7 nm/sqrt(391)).

Often the shape of the tip or the particle is not very well approximated by a sphere and the circular fit does not yield the correct height value for the particle. A three-point height average was used for the results presented here on gold colloids. On the other hand, the circular fit allowed also an estimate of the tip radius. It was already suggested that such gold colloid particles could be used as AFM tip characterizers [13, 14]. Unfortunately, a perfect, fresh tip with a tip radius of only

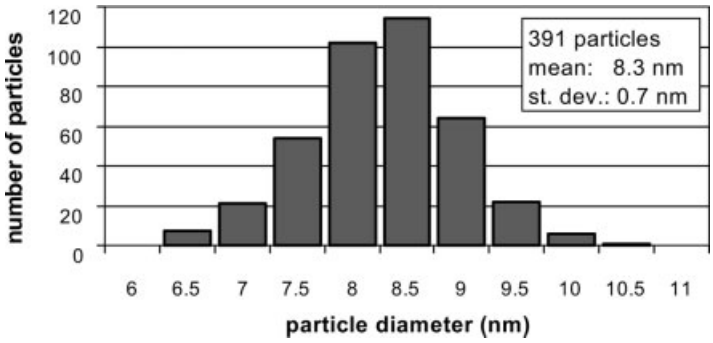

Fig. 27.4 Particle diameter distribution of 8.3 nm gold colloids deposited on mica and measured by AFM microscopy.

1 nm as estimated on a tip characterizer [10] is quickly contaminated by picking up gold colloids. The observed AFM tip radii were then in the same range as the measured particles, i. e., 10–30 nm. This had mostly no direct influence on the AFM height measurement because no twin or multiple tip image artifacts appeared.

Table 27.1 summarizes the results obtained on five different gold colloid particles. The size variation of the monodisperse particles gives only a small contribution to the uncertainty of the average particle diameter (0.03–0.2 nm) because a large amount of particles was analyzed. The AFM *z*-scale calibration, which is better than 0.5 %, has also a minor influence on the diameter uncertainty (0.02–0.13 nm) as will be seen in the following discussion.

Table 27.1 Evaluated mean particle diameters and size distributions of five different gold colloids

No. of particles	Mean (nm)	SD (nm)	SD of mean (nm)
185	4.16	0.67	0.05
391	8.28	0.69	0.03
131	13.70	1.32	0.12
222	17.14	1.24	0.08
139	26.73	2.40	0.20

27.3.2
Possible Systematic Deviations with Height Measurements on Gold Colloids

The average particle size can be measured reproducibly using an AFM by statistical evaluation of many particles. However, some fundamental questions related to the tip sample interaction need clarification before the full uncertainty can be given.

First the influence of the AFM tapping mode setpoint was investigated. In tapping mode the tip oscillates at its resonance frequency with a certain amplitude. As the tip approaches the surface this amplitude is reduced until the so-called setpoint amplitude is reached. This setpoint amplitude is then kept constant by the feedback mechanism. Additionally, the phase of the oscillation is imaged. On the same sample location various images were measured using different setpoints. Between light and hard tapping a particle height change of 1 nm on the 17 nm particles was observed (Figure 27.5). Harder tapping reduced the apparent particle height as if the particles were softer than the mica. The tapping mode is sensitive to the force gradient between the tip and the sample [15] while in the contact mode the tip is held at a distance of constant force, i. e., constant AFM cantilever deflection. Contact and tapping mode particle heights should be the same. With contact mode measurements, however, usually most of the particles were removed from the surface so that only some very good adhering species were left for their height determination. Especially sharp tips removed the particles easily while with dull tips, with a tip radius above 30 nm, the removal rate was lower. At sites where particles were removed by the AFM tip a small bump of about 1 nm could be observed that consist maybe of some gold removed from the particles.

On 44 individually selected particles the height obtained with contact mode and light tapping mode was compared. The mean diameter measured with tapping

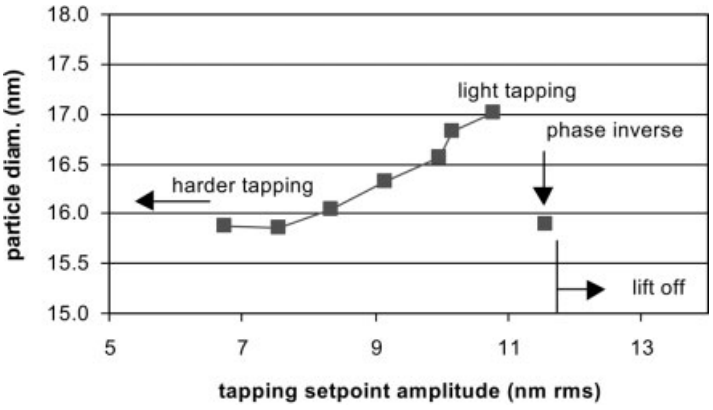

Fig. 27.5 Dependence of the measured gold colloid particle height with respect to the AFM tapping mode setpoint.

mode of 17 nm was only 0.3 nm larger (Figure 27.6). The standard deviation of the mean difference between the two modes was 0.2 nm so the deviation was not significant.

Measurements made by Mulvaney and Giersig [2] comparing TEM and contact mode AFM measurements on 16 nm diameter gold colloids showed that the mean diameter determined from TEM measurements was 0.2 nm larger than the contact AFM height value. Using this result the difference between TEM and tapping mode AFM diameter would be only 0.1 nm.

It seems that there is no big systematic height difference between light tapping and contact mode. However, the possibility still exists that there is a systematic effect for both methods due to the different tip sample interaction on mica and on the gold colloid particle (Figure 27.7).

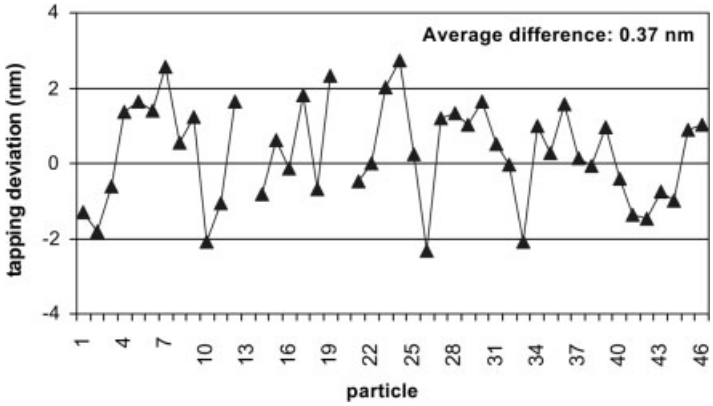

Fig. 27.6 Measured particle height differences between light tapping and contact AFM mode.

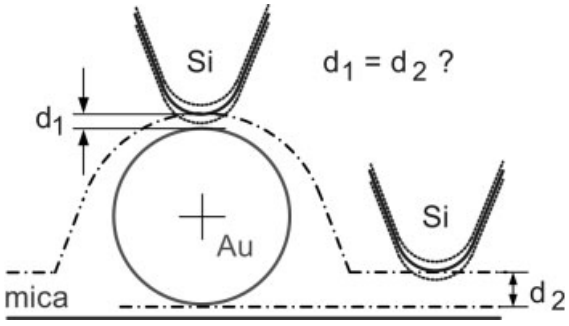

Fig. 27.7 The measured particle diameter could be systematically influenced by differences between the tip sample interaction on mica and the one on a particle.

27.3.3
Lateral Measurements on Polymer Spheres

With polymer particles instead of gold colloids it was in some cases possible to deposit a close-packed particle monolayer layer on a mica surface [16]. For such a layer the particle diameter can be determined from the lateral distance. This distance might be only influenced by particle–particle interaction forces but not by the AFM tip shape or the tip–surface interaction as for height measurements. Again the particles were deposited on atomically flat cleaved mica that was pretreated with poly-l-lysine. To obtain a close-packed layer the particle size distribution must be very narrow. Single larger or smaller particles can introduce defects. Good results were obtained with polymer spheres from Duke Scientific Corp. (Nanoshpere™ Size Standards, type 3200A) with a nominal size of 198 nm. For the evaluation of the lateral distance only perfect single lines of particles were used. The sample was aligned such that the particle rows were parallel to the fast scanning *x*-axis (Figure 27.8).

The individual particle positions were determined from their center of gravity on a single image profile. The average diameter was then obtained by a linear fit to lateral particle locations.

These measurements are very accurate. An average particle diameter of 193.9 nm was found with a standard uncertainty of only ± 0.25 nm. Deviations of single particle positions from the linear fit were within a range of ± 8 nm (Figure 27.9).

From lateral measurements it is difficult to deduce the particle size distribution because the local position variation is not only influenced by the size of a single particle. Also the height method cannot be applied to the image shown in Figure 27.8 as the mica reference plane can be seen only in a few locations.

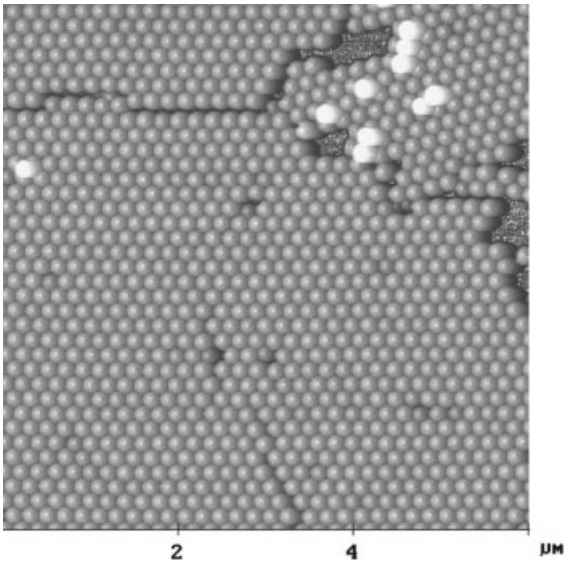

Fig. 27.8 AFM top view image of a close-packed layer of polymer spheres deposited on cleaved mica.

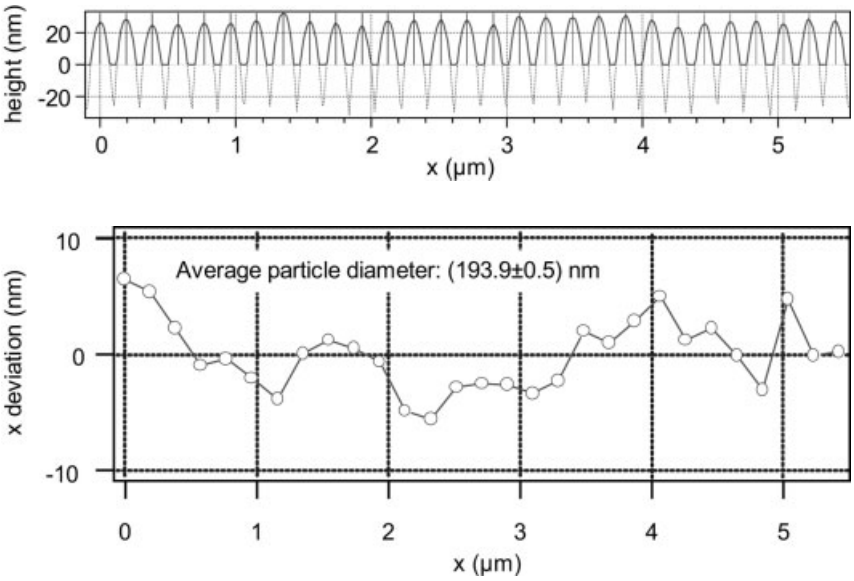

Fig. 27.9 Top: A profile across a close-packed particle row was evaluated to obtain the lateral particle positions. Bottom: The deviation from a linear fit to the particle positions gives the average particle diameter and the local variation.

On the other hand, it would also be interesting to have a direct comparison between lateral and vertical particle measurements on the same sample to see if systematic differences exist.

As very often the close-packed particles form small islands on the surface, there is also a good chance to find a place that looks like the one shown in Figure 27.10. Here a part of a long slender island can be seen with a visible mica reference surface on the left and right sides of the image. The left and right sides of the image are also the beginning and the end of single profiles in the fast scanning direction. This situation allows again a similar evaluation as for the gold colloids with the difference that in this case not each particle is surrounded by a reference plane but that still the entire image can be flattened line by line, using the left and right border parts as background reference (Figure 27.11). In the flattened image, particles are automatically recognized and particles on the border of the image and a few outliers are discarded. To the remaining particles a circular fit is applied to obtain the height as well as the AFM tip radius.

Based on the evaluation of 415 particles in the image, the particle size distribution with median diameter and standard deviation was determined (Figure 27.12). The particle standard deviation was 3 nm resulting in a standard deviation of the mean of 0.15 nm. As the size distribution is slightly asymmetric the more robust median value is used instead of the mean value. The mean value was roughly 0.4 nm smaller.

Again, as for the gold colloids, the particle height varied with the tapping mode setpoint. The median values were in the range from 193.8 nm to 194.9 nm for setpoints from 90 % to 60 % with respect to the tip lift off amplitude. Also the tip radius varied depending on the setpoint between 13 nm and 24 nm whereby lighter tapping increased the radius. This could also have been influenced by the feedback setting and the scanning speed. A relatively slow scan speed of 5 μm/s was used to acquire the images.

The final standard uncertainty estimation of 1.5 nm is mainly influenced by the height variation with the tapping mode setpoint and the *z*-calibration. Figure

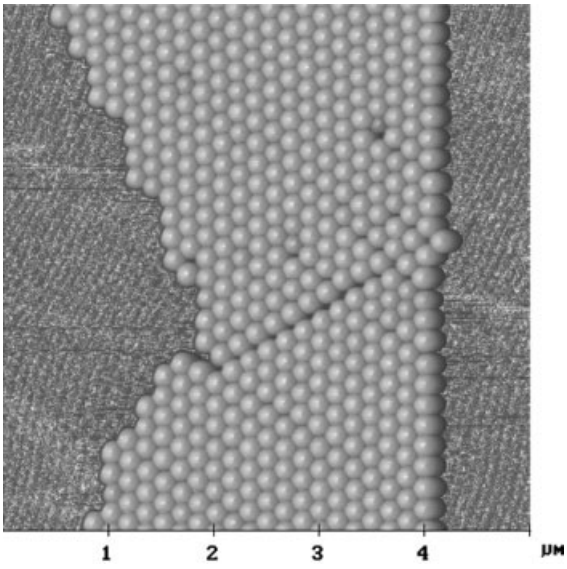

Fig. 27.10 Region of a long slender island of close-packed polymer spheres with 194 nm diameter deposited on cleaved mica allowing correct line-by-line image flattening to be applied.

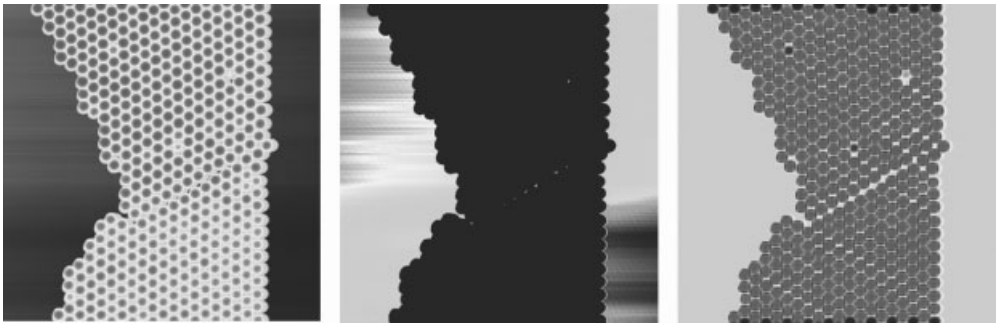

Fig. 27.11 Steps of the AFM image evaluation showing a region of a long slender island of 194 nm polymer spheres. Image size 5 μm × 5 μm. Left: Raw AFM image with height data. Middle: Background selection for image flattening using a height threshold. Right: Selecting valid particles by size filtering and individual particle height evaluation by fitting a circle segment to the measured points of the particle bump.

27.13 shows the comparison between the average particle diameter determined from the lateral particle distance and the particle height obtained for various AFM tapping mode settings. Considering the estimated uncertainties for both types of measurements the results are in a good agreement indicating that no additional significant systematic error is involved here.

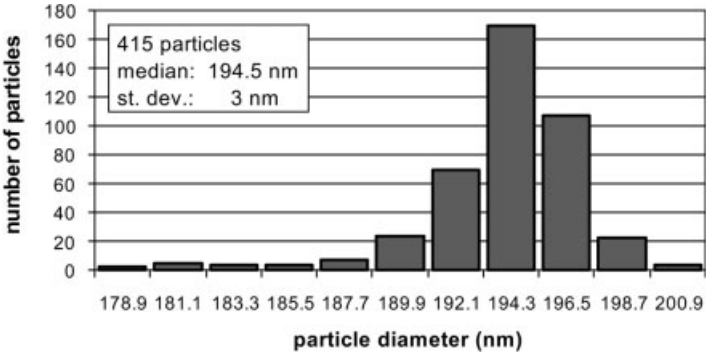

Fig. 27.12 Diameter distribution of 194 nm polymer particles deposited on mica determined from particle heights measured with AFM tapping mode.

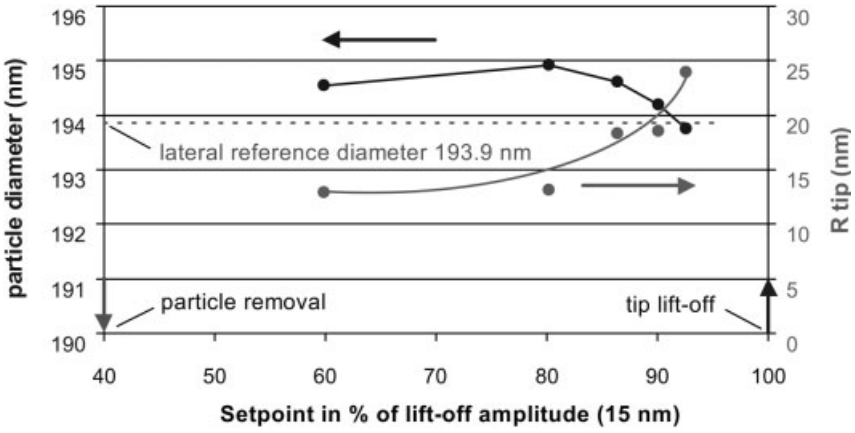

Fig. 27.13 Comparison of the polymer particle diameter determined from the lateral measurement with the ones from the particle height evaluations obtained for various AFM tapping mode setpoints.

27.4 Conclusion

A metrology AFM with tapping mode is well suited for traceable diameter calibrations of small particles in the range of 4 nm to 1 μm. Two methods can be used for the diameter determination: Lateral measurements on close-packed particle monolayer do not suffer from tip effects and give the smallest uncertainty. This method, however, is not always applicable and it does not indicate the particle size distribution. Alternatively, height measurements are possible for most types of particles as it is only necessary that a few particles stick somewhere on a flat surface. As the apparent height is influenced by the interaction distance of the AFM tip, these measurements are less accurate. With the work presented here these effects are considered to be smaller than ±1.5 nm. No evidence within the uncertainty of the results was found that indicates a systematic effect larger than the tapping setpoint dependence. In contrast to hard tapping, light tapping leads to better AFM particle height results when compared with the lateral measurements.

Usually particle and substrate material are not the same, and therefore, besides different mechanical properties, also the different surface potential must be considered [17]. Understanding the tip sample interaction as a function of the material, the sample topography and the tip shape are of great importance. Further investigations in this field will be of general interest to people who use metrology AFMs for height and structure width calibrations.

References

1 G. W. Mulholland, B. P. Nelson, and C. Croarkin, Aerosol Sci. Technol. **31**, 39–55 (1999).

2 P. Mulvaney and M. Giersig, J. Chem. Soc., Faraday Trans. **92**(17), 3137–3143 (1996).

3 Chr. Hoffrogge and H.-J. Rademacher, PTB-Mitteilungen **2/73**, 79 (1973).

4 S. T. Smith, D. G. Chetwynd, and D. K. Bowen, J. Phys. E: Sci. Instrum. **20**, 977 (1987).

5 M. J. Downs and W. R.C. Rowley, Prec. Eng. **15**(4), 281 (1993).

6 P. L.M. Heydemann, Appl. Opt. **20**, 3382 (1981).

7 Q. Zhong, D. Inniss, K. Kjoller, and V. B. Elings, Surf. Sci. Lett. **290**, L688 (1993).

8 F. Meli and R. Thalmann, Meas. Sci. Technol. **9**(7), 1087–1092 (1998).

9 F. Meli, PTB-Bericht **F-34**, 61–67 (1998).

10 F. Meli, PTB-Bericht **F-39**, 58–65 (2000).

11 F. Meli, in *Proc. of the 2nd Int. Conf. of Euspen, Turin, Italy* (May 2001), Vol. 2, pp. 358–361.

12 F. Meli, in *Proc. of 3rd Int. Conf. of Euspen, Eindhoven, NL* (2002), Vol. 2, pp. 533–536.

13 J. Vesenka, S. Manne, R. Giberson, T. Marsh, and E. Henderson, Biophys. J. **65**, 992–997 (1993).

14 A. W. Marczewski and K. Higashitani, Comput. Chem. **21**(3), 129–142 (1997).

15 N. A. Burnham, O. P. Behrend, G. Gremaud, P.-J. Gallo, D. Gourdon, E. Dupas, A. J. Kulik, H. M. Pollock, and G. A.D. Briggs, Nanotechnology **8**, 67–75 (1997).

16 Y. Li and S. M. Lindsay, Rev. Sci. Instrum. **62**(11), 2630–2633 (1991).

17 S. Sadewasser and M.Ch. Lux-Steiner, Phys. Rev. Lett. **91**(26), 6101 (2003).

28
Pitch and CD Measurements at Anisotropically Etched Si Structures in an SEM

C. G. Frase, S. Czerkas, H. Bosse, Yu. A. Novikov, and A. V. Rakov

Abstract

Pitch and CD measurements were performed on a calibration standard developed for SEM and AFM application (Ch. P. Volk, E. S. Gornev, Yu. A. Novikov, Yu. V. Ozerin, Yu. I. Plotnikov, A. M. Prokhorov†, and A. V. Rakov, Linear standard for SEM–AFM microelectronics dimensional metrology in the range 0.01–100 μm, Russ. Microelectron. **31**(4), 207ff (2002)). The specimen consists of several structure groups centered on a 15 mm × 15 mm silicon chip that contains arrays of anisotropically etched trenches with a sidewall angle of 54.7°, a depth of approximately 630 nm, a nominal pitch of 2.0 μm, and a length of 100 μm. Subject to measurements were pitch and width (critical dimension or CD) of the trenches in the central structure group. The measurements were performed with the electron optical metrology system (EOMS) at the PTB (W. Häßler-Grohne and H. Bosse, Electron optical metrology system for pattern placement measurements, Meas. Sci. Technol. **9**, 1120–1128 (1998)), a low-voltage SEM equipped with a laser-interferometer controlled specimen stage that was used for calibration of scan magnification by means of laser-interferometrical displacement measurements. For a correct interpretation of signal profiles, secondary electron (SE) image formation was modeled by Monte Carlo simulations including an SE ray-tracing algorithm considering the detector's collecting electric field. The simulations showed good conformity with measured data. For each structure in the array, a measuring window of 6 μm (covered by three images of about 2 μm × 2 μm) was defined. Signal profiles averaged over 50 scan lines (i. e., over a length of 220 nm) were extracted from the images for subsequent evaluation of CD, pitch, and line edge roughness. A CD evaluation algorithm based on prior workings (Ch. P. Volk, Yu. A. Novikov, and A. V. Rakov, SEM calibration in the micrometer and submicrometer range by means of a periodic linear measure, Meas. Technol. **43**(4), 346–352 (2000)) and adapted for imaging of structures in the EOMS instrument was developed. The algorithm separates the signal profiles in sections that can be approximated by linear regression. The resulting linear functions are extrapolated to determine the intersection points of the straight

Nanoscale Calibration Standards and Methods: Dimensional and Related Measurements in the Micro- and Nanometer Range.
Edited by Gunter Wilkening, Ludger Koenders
ISBN: 3-527-40502-X

regression lines. On the basis of this linearization of the profile, the algorithm determines the upper width and the basis width of trenches and deduces CD and pitch values. The main advantages of this method are a good robustness against signal noise due to the large number of data points used, and a minimization of the probe diameter's influence because of automatic rejection of nonlinear parts of the profile from regression. Furthermore, an estimation of the effective SEM probe diameter can be derived from the analysis of signal flanks. At the moment, structures with an upper width of about 100 nm and below are created (Yu. A. Novikov, A. V. Rakov, and Yu. V. Ozerin, Test object of solid surface micro and nanorelief, *Seminar NanoScale 2004* (Abstract)) that will be investigated next.

28.1 Introduction

The GWPS-2.0Si standard (Gauge of Width and Periodicity Special, nominal pitch 2.0 μm, made of (100) silicon) is a linewidth standard proposed by the Russian Academy of Sciences. It is usable for pitch and CD calibration in nanometrology. The structures of the standard are etched anisotropically with a sidewall angle of exactly 54.7°, the angle between the silicon (100) and (111) lattice plane. This design has the advantage that the projection of the sidewalls into the *xy*-image plane is quite broad and upper and lower linewidths can be measured separately and largely independent of the electron probe diameter. Therefore, CD calibration has the potential to provide smaller uncertainty than for approximately rectangular structures.

The first subject of this contribution is a detailed analysis of the SEM image formation at the structures by means of Monte Carlo simulations. From this, an algorithm for pitch and CD evaluation is derived that uses the advantages of the specimen's special design. This algorithm is used for SEM measurements at the structures that are compared with additional AFM measurements.

28.2 GWPS Specimen

The GWPS standard is incorporated on a 15 mm × 15 mm silicon chip together with "find me" structures. In an active area of 1 mm × 1 mm, five structure groups are centered. Every structure group contains three arrays of 11 trenches with a nominal pitch of 2.0 μm and a length of 100 μm. The sidewall angle of the anisotropically etched structures is 54.7° and the depth of the structures is approximately 630 nm. The arrays are marked with roman numerals I, II, and III and a horizontal line denoting the center of the trenches (Figure 28.1). Subject to the measurements were pitch and critical dimension (CD) of the trenches in the array II of the chip's central structure group.

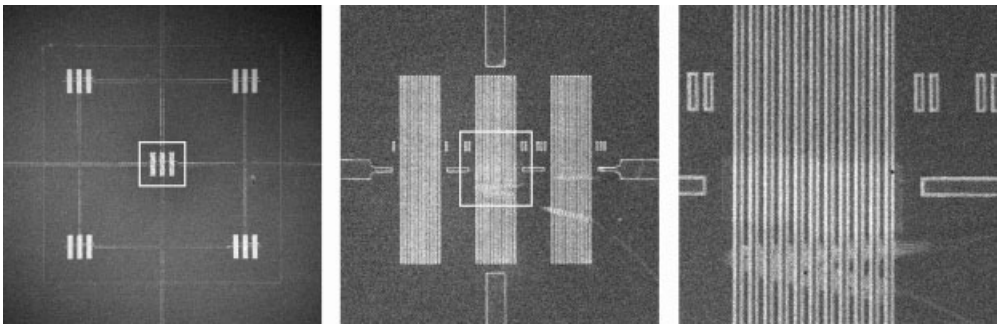

Fig. 28.1 Overview of the GWPS 2.0-Si layout. In the left image the whole active area with five structure groups, in the central image the central structure group, and in the right image the central array II with 11 trenches are shown.

28.3 SEM Instrumentation

The SEM we used for these measurements, the electron optical metrology system (EOMS), is described in detail in [1]. Briefly, it can be described as a low-voltage SEM mounted on top of a large vacuum chamber that can load planar objects of up to 300 mm. The main task of this instrument was to perform 2D coordinate measurements on photomasks. The low-voltage SEM column features a thermal field emitter (Schottky emitter), a beam booster, i. e., the electron beam is held on a high potential of 8 kV within the SEM column and decelerated to the intended landing energy in the objective lens, a magnetic-electrostatic detector objective lens (MEDOL), and an on-axis scintillation SE detector to obtain highly symmetric image contrasts. Typical primary electron energy we use is 1 keV. The *xy*-coordinate stage consists of a "one-level-table" supported by four Teflon pads, which moves on a lapped ground plate. It offers a travel range of 300 mm in both directions. The position of the stage is measured by laser interferometry with a resolution of about 0.6 nm. The interferometer controlled specimen stage is used for calibration of magnification and for characterization of scan field distortions as well.

28.4 SEM image formation and Modeling

Contrast formation in the low-voltage SEM's secondary electron (SE) imaging mode results from the elastic and inelastic scattering of primary electrons in solid state together with excitation and emission of secondary electrons. When the SEM's focused electron beam with a diameter of a few nanometers is scanned over the specimen surface the electrons undergo processes of elastic and inelastic scattering that form a characteristic diffusion cloud in the specimen. The inelastic

scattering process results in the excitation of secondary electrons (SE) with an energy by definition to be smaller than 50 eV. Therefore, SE can only escape from surface layers of a few nanometers. The emitted SE are absorbed by the objective lens and projected on a scintillation detector above the lens that measures the image signal.

The contrast in secondary electron imaging mode is affected by three main contrast mechanisms, the surface tilt contrast, the SE reabsorption in trenches (shadowing), and the conversion of high-energy backscattered electrons (BSE) in secondary electrons.

Surface tilt contrast is a result of the reduced penetration depth of the electron probe when hitting a tilted surface such as the sidewalls of the structures, resulting in a higher SE signal. It was often described in literature, see, e. g., [2]. The other two effects, SE reabsorption and backscatter conversion, are antagonistic effects: The reabsorption of SE generated in trenches by the sidewalls results in a signal decrease in the trenches, whereas the reabsorption of high-energy backscattered electrons by the sidewalls results in the generation and subsequent emission of additional secondary electrons and therefore in a signal increase. The balance between the two effects is strongly influenced by the electric field of the objective lens. In the case of the GWPS specimen measured by EOMS, we observed a contrast inversion: The SE signal from the trenches is slightly higher than the signal from the lines.

An additional contrast mechanism is the diffusion contrast that introduces nonlinear effects in the SE signal profile close to the specimen edges. The edge detection algorithm that was applied here suppresses nonlinearities. However, the diffusion contrast can also form the basis of a CD edge detection algorithm, see, e. g., [3].

The image formation was modeled by Monte Carlo simulations of electron diffusion in solid state and SE excitation and emission. For these investigations, the Monte Carlo program package MOCASIM (developed at the University of Münster) was used [4]. It is a Monte Carlo simulation program adapted for low-voltage SEM modeling, so it uses the quantum mechanical Mott cross section instead of the classical Rutherford cross section. However, comparison of the modeled signal profiles with experimental results on the GWPS structures showed a completely different contrast behavior. Therefore, the simulation was extended for secondary electron ray tracing in the electric field above the specimen. The combined simulation of Monte Carlo and electron ray tracing in vacuum showed a good conformity with experimental results, even the contrast reversal could successfully be modeled, see Figure 28.3. Figure 28.2 shows the simulated electron trajectories in solid state in the original simulation and the SE trajectories in vacuum in the extended simulation with SE ray tracing.

The finite diameter of the electron probe also has to be taken into account for a correct analysis of the SE intensity profiles. For the case of a well-aligned, nearly parallel electron beam, the real profile can be approximately regarded as a convolution of an ideal profile (i. e., probe diameter zero) with the intensity distribution of the probe electrons on the specimen surface (see Figure 28.4). From the result-

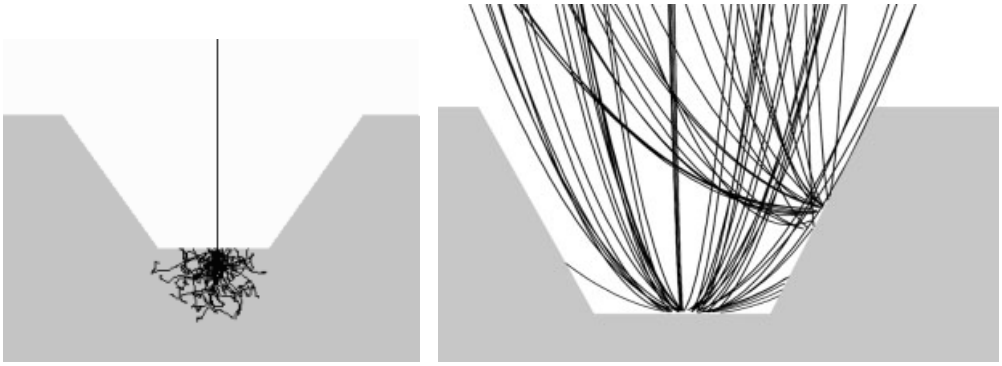

Fig. 28.2 Left: Monte Carlo simulation of electron diffusion in solid state. Right: Simulation of secondary electron trajectories in an electric field above the specimen surface. Electron probe position is the center of the trench. The second source of SE emission on the right sidewall is due to backscatter conversion.

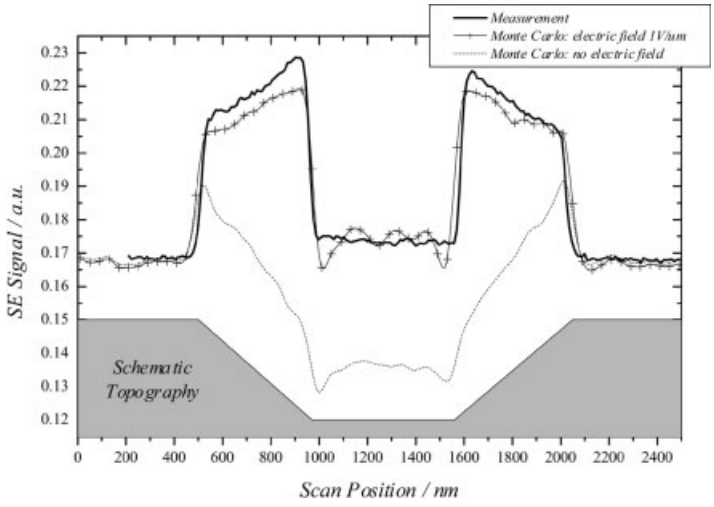

Fig. 28.3 Experimental and simulated SE intensity profile. The extended simulation with consideration of the electric field reproduces the slight contrast inversion satisfactorily whereas the original simulation without electric field consideration shows a strong signal decrease in the trench that was not observed in experiments.

ing profile, one can see that there remain linear parts in the profile that can be approximated by linear functions and that the center positions of the peak flanks are isofocal.

The influence of the finite probe diameter can also be shown in a geometric model of probe–specimen interaction (see Figure 28.4). At point 1 the probe begins to hit the sidewall. The signal rises sharply until the whole probe is located on the sidewall at point 2. The contrast difference between points 2 and 3 is due

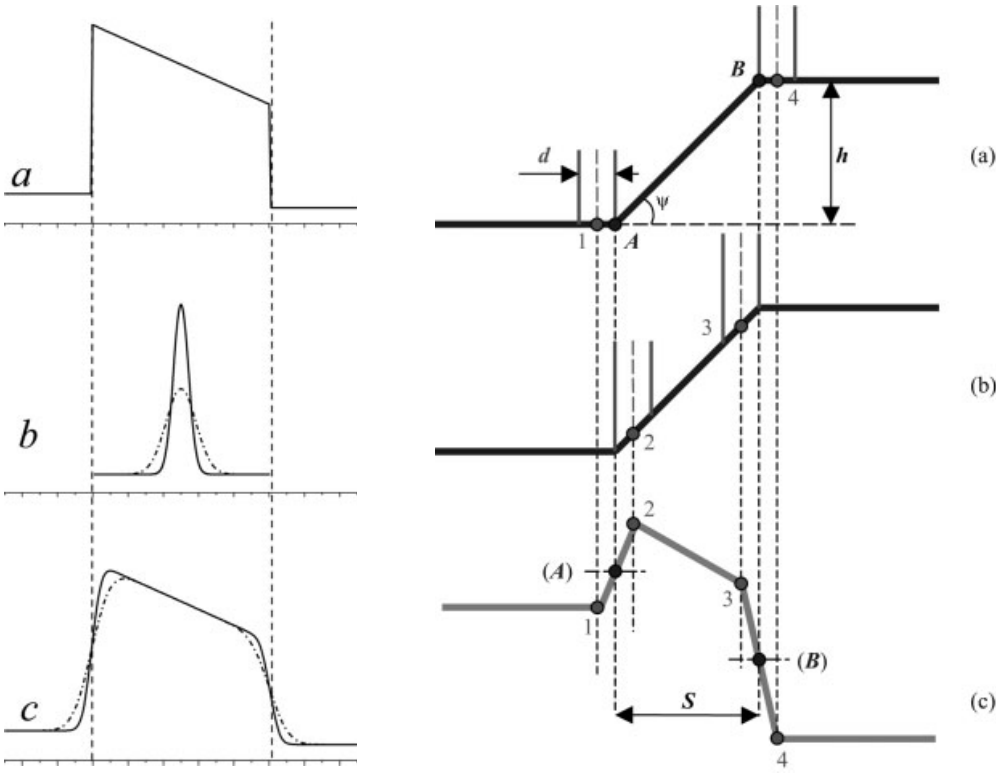

Fig. 28.4 Left: Scheme of the convolution of the ideal profile (a) with probe intensity profiles of different diameters (b) resulting in the real profiles (c). Right: Geometric model of the interaction between an assumed uniformly distributed electron probe with the diameter *d* and the specimen topography. (a) and (b) show the specimen topography and the impact points of the electron probe, and (c) shows the resulting intensity profile.

to the contrast mechanisms of shadowing and backscatter conversion. At point 3, the probe starts leaving the sidewall and at point 4 it has completely left the sidewall. The flanks 1–2 and 3–4 of the sidewall peak have the width *d* equal to the probe diameter. The control points *A* and *B* that are located in the center of the flanks are isofocal, i. e., they are largely independent of the probe diameter *d*. The projection *S* of the sidewall is defined as the distance *A*–*B* and thus is also independent of the probe diameter.

For our CD evaluation algorithm, two points are crucial: A profile that is distinguishable into approximately linear parts and the center of the peak flanks being isofocal. Prerequisite for this is the condition $S >> d$. Otherwise, the two peak flanks would merge into a single, Gauss-like peak. Therefore, the anisotropically etched sidewalls of the GWPS sample with a low sidewall angle and a broad sidewall projection *S* offer the possibility of CD measurements to be performed and evaluated largely independent of the probe diameter.

28.5
SEM Measurement Method

The analysis of the image formation revealed that the SE intensity profile can be segmented into parts that can be approximated by linear functions. A complete linear parameterization of the profile is therefore achievable.

From the SEM image (512 × 512 pixel) of one silicon trench, an intensity profile, averaged over 50 scan lines, is extracted. The first derivative is calculated and the two maxima respectively minima are detected that refer to the signal flanks of the two sidewall peaks. The full-width-half-maximum (FWHM) of the derivative peaks is defined as "flank regions" and a linear regression is applied in the individual regions of the original profile. The profile is then divided into four flank regions and five intermediate segments with approximately constant slope. In each intermediate segment, a slope histogram is calculated and the most probable slope is determined. Then, a subset of data points within the segment is taken, considering only data points lying in a slope window of, e. g., the most probable slope $\pm\sigma$. This eliminates all profile parts with nonlinearities from the subsequent linear approximation of the subset. As a result, four linear functions of the peak flanks and five linear functions of the intermediate segments are determined. The functions are extrapolated to determine the intersection points and this procedure finally results in a completely linear parameterized signal profile (see Figure 28.5). The center positions of the flank regions are defined as control points *A*, *B*, *C*, and *D*. The model of image formation shows that *A* and *D* are assigned to the upper left and the upper right positions of the trenches' sidewalls, and *B* and *C* to the lower left and lower right positions. The distance *A*–*D* is there-

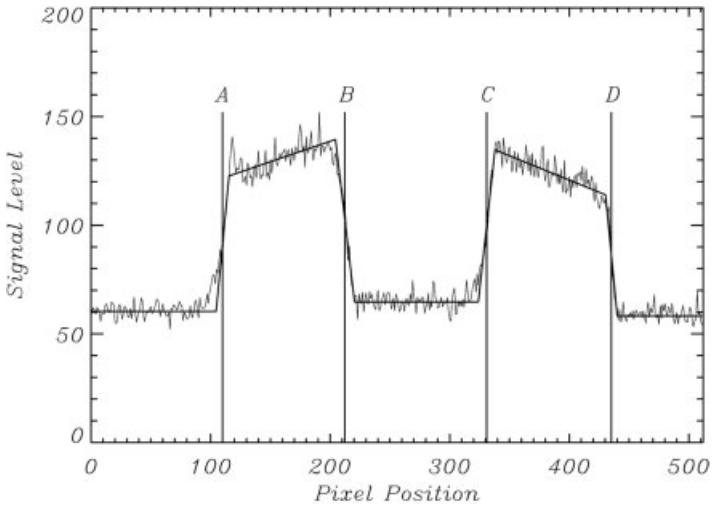

Fig. 28.5 Measured intensity profile and linearized profile. The control points *A*–*D* are placed in the center of the sidewall peak flanks.

fore the upper width of the trench, and the distance *B–C* the lower trench width. The above-described algorithm was applied to the CD evaluation in the measurements.

28.6 Measurement Results

The following measurement scheme was applied to the central array of the GWPS specimen: For each of the 11 trenches, a measuring window of 6 μm was defined that is covered by three images of 2 μm × 2 μm field of view (see Figure 28.6). In each image, 10 profiles averaged over 50 scanlines are extracted. So, in total 30 profiles were extracted for each of the 11 trenches. The measurements were repeated five times.

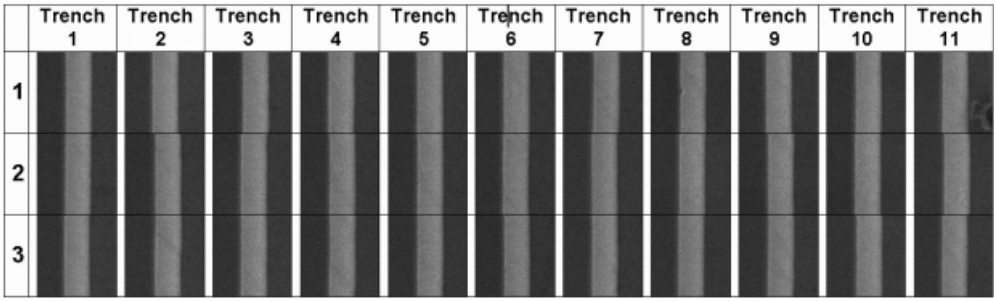

Fig. 28.6 Measuring scheme of the 11 trenches in the central array.

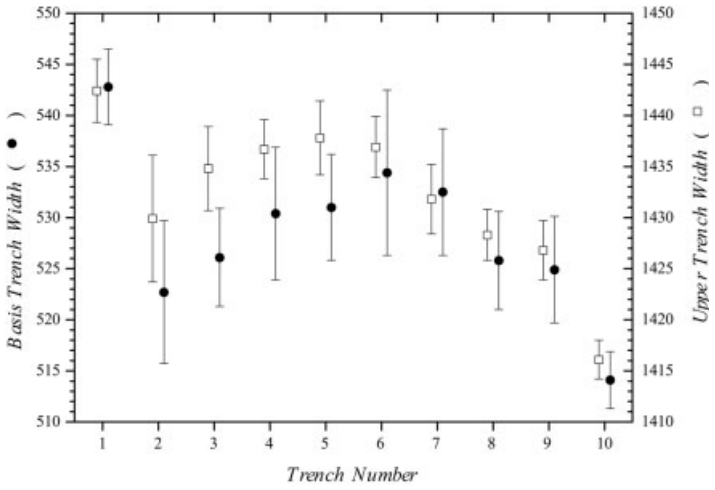

Fig. 28.7 Measurement results for the upper and basis trench widths.

The results for upper and basis trench width are shown in Figure 28.7. In trench number 11 a dust particle was observed, so the results were not further analyzed for this trench. Trench numbers 1 and 10 showed larger deviations in trench width; the other trench width variations lie in a range of 12 nm. The error bars shown in Figure 28.7 refer to the 1σ repeatability of the measurements and the CD variations in the 6-μm measuring window for each trench. The repeatability of the EOMS tool was determined from five repetitions at all 30 × 11 measuring positions as 2 nm (1σ). The CD variations observed in the 6 μm measuring window at trench numbers 1–10 are 3.5 nm (1σ) for the upper trench width and 5.4 nm (1σ) for the bottom trench width.

For pitch evaluation, images of two adjacent trenches were analyzed. The positions of the control points *A*, *B*, *C*, and *D* were determined in both images and the absolute distance of the two measurement positions was measured by laser interferometry. Then, the absolute distances *A–A*, *B–B*, *C–C*, and *D–D* were evaluated and a mean pitch from the four values and the 30 intensity profiles was calculated. Figure 28.8 shows the pitch results for trenches 1–2 to 9–10. The mean pitch variation over the 6-μm measuring window of 10 trenches is 4.4 nm (1σ).

In addition to the SEM measurements, AFM measurements have been performed with a commercial AFM tool. Figure 28.9 shows a comparison of trench width variation at trench number 10 between both measurement tools. The measured curves show an offset of 50 nm due to a large AFM tip radius because a worn tip was used. No absolute CD comparison was intended but a comparison of CD variation within the measurement window. The variation curves of SEM and AFM measurements follow each other smoothly.

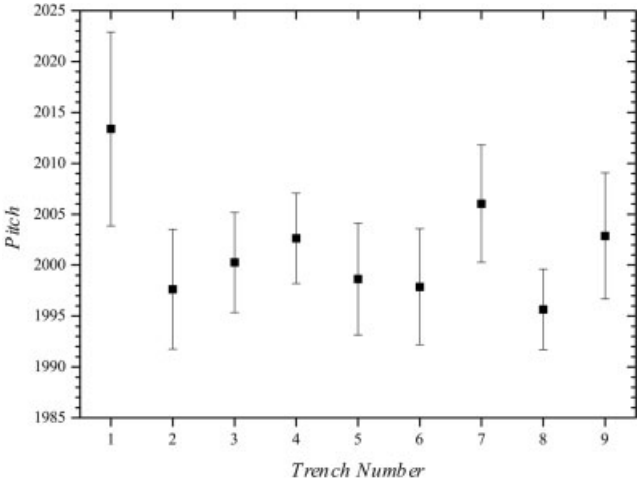

Fig. 28.8 Pitch measurement results for trenches 1–2 to 9–10.

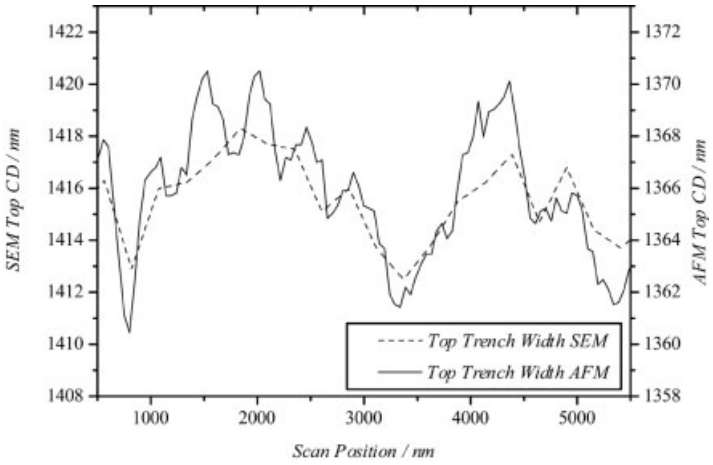

Fig. 28.9 Comparison of SEM and AFM measurements for top trench width variation at trench number 10.

28.7 Conclusion

A robust algorithm for CD evaluation at anisotropically etched silicon structures was presented. The trapezoidal topography of the structures together with the special algorithm allows CD measurements that are largely insensible to defocusing effects. The investigations will be continued at structures with a much smaller CD range (20–100 nm top linewidth). It has to be tested, down to which minimum structure size the algorithm is applicable. Furthermore, it has to be tested in Monte Carlo simulations to what extent the algorithm is influenced by electron diffusion in solid state.

References

1 W. Häßler-Grohne and H. Bosse, Electron optical metrology system for pattern placement measurements, Meas. Sci. Technol. **9**, 1120–1128 (1998).

2 L. Reimer, in *Scanning Electron Microscopy*, Springer Series in Optical Science (Springer, Berlin, 1998), 2nd ed., Vol. 45.

3 W. Mirandé and C. G. Frase, Comparison of linewidth measurements on Si structures performed by atomic force microscopy (AFM) and low voltage scanning electron microscopy (SEM), in *Proceedings Quantitative Microscopy (QM '99), Kopenhagen, 1999*, PTB-Bericht PTB-F-34, 1999, pp. 89–89.

4 L. Reimer, M. Kässens, and L. Wiese, Monte Carlo program with free configuration of specimen geometry and detector signals, Microchim. Acta **13**, 485–492 (1996).

29
Analysis and Comparison of CD-SEM Edge Operators: A Contribution to Feature Width Metrology

C.G. Frase, W. Häßler-Grohne, E. Buhr, K. Hahm, and H. Bosse

Abstract

We report on feature width or critical dimension (CD) measurements by the means of scanning electron microscopes (CD-SEM). For CD evaluation, CD-SEM edge operators are used to deduce the critical dimension of structures in the submicrometer region from SEM measurements. Three algorithms are presented and discussed that extract information about microstructures, especially chromium structures on chromium-on-quartz photomasks, from SEM images, respectively, secondary electron intensity profiles. An exponential fit operator (peak flank fit) is used in two variations to determine the top edge position of a feature, a Gaussian peak fit operator is applied for line edge roughness (LER) measurements. Furthermore, a signal decay operator is presented that is used to estimate the degree of charging of the quartz substrate. A Monte Carlo model of the SEM image formation is applied to investigate the effect of parameter variation, both specimen and measurement tool parameters, on signal formation and CD evaluation. It will be shown that for the low-voltage SEM instrumentation used in our group the application of the exponential rise operator allows to determine the top edge position of a feature from the measured SEM images with achievable uncertainties of about $U = 15$ nm ($k = 2$).

29.1 Introduction

Scanning electron microscopes (SEM) are widely used today as metrology tools offering high resolution and good linearity in wafer and mask manufacturing process control. This type of instruments are mostly used in parallel to other CD metrology instrumentation like optical transmission microscopes and scanning force microscopes (SFM or AFM). The measurement results of the different metrology instruments used in industry have to be compared and carefully matched in order to operate with sound, reliable, and appropriate CD specifications during the

Nanoscale Calibration Standards and Methods: Dimensional and Related Measurements in the Micro- and Nanometer Range.
Edited by Gunter Wilkening, Ludger Koenders
ISBN: 3-527-40502-X

manufacturing and qualification process. It is thus important to analyze and understand the possible physical reasons for discrepancies which might be observed in the results of different or even similar instruments [1].

Therefore, sound physical modeling of the SEM image formation is necessary which correlates the SEM images with the specimen topography. This analysis of the image formation is done by the means of Monte Carlo simulations which simulate the diffusion of probe electrons in solid state and the excitation and emission of secondary electrons. All the Monte Carlo simulations have been performed with the program package MOCASIM, developed at the University of Muenster [2]. It uses the tabulated Mott scattering cross sections [3] for elastic scattering and the Bethe continuous slowing down approximation (CSDA) for inelastic scattering processes [4]. SE generation and diffusion is taken into account by a simple but effective parametric model based on a mean SE generation energy and a mean SE exit depth. The simulation offers a free configuration of specimen geometry and detector strategy. In the model, specimen topography is defined by structure height, top linewidth (as the distance of the left and right top corner positions), top corner rounding radius, and edge slope angle. The top edge position is defined as the intersection point of the tangent terminating the upper plateau with the edge slope tangent. Therefore, the corner roundness does not affect the position of the top edge (Figure 29.1).

From the model, algorithms for edge determination are derived. These CD-SEM edge operators are applied to determine feature width measurement values especially at chromium-on-quartz photomasks from SEM images, respectively, measured secondary electron line profiles. In this contribution, three different edge operators are investigated: an exponential fit operator (peak flank fit) in a low and high sidewall angle application and a Gaussian fit operator (peak fit) for CD evaluation and a signal decay operator that estimates the degree of electrical charging of the quartz substrate.

We will report on the dependencies of these edge operators on different measurement conditions. Moreover, the correlation of the results of the different CD-SEM edge operators to geometrical details of the line features will be discussed. This discussion is related to the question of appropriate definition of

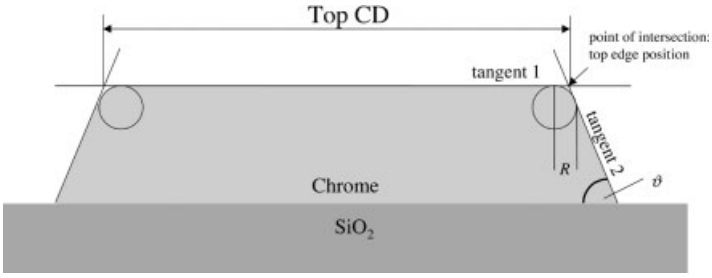

Fig. 29.1 Definition of top CD, here for CoG structures. For a finite edge roundness radius *R*, the intersection point of tangent 1 and tangent 2 defines the top edge position. The distance of the left and right top edge positions is defined as top CD.

the measurand 'CD' on an imperfectly defined feature. This point also has been addressed by the NIST as the pilot laboratory of the Nano1 international comparison on CD measurements, scheduled to be started in 2004.

29.2
Exponential Fit Operator

29.2.1
Secondary Electron Image Formation at Structural Edges

When SEM's electron beam impinges the specimen surface the electrons undergo several processes of elastic and inelastic scattering that form a characteristic diffusion cloud. Inelastic scattering processes result in the excitation of secondary electrons in the whole diffusion region. But due to their low energy of some electron volts they can escape only from a thin surface layer of a few nanometers. Secondary electrons (SE) are separated into SE1 that are excited by the primary electron beam on it's way into the specimen and SE2 that are excited by backscattered electrons on their way out of the specimen. Figure 29.2 shows a schematic presentation of the diffusion cloud and the lateral distribution of generated SE within the diffusion region, calculated by the Monte Carlo simulation. The lateral distribution of generated SE can be approximated by an exponential distribution:

$$N_{SE}(x) = A \exp[-x/w] \tag{29.1}$$

where N_{SE} is the number of generated SE, A is the amplitude, and w is the width of the distribution.

Only a small amount of the generated SE can escape the specimen. But when the electron beam approaches a surface step the amount of SE2 increases due to SE escaping through the step's sidewall. Because of the exponential distribution of SE generation within the diffusion cloud, an increase of SE signal at surface steps is observed that is well approximated by an exponential function.

$$S(x) = S_0 + A \exp[-x/t] \tag{29.2}$$

where S_0 is the signal in infinite distance to step, A is the amplitude, and $t = 1/e$ width.

Figure 29.3 shows the Monte Carlo simulated SE intensity profiles in front of a surface step of 400 nm height for the energy range 0.5–25 keV. The width t of the signal curves differs with energy but in all cases an exponential increase is observed which reaches its maximum at the step.

For further considerations, two cases have to be distinguished: the cases of a sidewall angle of 90° and larger (undercut) and a sidewall angle smaller than 90°. For an angle of $\geq$90°, the SE signal shows a sharp drop of intensity at the step whereas for sidewall angles <90° the SE peak broadens into a plateau.

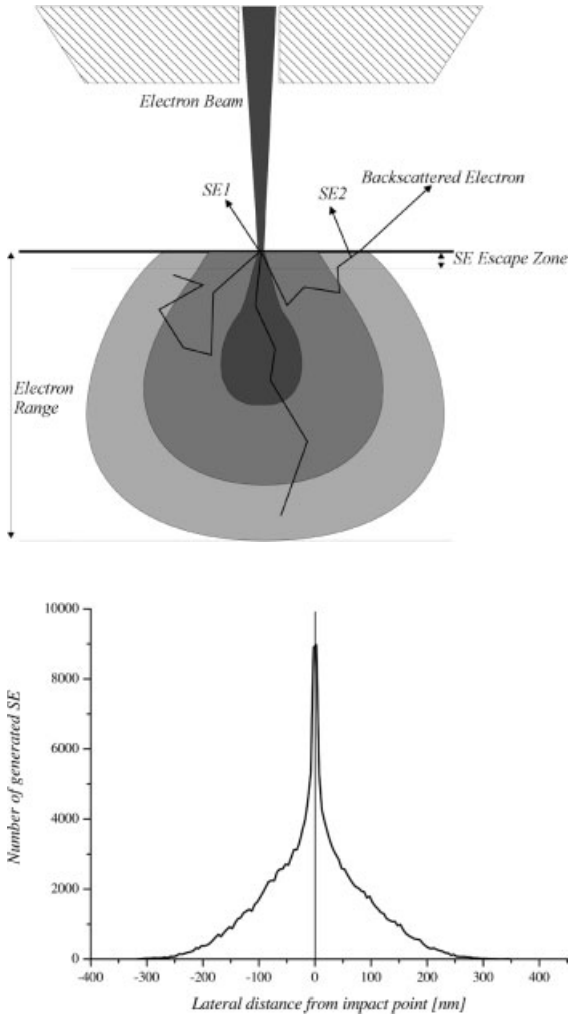

Fig. 29.2 Top: the schematic presentation of the electron diffusion cloud. The grey level indicates the amount of generated secondary electrons. Bottom: the lateral distribution of generated SE (Monte Carlo simulation, silicon, 5 kV).

This is caused by the surface–tilt contrast that intensifies the SE signal due to the reduced penetration depth of the electron beam at tilted surfaces. The effect has already been described by other authors, see e. g., [5]. Figure 29.4 shows the Monte Carlo calculated SE intensity signals for the cases of a sidewall angle of 90° and 79°, respectively. In both cases, the maximum intensity is reached at the upper sidewall position.

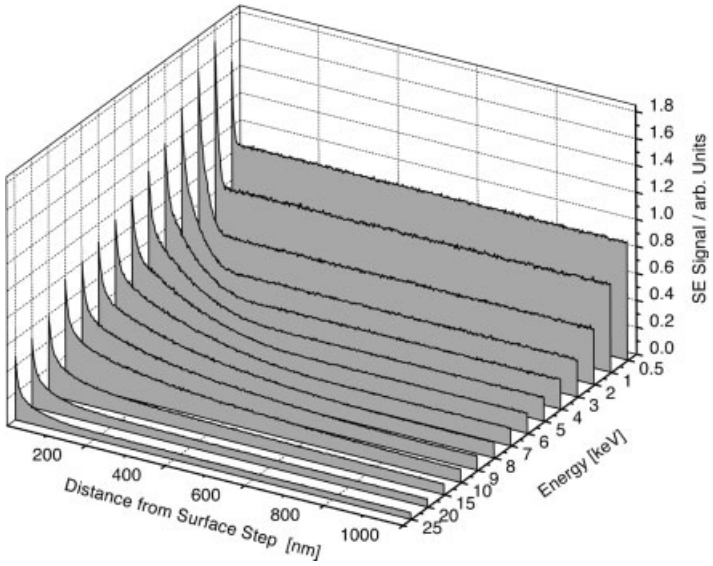

Fig. 29.3 Monte Carlo simulation of SE intensity as a function of beam energy and distance from a surface step of 400 nm height.

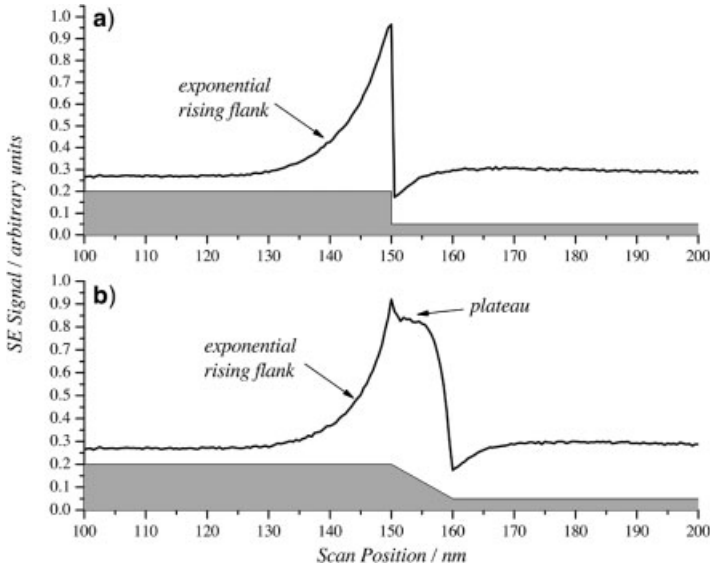

Fig. 29.4 Secondary electron intensity profile for a 50 nm silicon surface step: (a) for 90° sidewall angle and (b) for 79° sidewall angle.

29.2.2
Definition of Top CD Operator

It has been shown that the exponential signal rise in front of surface steps is solely produced by the basic mechanism of electron diffusion in solid state and is therefore largely independent of specimen features as material composition, edge slope, etc. In consequence, a robust and well-defined edge criterion can be derived that determines the upper position of feature's edge.

An exponential function is approximated to the exponential growing flank of the edge peak. The fit range is restricted to values below a threshold of 50 %–75 % of the peak maximum. Thus, deviations from the exponential behavior near the peak maximum due to SEM's finite probe diameter are excluded from fitting. The approximated function is then extrapolated to a value of 100 % peak maximum and this position is defined as a top edge position (see Figure 29.5). The distance of the left and right top edge positions is defined as top CD. Top CD linewidth measurements based on the exponential fit CD operator already showed good conformity with AFM measurements at silicon structures [6].

An important constraint for this CD operator has to be mentioned: the feature to be measured has to be large enough so that the left and right SE peaks do not overlap because otherwise the base level S_0 cannot be found. For an acceleration voltage of 1 kV, the minimum feature size is about 50 nm.

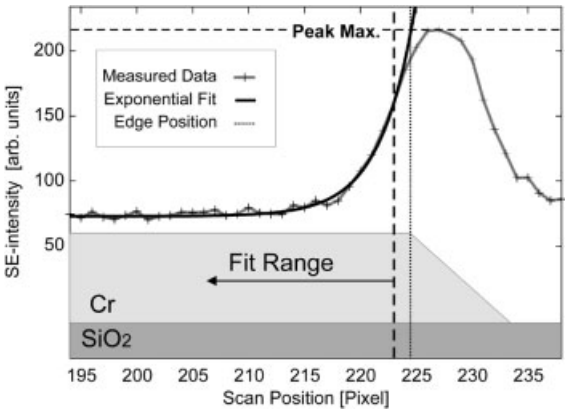

Fig. 29.5 Definition of exponential fit operator. An exponential function is approximated to the peak flank. The region next to the peak maximum is excluded from fitting because the upper plateau is rounded due to the finite probe diameter.

29.2.3
SEM Model Input Parameter Variations

The model input parameters of the Monte Carlo simulation were varied to investigate the effects on the simulated signal profiles and top CD evaluation. Subject to parameter variations were: electron probe diameter, edge slope, and top corner radius. In the model, the shape of the electron probe is assumed to be Gaussian. The probe diameter was varied from 0 nm to 20 nm FWHM for different para-

meter compositions of edge slope and top corner rounding. Acceleration voltage of the electron probe was set to 1 kV which is a typical value for low-voltage SEM.

The effect of the finite electron probe is quite different for edge slope angles ca. <85° (i. e., a plateau is observed) and edge slope angles >85° (no plateau). Figure 29.6 shows simulated SE signal profiles for a surface step of 90° and 79° and Gaussian beam diameters of 0–2.5 nm (FWHM). The signal profile at the 90° step is strongly affected; a loss of peak maximum and a shift of the peak maximum position are observed. In contrast, the signal profile at the 79° conserves its shape in the case of finite probe diameters. In consequence, for typical edge slopes of 60°–80°, top CD measurement results are little affected by the probe diameter. Typical SEM probe diameters smaller than 8 nm introduce a systematic shift of less than 0.5 nm with a variation range of 2.5 nm. On the other hand, for edges with a slope angle >85° the projection of the edge transition is smaller than the probe diameter and a loss of peak maximum intensity results due to resolution limitation. In consequence, if the probe diameter is increased to 10 nm the top CD value shifts about 10 nm. Therefore, a modified exponential fit operator for high sidewall angle structures is presented in the next section.

Top corner roundness results in a signal increase slightly slower than exponential behavior. For corner radii smaller than 20 nm this results in a systematic shift of 0.5 nm with a maximum variation range of 2 nm. Simulations showed no significant effect of chromium layer thickness on top CD because for typical COG masks, the chromium layer thickness (60–100 nm) is much larger than the electron penetration depth of <20 nm. The trends in CD variation due to the variation of model parameters which are presented here are confirmed by other Monte Carlo investigations for silicon structures and bottom CD evaluation [7].

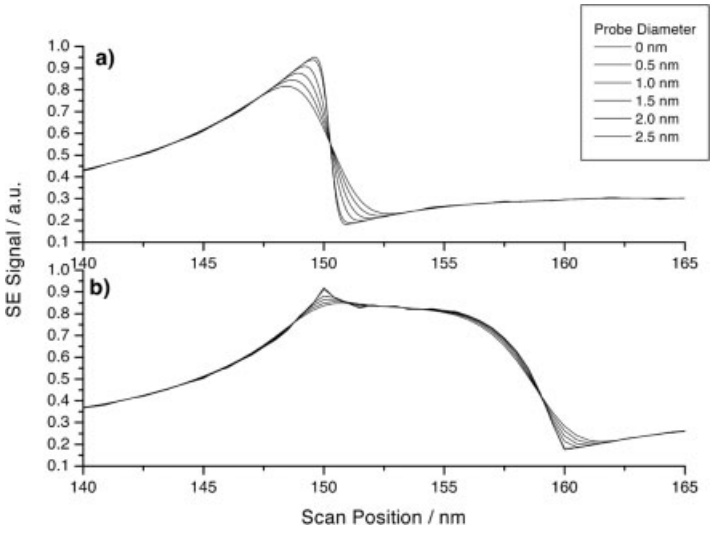

Fig. 29.6 SE intensity profiles for different electron probe diameters (Gauss, FWHM): (a) for a 90° surface step and (b) for 79° surface step. The 90° profile is affected much stronger by the finite probe diameter than the 79° profile.

29.2.4
Experimental Parameter Variations

Several experimental parameters have been varied to investigate the effect on top CD evaluation: the fitting range threshold of the exponential fit operator was varied in the interval of 50 %–75 % peak maximum. It is assumed that threshold variations in the range of 50 %–70 % will result in a robust exponential fit edge determination. The threshold variation of 20 % results in a CD variation of about 3 nm (Figure 29.7). During experiments, a maximum variation of the

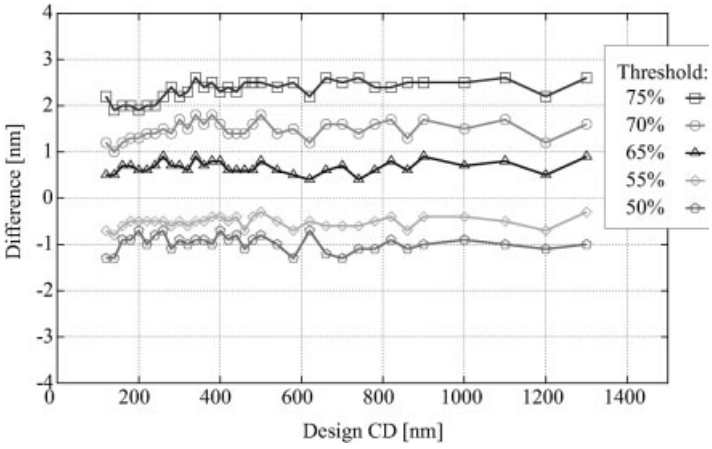

Fig. 29.7 Threshold sensitivity of exponential fit operator for CD measurements in the range of 100–1300 nm. A threshold variation of 20 % results in a CD variation of about 3 nm.

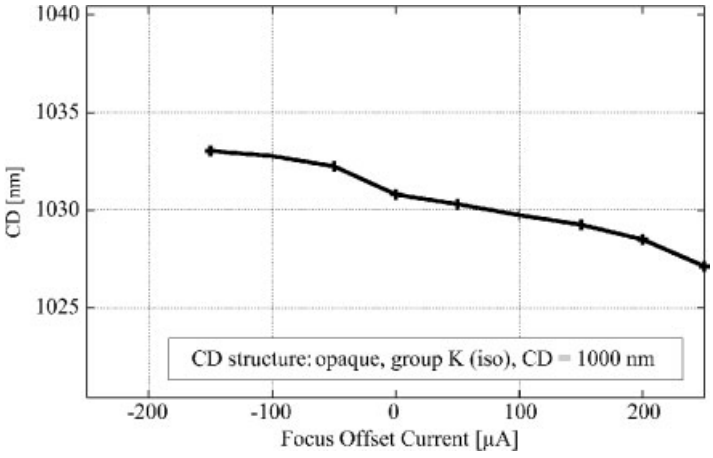

Fig. 29.8 Focus dependency of exponential fit operator. In experiments, the focus current can be kept in a range of ±100 μA.

focus current (i. e., objective lens current) of ±100 μA was observed. Focus series were performed that resulted in a corresponding CD variation of 5 nm at maximum (Figure 29.8). For a test series of 40 repeated measurements, a systematic drift of CD values of 3 nm was measured which can be attributed to electron-beam-induced carbon contamination. This means that in a typical series of about 10 measurements, the maximum corresponding drift is below 1 nm. In addition to the evaluation of the model dependencies and the experimentally determined influences of input parameter variations on the CD uncertainty, the following paragraph will cover the long-term reproducibility for top CD results inferred by the described exponential fit on a COG mask.

29.2.5 Measurement Results

Characterizations of the long-term reproducibility including reload of the mask into the SEM vacuum chamber were carried out on several CD structures. Figure 29.9 shows an example for clear structures on one CD test mask. Additional AFM measurements showed a slope angle >70° for this mask. Measurement windows of 5 μm length were used to define the area of interest for the repeated measurements at the opaque and clear line structures embedded in different environments. Three subsequent high-resolution SEM image scans of 1.7 μm each were performed to cover the 5 μm window.

Within each of the scans, subsequent integrations over 50 lines each (i. e., over a length of 160 nm) were made to determine accumulated line profiles on which the exponential CD fit was calculated to extract the corresponding top CD value. This integration window was stepped subsequently by 25 lines to cover the whole quadratic SEM image and 19 integrated line profiles were analyzed per image.

At least five repeated SEM image scans were made on each position to increase the reliability of measurement and to be able to exclude missed measurements

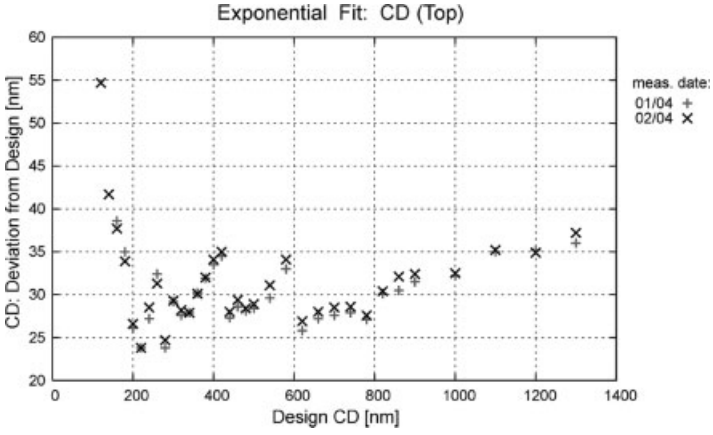

Fig. 29.9 Measurement of long-term reproducibility on a CD test mask.

due, e. g., to stage instabilities. In summary, $19 \times 3 \times 5 = 285$ CD measurement results could at maximum be used to calculate the mean CD over the defined 5 μm measurement window.

Achievable measurement uncertainty depends on the line edge variations, namely, line edge roughness and waviness of the structures. On good line structures, with small line edge roughness values of about 5 nm (3σ rms), our preliminary uncertainty budget yields measurement uncertainties U smaller than 15 nm ($k = 2$) for the top CD, measured by SEM and the described exponential fit algorithm. The dominant uncertainty contributions in this case are the long-term reproducibility, the focus setting stability, the scan calibration, the fit threshold dependency, and the line edge roughness.

29.3 Modified Exponential Fit Operator for High Sidewall Angles

In the preceding section, it was shown that the exponential fit operator shows deviations for edge angles $\geq 90°$ and larger probe diameters. Therefore, a modified exponential fit operator was developed that takes the Gaussian electron probe into account and can be applied to perpendicular edges. Two assumptions are made to derive the model SE profile:

1. The spatial intensity distribution of the incident electron probe can be described by a Gaussian function, i. e., the intensity profile in the scan direction can be written as

$$I(x) = \frac{1}{\sqrt{2\pi}\sigma} \exp\left(- \frac{x^2}{2\sigma^2} \right). \tag{29.3}$$

2. The edge profile which would be obtained for an infinitesimal small electron probe is given by an exponential function on the line ($x > x_0$) and a constant level on the substrate ($x \leq x_0$):

$$S(x) = \begin{cases} S_0 & \text{for} \quad x \leq x_0 \\ S_1 + A \exp(- (x - x_0)/t) & \text{for} \quad x > x_0 \end{cases}, \tag{29.4}$$

where, x_0 is the edge position, S_0 and S_1 are the signal levels for substrate and line structure, A is the amplitude of the exponential, and t is the parameter describing the width.

The edge profile for a Gaussian-shaped electron beam is the convolution P of the two functions I and S,

$$P(x) = S(x)^* I(x) = \int_{-\infty}^{\infty} S(x') I(x - x') \, \mathrm{d}x'. \tag{29.5}$$

The convolution can be solved analytically. One obtains for $P(x)$:

$$P(x) = S_0 + (S_1 - S_0)G\left(\frac{x - x_0}{\sigma}\right) + A\exp(-(x - x_0)/t)\,\exp\left(\frac{\sigma^2}{2t^2}\right)G\left(\frac{x - x_0}{\sigma} - \sigma/t\right) \tag{29.6}$$

with the Gaussian integral $G(x)$ defined by

$$G(x) = \frac{1}{\sqrt{2\pi}}\int_{-\infty}^{x}\exp\left(-\frac{x'^2}{2}\right)dx'.$$

The model SE profile $P(x)$ is approximated to the experimental SE profile and the edge position x_0 as well as the parameter σ describing the Gaussian probe profile is returned. The operator was tested at a series of Monte Carlo generated SE intensity profiles with Gaussian probe diameters ranging from 0 nm to 20 nm FWHM. As a model structure, a single line of 500 nm width and 300 nm height with rectangular sidewalls was chosen and the acceleration voltage was set to 7.5 KeV. The modified exponential fit operator was then used to determine the linewidth and the Gaussian parameter σ from the profiles. For the whole range of modeled probe diameters, the linewidth deviation from the exact value was less than 1 nm.

Figure 29.10 shows the application of the modified exponential fit operator to a Monte Carlo generated SE profile for a probe diameter of 10 nm. The approximated functions for the left and right sidewall regions show a good conformity

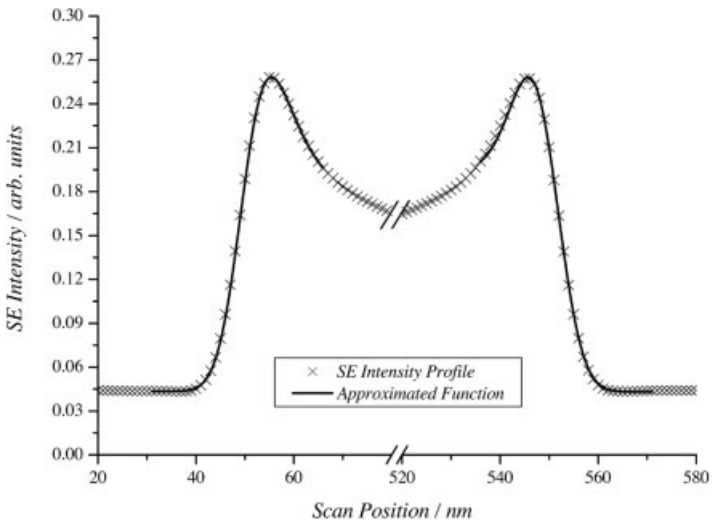

Fig. 29.10 Application of the modified exponential fit operator at a Monte Carlo generated SE profile. The model describes a single silicon line of 500 nm width and 300 nm height on silicon substrate. Acceleration voltage is 7.5 kV and Gaussian beam diameter is 10 nm FWHM.

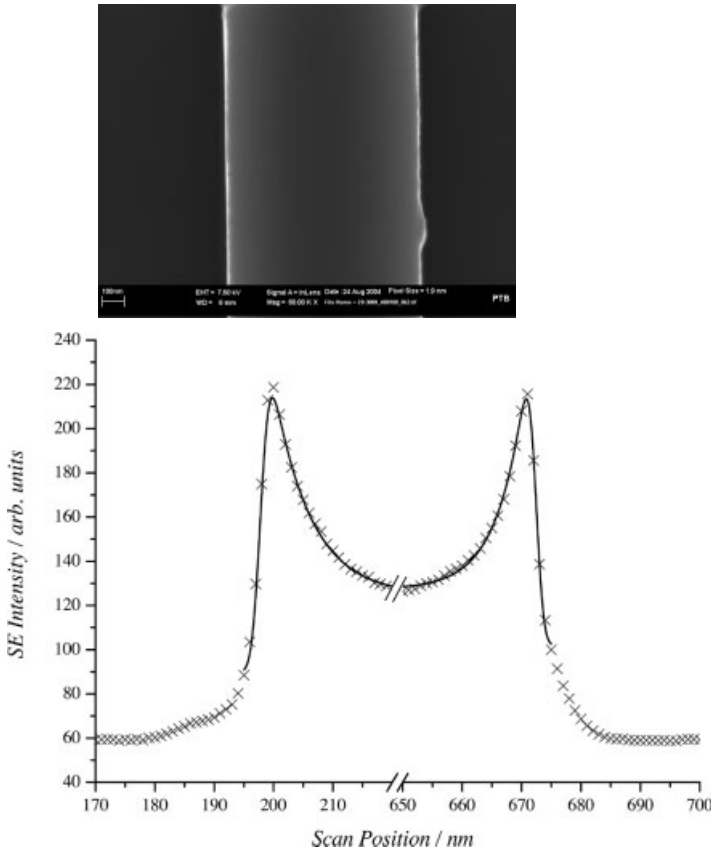

Fig. 29.11 Application of the modified exponential fit operator at experimental data. Top: secondary electron image of a silicon structure within a grating. Structure height 0.7 μm, width 0.9 μm, and acceleration voltage 7.5 kV. Bottom: extracted intensity profile and approximated functions for the left and right sidewall regions.

with the modeled profile. An example for the application of the operator to experimental data is shown in Figure 29.11. Although the characteristics and the achievable uncertainty have to be tested in detail, yet the first experimental results show a good stability and accuracy of the operator.

29.4 Gauss Fit Operator

In contrast to the exponential fit operator, the edge position determined by the Gauss fit operator is not strictly correlated to a specific point in the specimen topography. It is not based on a physical model but experimental results show that the SE edge peak convoluted with the Gaussian SEM electron probe profile can be

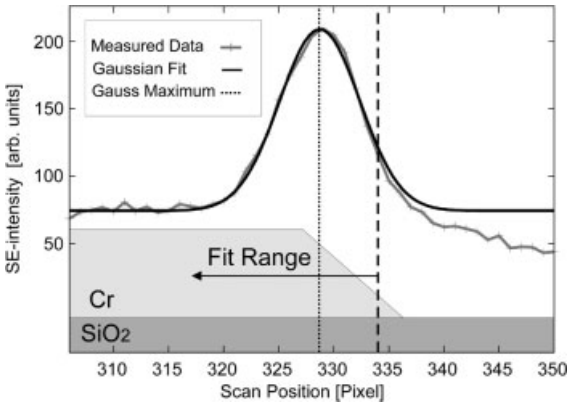

Fig. 29.12 Definition of Gauss peak fit operator. A Gaussian function is fitted to the whole waveform of the peak.

well approximated by a Gaussian peak function. Figure 29.12 shows the definition of the Gauss fit operator. Fitting range is the full waveform of the peak, restricted to values above the chromium signal level S_0. A Gauss function $S(x)$ is approximated to the measured data within the fitting range:

$$S(x) = S_0 + A\exp[-(x - x_{\max})^2/t^2] \tag{29.7}$$

where S_0 is the chromium signal level, A is the amplitude, $x_{\max}$ is the position of peak maximum, and t is the peak width.

The Gauss operator returns two parameters: the position of the Gauss maximum $x_{\max}$ and the width of the Gauss peak t. The advantage of this operator is

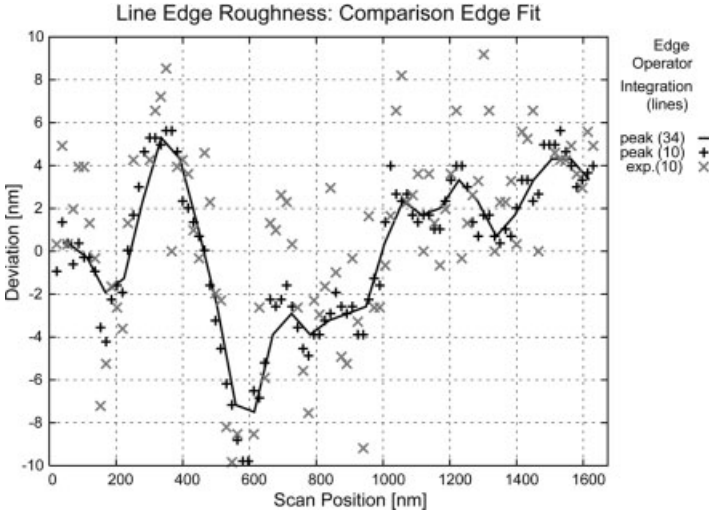

Fig. 29.13 Comparison of noise dependency for Gauss peak fit (after line average of 10, 34 resp.) and exponential fit operator.

a low dependency to noise because the full waveform of the SE peak is used for fitting. Therefore, line integration (for noise reduction) can be limited to a few scan lines. Because of this, the operator is especially suitable for application in line edge roughness (LER) characterization. Figure 29.13 shows the edge position along a measuring window of 1.7 μm, measured by the Gauss operator with a scan line integration of 34 and 10, respectively, and also measured by the exponential fit operator with a scan line integration of 10. The Gauss operator shows much smaller variation than the exponential fit operator. Therefore, high-frequency contributions to LER can be observed by application of the Gauss fit operator. Moreover, comparative investigations by SFM indicate a correlation between the width of the Gauss peak and the edge slope angle of the structure.

29.5
Signal Decay Operator

The signal decay operator is not a CD operator but a useful tool for the analysis of charging behavior of dielectric specimen, especially for uncovered quartz surfaces on photomasks. Specimen charging is a severe problem in SEM metrology. In the conventional range of acceleration voltage (typical 10–30 kV), negative charging of the specimen is observed that can reach some kilovolts and leads to beam deflections and electric discharge. Therefore, in SEM photomask metrology the so-called low-voltage SEM is applied with a typical accelerating voltage of 1–3 kV. In this region, the total electron yield (i. e., backscattered electrons plus secondary electron) exceeds unity. As a result, a positive chargeup of the specimen occurs that is self-limiting: positive charging generates a positive electric field that reabsorbs secondary electrons until the effective electron yield becomes unity. Therefore, positive charging cannot exceed the typical SE energy of ca. 2–5 eV. Although deflections of the electron beam and discharge is avoided in low-voltage SEM, even slight surface charging has an impact on image formation. If the electron beam hits the surface for the first time, the electron yield δ_0 is about 2.5 (for quartz at an accelerating voltage of 1 kV). Because of the chargeup, the electron yield (and the corresponding SE detector signal) decreases to unity.

At conducted and grounded parts of the specimen (like chromium), electron absorption and emission follow the Kirchhoff law. We define the current direction into the specimen as positive and the current out of the specimen as negative.

$$I_{\text{Probe}} - I_{\text{Emission}} + I_{\text{GND}} = 0 \tag{29.8}$$

where I_{Probe} is the probe current, I_{Emission} is the emission current, and I_{GND} is the specimen current.

Probe current and emission current are connected via the secondary electron yield δ_0 (emission of high-energy backscattered electrons is neglected here due to a comparatively small yield):

$$\delta_0 = \frac{I_{\text{Emission}}}{I_{\text{Probe}}} \Rightarrow I_{\text{Probe}}(1 - \delta_0) + I_{\text{GND}} = 0. \tag{29.9}$$

At nonconductive parts of the specimen (like quartz), imbalance between probe current and emission current cannot be compensated by the specimen current. Therefore, a charge Q builds up.

$$I_{\text{Probe}}(1 - \delta_0) + \frac{\mathrm{d}Q}{\mathrm{d}t} = 0. \tag{29.10}$$

For constant currents I_{Probe} and I_{Emission} the charge increases linearly. In the case considered here, the secondary electron yield δ_0 exceeds unity and therefore the specimen surface charges positively. The surface charge Q leads to a surface potential U that can be calculated by solving the Poisson equation and depends on the way of exposure (i. e., it will be different for a small spot of exposure and for a larger area). Because of the potential U all emitted electrons with an energy smaller eU will be recollected by the specimen and the effective electron emission δ_{eff} decreases. The buildup of the potential continues until the effective electron emission reaches unity and $I_{\text{Emission}} = -I_{\text{Probe}}$.

The energy distribution of the secondary electron emission is approximately a Maxwell distribution, i. e., for higher energies the exponential part is dominant (the low-energy part is neglected here):

$$\frac{\mathrm{d}\delta}{\mathrm{d}E} = \delta_0 \exp(-E). \tag{29.11}$$

The effective electron emission δ_{eff} covers the emission of all secondary electrons with an energy $E > eU$.

$$\delta_{\text{eff}} = \delta_0 \int_{\text{eU}}^{\infty} \exp(-E)\,\mathrm{d}E = \delta_0 \exp(-eU). \tag{29.12}$$

Therefore, the secondary electron signal decreases exponentially with increasing surface potential. Figure 29.14 shows a schematic SE energy distribution together with the emitted and reabsorbed part of the electrons for an assumed surface potential of 2 V.

Next, the time-dependent charge Q and SE emission δ_{eff} is calculated. For reason of simplicity, we assume that U is proportional to Q. The probe current remains constant but the emission current decreases exponentially with the charge.

$$\frac{\mathrm{d}Q}{\mathrm{d}t} = I_{\text{Probe}}(\delta_0 \exp(-Q(t)) - 1). \tag{29.13}$$

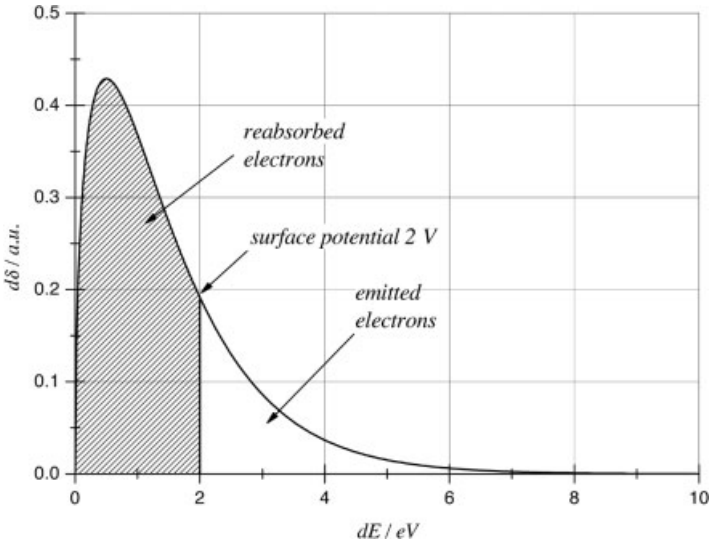

Fig. 29.14 The schematic presentation of the SE energy distribution. Electrons with an energy smaller than the surface potential are reabsorbed, the other electrons can escape the specimen.

The equation is approximated linearly and we get the time-dependent charge Q and the effective emission:

$$Q(t + \Delta t) = Q(t) + \Delta t I_{\text{Probe}}(\delta_0 \exp(-Q(t)) \qquad \text{and} \qquad \delta_{\text{eff}} = \delta_0 \exp(-Q(t)). \tag{29.14}$$

Equation (29.14) is solved iteratively with the start condition $Q(t = 0) = 0$, so $\delta_{\text{eff}} = \delta_0$. For $t \rightarrow \infty$, we get $\delta_{\text{eff}} \rightarrow 1$, i. e., emission current and probe current are in equilibrium. It was shown that for a *stationary* electron probe an exponential signal decrease can be observed. In the case of a *scanning* electron probe we assume that at least a part of the charge Q is moving with the probe. Otherwise, no signal decrease would be observed.

The signal decay operator approximates the signal profile at the chromium–quartz transition by an exponential function

$$S(x) = S_0 + A \exp[-x/t], \tag{29.15}$$

where S_0 is the quartz signal level, A is the amplitude, and t is the decay length.

Amplitude and quartz signal levels are fixed, so the only free fitting parameter is the decay length (see Figure 29.15); the operator returns the double decay length, i. e., the length in which the signal drops to exp[−2] or 13.5 %. Figure 29.16 shows the decay length measured five times in succession at a single, grounded chromium line on a photomask. On the right edge (i. e., the

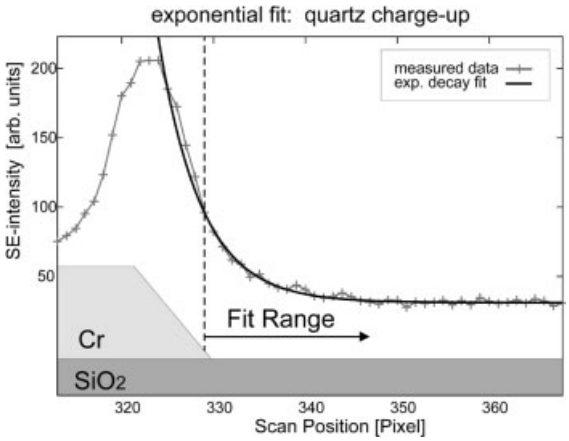

Fig. 29.15 Definition of exponential decay operator. An exponential function is fitted to the signal profile at the chromium–quartz transition. The decay length of the function is a measure for the degree of charging.

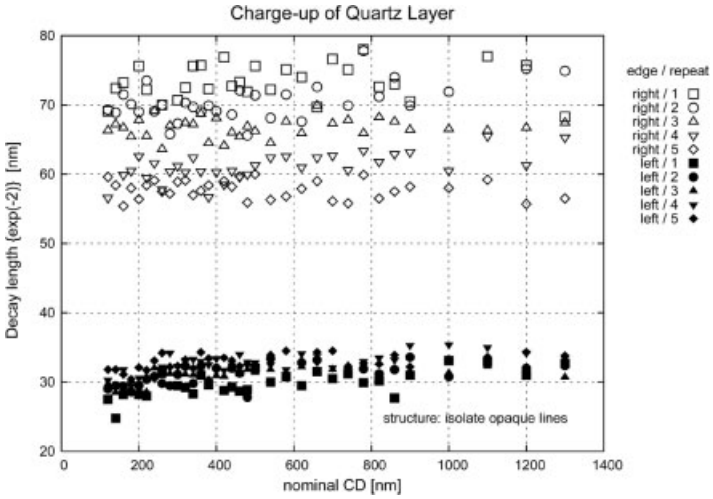

Fig. 29.16 Application of the signal decay operator to a chromium line on quartz. At the chromium–quartz transition (right) the signal decay decreases with every measurement whereas at the quartz–chromium transition (left) the decay remains unchanged because a condition of equilibrium is already reached.

chrome–quartz transition) the decay length becomes smaller with every measurement due to the residual charging of the preceding scan. The loss of decay length due to the precharge becomes evident in Figure 29.17 which shows a combined Monte Carlo model (for topographic contrast) and analytical model (for quartz chargeup). The operator sets a fixed threshold (i. e., a signal level corresponding to the chromium signal level) as unity and then determines the scan position at which the signal level has dropped to 13.5 % of the threshold level. Because of the precharge, the initial amplitude of the chargeup function is lowered and therefore

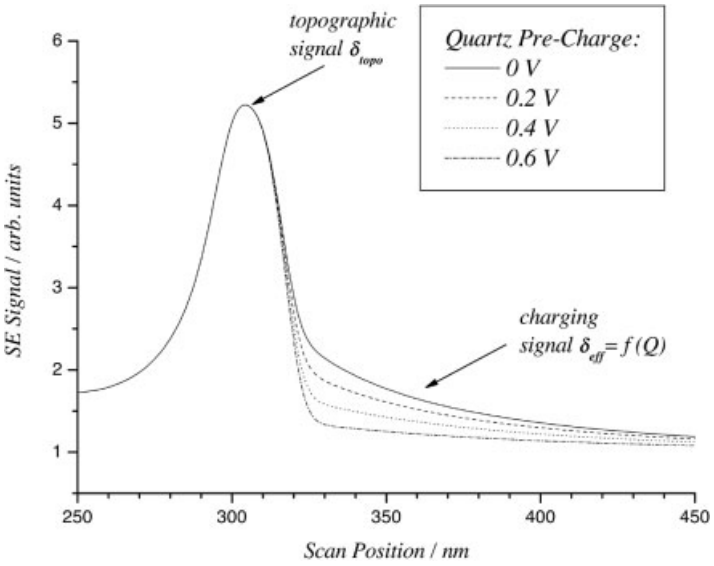

Fig. 29.17 Monte Carlo model of topographic contrast (for scan position < 320 nm) combined with analytical model (for scan position < 320 nm), calculated for different values of precharged quartz. Profiles were convoluted with a Gaussian probe profile of 10 nm FWHM.

the scan position corresponding to the exp[−2] signal level (i. e., the double decay length) becomes smaller.

In contrast to the chrome–quartz transition, we observe on the left edge of the line (i. e., the quartz–chrome transition) an exponential increase of the signal with a stable decay length of about 30 nm. In this case, the electron probe comes from the quartz direction and the effective electron yield has already reached equilibrium. When the electron probe establishes electrical contact to the chromium line (the electron range in quartz is about 30 nm for 1 keV) the surface charge Q discharges and in consequence, the effective emission current increases to its original value.

29.6 Conclusion

Three CD-SEM edge operators have been presented: The exponential fit operator allows a precise definition of top CD and is therefore comparable to other experimental results, e. g., SFM measurements. The measurement uncertainty for our instrumentation and application of the exponential fit operator is $U = 15$ nm ($k = 2$). The exponential fit operator was modified for application at high sidewall angle structures and shows a good stability and accuracy both for the Monte Carlo modeled and experimental data. In addition to the exponential fit operator,

a Gauss fit operator has been presented that fits a Gauss function to the full waveform of the sidewall peaks. In consequence, this operator is little affected by noise and can be used in particular for line edge roughness characterization. The signal decay operator is used to supervise the charging behavior of the specimen and therefore assures that the other edge operators are not affected by specimen charging. It is further planned to investigate the performance characteristics of the described edge operators on other type of CD-SEM instrumentation.

References

1 Th. Schätz et al., Development and characterization of new CD mask standards: a status report, in *EMC 2003, 19th European Mask Conference on Mask Technology for Integrated Circuits and Micro-Components, GMM-Fachbericht Band* (2003), Vol. 39, pp. 37–47.

2 L. Reimer, M. Kässens, and L. Wiese, Monte Carlo program with free configuration of specimen geometry and detector signals, Microchim. Acta **13**, 485–492 (1996).

3 F. Salvat and R. Mayol, Elastic scattering of electrons and positrons by atoms. Schroedinger and Dirac partial wave analysis, Comput. Phys. Commun. **74**, 358–374 (1993).

4 H. A. Bethe, Zur Theorie des Durchgangs schneller Korpuskularstrahlen durch Materie, Ann. Phys. **5**(5), 325–400 (1930).

5 L. Reimer, *Scanning Electron Microscopy*, 2nd ed. (Springer Series in Optical Science, Berlin, Vol. 45, 1998), p. 152 ff.

6 W. Mirandé and C. G. Frase, Comparison of linewidth measurements on Si structures performed by atomic force microscopy (AFM) and low voltage scanning electron microscopy (SEM), in *Proceedings Quantitative Microscopy* (QM'99) (PTB-Bericht PTB-F-34, Kopenhagen, 1999), pp. 89–96.

7 A. Karabekov, O. Zoran, Z. Rosenberg, and G. Eytan, Using Monte Carlo Simulation for Accurate Critical Dimension Metrology of Super Small Isolated Poly-Lines, SCANNING **25**, pp. 291–296 (2003).

30
Measurement of High-Resolution Interferential Encoders Using the PTB Nanometer Comparator

J. Flügge, R. Koening, and H. Bosse

Abstract

The PTB nanometer length comparator was developed in cooperation with the Dr. Johannes Heidenhain GmbH and the Werth Messtechnik GmbH. The comparator was designed to be applied for calibrations of graduations on objects like line scales and photomasks, and for calibrations of length measurement systems like displacement probes, interferometers, and incremental linear encoders. The maximum translation range of the 1D comparator is 610 mm. In this chapter measurements on high-resolution incremental linear encoders are presented, which were performed to verify the current measurement performance of the nanometer comparator.

30.1
Principle

The base of the comparator is a stiff granite block (Figure 30.1). A slide that moves on air bearings supports the calibration object, for example, a line scale, a grating of an incremental encoder or a measurement mirror of an interferometer. The translation of the slide is measured by an interferometer, whose beams are located in an evacuated metal bellow and metal pipes. In this way, the interferometer is completely located in vacuum, although the calibration objects can still be mounted under atmospheric conditions. This approach also ensures the highest level of measurement performance on calibration objects which are applied under ambient conditions. Different structure localization sensors can be applied to a universal carrier, which is mounted on a solid bridge above the measuring slide. Incremental scanning heads and two photoelectric microscopes, one equipped with a measurement slit and a photomultiplier and the other with a CCD camera are available.

Nanoscale Calibration Standards and Methods: Dimensional and Related Measurements in the Micro- and Nanometer Range.
Edited by Gunter Wilkening, Ludger Koenders
ISBN: 3-527-40502-X

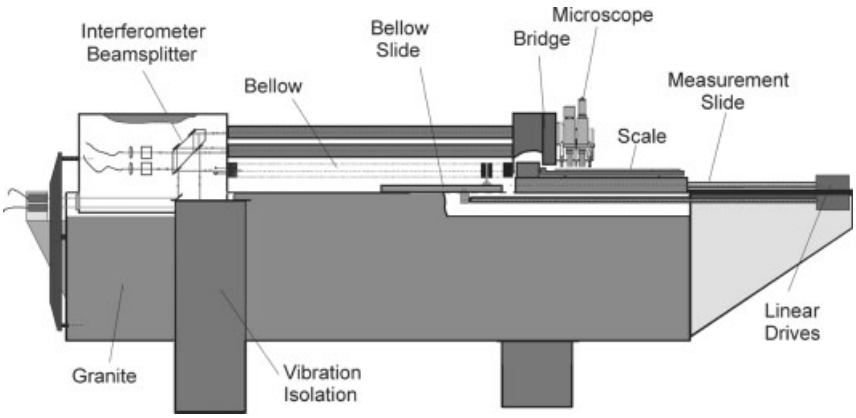

Fig. 30.1 Principle of the nanometer comparator.

30.2
Laser Interferometer

The integration of the laser interferometer into the comparator setup is a key component of the nanometer comparator [1]. The interferometer is based on the Jamin type where the reference beam is connected to the carrier bridge to compensate for the dilatation and bending of the granite base. Because the measurement and reference beams are not in line, a tilt between the carrier bridge and the interferometer beamsplitter results in a measurement deviation. Therefore, a second interferometer of the same type compensates for these angular movements. Because of the interferometer setup, only rather small and therefore more stable mechanical parts made of material with low thermal expansion are within the effective measurement frame of the comparator. This approach minimizes the influence of the thermal and mechanical distortions.

The interferometer utilizes the heterodyne principle. Interpolation nonlinearities in classical heterodyne interferometers are mainly caused by mixing the two frequencies in the interferometer arms due to an imperfect separation of the associated polarizations. This problem can be solved by keeping the two frequencies spatially separated until interference. A reference interferometer is used in this design to compensate phase changes between the two separated beams, for example, due to the frequency shifting by an acousto-optical modulator (AOM) [2]. In the nanometer comparator the angle compensation interferometer also acts as the reference in the spatially separated beam interferometer design, which is shown in Figure 30.2. Both incoming beams are splitted by neutral beamsplitters and the transmitted beams are reflected at the upper part of the zerodure spacer. The measurement and reference reflectors are roof mirrors and the two returning beams of the right incoming beam are reflected by mirrors fixed on the upper spacer to bring the spatially separated beams in pairs to interference.

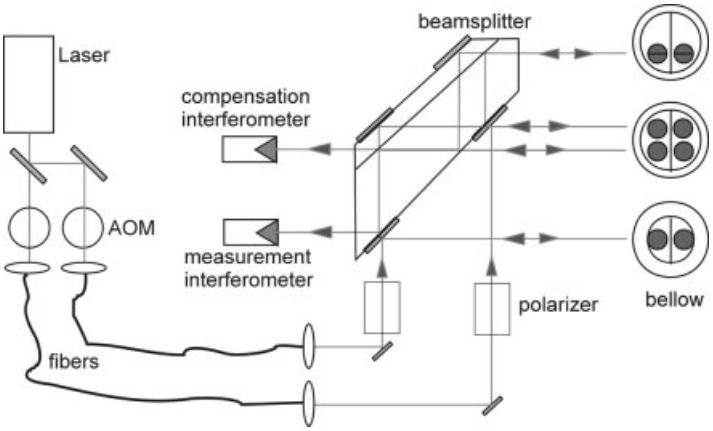

Fig. 30.2 Principle of the laser interferometer.

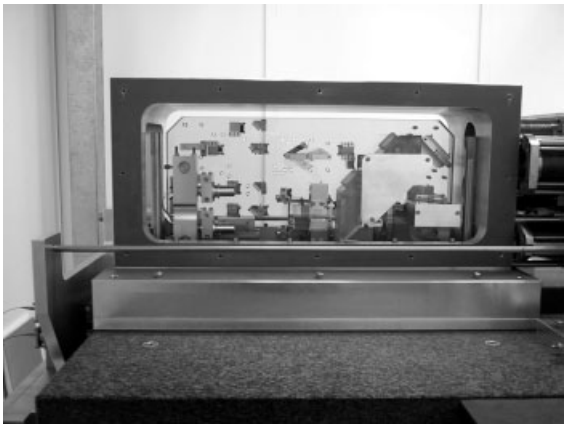

Fig. 30.3 Photo of the interferometer beamsplitter in the vacuum chamber.

This design also allows the use of optical fibers to feed the light of the laser to the interferometer. The light source is a frequency-doubled, iodine-stabilized Nd:YAG laser [3]. A photo of the interferometer parts in the vacuum chamber is shown in Figure 30.3.

30.3 Incremental Linear Encoders

Two incremental encoders, a LIP 382 with 70 mm and a LIP 481 with 520 mm measurement length and a U-shaped scale profile, both with zerodure scales, were measured. The LIP 481 which has a signal period of 2 μm has mainly been used to perform repeatability and reproducibility investigations. The grating was mounted directly on the aluminum slide. The LIP 381 has a signal period of

only 128 nm and a grating period of 512 nm and is therefore suitable to investigate the noise level and the interpolation nonlinearities of the nanometer comparator. Additionally, it was possible to mount the short scale directly on an Invar console fixed at the holder of the measurement mirror to check for the time-dependent drift of the comparator. The mounting possibility of long and short scales on the comparator is shown in Figure 30.4.

The signal detection of encoders are mostly based on the homodyne principle. Because of a movement of the grating Δs a phase shift of $2\pi m\ \Delta s/g$ occurs in the diffracted beams with the diffraction order m. If two different diffraction orders are recombined, the same signal as in a homodyne laser interferometer is generated. The measurement spots on the scale are normally much larger than the grating period; therefore, a large number of lines are involved in the signal generation. This is the main reason for the high resolution, good repeatability, and robustness to contamination of the encoder system. Because of this principle of signal generation, it is not easily possible to compare the measurement results of an encoder with measurements of single structures on the same scale. As an example, the measurement principle of the LIP 382 is illustrated in Figure 30.5.

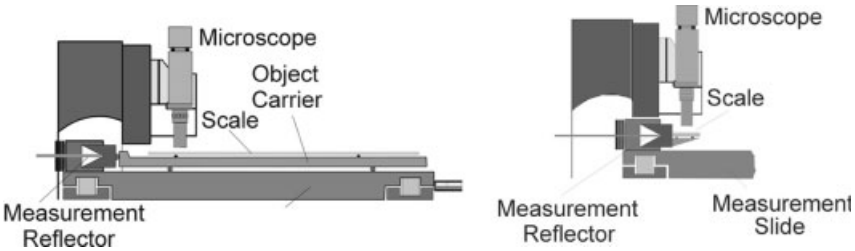

Fig. 30.4 Mounting of scales on the comparator. Left: long scales, right: short scales.

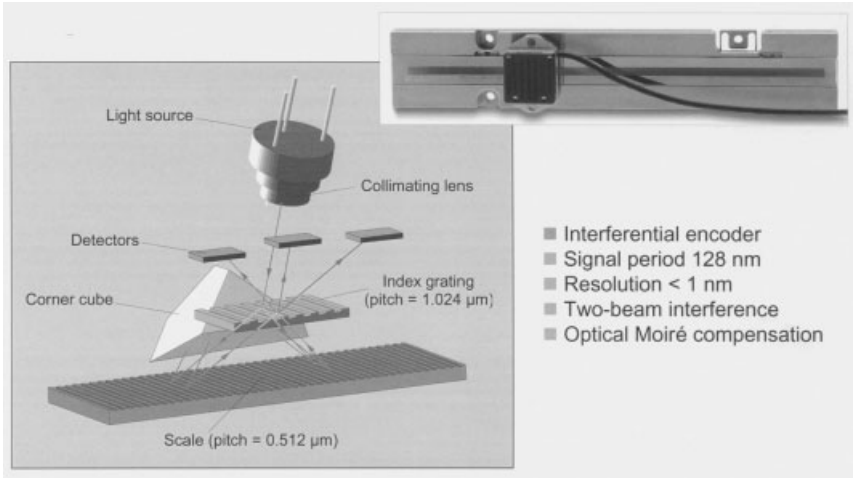

Fig. 30.5 Operation principle of the LIP 382 [4].

30.4 Measurement Results

The LIP 481 has mainly been used to demonstrate the reproducibility of the comparator. The counter card[1)] used achieves a resolution of 0.5 nm. The compensation of the interpolation nonlinearities was not activated but the encoder and the interferometer were triggered at multiples of the encoder signal period. The results of three measurement series are shown in Figure 30.6. Each measurement curve consists of three single measurements in both directions. The scale and the reading head have been removed after each measurement series and newly aligned for every new series. The measurements shown in Figure 30.6 have been carried out in dynamic mode at a constant speed of 2 mm/s.

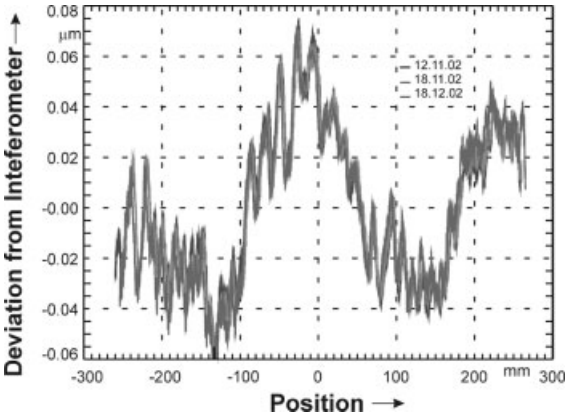

Fig. 30.6 Reproducibility of encoder measurements.

The observed difference of the measurements results of the LIP 382 and the laser interferometer over a few seconds was in a range of ±0.4 nm. Over some hours the difference shows a very good correlation with the temperature of the measurement slide. The coefficient was 1 nm/mK with a steel component of approximately 75 mm in the holder of the reading head, which will be replaced by Invar in the near future. The interpolation nonlinearities of the systems are shown in Figure 30.7. The encoder without signal correction showed a cyclic interpolation error of ±1 nm. After correction, using the Heydemann procedure [5], the signal period of the encoder is no longer visible and the current residual nonlinearity error of the interferometer can be determined approximately to be within ±0.2 nm.

1) The interpolation card used here is a Heidenhain IK 320. This VME-Bus interpolation card fits well in the data acquisition system of the nanometer comparator and interpolates the signal up to one part in 4096.

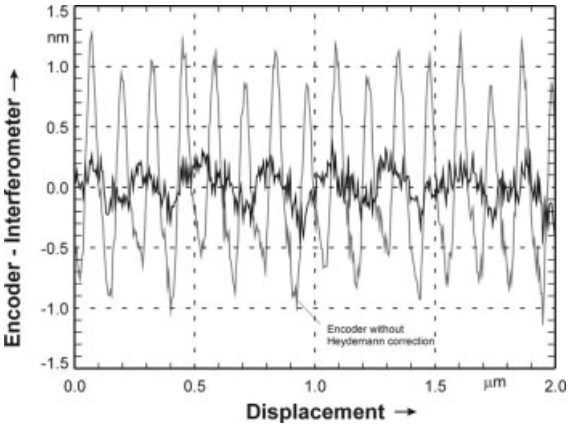

Fig. 30.7 Short-range deviations of the encoder and interferometer.

References

1 J. Flügge, H. Dangschat, A. Spies, J. Tschirnich, and H. Pieles, Concept of a interferometric length comparator with measurement uncertainties in the nanometer scale, in *1st Euspen International Conference, Bremen, Germany* (1999) pp. 227–230.

2 M. Tanaka, T. Yamagami, and K. Nahayama, Linear interpolation of periodic error in a heterodyne laser interferometer at subnanometer levels. IEEE Trans. Instrum. Meas. **38**(2), 552–554 (1989).

3 P. Cordiale, G. Galzerano, and H. Schnatz et al. International comparison of two iodine-stabilized frequency-doubled Nd:YAG lasers at $\lambda = 532$ nm. Metrologia **37**, 177 (2000).

4 W. Holzapfel, Optical principles and applications for ultraprecise linear and angular encoders. *EUSPEN Vision Online, Traunreut* (2003).

5 P. L.M. Heydemann, Determination and correction of quadrature fringe measurement errors in interferometers. Appl. Opt. **20**(19), 3382–4 (1981).

Part IX
Application – Surfaces

Nanoscale Calibration Standards and Methods: Dimensional and Related Measurements in the Micro- and Nanometer Range.
Edited by Gunter Wilkening, Ludger Koenders
ISBN: 3-527-40502-X

31
Experimental Characterization of Micromilled Surfaces by Large-Range AFM

P. Bariani, G. Bissacco, H. N. Hansen, and L. De Chiffre

Abstract

The chapter describes an experimental investigation of topography of surfaces obtained with ball nose end milling using sub-mm tools. Accurate characterization of fine surface details was achieved by the use of an atomic force microscope (AFM) mounted on a CMM. Other measuring techniques such as stylus profilometry, optical profilometry, and stereoscopic scanning electron microscopy were used for comparison. Surface characterization methods are compared with each other and with computer simulations based on ideal tool motion.

31.1
Introduction

Surface generation by ball nose micromilling can be simulated based on process parameters (ball nose radius, axial and radial depth of cut, feed rate, cutting speed).

However, surface 3D topography of such machined surfaces often widely differs from the simulated one due to the distinctive behavior of workpiece material, particularly when submicrometer chip thicknesses are considered and when machining hard materials.

Quantification of surface topography is of fundamental importance for the evaluation of the generated surface, high resolution and wide measuring range being highly desirable for the evaluation of tool–workpiece interaction. The goal of the experimental study was twofold:

- To compare experimental results obtained by a large-range AFM to simulations.
- To study which other measurement techniques can be used to characterize these surfaces in a similar fashion.

Nanoscale Calibration Standards and Methods: Dimensional and Related Measurements in the Micro- and Nanometer Range.
Edited by Gunter Wilkening, Ludger Koenders
ISBN: 3-527-40502-X

31.2 Micromilling of Hardened Tool Steel

Mechanical material removal techniques are valid alternatives to energy assisted micromachining techniques, and among them ball nose micromilling is gaining interest because of its capability of generating nearly any type of 3D surface. Moreover, its applicability to machining of hardened tool steel makes micromilling a popular choice for manufacturing of micromolds.

The reduction of end mills diameters, necessary for the reduction of machinable features' size, requires machine tools with high rotational speed capabilities in order to maintain the cutting speed at reasonable values. Although high-speed machine tools are used, the maximum rotational speed is rarely higher than 50 000 rpm, which, with micro end mills of 200 μm in diameter, means a maximum cutting speed of approximately 30 m/min. Furthermore, in ball nose end milling, the effective radius varies with the slope of the surface being machined. The effect is a further reduction of the actual cutting speed. Prediction of the generated surface in conventional size milling is possible by use of computer programs, based on ideal tool motion, when the process is unaffected by chatter [1].

In micromilling excessively low cutting speeds together with increasing cutting edge radius to chip thickness ratios and material hardness are responsible for an altered interaction between cutting edges and workpiece material. Therefore, surface generation modeling based on ideal tool motion can no longer be applied for the prediction of the machined surface. Smearing of the material behind the tool and formation of high ridges along the feed direction become dominant factors in the overall 3D surface topography. Considering the small values of the cutting parameters involved, understanding and evaluation of relevant tool–workpiece material interaction phenomena require 3D measuring instruments with high resolution and relatively large range. The latter in order to verify patterns as for instance repetitive built up edge formation and destruction. Furthermore, for measurements carried out by use of contact probing instruments, probe radius must be as small as possible, in order to avoid introducing undesired mechanical filtering that would bias the measurement results.

In the following, an experimental investigation on alternative measuring techniques for characterization of micromilled surfaces is presented. The two test workpieces examined consist of surfaces produced by ball nose micro milling on powder metallurgy tool steel in its hardened state at 58 HRC. Both surfaces were machined at 70° inclination angle on a three-axis milling machine equipped with a 50 000 rpm high-speed spindle. Cutting parameters for the two surfaces are reported in Table 31.1.

Table 31.1 Machining parameters

Surface ID	Surface 1	Surface 2
Tool radius (R)	100 μm	100 μm
Rotational speed (n)	31 831	31 831
Surface inclination angle (α)	70°	70°
Actual cutting speed (V)	20 m/min	20 m/min
Feed per tooth (a_z)	0.4 μm	1.6 μm
Step over (a_t)	10 μm	10 μm

31.3 Surface Topography Measurement

The action of the cutting tool generated a lay characterized by a wavelength on the order of 10 μm (step over value in Table 31.1) and amplitude of few micrometers. Such roughness is measurable by any topography-measuring instrument, at least in terms of range-resolution characteristics.

Appropriate surface sampling is the result of matching instrumental characteristics with the surface topography to be measured. Any topography measuring system, regardless of its working principle, can be characterized in terms of bandwidth. The short wavelength limit is given by the most restrictive among the following limiting factors:

- The frequency response of the instrument
- The probe size
- Sampling interval Δ

Frequency response and sampling interval can be adjusted within certain instrument specific limits; in contrast, the probe size is a fixed quantity. This cannot be matched with the surface topography and is in practice often the limiting factor. The long wavelength limit is often a tradeoff between functional and instrumental requirements. In general, measuring range should be sufficient to probe a region representative of the whole surface; on the other hand, instrument sampling interval should be as small as possible, but compatible with constraints regarding time and the resolution of the instrument analog-to-digital converter. However, at present, no standard guideline for selecting sampling conditions for topography measurement in three dimensions exists. This problem was addressed in the past by some researchers [2], and different criteria were proposed. According to Dong and others [3], optimal sampling conditions can be determined based on the normalized cumulative power spectrum of the roughness profile. However, in the present investigation, sampling conditions were fixed based on experience, taking into account the limits discussed above regarding instruments bandwidth. Cumulative power spectra from the different instruments were eventually compared and evaluated and three-dimensional roughness parameters were calculated.

31.4
Large-Range Atomic Force Microscopy

In the past few years, an integrated AFM-CMM instrument has been developed at IPL-DTU [4]. An AFM sensor was mounted on a CMM. The CMM is used as a positioning system for the sensor, the (x,y) axes are provided with electronic scales for measuring displacements. The purpose of such setup is to operate surface mapping. This measuring strategy consists of probing the surface with the AFM sensor, displacing the probe of amounts just few micrometers smaller than the scan side length, then operating the AFM again, and so forth. Data sets resulting from probing surface contiguous regions are eventually stitched together with a special software, developed for the purpose at IPL-DTU [5].

The use of the stitching routine based on surface features recognition, allows compensation of CMM (x,y) translational errors. Surface mapping with the AFM-CMM integrated instrument allows enlarging the AFM measurable range, but it brings also the possibility of enhancing range to sampling interval ratio through higher scan ranges, which is limited only by computers capability of handling large data files.

One relevant additional advantage of such measuring strategy consists of thermal drift effects avoidance, by scanning the desired range with some shorter scans rather than a single long scan.

Surface mapping of the machined surfaces was carried out taking three single scans with a range of $56 \times 56\ \mu m^2$, the overlap was on the order of 5 μm. The digitization was 512×512 pixels^2. Surface topography images before and after stitching are shown in Figures 31.2 and 31.3.

31.5
Techniques Used for Comparison

Optical profilometry, stereoscopic scanning electron microscopy, and stylus profilometry were used for comparison. The optical instrument was a UBM Microfocus 1080 scanning laser profilometer. This instrument is based on focus detection; area-sampling interval was $1 \times 1\ \mu m^2$. In the following, it will be referred to as focus detection profilometer (FDP). Topography reconstruction from SEM stereographs was accomplished by the stereo-pair technique, as implemented in a commercial software package [6]; the microscope used was a Jeol 5900 located at IPL-DTU. A magnification of 500× was used for the micrographs, corresponding to a pixel size of $0.2 \times 0.2\ \mu m^2$. Areal sampling interval for the stylus profilometer was $0.5 \times 0.5\ \mu m^2$. This will be referred to as the contact (CP) profilometer in the following. Theoretical surface topography, simulated as described above, was also considered in this study. For conventional size ball nose end milling operations, 3D surface roughness parameters calculated on the simulated surfaces are in excellent agreement with those measured on the actual machined ones as discussed in [1]. Software-simulated topography will be referred to as SW in the following.

31.6
Evaluation of Sampling Conditions for the Different Techniques

Surface roughness is the result of the distinctive interaction between the cutting tool and the workpiece. The choice of the long wavelength cutoff should be made on the basis of some aprioristic decision on what wavelength values are to be considered as roughness, what else are to be considered as waviness and therefore filtered out. In the present study, the theoretical surface texture being strongly anisotropic and periodic, with period determined by the step over value in Table 31.1, a Gaussian filter with cutoff frequency of 25 μm was chosen [7]. The evaluation of sampling conditions can be carried out on the basis of the Fourier transform of single profiles taken across the lay. In particular, power spectra can be used for the purpose.

For any given instrument, the maximum detected frequency is given by the Nyquist folding frequency:

$$f_c = \frac{1}{2\Delta},$$

where Δ is the sampling interval dimension. The roughness cumulative power spectrum should, in the case of effective probing, be well below the Nyquist folding frequency. On the other hand, the larger the sampling frequency, at the desired measuring range, the larger the amount of data points, and therefore measuring time. For any single instrument, frequency spectra of single profiles showed fairly small deviations. The spectrum from a single profile was therefore considered representative of the instrument sampling conditions.

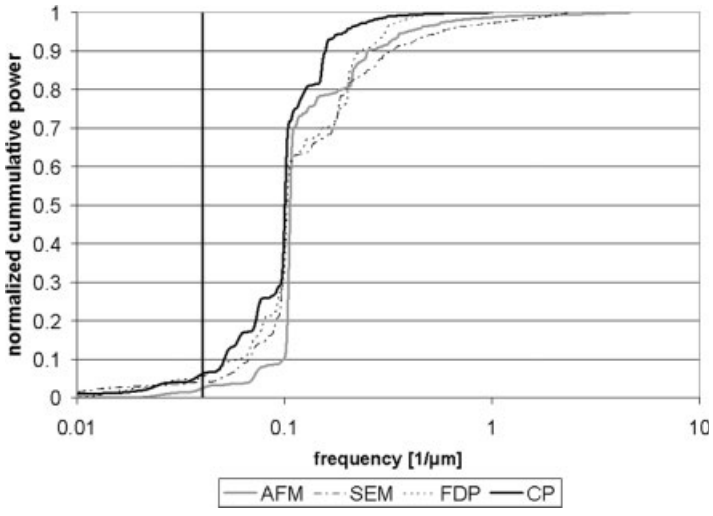

Fig. 31.1 Sampling conditions for the different instruments.

Cumulative power spectra for the four instruments are shown for comparison in Figure 31.1, based on profiles taken on Surface 1 (Table 31.1). Sampling length was approximately 150 μm.

From the curves of Figure 31.1, it is seen that a cutoff frequency value of 0.04 μm^{-1} is appropriate. The long wavelengths attenuated by filtering hold small percentages of the respective cumulative powers (given by the intersection between the line representing the cutoff frequency and the spectra). The dominant frequency, for all the instruments, is located at about $f = 0.1\ \mu m^{-1}$, corresponding to the milling step over value. The fundamental component of the roughness is therefore detected correctly by all the instruments used. For any of the curves shown in Figure 31.1, the Nyquist limit is given by the frequency value corresponding to cumulative power unitary value. The AFM shows the highest Nyquist to fundamental frequency ratio (approximately 40), while the optical profilometer (FDP) has a ratio of 5, meaning that only 10 points are sampled on the fundamental wavelength. The most effective probing is obtained by the AFM-based technique, at the cost of using a more complicated measuring procedure and of handling heavy data files.

31.7 Results

Visual representation of the topographies measured by the AFM-CMM instrument on Surface 1 is given in Figure 31.2. Three single AFM scans (respectively (a), (b), and (c)) were taken on adjacent surface regions, and stitched to produce the topography image shown in Figure 31.3.

In Figure 31.4 the topography of Surface 2 obtained using the AFM-CMM instrument is shown. The surface quality of Surface 2 seems improved compared to Surface 1. Computer simulated topography is shown in Figure 31.5, under conditions as for Surface 1.

Selected three-dimensional surface roughness parameters [8] were calculated on the data sets, over an area of $150 \times 50\ \mu m^2$. Results are shown in Figure 31.12.

Amplitude roughness parameters, namely *Sq* and *Sz*, calculated over the images from the four instruments show large deviations. Roughness amplitude, measured by the SEM-based technique and the optical instrument, is overestimated. Calculation of topography elevation with the stereoscopic SEM is rather uncertain, especially when relatively low magnifications are used to image surface regions of several hundred microns side length [9]. Measurements obtained with such technique are shown in Figures 31.6 and 31.7. Topographies measured with the optical profiler (FDP) are shown in Figures 31.8 and 31.9. It is seen that spikes artifacts are generated due to lack of reflection in correspondence of surface local slopes. In the presence of local spikes artifacts, *Sz* is seen not to be an appropriate parameter to evaluate surface finish. Local spikes are not eliminated by frequency filtering, leading eventually to wrong conclusions, the *Sz* value being based on local peak values indeed. Average amplitude parameters,

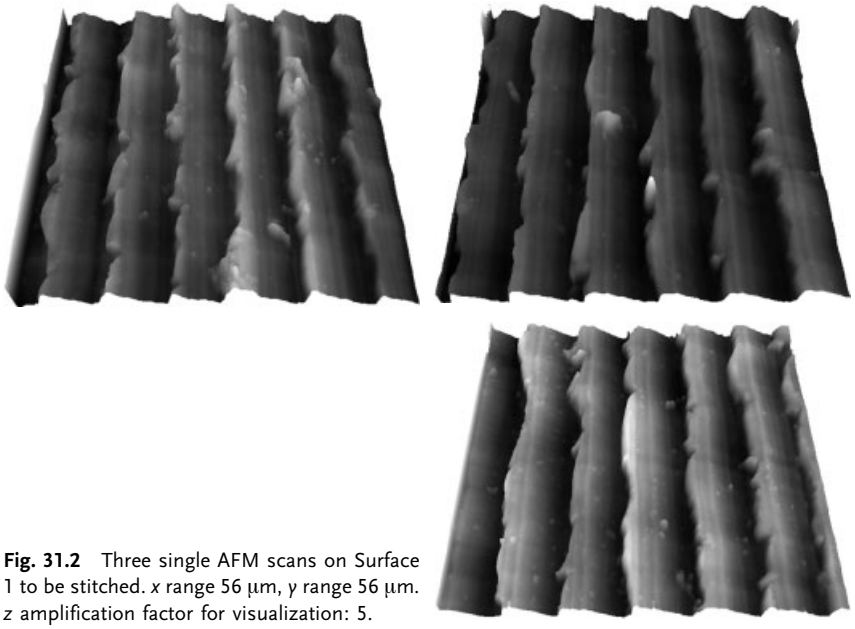

Fig. 31.2 Three single AFM scans on Surface 1 to be stitched. *x* range 56 μm, *y* range 56 μm. *z* amplification factor for visualization: 5.

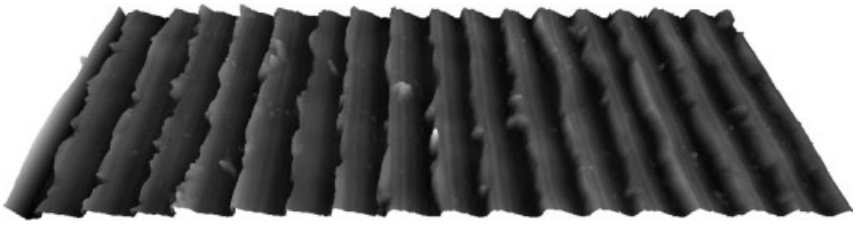

Fig. 31.3 Image resulting from stitching the three topography images shown in Figure 31.2. *x* range 155 μm, *y* range 55 μm, *z* range 1.762 μm. *z* amplification factor for visualization: 5.

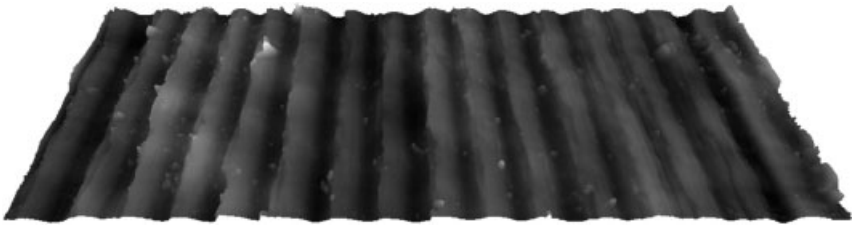

Fig. 31.4 Topography of Surface 2 resulting from the AFM-CMM instrument measurements. *x* range 154 μm, *y* range 56 μm, *z* range 1.248 μm. *z* amplification factor for visualization: 5.

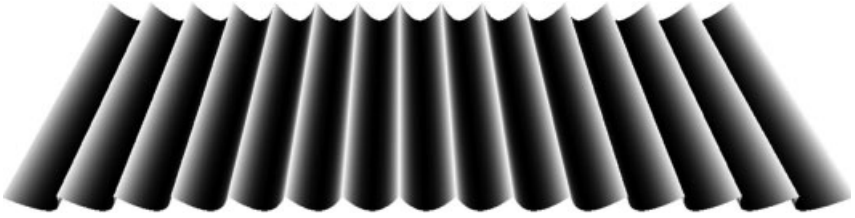

Fig. 31.5 Surface topography resulting from simulating ideal tool motion under conditions as for Surface 1. *x* range 150 μm, *y* range 50 μm, *z* range 0.125 μm. *z* amplification factor for visualization: 50.

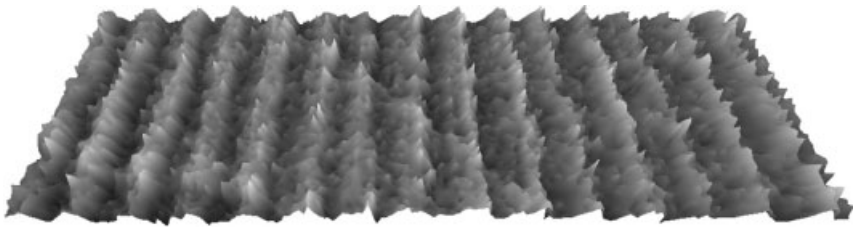

Fig. 31.6 Topography of Surface 1 resulting from the use of stereoscopic scanning electron microscopy (SEM). *x* range 149 μm, *y* range 50 μm, *z* range 2.962 μm. *z* amplification factor for visualization: 5.

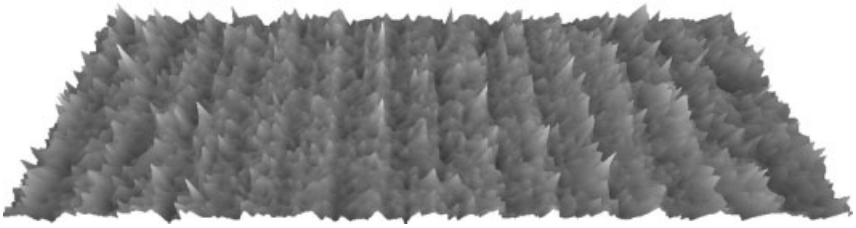

Fig. 31.7 Topography of Surface 2 resulting from the use of stereoscopic scanning electron microscopy (SEM). *x* range 148 μm, *y* range 50 μm, *z* range 3.971 μm. *z* amplification factor for visualization: 5.

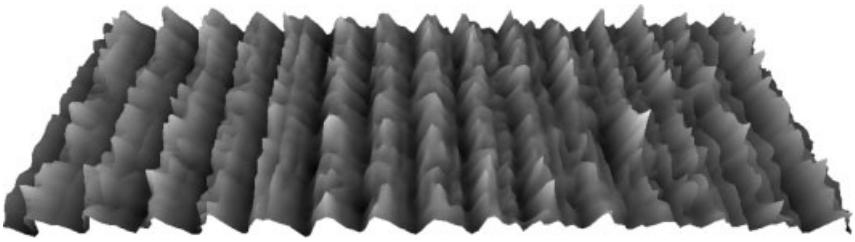

Fig. 31.8 Topography of Surface 1 resulting from the use of the focus detection profilometer (FDP). *x* range 150 μm, *y* range 50 μm, *z* range 3.463 μm. *z* amplification factor for visualization: 5.

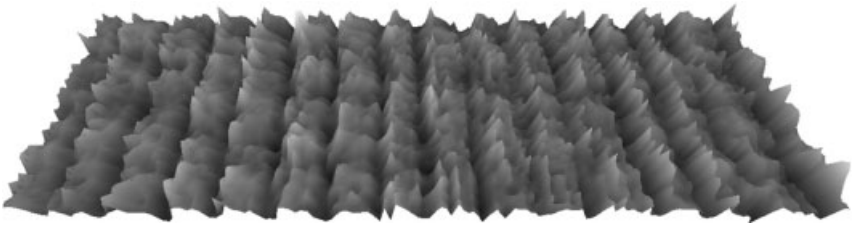

Fig. 31.9 Topography of Surface 2 resulting from the use of the focus detection profilometer (FDP). *x* range 150 μm, *y* range 50 μm, *z* range 3.589 μm. *z* amplification factor for visualization: 5.

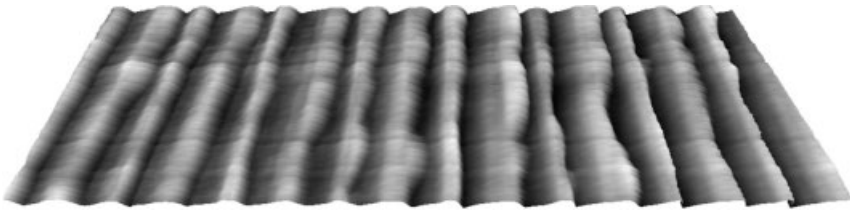

Fig. 31.10 Topography of Surface 1 resulting from the use of the stylus profilometer (CP). *x* range 150 μm, *y* range 50 μm, *z* range 0.886 μm. *z* amplification factor for visualization: 5.

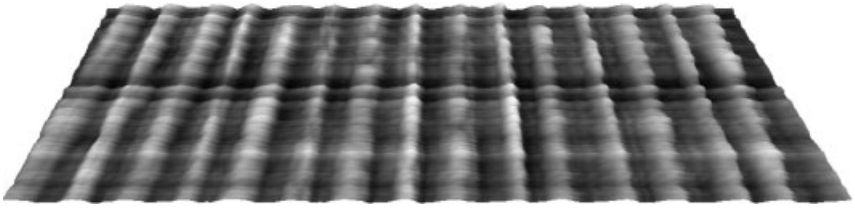

Fig. 31.11 Topography of Surface 2 resulting from the use of the stylus profilometer (CP). *x* range 150 μm, *y* range 50 μm, *z* range 0.633 μm. *z* amplification factor for visualization: 5.

such as *Sq*, in contrast, show the same trend as the AFM (Figures 31.12(a) and 31.12(b)). Measurements from the contact profilometer (CP) are shown in Figures 31.10 and 31.11. This is, to some extent, in agreement with the AFM. In particular, amplitude parameters (*Sq* and *Sz*) are systematically biased to lower levels. This is likely to be due to a better contact of the sharp AFM tip with narrow surface corrugations compared with the stylus instrument. Values calculated for the computer-simulated surfaces are much lower than those from measurements. The Surface-bearing index *Sbi* measures the bearing property of a surface; higher *Sbi* values indicate good bearing. Among the parameters selected, *Sbi* was the one showing smaller relative deviations between the instruments. The texture aspect ratio (*Str*) is an indicator of the degree of anisotropy of the detected surface roughness. (It refers to the texture direction determined on the surface angular spectrum.) An *Str* value close to zero indicates an anisotropic surface. The AFM-

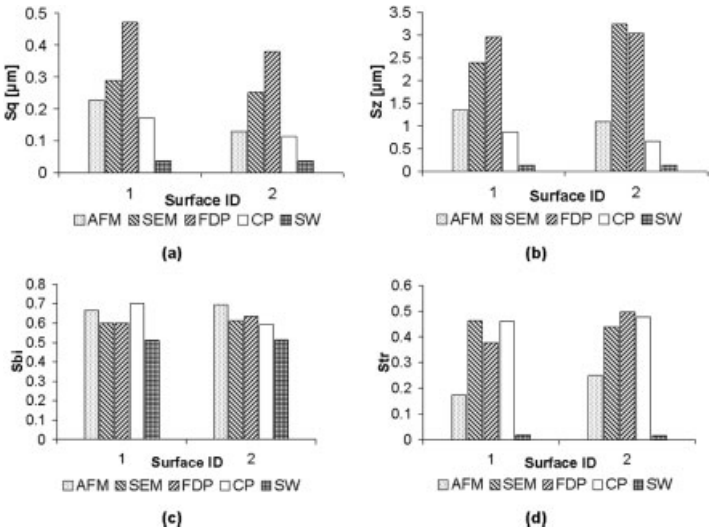

Fig. 31.12 Three-dimensional roughness parameters.

CMM instrument measurement detected surface anisotropy better than the other instruments, resulting in *Str* closer to the values obtained by software simulation. Measurement artifacts already discussed strongly affect correct detection of surface texture directionality. Spikes resulting from uncertain topography calculation (SEM) are isotropically distributed over the surface; the lay is eventually masked by such artifacts. Concerning the FDP instrument, spikes mainly occur on top of the existing peaks, namely over the main ridges along the feed direction (Figures 31.8 and 31.9). These artifacts, together with the low sampling frequency, are reckoned to be responsible for the higher apparent topography isotropy as compared to results from AFM. Measurements performed with the stylus instrument (CP) suffer from lack of straightness of the slow scanning direction (along the lay). This is particularly evident in Figure 31.11, where the smoother surface is imaged. A similar problem is often seen in AFM images due to relative thermal drift between the sensor and the sample. Use of mapping procedures based on stitching is seen to improve instrument performance with respect to this issue.

31.8 Discussion and Conclusions

Surface topography was measured with four different techniques. Sampling conditions for the instruments were discussed. These were found to be appropriate for any of the instruments used. The fundamental topography frequency was well below the Nyquist limit. The AFM-CMM instrument was found to be the most appropriate for measuring such topographies characterized by small fea-

tures resulting from the tool–workpiece interaction. This is mainly due to the small tip radius and aperture angle of the AFM tip.

Concerning the two ball nose end milled surfaces analyzed, all the calculated 3D surface roughness parameters show better values for Surface 2 than for Surface 1. This means that the tool–workpiece material interaction is more effective at higher feeds per tooth among those considered here. Although absolute values of roughness parameters are deviations between the instruments, the tendencies with different levels of the process parameters are recognized by all of them. Therefore, while quantitative determination of surface topography should be carried out with the AFM-CMM instrument, a comparative analysis for process parameters selection and optimization in ball nose micromilling is, in principle, possible also with the other instruments. As shown by the present study, prediction of the generated surfaces in ball nose end micromilling based on ideal tool motion is no longer reliable. This is presumably due to the tool–workpiece material interaction at micro scale, which becomes outstanding on the surface features generated considering ideal tool motion.

References

1 G. Bissacco, A software tool for simulation of surfaces generated by ball nose end milling, IPL-DTU 2004; Internal Report IPL.075.04 MM04.29.

2 T. Y. Lin, L. Blunt, and K. J. Stout, Determination of proper frequency bandwidth for 3D topography measurement using spectral analysis. Part I: isotropic surfaces, Wear **166**, 221–232 (1993).

3 W. P. Dong, E. Mainsah, and K. J. Stout, Determination of appropriate sampling conditions for three dimensional microtopography measurement, Int. J. Mach. Tools Manuf. **36** (12), 1347–1362 (1996).

4 H. N. Hansen, N. Kofod, L. De Chiffre, and T. Wanheim, Calibration and industrial application of instrument for surface mapping based on AFM, Ann. CIRP **51** (1), 471–474 (2002).

5 P. Bariani, Performance verification of surface mapping instrument developed at CGM, IPL-DTU 2003; Internal Report IPL.256.03.

6 MeX^{TM} software by Alicona Imaging GmbH.

7 ISO 11562-1. Geometrical Product Specifications (GPS)—Surface Texture: Profile method; Metrological characteristics of phase correct filters (International Organization for Standardization, Geneva, Switzerland, 1997).

8 K. J. Stout and L. Blunt, *Three Dimensional Surface Topography* (Penton Press, London, 2000) 2nd ed.

9 L. De Chiffre, P. Bariani, H. N. Hansen, and A. Horsewell, Traceability of dimensional measurements using the scanning electron microscope, in *Proceedings of the 4th International Euspen Conference, Glasgow* (2004).

32
Investigation of the Surface Roughness Measurement of Mass Standards

C. Zerrouki, L.R Pendrill J. M. Bennett, Y. Haidar, F. de Fornel, and P. Pinot

Abstract

The surface roughness of weights in the nanometer and micrometer range is an important surface quality factor that can affect the stability of these mass standards. The mass metrologist is faced with a choice between a wide variety of methods of measuring surface roughness. To aid the mass metrologist in this choice, a number of different laboratories participated in a EUROMET Mass Project 551 to investigate the applicability of five techniques in measuring the surface roughness of four "typical" mass standards ranging from 50 g to 2 kg. Most methods were noncontact, of particular interest for mass metrology, including the optical angle resolved scattering, total integrated scattering, and near field scanning optical microscopy, complemented by mechanical profilometry. Results obtained from these techniques yielded different roughness values because of the different vertical and lateral resolutions and surface spatial frequency bandwidth limits. Also, defects on the surfaces of some weights were associated with particular surface spatial frequencies. This review may be useful as a basis for future studies relevant to mass metrology, such as: the ranges of surface spatial frequencies that have a primary effect on mass stability; assessing the effectiveness of cleaning methods, by comparing roughness measurements made before and after cleaning; and improving the manufacturing process by measuring surface roughness for each polishing step.

32.1
Introduction

In mass metrology, the stability of weights, over a range of milligrams to tonnes, has naturally always been a major concern. Models have been used to describe the various factors that affect mass stability. Surface quality is one important factor that can include the amount and type of pollution (such as adsorbed water or various hydrocarbons) present on the surface. However, another important factor is

Nanoscale Calibration Standards and Methods: Dimensional and Related Measurements in the Micro- and Nanometer Range.
Edited by Gunter Wilkening, Ludger Koenders
ISBN: 3-527-40502-X

surface roughness, particularly in the nanometer and micrometer ranges [1]. Values of surface roughness need to be given that are commensurate with acceptable mass stability. Despite its importance, to date only a few international recommendations of limits on surface roughness for mass standards exist (see Section 32.2).

The mass metrologist is additionally faced with a choice amongst a wide variety of methods of measuring surface roughness. A multitude of methods for measuring surface roughness has been developed over the past 40 years, in part, in response to growing interest in surface roughness as a parameter that influences many physical or physico-chemical processes. These methods differ in their principles of operation, in their lateral and height resolution, and by the type of information that each method provides, such as profile, image of defects, power-spectral-density or auto-correlation function of the surface roughness, or different statistical parameters such as the root-mean-square (RMS) height (or roughness) δ and the correlation length σ [2].

In this article, we consider several methods that are appropriate for determining the surface roughness of mass standards (Section 32.3). The methods listed below were used in the Euromet Mass Project 551 by different laboratories to measure the surface roughness of four "typical" mass standards ranging from 50 g to 2 kg. Most methods were non contact, of particular interest for mass metrology, including the optical angle resolved scattering (ARS), total integrated scattering (TIS) methods, and near field scanning optical microscopy, complemented by mechanical profilometry. Some of these methods are appropriate for measuring surface roughness of mass standards both during the manufacturing process (especially during polishing) and during use.

32.2
Requirements for Surface Roughness of Mass Standards

Surface roughness of weights is included in the specifications and test procedures of the new version of an International Recommendation OIML R111. One of the principal aims of this Recommendation is to set limits on the maximum permissible errors (MPE) between the measured and the nominal value of a weight, against which individual weights are tested (verified) in order to determine the appropriate accuracy classification for each weight. As an example, a 1 kg mass should have an error in mass of less than ± 500 μg, while the smallest mass, 1 mg, must have an MPE of ± 3 μg, to be classed as an E_1 weight of the highest accuracy. In order to meet these accuracy limits over such a wide range of nominal mass values, from 1 mg to over 50 kg, and accuracy classes, the International Recommendation defines surface conditions of weights for use in legal metrology [3]. In many cases, a visual examination of the surface may suffice. However, in case of doubt or dispute, the new International Recommendation gives limits (Table 32.1) to the surface roughness according to the different accuracy classes. The maximum value of surface roughness permitted for weights greater than 50 kg shall be twice the values specified.

Table 32.1 Maximum values of surface roughness [3]

Class	E_1	E_2	F_1	F_2
R_z (μm)	0.5	1	2	5
R_a (μm)	0.1	0.2	0.4	1

A procedure recommended in the OIML R111 Recommendation is to compare the surface of the weight with a comparison specimen according to ISO 2632-2 [4] and two sets of comparison specimens shall be used, one with plane surfaces and one with cylindrical surfaces.

32.3 Surface Roughness Measurement Methods Applied to Mass Standards

In this review, some results of the recent Euromet Mass Project 551 are quoted to illustrate how a number of surface roughness methods are used to measure four "typical" mass standards. The basis for the choice of the five specific instruments, whose characteristics are summarized in Table 32.2, was either because they were available at one of the three National Metrology Institutes participating in the project, or were at laboratories that were collaborating with one of these laboratories. Thus, the study is not exhaustive, but is considered appropriate for metrologists who characterize the surface roughness of mass standards.

For more comprehensive studies of surface roughness measurement methods in general, see the references by Bennett [1, 5] and Whitehouse [6].

We will compare and discuss the advantages and limitations of each roughness measurement technique used to characterize mass standard surface quality in order to interest metrologists in systematic studies of correlation between the stability of mass standards and their surface roughness. This will make it possible to determine which fabrication methods lead to the most stable surface finish for the standards.

Table 32.2 Characteristics of the different instruments

Instruments	Illuminated surface area or profile length	Height resolution RMS δ (nm)	Spatial frequency bands (μm^{-1})
Mechanical profiler (NAWC-US)	< 2 mm	0.05	5×10^{-4}–13.1
Optical near field microscope (LPUB-Fr)	$< 100 \times 100$ μm^2	0.1	10^{-2}–50
ORM (BNM-INM/CNAM)	1.5 mm^2	2.5	7.94×10^{-2}–2.67
Lasercheck (US)	1×4 mm^2	0.1	1.89×10^{-3}–7.5×10^{-2}
Scatter sphere (SP)	< 49 mm^2	0.1	2.3×10^{-2}–1.5

32.3.1
Mechanical Profiler (NAWC-US)

A stylus instrument is conventionally used to measure the surface roughness of machined surfaces. With this instrument, a sharp stylus is traced very gently along a line on the surface and the vertical movement of the stylus is recorded as a function of the position along the line. In this way, a profile of the surface is recorded.

In the present study, a Talystep commercial profiler was modified and provided with Bennett–Fellows software [2]. Using a conical tip (as well as a shovel-shaped tip) with different stylus radii from 0.3 to 8 μm, and very light loads from 0.1 to 1 mg, the mechanical profiler can obtain high vertical and lateral sensitivity. Features of this instrument are summarized in Table 32.3.

In the operation of the Talystep, a linear variable transformer changes the vertical mechanical motion of the probe into an electrical signal, which is then digitized and fed to a computer for further data processing. The profile is detrended by using a least squares algorithm so that surface heights are measured above and below the mean surface level. In addition to the surface profile, various statistical parameters can be calculated: (RMS roughness δ, correlation length σ…) or power spectral density (PSD) and autocorrelation function.

Table 32.3 Features of the Talystep

Roughness measurement range (RMS δ)	0.04– 4.0×10^3 nm	Lateral measurement range	0.2 μm–2 mm
Noise level (RMS)	0.04 nm	Lateral sampling distance	0.03–0.3 μm
Step height measurement range	0.0002–25 μm	Lateral resolution (for $\delta < 1$ nm)	0.1 μm

32.3.2
Near Field Microscope (LPUB, FR)

The apparatus used by the LPUB combines two microscopes that give, respectively, the topography of the sample surface and information on the optical near field distribution using a scanning near-field optical microscope (SNOM).

Shear force regulation is used to obtain the topography of the surface at the same time as the probe, which is made from an optical fiber, detects the optical near field close to the surface and furnishes images of the optical field distribution. The probe tip is kept in the near field of the object at a constant distance (usually 5 nm) from the surface thus avoiding contact between the tip and the surface sample during the scanning [7, 8].

The optical image collected with the fiber probe depends on the nature and the topography of the surface, but it also depends on illumination parameters: wavelength, incidence angle, and polarization [9–11]. Moreover, the formation of the optical near-field image is a function of the nature of the fibre used to fabricate the probe (multimode or single mode fibre with a radius of curvature of the probe tip apex of the order of 25 nm) and to a certain extent of the shape of the probe tip. All these different parameters have to be considered to get an accurate analysis of the structure.

The surface topography will give the roughness in the scanned area, and optical images can give information, for example, about local inhomogeneities on the surface.

32.3.3
Angle-Resolved Light Scattering (BNM-INM, FR)

In the BNM-INM Optical Roughness Meter, the surface is illuminated at oblique incidence by p-polarized monochromatic light. Then measurements of the angular distribution of the scattered light are taken in the plane of incidence.

Angle-resolved scattering theory (ARS) allows the angular distribution of the scattered light to be related to the surface roughness [12–14]:

$$\frac{\mathrm{d}\phi}{\phi_0\,\mathrm{d}\Omega} = \frac{1}{4}\left(\frac{2\pi}{\lambda}\right)^4 \frac{1}{\cos\theta_0}\,|w|^2\,|S(\Delta k)|^2, \tag{32.1}$$

where ϕ_0 is the incident flux, $\frac{\mathrm{d}\phi}{\mathrm{d}\Omega}$ is the flux scattered in the direction θ per unit solid angle, λ is the optical wavelength, and θ_0 and θ are the incidence and the scattering angles, respectively. The function $|S(\Delta k)|^2$ is the Fourier transform of the surface roughness auto-correlation function [15], where $\Delta k = \left|\Delta\vec{k}\right| = \left|\frac{2\pi}{\lambda}(\sin\theta_0 - \sin\theta)\right|$ is the difference between the wave vector of the incident light and that of scattered light in the direction θ (components parallel to the surface). The term $|w|^2$ is a function of angles θ and θ_0, the dielectric permittivity ε, of the sample, and the polarization of the incident light.

The use of an appropriate analytic model for $|S(\Delta k)|^2$ allows us to determine the RMS height δ (also called R_q) of the asperities as well as their transverse correlation length σ, with which the surface roughness can be described by these two statistical parameters [15].

32.3.4
Angle-Resolved Light Scattering (Lasercheck, US)

Lasercheck is an instrument manufactured by Optical Dimensions, and is based on the same principle as the optical roughness meter of the BNM-INM. However, the angular distribution of the scattered light is measured by a linear array of

fixed detectors in the plane of incidence rather than by a single detector that moves in an arc of circle, also in the plane of incidence. The source is a laser diode emitting monochromatic light with a wavelength of 660 nm. The angle of incidence on the sample is 75°.

32.3.5
Total Integrated Light Scattering (SP, SE)

A traditional optical method of estimating roughness of length end gauge blocks [16, 17] and optical components [18] uses total integrated light scattering. The surface roughness is estimated either from measurements of the amount of specularly reflected light or from its complement, the total scattered light. The total integrated light scattering method is applicable over a wide range of surface roughness ($0 < \delta/\lambda < 0{,}3$). For smooth surfaces, ϕ_{spec} the light flux reflected in the specular direction is approximately equal to the total reflected flux $\phi_{tot} = \phi_{spec} + \phi_{scat}$ and its value is insensitive to changes in roughness. Here it is preferable to measure the integrated scatter ϕ_{scat}, which in the smooth-surface limit is directly proportional to the mean-square roughness:

$$\frac{\phi_{scat}}{\phi_{tot}} \approx \left(\frac{4\pi\delta\cos\theta_0}{\lambda}\right)^2 \tag{32.2}$$

an equation that is valid for any height distribution. The value of δ obtained from Eq. (32.2) does, however, depend on the bandwidth of spatial wavelengths sensed by the measuring instrument [19].

The light scattering method for surface roughness measurement may be calibrated by making measurements on the same surface samples with other techniques such as interferometry [16, 20]. However in the present work, Eq. (32.2) is found to give reasonable agreement with profilometer-calibrated gauge blocks within uncertainties (including filtering to match the different spatial spectral regions of the different methods) and is therefore used directly. Details of the method and equipment are given in [21]. In the present measurements, a diode laser (wavelength 650 nm) replaces the white light source used earlier.

32.4
Results and Instruments Comparison

As mentioned previously, only some results will be given here. For the complete study, see the final report of the EUROMET Project 551[22].

As a preliminary to using any of the roughness measuring techniques described here, it is preferable first to image the surface, for example by using an optical microscope. The image can give information about the best area to use for further measurements. As an example, the image of a site on the top of the 2 kg mass (Figure 32.1) shows one directional polishing scratches.

To provide more information on the roughness measurement instruments, each technique will be considered separately. First, we will consider the two scanning-probe devices and then the optically-based techniques.

As already been explained, the scanning probe devices (the mechanical profiler and the SNOM) does not involve, in general, any damage on the surface, because the two instruments can be used with very light loadings. With those instruments, the profile is a convolution of the true profile with the stylus tip. Therefore, any measurement is affected by the spatial-frequency response of the instrument. This effect becomes more significant when the surface has fine structure with steep slopes. The major advantage of these instruments is their excellent lateral resolution as well as the different types of information that they can provide.

The principal advantage of optically based techniques, on the other hand, is that they are nondestructive even for adsorbate layers. However, their lateral resolution is limited by several factors, including the optical wavelength.

We will now give examples of the results of surface roughness measurements of 2 kg mass made at BNM-INM (optical roughness meter) and at LPUB (SNOM).

Fig. 32.1 Optical microscopy picture of site pertaining to 2 kg mass (top).

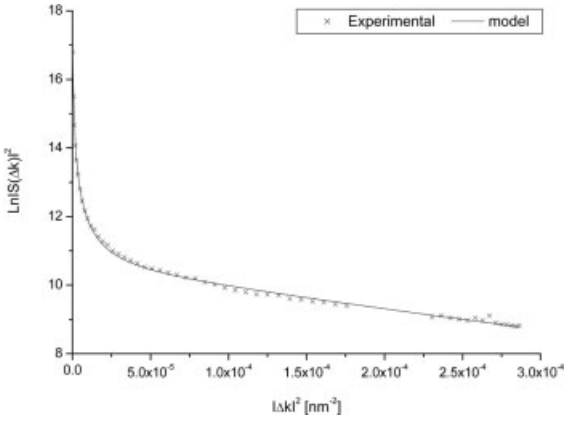

Fig. 32.2 PSD functions (measurement BNM-INM and model equation (32.1)) concerning one site on the upper base of 2 kg mass.

These are shown in the form of power spectral density function graphs where $|S(\Delta k)|^2$ is plotted versus $|\Delta k|^2$ (Figure 32.2) and versus spatial frequencies (Figure 32.3).

The best fit to the measured data is obtained by using the sum of Gaussian and Lorentzian terms describing the short- and long-range roughness (The autocorrelation function of the surface height is then represented by the sum of Gaussian and exponential functions). We emphasize, however, that the separation between short- and long-range roughness which depends critically on the particular surface, is an arbitrary choice because there is no definition of the bandwidth limits for short-range and long-range roughness. The RMS roughness δ determined from these measurements is about 7.5 nm.

One of the advantages of the SNOM is the ability to change the spatial frequency bandwidths by changing the measured size of the surface area:

$[0.25\ \mu m^{-1} - 32\ \mu m^{-1}]$ for $(4 \times 4\ \mu m)^2$,
$[0.025\ \mu m^{-1} - 3.2\ \mu m^{-1}]$ for $(40 \times 40\ \mu m)^2$.

The RMS roughness δ determined from these areas varies between 7 nm and 11 nm for the first spatial frequency band and between 11 nm and 14 nm for the second band, respectively.

Some measurement results from the EUROMET Mass Project 551 are summarized in Table 32.4. These are roughness values measured on 500 g and 2 kg mass standards by three of the optically-based instruments. For the optical roughness meters, taking account of the different spatial frequency bands (Table 32.2), it is clear that the values determined by TIS and SNOM $(40 \times 40\ \mu m)^2$ and those determined by ARS and SNOM $(4 \times 4\ \mu m)^2$ are comparable within uncertainties. The value of the RMS roughness δ generally depends on the bandwidth limits and especially on the lower limit. In summary, the results obtained by means of the three instruments agree well.

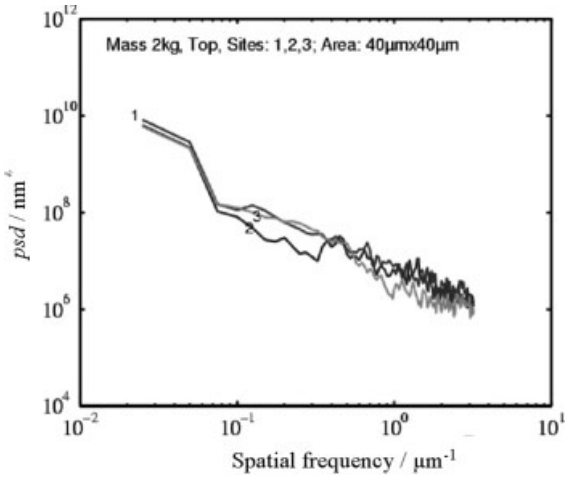

Fig. 32.3 PSD functions concerning one site on the upper base of 2 kg mass obtained by means of SNOM.

Table 32.4 Average values of δ (in nm) for 500 g and 2 kg masses

	500 g	2 kg
TIS/SE	11.5 ± 4.0	11.0 ± 3.0
ARS/FR	7.8 ± 1.8	7.5 ± 5.5
SNOM/FR $(40 \times 40\ \mu m)^2$	11.7 ± 1.2	12.4 ± 1.2
SNOM/FR $(4 \times 4\ \mu m)^2$	6.4 ± 0.6	9.1 ± 0.9

32.5 Conclusion

Five roughness measurement techniques have been described in this comparative study of measuring the surface roughness of weights. Results for 500 g and 2 kg masses obtained from three instruments are given for comparison. When measured with different instruments that have comparable surface spatial frequency bands (especially the lower band limit) [22, 23], the roughness values of the two masses agree well. However, the measured roughness is different even if the same instrument is used, but with different surface spatial frequency bands.

The present study emphasizes for the weighing community that no one single value of surface roughness for a particular surface can be given, not only because of actual local variations in roughness across the surface of a mass standard, but also due to the well-known fact that different methods cover different ranges of surface spatial wavelengths and surface spatial frequencies (reciprocals of the surface spatial wavelengths).

This review may be useful as a basis for future studies relevant to mass metrology:

- to determine which surface roughness techniques are most appropriate for mass metrology, i. e., the ones most sensitive to the ranges of surface spatial frequencies that have a primary effect on mass stability,
- to assess the effectiveness of cleaning methods, by comparing roughness measurements made before and after cleaning. Preliminary studies have already been performed at the BNM-INM [1],
- to improve the manufacturing process by measuring surface roughness for each polishing step. This is possible only for those laboratories that polish their own mass standards.

References

1 C. Zerrouki, F. Miserey, and P. Pinot, The nanometric roughness of mass standards and the effect of BIPM cleaning-washing techniques, Metrologia **36**, 403–414 (1999).

2 J. M. Bennett and L. Mattsson, Introduction to surface roughness and scattering, second edition *Optical Society of America*, Washington, D. C. (1999), pp. 1–130.

3 Weights of classes E_1, E_2, F_1, F_2, M_1, M_{1-2}, M_2, M_{2-3} and M_3, Part 1: Metrological and technical requirements OIML R 111-1 (Edition 2004) of International Recommendation OIML R 111, Technical Subcommittee OIML TC 9/SC 3.

4 Roughness comparison specimens – Part 2: Spark eroded, shot-blasted and grit-blasted, and polished, ISO 2632-2:1985.

5 J. M. Bennett, Recent developments in surface roughness characterization, Meas. Sci. Technol. **3**, 1119–1127 (1992).

6 D. J. Whitehouse, Trends in instrumentation for roughness and form measurement, SPIE **2088**, 2–17 (1993).

7 E. Betzig, P. L. Finn, and J. S. Weiner, Combined shear force and near-field scanning optical microscopy, Appl. Phys. Lett. **60**, 2484 (1992).

8 R. Toledo-Crow, P. C. Yang, Y. Chen, and M. Vaez-Iravani, Near-field scanning optical microscope with atomic force regulation, Appl. Phys. Lett. **60**, 2957 (1992).

9 L. Berguiga., F. de Fornel, L. Salomon, A. Gouronnec, and J. Bizeuil, Observation of optical fibers by near-field microscopies: effects of aging, SPIE Proc. **3848 (**1999).

10 L. Salomon, F. de Fornel, and J. P. Goudonnet, Sample-tip coupling efficiencies of the photon scanning tunnelling microscope, J. Opt. Soc. Am A **8**, **12**, 2009–2015 (1991).

11 F. de Fornel, *Evanescent Waves* (Springer Verlag, Heidelberg, 2001).

12 E. Kretschmann and E. Kröger, Reflection and transmission of light by rough surface, including results for surface-plasmon effects, J. Opt. Soc. Am. **65**, 150–154 (1975).

13 E. Kröger, and E. Kretschmann, Scattering of light by slightly rough surfaces, Zeit. Physik, **237**, 1–15 (1970).

14 J. M. Elson and Bennett J. M., Relation between the angular dependence of scattering and the statistical properties of optical surfaces, J. Opt. Soc. Am **69**, 31–47 (1979).

15 C. Zerrouki, La rugosité nanomètrique des surfaces polies : étude expérimentale par diffusion de la lumière. Aplication à l'étude des étalons de masse en alacrite XSH, 1998, Thèse de doctorat du Conservatoire National des Arts et Métiers, p. 175.

16 E. Engelhard, Precise interferometric measurement of gauge blocks, NBS Circular **581**, 1–20 (1957).

17 H. Darnedde, High-precision calibration of long gauge blocks using the vacuum wavelength comparator, Metrologia **29**, 349–359 (1992).

18 ASTM 1999, *Standard Test Method for Measuring the Effect of Surface Roughness of Optical Components by Total Integrating Scattering*, Standard F1084-87 (American Society for Testing and Materials, Philadelphia).

19 P. Beckmann and A. Spizzichino, *The Scattering of Electromagnetic Waves from Rough Surfaces* (Artech, Norwood, MA, 1987), Chapts. 3–5.

20 S. Ishikawa, G. Bönsch and H. Böhme, Phase-shifting interferometry with a coupled interferometer: application to optical roughness of gauge blocks, Optik, **91**, 103–108 (1992).

21 L R. Pendrill, Surface roughness measurable with total integrated light scattering, SP Progress Report 1995:**07**.

22 Euromet Mass Project 551, final report, BNM-INM/Cnam/Ma-2003-01, Paris.

23 C. Zerrouki, J. M. Bennett, F. de Fornel, Y. Haidar, Z. J. Jabbour, L. Pendrill, and P. Pinot, Study of several roughness measurement techniques applied to the characterisation of mass standard surface quality, (in preparation).

33
Surface Analysis of Precision Weights for the Study of Commonly Occurring Contaminants

Ulf Jacobsson and Peter Sjövall

Abstract

The increasing demand for mass precision measurements in the manufacturing industry raises the requirements on the stability of precision weights used for mass calibration. In this work, the results from a surface chemical analysis by time-of-flight secondary ion mass spectrometry (TOF–SIMS) are presented. Two types of precision weights were used, one wire weight used in the field, and one sheet weight used at the Swedish national laboratory for mass. From initial analysis results, silicone oil was found to be the major contaminant on both weights. The mass and the surface chemical composition of the precision weights were monitored (i) one day after cleaning, (ii) after approximately one year of laboratory or field use, respectively, and finally (iii) one day after undergoing an additional cleaning treatment. The TOF–SIMS results show that the silicone contaminant was efficiently removed by the cleaning procedure, while other contaminants, such as fatty acids, remained on the surface. The cleaning procedure used involved sequential immersion and agitation in n-heptane and ethanol. The weighing results showed no significant mass changes of the laboratory weights, while the field weights displayed a significant mass reduction upon the initial cleaning.

33.1
Introduction

The SI definition of mass is realized with a man-made object composed of noble metals (Pt–Ir), while the most common material currently used in precision weights is austenitic stainless steel engineered so that the density is 8000 kg/m^3. Therefore it is of high importance that primary mass standards as well as precision weights are as stable as possible and/or that the mass stability is monitored. Some important factors influencing weight stability are:

Nanoscale Calibration Standards and Methods: Dimensional and Related Measurements in the Micro- and Nanometer Range.
Edited by Gunter Wilkening, Ludger Koenders
ISBN: 3-527-40502-X

- Material choice
- Surface finish
- Environmental conditions
- Handling

In order to limit variations in the latter two factors, mass standards are stored and handled in clean environments using clean tools and cotton gloves, according to documented procedures [1]. However, low-level contamination of the mass standard surfaces will always take place and its significance will increase along with the increased requirements on weight stability. Water adsorption on the surface of mass standards is also a major concern in high precision mass metrology. The use of precision weights for calibration of balances for customers outside the clean laboratory environment poses new challenges in order to estimate stability and handling of contaminants.

The standard methods used when cleaning weights have several levels depending on the type and amount of visible pollutants on the weight's surface.

- Light brushing, gently blowing with a rubber ball
- Chamois leather
- Ethanol and chamois leather
- Water or ethanol in ultrasound bath
- Steam jet cleaning
- Soxhlet extraction

However, none of these methods is tailored to the specific chemical composition of the pollutants [2, 3].

A number of surface studies on high precision mass standards has been conducted using various techniques, such as X-ray photoelectron spectroscopy (XPS) [4], ellipsometry, [5] and secondary ion mass spectrometry (SIMS) [6]. The results from these studies all show different aspects of the surface properties. Ellipsometry provides information about the optical path through a contamination layer, but information about the chemical composition is limited. XPS and SIMS, on the other hand, give detailed information about the chemical composition.

33.2 Experimental

Two sets of high precision (OIML class E1) mass standards in the range 500–10 mg were used. One set of standards (sheet weights) was kept at the Swedish National Laboratory for Mass at SP. The other set (wire weights) was used for calibration and verification of high precision analytical balances by EXAKT Vågteknik AB. An example of the shape of small OIML-weights can be seen in Figure 33.1.

The experimental sequence of weighings, cleaning treatments, and TOF–SIMS measurements is shown in Table 33.1. The events are described as BC1 (Before Cleaning 1), AC1 (After Cleaning 1), and so forth.

The principle of the TOF–SIMS experiment is shown in Figure 33.2. A mass spectrum of the outermost molecular layer of the sample is obtained by using a primary ion source that irradiates the surface with high-energy primary ions. As a result of the primary ion bombardment, particles from the sample surface escape into the vacuum, some of them as ions, which then can be extracted into a time-of-flight mass spectrometer. The resulting mass spectrum contains detailed information about the chemical composition of the sample surface.

For TOF–SIMS analysis, the mass standard samples were mounted on the sample holder using metallic clips. Handling of the samples was done in a laminar-air flow box using clean tools and support surfaces. Before introducing the sample

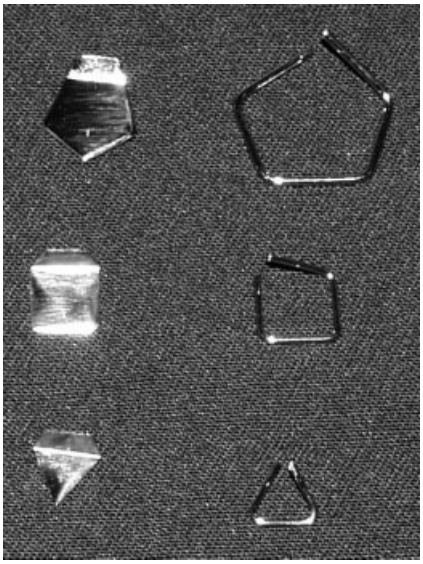

Fig. 33.1 Shapes of small precision weights in accord with OIML standard. The weight's nominal masses are coded by their form. The weights are from top to bottom: 500 mg, 200 mg and 100 mg.

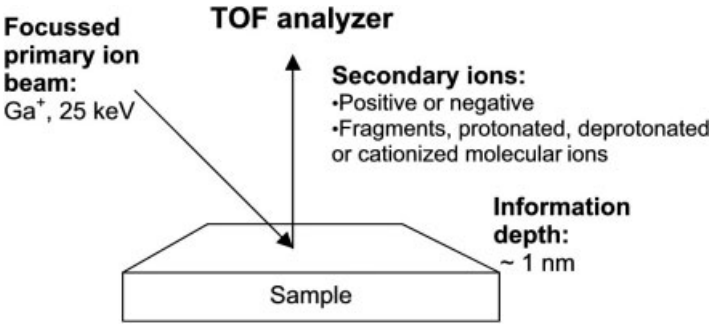

Fig. 33.2 Principle outline of the TOF–SIMS experiment.

into the vacuum chamber, possible dust particles were removed by gently blowing nitrogen gas across the sample surface. The TOF–SIMS analysis was carried out in a TOF–SIMS IV instrument (ION–TOF GmbH, Germany) using 25 keV Ga^+ as primary ions at a current of approximately 1 pA. The analysis area was typically $100 \times 100\ \mu m^2$ and the analysis time was 50 s, always keeping the accumulated ion dose below the static limit, $10^{13}\ cm^{-2}$ [7].

Table 33.1 Experimental sequence with dates when the different tasks were performed

Sheet weight set E11 owner: SP.

Designation	Date	Event	Note
BC1	2001-11-28	TOF-SIMS	
	2001-12-04	cleaning	n-heptane + ethanol
AC1	2001-12-07	TOF-SIMS	
AC1	2002-01-31	calibration	
AC1	2002-02-01	TOF-SIMS	
	2002-03-26	calibration	regular cal
	2002-04-18	calibration	together with 238:1
	2002-04-20 –2002-12-11		internal laboratory work
BC2	2002-12-11-13	calibration	
BC2	2002-12-13	TOF-SIMS	500 mg only
	2002-12-13	cleaning	n-heptane + ethanol
AC2	2002-12-16	TOF-SIMS	500 + 200 mg
AC2	2002-12-16-18	calibration	

Wire weights 238:1 owner: Exakt Vågteknik, Malmö.

Designation	Date	Event	Note
BC1	2002-04-09	Calibration	
BC1	2002-04-11	TOF-SIMS	500 mg only
	2002-04-11	Cleaning	n-heptane + ethanol
AC1	2002-04-15	TOF-SIMS	500 mg only
AC1	2002-04-16-18	Calibration	with E11
	2002-04-26–2002-12-11		field work with the weights
BC2	2002-12-11-13	Calibration	
BC2	2002-12-13	TOF-SIMS	500 + 200 mg
	2002-12-13	Cleaning	n-heptane + ethanol
AC2	2002-12-16	TOF-SIMS	500 + 200 mg
AC2	2002-12-16-18	Calibration	

The weighing procedure used is one of SP's Standard Operating Procedures for substitution weighing. The object under test is weighed against two standards, which in turn are compared with each other. The mass difference between the standards should not have changed significantly since their calibration, thus ensuring consistency in the high precision weighing process. The balance used was a Mettler Toledo/Metrotec A5 robotized comparator with max load 5.1 g and scale division 0.1 μg.

The cleaning procedure was tailored to the type of contamination found in the TOF–SIMS analysis. It consisted of a sequence of immersing and agitating the studied weights in first n-heptane and then ethanol. The first step was designed for removal of contaminants that are not soluble in ethanol. The second step was for removing contaminants soluble in ethanol and the residues of n-heptane.

33.3 Results

The chemical composition of contamination of two different mass standards, a 500 mg sheet weight and a 500 mg wire weight, was investigated by TOF–SIMS at four different measurement occasions: (i) before and (ii) after initial cleaning, and (iii) before and (iv) after a second cleaning treatment that was carried out after an extended period of storage (sheet weight) or field use (wire weight). Positive and negative spectra were recorded at each measurement occasion.

Figure 33.3 shows positive TOF–SIMS spectra from the sheet weight recorded before and after the initial cleaning treatment, respectively. At low ion masses ($<$100 u), the spectra are dominated by peaks corresponding to different hydrocarbon fragments ($C_xH_y^+$), indicating surface contamination by organic substances, and to metal ions from the weight material (Cr^+ and Fe^+). At higher masses ($>$ 70 u), the spectrum obtained before cleaning shows several strong peaks corresponding to fragments from polydimethylsiloxane (PDMS, marked P in spectrum). PDMS is a common form of silicone oil and the spectrum thus indicate considerable contamination of the sheet weight by PDMS before cleaning. After cleaning, the PDMS peaks have disappeared, as expected since the cleaning treatment was specifically designed to remove PDMS from the weight surfaces. Apart from the absence of PDMS peaks, the spectrum obtained after cleaning shows a somewhat increased signal from Na^+, significant signal intensity from di-isooctyl phthalate (DOP, common plasticizer in PVC, present e. g. in vinyl gloves) and similar signal intensities from hydrocarbon fragments as before cleaning. These spectra indicate that the cleaning treatment removed most of the PDMS, but that other contaminants may have been deposited during cleaning, such as sodium salts and DOP. The hydrocarbon fragments reflect the presence of organic contaminants on the sample surface and are always observed on samples that are handled in air before analysis.

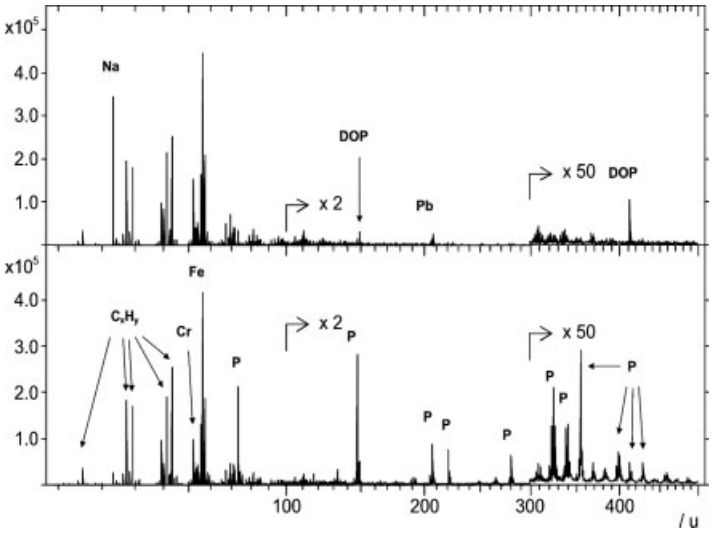

Fig. 33.3 Positive TOF–SIMS spectra of a mass standard (sheet weight, 500 mg) recorded before and after the first cleaning procedure (BC1 and AC1), respectively. The origin of the major peaks are indicated, where DOP stands for di-isooctyl phthalate and P stands for polydimethyl siloxane.

The negative TOF–SIMS spectra (not shown) provide additional information about the chemical composition on the sample surfaces. The signal intensities from Cl^-, PO_3^- and SO_3^- ions indicate the presence of substances containing these fragments on the surface. In addition, relatively strong signal intensities were observed for $C_{14}H_{27}O_2^-$ (227 u), $C_{15}H_{29}O_2^-$ (241 u), and $C_{16}H_{31}O_2^-$ (255 u), indicating the presence of fatty acids on the surfaces.

In Figure 33.4, the effect of the cleaning treatments on each of a selection of ion peaks in the TOF–SIMS spectra can be observed. The diagram shows normalized TOF–SIMS signal intensities for a selection of ions from the analysis of the sheet weight at the four different measurement occasions. The diagram should be analyzed by looking at how the signal intensity of each ion varies throughout the sequence of the four different measurement occasions. However, comparisons between ions cannot be interpreted in terms of abundance differences (due to the normalization procedure used, see figure caption).

From Figure 33.4 it can be concluded that the cleaning treatment is very efficient at removing PDMS from the surface, while other contaminants, such as salts (e. g., sodium chloride, phosphates, and sulphates), hydrocarbons and fatty acids, are not removed as efficiently as PDMS.

The efficient removal of PDMS and the less efficient removal of other contaminants by the cleaning treatment are also observed in Figure 33.5, which shows the normalized signal intensities before and after the second cleaning treatment, for the sheet and wire weights, respectively. The PDMS intensities are lowered dramatically by the cleaning procedure, both for the sheet and wire weight. For

the other ions, however, the signal decrease is considerably less pronounced and in some cases the signal intensity even increases after cleaning (notably the fatty acids on the wire weight). The signal increase may be due to unintentional deposition of contaminants during cleaning in combination with a cleaning procedure that is inefficient at removing this particular contaminant.

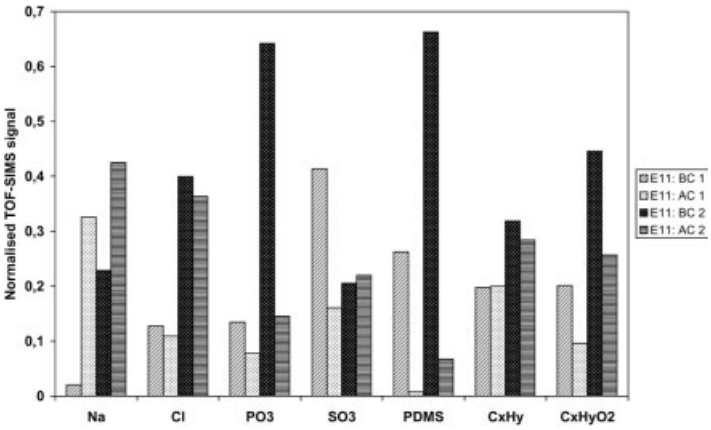

Fig. 33.4 Normalized TOF–SIMS signal for a selection of ions recorded at different stages of the experimental procedure on a 500 mg sheet weight (E11). The TOF–SIMS signals have been normalised first against the signal intensity of Fe^+ and FeO_2^- for the positive (Na, PDMS, and C_xH_y) and negative (Cl, PO_3, SO_3 and $C_xH_yO_2$) ions, respectively, and then against the sum of the signals from the specific ion at all four measurement occasions (the sum of all four bars for each ion is thus 1).

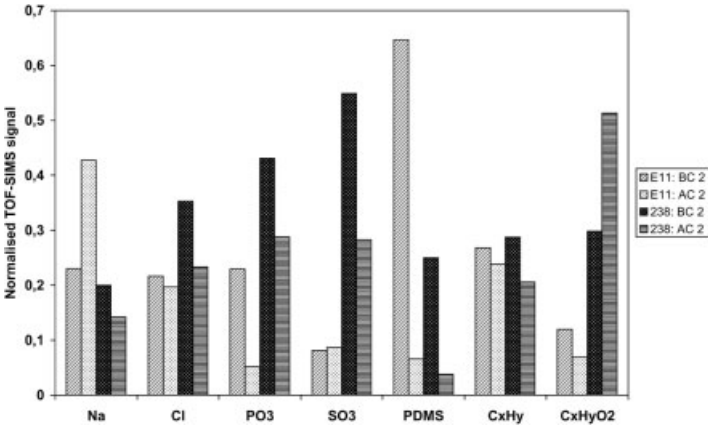

Fig. 33.5 Normalized TOF–SIMS signal for a selection of ions before and after the second cleaning procedure, comparing the results from the sheet weight (E11) and the wire weight (238). The normalisation procedure was the same as described in Figure 33.4.

In Figure 33.6, the intensity variations of the selected ions throughout the measurement sequence for the wire weight are shown. The results confirm that the cleaning treatment is efficient at removing PDMS, but less efficient for other contaminants. The increase in PDMS signal after the initial cleaning procedure is explained by the low PDMS signal before cleaning; this sample was not significantly contaminated by PDMS before the first cleaning treatment. The large decrease in the sulphate signal after the initial cleaning procedure suggest that the sample at this occasion may have been contaminated with a sulphate-containing substance that could be efficiently removed by the cleaning treatment, but that this particular substance was not present on any of the other analyzed surfaces.

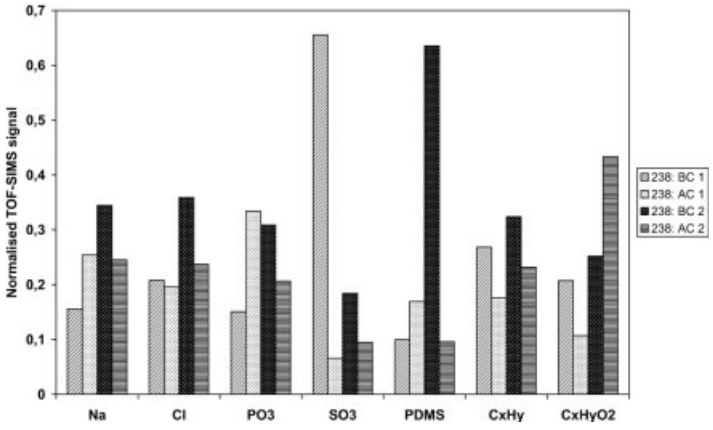

Fig. 33.6 Normalized TOF–SIMS signal for a selection of ions recorded at different stages of the experimental procedure on the 500 mg wire weight (238). The normalization procedure was the same as described in Figure 33.4.

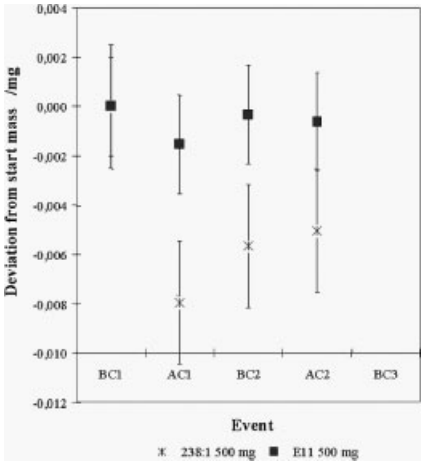

Fig. 33.7 Mass change in relation to the starting mass during the experiment sequence for 500 mg weights. E11 500 mg is the sheet weight, 238:1 is the wire weight.

Figure 33.7 shows the mass change for the weights throughout the experimental sequence. It can be seen that the mass decreased after initial cleaning for both weights. The decrease was more pronounced for the wire weights used in the field than the sheet weights kept at a laboratory. During the period between cleanings there was a mass gain for both weights. However, taking the uncertainty of calibration into account the results from weighing can be considered as inconclusive. No statistically significant mass change was observed after the second cleaning.

33.4 Discussion and Conclusions

The results in this work demonstrate the importance of surface chemical analysis for obtaining optimal cleaning procedures for mass standards and that TOF–SIMS is a particularly suitable method for this analysis. The sensitivity, chemical specificity, and lateral resolution (~200 nm, not demonstrated in this work) capabilities of TOF–SIMS can be used to provide detailed information about the nature of contaminants on the mass standard surfaces. This information can then be used to design optimal cleaning procedures.

Earlier works regarding contamination and cleaning of mass standards [2–5] have primarily focused on 1 kg primary mass standards kept at National Laboratories. To our knowledge, this is the first study using tailored cleaning and small weights used for balance calibration. The mass changes derived from the weighings were inconclusive. This depends mostly on the relatively high level of weighing uncertainty for this kind of small weights.

References

1 The NPL website: http://www.npl.co.uk/mass/guidance/handling.pdf

2 S. Davidson, I. Severn„ and D. Bayliss, Mass standards – a high precision study of commonly used methods for cleaning stainless steel weights, Meas. Sci. Technol. **13**, 1178–1182 (2002).

3 S. Davidson, A review of surface contamination and the stability of standard masses, Metrologia **40**, 324–338 (2003).

4 S. Ikeda et al., Surface analytical study of cleaning effects and the progress of contamination on prototypes of the kilogram, Metrologia **30**, 133–144 (1993).

5 B. R. Chakraborty, D. E. Lehman, and N. Winograd, "Time-of-flight static secondary ion mass spectrometry analysis of surface contamination on Pt/Ir standard mass material, Rapid Commun. Mass Spectrom. **12**, 1261- (1998).

6 R. Schwartz, and M. Gläser, Procedures for cleaning stainless steel weights, investigated by mass comparison and ellipsometry, Meas. Sci. Technol. **5**, 1429–1435 (1994).

7 J. C. Vickerman, in *ToF-SIMS: Surface Analysis by Mass Spectrometry*, edited by J. C. Vickerman and D. Briggs (IM Publications and Surface Spectra Limited, Charlton, Chichester, West Sussex, UK, 2001), pp. 1–40.

34
Tip-Shape Effect on the Accuracy of Capacitance Determination by Scanning Capacitance Microscopes

Štefan Lányi

Abstract

The capacitance measurement error, caused by the stray field of capacitance microscope probes of various designs, has been computed by means of the finite element method. Cylindrical islands and wells of varying radius and height or depth, in conducting surfaces and structures containing dielectric films, were used as test features for modeling. The results show that high accuracy and good contrast transfer are contradictory requirements. Probes with small tip radius yield smaller errors on features with small diameter but larger ones on features with large diameter, than tips with large radius of curvature. The stray field causes that the radius needed to image 25 nm high protrusions or deep depressions in air, with an error smaller than 10 %, is as large as 6 μm, assuming a shielded probe of realistic dimensions. For best results the probe should be shielded as close to the tip apex as possible. Unshielded microfabricated probes on cantilevers are little suited for quantitative analysis.

34.1
Introduction

The scanning capacitance microscopes (SCM) [1–6] are able to image and analyze structures on the free or insulator-coated surface of conductors, and buried structures in semiconductors and dielectrics. They are expected to satisfy the needs of semiconductor industry for high-resolution and high-accuracy determination of dopant concentration in semiconductor structures on the nanometer scale, identified for future generations of ULSI integrated circuits [7].

The factors influencing the accuracy of the capacitance measurement, when the amplitude of the applied voltage is limited, as in semiconductor structures, and high-lateral resolution is aimed, are the signal-to-noise ratio (SNR) of the capacitance transducer achievable at a reasonable bandwidth, and the ability of the probe to concentrate on the electrostatic field to a small volume. Though the

Nanoscale Calibration Standards and Methods: Dimensional and Related Measurements in the Micro- and Nanometer Range.
Edited by Gunter Wilkening, Ludger Koenders
ISBN: 3-527-40502-X

idea of SCM is one of the first among the scanning probe methods [1], attempts to describe or analyze the stray field of the probe, and of its consequences on the fidelity of imaging are scarce [3, 8–10].

The sensitivity of various types of capacitance transducers, applied in SCMs, has been analyzed in Ref. [11]. The expected limit of resolution, obtained by simulation respecting the achievable sensitivity, was found to be about 2 nm, albeit at rather low contrast [10], i. e., large error on small artifacts. The sensitivity of the probe, defined as a measurable capacitance between the probe and a surface element at a distance ϱ from the probe axis, not only depends on the tip/counter-electrode separation, but also on the shape of the probe. The steeper this dependence, the smaller is the influence of distant parts of the sample and higher the achieved contrast.

The requirement on measurement accuracy opens the question of calibration of microscopes. In the trivial case of conductors, the obtained surface topography can be compared with images obtained by means of a scanning tunnelling microscope (STM) or scanning force microscope (SFM). The microscopes using the RCA CED Video Disc, or similar capacitance transducer cannot measure the absolute value of the capacitance. They produce an output voltage proportional to capacitance difference and to an unknown measuring signal [1, 12]. Even if the transducer yields the true capacitance, like the low-frequency SCM [5], fine details of the tip shape, like the radius of curvature, which due to the stray field do not affect the measured capacitance markedly, may introduce serious uncertainty regarding the local contribution to the measured value. Thus a calibration is unavoidable. The aim of the present chapter is to quantify the measurement errors that would arise when imaging distinct topographic features or buried structures in a dielectric. It intends to show the expectable quality of raw data, which is important for further processing and reconstruction.

The effect of stray field, interpreted in the context of the present chapter as a measurement error, manifests itself most clearly as a distortion of nanometer- or even micrometer-size surface or sub-surface features. At present, no true three-dimensional simulations of probe/sample capacitance for nonplanar surfaces exist, but rather of simple 2D or combinations of 2D and 3D methods [13–16]. These simulations have shown that the least affected is the center of the protrusions or holes.

As a method of conservative estimation of measurement error, the difference between the capacitance sensed by the probe situated above the center of cylindrical protrusions or depressions in a plane and that sensed above a plane at the same distance, has been suggested [17, 18]. This approach has been now extended to a comparison of shielded and unshielded probes of different shapes, with accent on radius of curvature of the tip apex. The capacitance has been computed using the finite element method [19] by means of the MEP 6.0 code [20].

34.2
Probe geometry

The probes used in SCMs comprise sharpened wires [2, 21], conducting SFM cantilevers [22], and shielded sharpened wires [5, 23]. Both unshielded and actively shielded probes have been analyzed. The model of shielded probe had a radius of curvature $r = 25$ nm and cone angle 10°. The shield orifice radius R_o was 25 μm, and the tip protruding by 5 μm. The same tip geometry, as well as with larger cone angle (20°), and with a larger radius (1 μm), have been analyzed without shield. In a search for an ideal probe, a shield with orifice radius 1 μm and tip protruding 0.5 μm have also been included.

The shielding limits the fringing of the electrostatic field of the tip, thus rendering a good definition of boundary conditions possible. On the contrary, the stray field of unshielded probes is not limited. Even worse, the capacitance between an infinite plane and a cone grows approximately linearly with the size of the cone. However, simulation has shown that the flux density near the tip apex did not differ by more than 2.5 % when the size of the cone, except the tip radius, has been doubled. Therefore, the tasks were bounded by a force line in the form of a circular arc, in three dimensions a hemisphere, with radius 250 μm. Such model underestimates the stray capacitance of real unshielded probes mainly by ignoring the contribution of the cylindrical shaft or lead.

The cone angle of SFM tips, used in SCM, is usually about 25° to 35° and the tip radius 20 to 100 nm. In our model the angle, height, and radius were 30°, 15 μm and 25 nm, respectively. The parasitic capacitance of the probe cantilever and of its holder, which may be as large as 1 pF, has been first neglected and then introduced replacing the oblong or triangular cantilever by a cone with angle 160°. The models of the probes are seen in Figure 34.1.

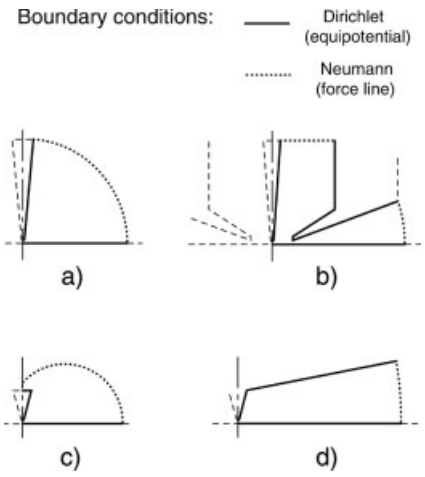

Fig. 34.1 Models of the probes. (a) unshielded probe (height 240 μm, cone angles 10° and 20°, tip radii 25 nm and 1 μm), (b) shielded probe (orifice radii 25 μm and 1 μm, protruding 5 μm and 1 μm, respectively, tip radius 25 nm), (c) microscopic tip (15 μm, cone angle 30° tip radius 25 nm), and (d) microscopic tip on cantilever.

34.3
Simulated topographic Artifacts

Cylindrical islands or holes may be considered the simplest approximations of topographic or structural features, representing practically important details in integrated circuits. Though the outer surface in semiconductor structures is usually flat, local variations of doping level affect the depth of depletion regions, which may be considered dielectric. Then the boundary between the depleted and unaffected semiconductor is equivalent to an internal insulator/conductor boundary with protrusions or depressions. The model is simplified in that it ignores the rounding of the boundaries in real structures.

The space between the tip apex and the conducting surface was assumed to be filled either with air (relative permittivity $\varepsilon_r = 1$) or with a dielectric with $\varepsilon_r = 5$. The models of the topographic features are shown in Figure 34.2. The height of an island was the normal distance from the tip apex to the plane surrounding the protrusion, with its top kept at constant distance (5 nm) from the tip. The depth of wells was the tip-to-bottom distance, with the surrounding plane 5 nm from the tip apex. They ranged from 5 to 500 nm, with radius from 0.05 to 12 μm. The probe has been positioned axially.

The employed software is able to compute the flux with fairly high accuracy. However, the solved models contained details ranging from a few nanometer up to tens to hundreds of micrometer. Since each data point is computed using a different geometry, with certain dimensions varying, the mesh cannot be the same in all cases. Then minor changes, caused by the mesh generator, occasionally lead to scatter of data. To keep it at acceptable level, the node spacing of the triangular mesh in critical areas was as low as 0.25 nm (over 13 000 elements and up to 6900 nodes in total). The capacitance has been obtained as the flux at unit potential difference. In the case of "sensitivity" the planar electrode has been considered split to concentric rings divided by narrow gaps, and the flux from the tip to each ring has been computed. In all other cases the capacitance has been obtained from the integral flux between the probe and surface.

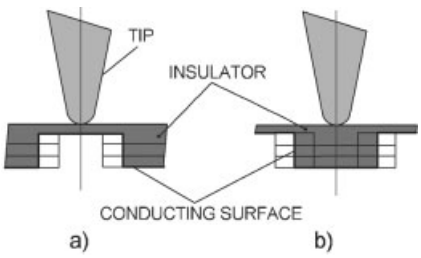

Fig. 34.2 Models of test structures. (a) cylindrical protrusion and (b) cylindrical depression.

34.4 Results

To link up with previous work [8–10], we shall use the shielded macroscopic probes as a basis for illustration of the performance of other probe geometries. Figure 34.3 shows the normalized dependence of the capacitance change on the radius of test features, sensed by such probe ($r = 25$ nm, angle 10°) for the more favorable case of $\varepsilon_r = 5$ that yield smaller errors [18]. The dashed lines mark 10 % deviation from the correct value. Figure 34.4 shows the sensitivity, the capacitance between the probe and a surface element of a conducting plane, in dependence on its distance from the probe axis, for tips with radii 25 nm and 1 μm, and a tip-to-plane distance 2 nm. Its gradient directly relates to the degradation of contrast transfer as a result of increasing tip radius, in

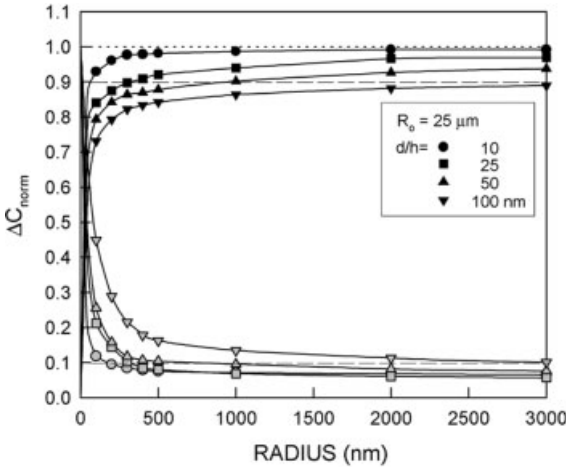

Fig. 34.3 Normalized dependence of capacitance change on artifact radius. Shielded probe.

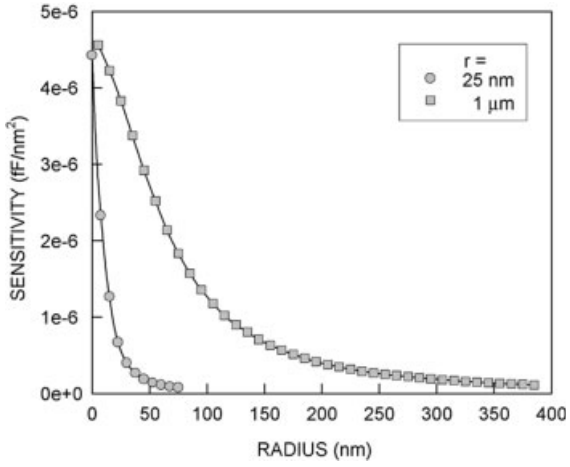

Fig. 34.4 Sensitivity of unshielded probes.

spite of the same sensitivity just in front of the tip apex. Its consequence is seen in Figure 34.5. Note the two *y*-axis scales that show the very different useful capacitance change achieved with the two tip radii. The absolute error, obtained on artifact radius exceeding approximately 3 μm, was nearly the same. This indicates that the error at large diameters is caused by the contribution of the conical part of the tip. The straightforward approach to its suppression would be as complete shielding as possible.

The performance of shielded probes with large orifice radius, radius reduced to 1 μm, of unshielded probe and of a microscopic tip at small depression radii and 50 nm depth is shown in Figure 34.6. All probes had the same tip radius of 25 nm. In spite of that the capacitance of the probes ranged from 4.23 fF (unshielded probe) to 0.023 fF (shielded with small orifice diameter), it changed within a radius of 500 nm only between 4.5 aF (shielded) and 3.9 aF (unshielded).

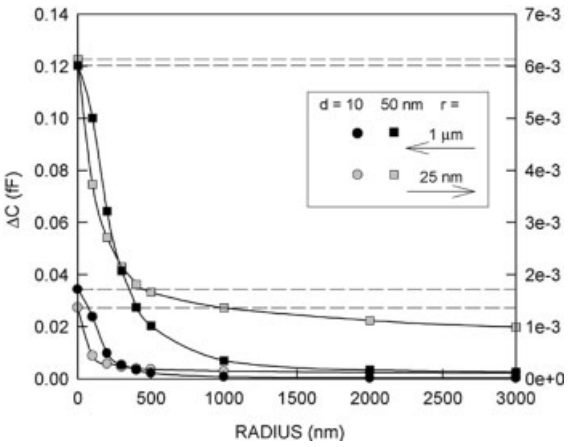

Fig. 34.5 Error with tips of different apex radii.

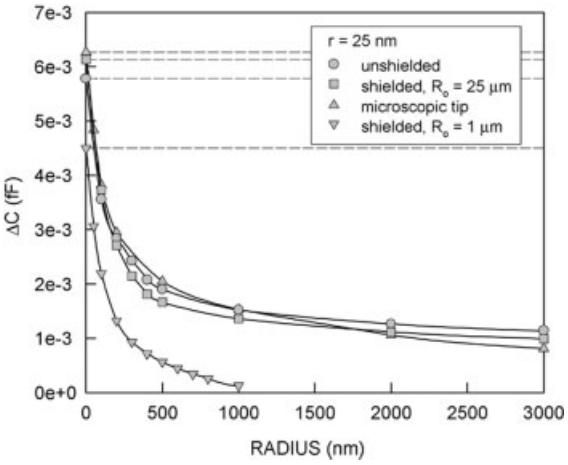

Fig. 34.6 Error with different probes.

The electrostatic field of the probe with small orifice diameter is best concentrated. The normalized capacitance change with such probe is seen in Figure 34.7. The improvement with respect to Figure 34.3 is evident.

The capacitance with an ideal probe in a fixed distance from the top of the protrusion would have to be independent of its diameter and height, and it would change with respect to a plane at the distance of the bottom of a hole. Figure 34.8 shows the results obtained with the shielded probe and $\varepsilon_r = 5$.

The capacitance of the microscopic tip was 0.66 fF. The value obtained using the complete model of the tip on cantilever yielded 112 fF and the "correct" value was not even approached on the length scale of the simulation.

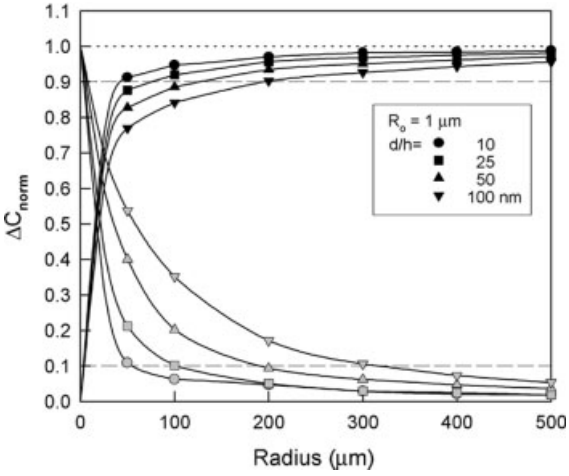

Fig. 34.7 Normalized dependence of capacitance change on artifact radius. Shielded probe with small orifice radius.

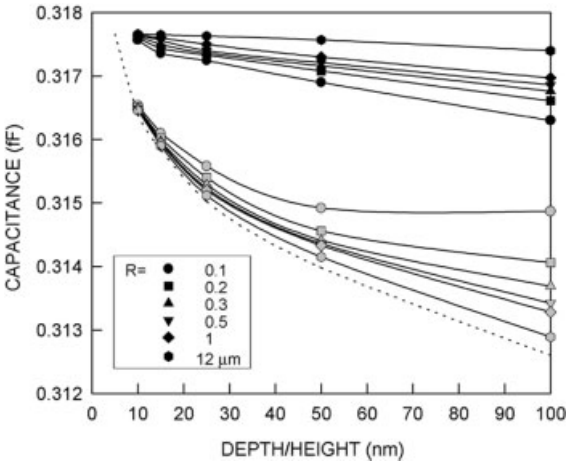

Fig. 34.8 Dependence of capacitance on protrusion height and hole depth. Shielded probe.

34.5 Discussion

Of all the probe models only the shielded are well defined, since the choice of the Neumann (force line) boundary condition connecting the shield with the plane has no effect on the tip-to-sample capacitance. On the other hand, the capacitance of the unshielded ones depends to some extent on the selection of the outer Neumann boundary condition. Changing it into a semicircle (similar to Figure 34.1(c)), comprising an area four times larger, increased the result only by 38 %, partly due to inclusion of the base of the cone. Therefore, the obtained stray capacitance is an acceptable approximation. It might be difficult to have an unshielded probe, made from a wire, as short as assumed in the models. The diameter of the cone base would be 40 μm and 85 μm for 10° and 20° cone angle, respectively. Even using wires of such diameter, the probes would be mostly longer, containing also a cylindrical shaft and a connection to it. However, as long as these components were perpendicular to the surface, their contribution to the stray capacitance would decay relatively rapidly.

Surprising is the much smaller relative error achieved with the tip having the 1 μm radius. Its advantage on larger artifacts is straightforward, but the very local contribution is the same as with the sharper tips. It means that the accuracy of local data may be comparable, in spite of worse contrast transfer on the deep sub-micrometer scale. In SCM the signal-to-noise ratio is an important and frequently limiting issue. Therefore, the higher capacitance change, correspondingly higher accuracy on large topographic features and the contrast transfer on small diameters, which is degraded far less than proportional to tip radius, poses the question of usefulness of very sharp probes in SCM. While on conducting surfaces or very thin insulating films tips with radii around 25 nm or less yield better results, for imaging structures containing not extremely thin dielectric films blunter tips would be superior.

Modeling the SFM cantilever by an obtuse angled cone may well approximate a triangular cantilever but it underestimates the influence of the end of an oblong beam. It still ignores the parasitic capacitance of the millimetre-sized cantilever chip. Disappointing is the effect of the stray capacitance of such probes. It might remain unrecognised in routine work, since the most frequently used transducers, based on a strip-line resonator, suppress the capacitance by tuning that obscures its real magnitude. The contrast transfer on small-scale features is little affected either. However, due to the closeness of the cantilever and the chip to the sample, the whole assembly acts as the probe. As it has been shown recently, differential sensing, i. e., modulation of the probe-to-sample separation, does not suppress its stray capacitance efficiently [24].

A tip with proper radius of curvature and shielded as close to its apex as possible, would be the correct choice, as long as the used capacitance transducer would allow its application. The cantilevers should be shielded at least on their side facing the sample.

The unaccounted stray capacitance makes any analytic method based on calibration standards problematic. It can yield reliable data only if the pitch of the standard and of the analyzed structure are the same.

References

1 J. R. Matey, US Patent 4 481 616 (applied 30 September 1981, filed 6 November 1984).
2 C. D. Bugg and P. J. King, J. Phys. E **21**, 147 (1988).
3 H. P. Kleinknecht, J. R. Sandercock, and H. Meier, Scan. Microsc. **2**, 1839 (1988).
4 C. C. Williams, W. P. Hough, and S. A. Rishton, Appl. Phys. Lett. **55**, 203 (1989).
5 Š. Lányi, J. Török and P. Řehůřek, Rev. Sci. Instrum. **65**, 2258 (1994).
6 D. T. Lee and J. P. Pelz, Rev. Sci. Instrum. **73**, 3525 (2002).
7 *International Technology Roadmap for Semiconductors*, 1999 ed. (Semiconductor Industry Association, San Jose, CA, 1999).
8 Š. Lányi and J. Török, J. Electr. Eng. **46**, 126 (1995).
9 Š. Lányi, J. Török and P. Řehůřek, J. Vac. Sci. Technol. B **14**, 892 (1996).
10 Š. Lányi and M. Hruškovic, J. Phys. D: Appl. Phys. **36**, 598 (2003).
11 Š. Lányi, Acta Phys. Slovaca **52**, 55 (2002).
12 G. H. Buh, Chi Tran, and J. J. Kopanski, J. Vac. Sci. Technol. B **22**, 417 (2004).
13 J. F. Marchiando and J. J. Kopanski, J. Appl. Phys. **92**, 5798 (2002).
14 Š. Lányi, Surf. Interface. Anal. **27**, 348 (1999).
15 N. C. Bruce, A. Garcia-Valenzuela, and D. Kouznetsov, J. Phys. D: Appl. Phys. **33**, 2890 (2000).
16 L. Ciampolini, M. Ciappa, P. Malberti, and W. Fichtner, Solid St. Electron. **46**, 445 (2001).
17 Š. Lányi, čs. čas. fyz. **53**, 120 (2003).
18 Š. Lányi and M. Hruškovic, in *ECOSS22 – European Conference on Surface Science, Prague*, September 8–12, 2003, Surf. Sci..
19 O. C. Zienkiewicz, *The Finite Element Method* (McGraw-Hill, New York, 1977).
20 L. Dědek and L. Dědková, MEP 6.0, Faculty of Electrical Engineering and Computer Science, Technical University of Brno, Brno, Czech Republic.
21 H. Tomiye, H. Kawami, and T. Yao, Appl. Surf. Sci. **117/118**, 166 (1997).
22 R. C. Barrett and C. F. Quate, J. Appl. Phys. **70**, 2725 (1991).
23 Š. Lányi and M. Hruškovic, Rev. Sci. Instrum. **73**, 2923 (2002).
24 Š. Lányi, Ultramicroscopy, in press.

35
Atomic Force Microscope Tip Influence on the Fractal and Multi-Fractal Analyses of the Properties of Randomly Rough Surfaces

P. Klapetek, I. Ohlídal, and J. Bílek

Abstract

In this chapter, several fractal and multi-fractal analysis methods are studied to characterize their efficiency on evaluating fractal properties of randomly rough surfaces. Moreover, results concerning the estimation of atomic force microscopy (AFM) tip influence on evaluation of fractal properties of rough surfaces are presented. Randomly rough surfaces are simulated by means of spectral synthesis method and AFM tip convolution with the simulated surface is numerically performed. The results of the fractal and multi-fractal analysis before and after tip convolution are compared. It is shown that significant discrepancies can be observed between different fractal analysis methods applied on the same simulated data. This fact is true, in particular, if the data are convolved with AFM tip having relatively large apex radius in comparison to objects forming surface roughness.

35.1
Introduction

In practice, objects exhibiting random properties are encountered. It is often assumed that these objects exhibit the self-affine properties in a certain range of scales. Self-affinity is a generalization of self-similarity which is the basic property of most of the deterministic fractals. A part of self-affine object is similar to whole object after anisotropic scaling. Many randomly rough surfaces are assumed to belong to the random objects that exhibit the self-affine properties and they are treated self-affine statistical fractals. Of course, these surfaces can be studied using atomic force microscopy (AFM). The results of the fractal analysis of the self-affine random surfaces using AFM are often used to classify these surfaces prepared by various technological procedures [1–4].

However, it is known that a process of measurement frequently influences the values of quantities characterizing the randomly rough surfaces determined using

Nanoscale Calibration Standards and Methods: Dimensional and Related Measurements in the Micro- and Nanometer Range.
Edited by Gunter Wilkening, Ludger Koenders
ISBN: 3-527-40502-X

AFM. Finite dimensions of the tip of the atomic force microscope mainly influence these results.

In this chapter, the influence of the tip on the fractal and multi-fractal properties will therefore be studied. It should be noted that the influence of AFM measurements on the results of the fractal analysis was partially investigated in several chapters [5, 6]. In these chapters, it was shown that it could be very problematic to compare the results of the fractal analysis of the surfaces obtained by different analytical methods. In this chapter, we compare results of different fractal analysis methods on simulated data having known fractal properties. This enables us to determine properties of different fractal analysis methods and to compare different methods mutually. Using the simulation of AFM measurement for our simulated data we can determine the tip convolution effect on determined fractal properties.

Moreover, we employ the multi-fractal analysis for studying the AFM tip influence on the fractal properties of randomly rough surfaces. In contrast to the fractal analysis the multi-fractal one is more complex and complicated. This multi-fractal analysis enables us to determine more parameters characterizing the random surfaces. For the multi-fractal analysis, we will also study the AFM tip convolution influence on the results of this analysis.

35.2 Data Simulation and Processing

For simulation of the surfaces with the well-defined multi-fractal properties, a spectral synthesis method is used (see, e. g., [7]). This method is designed to produce surfaces with the properties of the fractional Brownian surfaces. Fractional Brownian motion (fBm) is an extension of regular Brownian random walk for which the correlation between successive steps is controlled by a parameter H known as the Hurst exponent. The spectral synthesis method enables us to define the required Hurst exponent H of the surface (measure of the regularity) that is connected with the fractal dimension D_f of the surface as $D_f = 3 - H$.

The result of the spectral synthesis method is a surface with an important property – its intersection with any plane parallel to z-axis represents a fractional Brownian motion realization. The surface generated by means of this method has a self-affine property characterized by a given fractal dimension D_f.[7].

We have tested all the fractal and multi-fractal analysis methods on the sets of isotropic fractional Brownian surfaces generated by the spectral synthesis method. We used a set of 25 images (1024×1024 points) for each fractal dimension within the interval (2.1, 2.2, . . ., 2.9) and we averaged the results obtained by these images.

It is known that some artifacts (systematic errors) arise in AFM measurements of all fine structures. The main artifact concerns the "tip convolution" due to the fact that the tip exhibits finite linear dimensions (i. e., the tip has not an ideal form represented by the δ-function). This effect causes a misrepresentation of

the data describing a fine surface geometry studied. Here, we shall deal with the theoretical analysis concerning the influence of the tip dimensions on the values of the fractal and multi-fractal properties characterizing the surface roughness based on the following stages:

1. The self-affine surface structure is simulated by means of the spectral synthesis method (see above). Further, the fractal properties of this simulated surface are determined.
2. Using the Villarubia's algorithm [8] an AFM image of the simulated surface is simulated for a chosen AFM tip geometry.
3. The fractal and multi-fractal properties are determined using the data corresponding to this image, i. e., using the data corresponding to the structure influenced by the tip dimensions (uncorrected structure).

For this purpose, the procedure presented by Villarubia [8] has been employed in this chapter. This procedure (tip–sample dilation) enables us to include the influence of the finite dimensions of the tip on the geometry of the surface measured, i. e., it enables us to construct the surface measured using an AFM tip.

For the purposes of our theoretical analysis, we have selected a model of the standard pyramidal contact AFM tip (i. e., this tip is formed by a pyramid with a spherical apex). The apex radius was equal to 10–50 nm. This assumption corresponds to the real contact or noncontact tip properties.

35.3 Fractal Properties Analysis

We have used the four different methods for the determination of the fractal dimension of our simulated data. For each fractal dimension within the interval (2.1, 2.2, ..., 2.9) we have simulated 25 images and we have analyzed them by corresponding method. Error bars plotted in these figures show root mean square deviation of the fractal dimension obtained by averaging analyzed fractal dimensions over the set of 25 different images generated with same fractal dimension.

Cube counting method [1, 5] is derived directly from a definition of box-counting dimension

$$D_f = \lim_{l \to 0} \frac{\log N(l)}{\log l^{-1}},$$

where $N(l)$ is the smallest number of cubes with size l we need for covering whole surface. This means that we expect a self-similar character of the surface. The algorithm is based on the following steps: a cubic lattice with lattice constant l is superimposed on the z-expanded surface. Initially l is set at $X/2$ (where X is the length of the edge of the surface), resulting in a lattice of $2 \times 2 \times 2 = 8$

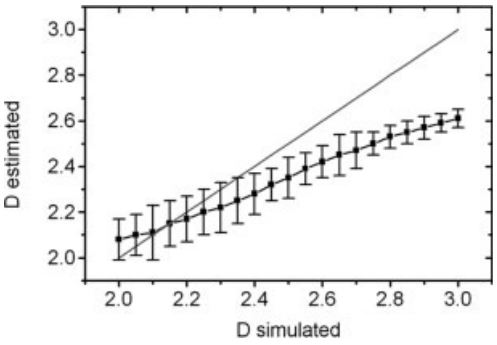

Fig. 35.1 Dependence of the estimated fractal dimension on real fractal dimension of the simulated surface using the cube counting method. Red line corresponds to the ideal result.

cubes. $N(l)$ is then number of all cubes that contain at least one pixel of the image. Lattice constant l is then reduced stepwise by factor of 2 and the process repeated until l is equal to the distance between two adjacent pixels. The slope of a plot of $\log(N(l))$ versus $\log(1/l)$ gives fractal dimension D_f directly. Results of the analysis of simulated surfaces by means of cube counting method are presented in Figure 35.1.

Triangulation method [1] is very similar to the cube counting method. Here, we again expect a self-similar character of the surface (Z is chosen to equal the X and Y ranges). For the surface area it is true that $S(l) \sim N(l)l^2$; moreover, $N(l) \sim l^{-D_f}$, thus we obtain relation for fractal dimension

$$D_f = \lim_{l \to 0} \frac{\log S(l)}{\log l^{-1}} + 2,$$

where l has the same meaning as in the cube counting method. A grid of unit dimension l is placed on the surface. This defines the location of the vertices of a number of triangles. When $l = X/4$, for example, the surface is covered by 32 triangles of different areas inclined at various angles with respect to the x–y plane. The areas of all triangles are calculated and summed to obtain an approximation of the surface area $S(l)$ corresponding to l. The grid size is then decreased by successive factor of 2, as before, and the process continued until l corresponds to distance between two adjacent pixel points. The slope of a plot of $\log(S(l))$ versus $\log(1/l)$ is then corresponding to $D_f - 2$. Results of the analysis of simulated surfaces by means of triangulation method are presented in Figure 35.2.

The *variance* method [2, 6] is based on the fact that variance of fractional Brownian motion obeys this law:

$$\mathrm{var}(Z(x_2) - Z(x_1)) \sim |x_2 - x_1|^{2H}.$$

As it is true that $D_f = 3 - H$, it is simple to calculate the fractal dimension.

In practice, in the variance method one divides the full surface into equal-sized squared boxes, and the variance σ^2 is calculated for particular box size as

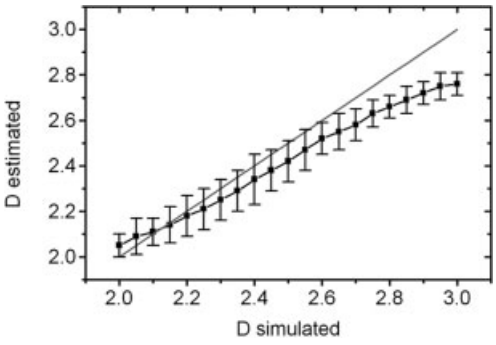

Fig. 35.2 Dependence of the estimated fractal dimension on real fractal dimension of the simulated surface using the triangulation method. Red line corresponds to the ideal result.

$$\sigma^2(B) = \left\langle \frac{1}{B^2-1} \sum_{i=1}^{B^2} (z_i - \bar{z})^2 \right\rangle$$

where B^2 is total number of data points in one box, z_i is the height in each point, $\bar{z}$ is the average height in a box, and $\langle \cdots \rangle$ denotes averaging over all nonoverlapping boxes covering the total image. Fractal dimension is evaluated from the slope β of a least-square regression line fit to the data points in log–log plot of $\sigma^2(B)$ as $D_f = 3 - \beta/2$. Results of the analysis of simulated surfaces by means of variance method are presented in Figure 35.3.

Power spectrum method [2, 6, 9] is based on the fact that the power spectrum of fractional Brownian motion obeys the following law:

$$P(\omega) \sim \omega^{-(2H+1)}.$$

In the power spectrum method, every line height profiles that forms the image is Fourier transformed and the power spectrum evaluated and then all these power spectra are averaged. Fractal dimension is evaluated from the slope β of a least-square regression line fit to the data points in log–log plot of $P(\omega)$ as $D_f = 7/2 - \beta/2$. The results of the analysis of the simulated surfaces by means of power spectrum method are presented in Figure 35.4.

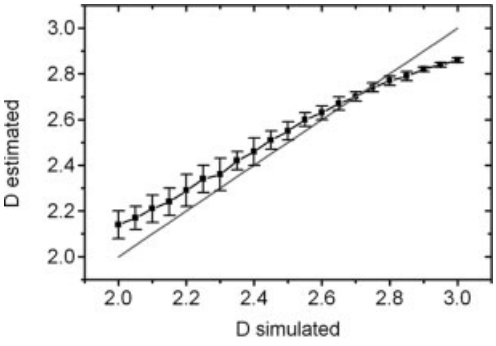

Fig. 35.3 Dependence of the estimated fractal dimension on real fractal dimension of the simulated surface using the variance method. Red line corresponds to the ideal result.

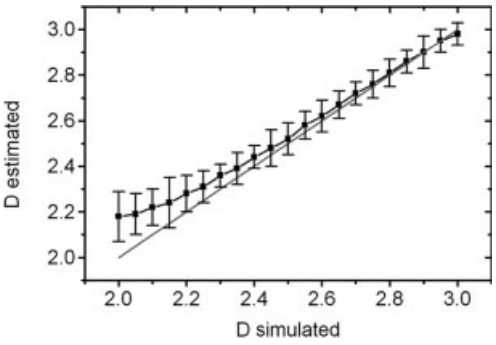

Fig. 35.4 Dependence of the estimated fractal dimension on real fractal dimension of the simulated surface using the power spectrum method. Red line corresponds to the ideal result.

35.4 Multi-Fractal Properties Analysis

For the multi-fractral analysis, we used two methods. the *correlation function* method [10] is based on the measurement of one-dimensional correlation function defined as follows:

$$G_{x,q}(\tau_x) = \frac{1}{N(M-m)} \sum_{l=1}^{N} \sum_{n=1}^{M-m} |z_{n+m,l} - z_{n,l}|^q,$$

where $m = \tau_x/\Delta$, $N \times M$ is scan size (N and M denote the numbers of rows and columns in the scan), z_{nl} and $z_{n+m,l}$ represent the values of the heights of the irregularities of the surface in two different points of this surface, τ_x is the distance between these two points along x-axis, Δ is the sampling interval, and q is the order of the correlation function. Note that the one-dimensional correlation function is only determined along the rows of the scan.

Below, it will be assumed that the scaling behavior of the function $G_{x,q}$ is given as

$$G_{x,q}(\tau_x) \sim \tau_x^{qH_q},$$

where H_q denotes the Hurst exponent corresponding to the given order of the correlation function. If all the coefficients H_q are equal, the above equation describes a self-affine surface with mono-fractal properties. If the coefficients H_q are different for at least some values of order q we talk about surface having multi-fractal properties. These surfaces can be described by a set of the values of H_q.

In Figure 35.5, the results of correlation function method applied on the simulated surfaces are plotted. It can be seen that the coefficients H_q are constant and the results of the evaluated fractal dimension correspond to the real fractal dimension of the simulated surfaces.

The *wavelet transform modulus maxima* (WTMM) method is based on the ability of the continuous wavelet transform to detect singularities. Wavelet transform of the one-dimensional signal $f(x)$ is defined as

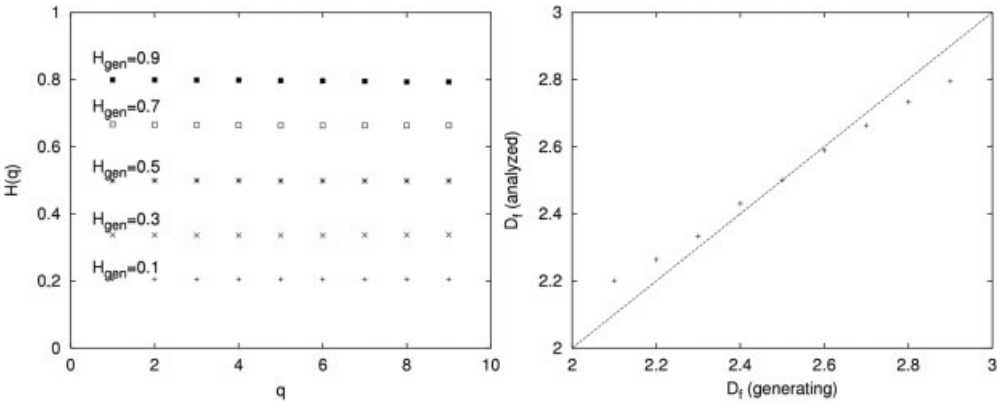

Fig. 35.5 The dependences of the Hurst exponent evaluated for different orders q of correlation function (right) and the dependence of the estimated fractal dimension on the real fractal dimension of the simulated surface using correlation function method (left). Line corresponds to the ideal result.

$$W[f](a,b) = \frac{1}{\sqrt{|a|}} \int_{-\infty}^{\infty} f(x)\varphi^*\left(\frac{x-b}{a}\right) \mathrm{d}x$$

where function $\varphi(x)$ is called wavelet, parameter a controls scale of the wavelet (its magnification), and parameter b controls its shift along the time axis. Wavelet transform does a decomposition of the signal into space–frequency domain in a way similar to windowed (short-time) Fourier transform. However, in contrary to windowed Fourier transform, the spatial resolution of different frequency components is not same, but depending on the frequency of the component (determined by corresponding scale parameter). When going toward smaller scales, the wavelet transform of a signal shows more and more details of the signal. Therefore, it is sometimes called as "mathematical microscope" [11]. It can be shown that these properties of the wavelet transform can be efficiently used for determining properties of singularities in the signal. For practical implementation, we used method developed by Arnéodo et al. [12] for multi-fractal analysis of the 2D data. We will only describe the method very roughly here (for details see [12]). The WTMM method is based on the following steps:

1. Wavelet transform modulus is computed for different scales a of the wavelet.
2. Local maxima of wavelet transform modulus are found in the directions of the wavelet modulus gradient. These maxima form connected chains.
3. Local maxima within connected chains are found. These points are used for further computation.
4. Points found in the previous step are interconnected through all scales a of the wavelet. This forms the so-called wavelet transform skeleton.

5. Scale adaptive partition function $Z(q,a)$ is computed from the wavelet skeleton.

It is then assumed that the scale adaptive partition function has the following scaling properties:

$$Z(q,a) \sim a^{\tau(q)}$$

where q is the order of scale adaptive partition function. The fractal properties of the surface can be then evaluated from the scaling exponents. For example, the fractal dimension is given by equation

$$D_f = \max(2,1-\tau(1)).$$

It can be shown that for the fractional Brownian motion the scaling exponents are connected with the Hurst exponent H of the surface as

$$\tau(q) = qH-2,$$

i. e., the $\tau(q)$ function is a linear function of q with slope given by the Hurst exponent. The linearity of the function is thus a sign of mono-fractal properties of the surface. Moreover, from the dependencies of $\tau(q)$ it is possible to determine the Hurst exponent of the surface.

In Figure 35.6, the results of WTMM method while analyzing the simulated data are plotted. It can be seen that the dependencies of $\tau(q)$ are linear and the estimated fractal dimension corresponds to the real fractal dimension of the simulated surfaces.

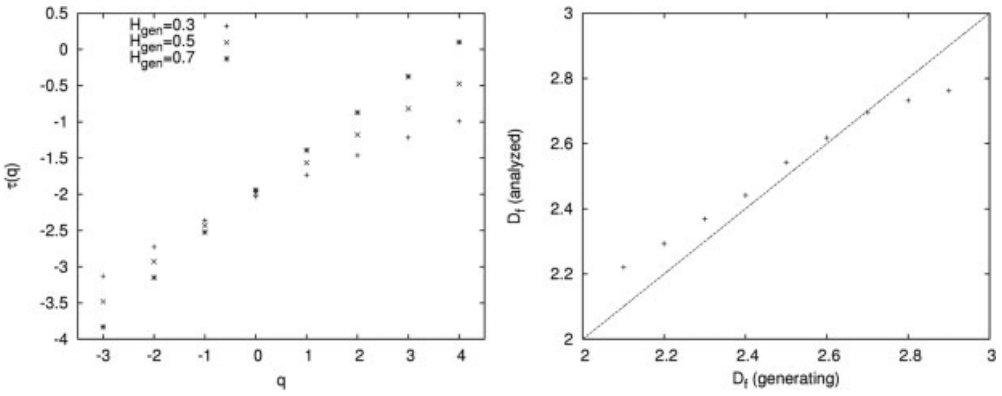

Fig. 35.6 The dependences of scaling exponent $\tau(q)$ evaluated for different orders q of scale adaptive partition function (left) and the dependence of the estimated fractal dimension on real fractal dimension of the simulated surface using WTMM method (right). Line corresponds to the ideal result.

35.5 Results and Discussion

From Figures 35.1–35.4, we can deduce some estimation about the efficiency of different fractal analysis methods. It can be seen that the two simplest methods based directly on fractal dimension definition – the cube counting and triangulation – produce relatively poor results. The results of the variance method and power spectrum method are relatively better. However, the methods generally fail for small and high fractal dimension values. Moreover, the error of the fractal dimension estimation (here based on repeated estimations on different realizations of fractional Brownian motion) is relatively high for all the methods.

In Table 35.1, the results of fractal analysis of the simulated surfaces convolved with AFM tip are presented. Tip convolution effects on evaluating fractal dimension of the simulated data can be seen. The influence of tip is different for different methods. In the cube counting and triangulation methods the effect is very similar. The convolution of the tip and image does not affect the linearity of the graphs from which the fractal dimension is evaluated. However, the estimated fractal dimension of the surfaces is lowered. In the case of the variance and power spectrum methods, the situation is inverse to situation before. The linearity is affected mainly in short values of the length, but if we use only the part of graph which is not affected we can obtain a good result; however, it is debatable whether we can ignore the nonlinear part.

In Figure 35.7, the results of the CF and WTMM methods by analyzing the multi-fractal properties of simulated and convolved data are plotted. It can be seen that the dependencies of $H(q)$ and $\tau(q)$ are losing their linear character. After the tip convolution, the image of surface loses its mono-fractal character as artificial multi-fractal properties are introduced. These effects could explain

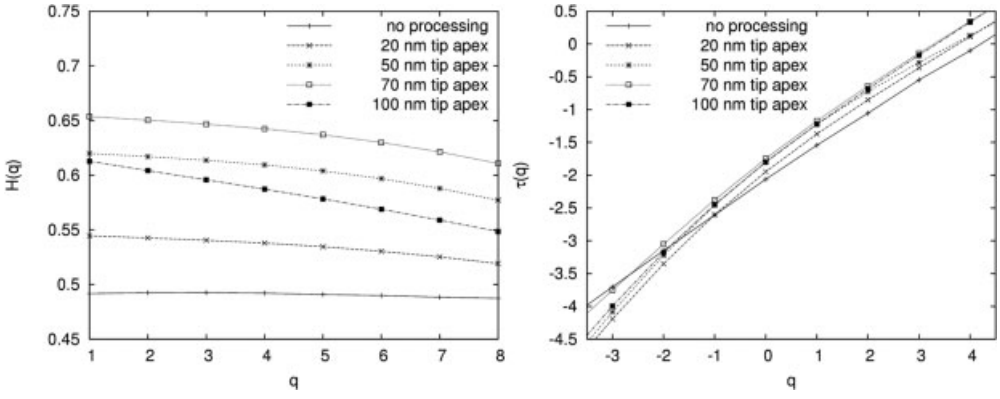

Fig. 35.7 The dependences of the Hurst exponent evaluated for different orders q of the correlation function for data convolved with AFM tip (left) and the dependences of scaling exponent $\tau(q)$ evaluated for different orders q of scale adaptive partition function for data convolved with AFM tip (right).

Table 35.1 Fractal dimension evaluated on the same simulated data convolved with the tips having radius of 0, 10, 30, and 50 nm

	$R = 0$ nm	$R = 10$ nm	$R = 30$ nm	$R = 50$ nm
Cube counting	2.48	2.44	2.36	2.33
Triangulation	2.59	2.56	2.47	2.44
Variance	2.71	2.69	2.67*	2.65*
Power spectrum	2.72	2.68	2.55	2.46

large errors obtained within fractal analysis of real surfaces measured by means of AFM, as the tip convolution can change the surface properties. Real surface fractal properties (predicted by means of growth or crack theories) can be therefore obscured by the AFM measurement influence.

35.6 Conclusion

It was shown that the accuracy of different fractal analysis methods varies very strongly. It is therefore difficult to compare the results obtained by means of different fractal analysis methods. The variance method and power spectrum method were found to produce satisfactory results. However, in the presence of the strong tip convolution effects the accuracy of all the methods is significantly decreasing.

It was also shown that the tip convolution effects could change the estimated value of fractal dimension. Moreover, they can also introduce a nonlinearity into the multi-fractal spectra that is not present in the original surface. This fact should therefore be respected when interpreting the results concerning the fractal properties of randomly rough surfaces evaluated using the AFM.

The practical meaning of both of these theoretical analyses consists in the numerical evaluation of the tip influence on the fractal properties of surfaces that are estimated to be self-affine. The results of this analysis can enable us to perform the rough estimation of the errors achieved within AFM studies of these surfaces.

References

1 C. Douketis, Z. Wang, T. L. Haslett, and M. Moskovits, Phys. Rev. B **51**(16), 15 (1995).

2 A. Van Put, A. Vertes, D. Wegrzynek, B. Treiger, and R. Van Grieken, Fresenius J. Anal. Chem. **350**, 440 (1994).

3 J. Krim and G. Palasantzas, Int. J. Mod. Phys. B **9**, 599 (1995).

4 J. M. Gómez-Rodríguez, L. Vázquez, and A. M. Baró, Surf. Int. Anal. **16**, 97 (1990).

5 W. Zahn and A. Zösch, Fresenius J. Anal. Chem. **365**, 168 (1999).

6 A. Mannelquist, N. Almquist, and S. Fredriksson, Appl. Phys. A **66**, 891 (1998).

7 T. H. Keitt, Landsc. Ecol. **15**, 479 (2000).

8 J. S. Villarubia, J. Res. Natl. Inst. Stand. Technol. **102**, 425 (1997).

9 W. Zahn and A. Zösch, Fresenius J. Anal. Chem. **358**, 119 (1997).

10 A. L. Barabási, R. Bourbonnais, M. Jensen, J. Kertész, T. Vicsek, and Y-Ch. Zhang, Phys. Rev. A **45**, R6951 (1992).

11 Z. R. Struzik, Fractals **8**, 163 (2000).

12 A. Arnéodo, N. Decoster, and S. G. Roux, Eur. Phys. J. B **15**, 567 (2000).

Part X
Application – Material Properties

Nanoscale Calibration Standards and Methods: Dimensional and Related Measurements in the Micro- and Nanometer Range.
Edited by Gunter Wilkening, Ludger Koenders
ISBN: 3-527-40502-X

36
Atomic Force Microscope Indentation Measurement Software

David Shuman

Abstract

Hardness testing could be a convenient method to measure the mechanical properties of materials from nanometer to millimeter deep indentations, however as the depth of the indentation decreases the difficulty in measurement increases. The objective of this chapter was to use an atomic force microscope to measure hardness indentations accurately. Automated computerized image analysis software was developed that measured the indentation depth, projected area, and contact area. The residual indent was digitally reconstructed into the same shape as the fully loaded indentation. The reconstructed image was used to calculate the projected area function and contact area function. This software was accurate enough to measure the hardness of a single indentation quantitatively. The measurement error was small enough to observe variation in hardness at the nanoscale. This computerized software provides all researchers with a standardized indentation measurement technique from any type of scanning probe microscope.

36.1
Introduction

There is a need for a method to measure hardness test indentations accurately at both the microscopic and nanoscopic scales (Figure 36.1). ISO 14577-1 describes two types of hardness, which will be discussed in this chapter, the Indentation Hardness H_{IH} (Equation 36.1) and Martens Hardness H_M (Equation 36.2) [1]. Martens hardness includes both the plastic and elastic deformation contact area and can be used for either Vicker's or Berkovich style indenters.

$$H_{IH} = \frac{\text{Force}}{\text{Projected Area}}\,, \tag{36.1}$$

$$H_M = \frac{\text{Force}}{\text{Contact Area}}. \tag{36.2}$$

Nanoscale Calibration Standards and Methods: Dimensional and Related Measurements in the Micro- and Nanometer Range.
Edited by G. Wilkening and L. Koenders

ISBN 3-527-40502-X

Small-scale hardness results for plastic, metals, and ceramics appear to increase with decreasing indentation size, commonly called the indent size effect (ISE) [2]. Rodríguez and Gutierrez carried out a series of indentation tests using a nanoindenter from the nanometer to micrometer depth on different metals with all of the results showing ISE. However, research by Nix and Doerner [3] observed that when the contact area was measured correctly for single crystal silicon the hardness remained constant.

A hardness test is done by forcing an indenter into a material. The projected area and contact area are then determine and used to calculate the desired hardness type. This chapter focused on improving the measurement of the projected area and contact area measurement at the nanoscale.

Hardness testing at the nanoscale refers to the depth of the indentation, but could be associated with grain size or film thickness. Monolithic, or amorphous materials should have a constant hardness from the nanometer to millimeter depths. As the indentation depth decreases into the nanometer depth regime a broad range of hardness are expected for most materials. At the nanoscale polycrystalline and multiphase materials should have a range in hardness depending on the location of the indenter. The shape of the indenter and how it is orientated compared to the crystal structure could also influence the hardness. Computer simulation predicts that as the grain size decreases it will reach a peak strength and then decrease. Similarly to this model of the grain size strength could also influence the hardness [4].

Current technology depends on using a device called a depth sensing indentation (DSI) tester to measure nanohardness [5]. A DSI records the displacement and force during indentation. By analyzing the shape of the unload curve it is possible to determine the penetration depth. The depth and geometry of the indenter are used to determine the contact area. The maximum force and contact area are used to calculate the hardness. The main advantage of using the DSI over other hardness testing technique such as Rockwell and Vicker's is that the resulting indentation does not have to be imaged and make a measurement manually. For example, Vicker's hardness testers require a person to visually measure using an optical microscope to measure the diagonal across the residual indentations.

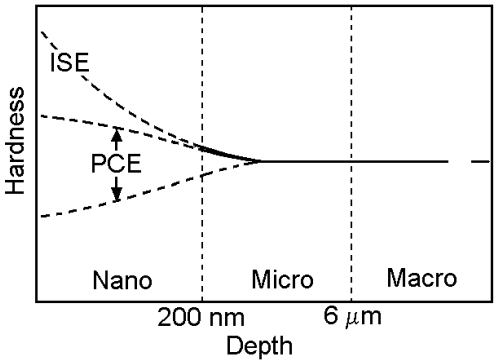

Fig. 36.1 The predicted hardness with decreasing indentation depth based on the indent size effect (ISE) and the polycrystalline effect (PCE).

How the microscope is focused and where the operator chooses to measure the diagonal causes a variation in the results. The DSI technique avoids having to measure the indentation shape manually. However, there are several uncertainties associated with the depth sensing indentation method such as frame compliance, thermal drift, zero contact point, tip rounding, and depth measurement sensitivity. Because of these technology problems it is uncertain whether the hardness test variation such as the ISE is caused by the material or by the instrument measurement error. Herrmann et al. wrote that the geometry of the indenter always causes the greatest uncertainty [6]. VanLandingham of National Institute of Standards and Technology (NIST) did a review study of nanoindentation testing in 2003 and concluded that better measurement methods are needed [7]. Nazarov et al. [8] published an article in Microscopy and Analysis magazine in September 2003 about nanoindentation testing and stated that the measurement of indents from an AFM image was too complicated and unreliable and preferred using a nanoindenter with the Oliver–Pharr method [5]. Several other research papers related to nanoindentation discussed the need to improve the indenter contact area measurement [9–12]. It would be advantageous to measure the indentation shape using the AFM instrument.

The state-of-the-art method for AFM indentation area determination is to use a technique called Threshold. Many image analysis software packages use threshold such as the popular NIH, or NanoScope. Threshold is done by dividing a grayscale image into a binary image above and below a grayscale value or in the case of AFM images its height. For the indentation research the threshold is commonly used to measure the projected area. After doing the threshold the highlighted binary pixels are summed to equal the projected area. In order to avoid the surrounding surface noise the threshold height is commonly slightly below the native surface height, which causes a projected area measurement error. However, the outline around indents are more complex than the flat plane assumption used for Threshold because of sink-in and pile-up.

The most critical scientific problem for this research is that the AFM residual indent image only presents the resulting plastic deformation. A standard AFM image could be used to measure the indentation hardness, which is the force divided by the projected area, because the projected area does not change during unloading (details see below). However, Martens and Vicker's hardness requires measuring the indenter to sample contact area at full load including both the elastic and plastic deformation. Hardness determination becomes even more complicated from an AFM image because of the three-dimensional shape, computer processors speed, graphical user interface, and RAM memory utilization.

This chapter describes new computerized image analysis software, called NanoMc, developed by the author [13]. The NanoMc automatically measures the indentation shape from an atomic force microscope (AFM) image. It was written using Microsoft® Visual C++. Two dynamic link library (DLL) programs were made that plug into NanoScope 5.12 or 5.13 from Veeco Instruments and into SPIP from Image Metrology. The NanoScope and SPIP software's handle the complicated graphical user interface. The advantage of the SPIP program is

that it imports a wide variety of scanning probe microscopes (SPM) image types. NanoMc automatically measures any size indent in any material with or without the pile-up area and the possibility of sink-in. By using this software only the force is required from an indentation tester to calculate the hardness.

An object character recognition type of technique was developed to locate the indent in the image. Then the NanoMc software measured the residual indent depth, projected area, and surface area. It has a function that digitally reconstructs the residual indent to equal the fully loaded indentation shape including both the elastic and plastic deformation. The contact depth and contact area are then measured from the elastically reconstructed image. The reconstructed image was used to calculate the projected area and contact area functions from a single indent. These functions have several useful applications for indentation analysis. For example, it could be used to calibrate a depth sensing indentation tester. Another application would be to use the projected area to calculate the contact depth and contact area based on the theory that the projected area stays the same after unloading [14].

36.2 Experimental Details

The experimental objective was to test the accuracy and usability of the NanoMc AFM indentation measurement software techniques. A Shimadzu DUH-W201S hardness tester was used to make the indentations with a Berkovich indenter. This test machine was only used to make the indentation and not to measure the hardness. Old and new Berkovich indenters were used. The contact area was measured using an AFM. The DSI owner's manual stated that the force range for this device was from 0.196 to 1961 mN with an accuracy of ± 19.6 μN and a displacement range from 0.001 to 10 μm $\pm 2\%$ of full scale. The force given by this DSI was assumed to be accurate to within the manufacture specifications. After indentation the samples were imaged with an AFM. There were 32 indents imaged with 13 in 6066-O aluminum, 15 in 1020 steel and four in electrolytic copper. Prior to imaging the AFM scanner was calibrated (for details see below).

AFM images were made of the indentations. The projected area and contact area were determine with the NanoMc and used to calculate the hardness. The contact depth was used to determine the Vicker's hardness. This Vicker's hardness is similar to that measured with a DSI, because it equals the contact area between the indenter and the sample at full load according to ISO 14577-1. However, this research is different from the ISO described method because it uses an AFM to measure the contact area.

Indenters wear down during service. When the indenter tip becomes too rounded the results are unreliable. It is therefore important to monitor the tip shape in order to know when it should be replaced. The NanoMc projected area function was used to determine the indenter angle and tip radius. The

NanoMc tip shape measurement technique was tested on an old and new Berkovich indenter.

36.2.1 Sample Preparation

Samples of 6066-O aluminum, 1020 steel, and electrolytic copper were chosen for these experiments because they are readily available. The samples came in the form of a 2.54 cm diameter rod. The rods were cut into round samples and then mechanically polished. They were hand sanded with 240, 400, 600, 800, and 1500 grit SiC wet sandpaper. Next suspended diamond 3 μm was used for 3 min and then 1 μm for 2 min. The final polish was done with an industrial polishing agent called Struers® OP-S. The resulting surface root-mean-square (RMS) roughness over a 10 μm by 10 μm scan area was 4.5 nm for aluminum, 2.6 nm for steel, and 3.8 nm for copper. Struers® OP-U was used for the final polishing step on a second steel sample. The OP-U solution highlighted the pearlite and ferrite microstructures of steel.

36.2.2 Indentation Procedure

Indents from 250 to 900 nm were made into the three samples. The laboratory conditions were temperature 20°C and relative humidity 60 %. The test setup was slightly different for the old and new Berkovich indenter. The approach rate on the old indenter samples was 10 s and on the new indenter samples was 30 s. A scratch mark was intentionally made on the sample as a reference point. The indentations were placed near the end of the scratch mark so that they could easily be found with the AFM optical microscope. Indents of the same force were placed in a straight line equally spaced so they could be distinguished from the randomly scattered debris.

36.2.3 AFM Calibration

A Veeco Instruments Dimension 3100 AFM was used to image the residual indents. However, before the indents were imaged the AFM was calibrated. The manufacture recommended calibration procedure was used with a 1 μm grid pattern. This method involves various scan rates, scan sizes, and scan orientations. After many images are recorded the length was measured for each image and used to determine the x and y calibration factors. The scanner z was calibrated by imaging a standard grid with a step height of 800 nm. Several other calibration samples were imaged to determine the scanner accuracy. It was determined that this AFM had an error of less than 5 % for the x-, y- and z-directions in the x–y scan size of 0.5–40 μm and z height from 0 to 800 nm using a 1 Hz scan rate, after the scanner had relaxed. The scanner was considered relaxed when the me-

chanical polishing scratches appeared straight. It usually required one scan area time for the scanner to relax. The scanning parameters were adjusted so that the scanning probe created an accurate image down to the lowest point inside the indent.

36.2.4 Surface Height and Roughness

The NanoMc software has many internal functions for locating and measuring the indent shape. Two of the main functions are surface height and roughness. The surface height is the plane of the virgin surface and roughness is one standard deviation from this plane. For a uniform indent free surface the average of all the pixels can be used to calculate the surface heights [15]. However, the averaging method does not work when there is an indent, which falsely decreases the depth and increases the roughness. This would cause an error in all the indentation shape measurements. Any pixels that were altered because of the indentation had to be eliminated. These pixels are in an area called the indent-effected-zone (IEZ). To avoid the IEZ pixels a height probability distribution was used to measure the surface height and roughness. This is a histogram of the pixel heights. A majority of the pixels occur at the surface height, which is at the apex of the histogram except for the surface roughness noise. By taking the full-width-half-maximum (FWHM) of this distribution avoids the IEZ and the surface roughness noise. The average at the FWHM equals the surface height and the width equals the roughness. This method works best when the indent covers less than half the image area. The distance between the "surface height" to the indent minimum gives the indent depth. The projected area and surface area also depend on the surface height and roughness measurement.

36.2.5 Projected Area

The indent area must be separated from the rest of the image in order to measure its shape. To do this the software creates digital outlines around the residual indent [16]. All the pixels inside this area are considered to be part of the projected area or surface area. There are two types of outlines called the "surface outline" and "pile-up outline" (Figure 36.2). The surface outline was the main topic for this research, because it is used to determine the projected area and contact area similar to that defined in ISO 14577-1. Placing the outline correctly is crucial for making accurate hardness measurements.

After finding the indent in the image area it was digitally divided into many *x*-sections 360° around the indent (Figure 36.3). All the *x*-section lines start at the indent minimum and go to the image edge. The pile-up outline was included for future research as a method to measure the hardness more accurately. Current standard hardness testing procedures only require the indenter contact area below the surface height.

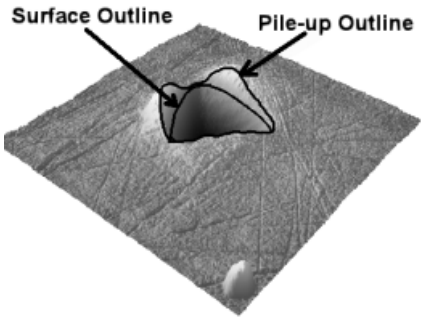

Fig. 36.2 A 3D AFM image of an indent with the surface outline and pile-up outline.

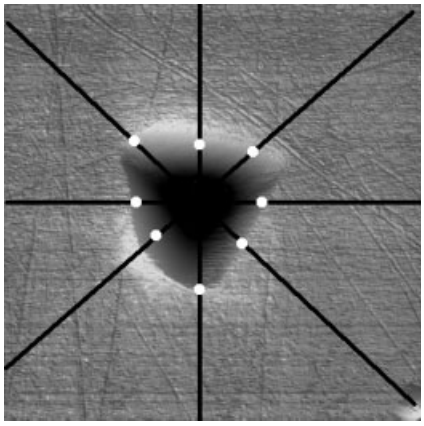

Fig. 36.3 X-sectioning 360° to locate the indent outline points.

Each of the section lines is analyzed to build the outlines. The surface outline is where the indent crosses the surface height plane or virgin sample surface as shown by white dots in Figure 36.3. The pile-up outline includes all the area where the indenter made contact with the sample surface.

The NanoMc software finds three possible points, called the "sink-in point", "pile-up point" or "surface point" for each section line (Figure 36.4). Pile-up and sink-in both have a similar characteristic when considering where the indenter last made contact with the sample. A tangent line was taken in the upper portion of the section line, just below the surface height. When the height between the tangent line and surface height is more than three sigma times the roughness indicated a sink-in or pile-up point. If there was sink-in then the surface outline must trace below the surface height. The section points are connected together by straight lines to form the surface outline.

Adjusting a function called the "Tangent Height %" controls the quality of the outlines. It is used to correct for outline errors such as when the outline sometimes goes far beyond the trench area do to surface roughness. Normally the Tangent Height % was set to 95 % causing the top end to be 5 % less than the surface height and the bottom end to be 45 % of the surface height. However, for indents

with sink-in the Tangent Height % must be decreased to keep it from straying outside the indent area. Changing the Tangent Height % usually only has a small effect on the projected area outline even when it was adjusted to its full range from 50 to100 % (Figure 36.5) for smooth faced indents. When the residual indent bottom is curved because of tip rounding the Tangent Height % should be set to the maximum height.

The tip radius influence was measured by comparing a new shape indenter to an old indenter. The Tangent Height % was varied for a new and old Berkovich indenter. The new Berkovich indenter had the same projected area down to 80 % of the indent depth, however the old indenter began to deviate at 90 % Tangent Height %. When the Tangent Height % was set between 90 and 100 % for both the new and old indenters the projected area function had the same residual error of ± 0.74 %.

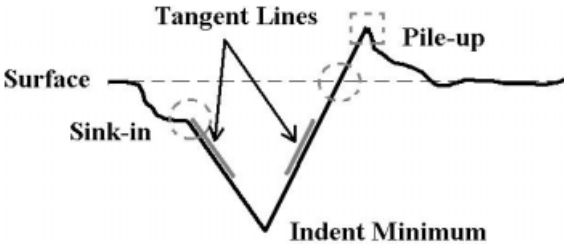

Fig. 36.4 A sketch of the tangent lines used by the software to locate the surface outline points (circled) and a pile-up point (squared).

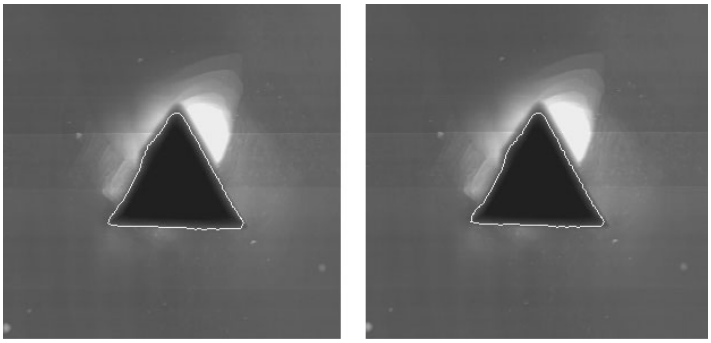

Fig. 36.5 The computer software generated surface outline shown in white at 50 % and 100 % Tangent Height %.

36.2.6
Projected Area

The projected area is the summation of the pixel area elements inside the surface outline that are in the same plane as the virgin sample surface. The area of each pixel is equal to the scan size divided by the sample rate. For example a 1 μm scan size with 512 pixels has a pixel width of 1.95 nm. A square pixel element has the area of 3.80 nm^2. A flood-fill technique was done from inside the outline to highlight each of the projected area pixels. As a test this projected area should be slightly more than the Threshold area discussed earlier. The new software automatically draws a white outline at the surface height on the results image for visual inspection. If the outline strays beyond the indent area then the Tangent Height % should be adjusted.

36.2.7
Surface Area

The surface area of the indent refers to the indent lining. It is the summation of all the pixel elements that cover the surface of the indent. The same pixels are used as with the projected area except now the height is considered. Each pixel surface area element has the shape of a quadrilateral because all four sides have different lengths (Eq. 36.5). A pixel quadrilateral element is made from the initial pixel at ($x0$, $y0$) to the neighbor pixels ($x1$, $y0$), ($x0$, $y1$), and ($x1$, $y1$). The distance measured between the pixel corners in three-dimensional space gives the four sides of the quadrilateral (s_1), (s_2), (s_3), (s_4), and its diagonal (d) from ($x1$, $y0$) to ($x0$, $y1$). The surface area is the summation of all the quadrilateral area elements under the projected area. The hardness contact area is measured in the same manner after doing the elastic reconstruction when the indent depth equals the contact depth.

Equation 5. The surface area of an indentation pixel element quadrilateral.

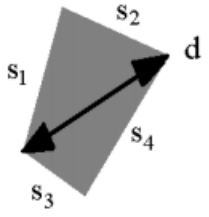

$$A = 0.5\,d\left[\sqrt{s_1^2 - \left(\frac{s_2^2 - s_1^2 - d^2}{-2\,d}\right)^2} + \sqrt{s_3^2 - \left(\frac{s_4^2 - s_3^2 - d^2}{-2\,d}\right)^2}\right]$$

36.2.8
Elastic Reconstruction

In order to measure the contact depth and contact area the indentation must be measured with both the plastic and elastic deformation. The NanoMc software adds the elastic deformation digitally back into the residual indent image. Stillwell and Tabor studied the shape of residual indents and found that the faces appeared to be smooth but at a lower slope than the actual indenter tip angle [14] (Figure 36.6). Finite element simulation and the observation of residual indents made in metals indicates that the diameter or the indent does not change upon unloading [17, 18]. The indent center experiences the greatest amount of force and therefore had the greatest elastic recovery. This software used the Stillwell and Tabor model as a basis for the elastic reconstruction method. However note that the Stillwell and Tabor model does not take into account asymmetric effects caused by crystallography, or microstructure.

Observe the difference from the indenter to the residual indent surface angles β_i and β_r in the schematic (Figure 36.6). By increasing the depth of each pixel proportional to its initial depth will increase the indent image face angle. To measure the contact depth and contact area it is desirable to make this angle equal to the indenter face angle. An equation was derived to calculate how much to increase the depth for each pixel element called the "elastic constant" (Eq. 36.3). The difference between the indenter angle (β_i) and the residual indent face angle (β_r) equals the elastic constant (ec).

$$ec = (\beta_i - \beta_r)/\beta_r. \tag{36.3}$$

Each pixel depth was increased by the elastic constant (*ec*) according to Eq. (36.4). The depth of each pixel $hf_{(x,\,y)}$ was measured from the surface height (h_{surf}). The elastic constant (*ec*) determined how much to increase the depth. All of the pixels inside the surface outline area increased in depth depending on its distance from the surface height. The pixel elements at the edge had little change in depth and the ones in the center had the most increase in depth. This effectively increased

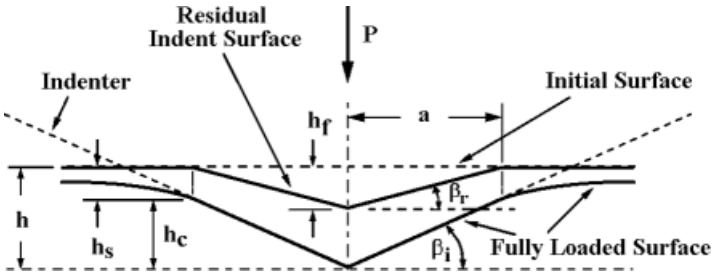

Fig. 36.6 The Stillwell and Tabor schematic of indentation loading and unloading with the indenter angle and residual angle added.

the face angle of the residual indent. By properly adjusting the elastic constant (*ec*) it is possible to reconstruct the indent image to have the same shape as the indenter even with tip rounding.

$$hc(x,y) = (h_{surf} - hf(x,y)) (1 + ec). \quad (36.4)$$

For verification of the elastic reconstruction process the resulting image should equal the contact depth and the angle of the sidewalls should equal the indenter face angle (β_i), typically 25° for a Berkovich indenter. The elastic reconstruction technique was tested on an AFM residual indent image in steel. The amount of elastic recovery was calculated using the known Berkovich indenter face angle which is $\alpha = 65°$. It was found more convenient to relate the indenter angle to the sample surface $\beta = (90° - \alpha) = 25°$. The angle of each sidewall face of the residual indent was measured as $\beta_1 = 21.335°$, $\beta_2 = 21.365°$, and $\beta_3 = 21.418°$ with an averaging of $\beta = 21.37°$. The elastic constant was calculated as the difference between the residual indent angle and the known indenter angle. In this case the elastic constant (*ec*) equaled 0.1699. The physical significance of the elastic constant value still needs to be studied. The software increased the depth of each pixel inside the indent surface outline. The resulting elastic reconstruction image was then re-measured to check if it correctly matched the indenter angle, $\beta_1 = 25.859°$, $\beta_2 = 24.650°$, and $\beta_3 = 24.509°$, which has an average of $\beta = 25.00°$ which equals the indenter face angle. The contact depth and contact area were determined from the elastically reconstructed image.

The average of all three faces of the Berkovich residual indent must be used to reduce the open-loop AFM scanner drift artifact. Scanner drift was seen by imaging the same indentation rotated 200°. The angle on each sidewall changed but the average was the same. For example the angle on one face was $\beta = 24.81°$. When the sample was rotated and re-imaged the same face was $\beta = 21.07°$, which showed that the AFM scanner caused an image artifact. This artifact was related to the trace direction of the scanner and the speed it enters and exits deep features. A closed-loop traceable scanning head could be used to reduce this error, however it was not studied as part of this research.

36.2.9
Building the Area Functions

The NanoMc software calculates the area functions from a single indent. First the indent image was elastically reconstructed. The elastic reconstructed image was digitally divided into several heights (Figure 36.7). At each height the projected area and contact area were measured. This array of measurements was used to derive the projected area function and contact area function. Whichever equation best fits the data should be used. The area-intercept must equal zero at zero depth. For indenters that have a rough tip rounded shape the popular Oliver–Pharr area function equation could be used [5]. However, caution should be taken because the tip shape can influence the hardness. Tests of indents from

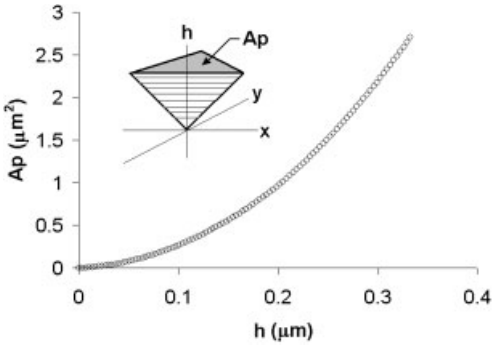

Fig. 36.7 A profile of an indent that has been digitally sliced to provide the area function data.

200 to 900 nm deep had a correlation coefficient of $R^2 = 0.999$ when using a second-degree polynomial linear-regression fit.

36.2.10 Indenter Angle and Radius

A second-degree polynomial projected area function (Eq. 36.6) can be used to calculate the indenter angle (Eq. 36.7) and radius (Eq. 36.8). This model assumes that the indenter has two basic shapes [19]. It is spherical at the tip and conical at the edge. Therefore, this model can be used to represent indenters from spherical to pyramid shape. This method of indenter angle and radius measurements could be used to help determine when to replace a worn out indenter. If there were debris attached to the indenter or it was severally deformed such as being broken at the tip than the linear regression correlation factor would indicate a problem with the indenter.

$$A = a_0\, h^2 + a_1\, h, \tag{36.6}$$

$$a_0 = \tan^2(\alpha), \tag{36.7}$$

$$a_1 = 2\,\pi\, R. \tag{36.8}$$

This method of indenter shape measurement was tested on an old and new Berkovich indenter. The average indenter angle determined from 'a_0' for all the indents in steel, copper, and aluminum was $A_p = 24.7\ hc^2$ for both the old and new Berkovich indenter, which closely corresponds to the ideal projected area constant $A_p = 24.5\ hc^2$. When all the indents made with the new indenter were used, the result was a tip radius of 63 ± 11.7 nm whereas the old indenter produced a tip radius of 924 ± 115 nm calculated from the 'a_1' term. The indents made with the old indenter below 200 nm were excluded because the indentation did not reach deep enough into the sample to include the pyramid part of the indenter. The large tip radius standard deviation was attributed to the crystallo-

Table 36.1 Old and new Berkovich projected area functions each from a single AFM image of a residual indent

Indenter	Projected area function	Indenter angle (α)	Tip radius (R)
Old Berkovich	$A_p\ (hc) = 25.264\ hc^2 + 6.3733\ hc$	70.6°	1014 nm
New Berkovich	$A_p\ (hc) = 24.633\ hc^2 + 0.1408\ hc$	70.3°	22 nm

graphic differences of each indentation as visible by the asymmetric pile-up shape.

The same method can be applied to a single indent to determine the indenter shape. The projected area was measured at various depths of the reconstructed indent image. A second-degree polynomial curve was fit to the depth versus projected area measurements using the method of least-squares. When the projected area intercept was set equal to zero the curve fit equaled Eq. (36.6). The first term 'a_0' was used to calculate the indenter angle and second term 'a_1' was used to calculate the indenter tip radius. Table 36.1 shows the NanoMc software results for the new and old indenters. The resulting indenter angle should be around 70.2° and the indenter radius should be near zero for a new Berkovich indenter.

36.2.11 NanoMc Hardness

As an example the NanoMc software was used to measure the Vicker's hardness of aluminum, steel and copper. The force was taken from the indentation machine and the contact area was measured from the residual indent impression using the NanoMc software and then dividing by the acceleration of gravity 9.80665 m/s^2. The hardness test results of each material were plotted together for comparison as shown in Figure 36.8. This is not a perfect example of the Vicker's hardness, because the Berkovich indenter has three sides instead of four however, Vicker's and Berkovich indenters have almost the same conical equivalent shape.

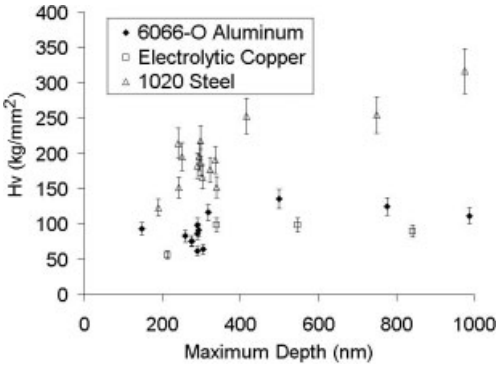

Fig. 36.8 The Vicker's hardness of aluminum, steel, and copper using the new and old Berkovich indenters.

The hardness test error bars were the summation of all the major measurement errors. The force error was ±19.6 μN according to the hardness tester manufacturer specifications. The contact area measurement was composed of several errors mainly caused by AFM scanner drift. The AFM scanner caused ±10% area error. Other sources of hardness measurement error were also included. The new software automatically measured the projected area so the accuracy of this software technique also was determined. A change in Tangent Height% caused a 0.74% error in the projected area measurement. The projected area function fits for the new indenter had an error of 0.010 μm^2 and the old indenter was 0.037 μm^2. The contact area function error was assumed to be the same as the projected area function because they were calculated using the same indent images. The maximum and minimum worst-case scenario was calculated for each hardness measurement. The maximum possible force error was divided by the minimum cumulative error for the contact area. The minimum error was the opposite extreme with a minimum force divided by the maximum contact area error. Table 36.2 shows the range in hardness for these metals at the nanoscale.

Several indentation tests were done at different locations on the sample surface using the same force. There were eight indentations made in aluminum using 2 mN force and ten indents made in steel using 5 mN force (Figure 36.9). Each of the indents were imaged with the AFM and measured by the NanoMc

Table 36.2 Hardness, force and depth range for aluminum, steel, and copper

Material	H_M (MPa)	Force (mN)	Depth (nm)	Samples
6066-O Aluminum	600–1330	1.5–34	160–960	13
1020 Steel	1200–3100	2.1–84	170–900	10
Electrolytic copper	550–970	1.5–21	225–840	4

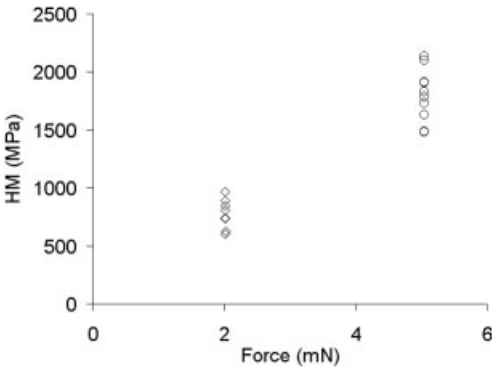

Fig. 36.9 Hardness measurements for 6066-O aluminum and 1020 steel using the NanoMc image analysis technique with a new Berkovich indenter.

software. It was assumed that this broad range in hardness was caused by the polycrystalline effect. Further research needs to be done to better understand why the hardness varies at the nanoscale.

36.3 Conclusion

The primary accomplishment of this chapter was reliable image analysis software to measure hardness test indentations using an AFM. The NanoMc software could automatically measure the indent depth, projected area, and surface area. It has a function called "Elastic Reconstruction", which can digitally reconstruct a residual indent image into the fully loaded indentation shape. The elastic reconstructed indent image was used to measure the contact depth and contact area. By digitally slicing the reconstructed indent image the projected area function and contact area function could be derived. A simple second-degree polynomial model was used to calculate the area functions. The advantage to this second-degree projected area model is that the first term relates to the indenter angle and the second term the tip radius. The hardness was measured for several indents. This software helped to observe a variation in hardness possibly caused by crystallography.

Acknowledgments

I thank Dr. Jaroslaw Drelich, Dr. Douglas J. Swenson and Dr. Margareth S. Andrade.

References

1 ISO 14577-1, Metallic material, Instrumented indentation test for hardness and materials parameters.

2 R. Rodríguez and I. Gutierrez, Correlation between nanoindentation and tensile properties influence of the indentation size effect, Mater. Sci. Eng. A **361**, 377–384 (2003).

3 M. F. Doerner and W. D.Nix, A method for interpreting the data from depth-sensing indentation instruments, J. Mater. Res. **1**, 601 (1986).

4 S. Yip, The strongest size, Nature **391**, 532–533 (1998).

5 W. C. Oliver and G. M. Pharr, An improved technique for determining hardness and elastic modulus using load and displacement sensing indentation measurements, J. Mater. Res. **7**(6), 1564–1583 (1992).

6 K. Herrmann, N. M. Jennett, W. Wegener, J. Meneve, K. Hasche, and R. Seemann, Progress in determination of the area function of indenters used for nanoindentation, Thin Solid Films **377–378**, 394–400 (2000).

7 M. R. VanLandingham, Review of instrumented indentation, J. Res. Nat. Inst. Stand. Technol. **108**(4), 249–265 (2003).

8 M. V. Nazarov, T. A. Nazarova, S. N. Dub, and G. K. Banini, SEM and AFM studies on micro- and nanoindentation of materials, Microsc. Anal. Issue 62, 17–19, September 2003.

9 T. A. Venkatesh, K. J. Van Vliet, A. E. Giannakopoulos, and S. Suresh, Determination of elasto-plastic properties by instrumented sharp indentation: guidelines for property extraction, Scripta Mater. **42**, 833–839 (2000).

10 J. M. Antunes, A. Cavaleiro, L. F. Menezes, M. I. Simões, and J. V. Fernandes, Ultra-mircohardness testing procedure with Vickers indenter, Surf. Coat. Technol. **149**, 27–35 (2002).

11 J. G. Swadener, E. P. George, and G. M. Pharr, The correlation of the indentation size effect measured with indenters of various shapes, J. Mech. Phys. Solids **50**, 681–694 (2002).

12 M. Sakai, Elastic recovery in the unloading process of pyramidal microindentation, J. Mater. Res., **18**(7), 1631–1640 (2003).

13 D. J. Shuman; NanoMc© Indentation Measurement Software, Michigan Technological University, 1999; http://www.nanomc.com

14 N. A. Stillwell and D. Tabor, Proc. Phys. Soc. London, London **78**, 169 (1961).

15 M. Madou, *Fundamentals of Microfabrication* (CRC Press LLC, Boca Raton, FL, 1997).

16 D. J. Shuman, Masters Thesis, Atomic force microscope software for measuring the mechanical properties of materials, Michigan Technological University, 2001.

17 R. Smith, D. Christopher, and S. D. Kenny, Defect generation and pileup of atoms during nanoindentation of Fe single crystals, Phys. Rev. B **67**, 245–405 (2003).

18 D. J. Strange and A. K. Varshneya, Finite element simulation of microindentation on aluminum, J. Mater. Sci. **36**, 1943–1949 (2001).

19 J. Thurn, R. F. Cook, Simplified area function for sharp indenter tips in depth-sensing indentation, J. Mater. Res. **17(**5), 1143–1146 (2002).

37
Nanodeformation Analysis Near Small Cracks by Means of NanoDAC Technique

Jürgen Keller, Dietmar Vogel, and Bernd Michel

Abstract

With the development of micro- and nanotechnological products such as sensors, MEMS/NEMS, and their broad application in a variety of market segments new reliability issues will arise. The increasing interface-to-volume ratio in highly integrated systems and nanoparticle filled materials and unsolved questions of size effect of nanomaterials are challenges for experimental reliability evaluation. To fulfill this need the authors developed the nanoDAC method (nano deformation analysis by correlation), which allows the determination and evaluation of 2D displacement fields based on scanning probe microscopy (SPM) data. In-situ SPM scans of the analyzed object are carried out at different thermomechanical load states. The obtained topography, phase, or error images are compared utilizing gray scale cross correlation algorithms. This allows the tracking of local image patterns of the analyzed surface structure. The measurement results of the nanoDAC method are full-field displacement and strain fields. Because of the application of SPM equipment deformations in the micro-, nanometer range can be easily detected. The method can be performed on bulk materials, thin films, and on devices, i. e., microelectronic components, sensors or MEMS/NEMS. Furthermore, the characterization and evaluation of micro- and nanocracks or defects in bulk materials, thin layers, and at material interfaces can be carried out.

37.1
Introduction

Scanning probe microscopy (SPM) has become a powerful imaging tool for submicron surface analysis and nanoscopic structures. Profile measurements and lateral pitch measurement, e. g., for semiconductor lines, have been established. Regarding deformation measurements at material defects or micro cracks most of the published approaches are qualitative or semiquantitative. Examples are in-situ straining experiments on magnetic thin films carried out by Bobji and

Nanoscale Calibration Standards and Methods: Dimensional and Related Measurements in the Micro- and Nanometer Range.
Edited by Gunter Wilkening, Ludger Koenders
ISBN: 3-527-40502-X

Bhushan [1] and the evaluation of crack propagation in NiAl single crystals that was analyzed by Göken et al. [2]. Recently, research on the combination of atomic force microscope (AFM) images and digital image correlation (DIC) algorithms has proved the ability to measure deformations on the nanoscale. The authors of the chapter made use of AFM equipment for deformation field measurement [3–5]. Chasiotis and Knauss [6, 7] and Soppa [8] used similar approaches to measure strain fields from AFM micrographs. In this chapter the underlying basic principles of the DIC method and the stability and reproducibility will be discussed. The application of the AFM-based image correlation on micro- and nanomaterials will be shown by a crack analysis of a thermoset polymer material. A second example is the thermal loading of a micromachined gas sensor.

37.2 Digital Image Correlation on SPM Images

37.2.1 Principle of NanoDAC

Digital image correlation methods on gray scale images were established by several research groups. Examples from different fields of application can be found in various publications, e. g., in [3–6, 9–11]. In previous research the authors developed and refined different tools and equipment in order to apply scanning electron microscopy (SEM) images for deformation analysis on thermomechanically loaded electronics packages. The respective technique was established as microDAC, which means micro deformation analysis by means of correlation algorithms [10].

The microDAC technique is a method of digital image processing. Digitized micrographs of the analyzed objects in at least two or more different states (e. g., before and during/after mechanical or thermal loading) have to be obtained by means of an appropriate imaging technique. Generally, the utilized cross cor-

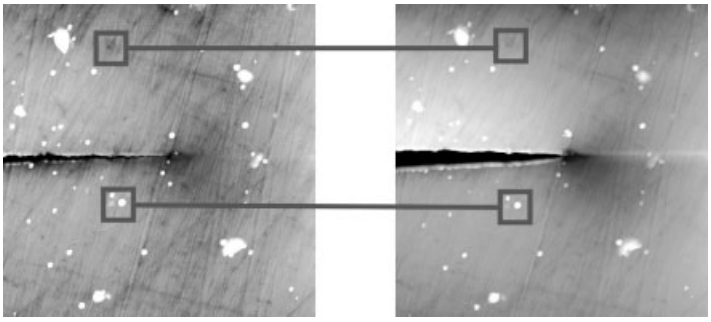

Fig. 37.1 AFM topography image of a crack in a thermoset polymer material for different crack opening displacements, scan size 15 × 15 μm.

relation algorithms can be applied to images extracted from a variety of sources such as SEM or laser scanning microscopy (LSM). The basic idea of the underlying mathematical algorithms follows from the fact that images commonly allow us to record local and unique object patterns, within the more global object shape and structure. These patterns are maintained if the objects are stressed by thermal or mechanical loading. Figure 37.1 shows examples of AFM images taken at a crack tip of a polymeric material. The markers indicate typical local patterns (i. e., topographic structures) of the images. In most cases, these patterns are of stable appearance, even if severe load is applied to the specimens so that they can function as a local digital marker for the correlation algorithm.

The cross correlation approach is the basis of the DIC technique. A scheme of the correlation principle is illustrated in Figure 37.2.

Images of the object are obtained at the reference load state 1 and at a different second load state 2. Both images are compared with each other using a cross correlation algorithm [5]. In the image of load state 1 (reference) rectangular search structures (kernels) are defined around predefined grid nodes (Figure 37.2, left). These grid nodes represent the coordinates of the center of the kernels. The kernels themselves act as gray scale pattern from the load state image 1 that has to be tracked, recognized, and determined by its position in the load state image 2. In the calculation step the kernel window ($n \times n$ submatrix) is displaced inside the surrounding search window (search matrix) of the load state image 2 to find the position of best matching pattern (Figure 37.2, right).

This position is determined by the maximum cross correlation coefficient that can be obtained for all possible kernel displacements within the search matrix. The described search algorithm leads to a two-dimensional discrete field of correlation coefficients defined at integer pixel coordinates. The discrete field maximum is interpreted as the location where the reference matrix has to be shifted from the first to the second image, to find the best matching pattern. For enhancement of resolution a so-called subpixel analysis is implemented in the utilized software [12].

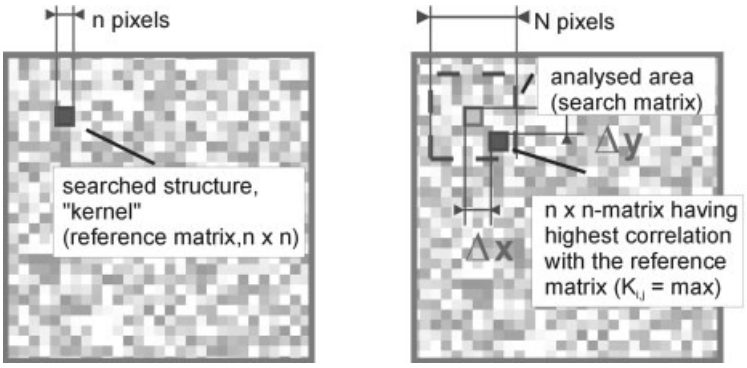

Fig. 37.2 Displacement evaluation by a cross correlation algorithm; left: detail of a reference image at load state 1; right: detail of an image at load state 2 [12].

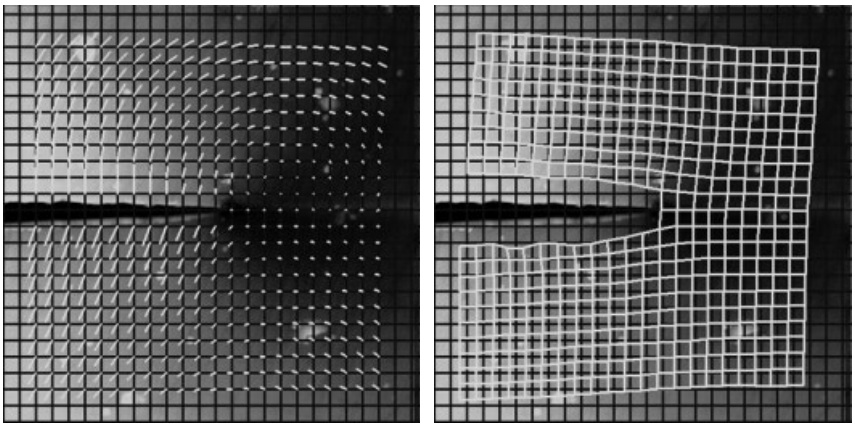

Fig. 37.3 Digital image correlation results derived from SFM images of a crack tip, scan size 15 × 15 μm; left: image overlaid with the user-defined measurement grid and vector plot; right: image overlaid with the user-defined measurement grid and deformed measurement grid; displacement vector and deformed grid presentation are enlarged with regard to the image magnification.

The result of the two-dimensional cross correlation and subpixel analysis in the surroundings of a measuring point primarily gives two components of the displacement vector. Applied to a set of measuring points (e. g., to a rectangular grid of points with a user-defined pitch), this method allows us to extract the complete in-plane displacement field. An example for the DIC-based displacement field is shown in Figure 37.3. For images originating from SPM techniques the described approach has been established as the so-called nanoDAC method (nano deformation analysis by correlation algorithms).

37.2.2 Stability Aspects of SPM Measurements

In comparison to DIC-based measurements treating optical or SEM images, some more essential difficulties have to be overcome for SPM-based imaging. They correspond to the extreme magnification of SPM techniques. Because SPM image scans are taken over a time interval from one to several minutes smallest system drifts can cause significant artificial object deformations. Classifying different drift sources it can be distinguished between

- SPM scanner drifts, which are related to time-dependent behavior of the piezo tube;
- relative movements between the scanning head and the sample fixture, mainly caused by temperature changes;
- drift of sample loading parameters (temperature, forces, load paths, etc.) within testing stages installed at the microscope; and

- incremental object deformations originating from viscoelastic material behavior of test specimens, i. e., time-dependent object deformations that take place even under constant loading parameters.

Substantial concerns regarding stability and reproducibility originate from drifts of the SPM scanner piezo and the variation of thermomechanical loading parameters over time. As a consequence, the accurate selection of SPM equipment and loading stages is a crucial issue. Moreover, the development and implementation of methods of drift control and compensation may be essential for particular applications. Practically serious problems arise from the fact that the drift effects described above are not evident from a single image achieved at a specific load state of the specimen. In some cases severe drift effects come to light by digital image correlation of several images acquired at the same load state. For example, significant pseudo displacements occur if the scanner is adjusted to a new position of its scanning range either by the zooming-in capability of the SPM control software or by a user-based definition of the new scanning range or scanning position. The application of DIC to images taken just after such positioning processes shows large pseudo displacements caused by scanner creep.

To underline the creep effect of the scanner a DIC displacement analysis is performed on two images acquired directly after each other using the repeat function of the SPM software. The 15 $\times$ 15 μm scans are carried out at an unloaded and stable mounted object with a metallic surface where the fast scanning is in the horizontal direction and the y-direction is scanned from top to bottom. The images are taken in noncontact mode and the data are extracted from one scan direction only to suppress artifacts caused by scanner hysteresis.

In this case only the y-direction of the displacement vector is of interest and the determined results are shown together with one of the images in Figure 37.4. The displacement results are given in pixel coordinates (1 pixel $\approx$ 59 nm). The first conclusion is that there is a general drift of several pixels across the vertical

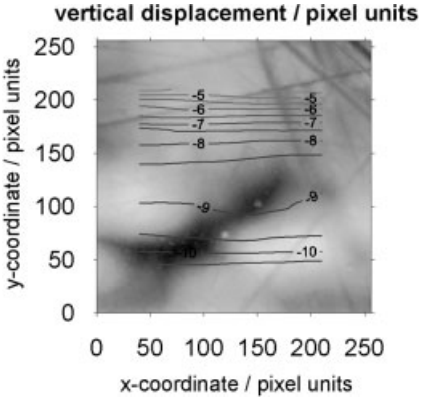

Fig. 37.4 Pseudo displacements caused by scanner creep; contour lines of identical displacement are closer to each other, indicating a larger strain level in the upper part of the image.

dimension of the image. Secondly, the displacement results clearly imply that there are larger strain values in the upper half of the image than in the lower half. This pseudostrain effect is caused by the creep behavior of the piezo scanner. After a running-in phase it will converge into steady-state scanning behavior. As a result the pseudostrain mainly occurs in the upper part of the image.

The presented example emphasizes the requirements of stable scanning behavior to avoid artificial object deformation. As mentioned above another important aspect is the thermal drifts of the apparatus including the AFM itself but also the specimen, loading device, and its positioning system. Moreover, these different drift sources superpose, so they cancel each other or enlarge each other depending on the actual environmental and system immanent influences. If one thinks about correcting the displacement by elimination of a specific stability source there will always be the problem of separation of the different sources.

Therefore, a strategy is necessary estimating the actual drifts of the complete system in their summation rather than separating a single drift source. A possible way to follow this objective is the description of the drift by a functional and applying a linearization to achieve an actual value for the system drift for a specific time period. A practicable way to determine the actual system drift would be to capture a series of two to three images at each of the load states that have to be compared. By a subsequent displacement analysis of each series utilizing the DIC code a mean drift value for each load state can be determined. If there is a difference between the mean drift at the specific load states a correction has to be applied to the obtained DIC results between these load states. The described strategy can be tested by a series of scans on a fixed specimen. In the following these tests will be called "zero displacement test."

The displacements and their standard deviation determined from a zero displacement test are also a measure for the accuracy of the DIC concept on SPM images. According to [12] the applied DIC code has a pixel resolution of 0.01 for in-plane displacement components for CCD camera images. Assuming that the code performs similar on AFM topographs, one expects a displacement resolution of 0.3 nm. Practically it is difficult to translate a macroscopic specimen with that accuracy. However, a zero displacement test and the resulting variation of the displacement are a measure for the precision of the measurements. In the following section these zero displacement tests are discussed. Nevertheless, it has to be mentioned that new or somehow modified SPM and loading equipment should be tested for stability and accuracy. The trend of the SPM manufacturer to develop scanning equipment with increased line scan frequency can be very helpful to minimize the thermal and creep induced drift. Furthermore, the application of closed-loop scanners comprising a positioning control unit will compensate scanning reproducibility problems.

The zero displacement tests were performed by 256×256 pixel scans on a Ni layer on silicon substrate with scan sizes of 10 μm and a line frequency of 1 Hz. The fast scan direction was the horizontal x-direction and noncontact topography data were picked up in the positive x-direction only in order to eliminate scanner hysteresis effects. The scans were carried out in a series of 15 images using the

"repeat" option of the AFM control software, so that nonstop scanning was performed for approximately 1 h.

A quantification of the prevailing drift can be easily performed by DIC techniques. The image sequence is analyzed by means of digital image correlation where each image is compared to its subsequent image. From the determined displacement fields the following statistical values are extracted:

1. Mean system drift determination over scan time.
2. Standard deviation of the measured displacement in fast (x) and slow (y) scan directions.

The results of the analysis are presented in Figures 37.5 and 37.6 where the evaluation of the mean displacement and standard deviation was carried out separately for the x- and y-directions. Mean displacement values of the analyzed

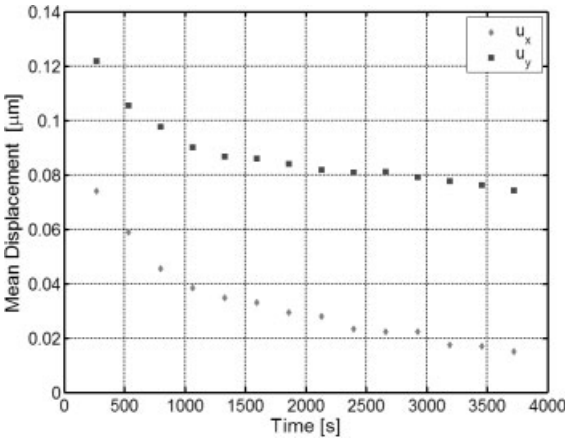

Fig. 37.5 Mean displacement, u, in the x- and y-directions calculated from displacement field vs. scanning time; scan size of the image 10×10 µm.

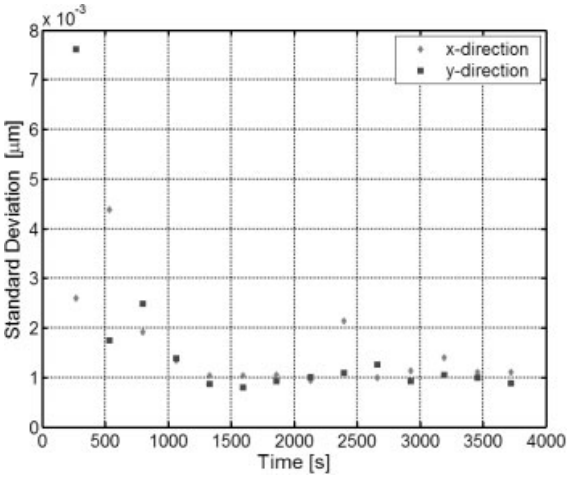

Fig. 37.6 Mean displacement, u, in the x- and y-directions calculated from displacement field vs. scanning time; scan size of the image 2×2 µm.

image series over scanning time clearly emphasize that system drifts can be described with simple polynomial functions. The extrapolation from two or three initial mean drifts to a subsequent image can be achieved with the obtained fitting function. With the calculated mean drift a strain component over the whole image can be calculated so that a pseudostrain can be eliminated from the actual displacement measurements.

The standard deviation calculation of the determined displacement values was also carried out separately for the *x*- and *y*-directions. Figure 37.6 shows that the relative error at the beginning of the 10 × 10 μm zero displacement test is in the range of ±7.5 nm for the *y*-direction and ±2.5 nm for the *x*-direction. This is caused by creep effects of the piezo scanner and thermal instabilities. After five scans the error is minimized to ±1 nm for both directions.

The presented results and the discussion lead to the following statements for system drift evaluation and compensation:

- By the application of the DIC analysis it is possible to quantify system drifts during in-situ loading tests.
- A system drift compensation can be done using the results from the drift analysis.
- For a scan size of 2.5 × 2.5 μm and a scanning field of 256 × 256 pixels a displacement value of 1 nm can be detected by the DIC analysis.

However, it has to be noted that the accuracy of the DIC analysis strongly depends on the experimental conditions (noise, image contrast, temperature stability).

37.3 Crack Evaluation

Cyanate ester resins and their modifications that are typically used in microelectronic applications show a high modulus of elasticity but poor resistance to fracture [13]. Because of the miniaturization in electronic packages micro material testing of such material systems will be a key for successful design of microelectronic packages. Therefore this type of material is chosen for crack evaluation experiments.

37.3.1 Experimental Setup

A simple specimen configuration is selected to demonstrate the fundamental approach. With a compact tension (CT) crack test specimen as shown in Figure 37.7 mode I (opening) loading of the crack tip is enabled. The CT specimen is loaded with the force *P* by a special tension/compression testing module, which can be utilized for in-situ SEM and SPM measurements. Figure 37.7 shows the CT specimen and parts of the loading device under the SPM.

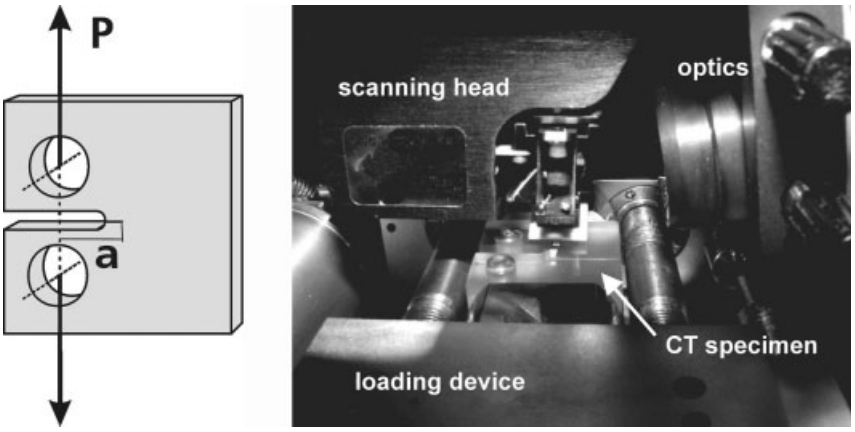

Fig. 37.7 Left: Compact tension (CT) specimen; right: in-situ loading under the AFM.

For the deformation measurements AFM noncontact topography scans are taken directly at the crack tip before and after loading. Afterward the DIC algorithms are applied to the set of images and displacements are determined at predefined grid nodes. Figure 37.9(left) shows the results in the form of a crack opening displacement field, u_y, extracted from the AFM scans at the cyanate ester resin CT specimen.

37.3.2
Crack Opening Displacement Analysis

A straightforward approach for crack evaluation in the AFM is the technique of crack opening displacement (COD) determination. In order to extract the mode I stress intensity factor K_I crack opening displacements, u_y^u and u_y^l, are measured along both the upper and lower crack boundaries (Figure 37.8).

If determined by linear elastic fracture mechanics they must be equal to

$$u_y^{u,l} = \pm \frac{K_I}{2\mu}\sqrt{\frac{x}{2\pi}}(k+1) \qquad \text{for} \quad x \leq 0 \tag{37.1}$$

$$u_y^u = u_y^l = 0 \qquad \text{for} \quad x > 0, \tag{37.2}$$

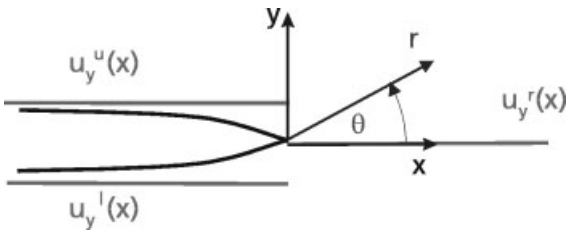

Fig. 37.8 Crack opening displacement according to linear elastic fracture mechanics (LEFM) for infinite bulk material and mode I crack opening.

where μ is the shear modulus and k is a function of Poisson's ratio, ν; $k = (3 - 4\nu)$ for plane strain and $k = (3 - \nu)/(1 + \nu)$ for plane stress. Taking the square of the difference of upper and lower displacements, we obtain a linear function of the x-coordinate or 0, depending on the position relative to the crack tip:

$$\left(\frac{u_y^u - u_y^l}{2}\right)^2 = Cx \qquad x \leq 0$$
$$= 0 \qquad x > 0. \tag{37.3}$$

For the equation above, the crack tip is set at location $x = 0$. The crack tip location on the real specimen can be found at the interception of a linear fit of the curve Cx with the x-axis. The slope C allows us to estimate the stress intensity factor K_I, which is a measure of the crack tip load. It is given by

$$K_I = \frac{E}{1+\nu}\frac{1}{k+1}\sqrt{2\pi C}, \tag{37.4}$$

where E is the Young's modulus.

The discussed analysis is applied to the displacement field measurements presented in Figure 37.9 (left). The results of the linear fit according to Eq. (37.3) are shown in Figure 37.9 (right).

The determined value for K_I with the application of Eq. (37.4) is equal to 0.056 MPa $m^{1/2}$, which is about 1/10 of the critical stress intensity factor for the cyanate ester resin. The value calculated from the applied loads is 0.085 MPa $m^{1/2}$. The comparison shows that the value calculated from the specimen loading is 1.5 times higher than the value extracted from the crack opening field. Possible reasons or error sources for the deviation are as follows:

- the value of the Young's modulus is assumed to be too low for this CT specimen;

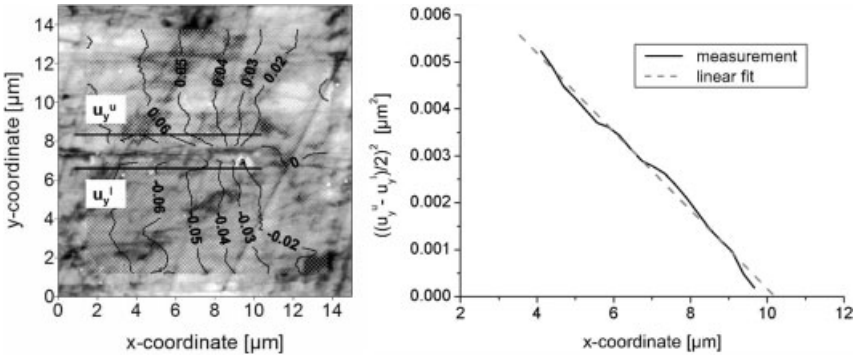

Fig. 37.9 Left: AFM image of the crack tip area (size 15 × 15 µm) with overlaid displacement results in the y-direction, u_y lines for the upper and lower crack face are included; right: evaluation of slope C for the calculation of the stress intensity factor K_I.

- the crack is not fully loaded at the surface of the specimen, due to the fact that the crack front is a relatively straight line normal to the specimen surface;
- the plane strain crack field solution is not accurate or is not completely predominating at the surface of the specimen.

Concluding the results discussed in this section a detailed analysis of the crack tip behavior by FE simulation is necessary.

37.4 Adaptation to Finite Element Analysis

The presented experimental results of the previous sections clearly underline the difficulties involved in the experimental crack tip evaluation at the micro- and nanoscale. Moreover, micro- and nanocracks in real electronic systems, MEMS or NEMS, are nested in a variety of materials with different material properties. In such cases the experimental approach on its own is not suited for the determination of critical stress/strain states or system reliability. A possible solution is the strategy of using a hybrid analysis tool combining SPM-based experimental displacement measurements and finite element concepts. The approach is realized by a definition of an adaptation concept (Section 37.4.1). The basis for the concept is the mesh adapter enabling the reduction of 3D-FE mesh data to 2D-DIC software node coordinate data (Section 37.4.2). Furthermore, a common platform for FEA and DIC results is defined and a verification algorithm for simulation/experimental results is developed (Section 37.4.3).

37.4.1 Adaptation Concept

The objective of an adapted finite element concept is the creation of a tool, which allows the verification of in-situ loading experiments and finite element results using a combination of finite element simulation and DIC-based displacement fields. FEA on its own is not sufficient to describe complex material and device behavior for future micro- and nanomaterial testing. Unknown material constitutive laws and complex interrelation between testing equipment and specimen make it unreliable to evaluate reliability exclusively by FEA or analytical approaches. Consequent validation of FE models by suitable experiments is inevitable.

Comparison between measured and simulated deformation fields is the way to achieve trustworthy testing results. Unfortunately in many cases simple determination of material properties by DIC measurements is impossible since there is the general access restriction of DIC measurements to surface and in-plane deformation. 3D and internal deformation data are indispensable for many testing purposes, e. g., for the determination of parameters for advanced fracture mechanics

criteria (J-integral, C*-, T-integral, etc.). Moreover, in some cases stress/strain data on three-dimensional objects are needed, which cannot be obtained from in-plane surface measurements. This information can be provided adapting FEA to DIC measurement. Because of the fact that both methods are implemented in completely different and therefore incompatible software packages an adaptation concept from FEA to DIC was developed. A flow chart of the concept is shown in Figure 37.10.

Basically, the concept allows one to match simulation and measurement results in order to provide material characterization on a best-fit strategy. At the end material properties such as Young's modulus or fracture mechanical properties are determined combining FEA and DIC results. FE meshes from either PATRAN/ABAQUS or ANSYS are utilized for simulation and DIC displacement field determination from load state images (see ① in Figure 37.10). Therefore a transformation interface of FE mesh nodes to respective measurement mesh nodes was developed.

Although determined in the same mesh nodes, simulation and measurements results cannot be compared directly. DIC deformation fields are superposed by rigid body displacements and rotations originating from, e. g., testing machine drifts, or FE boundary conditions that are not equivalent to the actual experimental loading. Therefore, original DIC results have to be derotated and a translation correction has to be applied before comparing them with FEA fields (see ② in Figure 37.10). Within the concept a set of finite element displacement fields is

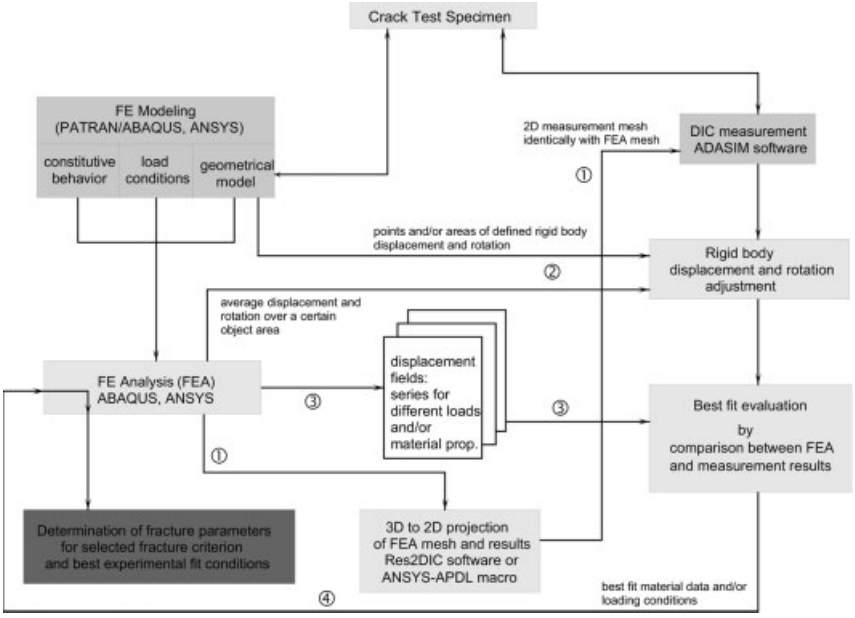

Fig. 37.10 Principle of nanoDAC measurement and adaptation concept to FEA.

compared with a set of derotated and displaced measurement fields (see ③ in Figure 37.10). Different simulated fields are provided varying specimen load conditions or material properties. The best fit between simulation and measurement field reveals the optimum input data (modeling) for simulation with regard to the specimen load conditions under consideration. Utilizing these best-fit conditions proven by experiment, additional or more advanced material properties can be employed (④ in Figure 37.10).

37.4.2
Mesh Transfer from FEA to Experiment

Transfer of finite element nodes to the measured experimental area is a straightforward approach for data comparison. This technique allows one to determine the experimental displacements at the position of the FE nodes, so that a direct validation of the results can be performed. Figure 37.11 illustrates the concept of the mesh adaptation from a three-dimensional FE model to a two-dimensional region of interest of the experimental approach.

The digital image correlation technique determines displacements at specific grid nodes that are similar to the nodes of the finite element mesh. In addition to meshing by means of an internal mesh generator the DIC software allows one to import user-defined meshes. During this mesh-import procedure the user has to specify *x, y*-scaling factors for the transformation of [mm]-based node location (from FE model data) to [pixel]-coordinates (of measurement images).

In the present case the mesh adaptation is carried out between the FE-code ANSYS or ABAQUS and the DIC software ADASIM. The interface macro produces mesh input files according to the interface definition of ADASIM.

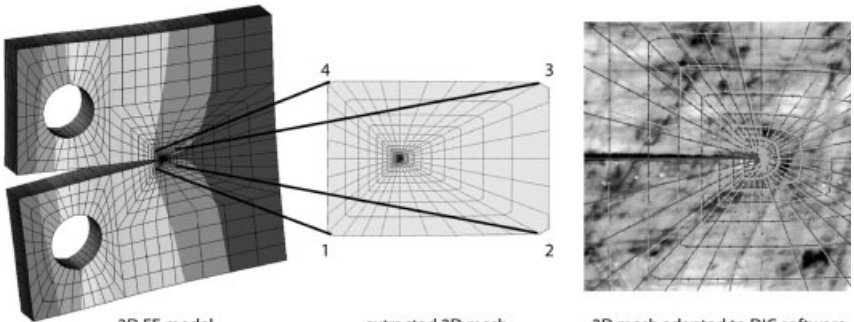

Fig. 37.11 Principle of nanoDAC measurement and adaptation concept to FEA; left: original 3D FE model, right: 2D DIC calculated displacement results based on 2D mesh, deformed and undeformed mesh is illustrated.

37.4.3 Verification Platform

Mathworks MATLAB software is used as a platform for finite element and DIC result data comparison. Import of finite element data is implemented by reading predefined file output formats already modified by the 3D FEA-DIC mesh adapter (compare to Section 37.4.2). The link between displacement values from different sources is performed by node number allocation of the FE mesh. In the most practical cases the mesh will consist of areas with varying node densities so that weighting functions have to be applied to node results. However, in this work weighting functions are not included.

The general aim is the verification of either FE model or DIC measurements. The accomplished verification process implemented as a MATLAB program comprises two main functions:

- variation of DIC results for the compensation of rigid body rotation and displacement within the region of interest and
- assessment of the degree of similarity between the FE and DIC results in order to figure out optimum matching conditions and the best fitting of FE results to the measurements.

In special cases information on appropriate rotation and displacement correction values can be extracted directly from the measured field, i. e., if special symmetry conditions are given in the loaded structure. However, for future application of the adaptation concept a more general approach has to be employed. Therefore the variation of the DIC results is done by addition of rotation and displacement terms to the measured field values depending on the location of the measurement point. The modification of the displacement field is done for different angles and displacement values so that a variety of displacement fields are generated.

In the second step the modified displacement fields have to be evaluated according to their similarity to the FE results. Therefore different statistical criteria are implemented in the verification algorithm, e. g., cross correlation coefficient, covariance, and least-squares methods.

In the following the verification algorithm is applied to the crack tip field of the CT specimen presented in Figure 37.9. The COD concept led to the conclusion that a combination of DIC and FE results will provide additional information for the evaluation of a crack tip displacement field. The analysis of the required fitting procedures reveals the following algorithm substeps: (1) derotation and displacement matching and (2) determination of material properties.

Derotation and Displacement Matching

The measured displacement field was rotated stepwise within a predefined interval of angle increments so that a set of modified displacement fields is generated. The rotation center was chosen with regard to the rotation field data obtained by the correlation software.

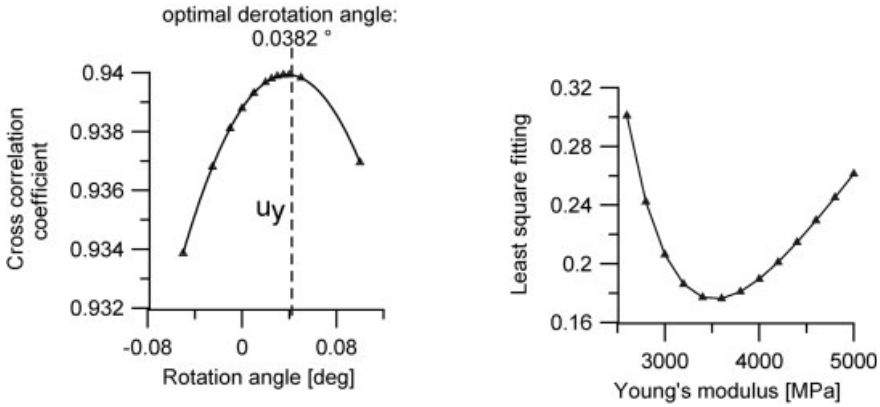

Fig. 37.12 Left: Determination of the ideal derotation angle by means of cross correlation of displacement fields, small derotation (0.038 grd) has taken place between finite element simulation and DIC measurement; right: determination of material model with best matching parameters (Young's modulus).

Each of the modified displacement fields was compared to the FE results by the three different statistical criteria mentioned above. Least-squares fitting and cross correlation result in graphs with well-defined extremum values. Therefore they can act as appropriate criteria for the determination of accurate derotation angles. Figure 37.12 shows the computed cross correlation coefficients for a pair of FE and modified displacement fields in dependence on the rotation angle.

Determination of Material Properties

For the determination of material properties the verification algorithm has to be applied to a pair of measured and simulated results. In this case the FE results are varied and the measured (or modified) field remain the same. FE simulations are performed with different Young's moduli within a reasonable scope of values, i. e., 2600–5000 MPa. Each of the obtained FE displacement fields is compared to the modified (derotated and rigid body displacement corrected) measured field by means of the least-squares method.

Figure 37.12 illustrates the least-squares parameter versus the Young's modulus of the FE simulation. A minimum value of the least-squares parameter at a Young's modulus of 3600 MPa is indicating the best matching pair of displacement fields.

The results of the verification algorithm clearly prove the capability of the adaptation concept in combination with the verification algorithm. The applied verification strategy by comparison of measured and simulated displacement fields leads to a well-defined best matching parameter set.

Unfortunately the recursively derived Young's modulus of 3600 MPa is not equivalent to tensile test measurements where a value of 2800 MPa was determined. A reason for this can be that unmodified cyanate ester resins tend to form a prestressed material configuration. This fact was indicated by the observation of cracks in the cured plates. Therefore a homogeneous material behavior cannot be guaranteed within the complete volume of the cured plates and the specimens. Especially at the surface of the plates the curing parameters are different from that of the middle resulting in varying material properties over the thickness of the plates.

37.5
Application of DIC to Micromachined Gas Sensor

Sensor applications with local temperature regulation such as a gas sensor (Figure 37.13) are usually thermally loaded with rapid and frequent change in temperature [14]. This thermal cycling and the temperature gradients over the structure imply thermal stresses and may cause failure of the component [15]. With in-situ AFM measurements on this micro system the capability of the nanoDAC approach is demonstrated by measuring material deformation resulting from mismatch of material properties.

The gas sensor is designed to tolerate several hundreds of °C thermal load. The thermal mismatch between the platinum electrodes (coefficient of thermal expansion (CTE) = 9 ppm K^{-1}) and the SiO_2 substrate (CTE = 0.65 ppm K^{-1}) leads to high local stresses, if the entire device is heated up to its service temperature. Local displacements resulting from the thermal load were measured by means of the nanoDAC technique.

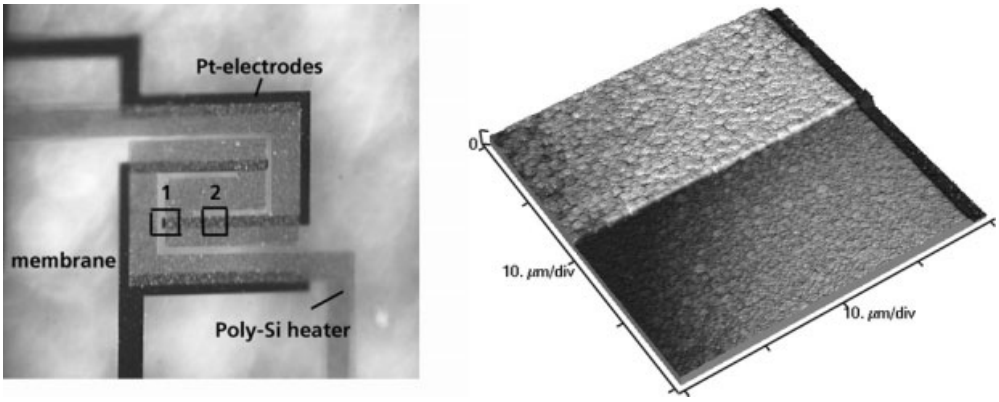

Fig. 37.13 Left: Gas sensor membrane, membrane thickness: 2 µm, field of view: 500 µm; right: AFM topography scan of platinum layer on top of the SiO_2 membrane (detail 2 on the left figure) [14].

In-situ noncontact AFM scans on top of the gas sensor membrane have been carried out at room temperature and at 100°C. The area that was observed is illustrated in Figure 37.13 as location 2. At this area an overlap of the SiO_2 membrane by the platinum electrodes should result in a thermally induced stress/strain field. The temperature was achieved by applying a defined voltage to the microheater of the gas sensor.

The determined thermally induced displacement field shows that the platinum layer with its higher CTE value reveals an inherent expansion toward the edge of the layer (Figure 37.14). In supplementary tests with heating cycles with maximum temperatures in the range of 450°C delamination of the platinum layer at the edges to the SiO_2 substrate layer is observed (Figure 37.14). Details of this testing cycle are described in more detail in [14].

Besides the information on deformation in the x–y plane the topographic AFM data allow the determination of the out-of-plane displacements. The height information of the AFM topography images before and after loading is analyzed for evaluation of movements or deformations in the z-direction. Applying this technique to in-situ measurements of thermal deformations by AFM on the top of the sensor membrane has revealed a high value of remaining deformations even after a single heat cycle (25–100°C). Inelastic strains remain after cooling down to room temperature.

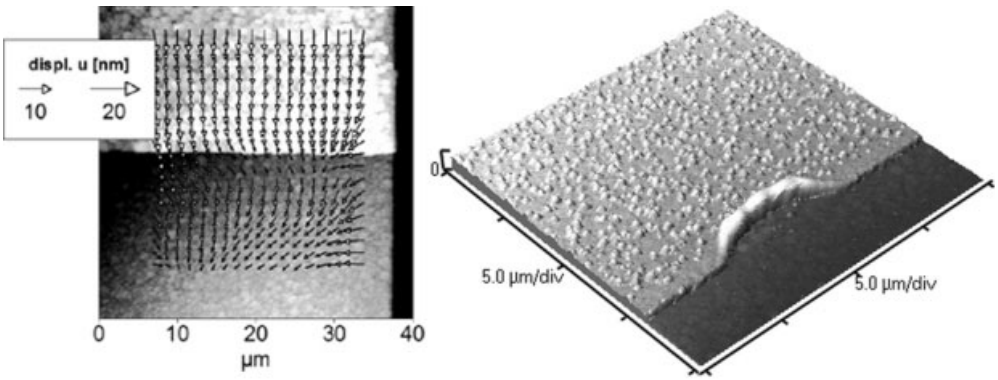

Fig. 37.14 AFM topography image of platinum and SiO_2 layers; left: vector plot of displacements, u, measured by nanoDAC; right: membrane after tempering at 450°C, Pt electrode destruction (compare to Figure 37.13).

37.6 Conclusions

In this chapter the principle of DIC-based displacement measurements at in-situ loaded structures under the AFM is successfully applied to crack tip evaluation of a polymer material. The measurements were carried out at a commercially available scanning probe microscope equipped with specially designed loading stages. In a second application example the capabilities for measurements at microelectronic components were shown. The presented nanoDAC method is suited for in-situ thermomechanical measurements of MEMS and sensor components. Material data such as fracture properties, Young's modulus, coefficient of thermal expansion, and Poisson's ratio can be determined. In the future the technique should also be used for tracking of structures or particles driven by diffusion processes or nanomanipulators.

Acknowledgments

The authors wish to acknowledge the collaboration with J. Puigcorbe and J. R. Morante from the University of Barcelona.

References

1 M. Bobji and B. Bushan, In situ microscopic surface characterization studies of polymeric thin films during tensile deformation using atomic force microscopy, J. Mater. Res. **16**(3), 844–855 (2001).

2 M. Göken, H. Vehoff, and P. Neumann, Atomic force microscopy investigations of loaded crack tips in NiAl, J. Vac. Sci. Technol. B **14**(2), 1157–1161 (1996).

3 D. Vogel and B. Michel, Microcrack evaluation for electronics components by AFM nanoDAC deformation measurement, in *Proceedings of the 2001 1st IEEE Conference on Nanotechnology. IEEE-NANO 2001* (2001), pp. 309–312.

4 D. Vogel, J. Keller, A. Gollhardt, and B. Michel, Evaluating microdefect structures by AFM based deformation measurement, Proc. SPIE **5045**, 1–12 (2003).

5 J. Keller, D. Vogel, A. Schubert, and B. Michel, Displacement and strain field measurements from SPM images, in *Applied Scanning Probe Methods*, edited by B. Bhushan, H. Fuchs, and S. Hosaka (Springer, Berlin, 2003), pp. 253–276.

6 I. Chasiotis and W. Knauss, A new microtensile tester for the study of MEMS materials with the aid of atomic force microscopy, Exp. Mech. **42**(1), 51–57 (2002).

7 W. Knauss, I. Chasiotis, and Y. Huang, Mechanical measurements at the micron and nanometer scales, Mech. Mater. **35**(3–6), 217–231 (2003).

8 E. Soppa, P. Doumalin, P. Binkele, T. Wiesendanger, B. Bornert, and S. Schmauder, Experimental and numerical characterisation on in-plane deformation in two-phase materials, Comput. Mater. Sci. **21**(3), 261–275 (2001).

9 Y. Chao and M. Sutton, Accurate measurement of two- and three-dimensional surface deformations for fracture specimens by computer vision, in *Experimental Techniques in Fracture*, edited by J. Epstein (VCH Publishers, 1993), pp. 59–93.

10 D. Vogel, A. Schubert, W. Faust, R. Dudek, and B. Michel, MicroDAC – a novel approach to measure in situ deformation fields of microscopic scale, Microelectron. Reliability **36**(11-12), 1939–1942 (1996).

11 D. Davidson, Micromechanics measurement techniques for fracture, in *Experimental Techniques in Fracture*, edited by J. Epstein (VCH Publishers, 1993), pp. 41–57.

12 M. Dost, E. Kieselstein, and R. Erb, Displacement analysis by means of grey scale correlation at digitized images and image sequence evaluation for micro- and nanoscale applications, Micromater. Nanomater. **1**(1), 30–35 (2002).

13 I. Hamerton, *Chemistry and Technology of Cyanate Ester Resins* (Blackie Academic, Glasgow, UK, 1994).

14 J. Puigcorbe, D. Vogel, B. Michel, A. Vila, I. Gracia, C. Cane, and J. Morante, Thermal and mechanical analysis of micromachined gas sensors, J. Micromech. Microeng. **13**(5), 548–556 (2003).

15 J. Puigcorbe, A. Vila, J. Cerda, A. Cirera, I. Gracia, C. Cane, and J. R. Morante, Thermo-mechanical analysis of microdrop coated gas sensors, Sensors Actuators A **97**, 379–385 (2002).

38
PTB's Precision Interferometer for High Accuracy Characterization of Thermal Expansion Properties of Low Expansion Materials

R. Schödel and A. Abou-Zeid

Abstract

Demands on dimensional stability and on the detailed knowledge of thermal expansion properties of "high tech" materials are growing considerably. These properties can be investigated by observing changes of the absolute length of macroscopic samples as a function of temperature and time. This chapter describes PTB's so-called precision interferometer that can be used for such measurements. The recent progress of this interferometer resolving sub-nm length changes of samples up to 400 mm in length is demonstrated. An overview of different measuring modes, including investigations of coefficient of thermal expansion (CTE) inhomogeneity, is given and measurement examples demonstrate that the attainable uncertainty can be less than 0.1 nm under certain conditions.

38.1
Introduction

Demands on dimensional stability and on the detailed knowledge of thermal expansion properties of "high tech" materials are growing considerably from year to year. One application is the further development of photolithography toward the so-called EUV lithography using 13 nm as wavelength of the light source light source, where it is very important to know the thermal expansion properties of the substrates used for the masks but also for the mirrors used as main optical components. These properties can be investigated by observing length changes of macroscopic samples as a function of temperature. Simple dilatometers (see Figure 38.1), commonly used for measurements of thermal expansion, are based on the observation of temperature induced length changes, ΔL, of the sample.

However, ΔL might be affected by unwanted contributions due to temperature changes of the solid arrangement used as a reference. In order to take this effect into account a calibration must be made. Conclusively, such dilatometers cannot be used for most precise determination of thermal expansion properties.

Nanoscale Calibration Standards and Methods: Dimensional and Related Measurements in the Micro- and Nanometer Range.
Edited by Gunter Wilkening, Ludger Koenders
ISBN: 3-527-40502-X

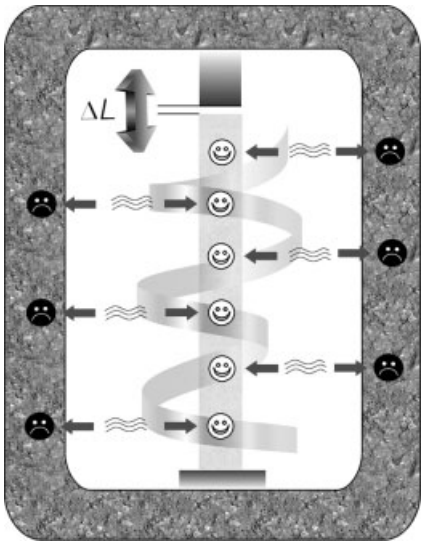

Fig. 38.1 Simple dilatometer design where length changes, ΔL, due to the sample temperature can be recognized simply by any kind of sensor. The disadvantage of this method originates from the unknown contribution to ΔL due to the solid arrangement.

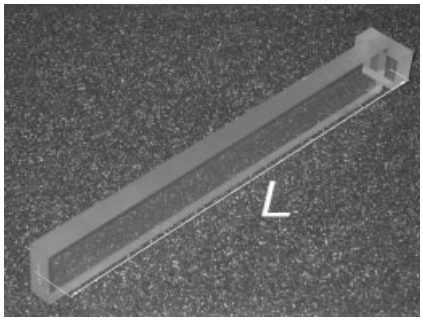

Fig. 38.2 Typical sample, connected to an end plate, designed for length measurements by interferometry.

A different concept for the investigation of thermal expansion is based on the measurement of the total length (absolute length, see Figure 38.2) of a sample as a function of the temperature. Length changes can then be extracted from the difference of the absolute length and a length measured at a reference temperature.

Length measuring interferometers are normally used for highest level calibrations of gauge blocks. According to industrial needs such interferometers have been improved drastically in the last decades [1–4]. With today's instruments using stabilized lasers and phase shift technique a measurement uncertainty of up to about 10 nm can be obtained [5, 6] depending on the sample length (ranging between about 0.5 mm and 300 mm). The limiting uncertainty contribution of the measured absolute length mainly originates from the unknown interaction between the sample and the end plate that is wrung to it. This regards to the deformation of the plate and the sample induced by the wringing forces.

Figure 38.3 illustrates the basic principle of length evaluation using optical interferometry. The length is defined as a multiple of the light wavelength, λ, used:

$$L = \tfrac{1}{2}\lambda \times (I + F), \tag{38.1}$$

where I is a large integer number (typically on the order of 1 million). F is the fractional order of interference, which is extracted from the interferogram:

$$F = \tfrac{1}{2\pi}(\phi_{\mathrm{P}} - \phi_{\mathrm{S}}). \tag{38.2}$$

Using only one wavelength would require the exact knowledge of integer interference orders (entailed with a large-scale mechanical premeasurement) before the exact length can be determined according to Eq. (38.1). The use of different wavelengths, however, results in three independent lengths, where the number of I can be varied in each case. The actual length can be assigned to the average of lengths that coincide best (method of exact fractions). This procedure drastically enlarges the range of unambiguity so that a rough estimate of the length, obtained from a simple measurement, is sufficient (see [7]). Therefore, such interferometers might be called "absolute measuring interferometers." PTB's so-called precision interferometer (PIF), described in this chapter, is such an interferometer. A rough measurement of the initial length using a simple dial gauge (with an uncertainty of about ± 100 μm) is sufficient because wavelengths of three stabilized lasers are used and the interference fraction, F, is measured very precisely (see below).

Strictly requirements for the design of the samples exist, i. e., the faces must be parallel to each other within about 5 μrad (1 arcsec). The faces of the sample and end plate must be flat within 30 nm to assure a good contact (wringing) between them. The effect of wringing itself can be considered as constant as long as the end plate has a similar coefficient of thermal expansion (CTE) and is not removed

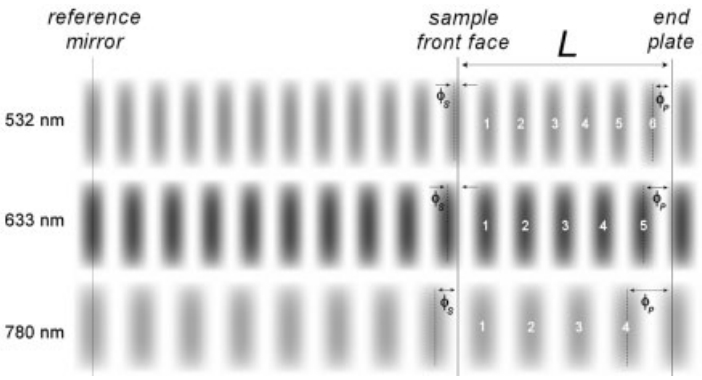

Fig. 38.3 Illustration of using different wavelengths for the determination of the sample length by interferometry.

from the sample during the measurement cycle. It is obvious that interferometers designed basically for length measurements (e. g., [1–7]) can be used for measurements of the thermal expansion. In such measurements, performed on "conventional" materials, the uncertainty of the temperature measurement and the refractive index of air at varying temperatures is a limiting factor, whereas the attainable uncertainty of the extracted length changes can be considerably lower than the uncertainty of the absolute length itself. The latter conclusion is based on the assumption that the interaction between the sample and the end plate is not dependent on the temperature.

PTB's PIF, optimized during the past few years (e. g., see [8, 9]), was designed in such a way that the interferometric length measurement can be performed in vacuum. Furthermore, special care was taken to reduce uncertainty contributions originating from the interferometer alignment [10]. Changes of the absolute length can be determined with an uncertainty in the sub-nm range. Besides the investigation of length changes induced by the sample temperature extracting the sample's CTE, length relaxations can be studied at a constant temperature using the PIF. An additional measurement capability of the PIF is the determination of the sample compressibility extracted from length measurements made under different air pressures [11].

38.2 Experimental Setup

38.2.1 Description of the Interferometer

Figure 38.4 shows the interferometer situated in a temperature-controlled chamber and installed into a vacuum-tight environmental chamber. Two measurement modes are possible: (i) measurements under air pressure where a constant and defined pressure is provided by a pressure balance (assembled and calibrated at PTB), (ii) measurements in vacuum ($<$0.1 Pa) where a turbo pumping unit is connected to the chamber.

The interferometer is equipped with three PTB-made stabilized lasers at 780 nm (Diode, Rb-stabilized), 633 nm (He–Ne, I_2-stabilized), and 532 nm (frequency doubled Nd:YAG, I_2-stabilized), where the latter is considered as the most stable (long time stability better than 10^{-12} [12]).The light provided by the three different lasers alternatively passes through a 200-μm multimode fiber that represents the entrance of the interferometer at the focal point of the collimator (600 mm focal length). The reference path of the interferometer can be varied for phase stepping by slightly tilting the compensation plate. The tilt angle is monitored by an auxiliary interferometer and is servo controlled. For measurements in air the measuring path contains a 400 mm vacuum cell close to the sample to determine the refractive index of air at the specific environmental conditions [11]. The surface temperature of the sample is measured by thermo couples near the sample's

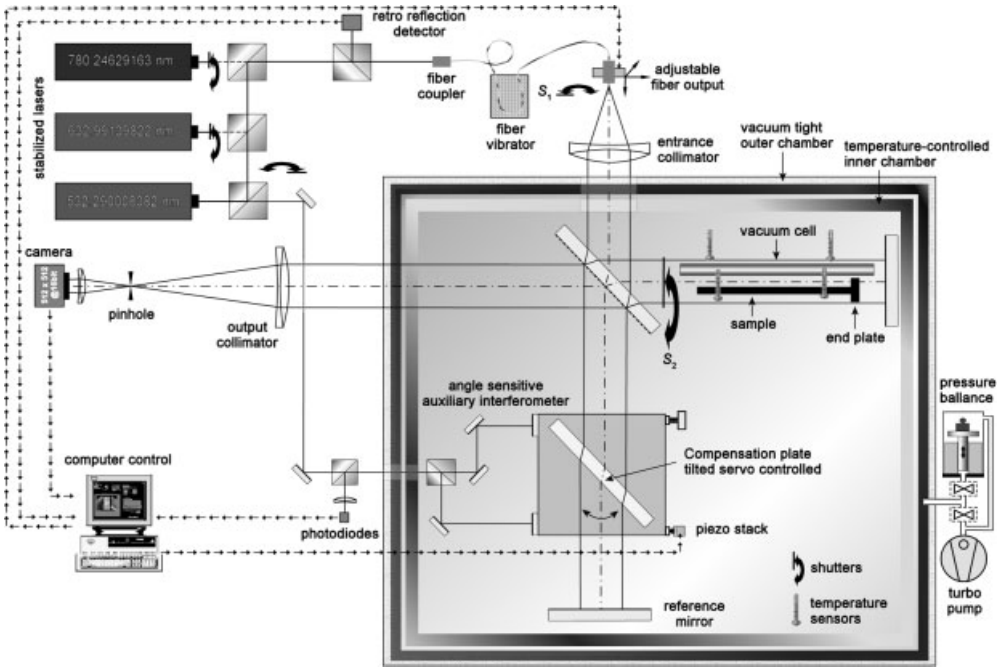

Fig. 38.4 Scheme of the precision interferometer (PIF).

front face and near the end plate. The temperature of a cupper block, used as a reference point for the thermo couples, is measured using an AC-bridge (F700, Automatic Systems Labs.) together with a PT-25 resistor. The uncertainty of the temperature measurements is below 1 mK [13] in the range from 15°C to 25°C.

Small wedges of all optical flats (windows, beam splitter, compensation plate, end plate) prevent multiple reflections that would interfere with the main beams and disturb the interference pattern. The pinhole at the interferometer output blocks the unwanted reflections and is also necessary for the adjustment of the arrangement.

The interference pattern is evaluated by phase stepping interferometry as described in [9]. Instability of the interferometer can easily be recognized by comparison of the phase topographies derived from two different data sets. A 512 × 512 pixel camera system (Photometrics CH 350) provides data frames at 16-bit per pixel.

38.2.2 Sample Design

Two different sample designs can be measured with the PIF: (i) gauge block shaped samples, (ii) cylindrical samples (Figure 38.5). Figure 38.6 shows the corresponding measured arrays of interference phase data.

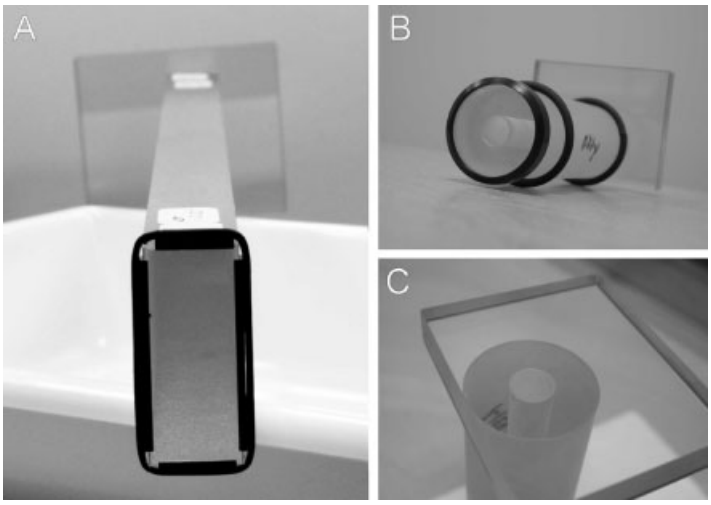

Fig. 38.5 Different sample designs that can be used. A: gauge block shaped samples, B: cylindrical samples. C shows a back view of B illustrating the tight connection between the sample and the end plate.

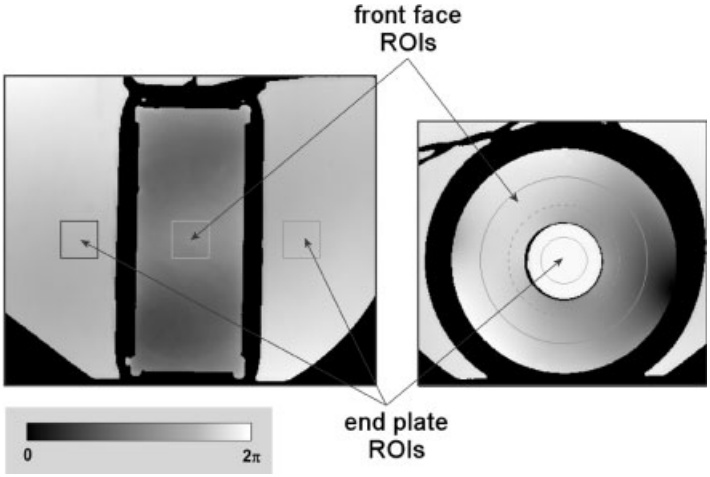

Fig. 38.6 Typical interference pattern of the two different sample designs (see Figure 38.5). These images are used to assign the interference data to a defined central position of the sample (see the text for details).

The interference array reflects the geometry of the respective sample. Accordingly these data can be used to define symmetrical regions of interest (ROIs) to be used for the length evaluation via Eqs. (38.1) and (38.2). The position of the ROIs must be defined accurately. Otherwise imperfect sample parallelism and surface texture drastically increase the measurement uncertainty. The assignment

of the ROIs is based on the center of the sample that has to be identified from the interference array. This is done by evaluating the central coordinate of the data representing a margin of the interference map. In fact, this margin is physically given by the masks surrounding the sample (see Figure 38.5) and is accentuated in Figure 38.6 by white pixels (left) and black pixels (right). The uncertainty of the central position evaluated in both directions is about 0.05 pixels only. The ROIs are generated according to the central position in two different ways: (i) three rectangular regions as in Figure 38.6 (left), where the left and right ROIs are located at the end plate and the central ROI is placed at the front face of the sample, and (ii) a ring-shaped ROI at the cylinder front face and a circular ROI at the end plate (Figure 38.6, right). The interference data averaged within the ROIs result in the values ϕ_P (average phase at the end plate) and ϕ_S (average phase at the sample face) and are further used for length evaluation (see above). Here the noninteger pixel position of the center is taken into account as described in [11].

13.2.3 Autocollimation Adjustment

Autocollimation misalignment can be regarded as one of the major uncertainty contributions in interferometric length measurement via the well-known "cosine error." Figure 38.7 illustrates the course of light beams when the fiber end is displaced by an amount of d from the optical axis corresponding to a misalignment angle of $a \approx d/f_{\text{collimator}}$, where $f_{\text{collimator}}$ is the focal length of PIF's collimator, 600 mm (see above). Thus, a displacement of 60 μm (typical for a visual alignment) would result in $a \approx 10^{-4}$ rad and the cosine error ($1 - \cos a \approx a^2/2$) would amount to 5×10^{-9}. Consequently, a 200 mm sample would be measured 1 nm to short.

In order to break this limit, autocollimation at the PIF is done more precisely by a scanning method described in detail in [8]. In short, the signal of the retro reflex of the interferometer reentering the fiber is observed as a function of the xy-position of the fiber itself. The return signal is extracted via a beam splitter close to the

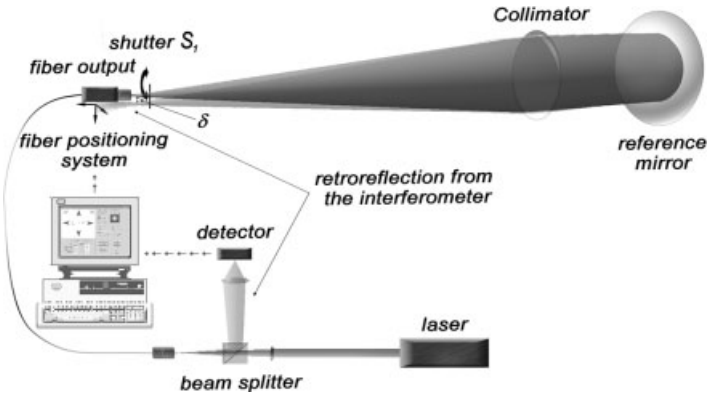

Fig. 38.7 Autocollimation setup used at the precision interferometer.

entrance of the fiber (see Figure 38.7). A computer-controlled translation stage is used to move the fiber in a plane perpendicular to the optical axis where the axial position (z) has to be set manually before. A PC program reads the signal data of the retro reflection at a certain xy-position.

After the scanning, the central xy-position is calculated and the fiber output is set to it. A second scan can be performed as a check. Accordingly, deviations of the central position found from scan to scan are well below 3 μm.

13.3 Check Measurements

Some check measurements are shown in the following in order to illustrate the performance of the PIF.

Usually the measurements are performed in fluffed out mode where no fringes appear because the wave fronts of the reference beam and the beam reflected from the sample face (and from the end plate) have exactly the same direction. Because of the initially performed autocollimation adjustment the sample and platen surface can be assumed to be perpendicular to the optical axis so that there is no cosine error (despite the constant influence originating from the aperture size [14] which is not relevant when length changes, as discussed here, are the focus of interest).

A subsequent tilt of the interferometer reference mirror causing fringes in the interference pattern should not influence the measured length (as can easily be shown). Various measurements using the green laser were performed at different tilt angles of the reference mirror. The results shown in Figure 38.8 clearly de-

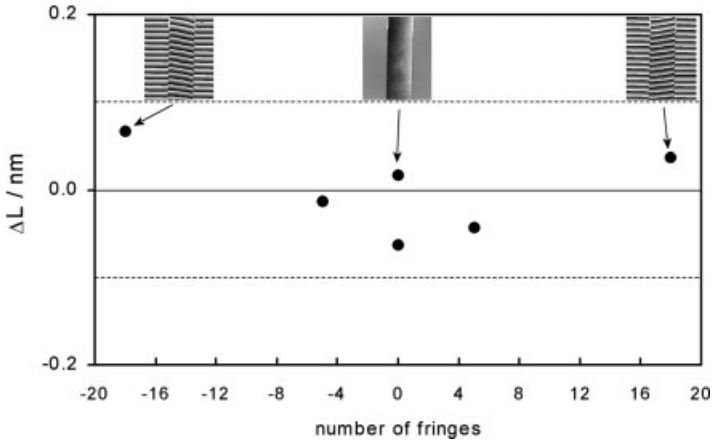

Fig. 38.8 Length evaluation at different vertical tilts of the interferometer reference mirror (given in units of the number of fringes covering the sample). The sample face is perpendicular to the optical axis as defined by autocollimation. The insets illustrate the mode of interference pattern. The absolute sample length is about 200 mm.

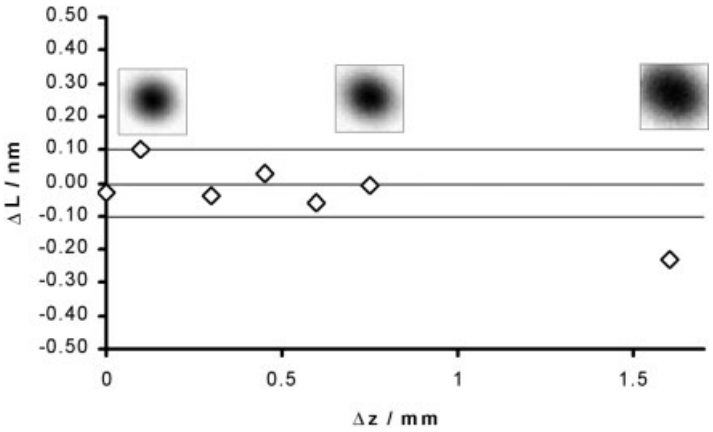

Fig. 38.9 Length evaluation at different axial (*z*-) positions of the fiber. Autocollimation was performed after *z* was set. The insets show the corresponding retroreflex scans as density graphics. The optimum *z*-position was assigned to zero. The same ≈200 mm sample was used as in Figure 38.8.

monstrate that a tilt of the reference mirror does not influence the measured length within 0.1 nm. This gives rise to the assumption that the interferometer is free from nonlinearities. This is supported by investigations of phase arrays measured with different tilts of the reference mirror (data not shown) and also by earlier investigations performed in the framework of camera nonlinearity [9].

In order to investigate the quality of the described autocollimation adjustment procedure, another kind of check measurement was performed. The fiber was displaced from an optimum *z*-position by a certain amount before the autocollimation adjustment procedure was applied. Figure 38.9 shows the results of several measurements using the green laser wavelength.

The deviations of the data from an average shown in Figure 38.9 are not larger than 0.1 nm as long as the misalignment of *z* does not exceed large values (>1 mm) which can easily be detected. Therefore adjustment with respect to the *z*-position of the fiber end is not critical.

38.4 Measurement Examples

Whereas the check measurements shown above were all performed under most stable conditions combined with a relatively short time interval, the uncertainty of measurements performed with the precision interferometer of course can be expected to be higher especially at varying temperatures. It is difficult to speculate about uncertainties in the sub-nm range where smallest (also unknown) disturbances can affect the measurement results. The measurement examples shown in the following may demonstrate the obtainable accuracy.

38.4.1
Thermal Expansion and Uncertainty

Figure 38.10 shows a typical thermal expansion measurement: The length of a 200 mm sample made from a low expansion material was investigated as a function of the sample temperature. An arbitrary reference length is subtracted so that a length change (compared to a reference length at approx. 20°C) is displayed.

The data points are shown as uncertainty bars. Additionally, two different fit functions are displayed: the gray line shows a third polynomial and the dotted line a fourth polynomial. The latter is almost identical to the third polynomial. This result may justify the assumption that a third polynomial function can be utilized for the subsequent calculation of the CTE. However, in general it is difficult to consider the influence of the unknown fit function.

Figure 38.11 shows the coefficient of thermal expansion (CTE) as a function of the sample temperature calculated from the two different polynomials of Figure 38.10 (gray line from the third polynomial and the dotted line from the fourth polynomial).

The upper curve shows that the difference between them is typically lower than 10^{-10} K^{-1} for the main temperature interval 8–42°C.

Assuming that the temperature-dependent length change may be described by a third polynomial, the uncertainty of the CTE can be calculated from the measured data assuming individual uncertainties for the length changes and for the temperature as described in detail in [11]. In short, the fit function can be expressed as a function of arbitrary data points $\{t_i, l_i\}$ so that partial derivations can be calculated before the actual measured data are inserted. Assuming that the

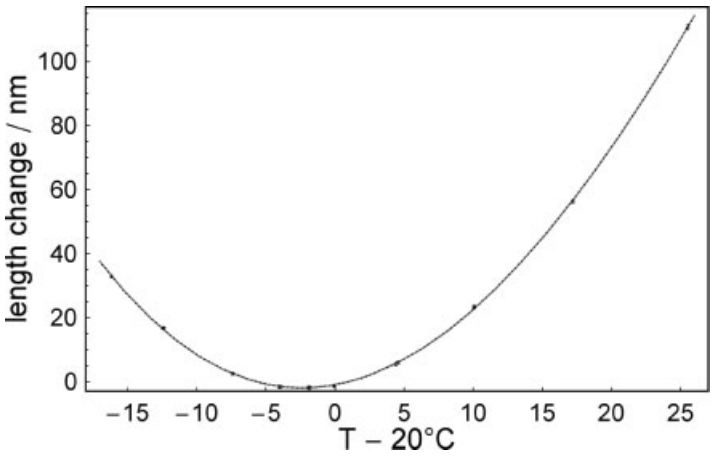

Fig. 38.10 Length change of a 200 mm sample of low expansion material as a function of the sample temperature. The data (uncertainty bars) were obtained from lengths measurements at different temperatures subtracting a reference length at 20°C. Two different fit functions are displayed (see the text for details).

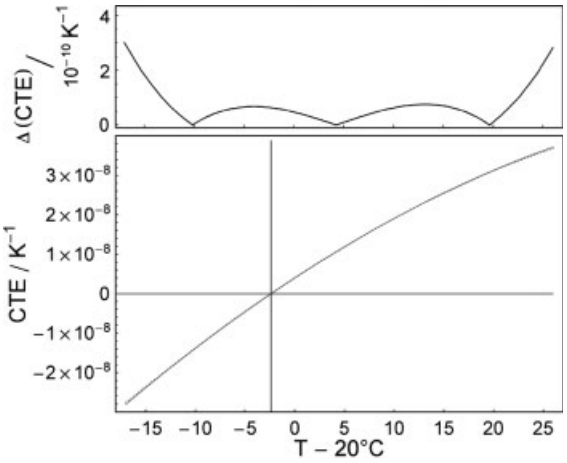

Fig. 38.11 CTE as a function of the sample temperature calculated from the two different polynomials of Figure 38.10 (see the text for details). The upper curve shows the difference between them.

data points are uncorrelated, the uncertainty of the coefficients appearing in the fit function can be calculated in this way and finally the uncertainty of the fit function is obtained. Figure 38.12 shows the result of this calculation as a filled plot. Here an uncertainty of 0.4 nm for the length changes was set as an estimate. This amount is dominated by contributions due to unsystematic changes of the interferometer optics observed at varying temperatures (data not shown).

The asymmetry of the uncertainty function originates from the fact that fewer data points exist at higher temperatures. However, the uncertainty in Figure 38.12 is in the range of $\pm 10^{-10}$ K^{-1} within the dominating temperature interval.

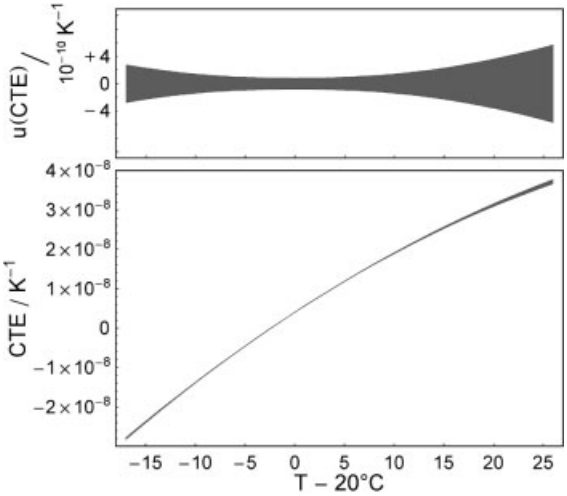

Fig. 38.12 CTE as a function of the sample temperature calculated from the third polynomial of Figure 38.10 within the limits of uncertainty (see the text for details). The upper curve shows the evaluated uncertainty at a magnified scale.

38.4.2
CTE Homogeneity

Besides length evaluation, the interference array covering the whole sample (as shown in Figure 38.6) can be used in order to investigate the topography of the sample front face related to the end plate. Figure 38.13 illustrates how this topography can be extracted from the original measured interference array. A plane that fits the end plate ROIs is subtracted (B) and the topography is obtained from $\frac{1}{2\pi}\phi_S \times \frac{1}{2}\lambda$ (C).

This topography can be investigated at different sample temperatures. Figure 38.14 shows measurement at a sample for which an orientation change of the front face with respect to the end plate was observed.

Besides possible surface effects on an orientation change, Figure 38.14 most likely indicates CTE inhomogeneity.

It might be remarked that such an effect was not found in Zerodur samples. Consequently, Zerodur material seems to be very homogenous with respect to its CTE.

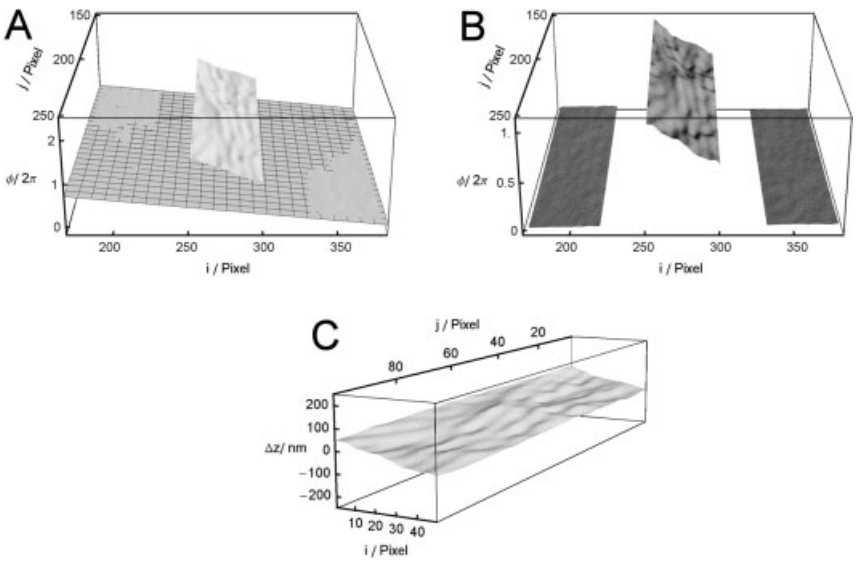

Fig. 38.13 A: Original measured interference array where the end plate ROIs are fitted by a plane, B: data of A where the plane is subtracted, C: front face topography obtained from B (see the text for details).

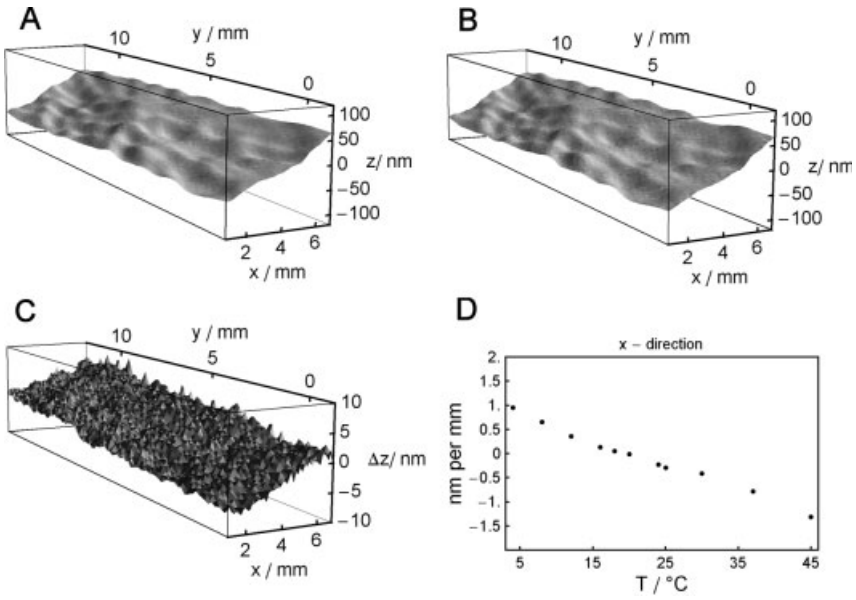

Fig. 38.14 A: front face topography at 20°C, B: front face topography at 45°C, C: difference between A and B revealing an orientation change of the front face with respect to the end plate caused by the different sample temperature, D: the slope change according to C in the *x*-direction as a function of the temperature.

38.4.3
Temporal Length Changes

A property of low expansion material concerns long-term stability. Figure 38.15 shows a measurement cycle in which the temperature was kept constant nearly 40 days before a temperature step from 20°C to 30°C was performed.

The observed shrinking of about 5 nm in 40 days is much more than that found in other samples made from the same base material and can be addressed most likely to too high temperatures during the sample preparation process. Besides the long-term shrinking another sample property is evident in Figure 38.15: The length change due to the temperature change is delayed on a time scale of several days. This can be seen more clearly in Figure 38.16 where the long-term shrinking was subtracted.

The detailed characteristic of the delayed length changes is not yet clarified. Deviations of the data points from an arbitrary smooth fit are well within 0.1 nm. This supports, together with the above check measurements, the assumption that the measurement uncertainty at constant temperature is lower than 0.1 nm.

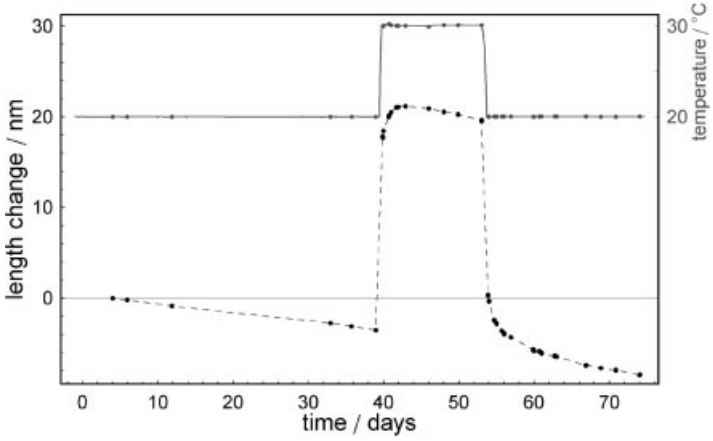

Fig. 38.15 Measurements at a 100 mm sample made of low expansion material. The temperature was kept constant nearly 40 day before a temperature step from 20°C to 30°C was performed and finally the original temperature was set.

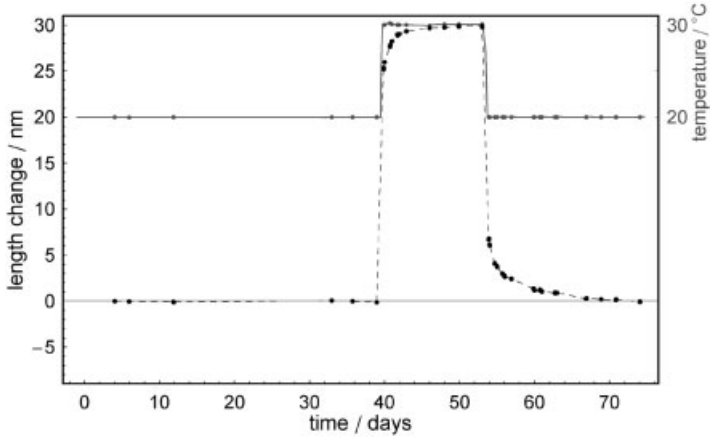

Fig. 38.16 Data of Figure 38.15 compensated for the effect of long-term stability.

38.5 Concluding Remark

The improved precision interferometer described and investigated in this chapter seems to have the potential for reliable measurements in the sub-nm range. This was demonstrated by check measurements, where the influence of the interferometer adjustment was investigated carefully. Although the measurement examples at varying temperature reveal a slightly increased uncertainty compared to the <0.1 nm spread found at a constant temperature, the instrument described seems to be a very good tool for most precise characterization of thermal expansion properties of low expansion material.

References

1 D. J. Pugh and K. Jackson, Automatic gauge block measurement using multiple wavelength interferometry, Proc. SPIE **656**, 244–259 (1986).

2 A. Lewis, Measurement of length, surface form and thermal expansion coefficient of length bars up to 1.5 m using multiple wavelength phase-stepping interferometry, Meas. Sci. Technol. **5**, 694–703 (1994).

3 I. Malinovsky, A. Titov, and C. A. Massone, Fringe-image processing gauge block comparator of high precision, Proc. SPIE **3477**, 92–100 (1998).

4 L. A. Salbut and M. Kujawinska, Modification of the Köster interferometer for automatization of gauge block measurements, Proc. SPIE **3477**, 116–126 (1998).

5 G. Bönsch, Automatic gauge block measurements by phase stepping interferometry with three laser wavelengths, Proc. SPIE **4410**, 1–10 (2001).

6 J. E. Decker, R. Schödel, and G. Bönsch, Next-generation Kösters interferometer, Proc. SPIE **5190**, 14–23 (2003).

7 J. E. Decker, K. Siemsen, R. Siemsen, A. Madej, L. Marmet, J. Miles, S. de Bonth, K. Bustraan, S. Temple, and J. R. Pekelsky, Increasing the range of unambiguity in step height measurement using multiple-wavelength interferometry – application to absolute long gauge block measurement, Appl. Opt. **42**, 5670–5678 (2003).

8 R. Schödel, A. Nicolaus, and G. Bönsch, Minimizing interferometer misalignment errors for measurement of sub-nanometer length changes, Proc. SPIE **5190**, 34–42 (2003).

9 R. Schödel, A. Nicolaus, and G. Bönsch, Phase stepping interferometry: methods for reducing errors caused by camera nonlinearities, Appl. Opt. **41**, 55–63 (2002).

10 R. Schödel and G. Bönsch, Highest accuracy interferometer alignment by retroreflection scanning, Appl. Opt. **43**, 5738–5743 (2004).

11 R. Schödel and G. Bönsch, Precise interferometric measurements at single crystal silicon yielding thermal expansion coefficients from 12°C to 28°C and compressibility, Proc. SPIE **4410**, 54–62 (2001).

12 P. Cordiale, G. Galzerano, and H. Schnatz, International comparison of two iodine-stabilized frequency-doubled Nd:YAG lasers at 532 nm, Metrologia **37**, 177–182 (2000).

13 G. Bönsch, H.-J. Schuster, and R. Schödel, High-precision temperature measurements with thermo couples, Technisches Messen **68**, 550–557 (2001).

14 C. F. Bruce, The effects of collimation and oblique incidence in length interferometers, Aust. J. Phys. **8**, 224–240 (1955).

Index

Nanoscale Calibration Standards and Methods: Dimensional and Related Measurements in the Micro- and Nanometer Range.
Edited by Gunter Wilkening, Ludger Koenders
ISBN: 3-527-40502-X